CRANFIELD UNIVERSITY

MOHAMMAD FAHMI BIN ABDUL GHAFIR

PERFORMANCE BASED CREEP LIFE ESTIMATION FOR GAS TURBINES APPLICATION

SCHOOL OF ENGINEERING
GAS TURBINE ENGINEERING

PhD
Academic Year: 2010 - 2011

Supervisor: YIGUANG LI
12/2011

CRANFIELD UNIVERSITY

SCHOOL OF ENGINEERING
GAS TURBINE ENGINEERING

PhD

Academic Year 2010 - 2011

MOHAMMAD FAHMI BIN ABDUL GHAFIR

PERFORMANCE BASED CREEP LIFE ESTIMATION FOR GAS TURBINES APPLICATION

Supervisor: YIGUANG LI

12/2011

This thesis is submitted in partial fulfilment of the requirements for the degree of Doctor of Philosophy

ABSTRACT

Accurate and reliable component life prediction is crucial to ensure both the safety and economics of gas turbine operations. In the pursuit of improved accuracy and reliability, current model-based creep life estimation methods have become more and more complicated and therefore demand huge amounts of work and significant amounts of computational time.

Because of the underlying problems arising from current life estimation methods, this research aims to develop an alternative performance-based creep life estimation method that is able to provide a quick solution to creep life prediction while at the same time maintaining the achieved accuracy and reliability as that of the model-based method. Using an artificial neural network, the existing creep life prediction sub-processes and secondary inputs are 'absorbed' into simple parallel computing units that are able to create direct mapping between various gas turbine operating and health conditions or gas path sensors and creep life. The outcome of this research is the creation of three proposed neural-based creep life prediction architectures known as the Range-Based, Functional-Based and Sensor-Based.

An integrated creep life estimation model was first developed and incorporated into an in-house performance simulation and diagnostics software. Using the integrated model, the effects of several operating and health parameters on a selected turbo-shaft engine model turbine blade's creep life was initially performed using an introduced Creep Factor approach. The outcomes of this investigation were then used to populate input-output samples to train and validate the neural-based creep life prediction architectures. To ensure that the proposed neural architectures are able to achieve generalisation and produce accurate creep life prediction for both clean and degraded engine conditions, four-stage assessments were carried out. Finally, the effects of input uncertainties on the creep life prediction were investigated to assess how sensitive the proposed architectures are to different levels of uncertainty.

The results show that all of the proposed neural architectures were able to produce accurate creep life predictions for both clean and degraded engine conditions. When comparing the three proposed architectures, the Sensor-Based architecture was found to be the most accurate in both conditions. Despite the accurate creep life prediction, it was also found that all of the proposed architectures were sensitive to input uncertainties with the Functional-Based architecture being the least sensitive to the uncertainty.

ACKNOWLEDGEMENTS

It is a pleasure to thank the many people who made this thesis possible.

Alhamdulillah and ‘syukur’ to Allah swt for His guidance and blessings upon me and my family.

I would like to express my sincere gratitude to my supervisor Dr Yiguang Li, Department of Power and Propulsion, School of Engineering for his guidance, advice, and continuous support throughout this work.

I owe my loving thanks to my wife Puteri Nur Sofwati, my daughters Puteri Nurin Balqis and Puteri Ayra Qistina. Without their prayers, encouragement, understanding and patience, it would have been impossible for me to finish this work. My special thanks also go to Mama, Adik, Tok Aim and Nekmok, Makcu and her family, Mak Ngah and her family, and also my wife’s family for their prayers and loving support.

Special thanks go to my dear friends and their families for all the wonderful times we had.

Finally I would like to thank the Ministry of Higher Education of Malaysia and Universiti Tun Hussein Onn Malaysia (UTHM) for sponsoring me and my family. Their financial support is gratefully acknowledged.

PUBLICATIONS

Y.G.Li, M.F.Abdul Ghafir, L.Wang, R.Singh, K.Huang and X.Feng, “Nonlinear Multiple Points Gas Turbine Off-Design Performance Adaptation Using a Genetic Algorithm.”, J. Eng. Gas Turbine Power, Vol. 133, Issue 7, July 2011.

M.F.Abdul Ghafir, Y.G.Li, L.Wang, R.Singh, K.Huang and X.Feng, “Impact of Operating and Health Conditions on Aero Gas Turbine Hot Section Creep Life Using a Creep Factor Approach”, ASME GT2010-22332, Proceeding of ASME Turbo Expo 2010, Glasgow, UK, June 2010

M.F.Abdul Ghafir, Y.G.Li, R.Singh, K. Huang and W.Zhang, “Comparative Study Between the Non-Linear Performance Adaptation and the Improved Least Square Non-Linear Adaptation Method”, Proceeding of the 24th International Congress on Condition Monitoring and Diagnostics Engineering Management, Norway, June 2011

M.F.Abdul Ghafir and Y.G.Li, “Impact of Operating and Health Condition on a Helicopter Turbo-Shaft Hot Section Component Using Creep Factor”, TSM 2011, Imperial College, London, July 2011

M.F.Abdul Ghafir, Y.G.Li, L.Wang, and W.Zhang, “Impact Analysis on Aero-Engine Performance Parameter Variation on Hot Section’s Creep Life Using Creep Factor Approach”, ISABE-2011-1609, International Symposium on Air Breathing Engines, Sweden, September 2011.

S.Eshati, M.F.Abdul Ghafir, P.Laskaridis, and Y.G.Li, “Impact of Operating Condition and Design Parameters on Gas Turbine Hot Section”, GT2010-22334, Proceeding of ASME Turbo Expo 2010, Glasgow, UK, June 2010

Y.G.Li, M.F.Abdul Ghafir, L.Wang, R.Singh, K.Huang and X.Feng, “Nonlinear Multiple Points Gas Turbine Off-Design Performance Adaptation Using a Genetic Algorithm.”, GT 2010-22285, Proceeding of ASME Turbo Expo 2010, Glasgow, UK, June 2010

Y.G.Li, M.F.Abdul Ghafir, L.Wang, R.Singh, K.Huang and W.Zhang, “Non-Linear Multiple-Point Adaptive Simulation Approach Using Aero-Engine Test Bed Data, ISABE-2011-1801, International Symposium on Air Breathing Engines, Sweden, September 2011.

TABLE OF CONTENTS

LIST OF FIGURES

LIST OF TABLES

LIST OF SYMBOLS

$\%T_{drop}$	Temperature drop percentage of each turbine stage
$\Delta V_{TanAvSec}$	Average tangential velocity difference
ΔV_{axial}	Axial velocity difference
Δw	Weight adjustment of connecting neuron
A	Cross sectional area where the gas travels
A_{AnSec}	Blade section annulus area
A_{CDM}	Constant used in Esposito and Bonora model
A_{CSSp}	Cross sectional area of a specified location along the blade span
A_{In}	Blade inlet annulus area
A_{OSD}	Orr-Sherby-Dorn constant
A_{Out}	Blade outlet annulus area
A_{wall}	Blade wall area
B_{MSP}	Manson-Succop constant
BIP	Burner inlet pressure
BMP_{Sp}	Bending moment about the specified location along the blade span
BMV_{AxSp}	Axial momentum bending moment at specified location along the blade span
BMV_{TanSp}	Tangential momentum bending moment at specified location along the blade span
C	Material constant
C_{CDM}	Constant used in CDM general constitutive equation
C_{LMP}	Larson-Miller parameter constant
CF	Creep Factor
CF_M	Mission Creep Factor
CF_{Sec}	Centrifugal force acting at the blade section

CF_{Sp}	Centrifugal force acting at the specified location along the blade span
CN	Relative non-dimensional rotational speed
CP_{hot}	Specific heat for hot gas
CP_{cold}	Specific heat for cold gas
D_{LDA}	Damage parameter used in Linear Damage Accumulation theory
DH	Enthalpy drop ratio
E	Prediction error percentage
$E(x)$	Expected value
E_{AVE}	Average errors for individual measurement for all operating points / average prediction error percentage
$E_{AVETOTAL}$	Total average errors for all measurements
E_{Abs}	Absolute prediction error percentage
E_{AbsAve}	Average absolute prediction error percentage
E_{max}	Maximum value of the prediction error
E_{min}	Minimum value of the prediction error
ETA	Isentropic efficiency
$F(x)$	Cumulative density function
$F_n(x)$	Empirical cumulative density function
FC	Flow capacity
G	Number of targeted parameters specified for DP performance adaptation
GSP	Goldhoff-Sherby parameter
$\boldsymbol{H}$	Hessian matrix
H	Hardening parameter
H_{Sec}	Blade section convective heat transfer coefficient
I	Identity matrix
I_{maxSp}	Maximum second moment of area at a specified location along the blade span
I_{minSp}	Minimum second moment of area at a specified location along the blade span
$J(\boldsymbol{w})$	Jacobian matrix
$L_{C\,M}$	Mission / operation blade nominal creep life
L_{CMin}	Minimum creep life
$L_{C\,Overall}$	Overall blade nominal creep life
L_C	Predicted blade creep life
L_{DP}	Design point relative non-dimensional rotational speed for compressor and turbine / design point burner inlet pressure
L_{OD}	Off design point relative non-dimensional rotational speed for compressor and turbine / off design point burner inlet pressure
LF	Life fraction
LF_M	Mission / operation life fraction
$LF_{Overall}$	Overall life fraction
LL	Lower limit
LMP	Larson-Miller parameter
$LU\%$	Life usage percentage
M	Mach number
M_{XXSp}	Resulting bending moment about the X-X direction at a specified location along the blade span
M_{YYSp}	Resulting bending moment about the Y-Y direction at a specified location along the blade span
MHP	Manson-Haferd parameter

MRM	Mandelson-Roberts-Manson parameter
MSP	Manson-Succop parameter
N	Number of sample generated / number of training pattern presented / rotational speed
N_s	Number of samples in each training, validation and test samples
$NGV_{mass\ frac}$	Mass fraction of coolant flow that enters the NGV
$Nu_g^*{}_{Sec}$	Nominal Nusselt number
Nu_{Sec}	Blade section Nusselt number
OF	Objective function
OH	Operating hour
OH_{Tot}	Total operating hour
OSD	Orr-Sherby-Dorn parameter
$P_{(actual)}$	Actual or target measurement obtained from real engine tests
$P_{(predict)}$	Predicted measurement obtained using the initial or adapted component characteristic maps
P_o	Gas stagnation pressure
P_{oNGV}	Turbine inlet stagnation pressure
P_{oOut}	Turbine outlet stagnation pressure
$P_{oOutStage}$	Outlet static pressure for each turbine stage
PF_{Sec}	Pressure force acting on the blade section
PCN	Relative compressor rotational speed
Pr	Prandtl number
Q	Representation of term $m\sqrt{T_o}/(AP_o)$
Qc	Material's activation energy
R	Ideal gas constant / Operation or health parameter using in neural network training / Regression coefficient / response
R_o	Universal gas constant
R_k	Ratio between the blade section wall temperature and the section gas temperature
R_v	Triaxial coefficient
RMS	Root mean squared
$RTDF$	Radial temperature distribution factor
Re	Reynolds number
Re_{Sec}	Blade section average Reynolds number
$Rotor_{massfrac}$	Blade mass fraction
$\bar{S}$	Marquardt sensitivity
$\overline{\boldsymbol{S}}$	Marquardt sensitivity vector in matrix formation
SD_E	Standard deviation of the prediction error
SF	Scaling factor
SF_{ac}	Safety factor
$Suth$	Sutherland constant
T	Neural network targeted output
Th_{TBC}	TBC coating thickness
T_{Blade}	Blade metal temperature
T_{CiSec}	Blade section inlet coolant temperature
T_{CoSec}	Blade section outlet coolant temperature
$T_{CoolantExit}$	Coolant exit temperature
$T_{CoolantIn}$	Coolant inlet temperature
$T_{cr(given)}$	Given critical blade metal temperature

$T_{cr(predict)}$	Predicted critical blade metal temperature
T_g	Gas temperature
$T_{G25\%}$	Blade inlet gas temperature at 25% distance of the blade root
$T_{G75\%}$	Blade inlet gas temperature at 75% distance of the blade root
T_{GMid}	Blade inlet gas temperature at the blade mid
T_{GRoot}	Blade inlet gas temperature at the blade root
T_{GSec}	Blade section inlet average gas temperature
T_{Gtip}	Blade inlet gas temperature at the blade tip
T_M	Blade / material metal temperature
T_{MA}	Manson-Haferd temperature constant
T_{MSec}	Blade section metal temperature
T_{Mixing}	NGV exit temperature
T_{NGV}	NGV bulk metal temperature
T_{OIN}	Blade inlet gas temperature
T_{io}	Reference temperature used in Sutherland equation
T_{max}	Maximum / peak temperature
T_{mean}	Gas mean temperature
T_o	Gas stagnation temperature
T_{oNGV}	Turbine inlet stagnation temperature
$T_{oOutStage}$	Outlet static temperature for each turbine stage
T_{ref}	Combustor temperature rise
$T_{wallSec}$	TBC outer wall temperature
U	Blade speed
UL	Upper limit
UTS	Ultimate tensile strength
V	Gas velocity
V_{Abs}	Gas absolute velocity
V_{Ax}	Gas axial velocity
VF_{AxSec}	Momentum force at axial direction
VF_{TanSec}	Momentum force at tangential direction
V_{Tan}	Gas tangential velocity
WAC	Corrected mass flow rate
W_{Tan}	Gas relative tangential velocity
X	X distance between the corresponding chord-wise location to the blade's root or mid CG
X_{Sec}	Exponent parameter for Nusselt number calculation
Y	Neural network simulated output
$Y_{(l)}$	Y distance between the corresponding chord-wise location to the blade's root or mid CG
Y_{Sec}	Exponent parameter for Nusselt number calculation
a	Slope parameter of Log-Sigmoid activation function
b, c	Scaling factor function coefficients
$\boldsymbol{b}$	Vector of b used in quadratic function
b	External bias for neuron / RES coefficient
c	Blade chord / scalar used in quadratic function
c_{sec}	Blade section average chord
$d_{(n)}$	Targeted outputs at learning iteration n
d_{Sp}	Distance between the section CG to the respective specified location along the blade span

$e_{(n)}$	Error signal at learning iteration n
$f(x)$	Probability density function
$\boldsymbol{g}$	Gradient matrix of a function
k	Number of OD points included in the adaptation process
k_{GSec}	Thermal conductivity for gas temperature
k_{MG}	Monkman--Grant constant
k_{TBC}	TBC thermal conductivity
m	Number of measurements
m_{Area}	Mass flow per unit area
m_{MG}	Monkman-Grant constant
$m_{NGV}{}^{*}$	NGV non-dimensional coolant mass flow
m_{Sec}	Mass of a specified blade section or shroud
$m_{coolant}$	Mass flow of the coolant
m_{gas}	Mass flow of the gas
n	Number of operating points used / number of learning iteration / number of synaptic weights available in the network / stress component
n_{obs}	Observed sample
n_{total}	Total sample
p	Gas static pressure
p_c	Effective accumulated equivalent creep strain
r	Average effective particle radius at $t = t$
r_o	Average effective particle radius at $t = 0$
r_{CG}	Radius between the rotation axis and the blade section or the shroud centre of gravity
s_{Sec}	Blade section average perimeter
ss	Sample step size
t	Gas static temperature / time
t_A	Manson-Haferd time constant
t_f	Time to failure
t_{fi}	Time to failure under condition i
t_i	Time spent under condition i
t_{rem}	Component remaining life
t_{spent}	Time already spent in service
u	Adder output
u_{CDM}	Constant used in MacLachlan model
v	Activation potential
v_{CDM}	Constant used in CDM general equation.
w	Synaptic weight
$\boldsymbol{w}$	Synaptic weight vector in matrix formation
w_{old}	Synaptic weight of previous iteration
w_{update}	Updated synaptic weight
x	Input signal / independent variable
$\boldsymbol{x}$	Parameter vector
y	Output signal produce by neuron
$y_{(n)}$	Output predicted by the output neuron at learning iteration n
z	Targeted parameter or output / measurement taken from the test rig
z_{norm}	Normalised targeted output
z_{ref}	Reference outputs predicted from the neural architectures using the 'true' inputs' value.

$\hat{z}$	Simulated parameter or output / measurement simulated using the to-be-adapted map at the same operating point
$\hat{z}_{norm}$	Normalised predicted output
$\hat{z}_{Uncertain}$	Predicted outputs obtained from uncertain input
$\mathcal{E}$	Error function with respect to a weight vector
α_{CDM}	Damage exponent
α_2	Blade outlet angle
α_o	NGV outlet angle
β	Conjugate gradient scaling factor
β_k	Statistical fitting constant
Δc	Comparison parameter
γ'	Metal gamma prime phase
γ_{hot}	Specific heat ratio of hot gas
ε_o	Instantaneous plastic strain
ε_C	Creep strain
ε_{Ct}	Creep strain at a given time
ε_f	Failure strain at which failure occurs
ε_{th}	Damage threshold strain at which creep damage initiates
$\dot{\varepsilon}_o$	Imaginary initial plastic strain rate
$\dot{\varepsilon}_C$	Creep strain rate
$\dot{\varepsilon}_{CS}$	Secondary creep strain rate
ε_{NGV}	NGV cooling effectiveness
ε_R	Blade cooling effectiveness
λ	Scaling parameter
$\check{\lambda}$	Increased scaling parameter
ϑ	Multiplication or division factor of Levenberg-Marquardt parameter
η	Learning rate parameter
η_P	Polytropic efficiency
η_{conv}	Convection efficiency
η_t	Turbine isentropic efficiency
θ	Theta projection model parameter
θ_{Sp}	Blade stager angle at a specified location along the blade span
μ	Gas viscosity / mean value
μ_o	Reference viscosity used in Sutherland equation
ρ_d	Dislocation density
ρ_g	Gas density
σ	Standard deviation / applied stress
σ_{eff}	Effective stress
$\sigma_{(l)Sp}$	Resulting bending moment stress at a specified chord-wise location.
σ_{CFSp}	Centrifugal stresses at the specified location along the blade span
$\sigma_{Tot(l)Sp}$	Total stress at a specified chord-wise location.
σ_{max}	Maximum stress
ω	Angular velocity
ω_{CDM}	Damage state variable in continuum damage mechanics
ω_{CR}	Critical damage
$\dot{\omega}_{CDM}$	Damage rate
$\varphi(.)$	Activation function
ζ	Denominator of Equation (5-56)
$\check{\zeta}$	Raised ζ

Ω	Omega method parameter

ABBREVIATIONS

0D	Zero dimension
1D	One dimension
2D	Two dimension
3D	Three dimension
ANN	Artificial neural network
CAD	Computer aided design
CAS	Calibrated air speed
CDF	Cumulative density function
CDM	Continuum damage mechanics
CFD	Computational fluid dynamics
CG	Centre of gravity / Conjugate-Gradient
DP	Design point
DT	Destructive test
EI	Erosion index
EPRI	Electrical Power Research Institute
FB	Functional Based
FE	Finite element
FI	Fouling index
GA	Genetic algorithm
HCF	High cycle fatigue
HL	High level
HP	High pressure
ISA	International Standard Atmosphere
LCF	Low cycle fatigue
LDA	Linear damage accumulation
LE	Leading edge
LL	Low level
LM	Levenberg-Marquardt
MFBP	Multilayer feedforward back propagation
ML	Medium level
MSE	Mean squared error
NDT	Non-destructive test
OD	Off-design
OEM	Original equipment manufacturer
PDF	Probability density function
PEC	Primary energy consumption
RB	Range Based
RSE	Response Surface Equation
RSM	Response Surface Method
SB	Sensor Based
SCG	Scaled-Conjugate-Gradient
SEM	Scanning electron microscope
TAS	True air speed
TBC	Thermal barrier coating

TE	Trailing edge
TET	Turbine entry temperature
TMF	Thermal-mechanical fatigue

1 INTRODUCTION

Since the first jet engine was put into service, the gas turbine has progressed considerably. In today's world, the gas turbine has become one of the most popular choices of power plant especially for power generation, aviation and in the oil and gas industries. Having the benefit of being designed in a modular and flexible fashion, the utilisation of gas turbines can vary from the small scale 200 kilowatt unit that powers schools and shopping malls to the large scale 200 megawatt unit that powers an entire city [1]; from land based, marine based to air based application; and from civil to military purposes.

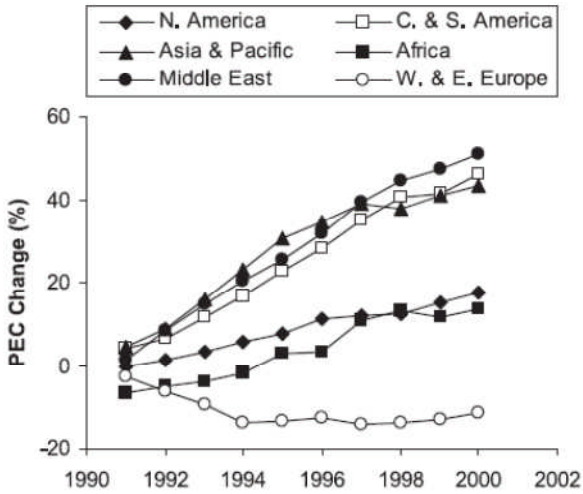

Figure 1-1: World primary energy consumption (PEC) trend by region (reference year 1990) [2]

The overall market for gas turbines has witnessed steady growth in recent decades as the primary energy consumption has rapidly increased, especially in the Asia & Pacific, Middle East, and Central & South American regions, as shown in Figure 1-1. Bhargava [2] suggested that one of the possible reasons for the observed trends is the overall increase in world energy demand. Wood [3] explained that the rise in demand is mainly caused by the economic development across the globe. Langston [4] wrote that in 1999, the value of gas turbine production was estimated to reach $34 billion worldwide, 21% more than the value estimated for 1998. In addition, it was estimated that from 2002 to 2011, the global production of all types of gas turbine engine may reach a staggering value of $414.5 billion (in 2002 US dollars) [5].

Besides the steady growth of the gas turbine market, the technological aspects of the gas turbine have also improved considerably. There are several contributing factors that have made these improvements possible. Advancement in materials such as the

introduction of high performance super alloys, improved manufacturing techniques, and superior thermal resistance coating mechanisms have paved the way for lightweight, super strength and high-temperature resistance materials to be extensively used as engine components. As a result, this reduces the component weight, increases the thrust to weight ratio and specific thrust. Figure 1-2 depicts the improvement of the thrust to weight ratio from 1940 to 2003. From the figure, it can be seen that up to 2003, thrust to weight ratio has increased approximately sevenfold.

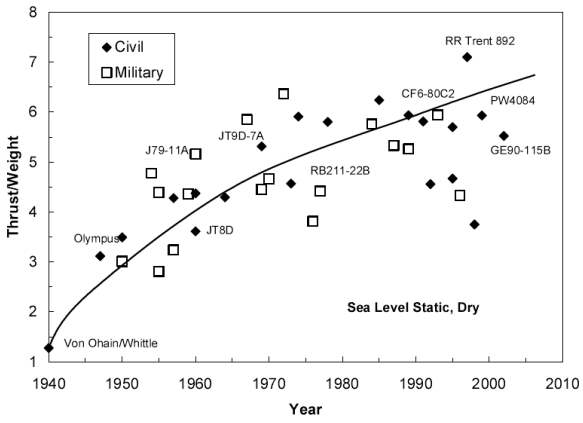

Figure 1-2: Thrust to weight ratio advancement for aero engine [5]

Advancement in computational capability to perform assisted structural design and three-dimensional (3D) numerical analyses are other aspects that also contribute to the technological progress. Geometrical blade optimisation, with improved design using finite element (FE) structural analysis and computational fluid dynamics (CFD), has improved blade aerodynamics which has therefore increased the compressor pressure ratio. Hence, it has improved the engine's thermal efficiency and specific fuel consumption, reduced the compressor stages, and the amount of blades required for each compressor stage. Figure 1-3 illustrates the historical improvement in compressor pressure ratio which shows the rise up to 40-fold.

Enhancement in turbine blades' cooling technology from a fully solid blade with convectional cooling, to the use of film and transpiration cooling has facilitated the rise in turbine entry temperature (TET) by improving the blade's cooling effectiveness, as shown in Figure 1-4. Also shown in the figure, as cooling effectiveness (measurement of how well the blades are being cooled between the incoming hot gas and the cooling air) increases, higher TET can be applied, resulting in a rise in the engine's thermal efficiency. Based on Figure 1-4, it was predicted that with the advanced cooling technology of the future, the cooling effectiveness can reach up to 0.8, thus is able to endure incoming gas temperatures up to 4200°F (2316°C).

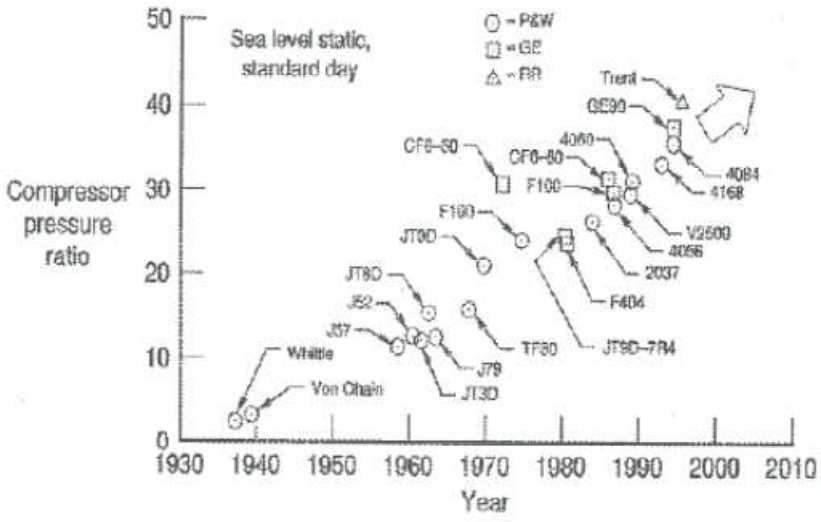

Figure 1-3: Compressor growth in pressure ratio [6]

1.1 Importance of Component Life Prediction

Although today's gas turbine can produce more power, use less fuel, provide higher thermal efficiencies, and reduce emission levels [7], the advantages have been eclipsed by several major problems such as lower availability (up to 10% lower), lower life of blades and vanes (averaging 15,000 hours), and higher degradation rates (5% to 7% in the first 10,000 hours of operation). Since it is running at higher TET, the blades and vanes are being operated near to its melting temperature despite the intricate and sophisticated blade cooling system [8].

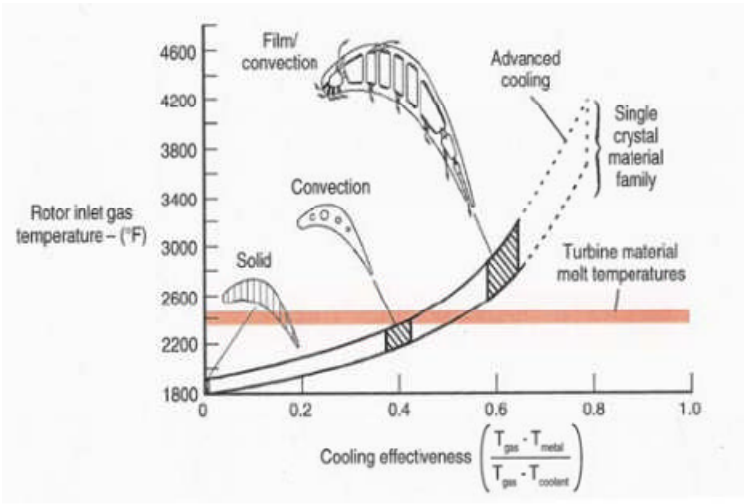

Figure 1-4: Blade cooling technology improvement [6]

Moreover, the trend for both compressor and turbine designs these days is towards fewer, larger, 3D airfoils with smaller clearance and higher pressure or expansion ratio [9]. As a result, both of these highly rotated components will need to tolerate higher mechanical loading, especially at higher rotational speeds. These mechanical loadings, normally in the form of large centrifugal loads and aerodynamic forces, will produce huge amounts of centrifugal and bending stresses.

When operating at this level of stress and temperature, gas turbine components, especially the hot section components such as the turbine blades and vanes, will become vulnerable to creep deformation. The presence of such deformation will cause a reduction in the components' useful life. It has been reported that an increase of 10 to 15°C in a component's metal temperature will significantly reduce by a half the component's useful life [10], [11].

Under varied gas turbine operating conditions, such as different rotational speeds, TETs, ambient conditions, and Mach numbers, the levels of stress and temperature endured by the components will vary, hence dictating the behaviour of the components' life consumption. For this reason, estimation of the gas turbine components' useful life has become increasingly important over the years. Both safety and economic reasons have driven the gas turbine manufacturers and operators to seek better estimation techniques that can accurately predict the gas turbine components' useful life.

The implication of overestimating the components' life can be devastating, especially when the component fails during operation. As an example, in July 1989, a tragic accident of a DC10-10 in Sioux City, Iowa killed 112 passengers due to in-flight separation of the stage 1 fan disc on the no 2 CF6 engine. It is reported that the fan life limit was estimated at 18,000 cycles but failed at 15,503 cycles [12]. Tragic events like this will not only impact on the operator financially, but can distort the operator's management and operations. Based on the report published by the Department of Transport and Regional Services [13], the cost due to aviation accidents can be divided into several categories, such as fatality costs which covers medical costs prior to death, productivity losses in the workplace and etc.; non-fatality injury costs which cover medical costs, rehabilitation costs and etc.; and common costs which cover property damage costs, legal costs, insurance administration costs, investigation costs etc.

On the other hand, underestimating the gas turbine components' useful life could also be costly to gas turbine operators. The greatest loss comes from maintenance cost which becomes a major part of the total operating cost [14]. The hefty safety

margin imposed by the original equipment manufacturer (OEM) to ensure safety, makes the components' life estimation too conservative [15], [16]. As a result, parts are removed prematurely during scheduled maintenance. It is reported that the cost of one HP turbine blade can be as much as $10,000; implying a total of $600,000 to $800,000 for a set of 60 to 80 blades [17].

In order to prevent such horrific incidents and to reduce the probability of premature parts removal, engine manufacturers and gas turbine operators spend huge amounts of money investing in research and development. Rolls Royce for example spent a gross average of £600 million annually from 1997 to 2006 [18]. This large amount of spending reflects the importance of expertise investment to an engine manufacturing organisation. Also, using OEM's maintenance guidelines as a starting point, operators also are striving to develop a more precise programme to 'individually' optimise service intervals, reduce maintenance costs and at the same time maintain or improve the reliability of their fleet [19].

1.2 Underlying Problems

As mentioned in the previous paragraphs, gas turbine hot section components' life estimation has becoming crucial for both safety and economic reasons. With the desire to always increase the gas turbine performance, the hot section components, in particular the high pressure turbine blades have to endure extremely high mechanical and thermal loadings. For this reason the high pressure turbine blades are often considered as the life limiting component of the gas turbine [20], [21] and often so influenced the inspection and maintenance interval of the gas turbine. Hence accurate prediction of the component life will assist the gas turbine operators in making informed maintenance decisions.

In pursuit of better outcomes, component life estimation methods today have become interdisciplinary. In an overall life estimation framework it requires the integration of aero-thermal dynamics, mechanical design, material sceince and failure mechanics.

In addition, the life estimation method has become multi-tasking. Depending on the approach selected, several analyses need to be carried out before the life of the component can be estimated. For example, the performance of the gas turbine corresponding to the gas turbine operating conditions need to be simulated in order to obtain the aero-thermal properties of the gas turbine. If the gas turbine has degraded, component diagnostics need to be applied first in order to obtain the health status of

the gas turbine. Next mechanical, thermal and microstructural analyses need to be performed in order to determine all of the functional parameters important to carry out the life estimation. Depending on the life estimation technique used, the life of the component will be assessed.

With so much complexity, the lifing assessment requires extensive work and a significant amount of computational time to obtain a solution. Because of this, in most cases the significant contributions in this area have been conducted at the technical lifing group of major OEMs [22]. Also, the complexity of the life estimation method places constraints on those who possess moderate levels of expertise and skills in this area, such as the performance engineers, maintenance engineers, supervisors, and technicians.

The complexity of the assessment also provides restrictions on the incorporation of the lifing methodology in the early design stages. Marcus [23] in his thesis explains that because the assessment is only possible towards the end of the design process, any errors or changes will cost the engine manufacturer a significant amount of money, which could be saved if a more comprehensive creep lifing prediction were possible in the early stages.

Because of the underlying problems arising from the current estimation method, there is a need to find alternative solutions. In principle, if all of the complex calculations previously done can be replaced or embedded into an alternative model while maintaining the current estimation accuracy, then the current complexity can be 'taken away' thus creating an accurate and rapid form of estimation technique.

In this research, a soft computing technique – the Artificial Neural Network (ANN) – is used to create neural-based component life estimation methods suitable to perform component life prediction under various operating and health conditions of gas turbines. Several questions will be answered as the research is being pursued:

a. Can the introduced neural-based component life estimation method reduce the complexity of the existing method?
b. To what extent can the previous complex calculations be embedded into the neural-based component life estimation?
c. What kind of network structure or architecture should be constructed in order to maintain the existing component life prediction accuracy?
d. Would it be possible to have a direct linkage between the gas turbine operating and health conditions with the components' corresponding life?
e. What sort of data are required as input to the alternative model?

1.3 Research Aim and Objectives

Life assessment of a particular gas turbine component depends on the failure modes acting on it. For components that are exposed to high mechanical and thermal loadings, fatigue and creep deformation are often considered as the dominant failure modes. However, in this research, only creep deformation will be considered. Therefore, all of the questions posed earlier will be tailored to create a neural-based creep life estimation method.

Based on the questions posed earlier, the research aims to develop an alternative creep life estimation model which will satisfy four important criteria:

a. The method will be based on the performance of the gas turbine.
b. The method will reduce the complexity of the current estimation framework.
c. The method should be able to perform rapid computation.
d. The method should maintain certain levels of accuracy.

In order to achieve this aim, several objectives have been laid out, and are summarised as follows:

a. To create an integrated creep life estimation model that enables the prediction of component creep life under different operating and health conditions.
b. To study the effects of different operating and health conditions on component creep life consumption using a simple relative analysis technique.
c. To construct an alternative neural-based creep life estimation model that enables a direct link between the gas turbine operating and health conditions and the components' corresponding life
d. To study the impact of input uncertainties on the creep life prediction accuracy obtained using the alternative creep life estimation method.

1.4 Research Scope

To ensure that the research can be completed within a reasonable time, certain boundaries need to be defined. For this reason, the scope of the research will be as follows:

a. Creep deformation is only considered in the research component of the life assessment.

b. The integrated creep life estimation model is developed for the calculation of high pressure turbine blade creep life.
c. ANN is used to construct the alternative creep life estimation model where the reduction of the complexity will be done at a macro level.
d. A turboshaft engine performance model is used to show the application of the alternative creep life estimation method.

1.5 Research Contribution

This thesis focuses on proposing alternative solutions to the presently complex creep life estimation method and therefore makes several contributions to knowledge. The main contribution of this work will be the development of several neural-based architectures that are able to provide good creep life prediction for gas turbine high pressure turbine blade's creep life under various gas turbine operating and health conditions.

In addition, a generic systematic approach used in designing the neural-based architectures is also proposed. Using this generic approach, readers will be able to form new and improved architectures not only for creep life estimation but also other forms of damage mechanism life prediction.

Apart from creating the neural-based life estimation model, the present model-based approach is also investigated and contribution to knowledge is also made. An improved integrated creep life estimation model is developed and incorporated with existing in-house performance simulation and diagnostics software in order to produce a newer version of the program with creep life prediction capability. In this integrated model, new parameters called Creep Factor and Mission Creep Factor are introduced to allow investigations into the effects of different operating and health conditions, and the effects of a particular mission/operation profile on component creep life consumption to be done using a simple relative analysis technique via the Creep Factor Approach.

1.6 Thesis Structure

The thesis is structured into nine chapters. As the first chapter is written to provide the overall picture of the research while defining its aim, objectives and scopes, the following chapters will discuss the work conducted in a progressive manner:

Chapter 2: Literature Review

In this chapter, the theory of creep deformation is given. In addition, the majority of the contents focus on providing an overview of the existing creep life estimation methods. Towards the end, the chapter focuses more on the application of soft computing techniques used in the field of component life estimation.

Chapter 3: Methodological Approach

This chapter presents the overall methodology of the research. It covers the idea implemented in this research and provides a research methodology diagram that summarises the research. In addition, a description of the method used to construct the alternative creep life estimation is presented.

Chapter 4: Integrated Creep Life Prediction Model

This chapter provides a thorough explanation regarding the integrated lifing system developed by the author. It includes a discussion on the system architecture and its corresponding sub-models. For each sub-model, the chapter provides the full algorithm including the equations and their corresponding assumptions. The chapter also describes how the sub-models are integrated with an in-house performance simulation software called PYTHIA to form an improved version of the software. In addition, a new form of relative analysis called the Creep Factor is introduced in order to provide a more meaningful representation of high pressure (HP) turbine blades' creep life consumption.

Chapter 5: Artificial Neural Network Based Creep Life Estimation

This chapter outlines the development of the alternative creep life estimation method proposed by the author using the ANN approach. At the beginning of the chapter the theoretical background of the ANN approach is given. The chapter then touches on the architecture design concept and explains how the proposed architectures are built using a process analysis. Also the general procedure developed by the author to create the architecture will be presented.

Chapter 6: Application of the Integrated Creep Life Prediction Model: Effects of Operating and the Health Conditions of HP Turbine Blades' Creep Life

In the first part of the chapter, the development of the selected engine performance model used as a test case in this research will be reported. This also covers the process undertaken by this research to ensure good performance prediction at both the design point (DP) and the off-design (OD) point. In the next part of the chapter, the

impact analysis of gas turbine operating and health conditions on the HP turbine blades creep life using the introduced Creep Factor is presented.

Chapter 7: Application of the Neural-Based Creep Life Prediction Method on the Aero-engine

The chapter discusses the implementation of the proposed architectures to the selected engine model in both clean and degraded conditions. At the end of the chapter, a comparison analysis between all the proposed architectures is given.

Chapter 8: Influence of Input Uncertainties on Creep Life Prediction

This chapter provides the results of the study conducted to investigate the effects of input uncertainties on the creep life prediction accuracy applied on the three clean engine neural network creep life prediction architectures. In this chapter, readers will be provided with the method used to perform the analysis and how the architectures respond to different levels of input uncertainties

Chapter 9: Conclusions and Future Work

This chapter summarises the key findings of the research, evaluates the research accomplishments and suggests suitable areas for future work.

2 LITERATURE REVIEW

2.1 Common Failure in the Gas Turbine Hot Section

The failure of metal parts is a complex phenomenon that depends on material, temperature, deformation, and the rate at which strain is applied [24]. When a metal component breaks, two major questions need to be answered; what are the modes of the failure and what is the origin of the damage; hence examination of the 'how' is essential to understand the deterioration phenomena [25].

When gas turbine hot section components are being operated at extreme operating conditions, several damage mechanisms such as fatigue, high temperature corrosion/oxidation, and creep deformation will inevitably emerge. The presence of such mechanisms will cause the component to lose its ability to sustain its intended function, increase its life consumption rate, and to some extent, will cause the component to fail prematurely.

2.1.1 Fatigue

Fatigue, broadly speaking, is caused by repetitive loads that produce fluctuations in the components' stress, σ, hence if large enough, will cause the component to fail even though the σ is much lower than that required for failure on single load application [26–28]. Consequently, it will lead to crack initiation and propagation which ends with a fracture.

Fatigue, in this context, can be either mechanical or thermal-mechanical fatigue (TMF). Mechanical fatigue is a failure occurring under cyclic loading which is, for example, caused by vibrational σ on turbine blades during gas turbine start-stop cycle and power change. Mechanical fatigue can be further divided into two: high cycle fatigue (HCF), and low cycle fatigue (LCF). The distinction between them is where the repetitive application of load is taking place. HCF is categorised by high frequency and low amplitude elastic strain. An example of HCF will be when the turbine or the compressor blade is subjected to repeated bending, such as when the blade passes behind a stator vane, hence emerges into the gas path which will bend the blade due to high velocity gas pressure. This will force the blades to vibrate and the excitation at some point will match the blade's resonant frequency causing the amplitude of vibration to increase significantly.

LCF on the other hand is categorised by low frequency and high amplitude plastic strain. When dealing with LCF, the yield limit of the material is often exceeded and the material becomes plastic; therefore, repetitive plastic deformation is the main cause of LCF [29]. Although there is no distinct border between the two types of failure, the traditional approach is to classify failures occurring above 10^4 cycles as HCF and those occurring below that value as LCF [28],

TMF on the other hand occurs when the component is not only exposed to cyclic loads but is also experiencing variations in temperature gradient, resulting in significant thermal expansion and contraction. According to Jacobsson [30], turbine blade cooling which is used to lower the turbine blade's temperature will induce high temperature gradients between the blades high and cold regions thus generating σ; and during service, the effect of variation results in TMF.

2.1.2 High Temperature Corrosion/Oxidation

Both turbine and compressor are exposed to aggressive corrosive and oxidising conditions that may be caused by several factors [31]:

a. Ingested air which contains sodium and chloride in the form of salt from the sea or from runaway de-icing treatment or marine environments.
b. Atmospheric contaminants resulting from pollutions from industry or forest fires which usually contain sulphur and sodium.
c. Volcanic activity which can generate significant levels of pollutants particularly sulphur.Gaseous combustion products which contain elements such as sulphur, vanadium or even lead and bromine from fuel at higher temperatures.

Although the blades have a protective coating, corrosive and oxidation attacks are unavoidable, especially when the blades are exposed to sufficiently contaminated surroundings or too much harmful fuel element.

2.1.3 Creep Deformation

Creep is a time dependent, thermally assisted deformation caused by prolonged high operating temperatures coupled with constant mechanical loading (below the yield stress of the material). Creep will cause the gas turbine hot section components to 'stretch' or elongate. Taking turbine blades for example, in the event of severe creep deformation, the physical shape of the blades will change and hence can no longer function properly. In addition, the elongation will cause the blades to be in contact with

the casing, causing the blades to fracture and finally lead to engine failure. Figure 2-1 depicts several deformed turbine blades under creep attack. Note that the blades have already lost their original features at the tip, indicating a severe creep attack.

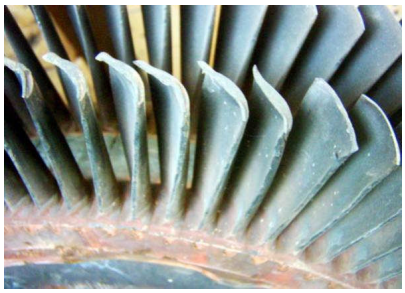

Figure 2-1: Deformed turbine blades under creep attack [32]

Although different materials have different strengths to resist creep deformation, it can generally be said that creep becomes significant when the homologous temperature (ratio between the material temperature and its melting temperature) is more than 0.5 but it can be in the range of 0.4 to 0.6 [8], [33–35].

2.1.4 Competition among Damage Mechanism

Table 2-1and Table 2-2 indicate how different components and applications have different influences on damage mechanisms. Compressor blading, for example, is prone to wet corrosion, LCF and HCF. According to Brun et al. [36], during engine shutdown, compressor cold surfaces can condense water where chemical species, such as salts or sulphur compounds, can be absorbed in the water producing an acidic, corrosive liquid resulting in wet corrosion. Moreover, since the compressor is being operated at much lower temperatures (low homologous temperature) creep is not significant compared to LCF or HCF.

Land-based power generations, the majority of the time, are being operated at uniform operating conditions and hence produce long periods of constant load conditions coupled with a high temperature environment. For this reason, creep becomes dominant compared to fatigue and oxidation. However, when compared with an aircraft engine, frequent stop-start cycles and changing of the throttle create cyclic loading which makes fatigue more dominant than creep. For marine engines, air ingested into the engine contains higher concentrations of sodium and chloride in the form of salt. During combustion in the gas turbine, sulphur from the fuel reacts with

high concentrated sodium chloride to form sodium sulphate which will then deposit on the hot section components resulting in accelerated corrosion attack [37].

Table 2-1: Life expenditure effects on gas turbine components [38]

	Design criteria and life expenditure effects					
	Time dependent life expenditure			Cyclic life expenditure		
Components	Oxidation, corrosion, erosion	Wet corrosion	Creep	LCF	HCF	Crack Propagation
Turbine blading	■	X	■	■	■	X
Compressor blading	X	■	X	■	■	X
Inner casing, mixing chamber, exhaust liner	■	X	■	■	□	X
Rotor parts (excluding blading)	X	X	X	■	X	■
Pressure-tight casing	X	X	X	■	X	X
Piping	X	□	X	■	■	X

■ Significant contribution □ Affects only locally X Irrelevant

Table 2-2: Comparison of problems for gas turbine applications [39]

	Oxidations	Hot corrosion	Creep	Fatigue
Aircraft engines	Severe	Moderate	Moderate	Severe
Land-based power generation	Moderate	Severe	Severe	Light
Marine engines	Moderate	Severe	Moderate	Moderate

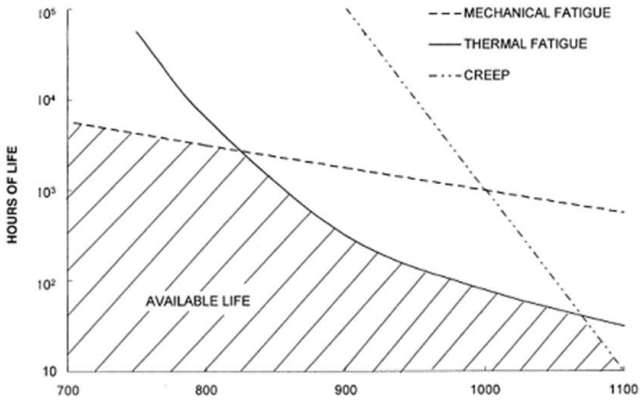

Figure 2-2: Factor influencing the turbine-component's life [40]

Figure 2-2 graphically summarises how different damage mechanisms exhibit different dominancies at different temperature regions. At lower metal temperatures, T_M approximately below 830°C, mechanical fatigue is more dominant than others. However, between 830°C and 1000°C, thermal fatigue becomes superior, although creep becomes a major threat as the temperature exceeds 1000°C.

2.2 Understanding Creep

Creep, as discussed in earlier sections is a natural progressive permanent deformation that is thermally activated and becomes significant at higher temperatures. Creep manifests itself as a progressive accumulation of plastic strain known as creep strain over a period of time. Because of such deformation, unacceptable dimension changes ending in rupture can occur.

Although creep deformation becomes significant as the metal homologous temperature is more than 0.4 to 0.6 (depending on the material), creep deformation can also happen at low temperatures. Figure 2-3 provides an illustrative comparison between the changes in material length due to creep deformation at two different homologous temperatures. From the figure it can be seen that at higher T_M, the change in length will be considerable as the metal will eventually fail due to creep rupture. In contrast, at lower temperatures, elongation will happen at a slower rate and it is unusual for failure to take place.

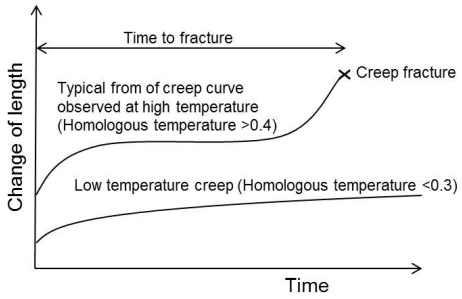

Figure 2-3: Creep curve at different metal temperature [8]

At higher homologous temperatures, the strength of the material will decrease, resulting in greater mobility of dislocation [41]. In addition, the high temperature causes the material's slip system to change and in some circumstances an additional slip system is created. With the additional slip system, which creates new 'routes' for dislocation to take place and higher mobility of dislocation, the creep strain at higher homologous temperatures will be considerably more than at low temperatures.

Webster and Ainsworth [35] mention that creep in polycrystalline materials occurs as a result of dislocations, grain boundary sliding and diffusion. As the material temperature increases, the atom will have enough thermal energy to jump from its original position to another while transmitting the energy to the adjacent atom. As a consequence, this diffusional process will alter the atomic arrangement and force the grain to extend with time.

The loss of metal strength can also happen due to irregular growing of the metal gamma prime phase γ'particles (γ'precipitation is used to strengthen the gas turbine blade) and carbide along metal grain boundaries [42–46]. These microstructural degradations will gradually decrease the total blade life [47–49]. A study conducted by Daleo et al. [46], [50] on GTD111 turbine buckets discussed the degradation process at a micro level. Figure 2-4(a) shows the virgin alloy with evenly distributed, γ' having an average size of 0.86 microns added with a very thin carbide layer. After 5,000 hours of thermal exposure at 900°C, the cubic shaped particles have transformed to a rounded morphology as shown in Figure 2-4(b); the size of γ' grew to 1.16 microns and the thick layer of carbide film was formed.

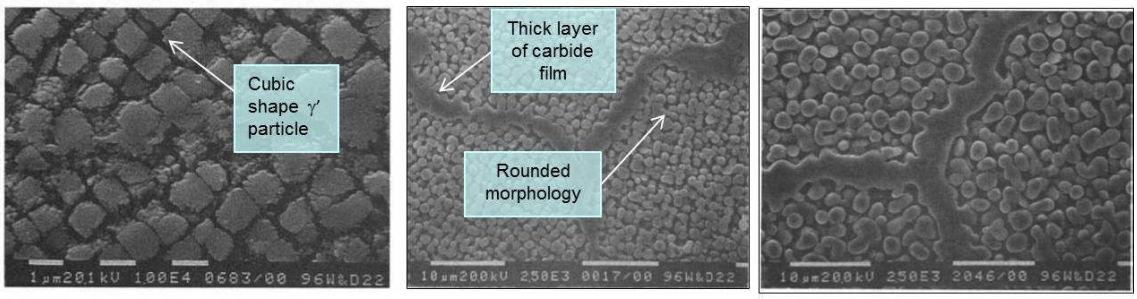

Figure 2-4: GTD 111 (a) virgin alloy (b) at 5,000 hours of exposure and (c) at 23,000 hours of exposure [46]

Figure 2-4(c) depicts the severe microstructure degradation as the bucket is exposed after 23,000 hours. Note that the carbide film along the boundaries has coarsened. Daleo et al. stressed that if the film continues to grow, the boundary will become brittle, notch-sensitive and prone to cracking.

2.2.1 Creep Curve and Stress Rupture Curve

The behaviour of creep is determined by means of laboratory tests in which a constant uniaxial load or σ is applied at a constant temperature. The resulting creep strain, ε_C is recorded as a function of time, t, and the creep curve, which plots ε_C against t, as illustrated in Figure 2-5, is generated.

After the instantaneous plastic strain, ε_O caused by the application of load, ε_C will continue to increase with t. During the first stage, known as the primary creep, the creep rate/plastic strain rate, $\dot{\varepsilon}_C$ will initially increase due to the higher dislocation motion of the material. As more material is dislocated, the density of the dislocation will increase until it becomes saturated. This will prevent more dislocation taking place,

thus creating strain hardening that will reduce the creep rate until it reaches a constant rate.

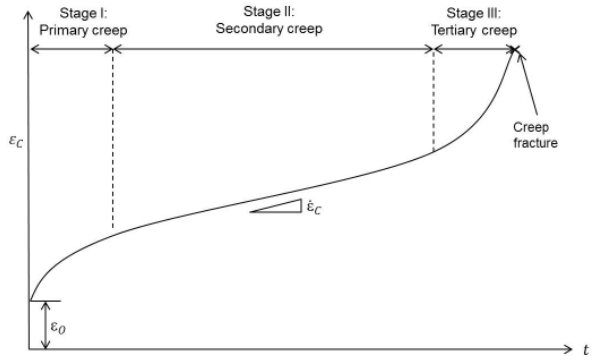

Figure 2-5: High Temperature Creep Curve

The secondary creep, known as the steady-state creep, will possess a fairly constant creep rate. The strain hardening rate will become proportional to the deformation rate which provides the balance between both, causing the rate to become steady. Figure 2-5 shows that the minimum creep rate will occur at this stage.

The final stage is termed tertiary creep. This is a period that will lead to fracture. It can be caused by a number of factors such as [8]:

a. mechanical instability, such as the occurrence of necking which results in a localised reduction in cross-sectional area,
b. microstructural instability, including grain growth or re-crystallisation with single-phase material or the gradual loss of creep strength as over-ageing occurs during creep of precipitation-hardened alloys; and/or
c. nucleation and growth of internal micro cracks which develop until the number and sizes of the micro cracks are sufficient to cause the creep rate to increase.

Figure 2-6 provides an example of a creep test result of Fe-Mn-Al Alloy at 600°C. As higher σ is applied, the minimum creep rate will increase. From the figure, 340MPa was required to achieve the minimum creep rate of 0.084%/hour while 180MPa was required for 0.0028%/hour.

Besides the creep curve, the creep behaviour of the material can also be represented using the stress rupture curve which provides the relationship between a specified applied σ and T_M to time to failure, t_f The test can be conducted either at specified T_M, with different values of σ or vice versa. Typical stress rupture curves are shown in Figure 2-7 generated at specified T_M with a variation of applied σ. As shown in

the figure, at the same T_M, the t_f of the steel reduces when the level of σ increases. Similarly, at the same σ level, a higher T_M has shortened the life of the steel.

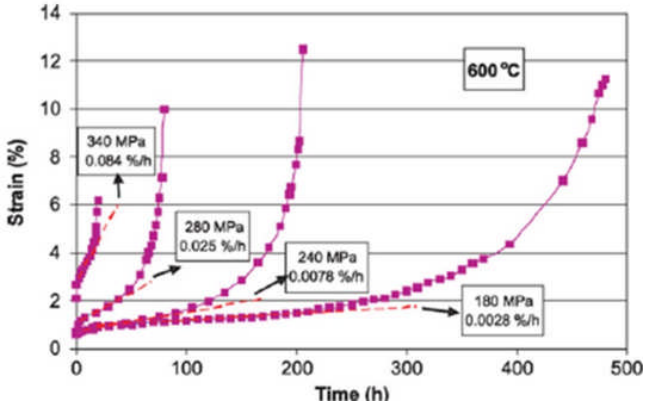

Figure 2-6: Creep curve of Fe-Mn-Al Alloy at 600°C during creep test [51]

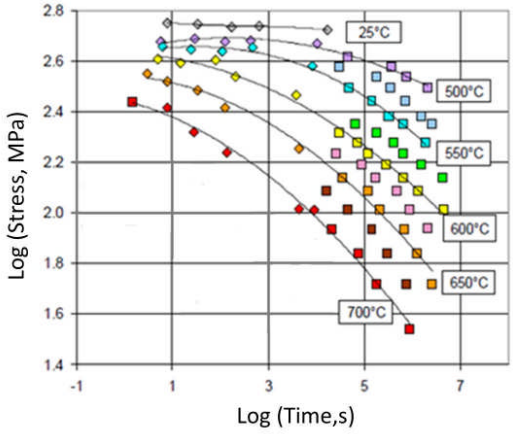

Figure 2-7: Creep rupture data for a 2.25Cr-1Mo steel [52]

2.2.2 Factors Affecting Creep Deformation

Creep characteristics depend on several factors such as σ, metal temperature, period of exposure, and material properties [15], [16], [31], [53–57]. Since creep is a time dependent, thermally assisted deformation, the longer the component is exposed to elevated temperature, the more deformed the component will become.

Different materials for instance will have a different creep resistance due to different microstructural arrangement, activation energy, grain size, and vacancy concentration within the materials. Figure 2-8 shows the variations of materials' creep resistance at 100 hours of creep rupture. Tungsten and Niobium alloys, for example, have higher temperature resistance than Nickel alloy but show lower stress resistance. 12%CrMoV steels in contrast have better stress resistance but can easily fail at lower temperatures.

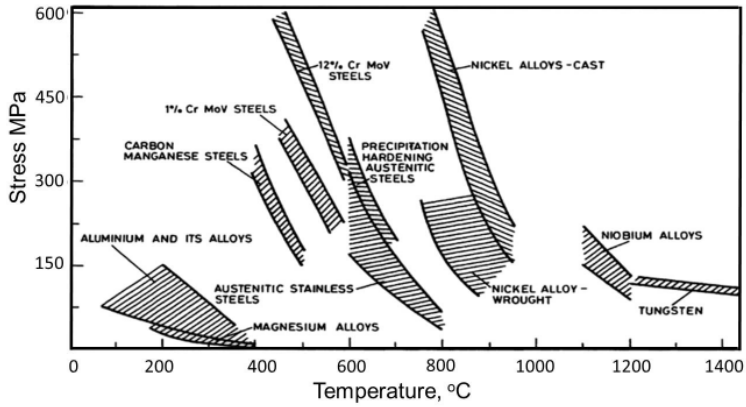

Figure 2-8: Stress and temperature to produce creep rupture in 100 hours in various alloys [35]

Since creep is a thermally activated process, higher temperature exposure will weaken the material due to increase in dislocation, grain boundary sliding, creep cavity nucleation, etc. [57]. As a result, $\dot{\varepsilon}_C$ will increase and hence shorten the t_f. Figure 2-9 illustrates the variation in the creep curve when the material T_M is increased at a constant applied load. The figure shows that when T_M is increased, t_f is shortened and the secondary creep rate, $\dot{\varepsilon}_{CS}$ also increases. In addition, the elongation of the material is also higher at the higher T_M although the time of exposure is shortened.

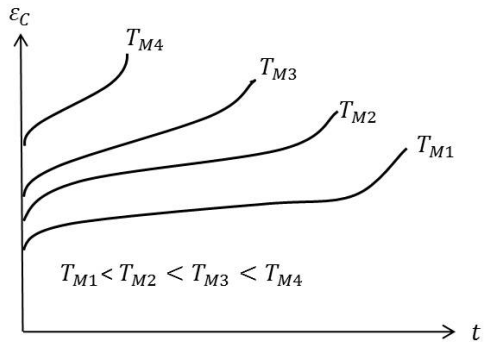

Figure 2-9: Schematic diagram of creep curves at different temperatures

$\dot{\varepsilon}_C$ is also sensitive to the level of applied σ. Figure 2-10 schematically shows how different levels of applied σ can influence the $\dot{\varepsilon}_C$ at constant temperature exposure. From the figure it can be seen that with the increase in σ, the primary and secondary creep stages are shortened or even eliminated, hence reducing the t_f. Similarly, the elongation of the material is also higher at the higher σ level, although time of exposure to the applied σ is shortened.

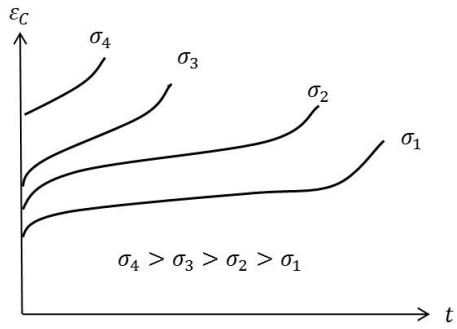

Figure 2-10: Schematic diagram creep curves at different levels of applied stress

2.2.3 Modelling the Creep Curve

Power law, Nabarro-Herring, Coble Creep, and Harper-Dorn Creep relations, which have been fully described in [33], have proposed some equations describing the secondary creep phenomena. Empirical relations such as the Monkman-Grant [58], Dobes-Milicka [59] and Koul [60] relations have also been valuable in providing relations between the $\dot{\varepsilon}_{CS}$ and t_f. Yet while the knowledge of t_f identifies the point of failure, analysis using only the secondary creep phenomena has disregarded the primary and tertiary creep stages in which the major proportion of the creep curve has been left out.

The Theta projection model has mathematically described the entire creep curve based on the concept of shape function obtained from constant stress creep curves. Beginning with 4 Theta [61], later improved to 6 Theta projection [62], the creep strain at a given time, ε_{Ct} can be defined as Equations (2-1) and (2-2) for the 4 Theta and 6 Theta models respectively.

$$\varepsilon_{Ct} = \theta_1\left(1 - e^{-\theta_2 t}\right) + \theta_3\left(e^{\theta_4 t} - 1\right) \quad \textbf{(2-1)}$$

$$\varepsilon_{Ct} = \theta_1\left(1 - e^{-\theta_2 t}\right) + \theta_3\left(e^{\theta_4 t} - 1\right) + \theta_5\left(1 - e^{-\theta_6 t}\right) \quad \textbf{(2-2)}$$

where θ_1 to θ_6 denote the Theta projection parameters which are obtained using non-linear optimisation algorithms based on the constant load experimental data. The first term in Equations (2-1) and (2-2) represents the decaying primary creep while the second term in both equations represents the accelerating tertiary creep. In order to cope with poor modelling of the creep curve at low ε_C and t, the third term in Equation (2-2) was introduced.

Once the θs are determined, various engineering analyses such as estimating the ε_{Ct}, $\dot{\varepsilon}_{CS}$, and t_f can be done. The $\dot{\varepsilon}_C$ for example can be estimated by differentiating

Equations (2-1) and (2-2) while t_f can be obtained by replacing ε_{Ct} in both equations with the rupture strain and solving numerically for t until the value of the rupture strain is obtained.

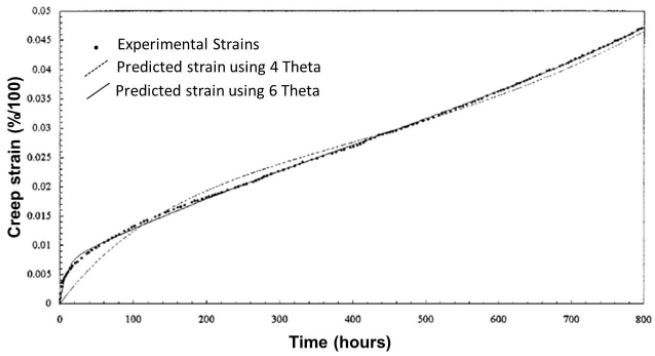

Figure 2-11: Creep curves of 1CrMoV modelled by 4 and 6 Theta models compared with experimental data measured at 863K and 165MPa [62]

Figure 2-11 depicts the creep curves of 1CrMoV modelled by both 4 and 6 Theta models compared to the experimental strains measured at specific T_M and σ. It can be seen how both Theta models are able to provide a good representation of actual creep behaviour over t with the 6 Theta model being more accurate at low ε_C and t.

Besides the Theta projection model, the Omega method proposed by the Material Properties Council (MPC) can also be used to model creep curve, especially when the primary and secondary creep stages are minimal [63]. $\dot{\varepsilon}_C$ in the method is expressed as

$$\ln \dot{\varepsilon}_C = \ln \dot{\varepsilon}_o + \Omega \varepsilon_C \tag{2-3}$$

where $\dot{\varepsilon}_o$ and Ω are the imaginary initial plastic strain rate and Omega method parameters. Integrating Equation (2-3) will give

$$\varepsilon_{Ct} = \left(\frac{1}{\Omega}\right) \ln\left[\frac{1}{1 - \Omega \dot{\varepsilon}_o t}\right] \tag{2-4}$$

Both $\dot{\varepsilon}_o$ and Ω are determined empirically when $\ln \dot{\varepsilon}_C$ against ε_C is plotted with $\dot{\varepsilon}_o$ is obtained at $\ln \dot{\varepsilon}_C = 0$ and Ω is obtained from the slope of the plot. In addition, t_f can be obtained using Equation (2-5).

$$t_f \approx \frac{1}{\Omega \dot{\varepsilon}_o} \tag{2-5}$$

2.2.4 Time Temperature Parameter

Data recorded from creep curves either by experiment or using the Theta or Omega method will not necessarily provide the most appropriate forms of creep life estimation. The experimental method is often insufficient to cover various σ and T_M hence extrapolation or interpolation to the required σ or T_M needs to be carried out.

The use of time temperature parameters provides another alternative solution. Time temperature parameters are correlated parameters which allow results obtained from the stress rupture test over a range of temperatures to be superimposed onto a single master curve. Although there are a number of time temperature parameters, only a few are widely used, such as the Larson Miller parameter (LMP), Orr-Sherby-Dorn parameter (OSD), Manson-Haferd parameter (MHP) and Manson-Succop parameter (MSP).

2.2.4.1 Orr-Sherby-Dorn Parameter (OSD)

OSD assumes $\log t_f$ forms a linear function with $1/T_M$ and can be expressed as

$$\log t_f = OSD + \frac{Qc}{R_o T_M} \quad \textbf{(2-6)}$$

with Qc and R_o being the material's activation energy and universal gas constant respectively. If Qc is assumed to be constant and taking A_{OSD} as Qc/R_o, Equation (2-6) can be expressed as Equation (2-7)

$$\log t_f = OSD + \frac{A}{T_M} \quad \textbf{(2-7)}$$

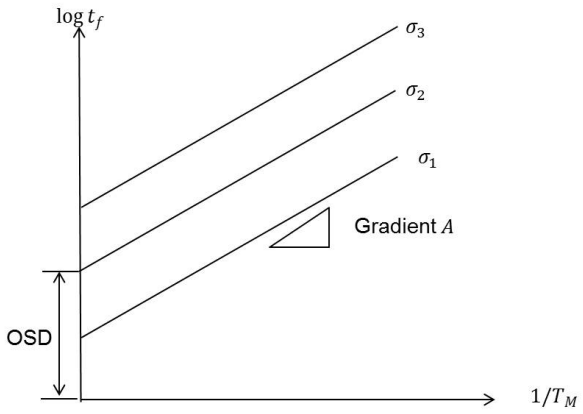

Figure 2-12: Schematic illustration of plot $\log t_f$ versus $1/T_M$ using OSD

Using Equation (2-7), data from the same σ but different T_M can be superimposed and plotted on $\log t_f$ versus $1/T_M$ to build iso-stress lines which are going to be parallel to each other as shown in Figure 2-12. When the values of OSD are obtained, a master curve can be generated. Later, for any given σ, OSD can be interpolated or extrapolated and t_f can be determined using Equation (2-7). The value of the A_{OSD} used in OSD formulation depends on the material. Figure 2-13 provides the master curve of ½Cr ½Mo¼V steel with A_{OSD} being 17,300.

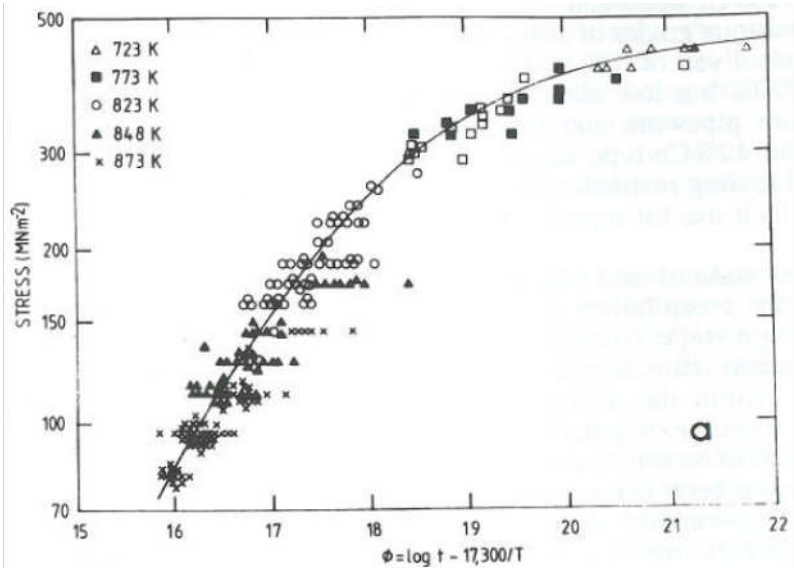

Figure 2-13: The OSD master curve of ½Cr ½Mo¼V steel [8]

2.2.4.2 Larson Miller Parameter (LMP)

The LMP equation is expressed as

$$\log t_f = \frac{LMP}{T_M} - C_{LMP} \qquad \textbf{(2-8)}$$

where C_{LMP} is the LMP constant. Plotting $\log t_f$ against $1/T_M$ (Figure 2-14) will create iso-stress lines which will converge to a point (constant C_{LMP}) on the $\log t_f$ axis. Similarly, the master curve for different values of σ can be generated. Figure 2-15 shows a Nimonic 105 master curve with C_{LMP} taken as 20. It is reported in most literatures that C_{LMP} can be in the range of 17-23, but it is normally generalised to 20.

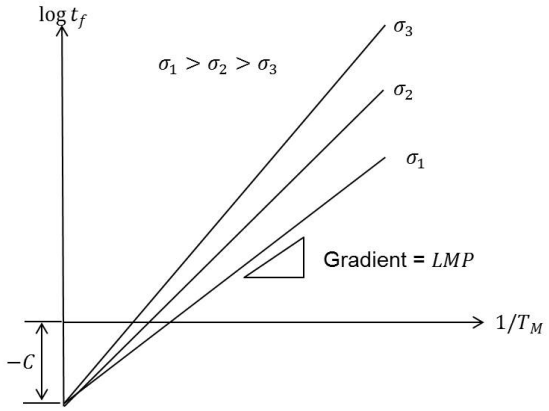

Figure 2-14: Schematic illustration of plot $\log t_f$ versus $1/T_M$ using LMP

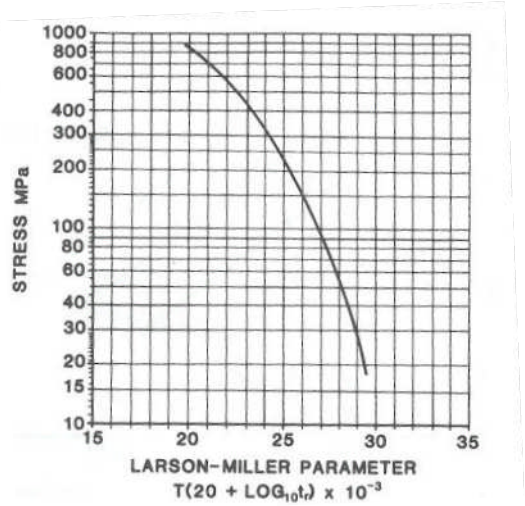

Figure 2-15: The LMP master curve for Nimonic 105 [35]

2.2.4.3 Manson-Haferd Parameter (MHP)

MHP is an improvement on LMP with the purpose of eliminating errors of using a C_{LMP} of 20 for any materials. MHP assumes that when $\log t_f$ is plotted against T_M (Figure 2-16), the convergence of the iso-stress line will happen at (T_{MA}, t_A) and will not intersect the axis of $\log t_f$. MHP introduces two more constants, T_{MA} and t_A which are the Manson-Haferd temperature and time constant respectively. Both constants can be identified by analysing the pattern of the iso-stress lines which indicate the converging point. The MHP equation can be written as

$$MHP = \frac{T_M - T_{MA}}{\log t_f - \log t_A} \quad \textbf{(2-9)}$$

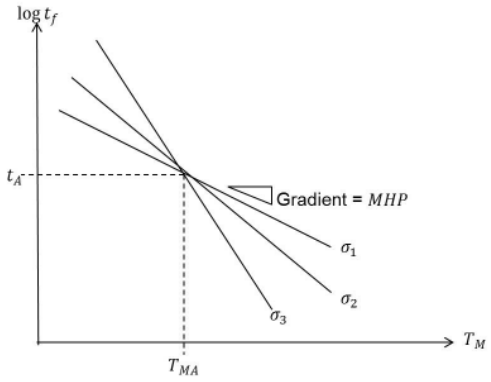

Figure 2-16: Schematic illustration of plot $\log t_f$ versus T_M using MHP

The MHP master curve for ASTAR 811C is shown in Figure 2-17.

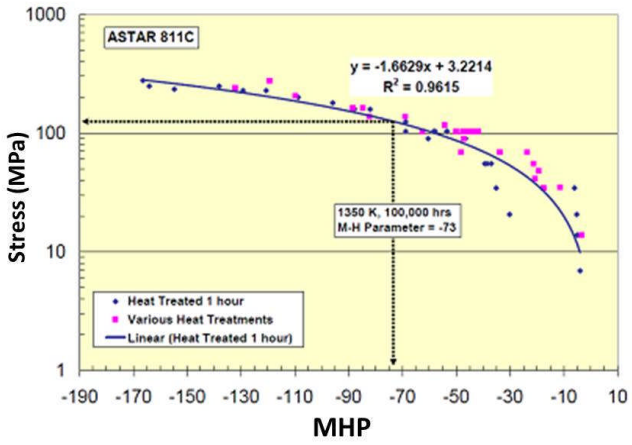

Figure 2-17: MHP master curve for ASTAR 811C [51]

2.2.4.4 Manson-Succop Parameter (MSP)

The MSP is similar to OSD which is based on the parallelism of iso-stress lines. MSP assumes that parallel iso-stress line can be achieved when graph $\log t_f$ against T_M is plotted (Figure 2-18). The MSP equation can be written as

$$\log t_f = MSP - B_{MSP} T_M \quad \textbf{(2-10)}$$

where B_{MSP} is the MSP constant. Similarly, the master curve can be generated for different σ. Figure 2-19 shows the master curve of 2.25Cr-1Mo steel extrapolated from the stress rupture test. Note that from the figure, the constant for the steel is taken as 0.02519.

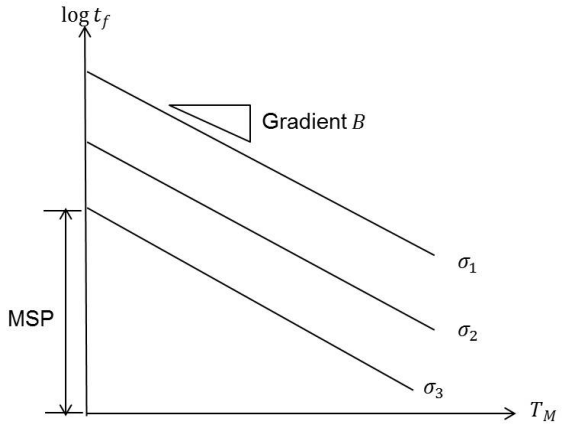

Figure 2-18: Schematic illustration of plot $\log t_f$ versus T_M using MSP formulation

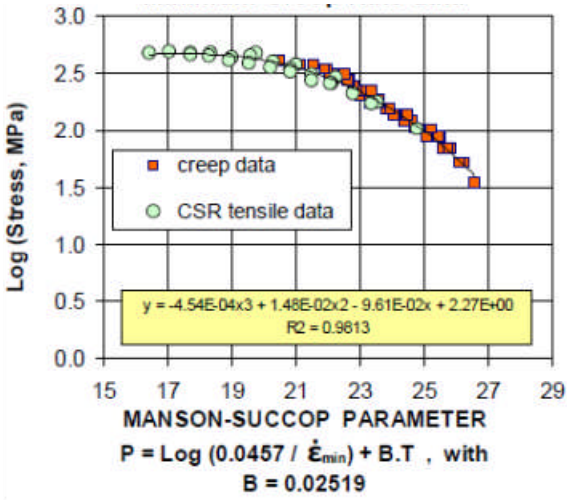

Figure 2-19: MSP master curve for 2.25Cr-1Mo Steel [52]

2.2.4.5 Selecting the Suitable Parameters

Selecting the most suitable time temperature parameter is still the subject of debate among researchers. One of the reasons is that the suitability of the parameters depends on the materials, T_M or σ range. Attempts have been made to compare these parameters in seeking the best and most accurate correlation.

Pink [64] compared both LMP and MHP in terms of their physical significance and reliability using the theoretical stress dependence which takes into account temperature difference and shear force. It was concluded that both parameters are in agreement with the theoretical equation for low temperature deformation. Furthermore, MHP was found to be more reliable at moderately high and high temperatures. Pink also added that LMP is widely accepted because it provides a fairly accurate description of rupture properties at the lower part of the high temperature range.

Nickel et al. [65] studied the creep rupture properties of chromium steel E911, P92 and P91 and the influence of oxidation on strength. From experimental works, the creep data were fitted using LMP, OSD and MHP before they were extrapolated at higher temperatures. It was found that MHP provides a slightly higher estimation when compared with the other parameters.

Sobrinho and Bueno [52] also made a comparison when they studied the correlation between creep and the hot tensile behaviour of Cr-Mo. Data from the experimental work were fitted using five parameters which are Goldhoff-Sherby (GSP), LMP, OSD, MHP, and MSP. The results revealed that the best fit was achieved using MHP followed by OSD, MSP, LMP, and GSP. The work was continued by Bueno and Sordi [66] who compared three different parameters which are LMP, MSP and OSD when they examined the behaviour of Fe-Mn-Al steel. They discovered that the best fitting was achieved using MSP, followed closely by LMP and then OSD.

Eno [67] compared Mandelson-Roberts-Manson (MRM), LMP, OSD, MHP, and MSP using two materials creep data for Alloy 617 and HAYNES® 230 alloy. For Alloy 617, the best fit was achieved using the MRM, followed by LMP, MHP MSP and OSD, whereas for Alloy 230, the best fit was achieved using MRM followed by MHP, LMP, MSP and OSD.

The works discussed in earlier paragraphs indicate that the parameters are unique and can be treated as special cases in a common general framework. Among all parameters, LMP is still considered to be the most favourable because of its ease of method and its widespread application [45], [48], [67], [68].

2.3 CREEP LIFE ESTIMATION APPROACHES

When a hot section component is put into service and operates at a creep regime, its life will be consumed progressively as shown in Figure 2-20. This is due to the fact that both the deformation and fracture are becoming time-dependent. The rate of useful life consumption will depend on the ability of the material to resist creep deformation and also the gas turbine operating condition. The more volatile the operating condition, the faster the material will be degraded thus the quicker the useful life will be consumed. As the material degrades progressively, micro-cracks will start to initiate on the surface and will propagate. According to Betten et al. [69], the influence of micro-cracks on creep behaviour begins even at the primary stage and the cracks become visible at the tertiary creep stage when the linkage of blunted micro-cracks into macro-crack occurs. The macro-cracks will propagate before the final creep fracture takes place.

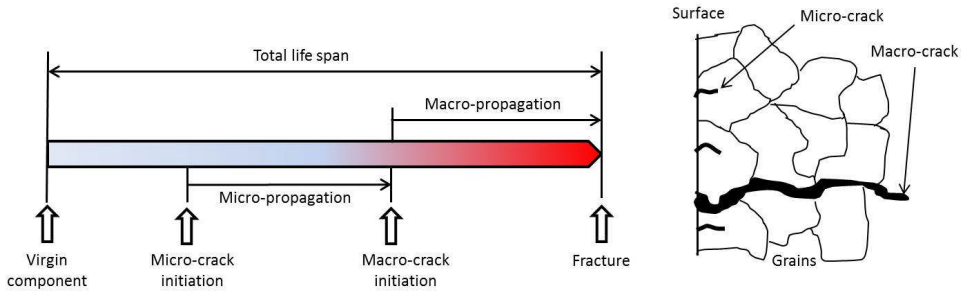

Figure 2-20: Life span of hot section component due to creep deformation [70], [71]

There are several methods for estimating creep life. In general, these methods can be classified into four broad approaches:

a. Model-Based approach
b. Service-Based approach,
c. Statistical/Probabilistic-Based approach, and
d. Soft Computing approach

It is important to note that in later sections of this thesis, some of the works related to the life estimation of turbine blades will be given for each approach. Nevertheless some works relating to the life estimation of other components are given as well.

2.3.1 Model-Based Approach

The model-based approach involves empirical, analytical or numerical model creation in order to calculate the component's creep life. Depending on how the model is created, external sources are needed to accompany the estimation such as the component's geometrical, material data, and engine operating and health conditions. According to Wood [72], non-destructive test (NDT) and destructive test (DT) should be carried out using conventional techniques when the life fraction is greater than 0.5 (50%).

The model-based approach can further be classified into two sub-approaches which are the total life approach and the damage tolerance approach. In the total life approach, the life span of the component is predicted prior to the failure of the component or at the time failure occurs. On the other hand, the damage tolerance approach focuses on modelling the crack initiation and propagation processes. It is important to note that in this section, only the total life approach will be discussed since the development of the author's integrated creep life prediction model is based on this approach.

Creep life estimation using the total life approach can be done by using either a life-based model, a strain-based model, or a damage-based model.

2.3.1.1 Creep Life Estimation Using the Life-Based Model

When predicting the creep life estimation using the life-based model, t_f of the component is directly predicted when the σ and T_M are presented. This can be done through the utilisation of the time temperature parameters, as discussed in Section 2.2.4. Although the time temperature parameters were established almost six decades ago, the empirical parametric method is still being widely used. Often these empirical parameters are being incorporated into an integrated, analytical or numerical thermal and stress model in order to perform creep life estimation based on various operating and health conditions.

Dedikin [73] incorporated the LMP into a non-linear FE code. In his method, CFD was first utilised to obtain convection boundary conditions over the external and internal surfaces of cooled turbine blades. The stresses and temperatures were then obtained using the non-linear FE method. By incorporating LMP into the FE code, t_f were computed, hence by using a linear damage parameter, the current damage due to creep deformation was displayed.

An integrated lifing analysis was also proposed by [74], [75]. The algorithm and system models which are comprised of an in-flight engine data acquisition, gas turbine performance simulation model, CFD model, FE model, and lifing model, were developed and integrated. The flight data were captured and stored using flight and engine data monitoring software and then downloaded into one dimensional performance simulation software where the entire transient of the aero-thermal properties from the flight profile were modelled and sent for further processing using the CFD and FE models. Then, the stress, strain and temperature distribution were estimated before the life was estimated.

Rosario et al. [76] utilised a window-based standalone creep life assessment called Creep-Fatigue Pro3 developed by the Electrical Power Research Institute (EPRI) for power plant application. The assessment consists of three main models which are the Stress Transfer Function model that receives measurements from existing plant data acquisition systems and converts the inputs into the component stress, Damage model which performs linear damage accumulation where the t_f is predicted using LMP, and crack model to calculate the fatigue crack growth.

[34], [77–83] also developed their own creep life prediction model by incorporating LMP. Except for [79], the inputs used to perform both thermal and stress analyses were obtained from a gas turbine performance simulation model. However, in [79], the temperature and gas pressure were determined using the thermodynamics relations of a Bryton cycle. Moreover, in [34], [77], [80], [82], 0D thermal analysis was used to predict the component bulk metal temperature compared to [78], [81], [83], who used 1D thermal analysis to obtain metal temperature variation across the blade span. The stress models created by these authors also differ in terms of what sort of stresses contribute to the total blade stress. In [34], [77], [82], only centrifugal stress is considered as the main contributing stress factor; in [81], [83], both centrifugal stress and bending moment stresses are considered; in [78], centrifugal, bending moment, and thermal stresses are considered; while in [79], centrifugal, bending moment and shear stresses are considered.

DiCristoforo et al. [84] also utilised LMP, when they reviewed the design of the second stage turbine blade of the GE MS6001 in order to achieve low stress distribution in a high temperature region. In their method, the reduction of the creep deformation was reduced by iteratively redesigning the airfoils by shifting the blade section's centre of gravity, so that a favourable bending moment is imposed at the radial location of the highest temperature. In each iterative process, the blade stresses were minimised using a parametric 3D FE model. Detailed geometry was acquired through reverse engineering while operating parameters were obtained from the user's operating database. 3D FE heat transfer analyses were then made for the original and restacking designs. Based on both thermal and stress analyses, the t_f for each design was evaluated using LMP.

2.3.1.2 Creep Life Estimation Using the Strain Based Model

When using the strain based model, the life span of the material is predicted either by direct calculation the t_f via the $\dot{\varepsilon}_C$/ ε_C or by modelling the ε_{Ct} until certain critical creep strain is achieved or certain desired time is required.

Classical Monkman-Grant empirical relation [58] for example provides the means to compute the t_f based on the $\dot{\varepsilon}_{CS}$ obtained at a given component T_M and σ. Monkman-Grant assumes that the t_f increases linearly as the $\dot{\varepsilon}_{CS}$ decreases, thus defining an empirical relation as given in Equation (2-11), with k_{MG} and m_{MG} denoting the empirically determined Monkman-Grant constants. Once both constants have been

determined, t_f can be estimated when $\dot{\varepsilon}_{CS}$ is input for any given stress and temperature.

$$t_f = \frac{k_{MG}}{\dot{\varepsilon}_{CS}{}^{m_{MG}}} \quad \textbf{(2-11)}$$

In [85–87], experimental works were conducted on IN738C, Rene 80, and MAR-M-002 at different σ and T_M regimes. For each σ and T_M, creep tests were carried out and the t_f, ε_C etc. were recorded before the log $\dot{\varepsilon}_{CS}$ against log t_f graph were plotted. Their findings showed that the Monkman-Grant relation was suitable for creep life assessment.

Empirical curve fitting models, such as the Theta projection model and Omega method (see Section 2.2.3), have been successfully used in component creep prediction. Recently Evans [88], Ibanez et al. [89], Bagnoli et al. [90] and Baldan et al. [91] separately performed evaluations on the utilisation of the Theta projection model in providing accurate creep predictions for 1CrMoV rotor steel, NI100 and GTD111 superalloys. Based on their results, it was found that the t_f for any creep test at any combination of σ and T_M in the range studied can be accurately predicted.

In 2003, Yeom [92] used the Omega method to perform the creep life prediction of Alloy 718 which is widely used for turbine disc application. In his research, the Omega method was expressed by the hyperbolic sine law where the $\dot{\varepsilon}_o$ and Ω were expressed as a function of component σ and T_M and the constants used in the expressions were determined empirically. The results showed that the creep life predicted using the Omega method expressed by the hyperbolic sine law provides good agreement with experimental data.

A strain-based model that considers the properties of individual phases has been modelled to reduce the use of empirical properties (i.e. stacking fault energy, material constants, and the modulus) in order to perform creep life estimation. Miodownik et al. [93] used JMatPro (**J**ava-based **Mat**erials **Pro**perties), a software developed by Sente Software Limited to obtain the $\dot{\varepsilon}_{CS}$ and t_f for multi-component commercial nickel based alloys, In their work, the overall properties of the component are obtained through computation and integration of the properties of individual phases such as thermodynamic properties, mechanical properties, stacking fault energy etc. Access to individual phase properties allow self-consistent calculation of the respective parameters required for t_f computation.

A more advanced strain based model has been developed by taking into account the creep deformation at a micro-level. This was done by developing a numerical strain-based model that considers the anisotropic behaviour of the material and modelling the creep deformation at slip system level to determine the resolved shear stress and the local shear creep strain accumulation.

Such work has been reported by Harrison et al. [94] and Shepherd et al. [95] in which they assume that the creep deformation occurs at 12 octahedral and 6 cuboidal slip systems. When a uniaxial load is applied for each slip system, the resolved shear stress was determined before the shear creep strain was calculated using a modified Graham-Walles equation to obtain the shear creep strain for a given increment of time. The contribution of shear creep strain for every slip system was then resolved to give the total creep strain on the global axis of the model. Determination of the creep life is done by investigating the time required to achieve a certain limiting strain.

Apart from those authors, there are also several other models that are similar, such as in [22], [96], [97]. However, all of the works also incorporated damage parameters in their models which will be discussed in a later section.

2.3.1.3 Creep Life Estimation Using the Damage Based Model

The progress of creep deformation can be viewed as a progressive damage occurring in a material which in time will lead to material failure. In view of this, the two most prominent damage theories, which are the linear damage accumulation (LDA) theory and the continuum damage mechanics (CDM), have often been used in component lifing models.

In LDA, the damage accumulation is assumed to be a linear process with damage, D_{LDA} beginning from zero (for undamaged material) and increasing linearly during the creep deformation until D_{LDA} reaches unity when the material fails. The most widely used LDA equation is given by Robinson [98] which defines the D_{LDA} as

$$D_{LDA} = \sum \frac{t_i}{t_{fi}} \quad \textbf{(2-12)}$$

where t_i and t_{fi} denote the time spent and time to failure under condition i respectively. According to him, the life consumption of each particular fraction of the life span, at an elevated temperature, is independent of and without influence upon the expenditure of all other fractions of the rupture life [98]. Equation (2-12) in some other literatures is also known as the Robinson rule or the life fraction rule.

Equation (2-12) allows the computation of damage when the material is exposed under various mechanical and thermal loadings such as when the gas turbine is being operated under different operation or mission profiles. Under these conditions, different t_{fi} will be calculated with higher σ and T_M exhibit the lowest t_{fi}.

The t_{fi} in Equation (2-12) can be done either by using creep rupture data obtained from various recorded experiments or by using the life-based models or strain-based models as discussed in the previous section. Works as such as [22], [34], [73–77], [99], [100] have incorporated the LDA in their component creep life assessment.

In CDM, damage accumulation occurring in a material is done by introducing a damage state variable, ω_{CDM} that describes the irreversible evolution of the material damage with t. Similar to LDA, in CDM, ω_{CDM} changes progressively from zero (undamaged material) to unity at which failure occurs. The theory was developed by Kachanov and Rabotnov in the 1960s and has found widespread application in the analysis of stress rupture and creep [101]. Generally, the damage rate, $\dot{\omega}_{CDM}$ or $d\omega_{CDM}/dt$ is defined as a function of σ, T_M and ω_{CDM} ($\dot{\omega} = f(\dot{\sigma}, T, \omega)$) and can be written as

$$\dot{\omega}_{CDM} = C_{CDM}\left(\frac{\sigma}{1-\omega_{CDM}}\right)^{v_{CDM}} \quad \textbf{(2-13)}$$

where C_{CDM} and v_{CDM} are constants of the constitutive equation. Integrating Equation (2-13) between the limits $\omega_{CDM} = 0$ at $t = 0$ and $\omega_{CDM} = 1$ at $t = t_f$ will give Equation (2-14). Also, integrating Equation (2-13) between the limits $\omega_{CDM} = 0$ at $t = 0$ and $\omega_{CDM} = 1$ at $t = t$ will give the relation of damage evolution as given in Equation (2-15)

$$t_f = [C_{CDM}(v_{CDM}+1)\sigma^{v_{CDM}}] - 1 \quad \textbf{(2-14)}$$

$$\omega_{CDM} = 1 - \left(1 - \frac{t}{t_f}\right)^{\frac{1}{v_{CDM}+1}} \quad \textbf{(2-15)}$$

The creep life prediction using the CDM approach has shown remarkable progress since it was first introduced. The work involves incorporating several damage mechanisms into the CDM formalism, re-formulation of the classical CDM constitutive equations, applying the CDM into complex 3D FE analysis with consideration of the material's anisotropic behaviour, hence turning CDM into more complex creep life

modelling and estimation approach. Some of the recent work involving creep life modelling and life estimation is given below.

Betten et al. [69] developed a 3D creep damage model for polycrystalline materials with parallel flat micro-cracks. In their work, they assumed that the creep damage is related to the degradation properties of surface discontinuities with a coinciding orientation of parallel planar micro-cracks. By taking the coinciding orientation as a unit vector, a damage vector was introduced as a function of ω_{CDM} and the coinciding orientation unit vector. In their model, ω_{CDM} was defined as the integral product of specific energy dissipation rate with t; where the specific energy was calculated by multiplying the equivalent creep strain rate and equivalent stress.

Qi and Bertram [102] have also developed a 3D anisotropic creep damage model for face-centred cubic (FCC) single crystals. The scalar form of ω_{CDM} is converted into a damage tensor to describe the anisotropic nature of the material. The model accounts for the initial anisotropy of the crystal in the evolution function of the creep and damage variables, and the crack-opening/closure behaviour due to micro-voids and micro-cracks via the activation and deactivation mechanism of the damage. The model has been applied to monotonous creep tests at an elevated temperature in different orientations. The results show that the proposed model is capable of describing both the strong orientation dependence and the non-linearity with respect to the applied load of the entire creep process.

The capability of the model was further tested for the case of multi-dimensional non-proportional loading conditions using the single crystal SRR99 as a case study and has been reported in [103]. Additionally, the model has been coupled with the unified model of Chaboche by replacing the stress tensor in the Chaboche model – this work has been reported in [104].

MacLachlan et al. [105], [106] have investigated the creep behaviour of the single crystal superalloy. In their model, the damage mechanics and the strain rate functions of Kachanov-Rabotnov were revised to include the ultimate tensile strength, UTS as given in Equations (2-16) and (2-17) where u_{CDM} denotes the functions' constant and σ_{eff} denotes the effective stress respectively.

$$\dot{\omega} = C_{CDM}\left(\frac{\sigma_{eff}}{UTS - \omega_{CDM}}\right)^{v_{CDM}} \quad \textbf{(2-16)}$$

$$\dot{\varepsilon}_C = E_o\left(\frac{\sigma_{eff}}{UTS - \sigma_{eff}}\right)^{u_{CDM}} \quad \textbf{(2-17)}$$

Integrating Equation (2-16) while specifying σ_{eff} as $\sigma/(1-\omega_{CDM})$ gave t_f as

$$t_f = \frac{(UTS-\sigma)^{v_{CDM}+1}}{C_{CDM}(v_{CDM}+1)UTS\sigma^{v_{CDM}}} \quad \textbf{(2-18)}$$

and damage profile as

$$\omega_{CDM} = 1 - \frac{\sigma}{UTS} - \left(\frac{UTS-\sigma}{UTS}\right)\left(1-\frac{t}{t_f}\right)^{1/(v_{CDM}+1)} \quad \textbf{(2-19)}$$

It was found that by incorporating the UTS into the revised damage mechanism formulations, the curvature of the stress rupture data can be modelled more accurately.

The MacLachlan model has been utilised by Karaivanov et al. [107] when they developed a 3D FE-based damage mechanism creep modelling for an advanced hydrogen fired turbine system. They used Fluent and ANSYS to perform thermo-mechanical analyses and developed a creep user routine (with the incorporation of the MacLachlan model) for ANSYS to simulate the creep strain, damage equivalent stress, damage parameter and their evolution simultaneously. A solid model of the NASA E^3 blade was created using Pro/Engineering and the airfoil was modelled as a single crystal with material parameters taken from CMSX-4. Using their model, the creep damage distributions were obtained for various projected operating times while the critical regions were identified.

MacLachlan et al. [108], [109] and Knowles and MacLachlan [110] have also developed an FE slip system-based damage mechanism creep model by considering the effects of rigid body rotation, slip system softening, strain rate hardening, threshold behaviour and high temperature rafting. In their model, the slip was considered on the two most activated families of the slip system occurring on modern single crystal superalloys. The model was implemented as an ABAQUS User Material (UMAT) and the framework was based on established theory of crystal plastic. The implementation of the model to analyse the creep deformation on a cooled HP turbine blade has been reported in [109]. A constant cross section blade design was constructed using ABAQUS. Using the model, several contour plots, such as the blade temperature profile, elastic thermal stresses, damage for both activated slip system and angle of rigid body rotation were simulated.

Vladimirov et al. [111] have also developed an FE slip system-based damage mechanism creep model by using the single crystal plastic model developed by Cailletaud [112] and combining the CDM approach by introducing ω_{CDM} for each slip

system in order to provide accurate anisotropic creep modelling at all three creep stages. The work differs from that of MacLachlan et al. [108] who also used single crystal plasticity theory in their model in the way ω_{CDM} is incorporated into the model. For the MacLachlan model, ω_{CDM} was incorporated in the σ_{eff} formulation while in the Vladimirov model, ω_{CDM} was included in the resolved shear stress formulation (for each slip system).

Yu et al. [113] have also developed an FE slip system-based damage mechanism creep model using a modified form of the Kachanov-Rabotnov damage law. The creep damage equations developed were based on the relationship between shear creep strain rate, damage rate and the resolved shear stress. Similar to the MacLachlan model [108], the resolved shear stress was calculated via the slip plane normal and slip direction. The proposed constitutive equations have been implemented into UMAT of ABAQUS.

Esposito and Bonora [114] have proposed a new formulation of damage mechanism by defining the damage evolution based on the accumulated creep strain rather than time. By incorporating ω_{CDM} in the Norton Law relation, $\dot{\varepsilon}_C$ was defined as Equation (2-20) with A_{CDM} denoting the equation constant and n denoting the stress exponent.

$$\dot{\varepsilon}_C = A_{CDM} \left(\frac{\sigma}{1-\omega_{CDM}}\right)^n \quad \textbf{(2-20)}$$

In their model, ω_{CDM} used in Equation (2-20) is defined as

$$\omega_{CDM} = \omega_{CR}\left\{1 - \left[1 - \frac{\ln(p_c/\varepsilon_{th})}{\ln(\varepsilon_f/\varepsilon_{th})} R_v\right]^{\alpha_{CDM}}\right\} \quad \textbf{(2-21)}$$

where ω_{CR} is the critical damage, p_c is the effective accumulated equivalent creep strain, ε_{th} is the damage threshold strain at which creep damage initiates, ε_f is the failure strain at which failure occurs, α_{CDM} is the damage exponent that determines the shape of the damage evolution and R_v is the triaxial coefficient that accounts for the stress triaxiality effect.

A_{CDM} and n in Equation (2-20) were determined empirically using available creep data. Using the plot of $\log \varepsilon_C$ and ε_C, ε_{th} was determined as a point at which the slope of the plot changes at the end of the secondary and the beginning of the primary creep, while both ω_{CR} and α_{CDM} were determined by an iterative numerical solution fitting procedure. The application of the model was done by investigating the creep damage evolution of IMI834 Titanium alloy (widely used in HP parts of axial compressors).

Ashby and Dyson [115] have introduced a physically-based CDM in recognition of the in-service material microstructural degradation. The effort was to place published knowledge relating to the mechanism of microstructural degradation within the mathematical framework provided by CDM. According to Dyson [116] if the material damage can be categorised based on the kinetics of the damage evolution, then broad categories will emerge which are Strain induced damage such as the mechanism of grain boundary cavitation, sub-grain coarsening, and mobile dislocation; Thermally induced damage such as particle coarsening and solid solution elements and Environmentally induced damage in which the damage rate follows either the strain induced or thermally induced damage with the additional incorporation of chemical interaction with containment fluid.

Dyson had summarised (see Table 1 in his paper) the equations used to relate the above mentioned damage mechanisms with, ω_{CDM}, $\dot{\omega}_{CDM}$, and $\dot{\varepsilon}_C$. For example, the ω_{CDM}, $\dot{\omega}_{CDM}$, and $\dot{\varepsilon}_C$ for multiplication of mobile dislocation are written in Equations (2-22), (2-23), and (2-24) with ρ_d, C, and H denoting the dislocation density, material constant and hardening parameter respectively.

$$\omega_{CDM} = 1 - \frac{\rho_{d_o}}{\rho_d} \tag{2-22}$$

$$\dot{\omega}_{CDM} = C(1 - \omega_{CDM})^2 \dot{\varepsilon}_C \tag{2-23}$$

$$\dot{\varepsilon}_C = \frac{\dot{\varepsilon}_{C_o}}{(1 - \omega_{CDM})} \sinh\left(\frac{\sigma(1 - H)}{\sigma_o}\right) \tag{2-24}$$

The equations described by Dyson have been recently used by Djakovic et al. [117] when they developed a CDM model to predict the creep deformation of aluminium alloy 2650-T8. The model developed considers several microstructural degradation mechanisms such as the hardening defined by the H, multiplication of mobile dislocation with damage parameter given in Equation (2-22), particle coarsening with ω_{CDM} as defined in Equation (2-25) and grain boundary cavity growth.

$$\omega = 1 - \frac{r_o}{r} \tag{2-25}$$

where r_o and r denote the average effective particle radius at $t = 0$ and at $t = t$. By combining all the damage mechanisms, the total creep strain was computed. Although aluminium alloy 2650-T8 is not used for gas turbine components (it is mainly used for supersonic aircraft fuselage skin), the method used by Djakovic can be applied to other materials.

2.3.2 Service-Based Approach

The service-based approach involves damage evaluation and remaining life assessment of the service exposed component, which requires direct access to the components. The present status of the component's material is positioned within the standard scatter band either by measuring its properties, hence providing a refined prediction or direct assessment of the extent of the damage experienced by the component as a result of actual service exposed [55].

The main methods of assessing the remaining life will involve both non-destructive tests (NDTs) and destructive tests (DTs).

2.3.2.1 Remaining Life Assessment Using the NDT technique

NDT is a non-invasive technique used to assess or predict the performance and service life of a component [118]. Although there are numbers of NDTs reported in [118], several techniques are found to be favourable in assessing the anomalies of the gas turbine blades such as visual inspection using tools such as a fiberscope or boroscope to perform surface inspection, dye penetrant testing to examine surface opening cracks, eddy current technique for detecting and sizing of a crack, ultrasonic technique to detect cracks in the shoe of the blade, and radiographic technique normally through wall measurement with film or real time radioscopy, X-ray diffraction method, X-ray tomography, neutron tomography and neutron radiography [119–123]

Metallographic analysis by means of replication technique [124], [125] is another form of NDT often used to assess the microstructural degradation of the material. Using the replica sample, qualitative and quantitative assessments are done to relate the levels of microstructural damage to life usage. Neubauer and Wedel [126] have classified creep damage due to creep cavitation into different stages (undamaged, A, B, C and D) and for each stage remedial action is prescribed, as shown in Figure 2-21. When non-destructive metallographic analysis is performed, the present level of damage can be classified according to the proposed classification, hence proper remedial action can be taken.

According to Viswanathan [127], the damage classification made by the Neubauer and Wedel scheme can be correlated with the component life fraction, LF. Figure 2-22 provides an example of the correlation between cavity classification and life fraction for 1Cr-0.5Mo tested at 570°C.

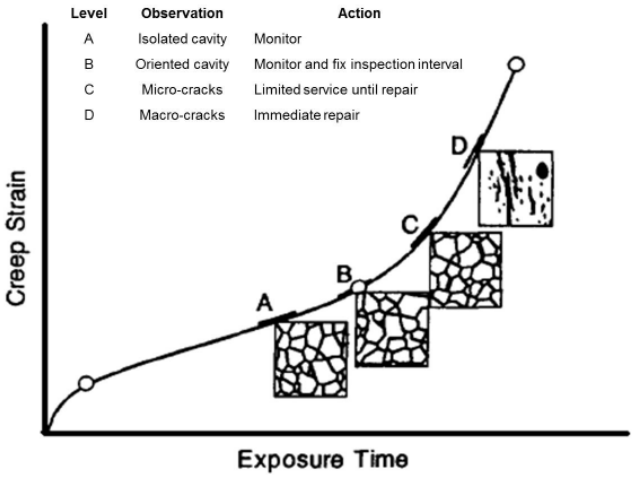

Figure 2-21: Classification of creep damage [127]

Similarly, when non-destructive metallographic analysis is performed, LF can be determined hence the component remaining life, t_{rem} can be calculated using Equation (2-26).

$$t_{rem} = t_{spent}\left(\frac{1}{LF} - 1\right) \quad \textbf{(2-26)}$$

where t_{spent} denotes the time already spent in service.

A similar technique has also been used in correlating other microstructural degradation with LF, service time or temperature exposure time. Such correlations have been reported in [128], [129].

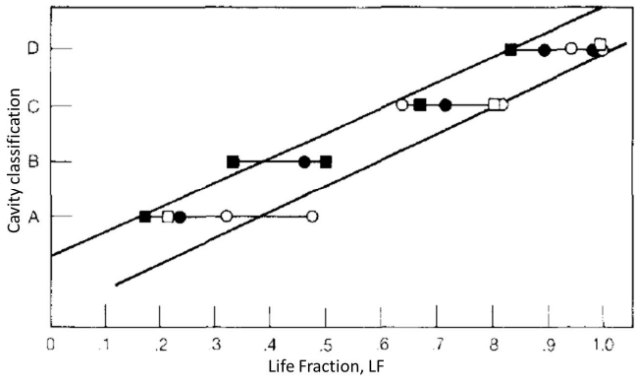

Figure 2-22: Correlation between cavity classification and life fraction of 1Cr-0.5Mo

2.3.2.2 Remaining life assessment using DT technique

Although the NDT life assessment techniques provide invaluable evidence as to the condition of a component, the most reliable method of life prediction is that of direct

creep testing of material removed from service [128]. Using the removed component, a standard sized creep specimen will be tested using the DT technique. A typical destructive evaluation includes metallography to identify cracks, cavities, coating degradation and grain boundary carbide particles, tensile tests to determine the strength or ductility degradation, impact tests to determine the extent of toughness degradation, hardness test, stress rupture test, and creep test. Using the destructive evaluations, the remaining life of the component will be determined.

Maraleh et al. [45] conducted a creep life prediction for a service exposed nickel-based superalloy IN738 turbine blade. A stress rupture test at 850°C with different applied stresses was conducted using four turbine blade samples from different service lives (30,000 hours, 45,000 hours, 60,000 hours and 80,000 hours) and compared with an unexposed sample from the same material. Based on the test data, the residual life of each service exposed turbine blade was calculated using LMP and life fraction rule and plotted, as shown Figure 2-23.

Similar work has been carried out by Vaezi and Solaymani [130] when they investigated the remaining life of an ABB-130 gas turbine blade which had been in service for 61,000 hours. Three DT techniques, i.e. metallographic assessment, creep test and hardness test, were first used to investigate the damage level of the blade. Then, using LMP relationship, t_f was determined. Based on the calculation, it was found that despite the blade being in service for 61,000, the remaining life of the blade was approximately 32,000 hours.

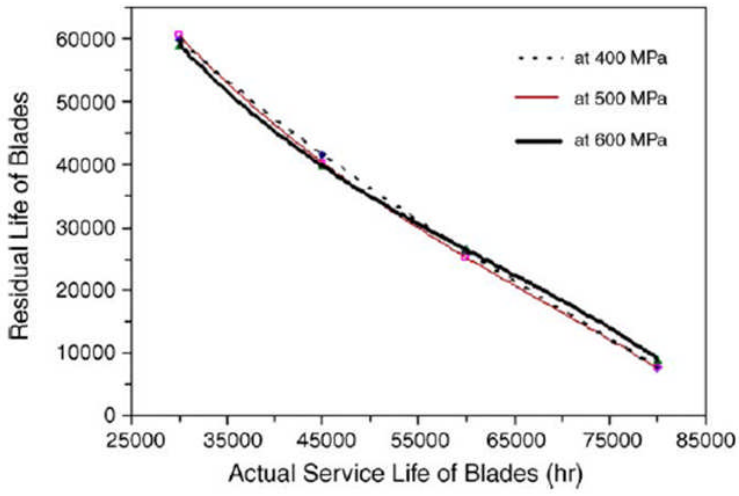

Figure 2-23: Relationship between the actual service and residual life [45]

2.3.3 Statistical / Probabilistic Approach

Although a statistical approach has been partially used in some of the approaches discussed earlier, most of the approaches (empirical-based model, such as the time temperature parameter, Omega method, Theta projection method, etc.) used statistics in order to assist the model development which in general is deterministic in nature.

In a statistical/probabilistic approach, statistical/probabilistic theory is used as the main lifing method. This approach is used either as a means to substitute the existing model, or as a means to account for uncertainties in the influencing parameters or variables that will affect the creep life behaviour, or to provide the basis of performing failure risk analysis. In this section, some works relating to this approach are discussed.

Holdsworth and Davies [131] reported a new procedure for the assessment of creep rupture data developed in the UK under BSI PD 6605 [132], [133]. In the new procedure, three classical algebraic models and four time temperature parameters were substituted with 18 statistical fitting models. Some of the proposed statistical fitting models are given in Equation (2-27) and (2-28) for substituting LMP and OSD. The other forms of the fitting models suggested by the standard can be seen in [131–133]. In both equations, β_k is known as the statistical fitting constant.

$$\log t_f = \{\sum_{k=0}^{n} \beta_k \log[\sigma]^k\}/T_M + \beta_5 \qquad (n = 2,3,4) \tag{2-27}$$

$$\log t_f = \{\sum_{k=0}^{n} \beta_k \log[\sigma]^k\}\beta_5/T_M \qquad (n = 2,3,4) \tag{2-28}$$

In BSI PD 6605, the initial 18 fitting models were all fitted to a given material creep data using maximum likelihood statistics where, by using this method, β_ks were numerically estimated. The most suitable fitting model was then selected on the basis of its deviance and the results of several post assessment tests suggested by the standard. The application of BSI PD 6605 on Alloy 617 can be found in [134], and on 12Cr alloy steel, with two improved fitting models designated as ADA and SDS models, can be found in [135]. In addition, similar work has also been done by Eno and Young [67] using similar forms of statistical fitting models for Alloy 617 and HAYNES® 230.

Uncertainties in measurements and influencing parameters can be investigated using the statistical/probabilistic approach. Koul et al. [136] had performed a Weibull probabilistic analysis in order investigate the variation in some microstructural parameters such as grain size, grain boundary precipitate size and inter-particle spacing. Prior to conducting the probabilistic analysis, a deterministic analysis was

initially performed using the numerical damage-based creep model (model-based approach) [137] in order to obtain the critical nodes. By randomising the microstructural parameters, a three-parameter Weibull distribution was formed. Then the critical nodal creep lives at a cumulative probability failure of 0.1% were estimated.

Koul et al. [138] extended their work when they performed a probabilistic analysis on an F5001P turbine disc. Using a 3D FE damage-based model which constituted a combined creep and oxidation damage, fracture critical locations were initially determined. By randomising the grain size, a Log-normal plot was constructed before the combined creep life at the fracture critical location at a cumulative probability failure of 0.1% was estimated.

Liu et al. [139], [140] have proposed a simplified model of creep life assessment using the statistical-based Response Surface Method (RSM) in order to reduce the complexity and computational burden of the current creep life prediction. Log creep life was taken to be the response, R while several variables were taken as independent variables. In [139], only gas temperature and rotational speed were considered while in [140], seven variables were considered before four of them were finalised. Relationship between the independent variables and creep life was developed using a Response Surface Equation (RSE), as given in Equation (2-29), with b and x denoting the RSE coefficient and independent variable respectively. To obtain the creep life 3D-FE based creep models (model-based approach) were used as inputs to generate RSE. The final RSE for [139] is given in Equation (2-30) with T_g and N denoting the gas temperature and rotational speed.

$$R = b_0 + \sum_{i=1}^{k} b_i x_i + \sum_{i=1}^{k} b_{ii} {x_{ii}}^2 + \sum_{i=1}^{k} \sum_{j=i+1}^{k} b_{ij} x_j \quad \textbf{(2-29)}$$

$$\log t_f = 5.31 - 0.592T_g - 0.172N + 0.00011T_g N + 0.263{T_g}^2 + 0.009N^2 \quad \textbf{(2-30)}$$

Once the RSE has been established, probabilistic analysis is done by using Monte Carlo simulation [140] where, for a given constant operating condition, variations of the independent variables were specified according to normal distribution hence the distribution of R was formed. Based on their results, they discovered that the component could be in service for 129,526 hours, some 97,918 hours longer than the traditional method. Lui et al. [141] expanded the utilisation of RSM and Monte Carlo simulation to develop a computationally efficient probabilistic creep-fatigue life assessment by integrating a historical operational profile and forecasting a future

operating profile. Similarly, for each segment of the operational profile, a probabilistic distribution of independent variables were fed into the RSE and accumulative probabilistic distribution of the R was computed. Some works that also used RSM and Monte Carlo simulation for probabilistic analysis on gas turbine blades can also be found in [142] and [143].

2.3.4 Soft Computing Approach.

Although the model-based and service-based approaches have been successfully used over the years, limitations and complexity of the approaches have driven researchers to use another form of creep life estimation approach. For this reason, soft computing techniques such as ANN, fuzzy logic and evolutionary algorithm have been used. Among these soft computing approaches, ANN has been predominantly used. In this section some of the works which involve the application of ANN in creep modelling and life prediction will be given.

The majority of the works at present involve creating an ANN model that is capable of predicting t_f when different combinations of influencing parameters are used as inputs to the ANN model. Sourmail et al. [144] have used the Bayesian neural network in order to express t_f and creep rupture strength (stress required to cause failure) of austenitic stainless steel as a function of chemical composition, test condition, stabilisation ratio, and solution treatment temperature. In their work, samples used to train and test the network were obtained from a gathered material database which contains a wide range of composition of the material group. Similar work was done by Maritza et al. [145]. In their work, chemical composition and operating condition were used as inputs to predict t_f, creep rupture strength, yield stress and UTS of a new iron-based superalloy. The database of the material group was also used to train and test the network. In both works, predicted outputs were in agreement with outputs obtained from the database.

Yoo et al. [146] have also used the Bayesian neural network to predict t_f of a single crystal Nickel-based superalloy with alloy composition, creep stress and temperature used as inputs. However, in their work, the Markov-Chain Monte Carlo training algorithm was used to train the network. It was found that the network is able to produce good t_f prediction with a correlation coefficient of 0.932.

Both Ibanez et al. [147] and Frolova et al. [148] have used a multilayer feedforward back propagation (MFBP) neural network in predicting the t_f of GTD 111

superalloy and 9%Cr Steel respectively. However, in the work of Frolova et al., the creep rupture strength was also predicted. Inputs to perform the prediction were different between the two works. In the work of Ibanez et al., temperature, stress, orientation of how the specimen is machined and batch number were used as inputs while in the work of Frolova et al., chemical composition, heat treatment parameters and product form were used as inputs. In addition, samples used to train and test the network in the work of Ibanez et al. were taken from the creep testing conducted by them while in the work of Frolova et al., samples came from the material database.

Gupta et al. [149] have also used an MFBP neural network to predict the creep properties of a rotating composite disc. In their work, a mathematical model of steady state creep behaviour has been developed in order to provide the inputs-outputs samples to train and test the network. Radial and tangential stress, radial and tangential strain rates were selected as the network outputs while particle size, particle content, operating temperature, and radial distance have been specified as the network inputs. A 4-30-30-4 sized network was created and trained using the training samples obtained from the mathematical model. Once training was completed, the network was tested using unseen samples and comparison between the output produced by the network and the mathematical model was made. It was found that excellent agreement was achieved especially near the inner radius of the disc. Maximum variations, however, were observed in radial and tangential strains with values reaching 16 to 13%.

Besides using the ANN to predict the material t_f for a given set of inputs, ANN has also been used to predict the influencing parameter(s) prior to creep assessment. Jeong and Kim [150] have used ANN to predict the porosity content in a material in order to develop an NDT technique for the quantitative estimation of creep damage. Based on the experimental results obtained at different creep life fractions, ultrasonic velocities and material porosity were measured; the material void aspect ratio was then calculated using a micro-mechanical equation. Two types of network (Types 1 and 2) were constructed using MFBP. In Type 1 network, ultrasonic velocities and material porosity were selected as model inputs and output respectively. On the other hand, in Type 2 network, ultrasonic velocities and void aspect ratio were used as model inputs while material porosity was selected as model output. In addition, in the Type 2 network, an additional MFBP network was constructed in order to predict the void aspect ratio for given ultrasonic velocities. It was found that both networks were able to give good porosity prediction with Type 2 network being better than Type 1.

Zarrabi et al. [151] incorporated ANN into their proposed creep damage model in order to obtain the creep internal energy which they assumed to be proportional to the material creep damage. MFBP neural network was used in their study where the output and input to the model are the creep internal energy and time respectively. The predicted internal energy using the ANN model was further used to obtain the creep life of the component. Validation was carried out on 2.25%Cr1%Mo steel and the predicted and experimental creep lives were then compared.

Parthasarathy et al. [15] used a dynamic neural network to predict the critical location metal temperature of a given mission profile based on the inputs of rotational speed, near-critical location gas temperature and mass flow. Once training had been completed, an unseen mission profile was then used to test the performance of the network. The neural network predicted temperature for the given unseen mission profile was found to be in good agreement with the FE predicted temperature with maximum prediction error to be around 10%.

The works discussed in the previous paragraphs have shown the capability of ANN as an approximator to approximate creep properties. Beside its approximating function, ANN has also been used to perform creep damage classification. Dobrzanski et al. [152] have used a self-organising neural network to perform damage classification of different levels of microstructural damage by means of image recognition. In their work, five classes of damage level: Class I – structure close to initial stage, Class II – possibly of singular void, Class III – oriented voids, chains of voids, linking of voids, Class IV – micro-fractures, and Class V – macro-fractures, were defined. Images taken from the scanning electron microscope (SEM) for each class of damage level were digitally processed, hence features defining each class of damage level were defined and used as input vectors. The output of the network is the classification of the defined damage level. Several sizes of network were created and the best network was chosen based on the classification efficiency. Using unseen samples of different damage levels, classification efficiency was measured. It was found that the efficiency of the classification was 92%.

Dobrzanski et al. [153] further extended his damage classification method by replacing his previous self-organising network with an MFBP neural network. In this work, although the same damage classes were used to classify the damage level of 13CrMo4-5 low alloy steel, different features were used to define each class of damage level.

2.3.5 Summary of the Creep Life Estimation Approach

Figure 2-24 provides a visual summarisation of the creep life estimation approaches discussed in Section 2.3 which in general can be classified into four broad approaches which are the Model-Based approach, Service-Based approach, Statistical /Probabilistic-Based approach and Soft Computing approach.

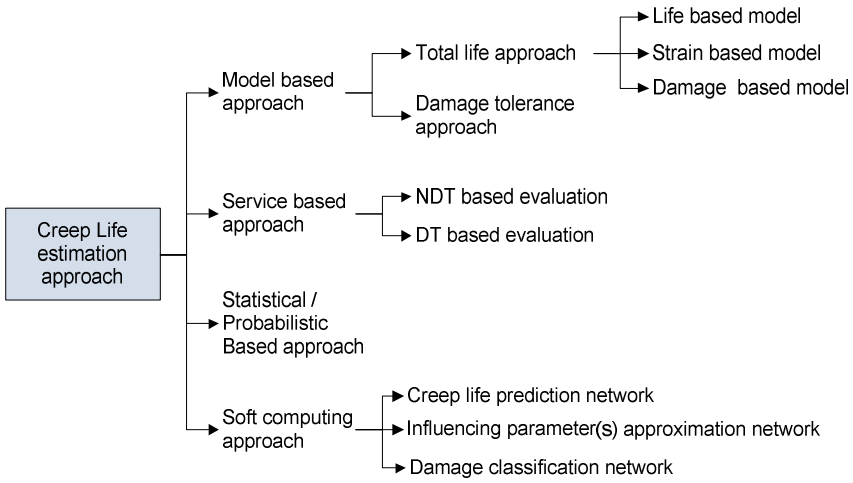

Figure 2-24: Summary of creep life estimation approach

The model-based approach which involves model creation for creep behavioural representation and life prediction can be further classified into two sub-approaches: which are the total life approach and damage tolerance approach. The main features and methods of different models in the total life approach are given in Table 2-3.

The utilisation of time temperature parameters provides the simplest form of creep life estimation. Because of the simplicity of the approach and the ease of obtaining the parameter master curves in the open literature, this method is still widely accepted. The challenge with this approach is how the external analytical or numerical models (i.e. the performance, diagnostic, thermal and stress models) are developed and coupled to form an integrated lifing framework.

When dealing with an analytical model in order to perform thermal or stress analyses, the accuracy of the analyses will depend on the decision whether to perform the analysis in 1D, 2D or 3D; it also depends on how many contributing elements are included in the models (i.e. incorporation of bending stress, centrifugal stress, thermal stress, uniform or non-uniform gas temperature distribution, type of cooling technology etc.). As more elements are considered, the complexity of the model and the amount of information required for the model will increase.

Table 2-3: Features and method of different models in total life approach

	Main Features	Method
Life-based model	t_f is directly predicted by form influencing parameters.	Utilisation of time temperature parameter
Strain-based model	t_f is directly predicted via $\dot{\varepsilon}_C$ or ε_C or modelling ε_C until critical state.	• Utilisation of Monkman-Grant, Dobes-Milicka or Koul relation. • Utilisation of fitting model such as Theta projection and Omega method • Inclusion of material individual phase • Consideration of a material anisotropic behaviour
Damage-based model	Damage is accumulated until material fail. Fractional life span and damage parameter is introduced.	• Utilisation of LDA theory by accumulating fractions of life span until it reaches unity. • Utilisation of CDM to account for irreversible evolution of material damage with time

Accuracy of the thermal and stress FE analyses on the other hand will depend on the complexity of the constructed model (2D or 3D), mesh density, types of element, determination of boundary conditions, and also how creep constitutive equations should be incorporated in the code. Often CFD analyses are performed in order to obtain proper boundary conditions of the internal and external surfaces. In addition, as the complexity of the current approach increases, the computational time also increases.

Both numerical and analytical models used to perform the thermal and stress analyses require inputs from a performance simulation model. Input for the performance model, however, can come from either a data acquisition system or be manually input.

A strain-based empirical model, such as the Monkman-Grant, Dobes-Milicka and Koul relationships, also offer the simplest solution to creep life estimation. More complicated empirical models are those of empirical curve fitting models such as the Theta projection or Omega method. These methods, although relatively simple, require the determination of respective constants via creep test data, manipulation of natural logarithm/logarithmic plots or non-linear optimisation algorithms.

A strain-based model that considers detailed analysis of individual phases of the material, modelling the anisotropic behaviour of the material and developing constitutive creep equations at a micro-level, provide a more advanced solution. These models minimise the dependency on empirical data and provide a more realistic investigation of creep deformation, thus improving the creep life estimation.

LDA theory provides the simplest form of damage-based life assessment. Due to the underlying principle that discounts the historical influence of the progressing damage, the damage calculation becomes rather crude and less accurate. A better damage-based life assessment that accounts for damage evolution of the material has been developed using the CDM approach. Within recent decades, improvements to the CDM approach have been made in several ways. These involve modification of the classical CDM constitutive equations at a macro or micro level, consideration of in-service microstructural degradation and different creep damage mechanisms, performing creep damage assessment via 3D FE analysis, incorporating CDM in slip systems deformation through FE analysis, and proposing new formulation of CDM by defining the damage evolution based on the accumulated creep strain rather than time.

Life assessment using a service-based approach requires direct access to the service exposed component through NDT or DT. NDT techniques such as visual inspection, dye penetrant testing, eddy current testing, radiographic testing are often used to detect anomalies in gas turbine blades. In addition, metallographic analysis by means of a replication technique provides another way to access the state of microstructural damage, hence by using a correlated component life fraction, the remaining life of the component can be assessed.

The DT technique is seen as the most reliable method of creep life prediction and is done by removing the components from service. Using the removed component, several destructive evaluations such as metallography examination, impact test, hardness test, stress rupture test and creep test can be performed; the remaining life is then determined using any parametric method such as LMP and the life fraction rule.

The statistical fitting model used in the statistical/probabilistic-based approach provides another form of creep rupture data assessment. The fitting model can be derived either from the existing classical algebraic models or time temperature parameters. In addition to that, statistical RSM can also be used to simplify the existing complex model-based approach by creating a functional relationship between the creep life and several functional parameters.

Apart from that, statistical/probabilistic theory has also been used to account for variations in the microstructural parameters and their effect on creep life prediction. Weibull and log-normal distributions are often used in the analysis. Additionally, the probabilistic analysis can also be done using Monte Carlo simulation. In some work, both Monte Carlo simulation and RSM have been incorporated to develop a computationally efficient probabilistic analysis.

A soft computing approach by means of ANN has formed another dimension in creep modelling and life estimation due to the limitations and complexities of both model-based and service-based approaches. In the majority, ANN has been used to create a direct mapping between the material t_f and different combinations of the influencing parameters using different types of network. In addition, ANN has also been used to predict influencing parameter(s) prior to creep assessment. The capabilities of ANN to perform image recognition and classification have also been used to create damage classification techniques in order to assess material.

The application of ANN in creep properties' prediction and classification has been, in the main, material oriented. What this means is that most of the inputs selected for the network construction are material featured parameters (i.e. material chemical compositions, stabilisation ratio, heat treatment parameters, and particle size). So far only Parthasarathy et al. [15] have used engine performance parameters (i.e. mass flow, rotational speed and hot gas temperature) as inputs to ANN in order to predict T_M which has been considered to be one of the most influencing factors in changing creep life consumption. The work of Parthasarathy et al. has opened another door to how another form of functional relationship that ties creep life prediction to gas turbine performance parameters in ANN formalism can be created. The success of their work means that it is possible to use ANN as a tool to create a performance-based creep life prediction that could simplify the overall process of creep life prediction for gas turbine application which, at the moment, is complex and multi-disciplinary.

2.4 Chapter Conclusion

The writing in this chapter is divided into three parts. In the first part, a broad discussion regarding different damage mechanisms in gas turbine hot sections is presented. This includes a discussion of HCF, LCF, TMF, high temperature corrosion/oxidation and creep. Also, discussions on how different component functions and applications can influence the dominancy of one particular damage mechanism over another are also given.

In the second part of the chapter, discussion regarding creep deformation is given in a more detailed manner. This includes a discussion on the impact of elevated temperature exposure to microstructural degradation, the phenomena of creep deformation, the creep curve and stress rupture curve, the factors affecting creep deformation, the different methods to model the creep curve, and time temperature parameters.

The last part of the chapter provides an overview of the existing methods in performing component creep life estimation. In this part, the existing methods are classified into different categories and for each category examples of several recent works are provided and discussed. At the end of the chapter, a summary of the creep life estimation approach is given.

3 METHODOLOGICAL APPROACH

This chapter provides the fundamental ground on which the research will be built. In the first part of the chapter, the idea implemented in this research is provided before the research methodology diagram is presented. In the later part of the chapter, explanations are given regarding major research works conducted in order to develop the alternative creep life estimation model. At the end of the chapter, a description of the evaluation process of the proposed model is given.

3.1 Research Idea

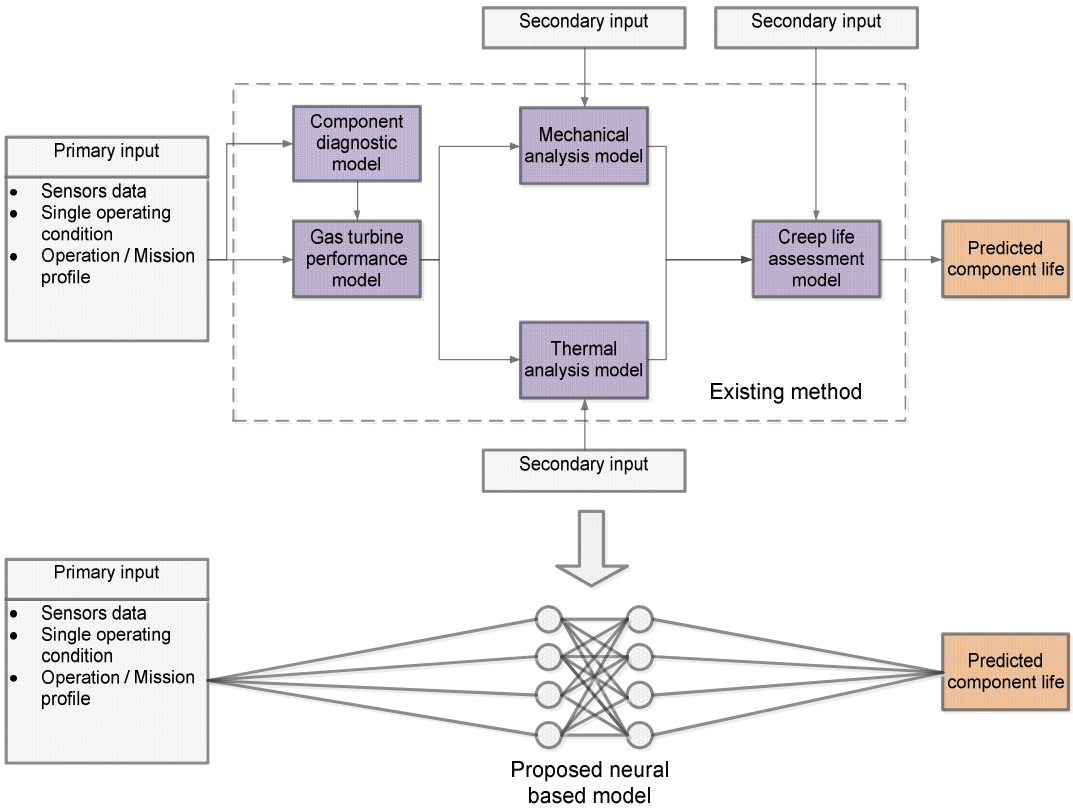

Figure 3-1: Illustration of research idea

As mentioned in the first chapter, the aim of this research is to develop an alternative creep life estimation model that is able to 'absorb' the complexity of the existing creep life estimation methods at a macro level using the ANN technique. The idea of this research is illustrated in Figure 3-1. The existing method shown in Figure 3-1 is an example of a typical integrated creep life estimation process based on the model-based approach which requires both primary and secondary inputs and many complicated sub-processes. Primary inputs are the user's main inputs on which the estimations of

the component creep life are based, such as the operation profile input and the health status of the engine. On the other hand, secondary inputs are those used for sub-processes such as component geometry, material property and thermal characteristics. These inputs remain unchanged and are considered as one-off data entries.

In principle, when the alternative neural-based model is developed, the existing sub-processes and secondary inputs will be absorbed, thus creating a simple alternative solution that can meet the criteria defined in the first chapter. By incorporating the existing sub-processes and secondary inputs, a direct link between the user's desired inputs and the component's estimated creep life can be established. This will permit rapid calculation while maintaining prediction accuracy.

3.2 Research Methodology Diagram

The research methodology diagram depicted in Figure 3-2 provides a summary of how the research was being carried out in order to develop the alternative neural-based model. As shown in Figure 3-2, an integrated creep life prediction model was first developed and integrated with existing in-house performance simulation software called PYTHIA [154]. Then, using the developed integrated model, the neural-based prediction model was constructed. Note also that prior to the development of the neural model, several tasks were performed. These include performing parameter impact analysis on blades' creep life, populating training samples for the construction of the neural-based model, performing a process analysis etc.

Creep lives predicted by both models (integrated and neural) were then compared in order to investigate the performance of the neural model. In addition, a comparison between different proposed architectures developed within the neural model was made. Finally, uncertainty analysis was carried out to measure how well the neural model responds to different levels of noisy or uncertain inputs.

3.3 Development of an Integrated Creep Life Estimation Model

Before the model was developed, several important decisions needed to be made regarding how it should be built. This involved decisions on:

a. the main lifing approach that is going to be implemented;
b. the number of sub-models required and how data will be transfer from one sub-model to another;
c. the governing equations that are required for each sub-model;

d. whether to use analytical, numerical or empirical method for each sub-model created;
e. whether to use a parametric model, damage model or crack model for predicting the blade's creep life;
f. the extent of the model created, i.e. whether to apply the life prediction model to all the major gas turbine components or should the model focus on the most critical one; and
g. the level of improvement that the model will offer.

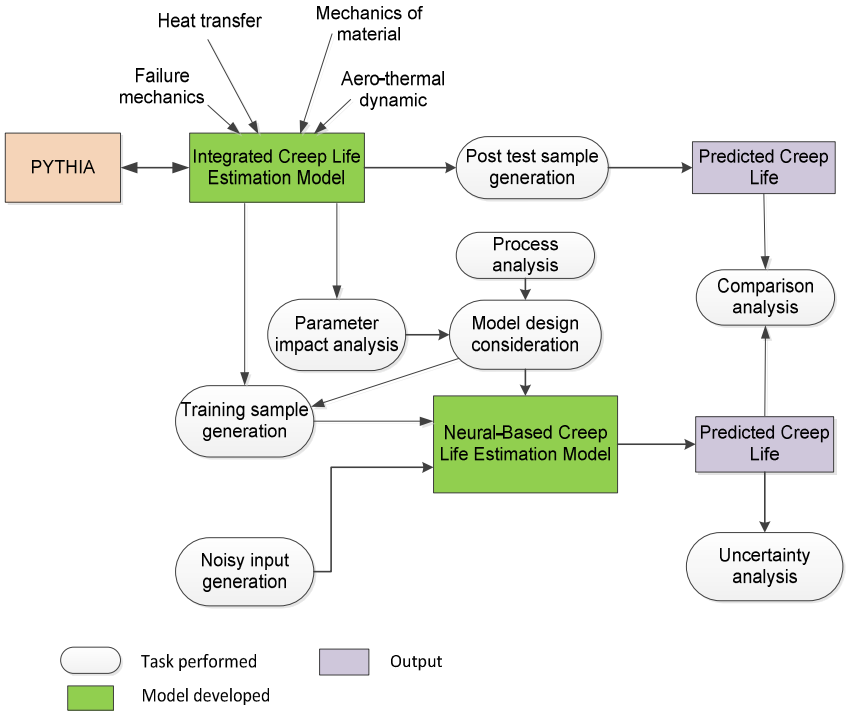

Figure 3-2: Research methodology diagram

Once the decision was made, the integrated creep life estimation model was developed. Using PYTHIA as the main platform, the model was then incorporated to produce a new version of the program with a creep life prediction capability. Several new interfaces were created to tailor the functionality of the developed integrated model. This enabled the user to perform single or multiple stage, cooled or uncooled HP turbine blades' creep life prediction under any given operating and health conditions, either for a single operation point or for any given mission profile, automatically.

In order to perform the parameter impact analysis, as shown in Figure 3-2, a simple relative parameter called Creep Factor was introduced. Using the Creep Factor, the influence of selected operating (i.e. altitude, ambient temperature, rotational speed etc.) and health parameters (i.e. compressor fouling and turbine erosion index) were

quantified. This is necessary as the outcomes of the analysis are used in designing the neural-based model.

Using the developed model, training samples for the development of the neural-based model were also populated; these consist of input parameters at different engine operating and health conditions together with their corresponding creep life. In addition, the model was also used to generate post test samples in the form of either a single operating point or multiple operating points (mission/operation profile) so that comparison analyses between the two integrated and neural-based models could be done.

3.4 Impact Analysis of Different Operating and Health Conditions on the Blade's Creep Life

The analysis aims to investigate how several selected operating and health parameters can have an influence on changing the HP turbine blade's creep life. Using the Creep Factor, the analysis was divided into two parts. In the first part, an impact analysis of several selected parameters on the blade's creep life was individually executed in order to quantify individual impact weight when a unit of the corresponding parameter deviates from a reference operating condition. Having to calculate the impact weight, the sensitivity of each parameter in changing the HP turbine blade's creep life was assessed. This is crucial as the results provide some insights on how samples should be populated via the integrated creep life estimation model in order to construct the neural-based creep life model.

In the second part of the study, the influence of a given mission profile on the HP turbine blade's creep life was investigated with the inclusion of component degradations such as compressor fouling and turbine erosion. The given mission profile was simulated using a clean engine before the same mission profile was simulated using a degraded engine. Using the Creep Factor approach, the impact of both the clean and degraded engines on the HP turbine blade's nominal creep life will be measured.

3.5 Development of a Neural-Based Creep Life Estimation Model

The work focuses on proposing several architectures that can be used to construct a neural-based creep life estimation model suitable to predict the HP turbine blade's creep life in a clean and degraded engine. But before the architectures can be proposed, several considerations need to be made. One of the processes in

determining how the architectures can be moulded is to understand the requirements and the procedures of the existing creep life method which can be called the process analysis, as shown in Figure 3-2. In this analysis, an output-input process tree was constructed. As the neural-based model is treated as an alternative solution to the existing estimation process, the focus of the analysis was to provide a process tree representing the developed integrated creep life prediction model. The outcome of the process analysis was several proposed architectures for both a clean and degraded engine.

Another consideration during the development of the neural-based model is how the sample should be populated. The concern during this stage is what should be made as the inputs and outputs to the proposed architectures. As the proposed architecture is different from one to another, the topology of the neural network for each proposed architecture was decided as well.

Another consideration that is also crucial in implementing the proposed architecture to a specific engine model, is the size of the samples required to train the network. This is dictated by how sensitive each input parameter is in changing the blade's creep life. The outcome from the impact analysis performed using the Creep Factor approach, via the integrated model in this case, is important as the comparison of the impact weight provides a good understanding of how one parameter is different from another. Also, issues such as the appropriate size of the network and the types of training algorithm used to train the network are important when the proposed architectures were applied to the selected engine model.

3.6 Evaluations of the Proposed Architecture

Evaluation of the neural-based model is divided to two parts. The first part looked at the prediction accuracy of the neural-based model when the predicted creep life was compared with the integrated model. Prediction errors were calculated and the overall performance of the proposed architectures was quantified. After having performed the analysis, a comparison between the different proposed architectures was made. In addition, the performance of the proposed architectures was again assessed using the same clean and degraded mission profiles previously used in Section 3.4. Using the integrated and neural-based creep life estimation methods, the mission segment and the nominal turbine blade's creep lives were compared.

The second part evaluates the effects of input uncertainties on the creep life prediction accuracy when different levels of input uncertainty were applied to each

clean engine proposed architecture. Several operating points within the gas turbine operating envelope were randomly selected and treated as the reference operating points. Then for each reference point, random input samples with different levels of uncertainty were populated before they were input into each clean engine's proposed architecture. The predicted creep lives (at each level of input uncertainty and at each reference operating point) were then compared with their corresponding creep lives predicted using their corresponding 'uncertain-free' inputs.

3.7 Chapter Conclusion

This chapter reports the methodology used to carry out the research. The first part of the chapter discussed the idea of the research. By implementing the research idea, the methodological approach is designed and the major tasks involved in this research are clustered, specified and linked to each other which include the development of an integrated creep life estimation model, the impact analysis of different operating and health conditions on the blade's creep life, development of the neural-based creep life estimation model, and evaluation of the proposed neural-based creep life estimation architectures. Later, a description of each major task is given.

4 INTEGRATED CREEP LIFE PREDICTION MODEL

This chapter discusses the overall structure of the integrated creep life prediction model before a detailed algorithm for each sub-model is presented. In addition, it depicts the samples of the program interfaces when the prediction model is incorporated with the existing in-house gas turbine performance and diagnostic software, PYTHIA.

As mentioned in Chapter 3, this integrated model serves several purposes:

a. It is used to generate training samples for the construction of the proposed neural-based creep life prediction architectures
b. It is also used to generated post test samples in order to assess the performance of each suggested neural-based creep life prediction architecture
c. It is used to study the effects of different operating and health conditions on a selected engine model HP turbine blade's creep life.

Although the engine selected for this research is a turboshaft engine, as outlined in the research scope, a generic integrated model is constructed. This is to allow future studies to be carried out using different engines with a different turbine design and cooling technology.

4.1 Model Consideration

Before the model is constructed, several important decisions need to be made. The decisions involve whether to use a model-based approach, a service-based approach, or a statistical/probabilistic-based approach as the main lifing approach; whether to use an analytical, numerical or empirical method for each sub-model created; or whether to use a parametric, damage or crack model for the prediction of creep. Also the research needs to decide whether to apply the life prediction model to all the major gas turbine components or if the model should focus on the most critical one.

It was decided to choose the model-based approach, as discussed in Chapter 2, as the main lifing approach. The main reason for selecting the model-based approach is to reduce any complications when the integrated model is incorporated with PYTHIA which has been constructed using the model-based approach. Moreover, other approaches, such as the service-based approach, were deemed unsuitable for this research as no facilities were available in the Department to perform the necessary testing.

In addition, an analytical approach is selected to perform all of the preceding analyses used to estimate the HP turbine blade's creep life. The decision to use an analytical approach is similar to why the model-based approach was chosen, which was to ensure that integration with PYTHIA could be made easily. Furthermore, the research was looking for a flexible and inexpensive approach that was capable of generating different sizes of training samples to construct the neural-based creep life estimation models.

Despite having several options in hand from which to choose, LMP parametric method was chosen to estimate the HP turbine blade's creep life. Among the reasons for selecting this method is that the method has been applied successfully for a variety of metals over many years [155]. In addition, the master curves are easily accessible in open literature. Also, compared to other methods, the parametric method is relatively easy and covers a wide spread of applications [34], [45], [46], [68].

The life estimation model focuses only on the HP turbine blades. The selection of HP turbine blades is due to the fact that by comparison with other major gas turbine components, HP turbine blades are exposed to the most volatile conditions (high thermal and mechanical loading) which make them vulnerable to creep damage. For this reason, HP turbine blades are considered to be the life limiting component and often influence the inspection and maintenance interval [20],[21].

It was also decided that the model should be flexible enough to perform the life prediction for both single stage and multi-stage HP turbine design with either cooled or uncooled blades coated with thermal barrier coating (TBC). However, at this stage, the model is capable of performing the creep life prediction for up to a 3-stage HP turbine design.

4.2 Overall Structure of the Model

Since the prediction of HP turbine blades' creep life can be computationally very expensive, especially if the most elaborate and time-consuming finite element procedures are applied, the model developed was simplified using a zero(0D) and one dimensional (1D) analytical approach. The overall structure of the integrated creep life prediction model is shown in Figure 4-1. The figure indicates the sub-models created by the author and how the models relate to one another. The figure also depicts the input required for each model before output is delivered from the life usage model and the life estimation model respectively.

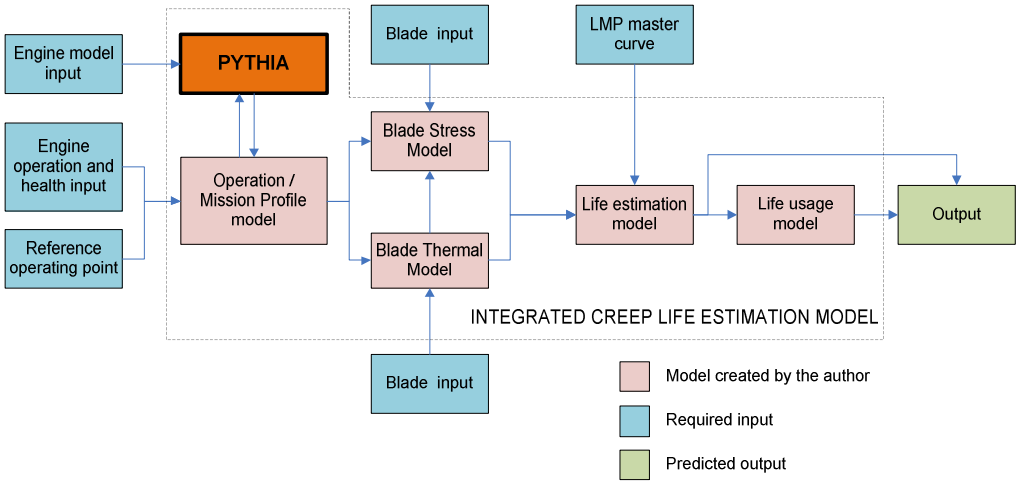

Figure 4-1: Overall structure of the integrated creep life prediction model

From Figure 4-1, it can be seen that there are five sub-models created by the author in order to construct the integrated creep life estimation model which are:

a. The Operation/Mission Profile Model that simulates the performance of a model engine for a given operation/mission profile, a single operating point or a user-defined reference operating condition
b. The Blade Stress Model that calculates the blades stresses
c. The Blade Thermal Model that performs the blade thermal analysis
d. The Life Estimation Model that calculates the blade's creep life; and
e. The Life Usage Model that provides the percentage of blade creep life usage for a given operation history.

4.3 Operation/Mission Profile Model

This model enables the research to carry out performance simulation for a single point or for a given operation or mission profile. This can be done for both clean and degraded engines. Figure 4-2 illustrates the flow diagram of the model.

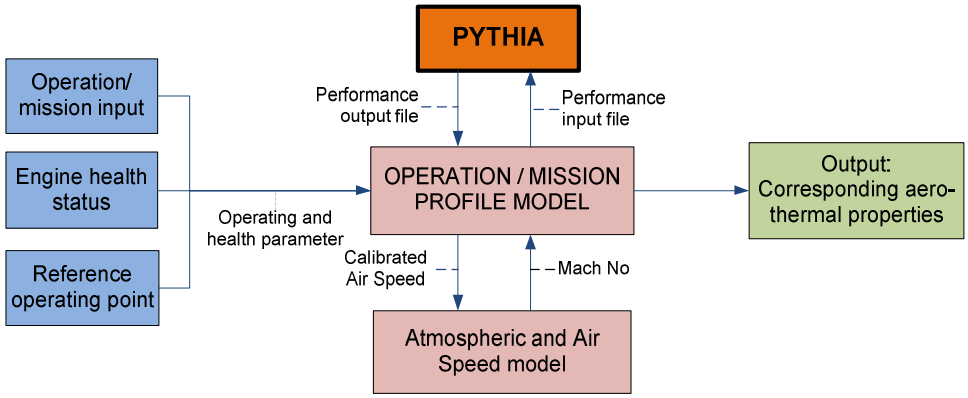

Figure 4-2: Flow diagram for the Operation/Mission Profile Model

When the users define the inputs, as shown in Figure 4-2, the operating parameters, such as the altitude, ambient temperature, rotational speed, calibrated air speed and Mach number, and the health parameters, such as isentropic efficiency and flow capacity indices, are input into the model.

If calibrated air speed (CAS) is defined by the user, the value is sent to the Atmospheric and Air Speed Model to calculate the corresponding Mach number. The reason for calculating the Mach number is because PYTHIA only recognises Mach numbers as the mean of speed. Thus any form of speed, such as the CAS or the true air speed (TAS), need to be converted to a Mach number.

For this model, CAS is used as one of the user's inputs. CAS is the speed shown by a conventional airspeed indicator after correction for position error (the amount by which the local static pressure at a given point in the flow field differs from free-stream static pressure is called the position error of the installation [156]) and instrument error [157]. Hence to calculate the Mach number, CAS needs to be converted to TAS. The procedure to perform the CAS to TAS conversion was adapted from [158] and the algorithm is given in Appendix A.1.

Once the Mach number is calculated, the value will be sent back to the Operation/Mission Profile Model. Together with the other operating and health parameters, a performance input file is generated in order to execute the performance simulation in PYTHIA. The output of the simulation, in the form of a performance output file is sent back to the Operation/Mission Profile Model before the corresponding aero-thermal properties needed for subsequent analysis are extracted.

If a mission/operation profile is inputted, each profile segment (take-off, cruise etc.) operating parameters and the respective operating hours (time spent for each segment) will be divided into smaller segments. The division of the segments will depend on the step size defined by the user. The reason for having smaller step sizes is to allow a rapid-change segment to be included in the life estimation process. Similarly, a performance input file accounting for all profile segments is then generated for subsequent performance simulation in PYTHIA.

4.4 Blade Stress Model

This model considers the effects of centrifugal loading and gas bending moment as its main sources of stress. Once the engine aero-thermal properties have been simulated, the values are inputted into the stress model to calculate the blade's stresses due to

the centrifugal load caused by engine rotation and the gas bending moment caused by the change in gas momentum and the presence of a static pressure difference.

A pseudo 2D analytical approach is applied where the variations of the blade stresses are predicted at several specified locations along the blade span and the blade chord. Along the blade span, four locations which are at the blade root, 25% distance from the blade root, mid span, and 75% distance from the blade root are specified. For the blade chord, three locations which are the blades trailing edge (TE), leading edge (LE), and the furthest point at the back of the blade are also specified. The reason for calculating the blade stresses only at the three locations is because these locations are most likely to have the highest tensional or compressible stress.

The aim of the Blade Stress model is to obtain the maximum stresses (combination of all sources of stress) at all of the specified blade span locations. However, in order to reduce the amount of input required for the blade stress model, the blade is divided into two sections which are the root to mid section and mid to tip section. By having the two sections, the maximum stress for the blade root, mean and tip are calculated. Once these maximum stresses are obtained, the maximum stresses at 25% and 75% distance from the blade root will be approximate.

The stresses calculated at the blade root, mean and tip are based on the summation of the centrifugal stress and the bending moment stresses. Since there are three chord-wise locations (TE, LE and the back of the blade) specified for the blade root, mid and tip, three blade stresses are computed. Thus the maximum stress would be the highest blade stresses of the three chord-wise locations.

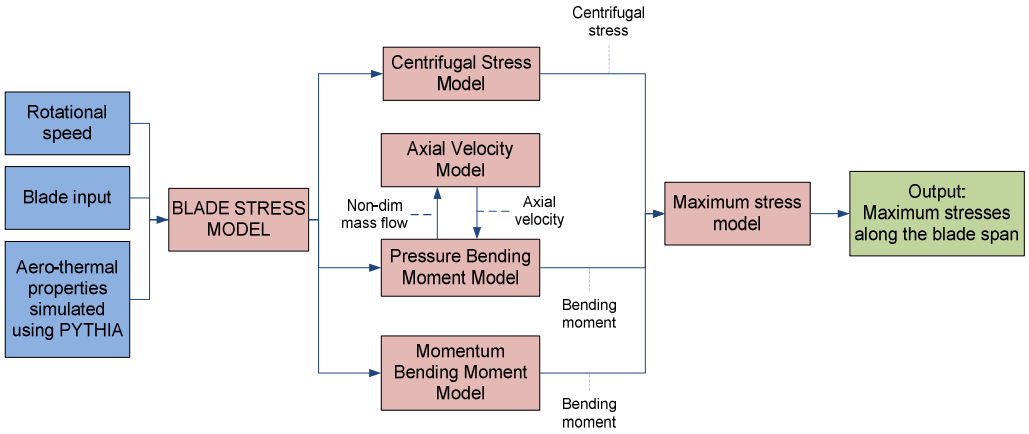

Figure 4-3: Flow diagram of the Blade Stress Model

The Blade Stress Model consists of five sub-models (see Figure 4-3) which are the Centrifugal Stress Model, the Pressure Bending Moment Model, the Axial Velocity Model, the Momentum Bending Moment Model, and the Maximum Stress Model. The

model receives simulated aero-thermal properties from PYTHIA together with rotational speed (either defined by the user or simulated by PYTHIA) and the blade input specified by the user. The user blade inputs required by the Blade Stress model are listed in Table 4-1 while the outputs predicted for each sub-model are listed in Table 4-2.

Table 4-1: Blade inputs used for the Blade Stress Model

Blade input			
1	Blade density	2	Number of blades
3	Shroud mass	4	Absolute rotational speed
5	NGV and blade cooling effectiveness	6	Stager angle at blade root at mid
7	Maximum second moment of area for blade root and mid	8	Minimum second moment of area for blade root and mid
9	NGV pressure recovery	10	NGV coolant stage mass fraction
11	Cross sectional area of blade root, mid and tip	12	Distance to blade section CG for blade root and mid
13	LE radius for blade tip and root	14	TE radius for blade tip and root
15	Stage temperature drop percentage		

Table 4-2: Outputs for Blade Stress Sub-Model

Sub-Model	Model Output
Centrifugal Stress Model	Centrifugal stresses on the tip, mean and the root of the blade
Pressure Bending Moment Model	Pressure bending moment about the blade root and blade mid height
Axial Velocity Model	Turbine blade inlet and outlet axial velocity
Momentum Bending Moment Model	Momentum bending moment about the blade root and blade mid height
Maximum Stress Model	Total stress at LE, TE and the back of the blade at blade root and mid, maximum stress at the blade root, mid, 25% and 75% distance from the blade root

4.4.1 Centrifugal Stress Model

This model calculates the centrifugal stress acting on the tip, mean and root of the blade. In order to calculate the centrifugal stress, the centrifugal force acting on each blade section is calculated first using Equation (4-1). It is assumed that for each blade section, the centrifugal force acts on the blade section's centre of gravity (CG) as shown in Figure 4-4.

$$CF_{Sec} = m_{Sec} \times \omega^2 \times r_{CG} \quad \textbf{(4-1)}$$

where m_{Sec} is the mass of a specified blade section or shroud, ω is the blade angular velocity, r_{CG} denotes the radius between the rotation axis and the specified blade section centre of gravity or the shroud centre of gravity.

Once the blade section centrifugal forces are calculated, the centrifugal forces acting on the blade tip, mid and root are calculated. As shown in Figure 4-4, the centrifugal force at the tip of the blade is caused by the centrifugal force of the shroud mass, while the centrifugal force acting at the mid of the blade is the summation of the centrifugal forces acting on the shroud and the blade mid-tip section. Similarly, the centrifugal force acting at the root of the blade is the summation of centrifugal forces acting on the shroud and the two blade sections (mid-tip section and root-mid section).

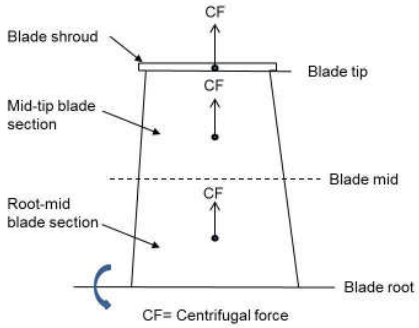

Figure 4-4: Blade sketch with centrifugal loading

The centrifugal stresses at the blade tip, mid and root, σ_{CFSp} are then calculated using Equation (4-2) with CF_{Sp} being the centrifugal force acting at each of the blade's tip, mid or root, and A_{CSSp} the corresponding cross sectional area.

$$\sigma_{CFSp} = \frac{CF_{Sp}}{A_{CSSp}} \quad \textbf{(4-2)}$$

The algorithm of this model was adapted from [26] and is given in Appendix A.2.1.

4.4.2 Pressure Bending Moment Model

As the gas travels across the blade, the static pressure changes accordingly. The difference between the inlet and outlet static pressure will produce a resultant pressure. Consequently, the resulting pressure will produce a pressure force that is able to generate a bending moment about the specified locations along the blade span.

Similar to the Centrifugal Stress Model, the Bending Moment model assumes that the pressure force, PF_{Sec} acting on each blade section calculated using Equation (4-3), acts on the blade section's CG as shown in Figure 4-5. From Equation (4-3), A_{AnSec} is

the blade section annulus area, Δp_{AvSec} is the average static pressure difference for each section (averaged between pressure static difference at the top of the section and the bottom of the section), and N_b is the number of blades.

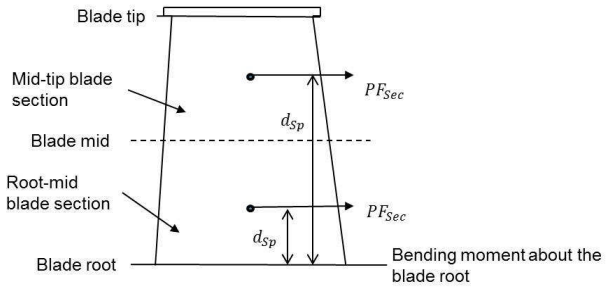

Figure 4-5: Blade sketch of the pressure force acting on the blade section

$$PF_{Sec} = \frac{A_{AnSec} \times \Delta p_{AvSec}}{N_b} \quad \textbf{(4-3)}$$

Once the pressure forces are calculated, the bending moment about the blade mid and root, BMP_{Sp} can be calculated using Equation (4-4) with d_{Sp} denoting the distance between the section CG and the respective blade mid or root. Figure 4-5 depicts the two d_{Sp} measured from both blade section CD to the blade root in order to calculate the bending moment about the blade root.

$$BMP_{Sp} = \sum \left(PF_{Sec} \times d_{Sp}\right) \quad \textbf{(4-4)}$$

Since PYTHIA only provides the inlet and outlet properties of the turbine blade as a whole, the model also calculates the intermediate properties of a multi-stage turbine if a multi-stage turbine design is used. The model assumes that the polytropic efficiency, η_P remains constant across the turbine stages [159] and the value can be calculated using Equation (4-5). In this equation, P_{oNGV} and P_{oOut} are the turbine inlet and outlet stagnation pressures simulated by PYTHIA respectively, γ_{hot} is the specific heat ratio of hot gas, and η_t is the turbine isentropic efficiency.

$$\eta_P = \frac{ln\left(1 - \eta_t\left(1 - \left(\frac{P_{oNGV}}{P_{oOut}}\right)^{\frac{\gamma_{hot}-1}{\gamma_{hot}}}\right)\right)}{\frac{\gamma_{hot}-1}{\gamma_{hot}} ln\left(\frac{P_{oNGV}}{P_{oOut}}\right)} \quad \textbf{(4-5)}$$

The outlet total pressure of the turbine stage, $P_{oOutStage}$ can then be calculated using Equation (4-6) where $T_{oOutStage}$ is the outlet static temperature and is calculated using Equation (4-7) with $\%T_{drop}$ denoting the temperature drop percentage of each

turbine stage defined by the user, and T_{drop} being the overall temperature drop across the turbine. Note that, for the subsequent stage analysis (second stage of the blade and so on), P_{oNGV} in Equation (4-6) and T_{oNGV} in Equation (4-7) are replaced with $P_{oOutStage}$ and $T_{oOutStage}$ from the previous stage.

$$P_{oOUTStage} = P_{oNGV}\left(\frac{T_{oOUTStage}}{T_{oNGV}}\right)^{\frac{\gamma_{hot}}{\eta_P(\gamma_{hot}-1)}} \quad \textbf{(4-6)}$$

$$T_{OutStage} = T_{oNGV} - \left(\%T_{drop} \times T_{drop}\right) \quad \textbf{(4-7)}$$

Since the focus of creep life prediction is on the HP turbine blade, it is necessary to calculate the gas properties at the inlet of the turbine blade (NGV exit properties). This is because as the gas flows across the NGV, there is a reduction in the gas properties, especially when NGV cooling is present. The calculation process is divided into two parts. In the first part, the NGV exit temperature T_{mixing} is calculated using an energy balance equation given in Equation (4-8) and shown in Figure 4-6.

$$T_{Mixing} = T_{oNGV} - \frac{NGV_{mass\,frac} \times m_{coolant} CP_{cold}}{m_{gas} CP_{hot}} (T_{CoolantExit} - T_{CoolantIn}) \quad \textbf{(4-8)}$$

where $NGV_{mass\,frac}$ is the mass fraction of coolant flow that enters the NGV input by the user, $m_{coolant}$ and m_{gas} are the coolant and gas mass flow simulated by PYTHIA respectively, CP_{cold} and CP_{hot} are the specific heats for cold and hot gas, $T_{CoolantExit}$ is the coolant exit temperature obtained from the Blade Thermal Model, and $T_{CoolantIn}$ is the coolant inlet temperature, also simulated by PYTHIA.

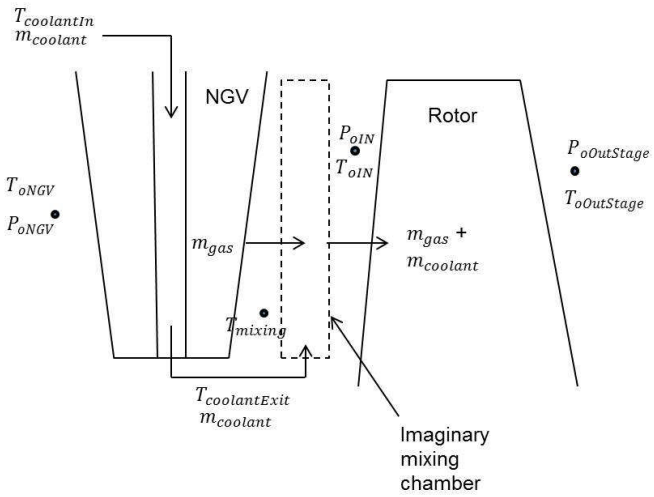

Figure 4-6: Imaginary mixing chamber to calculate blade inlet temperature

In the second part, an imaginary mixing chamber, as shown in Figure 4-6, is introduced to measure the blade inlet gas temperature with the effect of coolant gas entering the system. It is assumed that all the coolant flow that leaves the NGV will mix together with the core gas flow m_{gas}. From the thermodynamics mixing chamber relation, the blade inlet gas temperature, T_{OIN} is calculated using Equation (4-9).

$$T_{OIN} = \frac{m_{gas}CP_{hot}T_{Mixing} + (NGV_{mass\,frac} \times m_{coolant})CP_{cold}T_{Coolant\,Exit}}{\left(m_{gas} + (NGV_{mass\,frac} \times m_{coolant})\right)CP_{hot}} \quad \textbf{(4-9)}$$

To be able to calculate the static pressure difference, the absolute velocities V_{Abs} of the gas at the inlet and outlet of the blade need to be calculated by applying Equation (4-10);

$$V_{Abs} = \sqrt{V_{Ax}^2 + V_{Tan}^2} \quad \textbf{(4-10)}$$

where V_{Ax} is the blade inlet and the outlet gas axial velocity calculated from the Axial Velocity Model, and V_{Tan} is the blade gas tangential velocity calculated using Equation (4-11) for blade inlet and Equation (4-12) for blade outlet.

$$V_{Tan} = V_{Ax} \times tan\alpha_o \quad \textbf{(4-11)}$$

$$V_{Tan} = U - W_{Tan} \quad \textbf{(4-12)}$$

where α_o is the NGV outlet angle, U is the blade speed, and W_{Tan} is the outlet gas relative tangential velocity calculated using Equation (4-13) where α_2 is the blade outlet angle [160].

$$W_{Tan} = V_{Ax} \times tan\alpha_2 \quad \textbf{(4-13)}$$

Once the velocities are determined, the static temperature t and pressure p are calculated using Equations (4-14) and (4-15) respectively. Note that T_o and P_o used in Equations (4-14) and (4-15) will depend on whether the calculation is made for the inlet or the exit of the blade. If it is for the inlet of the blade, T_o and P_o will be T_{oIN} and P_{oIN}. However, if the calculation is made for the outlet of the blade, $T_o$and P_o will be $T_{oOutStage}$ and $P_{oOutStage}$ respectively.

$$t = T_o - \frac{V_{Abs}^2}{2CP_{hot}} \quad \textbf{(4-14)}$$

$$p = P_o\left(\frac{t}{T}\right)^{\frac{\gamma_{hot}}{\gamma_{hot}-1}} \quad \textbf{(4-15)}$$

The detail of the algorithm is given in Appendix A.2.2.

4.4.3 Axial Velocity Model

The axial velocity model is used to calculate both the inlet and outlet axial gas velocities of the blade. From the mass flow continuity [159], we know that the term $\frac{m\sqrt{T_o}}{AP_o}$ and $\frac{V}{\sqrt{T}}$ can be expressed in relation to the Mach number, stagnation and static temperature as given Equations (4-16) and (4-17).

$$\frac{m\sqrt{T_o}}{AP_o} = M\sqrt{\frac{\gamma}{R}}\left(\frac{T_o}{t}\right)^{\frac{-(\gamma_{hot}+1)}{2(\gamma_{hot}-1)}} \quad \textbf{(4-16)}$$

$$\frac{V}{\sqrt{T_o}} = M\sqrt{\gamma R}\left(\frac{T_o}{t}\right)^{-1/2} \quad \textbf{(4-17)}$$

where V is the velocity, M is the Mach number, R is the ideal gas constant and A is the cross sectional area where the gas travels.

In this model, the term $m\sqrt{T_o}/(AP_o)$ is denoted as Q and for each blade inlet and outlet Qs are obtained from the Pressure Bending Moment Model where $m, T_o, A,$ and P given in Equation (4-16) are taken as m_{gas}, T_{oIN} (for inlet) or $T_{oOutStage}$ (for outlet), A_{In}(for inlet) or A_{Out}(for outlet) and P_{oIN} (for inlet) or $P_{oOUTStage}$ (for outlet). Note that A_{In} and A_{Out} are the blade inlet and outlet annulus area.

Taking the Q values from Pressure Bending Moment Model as target values Q_{Target}, the inlet and outlet M are guessed and changed iteratively until the values of Q_{Guess} calculated using Equation (4-16) are similar. This is done by observing the error value, E calculated using Equation (4-18) and letting the iteration process stop when the threshold margin error is achieved which is $-0.005\% < E < 0.005\%$. Once the values of inlet and exit Mach numbers are determined, using Equation (4-17), the axial velocities are calculated.

$$E = \frac{Q_{Target} - Q_{Guess}}{Q_{Guess}} \times 100 \quad \textbf{(4-18)}$$

The algorithm of the Axial Velocity Model is given in Appendix A.2.3.

4.4.4 Momentum Bending Moment Model

When the gas traverses the blades, there exist forces acting on the blades due to the velocity difference between the inlet and the outlet. These forces are produced by the momentum change of the gases in both axial and tangential directions. In this model, the blade section momentum forces for both axial, VF_{AxSec} and tangential direction, VF_{TanSec} are computed using Equations (4-19) and (4-20) respectively

$$VF_{AxSec} = \frac{m_{Area} \times A_{AnSec} \times \Delta V_{axial}}{N_b} \quad \textbf{(4-19)}$$

$$VF_{TanSec} = \frac{m_{Area} \times A_{AnSec} \times \Delta V_{TanAvSec}}{N_b} \quad \textbf{(4-20)}$$

where m_{Area} is the mass flow per unit area, A_{AnSec} is the blade section annulus area, ΔV_{axial} is the axial velocity difference and $\Delta V_{TanAvSec}$ is the blade section average tangential velocity difference.

Note that the velocity difference calculated in the axial direction (Equation (4-19)) and the tangential direction (Equation (4-20)) is different. This is because in the axial direction, the axial velocity along the blade span is constant. Because of this, the difference in the axial velocity for each blade section is similar, hence does not require any averaging. However, for the tangential direction, velocity at the tip, mid and root is different. As a result, the velocity difference for each blade section is taken as the average of the velocity difference of the top and the bottom of the blade section. For example, the velocity difference at the root-mid section is the average of the velocity difference at the blade mid and blade root.

Equations (4-21) and (4-22) are then used to compute the axial and tangential momentum bending moment, BMV_{AxSp} and BMV_{TanSp} about the blade mid and root, with d_{Sp} denoting the distance between section CG and the respective blade mid or root. The algorithm of the model is given in Appendix A.2.4 and most of the equations used in this model are adapted from [26].

$$BMV_{AxSp} = \sum \left(VF_{AxSec} \times d_{Sp} \right) \quad \textbf{(4-21)}$$

$$BMV_{TanSp} = \sum \left(VF_{TanSec} \times d_{Sp} \right) \quad \textbf{(4-22)}$$

4.4.5 Maximum Stress Model

Before the maximum stress can be computed, the resulting moment about the blade direction, as shown in Figure 4-7, is calculated using Equations (4-23) and (4-24) for the blade root and mid.

$$M_{XXSp} = \left(BMP_{Sp} + BMV_{AxSp}\right)sin\theta_{Sp} + BMV_{TanSp}\cos\theta_{Sp} \quad \textbf{(4-23)}$$

$$M_{YYSp} = \left(BMP_{Sp} + BMV_{AxSp}\right)cos\,\theta_{Sp} - BMV_{TanSp}\,sin\,\theta_{Sp} \quad \textbf{(4-24)}$$

where M_{XXSp} and M_{YYSp} are the resulting bending moments about the X-X direction and Y-Y direction at a specified location along the blade span; and θ_{Sp} is the blade stager angle at a specified location along the blade span.

The conversion of the resulting bending moment from the engine direction (axial and tangential) to the blade direction (X-X and Y-Y) is to allow the calculation of the resulting bending moment stress, $\sigma_{(l)Sp}$ at three different chord-wise locations which are at the leading edge (LE), trailing edge (TE), and the farthest location at the back of the blade section for blade root and mid. This is done by applying Equation (4-25).

$$\sigma_{(l)Sp} = \frac{M_{XXSp}Y_{(l)}}{I_{minSp}} + \frac{M_{YYSp}X_{(l)}}{I_{maxSp}} \quad \textbf{(4-25)}$$

where $Y_{(l)}$ and $X_{(l)}$ are the Y and X distances between the corresponding chord-wise location to the blade's root or mid CG, as illustrated in Figure 4-7; and I_{minSp} and I_{maxSp} are the minimum and maximum second moment of area respectively.

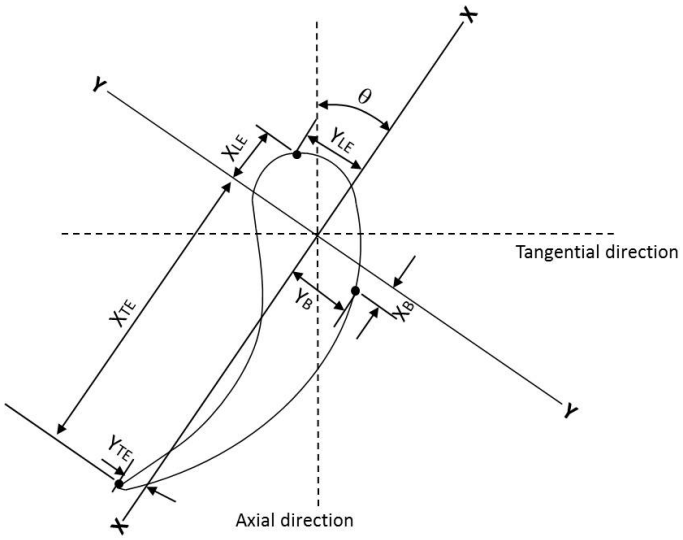

Figure 4-7: Schematic diagram of the blade and gas flow directions

The total stresses, $\sigma_{Tot(l)Sp}$ at the three chord-wise locations are then calculated by summing the respective bending moment stress and the centrifugal stress calculated in the Centrifugal Stress Model. This is done for both the blade root and mid using Equation (4-26). Thus the maximum stress at the blade root and mid would be the highest blade stresses of the three chord-wise locations. It is worth noting that the maximum stress at the blade tip is the blade tip centrifugal stress since there is no bending moment present at the tip of the blade.

$$\sigma_{Tot(l)Sp} = \sigma_{CFSp} + \sigma_{(l)Sp} \quad \textbf{(4-26)}$$

Finally the maximum stresses at the 25% and 75% distance from the blade root are approximated by taking the average of the corresponding lower and upper location along the blade span (i.e. the maximum stress at 25% is the average of the maximum stress at the blade root and mid). The algorithm for the Maximum Stress Model is given in Appendix A.2.5 and is adapted from [26].

4.5 Blade Thermal Model

The purpose of the Blade Thermal Model is to predict the blade's metal temperature. In general, 0D and pseudo-1D thermal models have been developed for cooled and uncooled blades as illustrated in Figure 4-8.

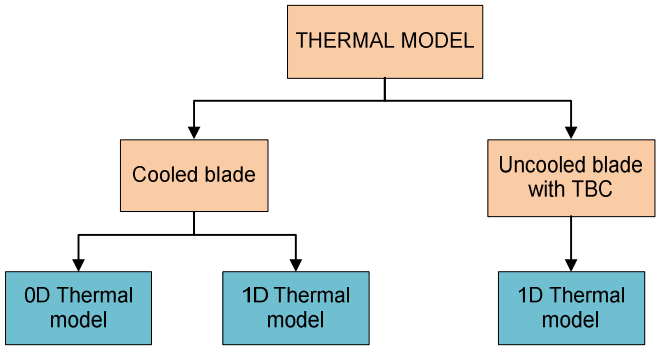

Figure 4-8: Blade Thermal Model Diagram

The difference between the 0D and 1D model is that for the 0D model, the bulk metal temperature will be calculated and the temperature is assumed to be uniform at both chord-wise and span-wise [34], [80], [82], [161]. Since temperature variation across the blade span is not included, the minimum creep life will always be located at the blade root due to the fact that the metal temperature is the same at all points on the blade while the maximum stress occurring at the blade is at the blade root (highest centrifugal stress).

However, the 0D thermal model can be very flexible as different cooling technology can be applied in order to predict the metal temperature. In addition, the model is simple and is helpful to users who have limited information regarding the blade geometry and thermal properties of the gas.

The variation of metal temperatures predicted by the 1D model is useful to determine the location of the minimum creep life. This provides useful information to users as it can show the effects of creep life variation along the blade span when different combinations of blade stresses and temperatures are applied to the HP turbine blades.

The Blade Thermal Model receives simulated aero-thermal properties from PYTHIA together with some inputs specified by the user. Table 4-3 summarises the user inputs required by the model.

Table 4-3: Thermal model inputs required from users

Model User's Inputs			
1	NGV and blade cooling effectiveness	2	NGV and blade coolant mass fraction
3	Blade radii, chords and perimeter	4	Ratio of wall to gas temperature
5	Blade angles	6	Radial temperature distribution
7	TBC properties		

4.5.1 Cooled Blade 0D Thermal Model

The model calculates the bulk metal temperature where it is assumed that the temperature is uniform throughout the blade. Equation (4-27) is used to calculate the bulk metal temperature, T_{Blade} where ε_R denotes the blade cooling effectiveness specified by the user.

$$T_{Blade} = T_{oIN} - \varepsilon_R(T_{OIN} \times T_{CoolantIn}) \quad \textbf{(4-27)}$$

The coolant inlet temperature $T_{CoolantIn}$ is simulated by PYTHIA while the blade inlet temperature T_{oIN} is obtained from the Pressure Bending Moment model using Equation (4-9). In Equation (4-9), the NGV coolant exit temperature, $T_{CoolantExit}$ is calculated using Equation (4-28).

$$T_{CoolantExit} = T_{CoolantIn-}\eta_{conv}(T_{NGV} \times T_{CoolantIn}) \quad \textbf{(4-28)}$$

Where η_{conv} and T_{NGV} are the convection efficiency and the NGV bulk metal temperature calculated using Equations (4-29) and (4-30) respectively [162].

$$\eta_{conv} = \frac{\varepsilon_{NGV}}{m_{NGV}{}^{*} - (m_{NGV}{}^{*} \times \varepsilon_{NGV})} \quad \textbf{(4-29)}$$

$$T_{NGV} = T_{oNGV} - \varepsilon_{NGV}(T_{oNGV} \times T_{CoolantIn}) \quad \textbf{(4-30)}$$

where ε_{NGV} and $m_{NGV}{}^{*}$ are the NGV cooling effectiveness and the NGV non-dimensional coolant mass flow respectively. Similar to ε_R, the ε_{NGV} is also specified by the user while $m_{NGV}{}^{*}$ is assumed to be around $1/2.5$ of the NGV coolant mass percentage [163].

4.5.2 Cooled Blade 1D Thermal Model

In order to create variation in the metal temperatures, the blade inlet gas temperature is varied. This is done by defining the gas radial temperature distribution factor, $RTDF$. The $RTDF$ is the ratio of the difference between the circumferentially peak gas temperature, T_{max} and gas mean temperature, T_{mean} to the combustor temperature rise, T_{ref} given in Equation (4-31). In this model the blade inlet temperature T_{oIN} is taken as T_{mean}. Having to define the $RTDF$, T_{max} can be obtained as T_{ref} is obtained from PYTHIA.

$$T_{max} = T_{oIN} + \left(T_{Ref} \times RTDF\right) \quad \textbf{(4-31)}$$

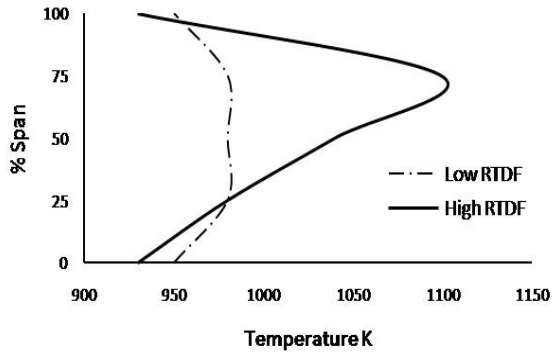

Figure 4-9: High and low radial temperature profile [81]

$RTDF$ identifies the profiles of the temperature distribution on the turbine blade. A higher $RTDF$ value will produce a distorted profile, as shown in Figure 4-9, with a substantial difference between the maximum and the minimum gas temperature along the blade radius. In contrast, a lower $RTDF$ value will produce a uniform distribution with small temperature variation along the blade span. As the profile of the gas temperature changes, the metal temperature at the designated blade section will also change accordingly, thus creating a profile of the turbine metal temperature. In the

model, the user is able to change the $RTDF$ value although it is recommended that the value should be less than 0.2 [163].

Five gas temperature points are created along the blade span which characterise the gas temperature profile defined as T_{Gtip}, T_{GMid}, and T_{GRoot} for the gas temperature at the blade tip, mid and root respectively; and $T_{G75\%}$ and $T_{G25\%}$for the gas temperature at 75% and 25% distance from the blade root respectively. In having to define those gas temperature points, several assumptions were made:

a. The maximum temperature, T_{max} occurs at 75% height from the blade root. The assumption is based on the explanation given in [164] which states that due to the rotation of the turbine blade, the peak temperature will shift from the mid blade towards the tip region.
b. The minimum gas temperature, T_{min} occurs at the tip and the root of the blade ($T_{min} = T_{Gtip} = T_{GRoot}$).
c. The reduction in gas temperature from the maximum temperature, $T_{G75\%}$ to the tip of the blade, T_{Gtip} is linear.
d. The rise in gas temperature from the root, T_{GRoot} to $T_{G75\%}$ is also linear.
e. The average of those defined temperature points should equal to the blade inlet temperature, T_{OIN}

By extrapolating those gas temperature points, the minimum temperature can be derived as shown in Equation (4-32).

$$T_{min} = \frac{(5T_{oIN} - 2T_{max})}{3} \quad \textbf{(4-32)}$$

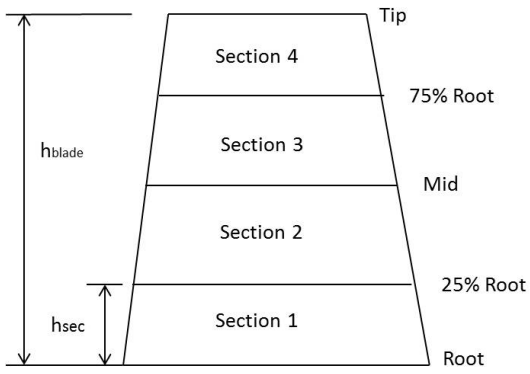

Figure 4-10: Blade section used in the 1D Thermal Model

In order to predict the metal temperature, the blade is divided into four sections as shown in Figure 4-10. Each blade section is treated as an individual blade where the

metal temperature is assumed to be constant both chord-wise and span-wise. It is also assumed that all blade sections have the same cooling effectiveness and the inlet coolant temperatures for the blade section are the coolant exit temperature of the section below it (i.e. blade section at the root will take the blade coolant inlet temperature as its coolant inlet temperature) as shown in Figure 4-11. Further, the model also treats the cooling in the blade as a single-passage cooling where the cooling air passes through the blade from the blade root to the tip.

The section metal temperatures T_{MSec} are calculated using Equation (4-33) where T_{GSec} and T_{CiSec} denote the average gas temperature of each blade section and blade section inlet coolant temperature respectively.

$$T_{MSec} = T_{GSec} - \varepsilon_R(T_{GSec} - T_{CiSec}) \quad \textbf{(4-33)}$$

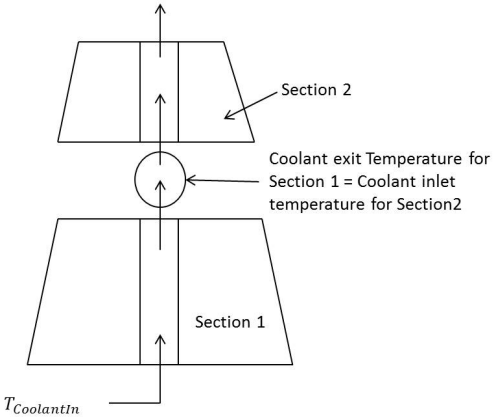

Figure 4-11: Relationship of coolant temperature between each blade section

Note that T_{CiSec} for each subsequent section is taken as the coolant exit temperature, T_{CoSec} of the lower section, as shown in Figure 4-11, while for blade Section 1, $T_{CiSec} = T_{CoolantIn}$. Furthermore, T_{GSec} is calculated by taking the average of the gas temperature point at the bottom and the top of the corresponding blade section (i.e. T_{GSec} for Section 1 is the average value of T_{GRoot} and $T_{G25\%}$).

The section coolant exit temperature T_{CoSec} is determined using Equation (4-34) where H_{Sec} is the blade section convective heat transfer coefficient, s_{Sec} is the average perimeter of each blade section, h_{Sec} is the height of the blade section, and $Rotor_{massfrac}$ is the blade mass fraction.

$$T_{CoSec} = T_{CiSec} + \left[\frac{H_{Sec}s_{Sec}h_{Sec}\varepsilon_R(T_{Gsec} - T_{CiSec})}{\left(\frac{m_{coolant}Rotor_{massfrac}}{N_b}\right)CP_{cold}}\right] \quad \textbf{(4-34)}$$

Equation (4-34) is formed based on the energy balance between the energy released by the gas and the energy absorbed by the coolant given in Equation (4-35).

$$\left(\frac{m_{coolant}Rotor_{massfrac}}{N_b}\right)CP_{cold}\left(T_{CoSec}-T_{CiSec}\right)=H_{Sec}S_{Sec}h_{Sec}\left(T_{GSec}-T_{MSec}\right) \quad \textbf{(4-35)}$$

Since $T_{GSec}-T_{MSec}=\varepsilon_R(T_{GSec}-T_{CiSec})$, then arranging Equation (4-35) with this equation will give Equation (4-34).

The blade section convective heat transfer coefficient H_{Sec} in Equation (4-35) is calculated using Equation (4-36) where Nu_{Sec} , k_{GSec} and c_{Sec} are the blade section Nusselt number, thermal conductivity for gas temperature, and average chord of each blade section respectively.

$$H_{Sec}=\frac{Nu_{Sec}\times k_{GSec}}{c_{Sec}} \quad \textbf{(4-36)}$$

In this model, the Nu_{Sec} is determined empirically using Equation (4-37) [165] where $Nu_g^*{}_{Sec}$ and Re_{Sec} is the nominal Nusselt number and average Reynolds number of each blade section; X_{Sec} and Y_{Sec} are the exponent parameters respectively.

$$Nu_{Sec}=Nu_g^*{}_{Sec}\left(\frac{\mathrm{Re}_{Sec}}{2\times10^5}\right)^{X_{Sec}}\left(\frac{T_{GSec}}{T_{MSec}}\right)^{Y_{Sec}} \quad \textbf{(4-37)}$$

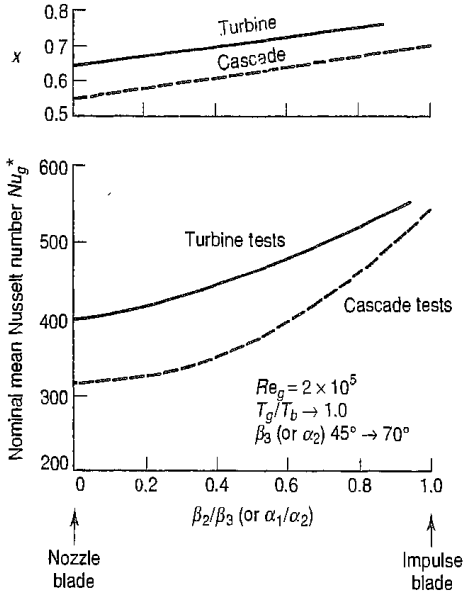

Figure 4-12: Heat transfer data for conventional blade profile [165]

Both the values of $Nu_g^*{}_{Sec}$ and X_{Sec} are obtained from Heat Transfer Data for Conventional Blade Profile plot obtained from [165] and shown in Figure 4-12. It is

important to note that the value of β_2/β_3 given in [165] is equal to α_1/α_2 in this thesis where α_1 is the blade inlet angle while α_2 is the blade outlet angle.

Re_{Sec} in the equation is calculated by taking the average of the bottom and the top outlet Re of the respective blade section which individually is calculated using Equation (4-38) [165].

$$\mathrm{Re}_{Sec} = \frac{\rho_g \times V_{AbsOut} \times c}{\mu} \quad \textbf{(4-38)}$$

where ρ_g and μ are the gas density, blade chord, and gas viscosity respectively. In this model, both ρ_g and μ are calculated using Equations (4-39) and (4-40) respectively. Note that the values of p and t presented in Equation (4-39) are the static temperature and pressure obtained from the Pressure Bending Moment Model.

$$\rho_g = \frac{p}{R \times t} \quad \textbf{(4-39)}$$

$$\mu = \mu_o \frac{0.555T_{io} + Suth}{0.555t + Suth}\left(\frac{t}{T_{io}}\right)^{3/2} \quad \textbf{(4-40)}$$

where μ_o is the reference viscosity, $Suth$ is the Sutherland constant, and T_{io} is the reference temperature. Gas viscosity μ in Equation (4-40) is known as the Sutherland Equation [166] where for air μ_o is $0.00001827\frac{Nsec}{m^2}$, $T_{io} = 524.07K$ and $Suth = 120$.

Once all the blade section metal temperatures, T_{MSec} are computed, the blade metal temperature, T_M at the blade root, 25% distance from the root, mid, 75% of the blade root and blade tip is calculated by taking the average of the corresponding upper and lower blade sections (i.e. metal temperature at the blade mid is the average of the blade section metal temperature of Sections 2 and 3)

The algorithm for this model is given in Appendix A.3.2.

4.5.3 Uncooled Blade 1D Thermal Model

The aim of this model is to predict the variation of metal temperatures along the blade for an uncooled turbine blade which has been coated with TBC. Most of the calculations in this model are similar to the previous thermal model. The blade is divided into four sections, as shown in Figure 4-10, and five gas temperature points are also created along the blade span to characterise the gas temperature profile. Also, the properties at the exit of the NGV are determined in the same way those properties are determined in the previous thermal models.

However, since no blade cooling is present, Equation (4-33) in the previous model cannot be used, hence a different form of metal temperature and gas relation is needed. In order to establish the relation, energy balance is applied. The energy released from the gas to the outer wall of the TBC for each blade section is equal to the energy transferred from the wall to the section blade's metal. This can be mathematically written as Equation (4-41).

$$H_{Sec}A_{wall}(T_{GSec} - T_{wallSec}) = \frac{k_{TBC}A_{wall}(T_{wallSec} - T_{MSec})}{Th_{TBC}} \quad \textbf{(4-41)}$$

where A_{wall} denotes the blade wall area, $T_{wallSec}$ is the TBC outer wall temperature, Th_{TBC} is the TBC coating thickness and the k_{TBC} is the TBC thermal conductivity. Taking R_k as the ratio between the blade section wall temperature and the section gas temperature ($R_k = T_{wallSec}/T_{GSec}$), hence Equation (4-41) can be re-written as:

$$\left(\frac{T_M}{T_G}\right)_{Sec} = R_k - \left[\frac{H_{Sec} \times Th_{TBC}}{k_{TBC}}(1 - R_k)\right] \quad \textbf{(4-42)}$$

Equation (4-42) provides the ratio between the metal temperature and the gas temperature for each blade section. Using this relation, the blade section metal temperature, T_{MSec} can be calculated using Equation (4-43).

$$T_{MSec} = T_{GSec}\left(\frac{T_M}{T_G}\right)_{Sec} \quad \textbf{(4-43)}$$

This model assumes that the R_k value remains constant, hence can be determined if the heat transfer across the blade can be calculated. However, if the heat transfer across the blade cannot be determined, R_k can also be inversely determined using other experimental or numerical methods.

The blade convective heat transfer coefficient H_{Sec} in Equation (4-42), is calculated using Equation (4-36) given in the previous thermal model. However, in this model, the blade section Nusselt number Nu_{Sec} is determined using a flat plat empirical relation as given in Equation (4-44) [167] where Pr denotes the Prandtl number and is taken to be 0.71[165]

$$Nu = 0.037Re^{4/5}Pr^{1/3} \quad \textbf{(4-44)}$$

Similar to the previous thermal model, once all the blade section metal temperatures, T_{MSec} are computed, the blade metal temperature at the blade root, 25% distance from the root, mid, 75% of the blade root and blade tip is calculated by taking the average of the corresponding upper and lower blade section (i.e. metal temperature

at the blade mid is the average of the blade section metal temperature of Sections 2 and 3).

The algorithm of the 2D thermal model for the uncooled blade with TBC is given in Appendix A.3.3.

4.6 Life Estimation Model

In the life estimation model, new parameters named Creep Factor and Mission Creep Factor are introduced as improvements to the existing life estimation model. Using both parameters, investigation into the impacts of different operating and health conditions and the effects of a particular mission/ operation profile on the HP turbine blade's creep life consumption can be done using a simple relative analysis technique via the Creep Factor Approach.

4.6.1 Creep Factor and Mission Creep Factor

In order to perform an impact analysis, comparison to a certain reference value that will act as a 'yardstick' needs to be done. In the case of blades' creep life assessment, knowing only the creep life of, say 17,000 hours, would not be sufficient as it does not reflect how well the engine is being used. Instead, if we could also quantify that the 17,000 hours is actually 40% shorter than it is supposed to be, this will indicate that the engine, under present operating condition has experienced more severe mechanical and thermal loading. The value of 40% in this case indicates the magnitude of impact that an operating condition has when the engine is being operated away from the normal operating condition. Possessing this information will allow users to seek a better solution, optimise the mission profiles or establish an effective maintenance planning that will reduce the operating and maintenance costs.

To represent such an impact on the deviation of operating conditions or even the deviation in the components' health conditions, a relative creep life parameter defined as the Creep Factor, CF is used in this model. The CF can measure how quickly the creep life is being consumed relative to a specific operating condition desired by the user. It is defined as a ratio between the actual blade's creep life, L_{CMin} calculated at the corresponding operating condition and the reference blade's creep life, L_{Ref} at a user-defined condition, as given in Equation (4-45) . This reference condition can either be the nominal operating condition, baseline operating condition, cruise condition or the design point condition.

$$CF = \frac{L_{CMin}}{L_{Ref}} \quad \textbf{(4-45)}$$

By using L_{Ref} which is desirable to users, will allow those users to choose a suitable yardstick in order to perform a realistic impact analysis, as the value of CF helps the user to quantify the change in the component's creep life when the operating condition deviates from the normal users' operating condition. Furthermore, the CF will eliminate the dependency on the given OEM baseline operation which sometimes is not achievable when the user-defined normal operating conditions are far from the suggested baseline operation. In general when:

a. CF = 1, the engine is being operated at a similar creep life as the life at the reference condition with $L_{CMin} = L_{Ref}$

b. CF < 1, the engine is being operated in a much worse condition than its reference condition hence reducing the blades' creep life

c. CF > 1, the engine is being operated at a better condition thus increasing the blades' creep life

d. $CF = 0$, the blade will fail as L_{CMin} = 0.

For example, a CF value of 0.7 will indicate a 30% reduction of the component's creep life from its reference operating condition, whereas a CF of 2 will indicate that the creep life has increased twofold from its reference operating condition.

The concept of Mission Creep Factor, CF_M is similar to CF. Just as the CF is used to quantify the impact of an individual operation segment, CF_M is used to quantify the impact of a given mission/operation profile. The steps to calculate CF_M will be described in Section 4.6.4. Having to combine both CF and CF_M, for a given mission/operation profile, users will be able to examine individual profile segments by observing the respective values of CF while at the same time examining the overall impact of the mission/operation profile on the blade's nominal creep life by observing the value of CF_M.

To illustrate the use of both CF and CF_M, Figure 4-13 illustrates four operating profiles denoted as Case I, II, III and IV. For each case, the same reference operating condition (TET = 1,000K) is applied where the life at that condition is assumed to be 4,500 hours. The CF_M calculated using the steps in Section 4.6.4 are listed in Table 4-4.

From Table 4-4, it can be seen how different operating profiles can be assessed using the CF approach. The individual CF for each profile segment (given in Figure 4-13) will indicate the magnitude of impact when the operating condition deviates from

the reference operating condition. For example, in Case II it can be seen that profile segment 2 has a lower creep life than segment 1. The creep life reduction relative to the reference operating condition in Segments 1 and 2 are 11% and 16% respectively. Since the profile segment 3 in Case IV has a CF value that exceeds unity, this tells us that the the engine has been operated at a better condition thus increases the blades' creep life.

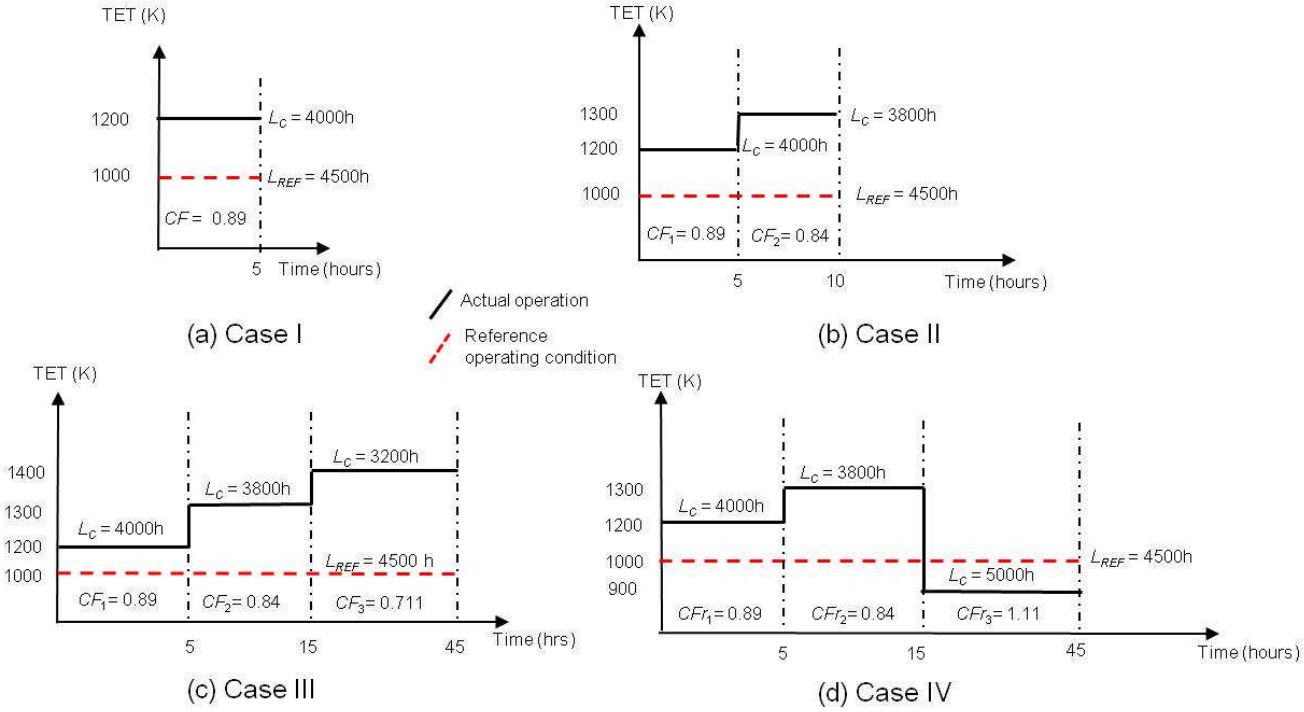

Figure 4-13: Different operating profiles with increase in TET

Table 4-4: Summary of the creep life analysis

	Mission Creep Factor CF_M
Case I	0.89
Case II	0.866
Case III	0.754
Case IV	1.01

By comparing all the cases depicted in Figure 4-13, it can be seen that the operation profile given in Case III has the highest threat in reducing the blade's creep life since the CF_M value is the lowest.

4.6.2 Creep Life Prediction Using Time Temperature Parameter

To obtain a reasonably conservative estimate of creep life, the LMP [168] which has been expressed in Equation (2-8) in Section 2.2.4.2, is used in this model hence t_f can be written as:

$$t_f = 10^{\left(\frac{1000LMP}{T_M} - C_{LMP}\right)} \quad \textbf{(4-46)}$$

For a known turbine blade material, stress and metal temperature obtained from the previous models, the blade t_f can be estimated. It is important to note that since at different blade sections, the amount of stresses and metal temperatures are different (1D thermal analysis), creep life at different blade sections will be different as well. The minimum creep life calculated will be taken as the value which represents the blade's creep life. Depending on the design and operating conditions, the location of the minimum creep life will vary. For a 0D thermal model, since the metal temperature is assumed to be constant and the maximum stress will occur at the blade root, the minimum creep life will be seen at the blade root.

The Life Estimation Model is divided into two sub-models. The first model is used to predict the blade minimum creep life of a single operating point; while the later model is used to predict the minimum nominal and mission/operation profile creep life for a given mission/operation profile.

4.6.3 Single Operating Point Creep Life Prediction Model

As the operating condition is input into the model, the blade maximum stress and metal temperature at each specified location along the blade span are computed using the Blade Stress and Thermal Models respectively. Based on the turbine blade material, the LMP value is obtained from the material LMP master curve at the corresponding maximum stress. Hence t_f at each specified location along the blade span is estimated using Equation (4-46).

In this model, the predicted blade creep life, L_C is determined by dividing each estimated t_f with a safety factor, SF_{ac} as given in Equation (4-48).

$$L_C = \frac{t_f}{SF_{ac}} \quad \textbf{(4-47)}$$

As the SF_{ac} becomes larger, the L_C will reduce even more. The values of L_C at the specified locations along the blade span are then compared and the minimum creep

life will be taken as the value which represents the blade's creep life, L_{CMin}. Once this is determined, CF is calculated using Equation (4-45).

The algorithm of this model is given in Appendix A.4.1.

4.6.4 Mission/Operation Profile Creep Life Prediction Model

The model is generally an extension of the Single Operating Point Creep Life Prediction Model whereby multiple single-operation point creep life predictions are estimated to form a complete mission/operation creep life assessment. The Robinson Life Fraction rule [98] is used in this model to compute the nominal creep life when a mission/operation profile is input by the users.

For a given profile, the life fraction LF, calculated using Equation (4-48), is obtained for each profile point. In Equation (4-48) OH denotes the profile point's operating hour.

$$LF = \frac{OH}{L_{C\,Min}} \quad \textbf{(4-48)}$$

The mission/operation blade nominal creep life $L_{C\,M}$ is then calculated using Equation (4-49) where OH_{Tot} and LF_M are the total operating hour and mission/operation life fractions respectively. Note that both OH_{Tot} and LF_M are the summation of the individual profile points OH and LF respectively.

$$L_{C\,M} = \frac{OH_{Tot}}{LF_M} \quad \textbf{(4-49)}$$

Finally CF_M is calculated using Equation (4-50).

$$CF_M = \frac{L_{C\,M}}{L_{Ref}} \quad \textbf{(4-50)}$$

The algorithm for this model is given in Appendix A.4.2.

4.7 Life Usage Model

The life usage model is used to estimate the blade nominal creep life when multiple mission/operation profiles are inputted. Similar to the previous model, the Robinson Life Fraction rule is used to calculate the overall nominal creep life and the blade life usage percentage when those profiles are specified.

Each mission/operation profile blade life fraction, LF_M and total operating hour, OH_{Tot} are individually added to produce the overall life fraction, $LF_{Overall}$ and $OH_{Overall}$.

Using both values, the overall blade nominal creep life $L_{C\ Overall}$ is computed using Equation (4-51).

$$L_{C\ Overall} = \frac{OH_{Overall}}{LF_{Overall}} \quad \textbf{(4-51)}$$

Besides the overall nominal creep life, the life usage percentage is also presented. As the overall life fraction represents the portion of the blade creep life that has already being consumed relative to the total available life, the life usage percentage, $LU\%$ is another way of representing the life fraction in a percentage manner. In addition, the blade's remnant creep life L_{Rem} is also calculated using Equation (4-52) with $CF_{M\ Overall}$ denotes the overall Mission Creep Factor which is calculated using Equation (4-53).

$$L_{Rem} = \left(CF_{M\ Overall} \times L_{Ref}\right) - OH_{Overall} \quad \textbf{(4-52)}$$

where

$$CF_{M\ Overall} = \frac{L_{C\ Overall}}{L_{Ref}} \quad \textbf{(4-53)}$$

The algorithm of the model is given in Appendix A.5.

4.8 Model Integration with PYTHIA

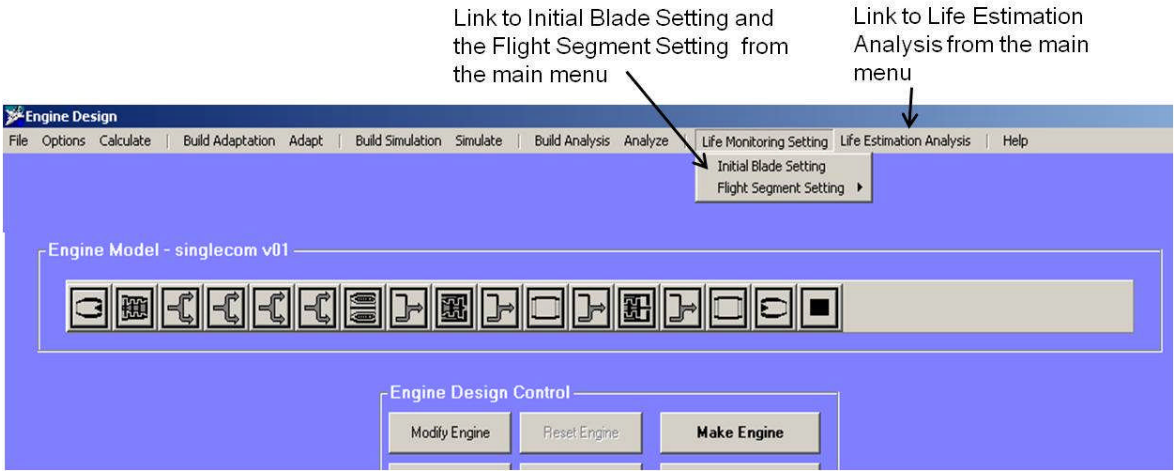

Figure 4-14: PYTHIA Engine Design Interface with links to the model interfaces

The Integrated Creep Life Prediction Model has been incorporated in the existing PYTHIA. Four main interfaces have been created:

a. Initial Blade Setting Interface
b. Flight Segment Setting Interface

c. Life Estimation Analysis Interface

d. Overall Life Calculation Interface.

From the main PYTHIA Engine Design Interface, given in Figure 4-14, the user is able to define the blade and the flight segments which are available in the main menu.

4.8.1 Initial Blade Setting Interface

In the Initial Blade Setting Interface, users are able to input the engine's blade data, as shown in Figure 4-15. In addition, users are able to define the stages of the HP turbine. The input data are saved automatically as a text file once the user exits the interface.

Once the data are stored, users will be able to automatically restore the blade setting when the engine model is uploaded. This will prevent the needs to enter the blade data each time the blade's creep life needs to be predicted . Note also during this stage, that users can choose either to perform the 0D or 1D thermal analysis.

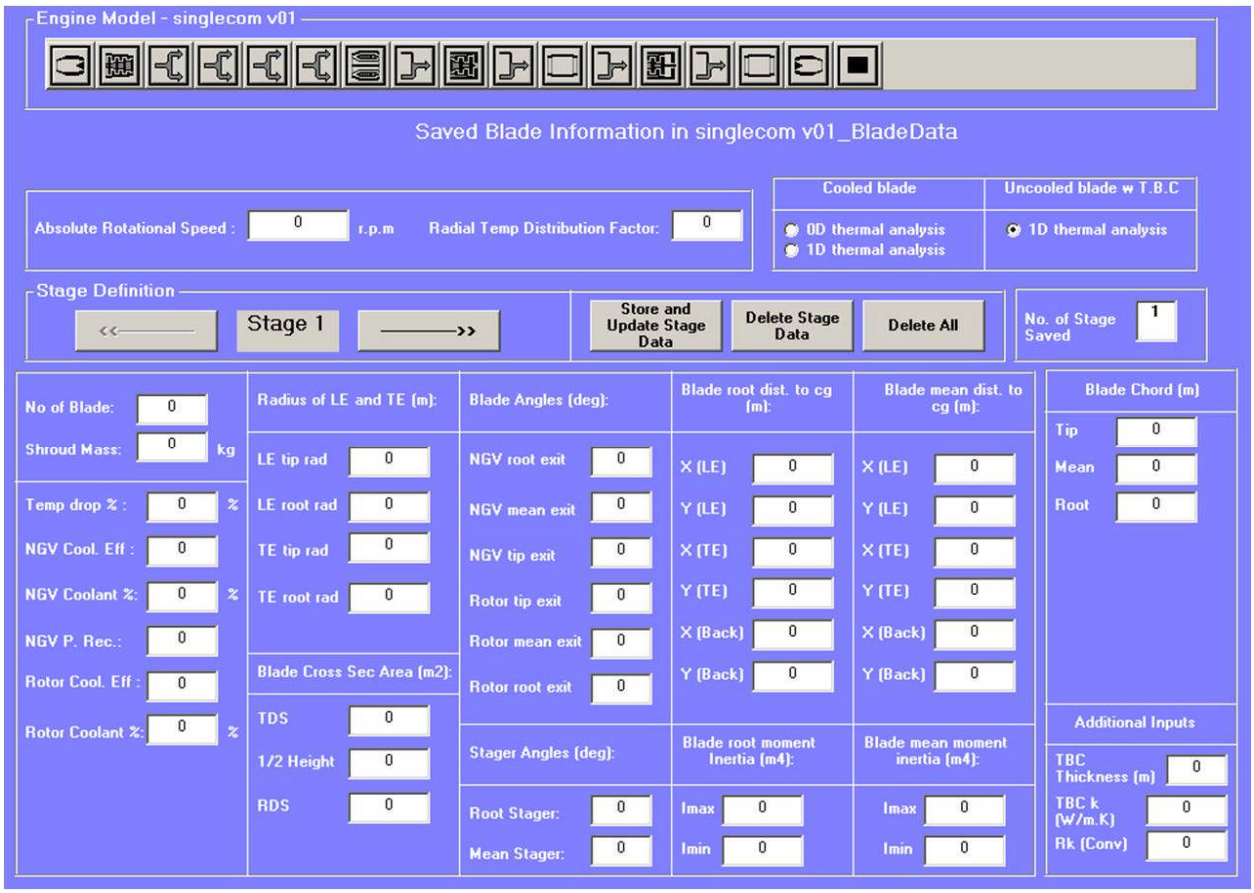

Figure 4-15 Initial blade setting interface

4.8.2 Flight Segment Setting Interface

The Flight Segment Setting Interface allows users to define up to 30 flight segments or operation segments. From the main menu (Figure 4-16) users can choose either to simulate a clean or a degraded mission profile. Figure 4-17 depicts the Flight Segment Interface for a clean engine mission profile simulation. From Figure 4-17, it can be seen that for each flight segment, users will be able to select up to three OD parameters that can define the flight characteristics. The OD parameters, such as the TET, relative compressor rotational speed PCN, altitude, shaft power, ambient temperature deviation, operating hours and many others, can be selected from the flight segment setting frame. The model will then simulate the mission/operation segments automatically once the flight segment data are saved.

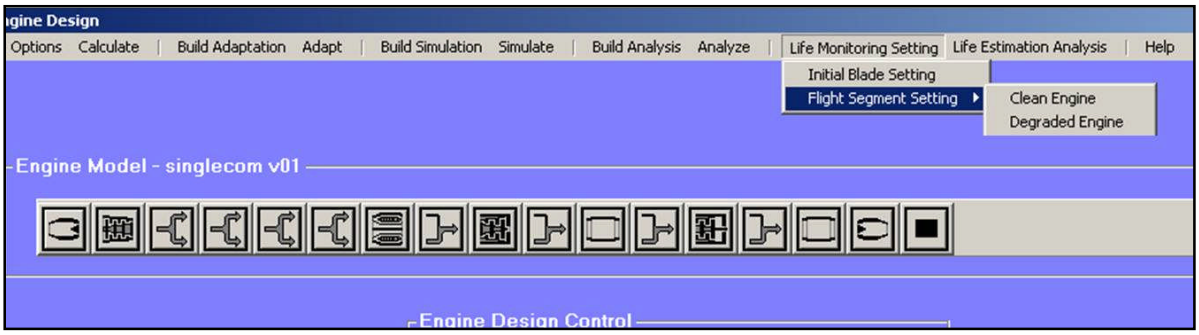

Figure 4-16: Clean and degraded mission/operation profile simulation option

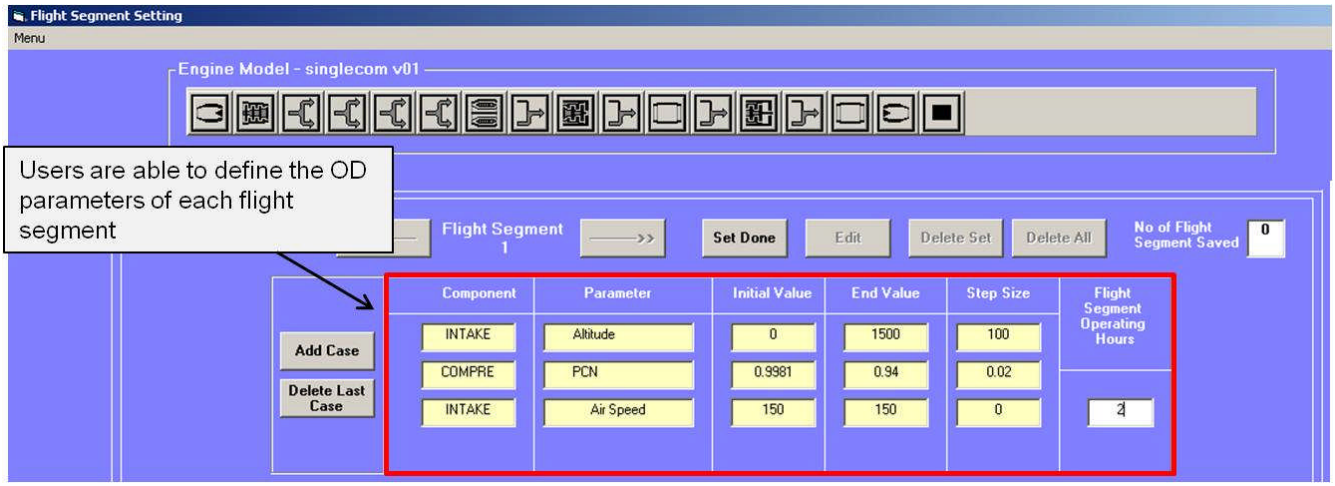

Figure 4-17: Flight Segment Interface for mission/operation with a clean engine

Figure 4-18 illustrates the Flight Segment Interface for a degraded engine mission/operation profile simulation. When users choose to simulate a mission/operation profile with a degraded engine, an additional degradation parameters

frame will be visible from which users will be able to define what component is degrading and the magnitude of that degradation. Figure 4-18 shows an example of a compressor degradation defined by the user with 3% degradation on efficiency, 1.5% flow capacity and 1.5% on pressure ratio. Once the degradation is defined, users can define the mission/operation segment in the same way the mission/operation segment for a clean engine is defined.

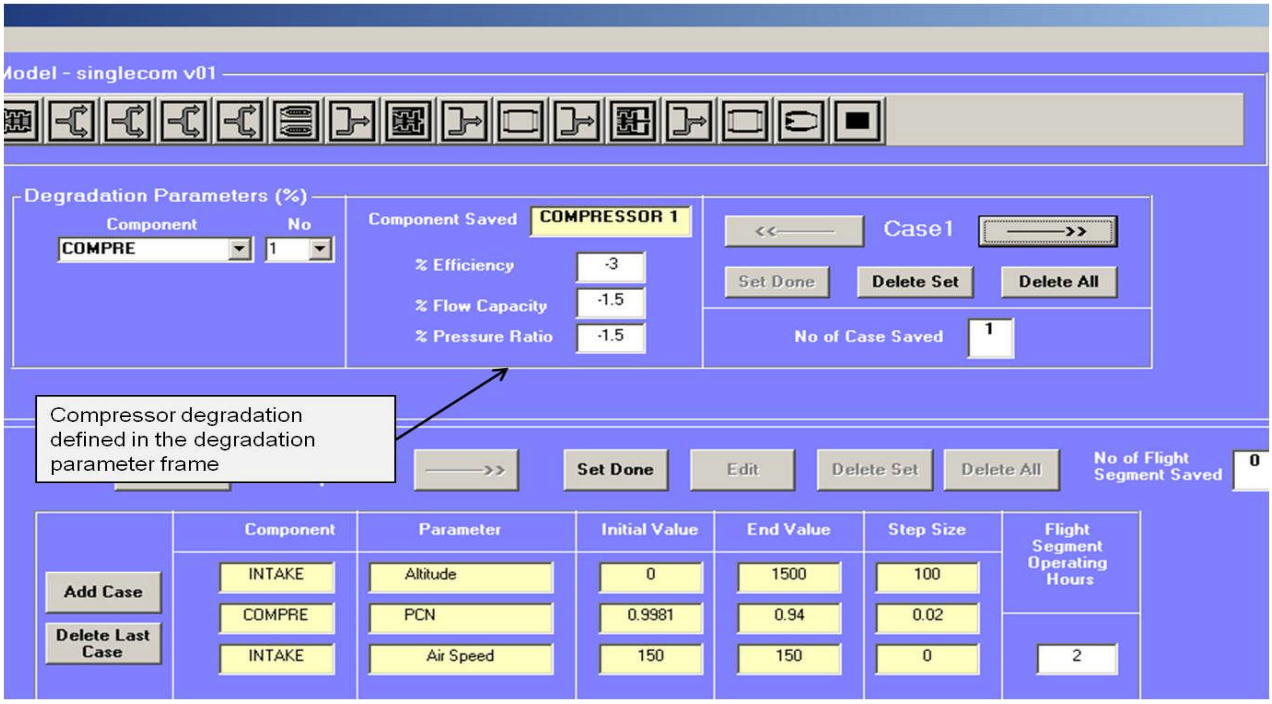

Figure 4-18: Flight Segment Interface for mission/operation profile with a degraded engine

4.8.3 Life Estimation Analysis Interface

After the blade data and the mission/operation segments are defined, the blade's creep life assessment can be carried out using the Life Assessment Analysis Interface as shown in Figure 4-19. As mentioned in Section 4.6, the results from the Life Estimation Model are divided into two parts. The first part provides the creep life assessment of each mission/operation segment while the second part provides the assessment for the entire mission/operation. This can be clearly seen in Figure 4-19, where on the left part of the interface, several columns are created to give the profile segment maximum stresses, rotor metal temperatures, LMP, blade's creep life, locations of the minimum creep life occurrence, life fractions, and Creep Factor, while next to it, the mission/operation blade's life assessment, which includes the mission life fraction, nominal creep life, Mission Creep Factor and the total operated hours, is provided. In

addition, users can also upload the material data which are already available in the system, or manually define the material during run time.

The output of the estimation is then automatically plotted, together with some operating parameters defined by users. Figure 4-20 depicts a glimpse of the plots automatically plotted by the system.

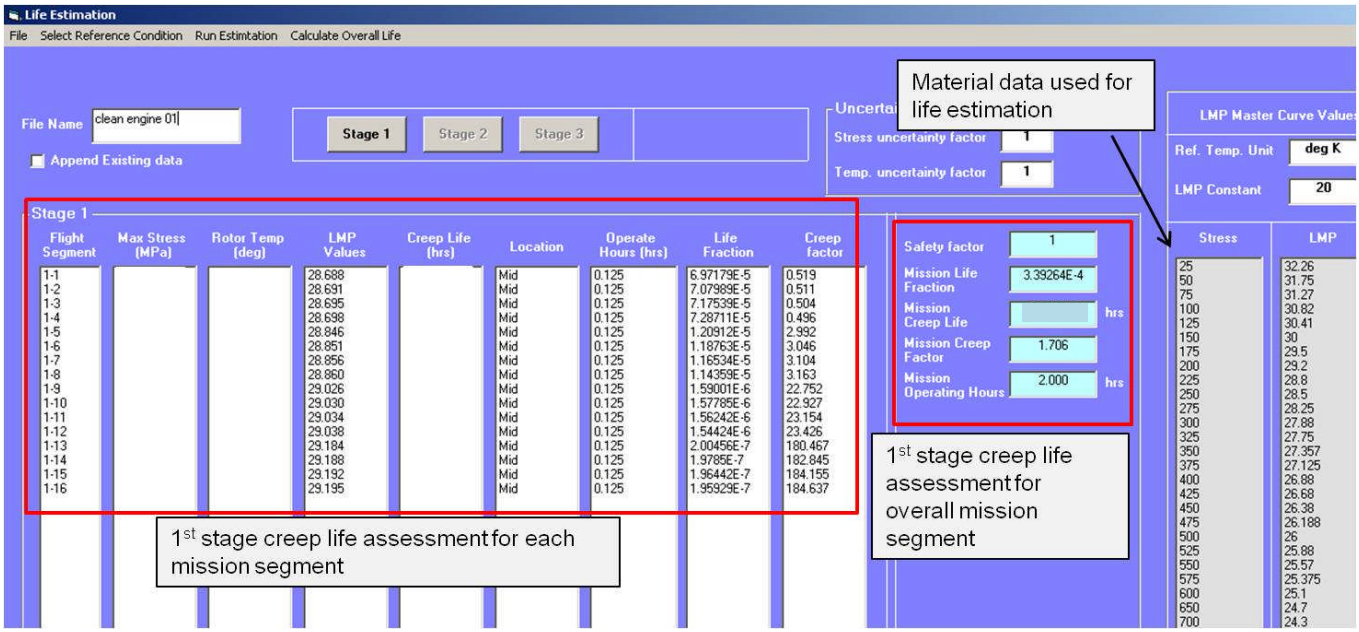

Figure 4-19: Life Assessment Analysis interface

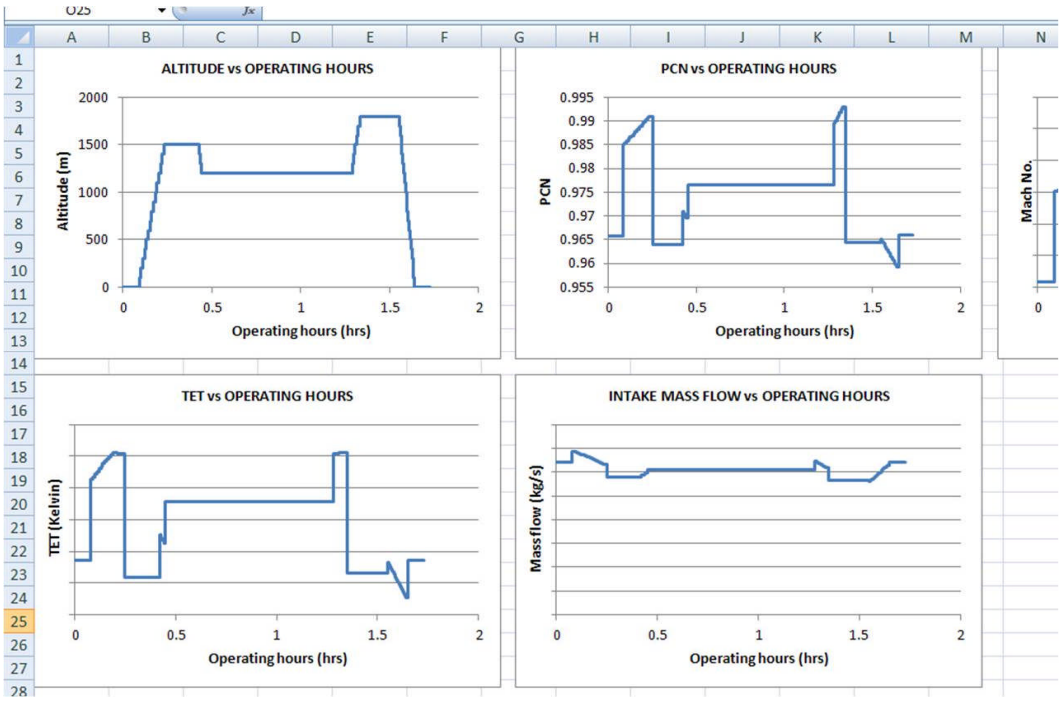

Figure 4-20: Estimation outputs are plotted against operating time

4.8.4 Overall Life Calculation Interface

The blade's life usage can be calculated after the single mission life assessment is carried out. Using the Overall Life Calculation interface, as shown in Figure 4-21, the summation of the mission's life fraction will be calculated using Equation (4-51) to form the life usage percentage, $LU\%$. Not only that, this interface will also provide the overall Creep Factor and the overall operating hours. From Figure 4-21 it can be seen that the engine has been through 145 hours of operation by which time the turbine blade's creep life has already being consumed by as much as 3.93% of the blade's useful life. The overall Creep Factor also indicates that the life of the blade is 31.3% better than the life predicted at the reference operating condition.

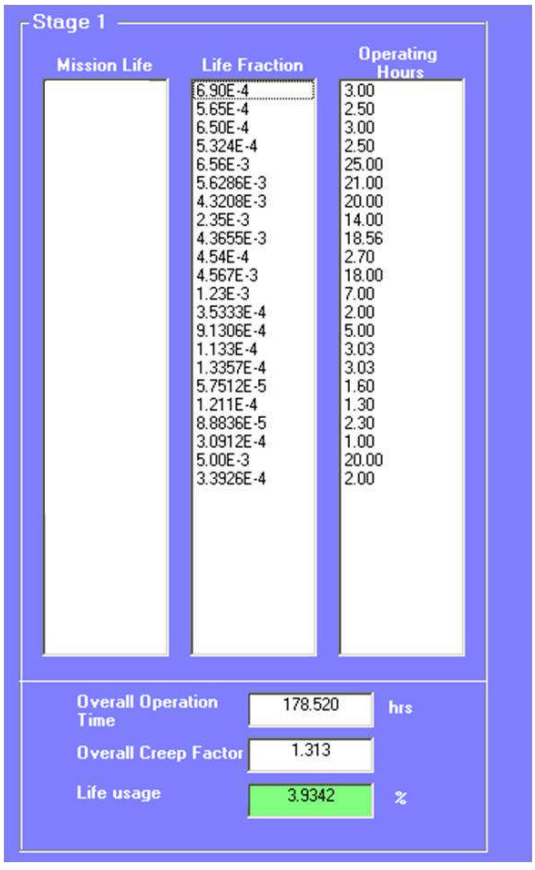

Figure 4-21: Overall Life Calculation interface

4.9 Benefits of the Developed Model

The benefits of the Integrated Creep Life Prediction Model developed by the author are as follows:

a. Flexibility to change and update turbine design features: The performance model used in PYTHIA is a 0D model which means the model will only simulate the gas path values at the inlet and outlet of the overall turbine design. It could never estimate the gas path conditions within the stages of the turbine. The model created is able to inversely predict the gas path values as the user defines the number of stages of the turbine.
b. Able to calculate the tangential and axial velocity and loading: Using a minimal set of geometrical data, the model is able to calculate the gas tangential and axial velocity, total and static temperature and pressure for each blade section, and at each stage. This allows the model to calculate the detailed gas bending moment due to momentum change and static pressure change.
c. Able to calculate the drop in gas temperature at the inlet of the blade due to the presence of cooling in the nozzle guide vane.
d. Able to predict the metal temperature variation across the blade span: Variation of the creep life across the blade span can be investigated. This is useful as the location where the blade might fail can be known.
e. Able to simulate an individual mission/operation segment or the entire mission/operation profile for both a clean and degraded engine.
f. Able to perform impact analysis for an individual flight/operation segment or the entire mission/operation profile: Both Creep Factor and Mission Creep Factor will provide additional information on how the engine is being operated. In addition, users will be able to know how individual flight/operation segments can influence the life consumption of the blade.
g. The model is relatively simple and requires only one person to perform the predictions: To some extent, as the current prediction becomes very complex, several people are required to perform individual analyses (thermal, stress, and creep). This model will require only one person to run the life estimation.

4.10 Chapter Conclusion

In this chapter, the Integrated Creep Life Prediction Model developed by the author has been reported. This includes the model design consideration and the overall structure of the model. Next, the chapter discusses each sub-model developed and a detailed algorithm for each sub-model has been presented in Appendix A. The chapter also

explains how the model is incorporated in PYTHIA and provides figures to show the reader the interfaces created. At the end of the chapter, the benefits of the developed model are given.

5 ARTIFICIAL NEURAL NETWORK BASED CREEP LIFE ESTIMATION

In this chapter, the development of the alternative creep life estimation method proposed by the author using the ANN approach is discussed. But before the discussion can begin, the theoretical background of the ANN approach is given in order to provide some understanding for readers.

5.1 Theoretical Background of ANN

In recent years, neural computing has emerged as a practical technology with successful applications in many field [169] such as in image processing and computer vision, signal processing, medicine, military systems, financial systems, power systems [170], material science [171–175], etc. ANN has evolved from a biologically inspired layer network connected by neurons into various categories of computational models with different algorithms and a large variety of architectural design [176].

ANN uses different approaches to solving problems than conventional computers. Computers use an ‘algorithmic’ approach which solves a particular problem by following sets of procedures and instructions. The approach, in a way, has restricted the problem solving capability, especially when the specific procedures required are unavailable. ANN on the other hand processes information similarly to the way the human brain does by using a large amount of interconnecting process units called neurons; these neurons work in parallel in order to solve a particular problem. Similarly to the brain, the ANN learns by example and finds its own way to solve the problem which sometimes can be unpredictable.

Because of the similarity it has with how the brain functions, it will be easier to understand how it functions first, i.e. before the mathematical model of the ANN can be discussed.

5.1.1 Biological Neural Units

In this section, the actual building block of the biological neural system is discussed. Neurobiologists estimate that the human brain consists of one hundred billion nerve cells or neurons [177] which in general act as a small processing unit, encoding their outputs as a series of brief voltage pulses. According to Kandel [178], a typical biological neuron found in vertebrates has three major morphologically defined parts (see Figure 5-1) which are:

a. The processing part: The cell body or soma, which consists of a cell nucleus typically 50μm in diameter.
b. The transmission part: The axon, a tubular construct with a diameter ranging from 0.2 to 20μm in width and with length up to 1m. The axon begins at the axon hillock which generates the cell action potential and is considered to be the main conduction mechanism of the neuron.
c. The receptive part: Dendrites, which branch out in a treelike fashion. Most neurons have multiple dendrites where the dendrite of one neuron is connected to the axons of other neurons via synaptic terminals. This is how the biological networks are formed.

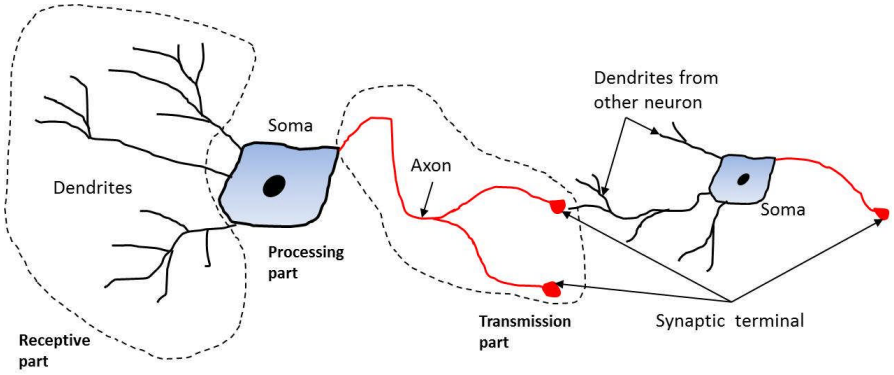

Figure 5-1: A typical biological neuron

Synaptic transmission involves complicated chemical and electrical processes. When one of the neurons fires, the voltage pulses are received by one of the other dendrites. The strength of the pulses given by the dendrite, together with other received pulses from other dendrites, forms an input signal to the soma. If the signal is below the axon hillock's threshold, no output signal is fired. However, if the input signal surpasses the axon hillock's threshold, regardless of how much above it is, the same output signal will be fired though the axon.

5.1.2 Models of a Neuron

A neuron is an information-processing unit that is fundamental to the operation of ANN. Figure 5-2 illustrates the model of a neuron which provides the basis for the ANN design. From the figure, it can be seen that there are three basic elements in a neuron model [179]:

a. A set of synapses or connecting links: Each synapse is categorised by a weight of its own. This weight w_{kj}, is multiplied by a signal x_j at the input of synapse j connected to neuron k.
b. An adder u_k which acts as a linear combiner that sums the input signals.
c. An activation function, $\varphi(.)$ used to limit the amplitude of the output.

From the figure it can be seen that the neuron model also has an externally applied bias denoted as b_k which increases and decreases the net input of the activation function.

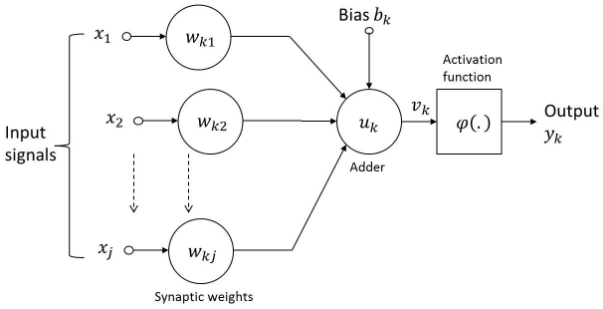

Figure 5-2: Model of a neuron [179]

Mathematically, adder, u_k and the output, y_k of neuron k can be written as Equations (5-1) and (5-2):

$$u_k = \sum_{j=1}^{m} w_{kj}\, x_j \qquad \textbf{(5-1)}$$

$$y_k = \varphi(v_k) \qquad \textbf{(5-2)}$$

with x_j, w_{kj} denoting the input and its corresponding synaptic weight, $\varphi(.)$ denotes the activation function, while v_k denotes the activation potential of neuron k written as Equation (5-3).

$$v_k = u_k + b_k \qquad \textbf{(5-3)}$$

By comparing the ANN neuron model and the biological neural unit, the synapses in the ANN model have the same function as the dendrites on the neural unit. The computation of the input using the adder and activation function follows the function of the soma. The y_k produced by the ANN neuron acts in the same fashion as the output signal fired through the axon of the biological neural unit.

5.1.3 Activation Function

The activation function, $\varphi(.)$ dictates how the output is being represented based on the values of activation potential, v_k. According to Haykin [179], there are three basic types of activation function:

a. Threshold function: The function can be visually represented in Figure 5-3. For this function, $\varphi(v_k)$ will take the corresponding argument:

$$\varphi(v_k) = \begin{cases} 1 & if \ \ v_k \geq 0 \\ 0 & if \ \ v_k < 0 \end{cases} \quad \textbf{(5-4)}$$

The function limits the neuron output to either 1 or 0, according to the values of v_k. From Equation (5-4), it can be seen that the neuron will take the value of 1 when v_k is non-negative or 0. As a result, the output of neuron k will be:

$$y_k = \begin{cases} 1 & if \ \ v_k \geq 0 \\ 0 & if \ \ v_k < 0 \end{cases} \quad \textbf{(5-5)}$$

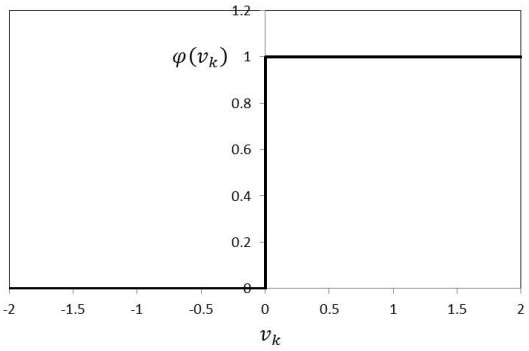

Figure 5-3: Threshold function

b. Piecewise-Linear Function: The function can have a value y_k of 0 to 1, but can also take on values between them depending on the amplification inside the linear region, as shown in Figure 5-4. Based on the figure, y_k will take the following argument:

$$y_k = \begin{cases} 1 & v_k \geq 0.5 \\ v_k & 0.5 > \ v_k > -0.5 \\ 0 & v_k \leq -0.5 \end{cases} \quad \textbf{(5-6)}$$

Again, this function can take on the values of 0 or 1, but can also take on values between, depending on the amplification factor in a certain region of linear operation.

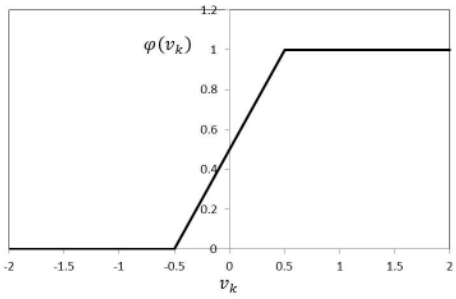

Figure 5-4: Piecewise-Linear function

c. Sigmoid Function: This function is by far the most common function used in the ANN design. The function can have v_k in a range of $-\infty$ to $+\infty$ and squash them into the range of 0 to 1 for a Log-Sigmoid Function (Figure 5-5) or -1 to 1 for a Hyperbolic-Tangent Function (Figure 5-6). The equations used for Log-Sigmoid and Hyperbolic-Tangent Functions are given in Equations (5-7) and (5-8) respectively.

$$\varphi(v_k) = \frac{1}{1 + \exp(-a_k v_k)} \quad \textbf{(5-7)}$$

$$\varphi(v_k) = \tanh(v_k) \quad \textbf{(5-8)}$$

In Equation (5-7), a_k denotes the slope parameter. As shown in Figure 5-5, as a_k increases, the slope of the function also increases.

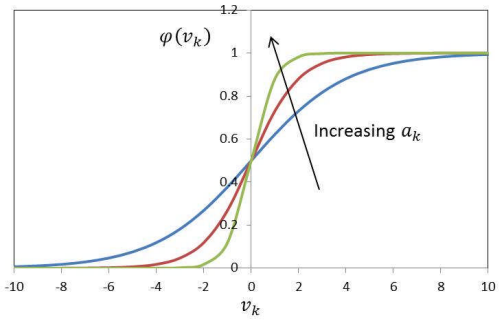

Figure 5-5: Log-Sigmoid Function

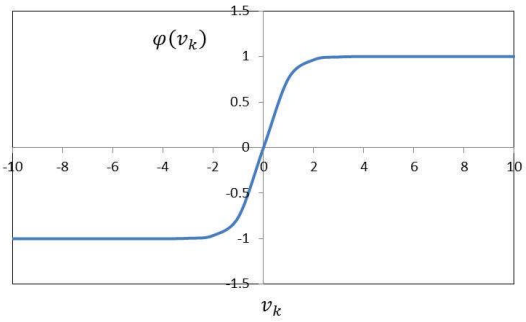

Figure 5-6: Hyperbolic-Tangent Function

5.1.4 Classes of Network Design

There are various designs of ANN currently available. However the designs can be classified into three:

a. Single-layer Feed Forward Network: It has the simplest form of a layered network where the output neurons are organised into a single layer connected

by an input layer, as shown in Figure 5-7. Note that the direction of the signal is only in a forward direction. Due to this the network is called the feed forward network. The term ‘single layer’ is referring to the output layer of computation nodes. Since the input layer does not perform any computation, the input layer is not counted as a ‘layer’ in the ANN design.

b. Multilayer feedforward network: The multilayer network distinguishes itself by having one or more hidden layers, as shown in Figure 5-8. From the input layer, the signals are sent to the respectively hidden layers for computation before the outputs of the hidden layer are sent to the next layers. Note that the outputs of the previous layer are taken as the inputs of the current layer. The process of forwarding the signals will continue until the signals reach the output layer. The output signals of the neurons in the output layer represent the overall response of the network towards the inputs given in the input layer.

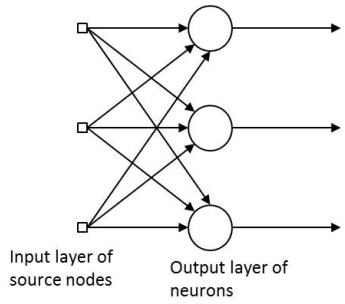

Figure 5-7: Single layer feedforward network

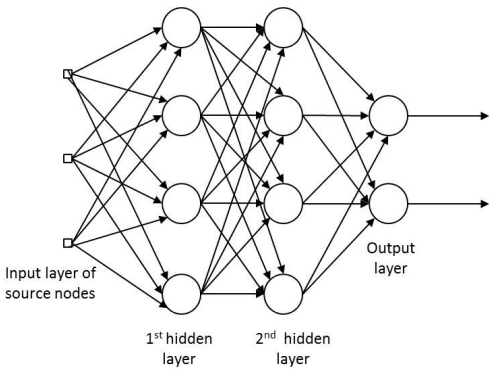

Figure 5-8: Multilayer feedforward network

The presence of the hidden layers enables the network to deal with higher complexity problems and is particularly valuable when the size of the input layer is large. The reason is that the hidden layers provide extra sets of synaptic connection and the extra dimension of neural interactions [180]. The network given in Figure 5-8 can be written as having a network size of 3-4-4-2 with 3

source nodes, 4 neurons in the first hidden layers, 4 neurons in the second hidden layers and 2 output neurons.

c. Recurrent Network: This network differs from the two previous feedforward networks in its feedback loop, with the outputs from particular neurons feeding its output back to the input of particular neurons. Figure 5-9 shows an example of a recurrent network with two hidden layers feeding back its output signals into two of its source nodes. The feedback is done using unit delay elements, z^{-1}. This produces a dynamic behaviour where layers are updated from both the external inputs and the activation from the previous forward propagation.

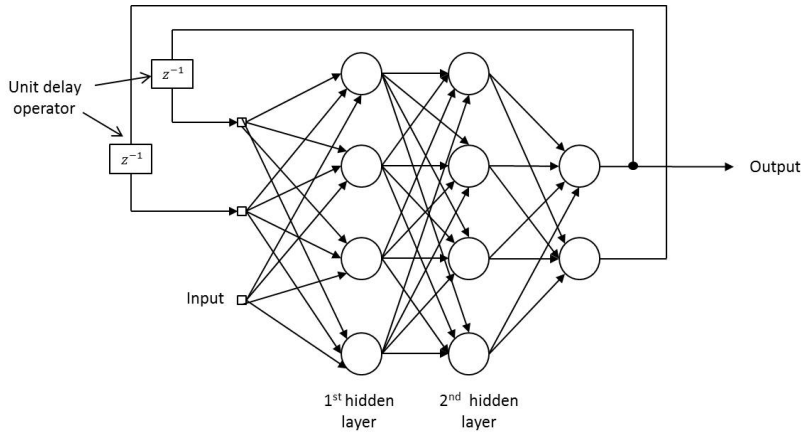

Figure 5-9: Recurrent Network

5.1.5 ANN Learning Process.

One of the most significant advantages of ANN is the ability to evolve while learning from its environment. The term 'evolve' refers to the iterative or repetitive process of adjusting its synaptic weights and bias hence improving its performance. Because of the adjustment it had experienced 'internally', the way the networks responded to its environment will change. Through this iterative process, the network becomes more familiar with its environment hence becoming more knowledgeable.

The types of learning dictate how the adjustments of both the synaptic weights and bias take place. Basically there are two types of learning paradigm which are unsupervised learning and supervised learning. Unsupervised learning can be considered as independent learning, where the network learns to represent particular inputs in a way that reflects the statistical structure of the overall collection input pattern [181]. Once the network has become tuned into the statistical structure of the input data, it will develop the ability to create new classes automatically [182].

Another form of learning paradigm is supervised learning which can be considered as assisted learning. In order to assist the network during the learning, the network requires training samples consisting of sets of inputs coupled together with their respective outputs. These outputs are taken as the targeted outputs which the network needs to achieve during the iterative learning process. The adjustments of the synaptic weights and bias can be done either by performing the adjustment while sequentially inputting the training sample at each learning iteration, or by performing the adjustment after all of the training samples are input in each iteration. The second method of inputting the training samples is called batch training and the learning iteration is called an epoch. 150 epochs means that the adjustments of weights using the same batch of training samples have been iterated 150 times.

One of the most commonly used learning rules in supervised learning is the error-correction learning. Using the error-correcting learning, as illustrated in Figure 5-10, the adjustments of the synaptic weights and bias (in each iteration) are in the direction of minimising the error signal, $e_{(n)}$ between the targeted outputs and the outputs predicted by the output neurons which can be defined as

$$e_{(n)} = d_{(n)} - y_{(n)} \quad \textbf{(5-9)}$$

where $d_{(n)}$ and $y_{(n)}$ are targeted and predicted outputs at a given learning iteration n.

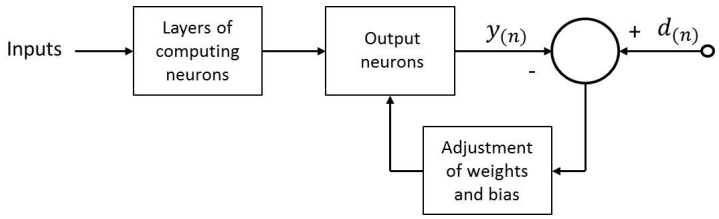

Figure 5-10: Illustration of error-correction learning

The $e_{(n)}$ acts as a controlling mechanism purposely to apply a sequence of adjustments to the synaptic weights and bias. However, the rate of the adjustment will depend on the training algorithm utilised. There are various parameter updating algorithms available from the simplest one, such as the Gradient Descent algorithm, to more sophisticated algorithms such as the Scaled Conjugate Gradient or the Levenberg-Marquardt algorithms. These will be discussed in a later section.

5.1.6 Learning Task

With the choice of having a single or multilayer network, and a supervised or unsupervised learning process with different training algorithms, ANN can be used to

perform several tasks such as pattern association, pattern recognition, function approximation, control, filtering, and beam forming. However, in this thesis, only pattern recognition and function approximation will be discussed. Descriptions of other learning tasks can be obtained in [179].

5.1.6.1 Pattern Recognition

Pattern recognition encompasses a wide range of information processing problems of great practical significance, from speech recognition and the classification of handwritten characters, to fault detection in machinery and medical diagnosis [169]. It is basically a process assigning a particular label or value to a given pattern or signal. One of the forms of pattern recognition is classification where data are assigned to a discrete class.

ANN performs pattern recognition by first learning the features extracted from a given input pattern during the training period before assigning the pattern to a designated class. According to Tou [183], features are defined as significant attributes which are to be used as the basis of classification. Chinese characters for example might have several discriminating features such as vertical stroke, horizontal stroke, dot, closed bottom and open bottom [183]. By learning these features during the training period, ANN will be able to distinguish one designated class from another. Later, when a new unseen pattern is presented, ANN will be able to identify the class of the pattern because of the information it has already learned during training.

In a multilayer feedforward network using a supervised learning algorithm, the task of feature extraction is performed by the computational units in the hidden layer(s) while the output layers allocate the pattern into the designated class [179]. The type of ANN that performs pattern recognition is known as a classifier.

5.1.6.2 Function Approximators

Function approximation is a process of finding the underlying relationship from a given finite input-output data and has been considered as the fundamental problem in a vast majority of real world applications [184]. According to Cybenko [185] and Hornik [186], a multilayer neural network has been proved to be capable of estimating any arbitrary non-linear function.

When ANN is used as a function approximator, the unknown functional relationship between the input and output is learned during the training period. This is done when sets of data or samples containing inputs and targeted outputs are

presented. During the training period, the synaptic weights and bias will be tuned in order to minimise the error between the approximated output and the targeted output.

Later, when new unseen data are presented, the ANN will be able to provide good approximations since the functional relationship between the input and output has been acquired during the training period. In general, the learning process of a function approximator network uses the error correction learning, as discussed in Section 5.1.5 and illustrated in Figure 5-10. The type of ANN that performs a function approximator is known as an approximator.

5.1.7 Multilayer Feedforward Back Propagation (MFBP) Network in Supervised Learning

According to Rumelhart et al. [187], the most widely used and successful supervised learning for multilayer feed forward networks is back propagation. The terms 'feed forward' and 'back propagation' used in MFBP network indicate that the network has two processing elements, as shown in Figure 5-11:

a. Element 1: The feeding of the input signals in a forward direction,
b. Element 2: The propagation of error signals in a backward direction.

In the first processing element, the input signals received from the input layer propagate forward from one hidden neuron to another until they reach the output neuron. In each forwarding movement, the input signals are processed as a function of both the neuron's associated synaptic weights and the input before transforming the signal into output signals at the end of the network. Based on the output signal, the error signals are calculated.

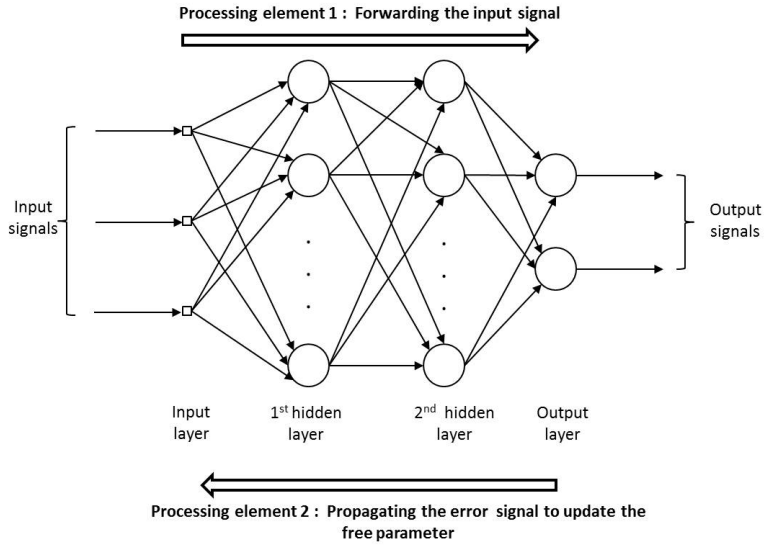

Figure 5-11: Illustration of the two processing elements in the MFBP network

In the second processing element, the error signals propagate backwards from the output neuron to the hidden neuron of the first hidden layer. As the error signals propagate from one neuron to another, the free parameters of the neurons (synaptic weights and bias) are changed or updated in the direction of minimising the error signals.

Once the free parameters are updated, in the next epoch, the input signals will again propagate from the input to the output layer, thus creating updated output signals and also reduced error signals. The signals will again propagate backwards in order to update the free parameters. The process of updating the free parameters will continue until the training process stops.

5.1.8 Parameter Updating Algorithm

The process of updating the free parameters depends largely on the parameter updating algorithm used. The simplest and most classical parameter updating algorithm is the Gradient Descent algorithm. In fact, in 1986 when Rumelhart et al. [187] first introduced back propagation in a neural network, a Gradient Descent algorithm was utilised. Today, more advanced numerical optimisation parameter updating algorithms have been developed such as the Conjugate Gradient, Quasi-Newton and Levenberg-Marquardt algorithms. In the subsequent sections, descriptions of several parameter updating algorithms will be discussed.

5.1.8.1 Gradient Descent Algorithm

Gradient Descent algorithm in neural network works on the principle of adjusting the free parameters in the direction opposite to the gradient of an error function $\mathcal{E}$. If the error function can be visualised as a surface located somewhere above a weight space, as shown in Figure 5-12, the movement of the weight updating will move until it reaches a point where $\mathcal{E}$ is minimum.

Looking at the neural network as a whole, the error signal given by output neuron j for each iteration n follows the same equation as Equation (5-9) which is $e_{j(n)} = d_{j(n)} - y_{j(n)}$. If an instantaneous error energy can be defined as $^1/_2\, e^2{}_{j(n)}$, correspondingly the summation of the instantaneous error energy can be taken as the error function which can be written as Equation (5-10) where set C includes all the neurons. Note that the parenthesis (n) indicates the error function $\mathcal{E}$ calculated at iteration n.

$$\mathcal{E}(n) = \frac{1}{2}\sum_{j \in C} e^2{}_{j(n)} \quad \textbf{(5-10)}$$

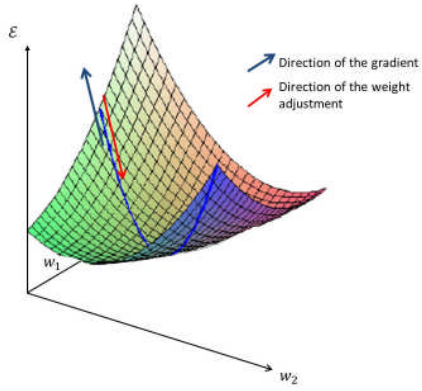

Figure 5-12: Error surface of an error function

In having to define the error function, the adjustment of the weight connecting neuron j to the preceding neuron, $\Delta w_{ji(n)}$ can be calculated using Equation (5-11) where η denotes the learning rate parameter and $\frac{\partial \mathcal{E}(n)}{\partial w_{ji(n)}}$ denotes the gradient of error function with respect to w_{ji}. Note that the negative sign shows that the direction of the weight updating is opposite to the direction of the gradient, as discussed in the earlier paragraph.

$$\Delta w_{ji(n)} = -\eta \frac{\partial \mathcal{E}(n)}{\partial w_{ji(n)}} \quad \textbf{(5-11)}$$

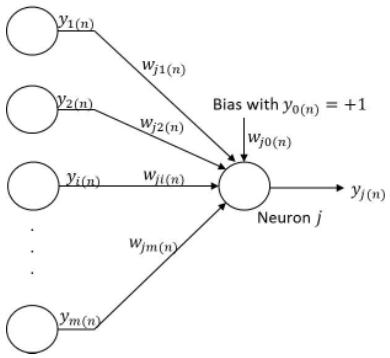

Figure 5-13: Illustration of neuron *j* with several preceding neurons

Consider Figure 5-13 which illustrates neuron j being fed by output signal, y coming from the several preceding neurons. Note that the bias is treated as weight w_{j0} with input signal y_0=1. From the figure, the output signal of neuron j can be written as

$$y_{j(n)} = \varphi\left(v_{j(n)}\right) \tag{5-12}$$

with

$$v_{j(n)} = \sum_{i=0}^{m} w_{ji(n)} y_{i(n)} \tag{5-13}$$

By applying the chain rule,

$$\frac{\partial \mathcal{E}(n)}{\partial w_{ji(n)}} = \frac{\partial \mathcal{E}(n)}{\partial e_{j(n)}} \times \frac{\partial e_{j(n)}}{\partial y_{j(n)}} \times \frac{\partial y_{j(n)}}{\partial v_{j(n)}} \times \frac{\partial v_{j(n)}}{\partial w_{ji(n)}} \tag{5-14}$$

Thus giving

$$\frac{\partial \mathcal{E}(n)}{\partial w_{ji(n)}} = -e_{j(n)}\, \varphi\left(v_{j(n)}\right) y_{i(n)} \tag{5-15}$$

The use of Equation (5-15) in (5-11) yields

$$\Delta w_{ji(n)} = \eta e_{j(n)}\, \varphi\left(v_{j(n)}\right) y_{i(n)} \tag{5-16}$$

Taking $e_{j(n)}\, \varphi'\left(v_{j(n)}\right)$ as the local gradient of neuron j, $\delta_{j(n)}$, Equation (5-16) can be written as

$$\Delta w_{ji(n)} = \eta \delta_{j(n)} y_{i(n)} \tag{5-17}$$

The computation of $\delta_{j(n)}$ will depend on the functionality of neuron j. If neuron j is an output neuron, Equation (5-18) can be used. However, if neuron j is a hidden neuron, a representation of $\delta_{j(n)}$ needs to be formulated.

$$\delta_{j(n)} = e_{j(n)}\, \varphi\left(v_{j(n)}\right) \tag{5-18}$$

Let us consider neuron j as a hidden neuron feeding an output signal $y_{j(n)}$ to an output neuron k. From Equation (5-18), $\delta_{j(n)}$ can be re-written as Equation (5-19). Using the chain rule, Equation (5-19), can be written as Equation (5-20).

$$\delta_{j(n)} = -\frac{\partial \mathcal{E}(n)}{\partial v_{j(n)}} \tag{5-19}$$

$$\delta_{j(n)} = -\frac{\partial \mathcal{E}(n)}{\partial y_{j(n)}} \times \frac{\partial y_{j(n)}}{\partial v_{j(n)}} \tag{5-20}$$

Using Equation (5-12), Equation (5-20) can be written as

$$\delta_{j(n)} = -\frac{\partial \mathcal{E}(n)}{\partial y_{j(n)}} \varphi\left(v_{j(n)}\right) \quad \textbf{(5-21)}$$

Since neuron k is now an output layer,

$$\mathcal{E}(n) = \frac{1}{2}\sum_{k \in C} e^2{}_{k(n)} \quad \textbf{(5-22)}$$

Again, using the chain rule,

$$\frac{\partial \mathcal{E}(n)}{\partial y_{j(n)}} = \frac{\partial \mathcal{E}(n)}{\partial e_{k(n)}} \times \frac{\partial e_{k(n)}}{\partial y_{j(n)}} \quad \textbf{(5-23)}$$

Using Equation (5-22), Equation (5-23) can be written as Equation (5-24) hence expended to be Equation (5-25)

$$\frac{\partial \mathcal{E}(n)}{\partial y_{j(n)}} = \sum_{k \in C} e_{k(n)} \times \frac{\partial e_{k(n)}}{\partial y_{j(n)}} \quad \textbf{(5-24)}$$

$$\frac{\partial \mathcal{E}(n)}{\partial y_{j(n)}} = \sum_{k \in C} e_{k(n)} \times \left(\frac{\partial e_{k(n)}}{\partial v_{k(n)}} \times \frac{\partial v_{k(n)}}{\partial y_{j(n)}}\right) \quad \textbf{(5-25)}$$

At neuron k, both $e_{k(n)}$ and $v_{k(n)}$ can be written as

$$e_{k(n)} = d_{k(n)} - y_{k(n)} = d_{k(n)} - \varphi\left(v_{k(n)}\right) \quad \textbf{(5-26)}$$

$$v_{k(n)} = \sum_{i=0}^{m} w_{kj(n)} y_{j(n)} \quad \textbf{(5-27)}$$

Differentiating both equations and using them with Equation (5-25) yields

$$\frac{\partial \mathcal{E}(n)}{\partial y_{j(n)}} = \sum_{k \in C} e_{k(n)} \left(-\varphi\left(v_{k(n)}\right)\right) w_{kj(n)} \quad \textbf{(5-28)}$$

Which can be simplified as

$$\frac{\partial \mathcal{E}(n)}{\partial y_{j(n)}} = -\sum_{k \in C} \delta_{k(n)}\, w_{kj(n)} \quad \textbf{(5-29)}$$

The use of Equation (5-29) in Equation (5-21) yields Equation (5-30). Once $\delta_{j(n)}$ has been formulated, then $\Delta w_{ji(n)}$ can be determined using Equation (5-17).

$$\delta_{j(n)} = \varphi\left(v_{j(n)}\right) \sum_{k \in C} \delta_{k(n)}\, w_{kj(n)} \quad \textbf{(5-30)}$$

From the algorithm presented, it can be said that when the Gradient Descent algorithm is used to update the free parameters, the weight adjustment for each synapse connecting the output neuron is determined by the learning rate, local gradient of the neuron and also the input signal of the respective weight. However, for a hidden neuron, the weight adjustment will not only depend on the learning rate and the input signal of the respective weight, but also the weighted sum of the local δs and the associate derivative of $\varphi'(v_{j(n)})$. In having to calculate the weight adjustment, the new updated weight can be calculated using Equation (5-31)

$$w_{update} = w_{old} + \Delta w \quad \textbf{(5-31)}$$

with w_{update}, and w_{old} denoting the updated weight and weight of the previous iteration.

The calculation of the local gradient requires the derivation of activation function. In order for the derivative to work, the activation function must be continuous. For this reason, activation functions such as the Log-Sigmoid and Hyperbolic-Tangent Function are commonly used in MFBP.

5.1.8.2 Levenberg-Marquardt (LM) Algorithm

In the Gradient Descent algorithm, $\partial\mathcal{E}/\partial w$ determines how the free parameters are being adjusted. This method is known as the first order method of error minimisation since only the first order derivative of the error function which describes the rate of the error function is considered. However, in the second order method of error minimisation, such as the LM algorithm, extra consideration is given by also including the deceleration of the error function which determines the curvature of the error surface [188]. According to Samarasinge [188], the deceleration of the error function at a given point in an error surface can be expressed by differentiating the error derivative i.e. $\partial^2\mathcal{E}/\partial w^2$ with respect to a weight. Consideration of both the gradient and also the deceleration of the error function, will not only help improve the performance of the network but also improve the training time by reducing the number of iterations required to achieve the optimal solution.

Different second order methods have different ways of utilising $\partial^2\mathcal{E}/\partial w^2$ in order to adjust the free parameters. The LM algorithm adjusts the free parameter by modifying Newton's method which uses Equation (5-32), written in matrix form to perform the weight adjustment.

$$\Delta \boldsymbol{w} = -[\nabla^2 \mathcal{E}(\boldsymbol{w})]^{-1} \nabla \mathcal{E}(\boldsymbol{w}) \tag{5-32}$$

where $\nabla^2 \mathcal{E}(\boldsymbol{w})$ and $\nabla \mathcal{E}(\boldsymbol{w})$ are the Hessian matrix, H and the gradient of the error function respectively. Note that the term $(\boldsymbol{w})$ in $\mathcal{E}(\boldsymbol{w})$ means that the error function is at some weight vector.

Taking the sum square error (Equation (5-33)) as the error function, both $\nabla \mathcal{E}(\boldsymbol{w})$ and $\nabla^2 \mathcal{E}(\boldsymbol{w})$ can be written as Equations (5-34)and (5-35) respectively.

$$\mathcal{E}(\boldsymbol{w}) = \sum_{i=1}^{N} e^2{}_i(\boldsymbol{w}) \tag{5-33}$$

$$\nabla \mathcal{E}(\boldsymbol{w}) = J^T(\boldsymbol{w}) \boldsymbol{e}(\boldsymbol{w}) \tag{5-34}$$

$$\nabla^2 \mathcal{E}(\boldsymbol{w}) = 2J^T(\boldsymbol{w}) J(\boldsymbol{w}) \tag{5-35}$$

Where N denotes the number of training patterns presented and $J(\boldsymbol{w})$ is the Jacobian matrix at some synaptic weight vector written as Equation (5-36) with n denoting the number of synaptic weights available in the network.

$$J(\boldsymbol{w}) = \begin{bmatrix} \frac{\partial e_1(\boldsymbol{w})}{\partial w_1} & \frac{\partial e_1(\boldsymbol{w})}{\partial w_2} & \cdots & \frac{\partial e_1(\boldsymbol{w})}{\partial w_n} \\ \frac{\partial e_2(\boldsymbol{w})}{\partial w_1} & \frac{\partial e_2(\boldsymbol{w})}{\partial w_2} & \cdots & \frac{\partial e_2(\boldsymbol{w})}{\partial w_n} \\ \vdots & \vdots & \ddots & \\ \frac{\partial e_N(\boldsymbol{w})}{\partial w_1} & \frac{\partial e_N(\boldsymbol{w})}{\partial w_2} & \cdots & \frac{\partial e_N(\boldsymbol{w})}{\partial w_n} \end{bmatrix} \tag{5-36}$$

The LM algorithm modified the Newton method given in Equation (5-32) by incorporating a scaling parameter λ (Equation (5-37)) which is (i) multiplied by factor ϑ>1 if a step would result in an increase in the error function or (ii) divided by ϑ>1 when the error function is decreasing.

$$\Delta \boldsymbol{w} = -[J^T(\boldsymbol{w}) J(\boldsymbol{w}) + \lambda I]^{-1} J^T(\boldsymbol{w}) \boldsymbol{e}(\boldsymbol{w}) \tag{5-37}$$

where λ, ϑ and I denote the scaling parameter, multiplication or division factor of the Levenberg-Marquardt parameter and identity matrix respectively.

To apply the algorithm to MFBP, a suitable Jacobian matrix needs to be formulated by means of modifying the previous back propagation method. This is done by considering the error instead of the sum squares of error. Consider a multilayer network, as shown in Figure 5-14, with R inputs, S neurons for each layer, and M layers being presented with N training patterns. Hence the error function vector at the output layer (layer M) can be written as

$$\boldsymbol{\mathcal{E}}^T = [\boldsymbol{\mathcal{E}_1}\ \boldsymbol{\mathcal{E}_2}\ \ldots\ \boldsymbol{\mathcal{E}_N}] \approx \left[e_{1,1}\ e_{2,1}\ \ldots\ e_{S^M,1}\ e_{1,2}\ e_{2,2}\ \ldots\ e_{S^M,N}\right] \quad \textbf{(5-38)}$$

Note that the term $e_{2,1}$ represents the error obtained from the second output neuron calculated using the first training pattern. Additionally the free parameter vector can also be written as

$$\left[w^1{}_{1,1}\ \ w^1{}_{1,2}\ \ldots\ w^1{}_{S^1,R}\ b^1{}_1\ \ldots\ b^1{}_{S^1}\ w^2{}_{1,1}\ w^2{}_{1,2}\ \ldots\ w^2{}_{S^2,S^1}\ b^2{}_1\ \ldots\ b^M{}_{S^M}\right] \quad \textbf{(5-39)}$$

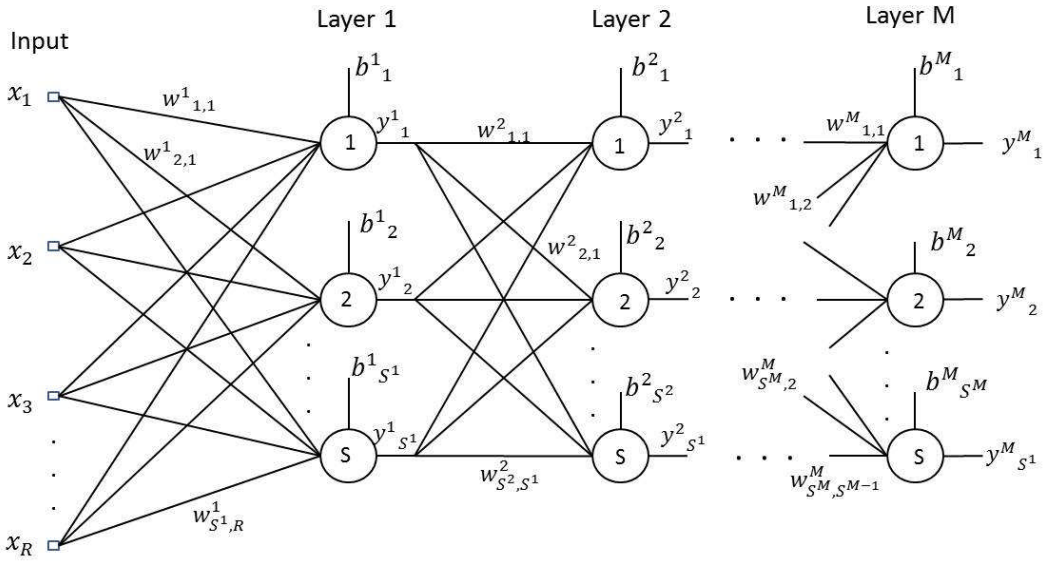

Figure 5-14: Schematic diagram of a multilayer network

Also the term $w^1{}_{1,2}$ represents the weight of the first layer neuron 1 connected by the previous input 2. In addition $b^2{}_1$ represents the bias of neuron 1 in layer 2. Imitating the Jacobian matrix for Equation (5-36) will give

$$J(\boldsymbol{w}) = \begin{bmatrix} \frac{\partial e_{1,1}}{\partial w^1{}_{1,1}} & \frac{\partial e_{1,1}}{\partial w^1{}_{1,2}} & \cdots & \frac{\partial e_{1,1}}{\partial w^1{}_{S^1,R}} & \frac{\partial e_{1,1}}{\partial b^1{}_1} & \cdots & \frac{\partial e_{1,1}}{\partial b^1{}_{S^1}} & \frac{\partial e_{1,1}}{\partial w^2{}_{1,1}} & \cdots \\ \frac{\partial e_{2,1}}{\partial w^1{}_{1,1}} & \frac{\partial e_{2,1}}{\partial w^1{}_{1,2}} & \cdots & \frac{\partial e_{2,1}}{\partial w^1{}_{S^1,R}} & \frac{\partial e_{2,1}}{\partial b^1{}_1} & \cdots & \frac{\partial e_{2,1}}{\partial b^1{}_{S^1}} & \frac{\partial e_{2,1}}{\partial w^2{}_{1,1}} & \cdots \\ \vdots & \vdots & & \vdots & \vdots & & \vdots & \vdots & \\ \frac{\partial e_{S^M,1}}{\partial w^1{}_{1,1}} & \frac{\partial e_{S^M,1}}{\partial w^1{}_{1,2}} & \cdots & \frac{\partial e_{S^M,1}}{\partial w^1{}_{S^1,R}} & \frac{\partial e_{S^M,1}}{\partial b^1{}_1} & \cdots & \frac{\partial e_{S^M,1}}{\partial b^1{}_{S^1}} & \frac{\partial e_{S^M,1}}{\partial w^2{}_{1,1}} & \cdots \\ \vdots & \vdots & & \vdots & \vdots & & \vdots & \vdots & \\ \frac{\partial e_{1,2}}{\partial w^1{}_{1,1}} & \frac{\partial e_{1,2}}{\partial w^1{}_{1,2}} & \cdots & \frac{\partial e_{1,2}}{\partial w^1{}_{S^1,R}} & \frac{\partial e_{1,2}}{\partial b^1{}_1} & \cdots & \frac{\partial e_{1,2}}{\partial b^1{}_{S^1}} & \frac{\partial e_{1,2}}{\partial w^2{}_{1,1}} & \cdots \\ \vdots & \vdots & & \vdots & \vdots & & \vdots & \vdots & \\ \frac{\partial e_{1,N}}{\partial w^1{}_{1,1}} & \frac{\partial e_{1,N}}{\partial w^1{}_{1,2}} & \cdots & \frac{\partial e_{1,N}}{\partial w^1{}_{S^1,R}} & \frac{\partial e_{1,N}}{\partial b^1{}_1} & \cdots & \frac{\partial e_{1,N}}{\partial b^1{}_{S^1}} & \frac{\partial e_{1,N}}{\partial w^2{}_{1,1}} & \cdots \end{bmatrix} \quad \textbf{(5-40)}$$

The terms $\partial e/\partial w$ and $\partial e/\partial b$ in the element of the Jacobian matrix were computed by defining the Marquardt sensitivity, $\bar{S}$. For element containing $\partial e/\partial w$,

$$[J]_{row,column} = \frac{\partial e_{k,q}}{\partial w^m{}_{i,j}} = \bar{S}^m{}_{i,q} \times y_{i,q}^{m-1} \quad \textbf{(5-41)}$$

and for element containing $\partial e / \partial b$

$$[J]_{row,column} = \frac{\partial e_{k,q}}{\partial b^m{}_i} = \bar{S}^m{}_{i,q} \quad \textbf{(5-42)}$$

The term $e_{k,q}$ represents the error at any neuron k calculated by presenting training pattern q. $\partial w^m{}_{i,j}$ indicates the weight at any layer m, connecting any neuron i with input j. Also $\bar{S}^m{}_{i,q}$ represents the sensitivity at any neuron i of layer m calculated when pattern q is presented while $y_{i,q}^{m-1}$ represents the output produced by the previous layer of neuron i when pattern q is presented.

The sensitivity $\bar{S}^m{}_{i,q}$ either for the weight and bias is almost similar to the local gradient defined in the previous back propagation algorithm. Because of that, when the neuron is the output neuron $\bar{S}^m{}_{i,q}$can be calculated using Equation (5-43).

$$\bar{S}^m{}_{i,q} = \varphi^{M}\left(v_{i,q}^{M}\right) \quad \textbf{(5-43)}$$

Instead, when the neuron is the hidden neuron, $\bar{S}^m{}_{i,q}$can be calculated using Equation (5-44)

$$\bar{S}^m{}_{i,q} = \varphi^{m}\left(v_{i,q}^{m}\right)(\boldsymbol{w}^{m+1})^T \bar{\boldsymbol{S}}_q^{m+1} \quad \textbf{(5-44)}$$

Once the Jacobian matrix is computed, Equation (5-37) can be used to calculate $\Delta \boldsymbol{w}$. The iterative process can be summarised as follows [Hagan]:

1. Present all input and compute all the corresponding output.
2. Calculate the error $e_{1,1}\ e_{2,1}$ ... $e_{1,2}$ ... $e_{1,N}$ ... and obtain the sum square error of all input.
3. Compute the Marquardt sensitivity using Equation (5-43) for output neurons and (5-44) for hidden neurons.
4. Build the Jacobian matrix using Equation (5-40).
5. Compute $\Delta \boldsymbol{w}$ using Equation (5-37).
6. Compute the updated weight using Equation (5-31).
7. Re-compute the sum square error using the updated weight. If the sum square error is smaller than in Step 2, divide λ by ϑ and go back to step 1.However, if the sum square is larger, then multiply λ with ϑ and go back to step 6.

5.1.8.3 Conjugate Gradient (CG) Algorithm

The CG algorithm is another form of second order method of error minimisation. The purpose of introducing this algorithm is not only to improve the performance of the network but to improve the training time by reducing the number of iterations required to achieve the optimal solution. In this method the adjustment of the weights is determined by utilising search direction vectors that are directionally conjugated with each other.

For a brief understanding, consider a quadratic error function $\mathcal{E}(\boldsymbol{x})$ as given in Equation (5-45) where $\boldsymbol{w}$ is the weight vector, $\boldsymbol{H}$ is the symmetric, positive definite Hessian matrix, $\boldsymbol{b}$ is a vector, and c is a scalar.

$$\mathcal{E}(\boldsymbol{w}) = \frac{1}{2}\boldsymbol{w}^T\boldsymbol{H}\boldsymbol{w} + \boldsymbol{b}^T\boldsymbol{w} + c \tag{5-45}$$

The gradient of the quadratic function, $\boldsymbol{g}$ can be written as

$$\boldsymbol{g} = \mathcal{E}(\boldsymbol{w}) = \boldsymbol{H}\boldsymbol{w} + \boldsymbol{b} \tag{5-46}$$

Therefore the change in the gradient at iteration $n+1$ can be written as

$$\Delta\boldsymbol{g_n} = \boldsymbol{g}_{n+1} - \boldsymbol{g}_n = (\boldsymbol{H}\boldsymbol{w_{n+1}} + \boldsymbol{b}) - (\boldsymbol{H}\boldsymbol{w_n} + \boldsymbol{b}) = \boldsymbol{H}\Delta\boldsymbol{w}_n \tag{5-47}$$

Consider $\boldsymbol{p}_n$ as a search direction vector, the change in $\boldsymbol{w}$ can be written as

$$\Delta\boldsymbol{w}_n = \boldsymbol{w_{n+1}} - \boldsymbol{w}_n = \eta_n\boldsymbol{p}_n \tag{5-48}$$

When the steepest descent is used to determine $\Delta\boldsymbol{w}_n$, $\boldsymbol{p}_n$ will be in the direction of the opposite gradient of the quadratic function. Additionally η_n can be computed using Equation (5-49).

$$\eta_n = -\frac{\boldsymbol{p}_n{}^T\boldsymbol{g}_n}{\boldsymbol{p}_n{}^T\boldsymbol{H}\boldsymbol{p}_n} \tag{5-49}$$

Since in the CG algorithm, the search direction vectors are taken to be directionally conjugate to each other, the search direction vector for $n+1$ should satisfy the conjugacy rule as given in Equation (5-50).

$$\eta_n\boldsymbol{p}_n{}^T\boldsymbol{H}\boldsymbol{p}_{n+1} = \Delta\boldsymbol{w}_n{}^{\boldsymbol{T}}\boldsymbol{H}\boldsymbol{p}_{n+1} = \Delta\boldsymbol{g}_n^T\boldsymbol{p}_{n+1} = 0 \tag{5-50}$$

From Equation (5-50) it can be seen that the search direction will be conjugate when the $\boldsymbol{p}_{n+1}$is orthogonal to the change in the gradient.

Having understood this condition, the first search direction $\boldsymbol{p}_0$ can be taken as directly opposite to its gradient with $\boldsymbol{p}_0 = -\boldsymbol{g}_0$. Then at each iteration, $\boldsymbol{p}_n$ which is

orthogonal to the change in the gradient, can be constructed using Equation (5-51) with β_n known as the scaling factor at iteration n.

$$\boldsymbol{p}_n = -\boldsymbol{g_n} + \beta_n \boldsymbol{p}_{n-1} \quad \textbf{(5-51)}$$

There are several methods that can be used to find β_n such as given by Hestenes and Steifel (Equation (5-52)), Fletcher and Reeves (Equation (5-53)), and Polak and Ribiere (Equation (5-54)).

$$\beta_n = \frac{\Delta \boldsymbol{g^T}_{\boldsymbol{n-1}} \boldsymbol{g_n}}{\Delta \boldsymbol{g^T}_{\boldsymbol{n-1}} \boldsymbol{p}_{n-1}} \quad \textbf{(5-52)}$$

$$\beta_n = \frac{\boldsymbol{g^T}_{\boldsymbol{n}} \boldsymbol{g_n}}{\boldsymbol{g^T}_{\boldsymbol{n-1}} \boldsymbol{g_{n-1}}} \quad \textbf{(5-53)}$$

$$\beta_n = \frac{\Delta \boldsymbol{g^T}_{\boldsymbol{n-1}} \boldsymbol{g_n}}{\boldsymbol{g^T}_{\boldsymbol{n-1}} \boldsymbol{g_{n-1}}} \quad \textbf{(5-54)}$$

The CG algorithm cannot be directly applied to MFBP since the error function used in MFBP is not quadratic. For this reason, Equation (5-49) cannot be used. Secondly the exact minimum cannot be reached in a definite number of iterations.

To overcome these constraints, the previous method of calculating Equation (5-49) is replaced using the iterative interval location and reduction method as described in [189]. Using these methods, $\Delta \boldsymbol{w}_n$ and $\boldsymbol{w_{n+1}}$ can be computed. In addition, since no exact minimum can be obtained in a definite number of iterations, the search direction is reset to the steepest gradient direction after n directions.

With MFBP, the computation of gradient $\boldsymbol{g}$ is computed using Equation (5-15). However the adjustment of the free parameter is determined using the CG algorithm via Equation (5-51).

5.1.8.4 Scaled Conjugate Gradient (SCG) Algorithm

In the previously discussed CG algorithm, it has been shown how the line search is used to adjust the synaptic weight. However, when the algorithm is implemented into the MFBP, the iterative process used in the interval location and reduction in each line search causes the implementation to be computationally expensive.

To overcome this problem, Moller [190] introduced the SCG algorithm as a way of avoiding the line search procedures of the CG algorithm. Referring to Equation (5-49), the determination of the η for each n iteration is influenced by the Hessian matrix, $\boldsymbol{H}$. As the error function can also be non-quadratic, $\boldsymbol{H}$ does not need to be

positive definite [169]. In order to ensure that $\boldsymbol{H}$ can be positive definite, modification on $\boldsymbol{H}$ needs to be done in the form of the Levenberg-Marquardt approach as given in Equation (5-55).

$$\boldsymbol{H} + \lambda \boldsymbol{I} \tag{5-55}$$

This modifies Equation (5-49) to

$$\eta_n = -\frac{\boldsymbol{p}_n{}^T \boldsymbol{g}_n}{\boldsymbol{p}_n{}^T \boldsymbol{H} \boldsymbol{p}_n + \lambda_n \|\boldsymbol{p}_n\|^2} \tag{5-56}$$

Equation (5-56) shows that when λ_n has large values, η_n will become small, hence reducing the step size of the weight adjustment. According to Bishop [169], the technique is also known as the model trust region method because the model is effectively only trusted in a small region around the current search point which is governed by λ_n, i.e. a larger λ_n will have smaller trust region and vice versa.

Consider now the denominator of Equation (5-56) which is

$$\zeta_n = \boldsymbol{p}_n{}^T \boldsymbol{H} \boldsymbol{p}_n + \lambda_n \|\boldsymbol{p}_n\|^2 \tag{5-57}$$

for a positive definite Hessian, $\zeta_n > 0$. However in the case of $\zeta_n < 0$, λ_n needs to be increased to $\breve{\lambda}_n$ so that $\zeta_n > 0$. When Moller [190] set $\breve{\lambda}_n$ to be

$$\breve{\lambda}_n = 2\left(\lambda_n - \frac{\mathcal{E}_n}{\|\boldsymbol{p}_n\|^2}\right) \tag{5-58}$$

The rise in $\breve{\zeta}_n$ becomes

$$\breve{\zeta}_n = -\boldsymbol{p}_n{}^T \boldsymbol{H} \boldsymbol{p}_n \tag{5-59}$$

Since the size of the trust region depends on λ_n, the decision to increase or decrease λ_{n+1} is determined using a comparison parameter Δc_n defined by

$$\Delta c_n = \frac{2\{\mathcal{E}_n - \mathcal{E}_{n+1}\}}{\eta_n \boldsymbol{p}_n{}^T \boldsymbol{g}_n} \tag{5-60}$$

When Δc_n is close to unity, it shows that the current approximation is good hence λ_n should be reduced in order to reduce the step size of the weight adjustment. However, if Δc_n has a low value, the current approximation needs to be improved hence λ_n should be increased in order to increase the step size of the weight adjustment. The following rules are then applied to change λ_{n+1}

$$\begin{aligned} &\text{If } \Delta c_n > 0.75 \text{ then } \lambda_{n+1} = \lambda_n / 2 \\ &\text{If } \Delta c_n < 0.25 \text{ then } \lambda_{n+1} = 4\lambda_n \end{aligned} \tag{5-61}$$

The SCG algorithm can be summarised as follows:

1. Initialise the weight vector, λ and set $\check{\lambda} = 0$.
2. Find the initial $\boldsymbol{g}$, $\boldsymbol{H}$ and $\boldsymbol{p}$.
3. Calculate ζ using Equation (5-57). If $\zeta < 0$, then calculate $\check{\zeta}$.
4. Calculate the η using Equation (5-56).
5. Update $\boldsymbol{w}$ using Equation (5-48) and set $\check{\lambda} = 0$.
6. Find the $\boldsymbol{g}, \boldsymbol{H}$ using the updated $\boldsymbol{w}$.
7. Calculate β using either Equation (5-52), (5-53) or (5-54).
8. Calculate $\boldsymbol{p}$ using Equation (5-51).
9. Calculate Δc using Equation (5-60) and, depending on the rules given in Equation (5-61), adjust λ for the use of the next iteration.
10. In the next iteration, use the adjusted λ and repeat steps 3 to 10.
11. When $\boldsymbol{g} = 0$, then stop the process.

5.1.9 Performance Improvement and Generalisation in MFBP

There are many factors that can influence the performance (reduction in error function) of a created network, such as the complexity of the problem in hand, the quality of the training samples, the selection of architecture and the application of the training algorithm. Nevertheless, there are some measures that can be taken in order to improve the performance of the network. Some of these are:

a. Selecting a proper input set to train the network: The inputs selected to form the input set should be good enough to provide significant change to the output response. The input pattern for pattern recognition, for example, should provide good features so the network can differentiate the pattern from one class to another. Sensitivity analysis can be a good way of accessing how strongly an input element can affect the predicted output. By knowing the strength of each input in changing the predicted output, not only does it help users to eliminate the unnecessary weaker inputs, it also ensures that the stronger inputs are not left behind. Methods used by Li et al. [191] and Ogaji et al. [192] can be used in performing the sensitivity analysis.

b. Selecting suitable activation function: MFBP in general will learn faster when the sigmoidal activation function used is antisymmetric than when it is nonsymmetric [193]. Antisymmetric function are functions that satisfy

$$\varphi(-v) = -\varphi(v) \quad \textbf{(5-62)}$$

This condition can be achieved when the Hyperbolic-Tangent Function is used. This can be clearly seen when the outputs of the activation function produced by both the Hyperbolic-Tangent and Log-Sigmoid Function are tested using the condition given in (5-62). Taking v as 5, the output of the Hyperbolic-Tangent Function (Equation (5-8)) is:

$$\varphi(-5) = -0.9991 \text{ and } -\varphi(5) = \text{-}0.9991$$

while for the Log-Sigmoid Function (Equation (5-7)) is

$$\varphi(-5) = 0.006693 \text{ and } -\varphi(5) = \text{-}0.9933$$

For this reason, the Hyperbolic-Tangent Function should be more preferable in ensuring faster learning.

c. Pre-processing the inputs and targeted outputs: Neural network training can be made more efficient if certain pre-processing on the network inputs and outputs is performed [169], [194]. This can be done by normalising both inputs and outputs to a specific range. Scaling of a particular input or output can be done using Equation (5-63)

$$Val_N = ValMin_N + (ValMax_N - ValMin_N)\left(\frac{Val - ValMin}{ValMax - ValMin}\right) \quad \textbf{(5-63)}$$

where Val_N, $ValMin_N$ and $ValMax_N$ denote the normalised value, minimum and maximum range of normalised value while Val, $ValMin$ and $ValMax$ denote the input/output present, minimum and maximum value respectively. For example, if the input has the maximum and minimum values of 3,000 and 100, the normalised value for input of 1,715 within the specified normalised range of -1 to 1 will be

$$Val_N = -1 + \big(1 - (-1)\big)\left(\frac{1715 - 100}{3000 - 100}\right) = 0.11379$$

The specified range is often influenced by the activation function used. For example, if the Hyperbolic-Tangent Function is used, than the suitable range for normalisation is -1 to 1. This is to ensure that all of the input within the minimum to maximum values can be properly activated within the limit of the activation function. Apart from that, the normalisation will also ensure that the speed of the free parameter adjustment can be done at the same rate.

Besides possessing good network performance, achieving good generalisation is also crucial. The network is said to achieve good generalisation when it is able to retain

its performance when unseen inputs (inputs never seen before) are presented. The network learning can be viewed as a 'fitting' process between the behaviours of predicted and targeted outputs. When too many input-output examples are presented during the learning, 'overfitting' will occur. This means that instead of understanding the behaviour of the outputs for given inputs, the network will end up memorising the examples and hence lose the ability to generalise.

Figure 5-15(a) and (b) depict a comparison between a properly fitted data and an overfitted data respectively. From the figure it can be seen that when overfitting occurs, the output of the unseen input predicted by the network deviates from its true value. However, when good generalisation is achieved, the true output behaviour is learnt, hence accurate prediction is also achieved.

According to Hagan [189], for a network to be able to generalise, the amount of free parameter should be less than the data used in the training. Clearly here both the amount of sample and free parameters play an important role in determining the success of achieving good generalisation.

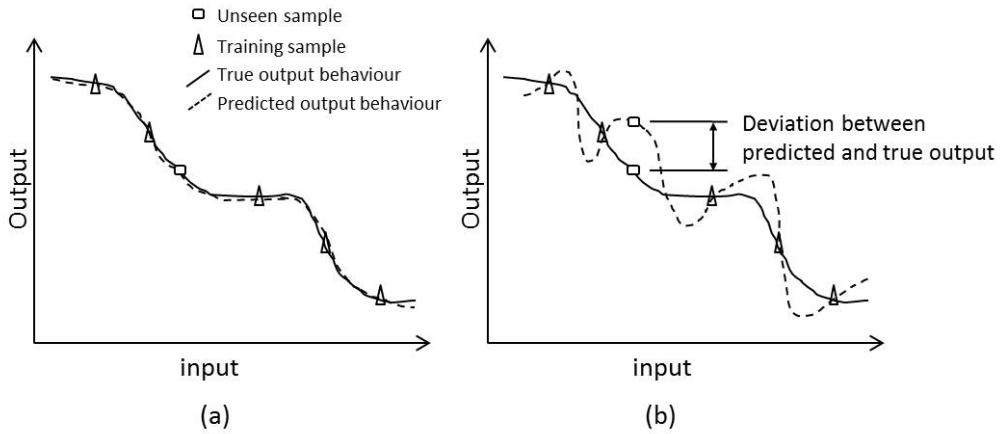

Figure 5-15: (a) Properly fitted data (good generalisation) (b) Overfitted data (poor generalisation)

One way of preventing overfitting is to use the early stopping method. According to Sarle [195], the early stopping method can be done by splitting the input samples into training samples and validation samples. The training samples will be used to perform the free parameter updates while the validation samples will be used to decide when to stop. When both samples are simultaneously used during the training, the error function of the validation samples is observed and the training is stopped when the error function begins to rise. Hagan et al. [189] added that additional test samples can also be taken from the input samples. When the test samples are used together

with the training and validation samples, they act as a mean to compare the performance between different networks.

5.1.10 Advantages and Disadvantages of ANN

It is obvious that by imitating the biological neural system, ANN originates its computing ability through its huge parallel distribution computing neurons and the ability to evolve while learning from its environment. This makes it possible to solve complex, large scale problems. Some of the advantages of ANN are:

a. Ability to solve non-linear problems. Since ANN is constructed using interconnected non-linear neurons, solving problems which are non-linear is not a problem.
b. ANN has the ability to adapt to its environment through the adjustment of free parameters during the learning period. This makes the network dynamic and can always be continuously improved.
c. By understanding the behaviour between the input and the output, the non-explicit relationship between both can be mapped, hence producing a model-free estimation.
d. Since the complexity of the problems is distributed among layers of computing neurons, computation is significantly shortened once the network has been trained, especially when the computation is done in parallel.
e. The ability to distribute the complexity of the problem ensures that ANN can work with large numbers of variables.
f. Because ANN can be trained to suit a particular unique system, it can be tailored to the condition of that system, hence provide a better representation of the system.
g. By using the multilayer network, ANN has the ability to approximate any arbitrary non-linear function.
h. ANN has the ability to carry out different learning tasks from pattern association, pattern recognition, control, function approximation etc.

Despite numerous advantages, there are also weaknesses in ANN. Some of the weaknesses are:

a. ANN is unable to retain its performance when it has to perform outside the range of data used during the training. As a result, massive data are required to ensure that the range exceeds the requirement of the estimation capability.

b. The amount of time required to train the network increases if the size of the samples or the complexity of the problems increases.
c. Its ‘black box’ nature makes it difficult to access the network ’reasoning’. Apart from defining the architecture and setting up the network parameters, users have no other role than presenting the input, watching it train and providing the output.

5.2 Developing ANN-Based Creep Life Prediction

In this section the development of the alternative neural-based creep life prediction, suitable to predict HP turbine blade’s creep life is presented.

5.2.1 Analysing the Process of the Current Model-Based Creep Life Prediction Approach

As mentioned in Section 3.5, since the proposed neural-based creep life prediction approach serves as an alternative to the existing prediction process, the focus of the study is to develop suitable architectures that are able to absorb the complexity of the developed Integrated Creep Life Prediction model. But before this can be done, the process of how the integrated model performs the creep life prediction needs to be analysed.

In this process analysis, an output-input process tree which imitates the decision tree used in operational research is first constructed. The process tree would graphically provide sufficient information on how data are being manipulated and linked from the final output (minimum creep life, L_{Cmin}) to the preceding sub-processes; and how data are transferred from one preceding variable to another until the model inputs are met at the end of the process tree.

Appendix B provides the output-input process tree of the Integrated Creep Life Prediction model for the case of an engine with a single stage HP turbine with the blades being analysed using the Uncooled Blade 1D Thermal Model. From Appendix B, it can be seen how the overall process of predicting the minimum creep life can be visualised using the process tree. The process tree can be divided into two major divisions where the first sub-process mainly calculates the blade’s metal temperature, T_M while the second calculates the LMP through the determination of the blade’s maximum stress, σ_{max}. The linking from one sub-process to another helps to identify which variables are being manipulated in order to obtain the output of the sub-

processes. It was found that the entire creep life prediction requires two main parameters and two main inputs which are

a. Calculated parameters: Parameters that are being calculated during the prediction process.
b. Simulated parameters: Parameters that are simulated using PYTHIA.
c. Primary input: User's main inputs on which the estimations of the component creep life are based.
d. Secondary inputs: One-off inputs that remain unchanged through the entire prediction process.

Note that the gas turbine sensors used to isolate and quantify the engine health conditions, together with the operating and health conditions, were categorised as primary inputs. To explain this decision, consider two scenarios which are scenario 1 where engine health conditions are known and scenario 2 where engine health conditions are unknown. In scenario 1, since engine health conditions are known, inputs from the sensors are not needed. However in scenario 2, since health condition are unknown, sensors' inputs become vital in order to perform the isolation and quantification. For this reason both the sensors and engine conditions are considered to be primary inputs.

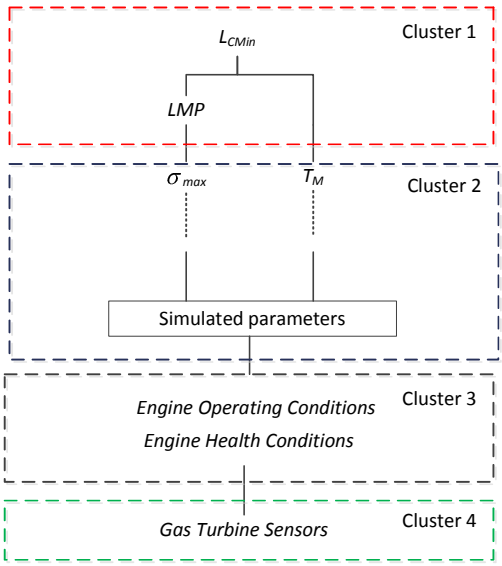

Figure 5-16: Clustering of analysed parameters

Based on the process tree, clustering of the parameters was done, as shown in Figure 5-16. The clustering of the parameters will become the basis of deciding how the proposed architectures should be designed to map those clusters. As shown in the figure, Cluster 1 clusters the two parameters that condition a Larson-Miller master

curve. Cluster 2 contains the parameters used to compute different forms of stresses, temperatures, pressures etc. in order to calculate the blade's metal temperature and maximum stress. Clusters 3 and 4 contain both primary inputs; Cluster 3 groups the parameters that define the engine operating and health conditions, while Cluster 4 groups all the gas turbine sensors.

Note also that the secondary inputs were not grouped into any clusters. This is because the inputs are not changing through the entire prediction process hence do not provide any sensitivity in changing the behaviour of the blade's creep life when the engine operating and health conditions are changed.

5.2.2 Conceptual Designs of the Neural Architectures

Using the clustered parameters, different mappings that link the clustered parameters were created. These mappings become the conceptual designs of the neural-based architectures.

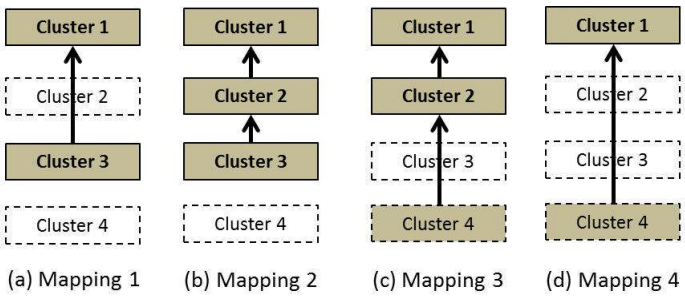

Figure 5-17 Different mappings between the cluster parameters

Four mappings (1 to 4) as shown in Figure 5-17(a) to (d) were created. In Mapping 1, a direct link from Cluster 3 to Cluster 1 was proposed with both Cluster 2 and 4 were left out. In Mapping 2, linking between Cluster 3 and 1 was proposed by introducing intermediate linkages that link Cluster 3 to Cluster 2 before linking Cluster 2 to Cluster 1. However in Mapping 2, Cluster 4 was left out. In Mapping 3, intermediate linkages were also used. However the aim is to connect Cluster 4 to Cluster 1 by first linking Cluster 4 to 2 before linking Cluster 2 to 1. In Mapping 3, Cluster 3 was left out. Finally in Mapping 4, direct mapping between Cluster 4 and 1 was proposed with Clusters 2 and 3 were left out.

Once the mapping was established, the parameter(s) for each cluster were finalised, as shown in Table 5-1. These finalised parameters were then used to construct the input and output of individual neural networks that form the proposed architecture.

Table 5-1: Finalised parameter(s) for each cluster

Cluster	Finalised parameter(s)
1	L_{CMin}
2	σ_{max} and T_M
3	Engine operating and health conditions
4	Gas turbine sensors

5.2.3 The Proposed Neural-Based Architectures

Based on the conceptual design, the neural-based architectures were formed. Although four conceptual designs were created, only three designs were pursued which are Mappings 1, 2 and 3 in order to developed three neural-based architectures. The main reason Mapping 4 was left out was because of the limited amount of time available to test all of the proposed architectures. For this reason, the construction of the neural-based architecture based on Mapping 4 will be done in future work.

As discussed in Section 5.1.9, the complexity of the problem in hand dictates the performance of the neural network created. For this reason two scenarios are considered:

a. Scenario 1: Low complexity problems
b. Scenario 2: High complexity problems.

5.2.3.1 Neural-Based Architecture for Low Complexity Problems

When dealing with low complexity problems, simple neural architecture can be used in order to realise the mappings created during the conceptual design. The architecture using conceptual design Mapping 1 is given in Figure 5-18. Based on the figure, it can be seen that only one approximator network (Creep Life Approximator) is needed to map the finalised parameters. This architecture is known as the Range-Based (RB) architecture where inputs from the engine operating conditions and known engine health conditions are sent to the approximator network in order to predict the blade's creep life within a certain user defined range.

It can be seen from Figure 5-18, the RB architecture creates a direct mapping between the selected inputs and the engine model HP turbine blade's creep life. In situations where users want to create an alternative neural-based solution for a clean engine case only, then the engine health conditions inputs can be excluded.

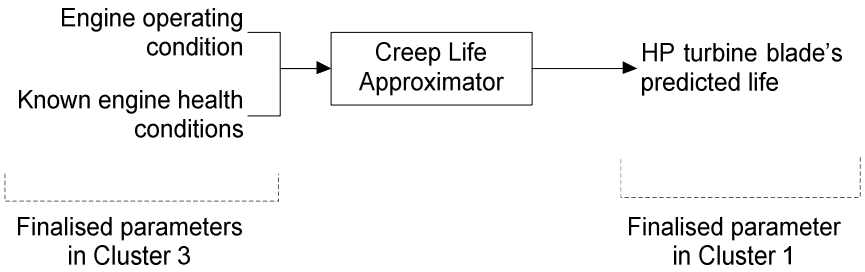

Figure 5-18: Range-Based architecture based on Mapping 1

The second architecture, as shown in Figure 5-19, is called the Functional-Based (FB) architecture and is proposed based on the second conceptual design, Mapping 2. From the figure it can be seen that the architecture uses two intermediate approximator networks known as the Blade Metal Temperature Approximator and the Blade Stress Approximator and one output approximator known as the Creep Life Approximator. The inputs, which are the engine operating conditions and known engine heath conditions, are sent to individual intermediate approximators in order to predict the two functional parameters which are the blade's metal temperature and stress before the predicted values are sent to the Creep Life Approximator to predict the blade's creep life.

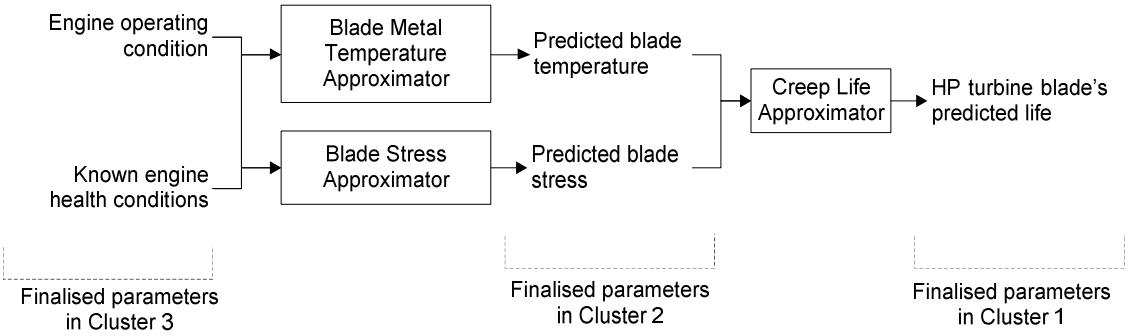

Figure 5-19: Functional-Based architecture based on Mapping 2

The proposed FB architecture in a way forms a cascade network where the networks are arranged in a successive manner with the intermediate approximators, which not only provide the outputs to the main inputs but also provide inputs to the network that produces the final output. Similarly to the previous architecture, when only a clean engine case is considered, the engine health conditions inputs can be excluded.

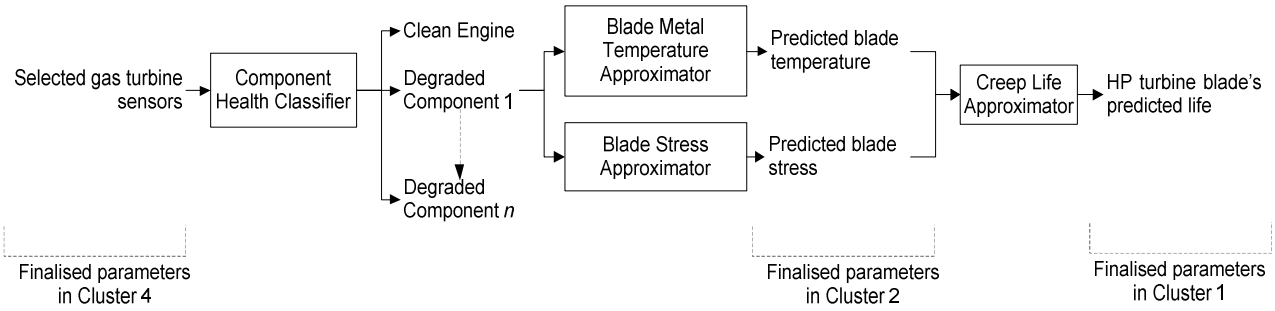

Figure 5-20: Sensor-Based architecture based on Mapping 3

The Sensor-Based (SB) architecture forms the final neural architecture created based on the third conceptual design, Mapping 3, as shown in Figure 5-20. The cascaded type of network receives inputs from selected gas turbine sensors and classifies the input patterns into different classes of engine health condition (i.e. Class 1 for clean engine, Class 2 for compressor degradation etc.) via the Component Health Classifier. Then the classed inputs are sent to the respective intermediate approximators to predict the blade's metal temperature and stress. Finally, using the predicted values, the blade's creep life is predicted using the output approximator.

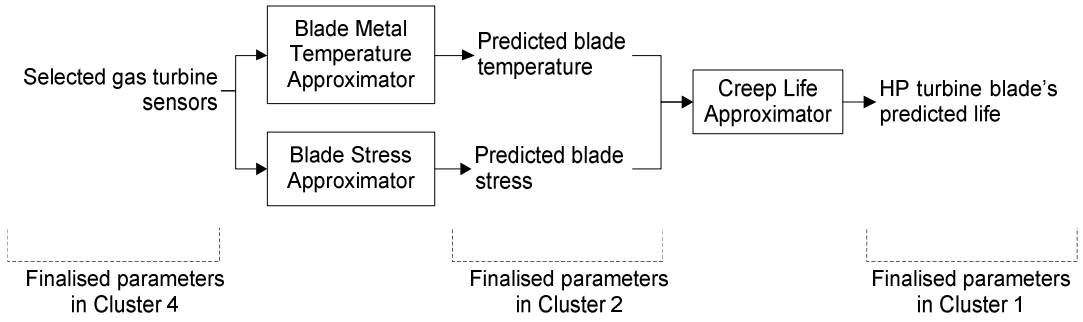

Figure 5-21: Simplified Sensor-based architecture for clean engine case

In dealing with only the clean engine case, the SB architecture can be simplified by utilising only three approximators, as shown in Figure 5-21. The simplified version of the architecture receives inputs from the sensors before predicting both the functional parameters and uses the predicted values to predict the blade's creep life.

5.2.3.2 Neural-Based Architecture for High Complexity Problems

There are several reasons why the complexity of creep life prediction using the alternative neural solution increases, including wider engine operation envelope, increase in the component degradation magnitudes, or because the engine performance becomes too non-linear. Consequently these create a complicated non-

linear error surface (in a synaptic weight space as shown in Figure 5-12) with many local minima. Hence it becomes difficult for the neural network to optimise the free parameters.

In order to improve the prediction capability, several actions can be taken:

a. The blade's creep life range can be divided into several smaller ranges with each smaller range having its own approximators.
b. The engine operation envelope can be divided into smaller divisions with each division having its own approximators.
c. If the engine health conditions are known, separate architecture can be constructed for each degraded component.
d. If the degradation magnitudes are too big, then magnitudes of the degradation can be divided into smaller divisions with each division having its own approximators.

Figure 5-22 provides an example of how the creep life prediction range can be divided into smaller ranges by first introducing a Range Classifier to classify the input pattern into the desired creep life range. Once the input has been classified, the input will be sent to the respective Class Range Approximator in order to predict the blade's creep life.

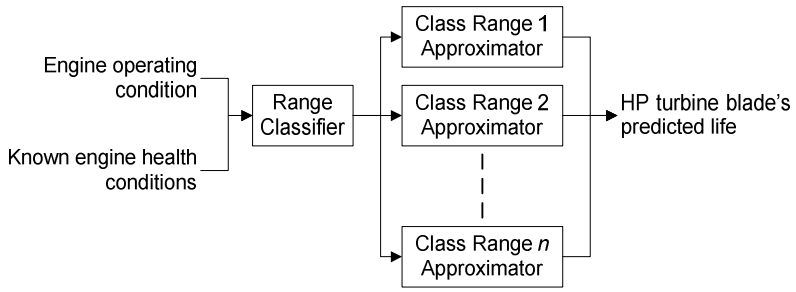

Figure 5-22: RB architecture with different ranges of creep life prediction

Figure 5-23 shows another example of how the degradation magnitude is divided into three levels (low, medium and high) before the operational envelope is divided into several divisions. Since in the example, the engine health condition is already known, different FB architectures can be built accordingly, i.e. FB architecture for compressor degradation, FB architecture for turbine degradation etc. According to Figure 5-23, the component degradation magnitude will be assessed first in order to determine the levels of degradation. Then using the engine operating input, the input will be assessed and then sent to the corresponding operation division. Here, the input will be presented to both intermediate approximators to estimate the blade's metal temperature and

stress before both estimated values are sent to the output approximators to estimate the blade's creep life.

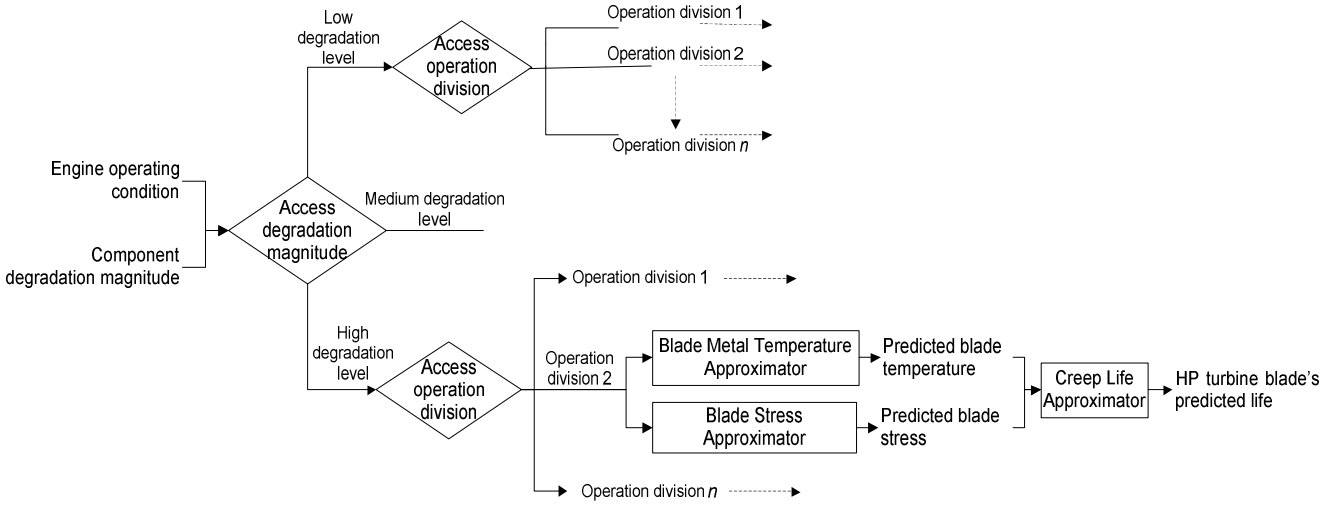

Figure 5-23: FB architecture with degradation levels and operation divisions

Figure 5-24 provides another example of how the SB architecture can be used with the incorporation of different levels of operation and degradation magnitude. Note that in Figure 5-24, altitude is chosen as a dividing criterion to divide the operating envelope into three levels of altitude. When the gas turbine sensors and altitude are input, the corresponding altitude is assessed. Then the sensor input is sent to the respective Component Health Classifier in order to classify the input into the corresponding engine health condition. Since the degradation magnitude is also divided into several levels, a Degradation Level Classifier is used to classify the input into the corresponding degradation level. Finally the input will be sent to the intermediate approximators before the blade's creep life is predicted using the output approximator.

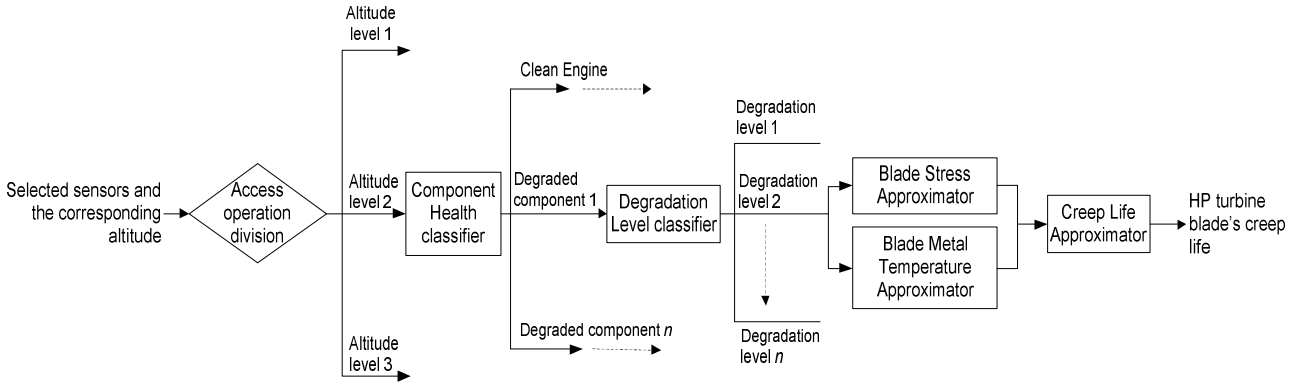

Figure 5-24: SB architecture with operation and degradation levels

The choice of what classes of network design (single layer or multi-layer) should be used, what learning paradigm should be applied (supervised or unsupervised) or even what type of training algorithm (first order or second order) for each proposed architecture will depends on the user. However, in this thesis, the application of the architecture was done using an MFBP network with a second order training algorithm. The implementation of the architecture is discussed in Chapter 7.

5.2.3.3 Advantages and Disadvantages of Each Proposed Architecture

Table 5-2: Advantages and disadvantages of the proposed architectures

Architecture	Advantages	Disadvantages
RB	1. Only one approximator network is needed to map the input to the main output. 2. Time required to train the network is less if one network is used. 3. Computational time is faster when one network is used. 4. Can cater for a much wider creep life range since the life range can be split into smaller divisions to maintain prediction accuracy.	1. Time required to train the network can increase if the smaller division of creep life range is required. 2. Becomes rigid to changes if functional parameters require any changing. 3. If classifier network is used, there will be a chance of misclassification. 4. Needs to know degradation magnitude prior to life prediction.
FB	1. Flexible to changes since separate networks are used to represent the intermediate and output parameters. 2. Easy to train when one network needs more training. 3. Can change one functional parameter to another without disrupting the whole architecture. 4. No need for classifier networks to perform any classification, hence eliminates the possibility of misclassification.	1. Requires more networks to map the input to the main output. 2. Requires more training since more networks are needed even in uncomplex situations. 3. Needs to know degradation magnitude prior to life prediction.
SB	1. Does not require any component diagnostics prior to life estimation 2. Flexible to changes since separate networks are used to represent the intermediate and output parameters. 3. Easy to train when one network needs more training. 4. Can change one functional parameter to another without disrupting the whole architecture.	1. Requires more networks to map the input to the main output and also to isolate component degradation. 2. Requires more training since more networks are needed even in uncomplex situations. 3. Misclassification can occur.

Since different neural architectures have different network arrangements, one architecture should have advantages over the other and vice versa Table 5-2 provides the advantages and the disadvantages of the RB, FB and SB architectures.

5.3 Chapter Conclusion

The aim of the chapter was to discuss the development of the alternative creep life estimation method using the ANN approach. However, in the first part of the chapter, the theory of the ANN was given. This covers:

a. explanation of how the ANN was modelled based on the functionality of the biological neural unit
b. descriptions of several activation functions commonly used in ANN design
c. descriptions of different classes of ANN design
d. description of ANN learning process and tasks
e. discussion on the functionality of the MFBP network
f. detailed discussions on several commonly used first and second order training algorithms
g. discussion on how to improve the network performance and generalisation
h. the advantages and disadvantages of ANN.

In the second part of the chapter, the development of the neural-based creep life prediction was discussed. Using an output-input process tree, the process of the current model-based creep life prediction approach was analysed. It was found that the entire creep life prediction requires two main parameters and two main inputs which are the calculated parameters, simulated parameters, primary inputs and the secondary inputs.

Based on the process tree, clustering of the parameters was done. Using the clustered parameters, four conceptual designs with different forms of mapping between the cluster parameters were proposed. Once the mapping was established, the parameter(s) for each cluster were finalised. These finalised parameters were then used to construct the input and output of individual neural networks that form the proposed architectures.

Three neural-based architectures known as the RB, FB and SB architectures were then finalised. In the RB architecture, the prediction of the blade's minimum creep life is done using the Creep Life Approximator network that receives inputs from the engine operating conditions and known engine health conditions. In both the FB and SB architectures, intermediate approximators known as the Blade Metal Temperature

Approximator and the Blade Stress Approximator networks were introduced to predict the blade's metal temperature and stress. However, both the FB and SB architectures use different inputs with the FB architecture uses the engine operating conditions and known engine health conditions, while the SB architecture uses the gas turbine sensors.

In this chapter, the evolution of the proposed architectures was also given from low to high complex prediction problems. Several actions such as dividing the creep life into several ranges or dividing the operational space into smaller divisions were also given. Finally the advantages and disadvantages of each proposed architecture were presented.

6 APPLICATION OF THE INTEGRATED CREEP LIFE PREDICTION MODEL: EFFECTS OF OPERATING AND HEALTH CONDITIONS ON HP TURBINE BLADE'S CREEP LIFE

This chapter presents the application of the developed Integrated Creep Life Prediction Model in order to investigate the effects of several selected operating and health parameters on a selected engine model HP turbine blade's creep life. In this analysis, the introduced Creep Factor, as discussed in Section 4.6.1, is used to assess the impact of individual selected parameters when the parameters deviate from a user-defined reference operating condition.

In addition, the influence of a given mission profile on the HP turbine blade's creep life is investigated. This is done for two conditions:

a. When the engine is clean, and
b. When the engine is degraded due to compressor fouling and turbine erosion.

Using the Creep Factor approach, the impact of both clean and degraded engines on the HP turbine blades' nominal creep life is measured.

6.1 Engine Model Construction

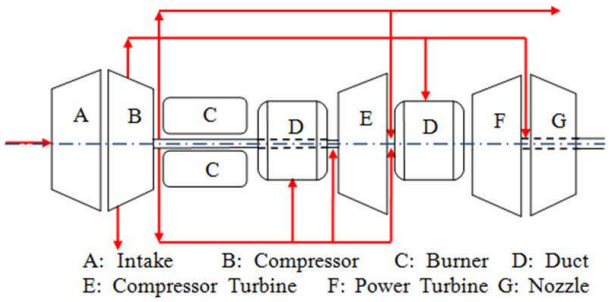

Figure 6-1: Engine model configuration

In order to perform the investigations, a helicopter turbo-shaft engine model is used. The configuration of the engine is given in Figure 6-1 which consists of a three axial-one centrifugal stage compressor, a reverse flow annular combustion chamber, a single stage compressor turbine (HP turbine) and a two-stage power turbine (LP turbine). Based on the engine configuration, an engine performance model was constructed using PYTHIA. It is important to note that the data used to construct the engine model are based on a newly designed helicopter engine given by an engine

manufacturer. However, for confidentiality reasons, the engine data will not be given in this thesis.

6.1.1 Design Point Performance Adaptation

Although most of the data are given by the engine manufacturer, some data are reasonably assumed. Consequently, the assumed data can lead to prediction errors. To reduce the DP performance prediction errors, non-linear DP performance adaptation was carried out using PYTHIA where the method was proposed and coded by Li et al. [191]. In their method, the parameters which are defined as the to-be-adapted parameters will be modified until the targeted performance parameters are met. Figure 6-2 provides a schematic diagram of the adaptation procedure which was used in the research. The theoretical and mathematical model used in this approach will not be discussed in this thesis as it has been reported in [191].

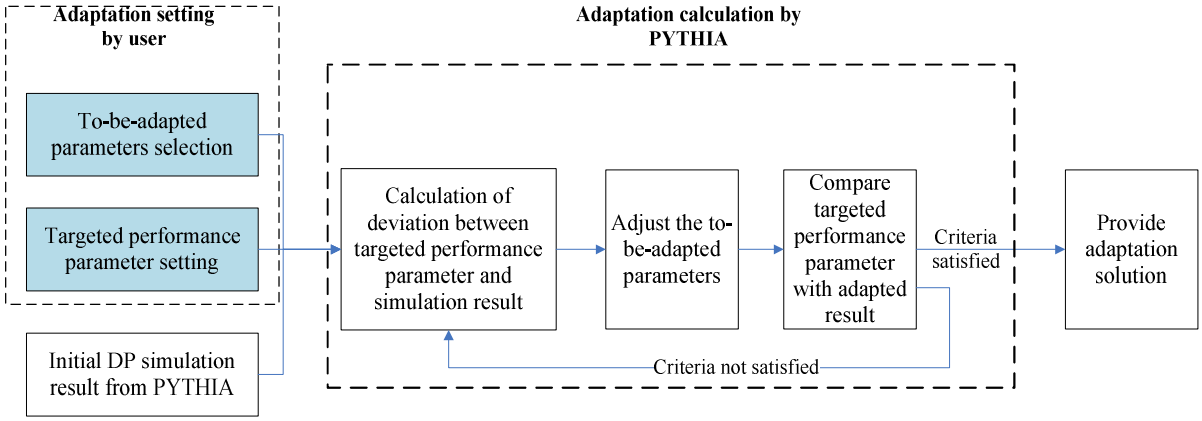

Figure 6-2: Schematic Diagram of the Non-Linear Adaptation Procedure

As shown in Figure 6-2, there are two parameters (shaded text boxes) that need to be specified [191]:

a. The to-be-adapted parameters which are parameters that will be changed during the adaptation. These parameters are also called the independent parameters or gas turbine component parameters, such as mass flow rates, compressor pressure ratios and isentropic efficiencies, turbine entry temperature, and turbine isentropic efficiencies. These parameters are independent of each other and determine the engine performance at DP.
b. The targeted parameters, which are also called the dependent performance parameters or measurable parameters, such as thrust or shaft power, specific fuel consumption or thermal efficiency, and gas path pressures and

temperatures. The quantity of these parameters is determined by the quantity of the independent component parameters or the to-be-adapted parameters.

Table 6-1 lists the targeted performance parameters and the to-be-adapted parameters selected in the research. It is worth mentioning that the targeted performance parameters were obtained from the engine DP performance data given by the engine manufacturer.

Table 6-1: Parameters selected of the DP performance adaptation

To-be-adapted parameters	Targeted parameters
Intake pressure recovery	Compressor inlet total pressure
Intake mass flow	Compressor outlet total pressure
Compressor pressure ratio	Compressor outlet total temperature
Compressor isentropic efficiency	Power turbine inlet total temperature
Compressor bleed pressure ratios	Power turbine outlet total pressure
Mass fractions extracted from the core flow	Fuel flow
Turbine entry temperature	
HP Turbine isentropic efficiency	
Power Turbine isentropic efficiency	

After the to-be-adapted parameters were chosen, performance adaptation was undertaken. As shown in Figure 6-2, during the adaptation process, the deviations between the targeted and the simulated parameters (based on the existing component parameters) are calculated. The to-be-adapted parameters are then changed iteratively until the adaptation criterion is achieved. The adaptation criterion used in [191] is that the root mean square, RMS of the difference between the targeted and simulated parameters calculated using Equation (6-1) must be smaller than 0.001.

$$RMS = \sqrt{\frac{\sum_{i=1}^{G}\left(\frac{\hat{z}_i - z_i}{z_i} \times 100\right)^2}{G}} \quad \textbf{(6-1)}$$

where $\hat{z}$ and z are the simulated and specified targeted parameters respectively and G is the number of targeted parameters specified for the adaptation.

Figure 6-3 depicts the prediction errors percentage, E, calculated using Equation (6-2) before and after the performance adaptation was carried out.

$$E = \frac{\hat{z}_i - z_i}{z_i} \times 100 \quad \textbf{(6-2)}$$

From Figure 6-3, it can be seen that the prediction errors of all the targeted measurements have significantly reduced from the average errors of 0.998% to 5.08E-

5%. Also, two of the parameters, which are the compressor outlet total pressure and power turbine inlet total temperature, have no prediction errors while the highest prediction error is given by the power turbine total pressure which drops from 4.78% to 0.0002%. Based on the figure, it can be clearly seen that after DP performance adaptation was performed, an accurate engine model was achieved at DP.

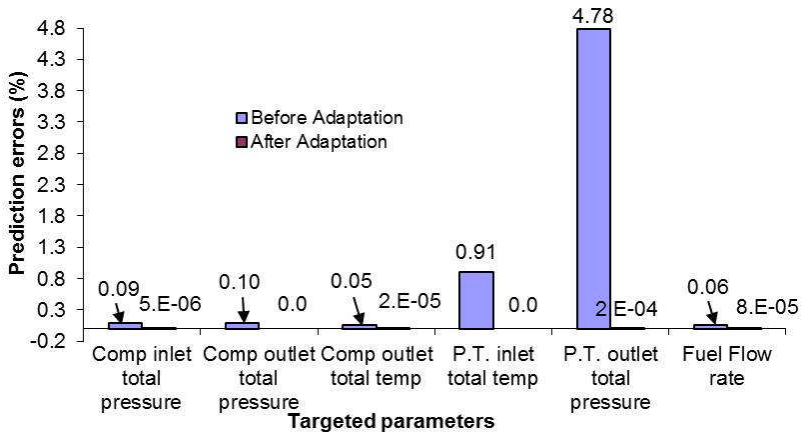

Figure 6-3: Prediction errors before and after the performance adaptation

6.1.2 Off-Design Performance Adaptation

Even though an accurate engine model has been accomplished at DP, prediction accuracy at OD conditions must also be realised. Therefore OD performance adaptation needs to be carried out. Since the accuracy of the engine performance model at OD conditions depends very much on the component characteristic maps in use, performance adaptation can be done by either scaling the characteristics map using a set of scaling factors [196–201] or by generating new component characteristic maps based on the engine test bed data [202], [203].

A typical turbine map is illustrated in Figure 6-4, where the initial map is represented in solid speed lines and a typical point on a speed line is denoted as *A* having characteristic parameters WAC_A, ETA_A and DH_A. In the figure, WAC, ETA and DH are the corrected mass flow rate, isentropic efficiency, and enthalpy drop ratio respectively. When the map is scaled, point *A* moves to *A** and its corresponding characteristic parameters are changed to WAC_{A^*}, ETA_{A^*} and DH_{A^*} If the scaling factors used to scale the corresponding characteristic parameters are SF_{WAC}, SF_{ETA}, SF_{DH}, then WAC_{A^*}, ETA_{A^*} and DH_{A^*} can be determined using Equations (6-3), (6-4) and (6-5) respectively.

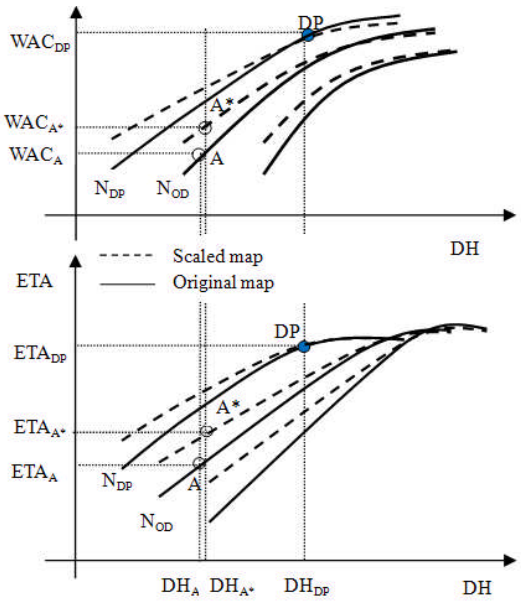

Figure 6-4: OD scaling of a turbine map

$$WAC_{A*} = SF_{WAC} \times WAC_A \quad \textbf{(6-3)}$$

$$ETA_{A*} = SF_{ETA} \times ETA_A \quad \textbf{(6-4)}$$

$$DH_{A*} = SF_{DH} \times DH_A \quad \textbf{(6-5)}$$

In this research, OD performance adaptation was carried out using the method proposed by Li et al. [204] which is already available in PYTHIA. A non-linear form of a quadratic scaling factor function given in Equation (6-6) is introduced to relate the scaling factors to the operating condition. By having to use the scaling factor function, a unique value of scaling factor can be applied as the operating condition changes.

$$SF_X = 1 + b\left(\left|\frac{L_{DP} - L_{OD}}{L_{DP}}\right|\right) + c\left(\left|\frac{L_{DP} - L_{OD}}{L_{DP}}\right|\right)^2 \quad \textbf{(6-6)}$$

In Equation (6-6), SF denotes a scaling factor for a typical characteristic parameter with coefficients b and c denoting two scaling factor function coefficients. In addition, subscript X represents a general characteristic parameter where for the compressor and turbine L_{DP} and L_{OD} represent the relative non-dimensional rotational speed, CN at OD point and DP respectively while for the burner, L_{DP} and L_{OD} represent the burner inlet pressure, BIP for OD point and DP, respectively.

The search of the optimum coefficients b and c, in [204] is done using the genetic algorithm (GA) and the effectiveness of the adaptation process is measured using an objective function (OF) given in Equation (6-7). In Equation (6-7), $P_{(predict)}$ is the

predicted measurements obtained using the initial or adapted component characteristic maps, $P_{(actual)}$ is the targeted measurements obtained from real engine tests, m denotes the number of measurements used for each OD point included, and k denotes the number of OD points included in the adaptation process. From Equation (6-7), it can be seen that the effectiveness of the adaptation increases if the value of the OF reduces.

$$OF = \frac{1}{k}\frac{1}{m}\left[\sum_{j=1}^{k}\sum_{i=1}^{m}\left|\frac{P_{(predict)i,j} - P_{(actual)i,j}}{P_{(actual)i,j}}\right|\right] \times 100 \qquad \textbf{(6-7)}$$

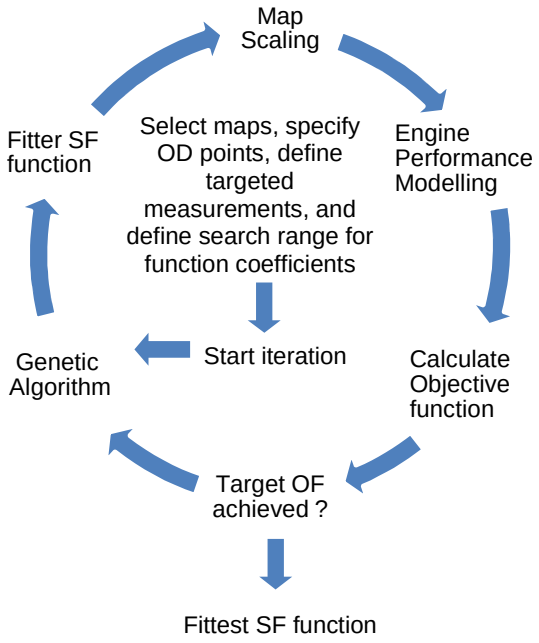

Figure 6-5: Flowchart of the OD performance adaptation in [204]

The process of obtaining an optimal set of scaling factor functions using a GA is illustrated in Figure 6-5. Each GA string represents a potential solution of a set of coefficients b and c which are required to form the necessary scaling factor functions for specified component characteristic map(s). Once component characteristic maps are selected as the to-be-adapted component maps (maps that are scaled during adaptation), OD points used in the adaptation process are specified. Then for each specified OD point, measurements which are used as the target (values to be achieved during adaptation) are defined. The fitter strings are then searched by the GA within the heuristically given range of the scaling factor function coefficients b and c.

During the optimisation process, each string is applied to scale the component maps, and the scaled maps are then used by the engine performance model to produce simulated measurements. Based on these simulated and targeted

measurements, an objective function, as in Equation (6-7), is calculated. If none of the strings can lead to the desired objective function, the GA reproduction process will continue until the fittest string is found or the maximum allowable generation is reached. Note that if the adaptation outcome is not desirable, scaling factor function coefficients b and c search ranges will be changed once again heuristically and the search for the fittest string will be repeated.

For this research, test rig data were used. The test data of the engine were obtained from the engine manufacturer who conducted the engine performance tests at various OD points. Using the engine performance model, a set of generic component characteristic maps were initially applied to the engine model to start the performance simulation. In this research, three component characteristic maps for the compressor, compressor turbine and power turbine were chosen as the to-be-adapted maps while the burner map remains unchanged.

Table 6-2: Operating points available from the test rig data

No.	PCN	Status
1	0.9981	Testing
2	0.98273	Adaptation
3	0.97862	Adaptation
4	0.96713	Adaptation
5	0.95442	Testing
6	0.9268	Adaptation

Based on the test rig data, six operating points, as listed Table 6-2, were available for analysis. “Adaptation” in the table implies that the data at these points were used for adaptation where “Testing” implies that the points were used to test the model accuracy after adaptation was performed. In addition, PCN in the table denotes the relative compressor rotational speed. The value of 0.9981 indicates that the compressor rotational speed at this point is 99.81% of its absolute design speed. In addition, for each point listed in Table 6-2, seven measurements, as listed in Table 6-3, were used as the targeted measurement.

Before the adaptation was conducted, the performances of the engine model using the to-be-adapted (generic) component characteristic maps were simulated according to the OD points and measurements listed in Table 6-2 and Table 6-3 respectively. Then, the E, for each measurement at each operating point was calculated using Equation (6-2).

Table 6-3: Measurements selected as targeted measurements

Measurement	Symbol	Unit
Compressor outlet total pressure	*P3*	atm
Compressor outlet total temperature	*T3*	K
Power turbine inlet temperature	*T12*	K
Power turbine outlet total pressure	*P15*	atm
Power turbine outlet total temp	*T15*	K
Fuel flow	*FF*	kg/s
Shaft power	*SP*	W

Table 6-4: Initial prediction error (%) at different $PCNs$

	Prediction error (%)					
PCN	0.998	0.9827	0.97862	0.96713	0.9544	0.9268
P3	0.0	0.83	1.65	3.82	5.64	13.29
T3	0.0	0.26	0.11	0.36	0.78	0.89
T12	0.0	0.96	1.33	2.35	3.04	5.64
P15	0.0	1.58	0.93	0.23	0.0035	0.47
T15	0.0	0.1	0.12	1.21	1.68	0.38
FF	0.0	1.45	2.99	5.88	8.07	20.5
SP	0.0	3.01	5.23	10.83	17.20	47.27

The initial engine model prediction errors are shown in Table 6-4 where several observations can be made. As PCN reduces from 0.9827 to 0.9268, the prediction errors for most measurements increase. *P3*, *FF* and *SP* have considerably higher prediction errors, especially at lower speeds, with the highest error reaching around 48%. It can also be seen that the errors vary non-linearly with PCN (refer to Figure 6-6 to Figure 6-11) suggesting that variable scaling factors for each operating point and component characteristic parameter are required to ensure minimal prediction errors across the operating envelope.

Figure 6-6 to Figure 6-11 represent the prediction errors calculated using Equation (6-2) for different measurements before and after the adaptation was carried out. In general, significant improvement has been achieved as the majority of the prediction errors (after the adaptation) for the OD points used in the adaptation or testing have fallen below the specified threshold which is E=2%. This can be seen in Figure 6-6 and Figure 6-7 where both *SP* and *FF* which initially possess considerably higher prediction errors (see Table 6-4) have been reduced significantly, especially at the lowest PCN with reductions from 45% to 0.07% for *SP* and 20% to 0.67% for *FF*.

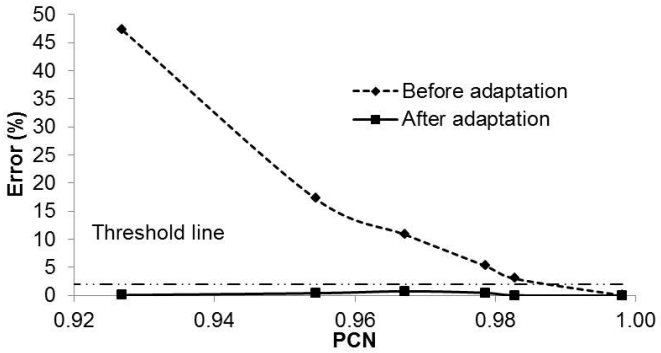

Figure 6-6: Prediction errors for SP before and after adaptation

From the initial simulation (before adaptation), the prediction errors for most measurements except for *P15* (see Figure 6-8) and *T15* (see Figure 6-9) are seen to increase when PCN is reduced. This indicates that if the rotational speed is further reduced, the prediction accuracy will deteriorate even more.

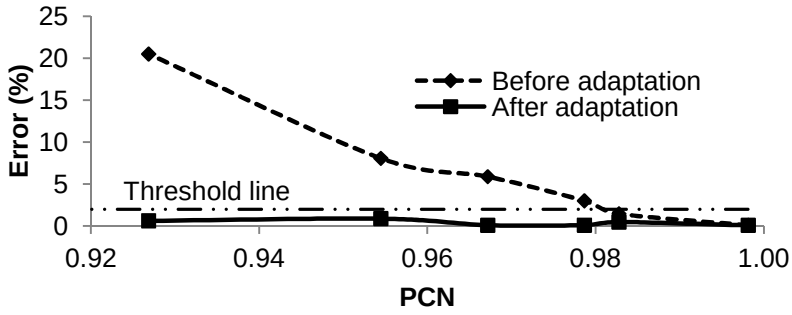

Figure 6-7: Prediction errors for *FF* before and after adaptation

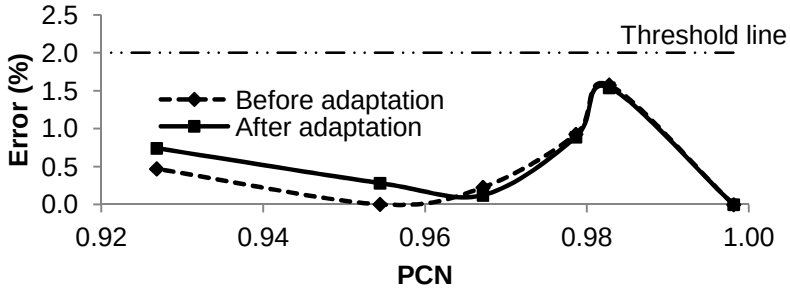

Figure 6-8: Prediction errors for *P15* before and after adaptation

However, for both *P15* and *T15*, the initial prediction errors are seen to fluctuate as PCN changes. Despite the fluctuations, the prediction errors were well below the threshold value (2% error) indicating that the occurrence of the fluctuation did not cause significant change in the accuracy of the prediction.

After performance adaptation was completed, only three measurements were found to exceed the threshold value, which were *T15* (4.5%), *T3* (3%), and *T12* (2.67%) as shown in Figure 6-9 to Figure 6-11 respectively. Note that the prediction

errors of these three measurements during the initial simulation were well below the threshold. This demonstrates that in order to reduce huge initial errors produced by other measurements, accuracy of some measurements needs to be compromised.

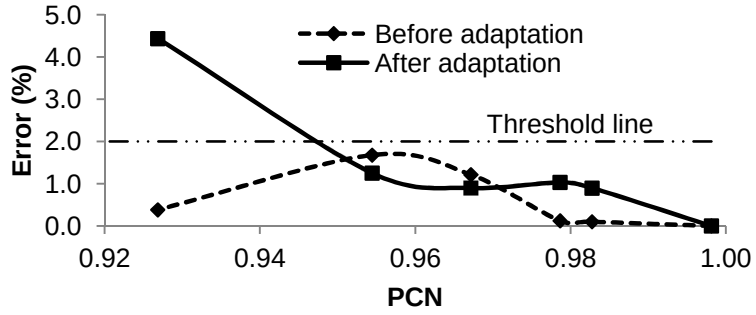

Figure 6-9: Prediction errors for *T15* before and after adaptation

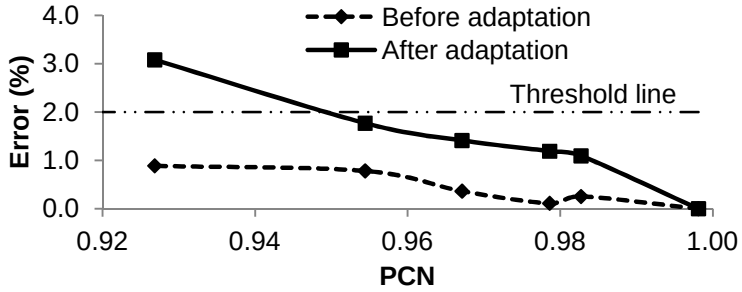

Figure 6-10: Prediction errors for *T3* before and after adaptation

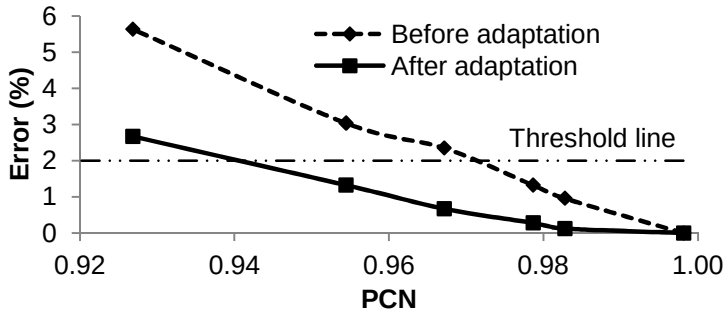

Figure 6-11: Prediction errors for *T12* before and after adaptation

Table 6-5 lists the average errors for individual measurements for all operating points listed in Table 6-2, E_{AVE}, and the total average errors for all measurements, $E_{AVETOTAL}$, before and after adaptation, calculated using Equations (6-8) and (6-9).

$$E_{AVE} = \frac{1}{n}\sum_{j=1}^{n}\frac{\hat{z}_j - z_j}{z_j} \times 100 \quad \textbf{(6-8)}$$

$$E_{AVETOTAL} = \frac{1}{nm}\sum_{i=1}^{n}\sum_{j=1}^{m}\frac{\hat{z}_{i,j} - z_{i,j}}{z_{i,j}} \times 100 \quad \textbf{(6-9)}$$

where m is number of measurements defined for each specified OD point, n denotes the number of operating points used for this study including all points for adaptation and testing, z is the measurement taken from the test rig while $\hat{\mathrm{z}}$ is the measurement simulated using the to-be-adapted map at the same operating point.

Table 6-5: Summary of average errors before and after adaptation

	Average Error (%)	
Measurement	Before adaptation	After adaptation
P3	4.2	0.34
T3	0.4	1.42
T12	2.22	0.85
P15	0.53	0.6
T15	0.58	1.42
FF	6.49	0.36
SP	13.92	0.29
Total Average Error (%)	4.05	0.75
Number of measurements exceeding the threshold	15	3

From Table 6-5, it can be seen that after the adaptation, the E_{AVE} of all the measurements selected for this study were significantly reduced. The average errors of all the measurements fall below the specified threshold, although measurements *T3* and *T15* are seen to have relatively higher errors compared with the others. Note that for both *T3* and *T15*, their final average errors are higher than their initial simulated values. As explained earlier, the increase in those errors is due to the compromise made to reduce the high initial errors caused by both *SP* and *FF*.

The overall improvement is indicated by the $E_{AVETOTAL}$ given in Table 6-5. It can be seen that $E_{AVETOTAL}$ has reduced considerably from 4% to around 0.75%. Furthermore, the number of measurements having prediction errors that exceed the specified threshold were reduced noticeably from 15 to only 3.

From the results shown in the previous paragraphs, it can be concluded that after performing both DP and OD point performance adaptations, the prediction accuracy of the engine model has been improved significantly. This is crucial for the research, as an accurate engine model can give the correct 'picture' on how different engine operating and health conditions can affect the behaviour of the blade's creep life consumption.

6.2 Method of Performing the Impact Analysis

The first part of the study investigates the effects of different operating and health parameters on the engine model HP turbine blade's creep life. The method of the analysis for the first part of the study is summarised in Figure 6-12. Each selected parameter within the specified range was simulated using the developed Integrated Creep Life Prediction Model. The aim is to obtain its corresponding Creep Factor, CF, calculated using Equation (4-45). The obtained CFs were then plotted against its respective parameter. This is to analyse the trend of the change on the blade's creep life. If the behaviour is exponential, a log CF against its corresponding parameter will be plotted to obtain a linear relation. The linear relation permits a specific impact weight, defined as the slope of the plot to be calculated which, in general, represents how much the blade's creep life will be affected when a unit of the parameter deviates from its reference value. Higher impact weight will indicate higher creep life consumption; thus having this value compared from one parameter to another can indicate which parameter is more sensitive in changing the blade's creep life.

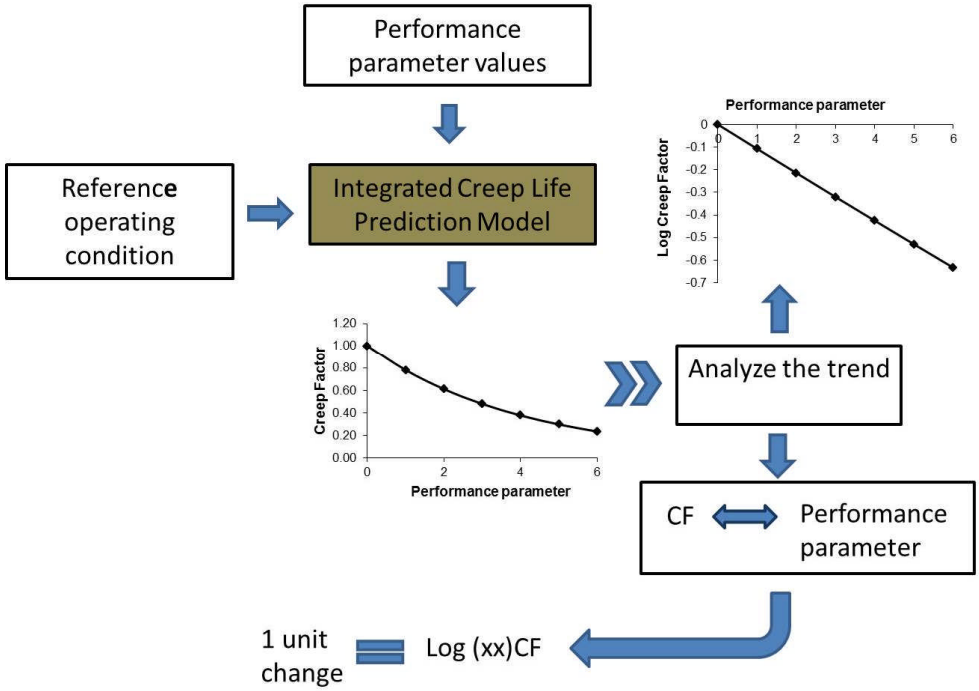

Figure 6-12: Method diagram for the first part of the impact analysis

The second part of the study examines the influence of clean and degraded mission profiles on the HP turbine blade's creep life. The degraded mission profiles

consider degradations in the engine model compressor due to compressor fouling and also degradations in both engine model turbines due to turbine erosions.

For each given mission profile, each mission segment creep life was first calculated using Equation (4-45). Then the life fraction LF of each mission segment was calculated using Equation (4-48) before the mission nominal creep life was calculated using Equation (4-49). Finally the mission Creep Factor CF_M was computed using Equation (4-50). Note that since some mission segments can have continuously changing performance parameters, these segments were divided into smaller segments in order to create a sequential step of continuously constant operating conditions.

By having to calculate each mission segment, CF and CF_M, the effects of each mission segment and the overall mission profile on the blade's creep life can be quantified relative to the reference operating conditions. By comparing the CFs of the mission segments, 'critical' mission segments can be identified.

6.3 Application

The study was conducted using the developed engine model. The hot section component selected for the study is the uncooled single stage unshrouded HP turbine blades coated with thermal barrier coating (TBC). Some of the inputs used in the integrated model are obtained from the engine manufacturer while some are reasonably assumed or calculated. Table 6-6 summarises the inputs used in the integrated model. For confidentiality reasons, those inputs provided by the engine manufacturer are not given in this thesis.

Since some of the values are reasonably assumed, these values are given in this thesis. For this study, the $RTDF$ value was set to 0.1. The chosen value of $RTDF$ was considered to be moderate ($RTDF$ value should be kept at not more than 0.2 [205]) as this value was found to be used in other literatures [162], [206], [207]. Also, the thickness and thermal conductivity of the TBC were assumed to be 150μm and $2W/m.K$ respectively [208].

The value of R_k which is the ratio between the blade section wall temperature and the section gas temperature was inversely determined by comparing the results of a numerical critical blade temperature analysis conducted by the engine manufacturer and the predicted metal temperature obtained from the Blade Thermal Model. The R_k value was initially guessed in order to predict the blade's metal temperatures (corresponding to the location of minimum creep life along the blade span) at the same

operating conditions used by the engine manufacturer. The predicted blade's metal temperatures were then compared to the critical blade metal temperatures provided by the engine manufacturer. R_k was then changed progressively until the prediction errors were minimised. The prediction errors, E were calculated using Equation (6-10).

$$E = \left| \frac{T_{cr(predict)} - T_{cr(given)}}{T_{cr(given)}} \right| \times 100 \quad \textbf{(6-10)}$$

where $T_{cr(predict)}$ and $T_{cr(given)}$are the predicted and the given critical blade metal temperature respectively.

Table 6-6: Summary of the inputs used in the integrated model

No	Input	Data Acquisition
1	Absolute rotational speed	Engine manufacturer
2	Number of blade	Engine manufacturer
3	NGV cooling effectiveness	Engine manufacturer
4	Blade chords	Engine manufacturer
5	Blade LE and TE radii	Engine manufacturer
6	Blade cross sectional areas	Engine manufacturer
7	Blade and NGV angles	Engine manufacturer
8	Blade density	Engine manufacturer
9	Blade LMP master curve	Engine manufacturer
10	Radial temperature distribution factor, $RTDF$	Assumed
11	NGV pressure recovery	Assumed
12	Blade TBC thickness	Assumed
13	Blade TBC thermal conductivity	Assumed
14	X and Y distances between the corresponding chord-wise location to the respective blade's cross section CG	Calculated
15	Blade cross section minimum and maximum second moment of areas	Calculated
16	R_k	Calculated

Table 6-7 provides the critical metal temperature prediction errors, E, at different operating conditions (PCN from 1.0 to 0.945) when different values of R_k were applied. PCN, as mentioned in Section 6.1.2, is the ratio between the engine compressor rotational speed and its absolute design speed. It can be seen from the table that the optimised value of R_k is 0.885 with the average prediction error, E at 1.3844%. Hence an R_k value of 0.885 was applied to the engine model.

Apart from the R_k, the X and Y distances between the corresponding chord-wise locations (LE, TE and the back of the blade) to the respective blade's cross section CG (refer to Figure 4-7 in Section 4.4.4), and the blade cross section minimum and maximum second moment of areas, were determined by the author. The determination of the values was based on the given 3D computer aided design (CAD) blade model.

Using commercial CAD software, the X and Y distances were measured and the second moment of areas were calculated.

Table 6-7: Prediction error at different R_k

	Critical Metal Temperature Prediction Error (%)			
PCN	R_k = 0.89	R_k = 0.887	R_k = 0.885	R_k = 0.88
1.0	1.3673	0.9319	0.6415	0.0843
0.9910	0.8589	0.4236	0.1334	0.5921
0.9820	0.3010	0.1342	0.4243	1.1496
0.9778	1.0529	0.6133	0.3203	0.4124
0.9711	1.0397	0.5979	0.3033	0.4331
0.9600	2.0520	2.4839	2.7718	3.4915
0.9550	1.6821	2.1173	2.4075	3.1329
0.9450	3.3534	3.7853	4.0732	4.7929
Average Error (%)	1.4634	1.3859	**1.3844**	1.7611

Table 6-8: Operating and health parameters selected for the study

Selected parameter	Test range
Operating condition	
PCN	0.9981 to 0.96
Altitude	0 to 1000 m
Ambient temperature (deviation in temperature from ISA)	36.1° C to ISA (21.1 to 0°C)
Health conditions	
Compressor fouling	0 to 5 FI
HP turbine erosion	0 to 5 EI
LP turbine erosion	0 to 5 EI

Operating and health parameters, together with their variations used in the first part of the study, are listed in Table 6-8. For all the tests, the PCN was chosen as the engine handle. Also two indices, the fouling index (FI) and erosion index (EI) were also used which hypothetically describe the magnitude of degradations [40]:

a. 1% of EI is defined as 1% decrease in efficiency accompanied by a 0.5% increase in flow capacity
b. 1% of FI is defined as 1% decrease in efficiency accompanied by a 0.5% reduction in flow capacity

The efficiency and flow capacity are health parameters of compressors and turbines and details are given in [209].

Clean engine running at a PCN of 0.98, zero altitude, Mach number equal to zero, with an ambient temperature of 36.1° C (21.1° ΔT from ISA sea level) was chosen as the reference operating condition. The reference condition chosen for this study was arbitrarily selected in order to show the effect of increase and decrease of the Creep Factor when the rotational speed was changed from 0.9981 to 0.96. It is important to note that when each parameter was changed, according to their specified variations as given in Table 6-8, other parameters remained at the reference condition. For example, when the altitude was simulated from 0 to 1000m, the PCN and ambient temperature were fixed at 0.95 and 36.1°C respectively.

Table 6-9: Mission profile created for the second part of the study

	Mission Segment	Altitude (m)		PCN		Power level % (approx.)	CAS (knot)	Time (min)
		From	To	From	To			
F1	Hover-taxi	0	0	0.966	0.966	71	5	5
F2	Take off from base	0	1500	0.985	0.991	88	100	10
F3	Cruise flight	1500	1500	0.964	0.964	66	150	10
F4	Land at training site	1500	1200	0.971	0.969	72	100	2
F5	Conduct training	1200	1200	0.977	0.977	78	0	50
F6	Depart training site	1200	1800	0.989	0.993	88	100	4
F7	Cruise flight	1800	1800	0.964	0.964	65	150	12
F8	Land at base	1800	0	0.965	0.959	66	100	6
F9	Hover-taxi	0	0	0.966	0.966	71	5	5

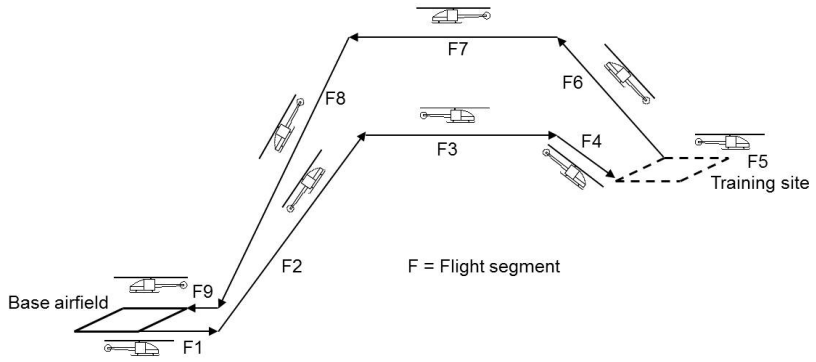

Figure 6-13: Graphical representation of the mission profile

As mentioned earlier, the second part of the study investigates the influence of a given mission profile on the blade's creep life with the inclusion of degradation. For this reason, a mission profile used for both the clean and degraded engine was created.

The mission profile created was adapted from [210] and the operating parameters and operating hours for each mission segment were reasonably assumed. The description of the mission profile is listed in Table 6-9 and the graphical representation of the mission is given in Figure 6-13. For the degraded engine, three cases will be considered which are the presence of compressor fouling with 2% FI, and HP and LP turbines' erosion with 2% EIs respectively.

6.4 Effect of Engine Operating and Health Conditions on the Blade's Creep Life

6.4.1 Effect of Engine Rotational Speed

As the engine rotational speed was used as the handle of the engine, the level of the handle represents the level of engine speed. Figure 6-14 illustrates the effect of engine rotational speed on the creep life of the HP turbine blades. It can be seen from the figure that when the engine's rotational speed, PCN was reduced from its reference value to 0.96, the Creep Factor, CF, increased substantially from 1.0 to around 20. This indicates that a 2% reduction in rotational speed from its reference operating condition will extend the blade life up to nearly 20 fold. In contrast, as the speed was increased from its reference operating condition to 0.9981, the CF dropped dramatically to a value of 0.12, indicating an 88% reduction in the blade's creep life from its reference life.

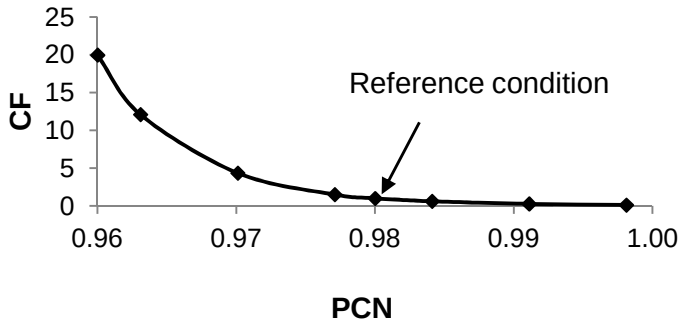

Figure 6-14: Plots of CF against rotation speed PCN

Figure 6-14 also indicates that CF varies exponentially with the engine rotational speed. A plot of log CF against the speed, as shown in Figure 6-15, depicts a linear relation between the log CF and the engine rotational speed and such a plot provides a much clearer representation of the relationship. Note that since the value of CF is unity at the reference condition, the log CF is zero. The impact weight which is the slope of the curve was found to be around -0.591 of log CF value. This means that for every 1%

increase in PCN from its reference condition, there will be a 0.591 drop in the value of the log CF.

The change in the CF resulted from a substantial change in both blade stresses and metal temperatures. Figure 6-16 illustrates the deviations of the blade stresses from their reference value. Delta stress represents the difference between the blade stress at the current operating condition and the blade stress at the reference operating condition. A negative trend as the engine rotational speed reduces indicates reductions in the blade stress values. This shows that when the engine speed reduces, the blade stresses are reduced due to the reduction in centrifugal forces, thus changing the maximum stresses. It is important to note that the stresses due to the bending moment also change but are relatively small compared with the stress resulting from the centrifugal force.

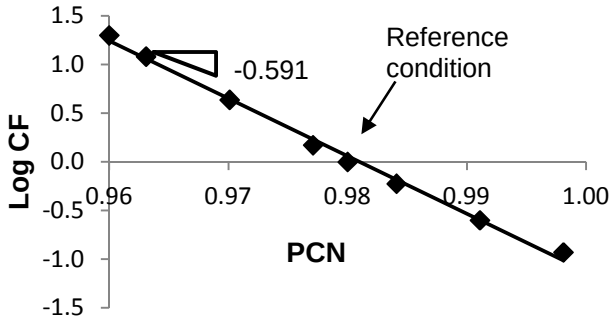

Figure 6-15: Plots of log CF against rotation speed PCN

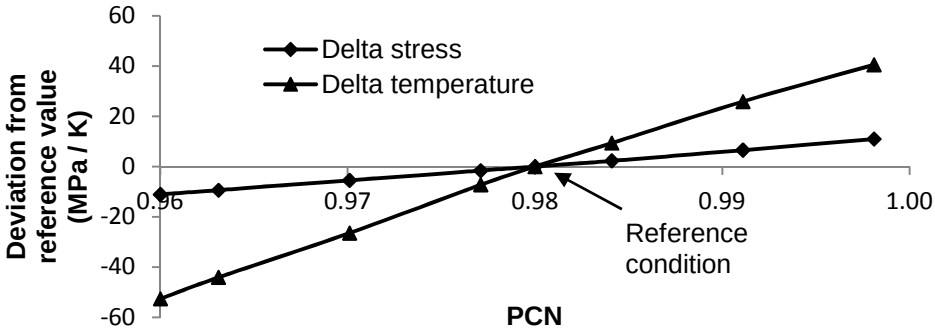

Figure 6-16: Deviations of metal temperatures and stresses from their reference values vs. engine speed

In addition, the reductions in rotational speeds will reduce the non-dimensional speeds. As the non-dimensional speed reduces, the non-dimensional mass flow in the compressor map will reduce. Since the inlet compressor remains unchanged due to the unchanged ambient conditions, the inlet mass flow of the compressor will reduce causing a reduction in the compressor work, hence reducing the TET. This can be

clearly seen in Figure 6-17 where the percentage deviations of mass flow, compressor power, and TET from the reference value are depicted. The negative trends of the plot as the rotational speeds were reduced show reductions of those parameters. As a result, the blade's metal temperatures will be brought down. This can be seen in Figure 6-16 where the negative trend as the engine rotational speed reduces indicates a reduction in the blade's metal temperatures.

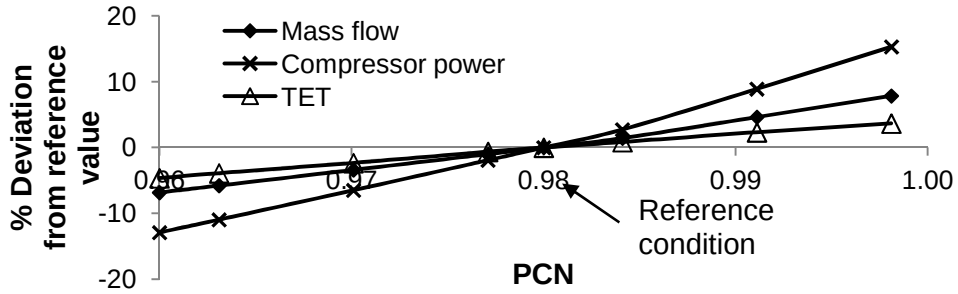

Figure 6-17: Percentage deviations of mass flow, compressor power and TET from its reference values vs. engine speed

6.4.2 Effect of Altitude

With the increase in altitude, the ambient static temperature falls linearly and so does the static pressure and air density, hence reducing the mass flow rate into the engine. Consequently this will result in a decrease in the compressor work, despite having an increase in pressure ratio due to an increase in non-dimensional speed. However, in seeking for continuity between the compressor and the high pressure turbine, the engine performance model was seen to produce a higher burner temperature rise as the altitude increases, resulting in a slight increase in TET. This can be seen in Figure 6-18. Consequently this will increase the blade metal temperature, as shown in Figure 6-19.

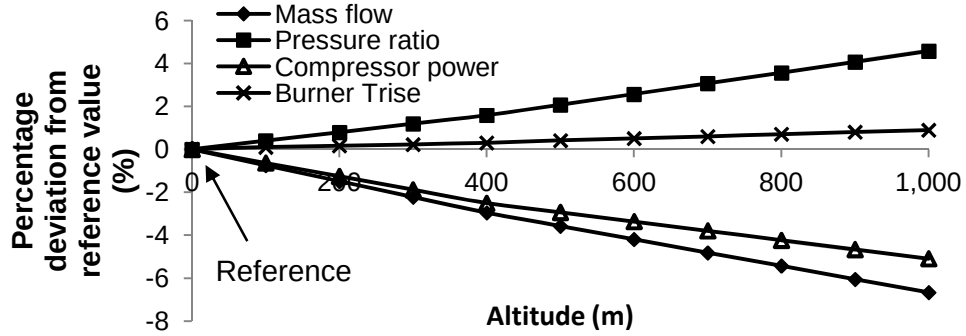

Figure 6-18: Percentage deviations of pressure ratio, compressor work, and burner temperature rise and intake mass flow from reference value vs. altitude

The increase in altitude also changes the blade stresses. As shown in Figure 6-19, although the metal temperature is rising as the altitude rises, the blade stress reduces slightly. The slight reduction in blade stresses is due to the reduction in the gas bending moment from the pressure and momentum difference between the inlet and outlet of the blade. This can be clearly seen in Figure 6-20, where in the figure the deviations of forces, due to momentum, change at the axial and tangential directions, and also deviation of forces, due to static pressure, change at the axial direction from its reference value. As shown in the figure, the negative trends depicted in all forces indicate reductions in the forces, hence reducing the gas bending moment stresses.

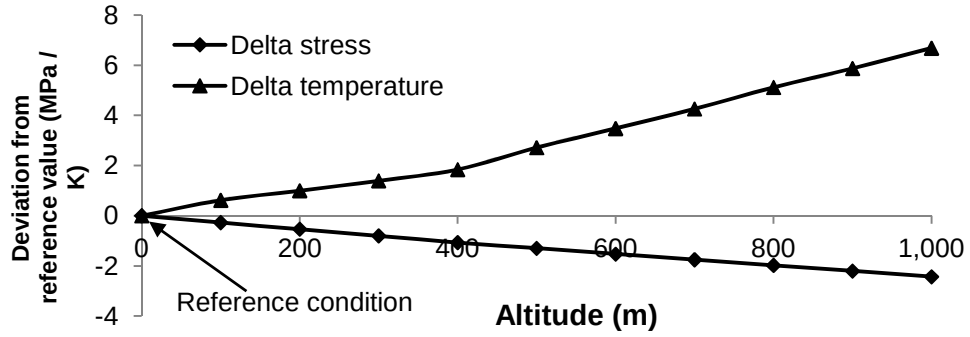

Figure 6-19: Deviation of metal temperature and stress from reference value vs. altitude

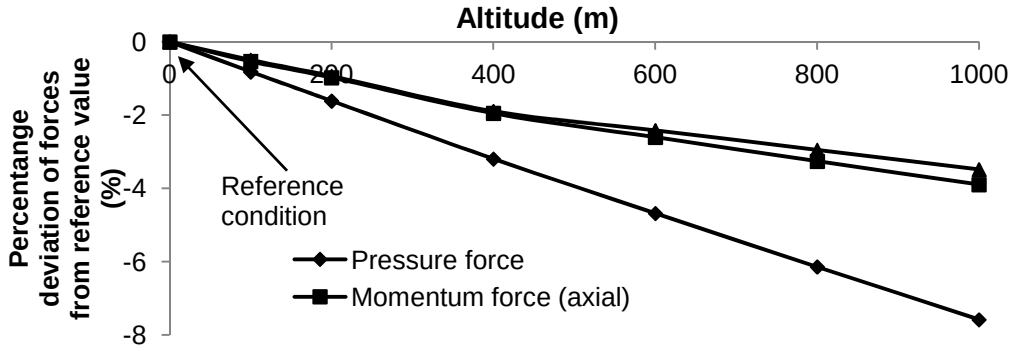

Figure 6-20: Percentage deviation between the forces from its reference value at different altitudes

Despite having an increase in metal temperature while at the same time a decrease in blade stress, the change in the blade stress is small since the centrifugal force which acts as the main stress contributor does not change. This can be clearly seen when comparing the stress deviation shown in Figure 6-19 with that in Figure 6-16. Because of this, the temperature is seen to be dominant in changing the HP turbine blade's creep life. This can be clearly seen when the CFs are plotted against

the altitudes in Figure 6-21. The reduction in CF is in accordance with the increase in metal temperature due to the fact that a higher metal temperature will cause lower blade creep life, thus lower CF.

Figure 6-21 illustrates the behaviour of the CF when the altitude was increased from its reference value 0 to 1000m. The figure shows that when the altitude increases, the CF reduces fairly linearly from 1.0 to around 0.8 indicating a 20% reduction in the blade's creep life. Treating the changes as linear, the impact weight for the increase in altitude is found to be -0.0002 of CF value. What this means is that for every 1m increase in the altitude, there will be a -0.0002 drop in the CF value.

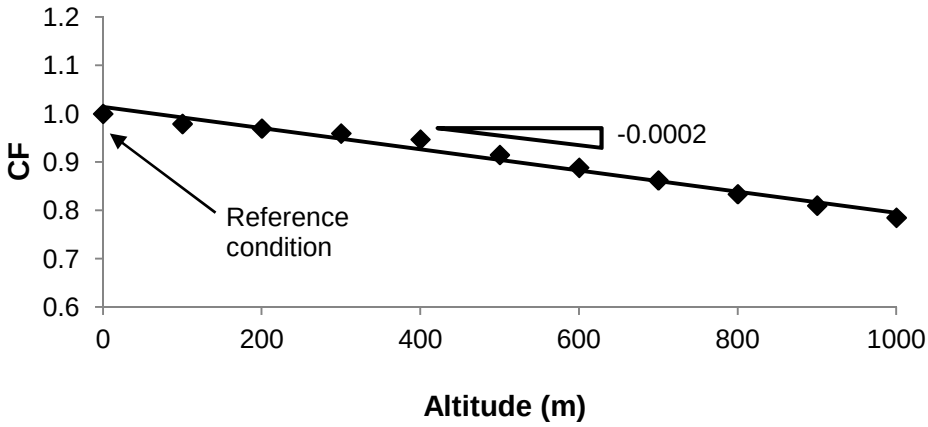

Figure 6-21: Plot of CF against altitude

6.4.3 Effect of Ambient Temperature

In this study, the ambient temperature was increased from ISA sea level condition to the reference ambient temperature 36.1°C (21.1° temperature deviation for ISA). When the engine performance was simulated, it was found that the compressor delivery temperature was increasing, despite having a reduction in the compressor pressure ratio, due to the reduction in the non-dimensional speed. At the same time, it was also observed that the burner temperature rise remained fairly constant as the ambient temperature was increased. This resulted in an increase of the TET (constant burner temperature rise + increase in compressor delivery temperature), as shown in Figure 6-22. The increase in TET consequently will increase the blade metal temperature, as shown in Figure 6-23.

The change in the ambient temperatures also changes the blade stresses. From Figure 6-23, it can be seen that as the ambient temperatures were increasing, the blade stresses were reducing. The trends of the blade stresses in Figure 6-23 are seen to be similar to the trends of blade stresses depicted in Figure 6-19. Since the

centrifugal stress remains unchanged, due to constant engine rotational speed, the change in the blade stresses is due to the change in the gas bending moment stresses. This can be clearly seen in Figure 6-24 where the deviations in the forces, due to momentum and static pressure change, have negative trends which hence reduces the gas bending moment stresses.

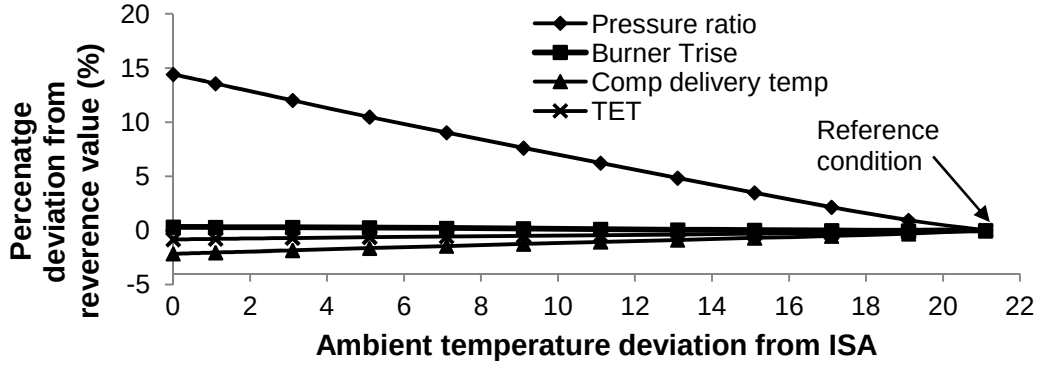

Figure 6-22: Percentage deviation of pressure ratio, burner temperature rise, compressor delivery temperature

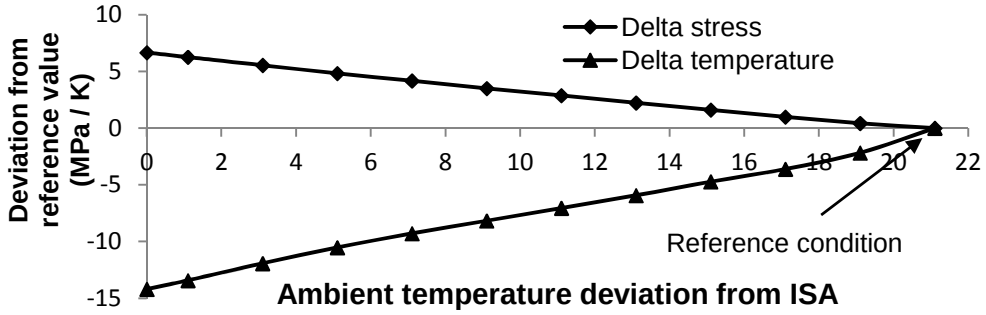

Figure 6-23: Deviation of metal temperature and stress from reference value vs. ambient temperature deviation from ISA

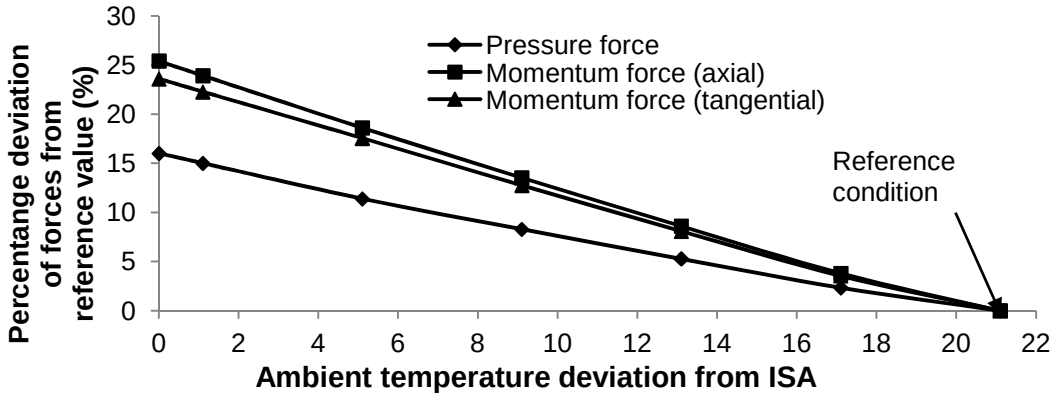

Figure 6-24: Percentage deviation between the forces from reference value at different ambient temperatures

Despite having an increase in metal temperature while at the same time a decrease in blade stress, the change in the blade stresses is small since the centrifugal force which acts as the main stress contributor does not change. Similar to the previous case, temperature is seen to be the most influential factor in changing the creep life of the HP turbine blades. A plot of CF against the ambient temperature deviation for the ISA, as shown in Figure 6-25, can validate the argument as the reductions of CFs are in agreement with the increase in the blade's metal temperature, as shown in Figure 6-23.

The effect of ambient temperature change on the blade's creep life is shown in Figure 6-25. It can be seen from the figure that as the ambient temperature was increased from the ISA sea level to the reference condition, CF reduced 1.7 times from its initial value indicating a 70% decrease in the blade's creep life. In addition the behaviour of the creep life change was seen to be fairly linear suggesting that a 1 degree increase in the ambient temperature deviation from the ISA will cause a 0.0292 drop in the CF value.

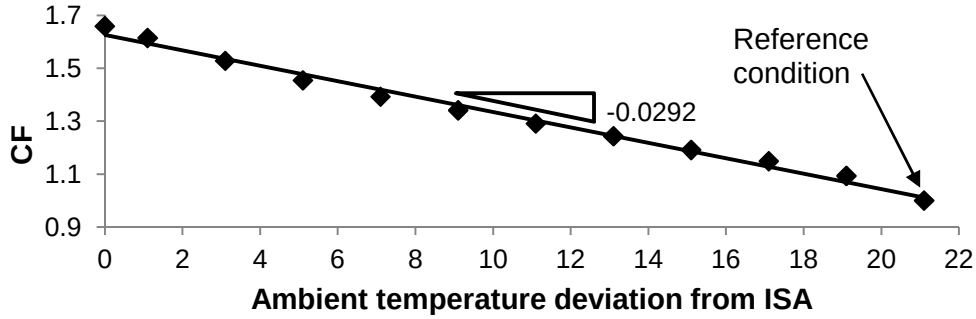

Figure 6-25: Plot of CF vs. ambient temperature deviation from ISA

6.4.4 Effect of Mach Number

When the Mach number was increased from 0 to 0.3, the compressor inlet pressure and temperature, and mass flow were seen to increase. This is due to the fact that the increase in Mach number increases the nozzle ram pressure, hence increases the outlet temperature [211]. In addition, as the Mach number increases, the amount of gas that can enter the engine increases and thus increases the mass flow.

The increase in the compressor inlet temperature means that the non-dimensional speed of the compressor will drop, thus reducing the compressor pressure ratio. Despite having a reduction in the pressure ratio, the increases in compressor inlet pressure and temperature were seen to be dictating the increase in the compressor outlet pressure and temperature.

However, the performance simulation results also indicate that despite having an increase in both temperature and pressure at the outlet of the compressor, the burner temperature rise was seen to be reducing in order to reach the continuity between the turbine and the compressor. Consequently this will produce a slightly lower TET as the Mach number was increased. The deviations of those parameters from their corresponding reference value are depicted in Figure 6-26.

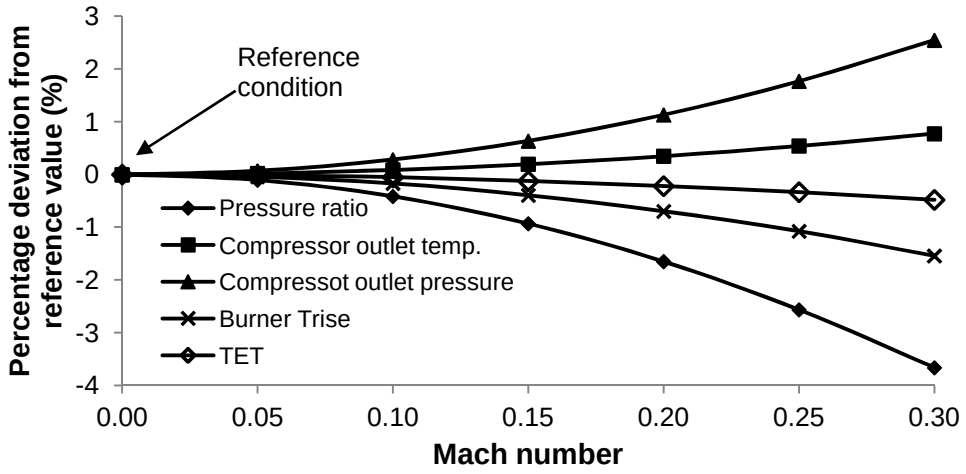

Figure 6-26: Percentage deviation of the dependent parameters with its reference value

The drop in the TET, as shown in Figure 6-26, has resulted in a reduction in the metal temperature as the Mach number was increased. This can be clearly seen in Figure 6-27 where the negative trend shows the reduction of the metal temperature as the Mach number was increased. From the figure, it can also be seen that the blade stress changes as the Mach number is changed. However, such change is relatively small since the centrifugal force which acts as the main stress contributor does not change. For this reason, the drop in the TET was seen to be the dominant effect in dictating the blade's creep life.

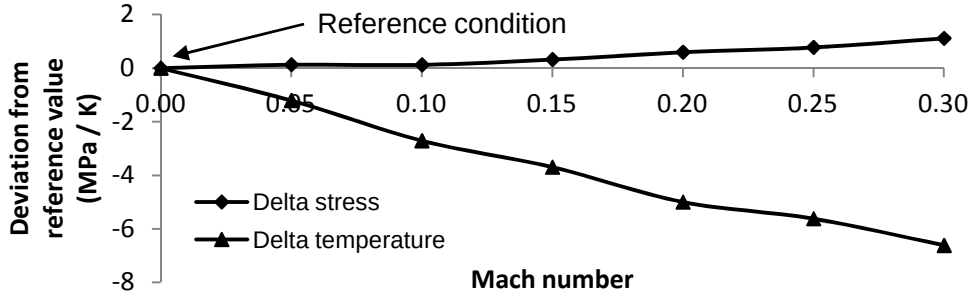

Figure 6-27: Deviations of metal temperatures and blade stresses from reference value vs. ambient temperature deviation from ISA

The effect of the Mach number change on the blade's creep life is shown in Figure 6-28. It can be seen from the figure that as the Mach number was increased from the reference condition to 0.3, the CF increased 1.25 times from its initial value, indicating a 25% increase in the blade's creep life. In addition, the behaviour of the creep life change was seen to be fairly linear suggesting that a 1 unit increase in Mach number can cause a 0.8953 increase in the CF value

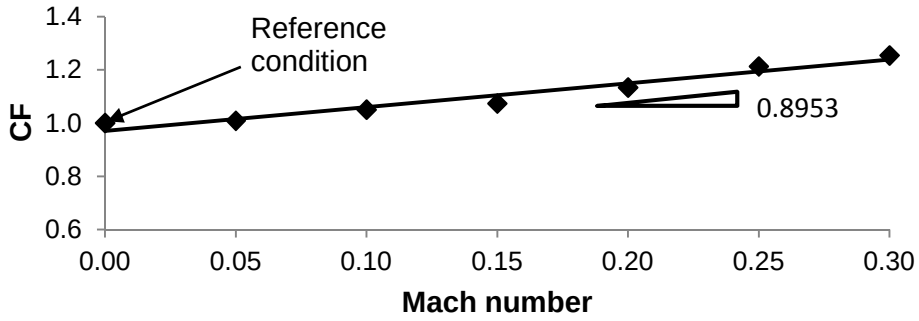

Figure 6-28: Plot of CF against the Mach number

6.4.5 Effects of Component Degradation

In this section, the effects of the engine health conditions on Creep Factor are discussed. The aims are to understand how much influence each individual component has on the HP turbine blades' creep life, and which components have the highest impact when they are being degraded. Figure 6-29 illustrates the effects of compressor fouling, and HP and LP turbines' erosions on CF. From the figure it can be seen that the CFs were reduced when the erosion and fouling indices were increased. At an index of 5.0, the CFs for compressor fouling, HP and LP turbine erosion are 0.28, 0.33 and 0.62 respectively. This means that the blades' creep life has reduced significantly to 72%, 67% and 38% respectively.

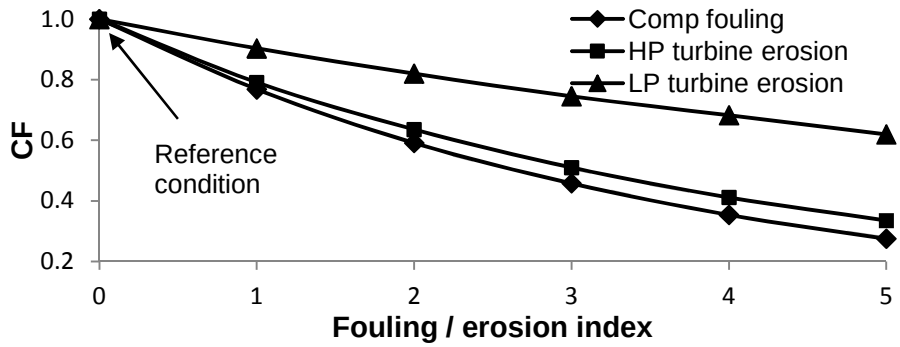

Figure 6-29: Effect of component degradation on CF

The main reason behind this is that the degradation on each component has different effects on the drop in the blades' metal temperature. Figure 6-30 shows the

change in the metal temperature as the fouling and erosion indices are changed. As can be observed, the highest rise in the blades' metal temperature is obtained when the compressor is fouled, followed by the HP turbine erosion and then LP turbine erosion.

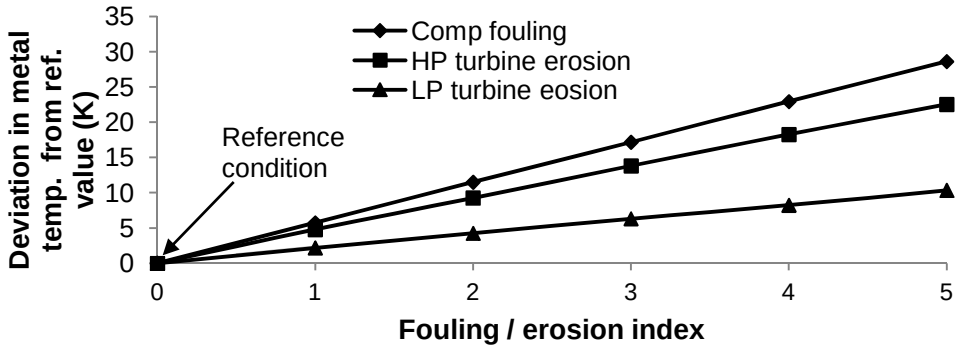

Figure 6-30: Deviation in metal temperature from its reference value

Similar to the previous cases, the blade stresses did not change significantly due to engine degradation as the engine rotational speed was the same. In the case of single component degradation, the main contributor to the deterioration of the blade's creep life is the change of blade metal temperature.

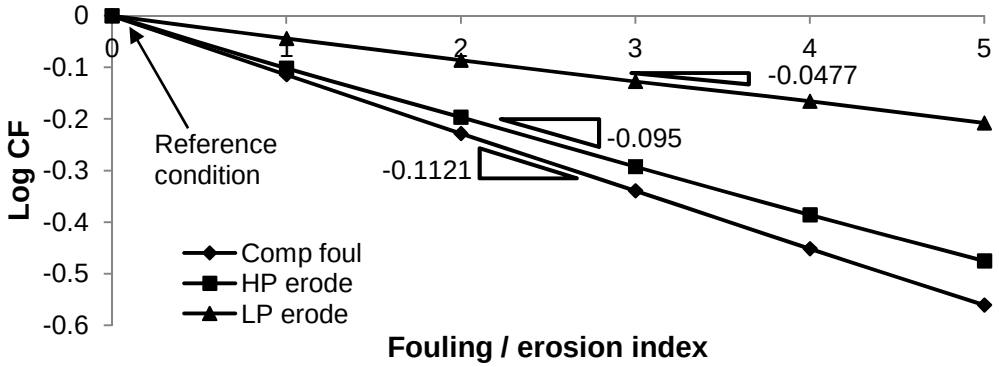

Figure 6-31: Log CF vs. degradation indices

The trend of the plotted graph in Figure 6-29 shows that CFs change exponentially with components' degradation. A plot of a log of CF against the fouling and the erosion indices (Figure 6-31) shows linear relations between them. Based on these relations, the impact weight for each degradation case can be calculated. It can be seen that a unit increment of fouling or erosion index will produce 0.1124, 0.095 and 0.0477 reductions in the value of the log CF for the compressor, HP turbine and LP turbine respectively from its reference value.

By comparing the impact weights, compressor fouling is seen to give the highest impact in reducing the blade's creep life. The value also indicates that the impact of

compressor fouling on the blade's creep life is 1.183 and 2.36 times 'exponentially' higher than HP and LP turbines erosion respectively.

6.4.6 Summary of the Results

The summary of the results obtain from Sections 6.4.1 to 6.4.5 is given in Table 6-10. Having compared the calculated impact weight, the sensitivity of each operating and health parameter can be assessed. By comparing all of the operating parameters, it can be seen that engine rotational speed is the most sensitive in changing the blade's creep life. Not only is the magnitude of the impact weight the highest, the logarithmic term indicates that the reduction in the blade's creep life is accelerating. On the other hand, altitude is the least sensitive as the impact weight, compared to the other operating parameters, is the lowest.

Table 6-10: Summary of the impact analysis

	Trend	Relation	Unit increase	Impact weight
Operating parameters				
Rotational speed	exponent	$PCN \uparrow$, $CF \downarrow$	1%	-0.591 LogCF
Altitude	linear	Altitude $\uparrow$, $CF \downarrow$	1m	-0.0002 CF
Ambient temperature	linear	Temperature $\uparrow$, $CF \downarrow$	1 degree	-0.0292 CF
Mach number	linear	M $\uparrow$, $CF \uparrow$	1 unit	0.8953 CF
Health parameters				
Compressor fouling	exponent	FI $\uparrow$, $CF \downarrow$	1% FI	-0.1121 LogCF
HP turbine erosion	exponent	EI $\uparrow$, $CF \downarrow$	1% index	-0.095 LogCF
LP turbine erosion	exponent	EI $\uparrow$, $CF \downarrow$	1% index	-0.0477 LogCF

Although it is a little 'unfair' to compare the impact weight in this manner since the unit increment used in each operating parameter is different, it still provides a useful indicator of the sensitivity of the parameter to the blade's creep since in all cases a unit change is considered throughout the entire analysis.

By comparing the impact weight of different health parameters, it can be seen that compressor fouling has the highest impact weight. The highest value of the impact weight means that compressor fouling possesses the highest threat in reducing the blade's creep life compared to turbine erosions. On the other hand, the LP turbine erosion is seen to have the lowest threat as the value of the impact weight is the lowest among the three degradations.

6.5 Effects of Both a Clean and Degraded Mission Profile on the Nominal Blade's Creep Life.

In this study, the effects of a given mission profile (see Table 6-9) on the blade's nominal creep life were quantified. For the degraded engine, three cases were included which are compressor fouling with 2% FI, HP and LP turbines erosion, with 2% EIs respectively.

Figure 6-32 plots each mission segment CF against its respective OH. In addition, Table 6-11 provides the summary of the change in CF for each mission segment. From Table 6-11, it can be seen that for mission segments that have no constant operating condition, such as F2, F4, F6, and F8, several mission points were created to construct sub-mission segments. As shown in the figure, from the nine specified mission segments, 54 sub-mission profiles were generated. It is worth noting that the notation F2-18 means that the number '2' represents the second defined mission segment and '18' represents the accumulated segments created for the entire mission profile.

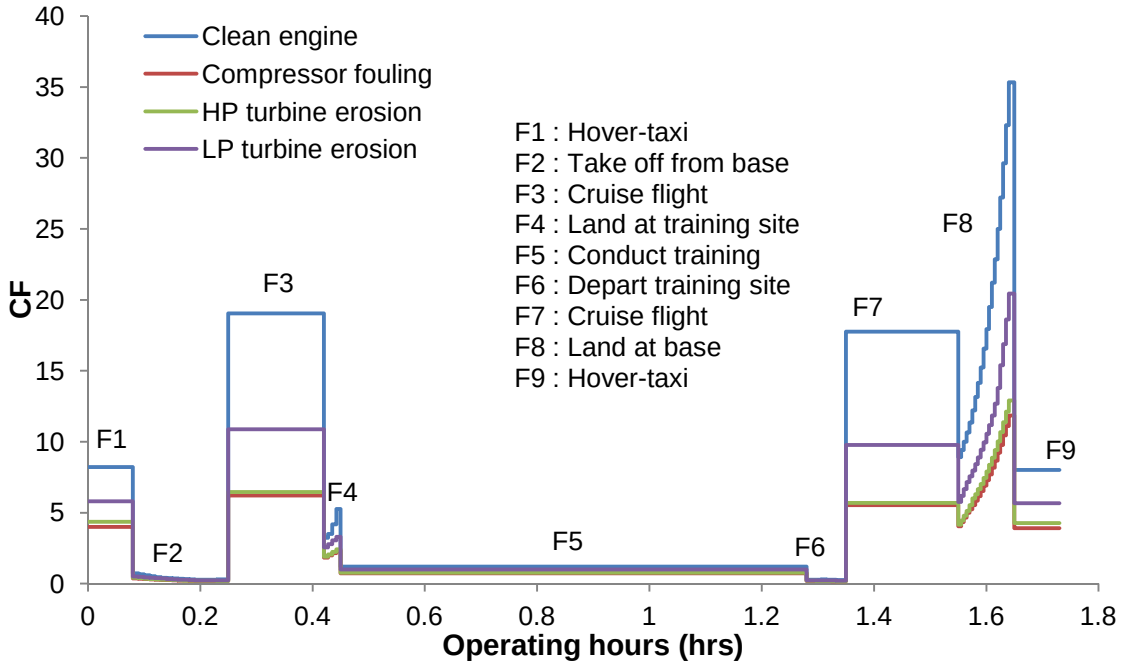

Figure 6-32: CF variation for a given mission profile

The variations in CF as shown in Figure 6-32 or Table 6-11 are caused by the change in the operating and health parameters which define the mission profile. The change in the parameters, as a result, leads to the change in the blade's metal temperatures and stresses which alters the blade's creep life.

The plot of individual mission segment CF with its respective OH provides insight on how each mission segment could influence the blade's creep life relative to a user defined reference condition. This can be very useful as the plot could visually indicate the impact of each mission segment on the blade's creep life. In addition, the different effects of component degradation can be easily observed.

Table 6-11: Summary of CF for each mission segment

Mission segment		Sub-mission created	Creep Factor, CF of each sub-mission segment			
			Clean	Compressor fouling	HP turbine erosion	LP turbine erosion
F1	Hover-taxi	F1-1	8.22	3.99	4.36	5.80
F2	Take-off from base	F2-2 to F2-18	0.72 to 0.29	0.37 to 0.18	0.40 to 0.19	0.51 to 0.23
F3	Cruise flight	F3-19	19.05	6.21	6.45	10.88
F4	Land at training site	4-20 to F4-23	3.23 to 5.26	1.83 to 2.33	1.91 to 2.43	2.56 to 3.31
F5	Conduct training	F5-24	1.20	0.72	0.77	0.99
F6	Depart training site	F6-25 to F6-32	0.28 to 0.24	0.18 to 0.17	0.2 to 0.17	0.27 to 0.20
F7	Cruise flight	F7-33	17.75	5.54	5.69	9.76
F8	Land at base	F8-34 to F8-53	8.9 to 35.3	4.04 to 11.84	4.16 to 12.91	5.76 to 20.43
F9	Hover-taxi	F-54	8.02	3.90	4.26	5.66

From the results, several observations can be made. Figure 6-32 shows that the clean engine possesses higher CFs compared to the degraded engine over the entire mission. This is to be expected since the presence of degradation, as discussed in the first part of the study, will produce a lower blade's creep life compared to a clean engine.

With the degraded engine, compressor fouling is seen to give the lowest CFs at all mission segments followed then by HP turbine erosion and LP turbine erosion. This is consistent with the results obtained in Section 6.4.5 which identifies compressor fouling as the main threat in changing the blade's creep life followed by HP turbine erosion and then LP turbine erosion.

For both the clean and degraded engine, three mission segments which are F2, F5 and F6 have low CFs relative to the others. However, by comparing the CF between the three mission segments, as given in Table 6-11, F6 has the lowest CF overall. This is due to the fact that during the entire mission segment, the power level is kept at the highest (highest rotational speed with PCN from 0.989 to 0.993) while operating at higher altitudes. Note that from the first part of the study, higher rotational speed and higher altitude will cause the blade's creep life to reduce.

From Figure 6-32, it can be seen that for both the clean and degraded engine, the highest creep life occurs at the end of mission segment 8 (F8). This is also to be expected as at that point, the rotational speed is lowest (PCN 0.959) and the engine is being brought down from 1800m to the ground.

The plot of CF in Figure 6-32, directly measures the impact of each mission segment on the blade's creep life. Taking mission segment F3 as an example, the CF for the clean engine, as given in Table 6-11, shows that the blade's creep life is 19 times higher than the life at its reference condition. However, due to compressor fouling, the blade's creep life has been shortened by six times of the life predicted at its reference operating condition.

The CF_M, as listed in Table 6-12, provides the overall weight of the impact relative to its reference condition. The table shows that the clean engine's nominal creep life is 46% higher than the life predicted at its reference condition. However, due to compressor fouling, the nominal creep life has fallen by 29% $\left((1.0 - 0.71) \times 100\%\right)$ from its reference value which gives a total drop of almost 39% $((1.17 - 0.71)/1.17 \times 100\%)$ from its clean engine value. The engine with HP turbine erosion has a slightly higher CF_M which is 0.76. This means that the presence of HP turbine erosion has reduced the blade's nominal creep life by as much as 24% from its reference value. This provides a total drop of almost 35% from its clean engine value. On the other hand, the reduction of the blade's creep life due to the LP turbine erosion is not as severe as both compressor fouling and HP turbine erosion. This is again consistent with the results obtained in the first part of the study.

Table 6-12: Mission life assessment

	CF_M
Clean Engine	1.17
Engine with compressor fouling	0.71
Engine with HP turbine erosion	0.76
Engine with LP turbine erosion	0.96

6.6 Chapter Conclusion

In this chapter the investigations of the effects of several selected operating and health parameters on a helicopter turbo-shaft engine model HP turbine blade's creep life using the developed Integrated Creep Life Prediction Model are reported. The investigations were divided into two parts where in the first part, the influence of individual operating and health parameters were quantified using the introduced Creep

Factor. In the second part of the study, the effects of clean and degraded mission profiles on the nominal blade's creep life were investigated using the same Creep Factor approach.

Prior to the investigations, the selected engine model was constructed using PYTHIA. In order to improve the engine performance prediction accuracy at both DP and OD conditions, DP and OD performance adaptations were carried out. Based on these results, it can be concluded that both DP and OD performance adaptations have significantly reduced the initial performance prediction errors at both conditions. At DP, the average error of the targeted parameters has been reduced from 0.998% initially to 5.08E-5% after DP performance adaptation was performed. Also, at OD, the overall performance prediction error has been reduced from a total average error of 4% to around 0.75%. Furthermore, the number of measurements having prediction errors that exceed the specified threshold are noticeably reduced, from 15 to only 3.

In the first part of the study, the effects of engine rotational speed, altitude, ambient temperature, Mach number and component degradation due to compressor fouling and turbine erosions on the blade's creep life have been quantified by measuring the impact weight as one unit of each parameter deviates from a defined reference operating condition. By comparing the impact weight, it was found that, for a clean engine, engine rotational speed is the most sensitive in changing the blade's creep life. On the other hand, altitude is the least sensitive as the impact weight compared with the other operating parameters is the lowest. By comparing different health parameters, it was found that compressor fouling possesses the highest threat in reducing the blade's creep life compared to turbine erosions. However, LP turbine erosion is seen to have the lowest threat as the value of the impact weight is the lowest among the three degradations.

By applying the same mission profile on a clean and degraded engine, the effects of clean and degraded mission profiles on the blade's creep life were quantified. For the degraded engine, three cases were investigated which were compressor fouling with 2% FI, HP and LP turbines erosion with 2% EIs respectively. Based on the plot of mission segment Creep Factors against its respective operating hours, the effect of the individual mission segment on the blade's creep life was assessed. It was found that, due to the variations in the operating and health parameters, difference impacts on the blade's creep life were encountered. However, the outcome of the analysis was always in agreement with the findings obtained in the first part of the study.

Finally, the CF_M for both clean and degraded mission profiles was calculated in order to assess the overall weight of the impact of the mission profiles relative to the defined reference condition. It was found that for the clean engine, the nominal blade's creep life is higher than the life predicted at the reference condition. However, the presence of component degradations have significantly reduced the nominal blade's creep life to values lower than the life predicted at the reference condition.

7 APPLICATIONS OF THE NEURAL-BASED CREEP LIFE PREDICTION METHOD ON THE AERO-ENGINE

This chapter reports the applications of the proposed neural-based creep life architectures on the developed engine model. The chapter is divided into three parts. The first part of the chapter will discuss the methods of implementing the architectures including the assessments conducted to evaluate the performance of the implemented architectures. The second part of the chapter then discusses the application of the proposed neural-based creep life architectures at clean engine conditions, before the application of the architecture at degraded engine conditions is presented.

7.1 Methodology of Implementing the Proposed Architectures

The general method used to implement the proposed neural architectures for the developed engine model at both clean and degraded engine conditions is given in Figure 7-1. Using the Integrated Life Estimation Model, samples are generated. For each sample, there will be a set of inputs coupled with its corresponding targeted outputs. For the approximator type of network, the corresponding targeted outputs will be the values that the network should be predicting, such as the blade's creep life, metal temperature or stress. On the other hand, if a classifier type of network is used, than the targeted outputs will be the desired class in which the network should be classified, such as to classify whether the engine is clean or degraded etc.

The amount of samples populated to train the network were determined by considering the sensitivity of each of the selected operating and health parameters obtained in Section 6.4. This was then translated into step sizes that dictate how the samples were being spaced when they were being populated. For example, in Section 6.4, it has been proved that for a clean engine condition, the rotational speed is most sensitive in changing the blade's creep life followed by Mach number, ambient temperature, and altitude. Thus the step size for rotational speed is smallest to allow more samples to be taken at smaller intervals while the step size for altitude is the largest. If n operations or health parameter R are chosen as the input, $R_1, R_2, R_3, \ldots R_n$ and the step size corresponding to each R is ss, then the size of the samples can be calculated using Equation (7-1).

$$\text{Sample size} = \left[\frac{UL-LL}{ss}+1\right]_{R_1} \times \left[\frac{UL-LL}{ss}+1\right]_{R_1} \times \ldots \left[\frac{UL-LL}{ss}+1\right]_{R_n} \quad \textbf{(7-1)}$$

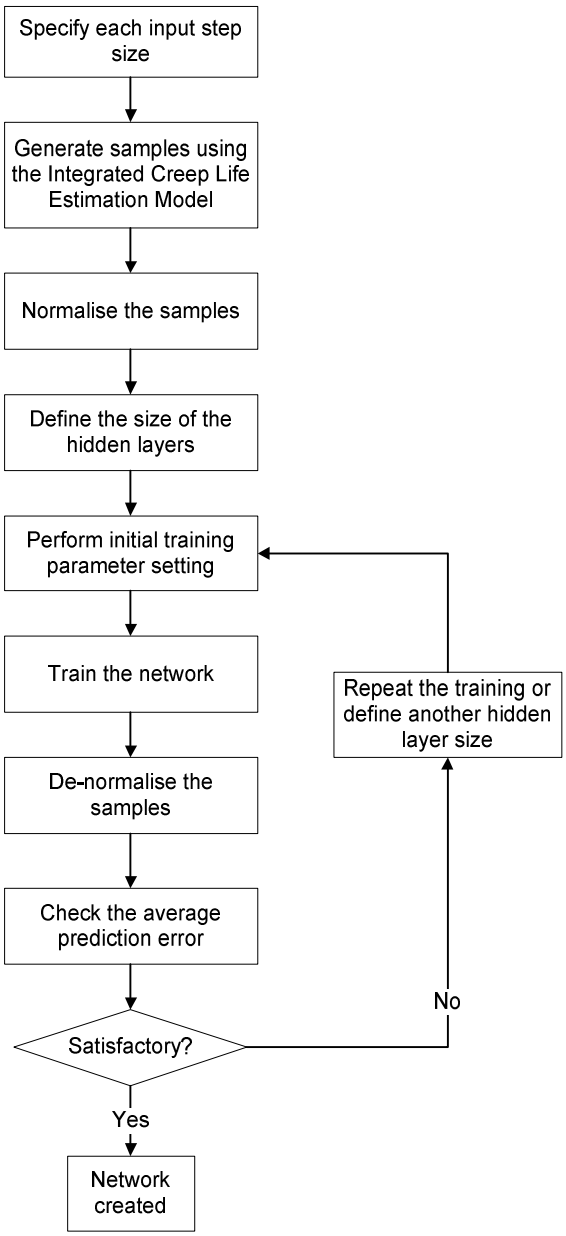

Figure 7-1: General method used to train the proposed neural architectures

Once the samples were generated, they were divided into three sets. The first set, known as the training samples, which contains 60% of the generated samples was used to train the network. These were samples that were used to change the neural network synaptic weights during the training process. Another set of samples containing 20% of the generated samples was used as validation samples. The validation samples were used to stop the training process before overfitting occurs.

Finally the last 20% of the samples were used as test samples which provided independent tests of network generalisation to data that the network has never seen.

In order to improve network generalisation, each sample input and output were normalised within the range of -1 (lowest input or output value) to 1 (highest input or output value). Then the size of the hidden layers was specified. In general, a smaller size was initially set and was progressively increased by the author when unsatisfactory results (high prediction errors) were obtained. In addition, the initial training parameters were also set. This involved specifying the number of maximum epochs, defining minimum performance gradient, maximum validation failure etc.

In this study, MFBP neural network was used as the basis to construct the network. The decision to use MFBP was because of the success the approach has in obtaining accurate approximation and classification. When an approximator type of network was used to approximate any forms of value, such as the blade's creep life or the blade's metal temperature, an LM training algorithm was used. However, when a classifier type of network was used to classify any output from a given input, an SCG algorithm was applied. In addition, the study used Hyperbolic-Tangent Function as the activation function for its hidden neurons while Linear Function for its output neurons.

The selection of both LM and SCG training algorithms was based on the fact that both training algorithms can provide fast convergence while maintaining high prediction or classification accuracy when the individual training algorithm was used for the desired purpose. The construction of the neural-based models was done using MATLAB Neural Network Toolbox™.

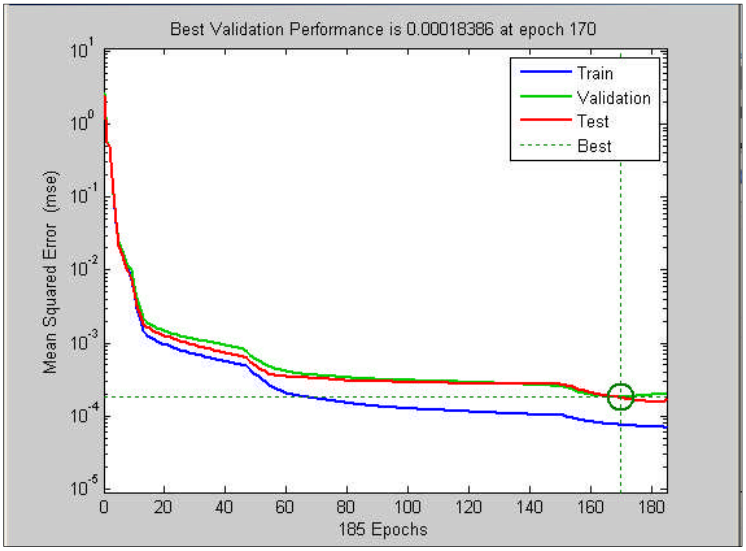

Figure 7-2: Observed $MSEs$ of training, validation and test samples during network training

During the training of the approximator type network, the mean squared errors ($MSEs$) of the three sets of samples were observed, as shown in Figure 7-2. It can be seen that the $MSEs$ which start from large values were decreasing at each epoch until the training was stopped either when the specified maximum epoch was reached or when the observed validation samples' MSE began to increase. From Figure 7-2, the training was stopped at epoch 170 (validation sample MSE is 0.000184) just when the validation sample MSE began to increase. This approach is very helpful in preventing overfitting from occurring. Note that the $MSEs$ observed during training are calculated using Equation (7-2),

$$MSE = \frac{\sum_{i=1}^{N_s} (\hat{z}_{norm} - z_{norm})_i^{\,2}}{N_s} \quad \textbf{(7-2)}$$

where N_s denotes the number of samples in each training, validation and test sample, with $\hat{z}_{norm}$ being the normalised predicted output predicted by the neural network and z_{norm} is the normalised targeted output which is taken from the normalised generated samples discussed in the previous paragraph.

Trend and value of the $MSEs$ during the network training were also observed in order to ensure the trained network can provide good generalisation. Low MSE will indicate that error between the predicted and targeted output is small. From Figure 7-2, it can be seen that the trend of $MSEs$ produced using test and validation samples are very close to each other while the trend of $MSEs$ of the training samples is slightly lower. This shows that the errors between the test and validation samples will be similar while for the training sample, it will be slightly lower.

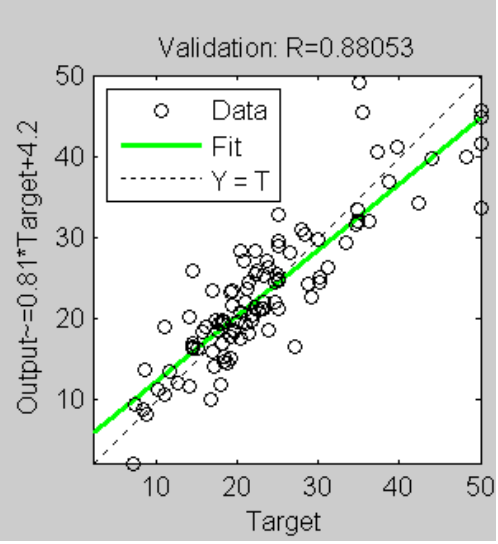

Figure 7-3: Sample of the regression plot [194]

Apart from the observed MSE, for the approximator network, linear regression plots between the normalised predicted and targeted outputs for each validation, training, and test samples were also observed. The sample of the regression plot is illustrated in Figure 7-3. The plot given in Figure 7-3 provides a graphical representation of how the predicted output is correlated to the targeted output. A well trained network will produce outputs that will scatter closely to the Y=T line, thus producing regression coefficient R close to unity. It is worth mentioning the Y=T line is the line when the network output is equal to the targeted output. In the MATLAB Neural Network Toolbox™, Y and T denote the network predicted and targeted output respectively.

Once the training of the approximator network had been stopped, the normalised outputs predicted by the network (for all of the three sets of samples) were de-normalised to obtain the true outputs. Then each true predicted output was compared with the respective targeted output and the absolute prediction error percentage, E_{Abs}, was calculated using Equation (7-3) with $\hat{z}$ and z denoting predicted and targeted outputs respectively.

$$E_{Abs} = \left|\frac{\hat{z} - z}{z}\right| \times 100 \quad \textbf{(7-3)}$$

Here, the average absolute prediction error percentage, E_{AbsAve} was calculated using Equation (7-4) with N denoting the number of samples generated.

$$E_{AbsAve} = \frac{\sum_{i=1}^{N}(E_{Abs})_i}{N} \quad \textbf{(7-4)}$$

The observation of the classifier network is similar to the approximator network. The trends and the values of the MSE were also observed. However, the focus of the observation was directed to the classifying ability of the classifier. This was done by observing the confusion matrices of the three samples. An example of the confusion matrix is depicted in Figure 7-4. The diagonal cells in the figure show the number of samples that were correctly classified while the off-diagonal cells show the misclassified samples. In addition, the blue cell in the bottom right of the figure shows the total percentage of the correctly classified samples (in green) and the total percentage of the misclassified samples.

During the training of the network, the value in the cells will change from a low percentage to a high percentage of correct classification. Similar to the approximator

network, the training was stopped either when the maximum epoch was reached or when overfitting started to happen.

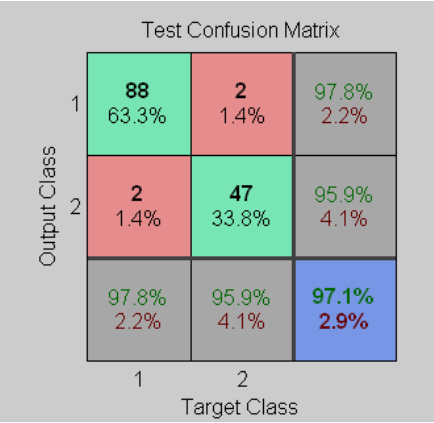

Figure 7-4: Example of the confusion matrix observed during network training [194]

In order to assess the performance of the trained network, several criteria were observed, as listed in Table 7-1. If the criteria were not satisfied, the training was repeated using the same, or with the new, hidden layers size. If the criteria were satisfied, then the network was stored for further applications.

Table 7-1: Criteria used to finalise the size of the network

Network	Criteria Used
Approximator	a. The value of E_{AbsAve} should be small. b. The maximum E_{Abs} should be less than 10% (if possible) c. No negative value of creep life prediction by the network (in some cases, in order to find the optimum synaptic weights, negative creep life value is predicted) d. Number of samples exceeding the maximum E_{Abs} should be minimised.
Classifier	a. The overall percentages of correct classification of the training, validation, and test samples should be close to 100%. b. The overall percentage of correct classification should be more than 99% (if possible)

7.2 Evaluation of the Performance of the Proposed Architectures

Once the training was completed and the network stored, further assessments were carried out in four stages for both the approximators and classifiers. In the first stage,

assessment was done using the previously used populated samples. For the approximators, since absolute forms of error were used to find the suitable sizes of hidden layers, how the errors were distributed above and below the average value is not described. For this reason, the aims of the assessment at this stage are threefold:

a. to see how many samples there are that are able to produce a predicted blade's creep life with errors that fall within a given range;
b. to know what would be the representative overall deviation between the prediction errors from its average value.

In order to achieve the first aim, the prediction error percentage, E of each de-normalised output (the predicted creep life prediction errors) was calculated using Equation (7-5).

$$E = \frac{\hat{z} - z}{z} \times 100 \quad \textbf{(7-5)}$$

Additionally, six ranges of a blade's creep life E were specified and are listed in Table 7-2. Based on the specified ranges, the percentages of samples that could produce E within the given range were counted and tabulated. The results will show into what error range most samples would fall. If a high percentage of samples is encompassed at a lower error range, it will suggest that accurate approximators have been established.

Table 7-2: Error ranges used to assess the performance of the trained approximators

Error Range	Description
T1	$-1\% \leq E \leq 1\%$
T2	$-2\% \leq E \leq 2\%$
T3	$-3\% \leq E \leq 3\%$
T4	$-4\% \leq E \leq 4\%$
T5	$-5\% \leq E \leq 5\%$
T6	$-6\% \leq E \leq 6\%$

To achieve the second aim of the first stage evaluation, the Es of the de-normalised outputs were averaged using Equation (7-6) with E_{Ave} as the average prediction error percentage. In addition, the prediction error standard deviation, SD_E was also calculated using Equation (7-7). If the E_{Ave} is very near to zero, then it indicates that the distributions of Es are unbiased. Furthermore, a low SD_E will indicate that most of the Es are close to E_{Ave} hence minimising the variance of E.

$$E_{Ave} = \frac{\sum_{i=1}^{N}(E)_i}{N} \quad \textbf{(7-6)}$$

$$SD_E = \sqrt{\frac{1}{N}\sum_{i=1}^{N}(E_i - E_{Ave})^2} \quad \textbf{(7-7)}$$

Since during the training, the overall classification accuracy was used to find the suitable size of the hidden layers, the assessment of the classifier network was done by further investigating the classification accuracy of each class via the confusion matrix. By using the confusion matrix, several observations will be made. These will include observing:

a. how many samples have been correctly predicted for each class,
b. how many extra samples being predicted as the observed class come from different classes, and
c. how many samples that are supposed to be classed in the observed class 'jumped' into different classes.

If the amount of misclassification relative to the correct classification is very small, it will suggest that a good classifier has been established.

Additionally, in order to investigate the effects of the misclassification on the prediction accuracy given by an incorrect class approximator, the misclassified samples were input into the wrongly classed approximator. Then the E of each misclassified sample was measured before E_{Ave} and SD_E were computed.

The second stage of assessment acts as post evaluation, aimed at providing validation to the generalisation of either the approximators or the classifiers. In order to do so, two sets of unseen samples were generated using the Integrated Creep Life Estimation Model and tested independently. It is worth noting that the unseen samples contain a set of inputs to the network coupled with their respective targeted unseen outputs.

For each set of unseen samples, the inputs were inputted into the trained network and the outputs were predicted, using the trained approximator or classifier respectively. For the approximator, the output E were computed before the percentage of samples that are capable of producing a predicted creep life within a specified range of E (given in Table 7-2) were plotted or tabulated. If generalisation has been achieved, the behaviour of the two unseen samples should be similar, thus validating the trained network. As for the classifier, the classification accuracy between the two unseen

samples will be compared via the confusion matrix. If the accuracies between the two unseen samples are similar, it will suggest that the classifier possesses good generalisation.

The second stage assessment can be seen as a very useful method in showing how consistently the trained networks responded when two different unseen samples were inputted. However, in order to obtain the overall picture of how the trained networks responded, suitable statistical distribution needs to be searched. This is to measure the realistic probability of obtaining a specific range of prediction error as given in Table 7-2.

In order to do so, in the third stage of evaluations, distribution fitting software called EasyFit 5.5 developed by MathWave Technologies [212] was used. Using the software, the calculated E for the combined sets of unseen samples were inputted and the best fitted distributions were searched from ten unbounded statistical distributions, as listed in Table 7-3. Note that in EasyFit 5.5, there are also bounded and non-negative distributions but only the unbounded distributions were selected because the calculated E are not restricted to any limits and can have both a positive and negative value with $-\infty < E < +\infty$.

Table 7-3: Unbounded statistical distribution used for the analysis

No.	Statistical Distribution	No.	Statistical Distribution
1	Cauchy	2	Error
3	Error Function	4	Gumbel Max
5	Gumbel Min	6	Hyperbolic Secant
7	Johnson SU	8	Laplace
9	Logistic	10	Normal
11	Student's t		

Based on the selected distributions, the software will then rank all the selected distributions by means of a Kolmogorov-Smirnov test [212] where the distribution that possesses the lowest Kolmogorov-Smirnov statistic parameter, D is taken as the best fitted distribution. It is worth noting that the statistic parameter D in the Kolmogorov-Smirnov test provides the magnitude of discrepancy between the empirical cumulative distribution function (based on the given sample) with the fitted theoretical cumulative distribution function (CDF). If the discrepancy between them is large, the degree of unsuitability will be higher and vice versa.

Once the best fitted distribution was obtained, the theoretical probability density function (PDF) and the CDF of the fitted distribution were plotted using the software. By plotting the corresponding PDF, $f(x)$ against its respective values of E, the density of

the probability was visualised. In EasyFit, the plot of the theoretical PDF was accompanied by the empirical PDF (based on the given samples) displayed as a histogram consisting of equal-width vertical bars where each represented the number of sample data values (falling into the corresponding interval), divided by the total number of data points. An example of the PDF plotted in EasyFit is given in Figure 7-5.

Having to plot both theoretical and empirical PDF is not sufficient as it does not represent the probability of the network obtaining a certain range of the blade's creep prediction error, such as the one given in Table 7-2. In order to calculate the probability at a given range, the theoretical CDF, $F(x)$ was plotted. In this study, the theoretical CDF describes the probability that E takes on a value less than or equal to the value. For example the $F(x)$ at E = 1% will provide the probability of E having a value less than or equal to 1%.

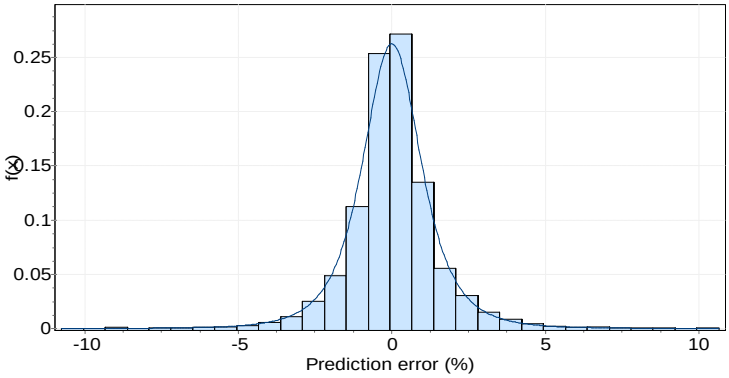

Figure 7-5: Sample PDF plot against the prediction error, E

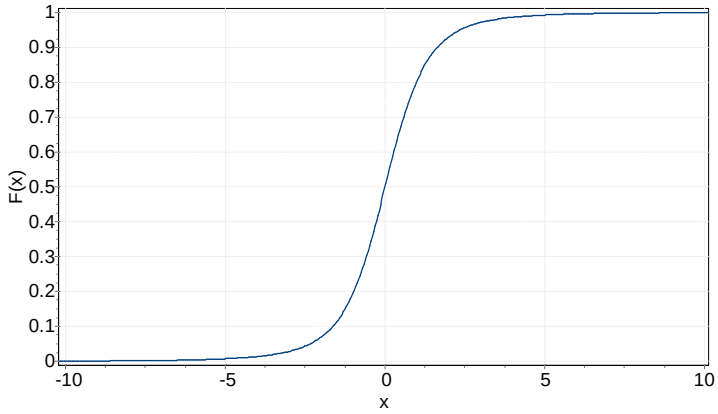

Figure 7-6: Sample of a plotted CDF for a given x

The general equation to calculate the CDF at any given value of x is given in Equation (7-8) and the plot of the CDF is illustrated in Figure 7-6. From Equation (7-8) it can be seen that the CDF is the integral of a given PDF. Therefore for a given prediction error range, the probability of obtaining E within the specified range can be

obtained by integrating the PDF within the upper, UL, and lower limit, LL, of the specified range, as given in Equation (7-9).

$$F(x) = \int_{-\infty}^{x} f(x) \quad \textbf{(7-8)}$$

$$F(x) = \int_{LL}^{UL} f(x) \quad \textbf{(7-9)}$$

In this third evaluation stage, the probabilities of achieving the specified error range given in Table 7-2 were computed and tabulated. If high probability can be achieved at a lower error range, it indicates that the network has a high tendency to provide an accurate blade's creep life prediction.

The last stage of the assessments looked at how well the proposed architectures responded to given mission profiles. Since the previous stages of the assessments focused on a single operating condition, the given mission profiles can determine the accumulation effects of the prediction accuracy when the individual operation conditions are tied together to form a continuous operation.

The mission profiles used in Section 6.5 were applied to the proposed network. Based on the mission profiles, the blade's creep lives were predicted before the CF and LF for each mission segment or mission sub segment were computed. Finally, as an overall assessment, the LF_M and CF_M were computed. Comparisons of the CFs, LF_M and CF_M between the proposed architectures and those obtained from Section 6.5 were then made before conclusions were drawn regarding the performance of the proposed architectures.

7.3 Implementation of the Proposed Neural Architectures on the Developed Engine Model at Clean Condition

The implementation of the proposed neural-based creep life prediction architectures on the selected engine model was first done using the RB architecture, followed by the FB architecture and finally the SB architecture. But before the implementation could even begin, the operational ranges covered by the developed architectures were first defined and are given in Table 7-4. In the table, the lower and upper limits were specified in accordance with the engine operating envelope (altitude and Mach number) given by the engine manufacturer. For the rotational speed, the lower rotational limit was set to PCN 0.94. It is worth noting that the value is arbitrarily selected to provide a reasonable

range of operation which creep life range could be between 1 to 1500 times the life predicted at design point (DP).

Table 7-4: Range covered by the developed neural-based model

Parameters	Lower limit (LL)	Upper limit (UP)
Altitude (m)	0	5000
PCN	0.94	1
Mach number	0	0.3
Ambient temperature deviation from ISA (K)	0	30

7.3.1 Implementation of RB Architecture

In this section the implementation of the proposed RB architecture on the selected engine model is reported.

7.3.1.1 Design Considerations and Realisation

The RB architecture creates a direct mapping between the selected operating parameters and the engine model HP turbine blade's creep life. Here, a multi-class network was implemented (as proposed in Section 5.2.3.2) where the predicted creep life was classed into several ranges, as shown in Figure 7-7. In the figure, it can be seen that the implemented architecture used six classes:

a) Class 1: Creep life predicted less than 3 times the life predicted at DP.
b) Class 2: Creep life predicted between 3 and less than 30 times of the life predicted at DP.
c) Class 3: Creep life predicted between 30 and less than 150 times of the life predicted at DP.
d) Class 4: Creep life predicted between 150 and less than 300 times of the life predicted at DP.
e) Class 5: Creep life predicted between 300 and less than 850 times of the life predicted at DP.
f) Class 6: Creep life predicted between 850 and 1500 times of the life predicted at DP.

The decision to use only up to six classes was based on two reasons. First, an initial investigation done by the author regarding the material's homologous temperature corresponding to the blade's creep life exceeding by 1500 times the creep life value at DP was found to be less than or close to 0.6. This shows that although

creep was present, the influence of creep deformation was less significant compared to the homologous temperature at DP which was above 0.75.

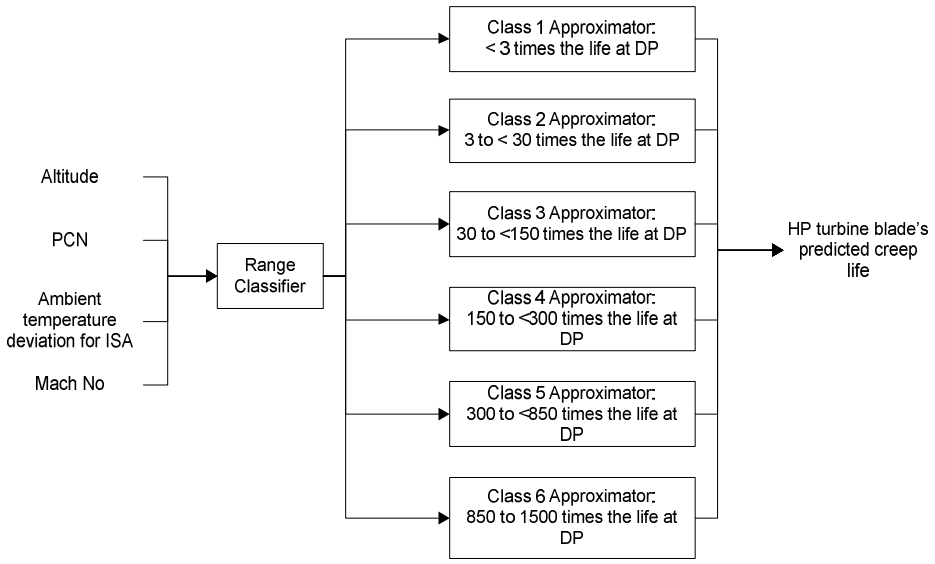

Figure 7-7: Implemented RB Neural Creep Life Estimation Architecture

Secondly, considerably high creep life will have considerably smaller LF thus becoming less crucial when the creep damage is accumulated. For example, if the creep life at DP is taken to be 10,000 hours, then the life when it is 1500 times greater would be 15,000,000 hours. If the engine has been operated for 1000 hours, the LF at DP is 0.1 (10%) while in the latter case it is 0.00006667 (0.006667%).

In addition, the range selected for each class was determined progressively. In an earlier stage of the architecture development, three classes were specified. However, the prediction accuracy obtained using the three-class architecture was unsatisfactory. Consequently, the division of classes was increased in order to improve the accuracy, hence it was found that with a six-class architecture, the prediction accuracy improved significantly.

From Figure 7-7, it can be seen that the classification of the classes was done using a single Range Classifier. Furthermore, since six classes were specified, the implemented architecture used six approximators to predict the blade's creep life. Also the figure indicates that four operating inputs, which are altitude, PCN, ambient temperature deviation from ISA and Mach number, were used to predict a single output which is the engine model HP turbine blade's creep life.

7.3.1.2 Number of Samples to Train the Classifier and Approximators

The number of samples generated depends on the step size specified for each input parameter which is listed in Table 7-5. From the table, it can be seen that altitude has the highest step size due to the fact that the parameter was found to be the least sensitive in changing the blade's creep life. On the other hand, rotational speed has the smallest step size to ensure that the non-linearity nature of the parameter is captured within the populated samples.

Table 7-5 also indicates that, despite having initial samples of 27,456, the finalised samples used to create the training, validation and test samples are 21,427. The reduction of the samples is caused by the removal of the samples which possess an unconverged simulated performance output and also samples with creep life more than 1500 times the life predicted at DP.

It is worth mentioning that the unconverged simulated performance output happened when the matching between the compressor and the turbine during the engine performance simulation at OD condition could not be achieved after 20 iterations (20 iterations is the maximum iteration that PYTHIA will perform before the final unconverged output is displayed). Because the unconverged performance output given does not resemble the true performance of the engine at that particular OD condition, the data must be removed from the populated samples.

Table 7-5: Step size used for each parameter and the distribution of samples for classifier and approximators

Parameter	LL	UL	Step size	Parameter	LL	UL	Step size
Altitude	0	5000	200	Mach number	0	0.3	0.06
PCN	0.94	1	0.006	Ambient temperature deviation from ISA	0	30	2
Initial samples generated			27,456	Finalised samples			21,427
Distribution of finalised sampled							
Class 1 approximator			1,410	Class 2 approximator			7,507
Class 3 approximator			5,364	Class 4 approximator			2,118
Class 5 approximator			3,472	Class 6 approximator			1,556
Range classifier			21,427				

Based on the finalised samples, the samples were then distributed according to the range specified in each class before the allocated samples were divided into training, validation and test samples, as listed in Table 7-6.

Table 7-6: Size of training, validation and test samples

Samples	Approximator						Range classifier
	Class 1	Class 2	Class 3	Class 4	Class 5	Class 6	
Training	862	4,460	3,201	1,282	2,098	954	12,857
Validation	282	1,508	1,097	402	695	301	4,285
Test	266	1,539	1,066	434	679	301	4,285

7.3.1.3 Training of the Approximator and Classifier Network

The final sizes of each approximator and classifier are listed in Table 7-7. It can be seen that most of the networks created for the RB architecture used two hidden layers except for the Class 3 and Class 5 Approximators which used three hidden layers. This indicates that both of the classes require a more optimised synaptic weight in order to achieve good generalisation during the training.

To demonstrate how the final sizes were obtained, Class 6 Approximator and Range Classifier were used as examples.Table 7-8 and Table 7-9 provide the results of each attempt made before the final Class 6 Approximator and Range Classifier sizes were obtained respectively. From Table 7-8 it can be seen that seven attempts were made before the size of the Class 6 Approximator was finalised. From Table 7-9, ten attempts were made before attempt six was finally chosen (highlighted row) as the Range Classifier.

Table 7-7: Finalised sizes of classifier and approximator networks

Network	Size of the network
Class 1 Approximator	4-15-15-1
Class 2 Approximator	4-15-25-1
Class 3 Approximator	4-15-15-15-1
Class 4 Approximator	4-20-20-1
Class 5 Approximator	4-15-15-15-1
Class 6 Approximator	4-30-30-1
Range Classifier	4-30-30-6

Table 7-8: Attempts made to achieve the final Class 6 Approximator network size

Attempt	Network size	E_{AbsAve} (%)	Maximum E_{Abs} (%)	Number of negative predicted creep life	Number of E_{Abs} exceeding 10%
1	4-10-10-1	1.32	9.99	0	0
2	4-15-15-1	0.87	11.84	0	1
3	4-17-17-1	0.93	15.25	0	3
4	4-15-20-1	1.07	14.07	0	5
5	4-20-20-1	1.35	39.37	0	32
6	4-25-25-1	1.01	24	0	8
7	4-30-30-1	0.77	8.79	0	0

The observed MSE during the training of the class approximator networks and the corresponding final regression plots are given in Appendices C.1 and C.2 respectively. However, the summary of the final MSE and R is given in Table 7-10. From the plots of the $MSEs$ in Appendix C.1, it can be seen that the training of the networks was stopped when the MSE of the validation samples starts to increase. Also, the MSE plots for all the samples have similar trends although the $MSEs$ of the training samples are lower in each epoch. Apart from that, the trends of the $MSEs$ for the validation and test samples are close to each other suggesting that good generalisation may have been achieved during the training. Furthermore the low values of the final MSE for each training, validation and test sample (as shown in Table 7-10) also suggest that the optimised synaptic weights may able to provide low prediction error.

Similarly, the plots of the final regressions, as shown in Appendix C.2, also show that the scattering of the data plotted was very close to the Y=T line, hence producing a high value of R. The high value of R indicates that the predicted and targeted normalised outputs were highly correlated.

Table 7-9: Attempts made to achieve the final Range Classifier

Attempts	Size	Training	Validation	Testing	Overall
1	4-20-20-6	97.9	97.5	96.4	97.5
2	4-20-20-6	97.6	96.9	96.8	97.3
3	4-20-20-6	98.3	97.7	97	97.9
4	4-20-20-6	98.4	97.1	97.1	97.9
5	4-25-25-6	99	97	97.5	98.4
6	4-30-30-6	99.7	98	97.8	99.1
7	4-40-40-6	99.6	98	97.6	98.9
8	4-15-15-15-6	97.7	97	97	97.4
9	4-20-20-20-6	99	97.7	97.5	98.4
10	4-25-25-25-6	92.6	91.4	91.4	92.2

Table 7-10: Summary of the final MSE and R for each class approximator

	Class Approximator					
	Class 1	**Class 2**	**Class 3**	**Class 4**	**Class 5**	**Class 6**
Training samples:						
MSE	5.49E-05	3.56E-5	6.97E-05	5.44E-04	1.67E-04	9.2E-04
R	0.99991	0.99994	0.99989	0.99924	0.99975	0.99865
Validation samples:						
MSE	1.63E-04	5.25E-05	1.84E-04	2.54E-03	1.19E-03	3.56E-03
R	0.99967	0.99992	0.99971	0.99662	0.99762	0.9942
Test samples:						
MSE	2.4E-04	7.77E-05	1.55E-05	1.90E-03	7.34E-04	3.6E-03
R	0.9996	0.99985	0.99974	0.99714	0.9986	0.99554

7.3.1.4 Assessment of the Performance of the Networks Using the Populated Samples

Based on the error ranges specified in Table 7-2, the percentages of samples that could produce E within the specified ranges were counted. The results of the analysis are given in Table 7-11. It can be seen that as the error range increases, the percentage of samples that can produce E within the range also increases. From Table 7-11, it can be seen that on average, around 97% of the samples are able to produce a predicted blade's creep life with E within -3 to 3% while most of the networks were seen to have 99% of the samples producing E within -5 to 5%. By comparison between the class approximators, Class 1 Approximator is seen to provide the most accurate approximation with 99% of the samples able to produce a predicted blade's creep life with E within -3 to 3%.

The calculated E_{Ave} and SD_E are given in Table 7-12. From the table it can be seen that the sample's E_{Ave} was found to be very close to zero with SD_E in the range between 0.84 to 1.3%. This shows that despite having a good E_{Ave}, the prediction errors were spreading out, hence producing a diverse distribution with 99% of the data able to produce a predicted creep life with E within -5 to 5%.

Table 7-11: Percentage of samples within the specified error range

Level of Error Range	% of Samples Within the Specified Level of Range						
	Class 1	Class 2	Class 3	Class 4	Class 5	Class 6	Average
T1	86.03	84.01	81.91	73.04	71.43	74.48	78.48
T2	96.31	95.70	94.03	91.17	91.01	93.89	93.69
T3	99.00	98.45	97.42	96.27	96.00	97.56	97.45
T4	99.50	99.29	98.77	98.21	98.36	98.97	98.85
T5	99.78	99.71	99.29	98.90	98.90	99.23	99.30
T6	99.85	99.89	99.51	99.30	99.30	99.61	99.58

Table 7-12: E_{Ave} and SD_E of each trained network

	Class Approximator					
	Class 1	Class 2	Class 3	Class 4	Class 5	Class 6
E_{Ave}(%)	-0.02681	0.01535	0.01923	0.03273	0.02401	-0.00802
SD_E (%)	0.83785	0.91782	1.0904	1.2906	1.245	1.2282

The performances of the Range Classifier using the training, validation and test samples are given in Appendix C.3 and the summary is given in Table 7-13. From the

results given in Table 7-13, the Range Classifier was found to have good classifying capabilities producing around 98% classification accuracy. In addition, although there were drops in the accuracy for both validation and test samples, the drops are relatively small and the Classifier is still able to produce a good classification.

Table 7-13: Summary of the classification results

	Training samples	Validation samples	Test samples
Overall classification accuracy	99.7%	98.0%	97.8%
Class 1 (C1):			
Samples correctly predicted	861	277	262
Extra samples predicted as C1	3 from C2	7 from C2	4 from C2
Samples that jumped to other class	1 to C2	5 to C2	4 to C2
Class 2 (C2):			
Samples correctly predicted	4457	1494	1529
Extra samples predicted as C2	1 from C1	5 from C1	4 from C1
		8 from C3	16 from C2
Samples that jumped to other class	3 to C1	7 to C1	4 to C1
		7 to C3	6 to C3
Class 3 (C3):			
Samples correctly predicted	3197	1077	1041
Extra samples predicted as C3	8 from C4	7 from C2	6 from C2
		8 from C4	9 from C4
Samples that jumped to other class	4 to C4	8 to C2	16 to C2
		12 to C4	9 to C4
Class 4 (C4):			
Samples correctly predicted	1270	383	412
Extra samples predicted as C4	4 from C3	12 from C3	9 from C3
	9 from C5	9 from C5	13 from C5
Samples that jumped to other class	8 to C3	8 to C3	9 to C3
	4 to C5	11 to C5	13 to C5
Class 5 (C5):			
Samples correctly predicted	2086	674	657
Extra samples predicted as C5	4 from C4	11 from C4	13 from C4
	7 from C6	8 from C6	11 from C6
Samples that jumped to other class	9 to C4	14 to C4	13 to C4
	3 to C6	7 to C6	9 to C6
Class 6 (C6):			
Samples correctly predicted	947	293	290
Extra samples predicted as C6	3 from C5	7 from C5	9 from C5
Samples that jumped to other class	7 to C5	8 to C5	11 to C5

Further investigation into the misclassified samples reveals that most of the misclassifications occurred when the estimated creep lives (at the corresponding operating condition) were located very close to the class upper and lower limits. The effects of the misclassification on the prediction accuracy given by an incorrect class

approximator are shown in Table 7-14. From the table it can be seen that although incorrect approximators were used to estimate the blade's creep life, the prediction errors were still at the acceptable level with small E_{Ave} and SD_E. In addition the highest maximum errors encountered during the analysis are around 8.5% (only three samples were seen to produce errors around this value) while the lowest minimum errors were around -6.2%.

Table 7-14: Summary of the prediction using a misclassified class approximator

	Class Approximator					
	Class 1	**Class 2**	**Class 3**	**Class 4**	**Class 5**	**Class 6**
E_{Ave}(%)	0.13	-0.02	-0.03	0.13	-0.13	0.31
SD_E (%)	1.08	1.87	2.66	2.30	2.56	2.53
Min error (%)	-2.31	-6.22	-6.28	-5.77	-8.52	-5.81
Max error (%)	2.34	3.00	6.56	8.54	8.45	4.49

7.3.1.5 Assessment of the Performance of the Network Using Unseen Post Test Samples

The step size for each input parameter and the distributions of samples for both sets of unseen samples are given in Appendix D. From the appendices, it can be seen that around 8,000 new unseen samples were generated for the post test. Based on the unseen samples, plots of the percentages of samples encompassed within the specified error ranges (Table 7-2) were constructed and are given in Figure 7-8 while the data used to generate the plots are available in Appendix E.

From Figure 7-8, it can be clearly seen that the distribution of samples able to produce a predicted creep life with E within the specified error range for both unseen samples are almost identical, thus producing patterns that are overlapping each other. The overlapping of the patterns has validated that good generalisation has been achieved in all of the trained networks.

Based on data given in Appendix E, it can be seen that on average, approximately 96% of their respective unseen samples were able to produce a predicted creep life with E within -3 to 3% while most of the networks were seen to have approximately 98% of the unseen samples producing E within -5 to 5%. In addition, by comparing the class approximators, Class 1 Approximator provides the most accurate approximation with 99% of the samples able to produce a predicted creep life with E within -3 to 3%. This is very beneficial as the Class 1 Approximator is most significant in producing a bigger life fraction (for given operating hours) as the predicted creep life within Class 1 is relatively close to the life at DP.

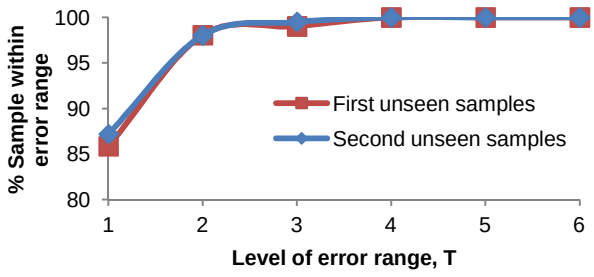

(a) Class 1

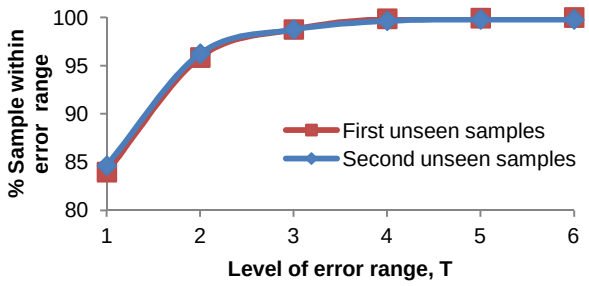

(b) Class 2

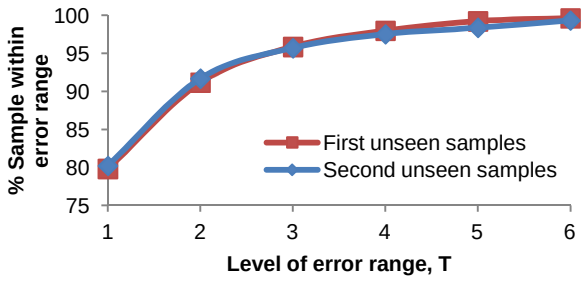

(c) Class 3

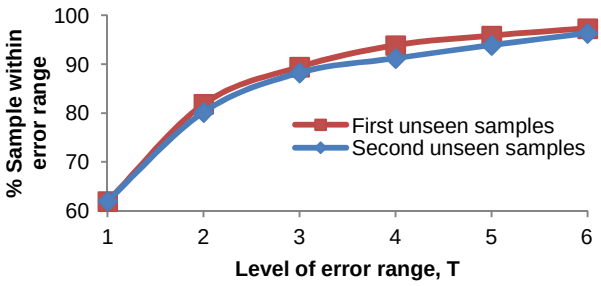

(d) Class 4

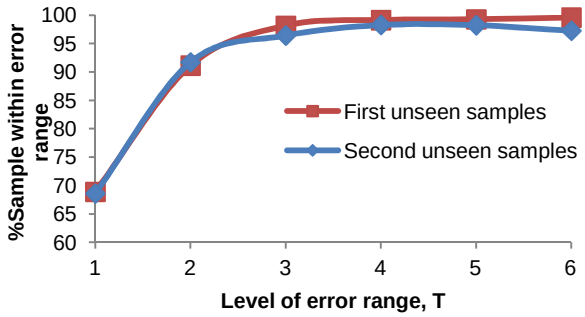

(d) Class 3

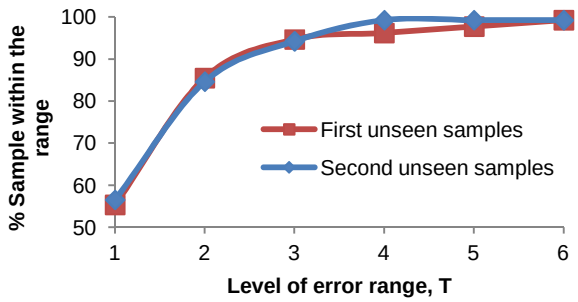

(e) Class 4

Figure 7-8: Percentage of samples within the specified range for all the class approximators

Having compared the sample's prediction error distribution analysis given in Appendix E, it can be seen that the Class Approximators, in general, were able to retain their performances, despite having small discrepancies in the average values when compared with the results obtained using the training samples (refer to Table 7-11). This was to be expected since most of the samples used to train the approximators were suited to provide the optimisation of the network's synaptic weights. Also, as mentioned in an earlier paragraph, the observed MSE of the training samples used to change the synaptic weights is lower than the validation and test samples. As a result, lower errors were going to be encountered when the three

samples were combined in the samples error distribution analysis as given in Table 7-11.

The post test results using both sets of unseen samples of the Range Classifiers are given in Table 7-15 and Table 7-16. From both tables it can be seen that the percentages of the correct classification across all of the classes are very similar with a small percentage of deviations, hence validating that the Range Classifier is able to provide good generalisations. Overall it can be said that the trained classifier is able to produce good classifying ability with accuracy around 98.7%.

Table 7-15: Confusion matrix constructed using the first set of unseen samples

Output Class \ Target Class	1	2	3	4	5	6	
1	**204** 5.0%	**3** 0.1%	**0** 0.0%	**0** 0.0%	**0** 0.0%	**0** 0.0%	**98.6%** 1.4%
2	**1** 0.0%	**1439** 35.4%	**9** 0.2%	**0** 0.0%	**0** 0.0%	**0** 0.0%	**99.3%** 0.7%
3	**0** 0.0%	**5** 0.1%	**1025** 25.2%	**0** 0.0%	**0** 0.0%	**0** 0.0%	**99.5%** 0.5%
4	**0** 0.0%	**0** 0.0%	**7** 0.2%	**407** 10.0%	**8** 0.2%	**0** 0.0%	**96.4%** 3.6%
5	**0** 0.0%	**0** 0.0%	**0** 0.0%	**0** 0.0%	**682** 16.8%	**13** 0.3%	**98.1%** 1.9%
6	**0** 0.0%	**0** 0.0%	**0** 0.0%	**0** 0.0%	**8** 0.2%	**249** 6.1%	**96.9%** 3.1%
	99.5% 0.5%	**99.4%** 0.6%	**98.5%** 1.5%	**100.0%** 0.0%	**97.7%** 2.3%	**95.0%** 5.0%	**98.7%** 1.3%

Table 7-16: Confusion matrix constructed using the second set of unseen samples

Output Class \ Target Class	1	2	3	4	5	6	
1	**199** 4.9%	**2** 0.0%	**0** 0.0%	**0** 0.0%	**0** 0.0%	**0** 0.0%	**99.0%** 1.0%
2	**4** 0.1%	**1424** 35.2%	**11** 0.3%	**0** 0.0%	**0** 0.0%	**0** 0.0%	**99.0%** 1.0%
3	**0** 0.0%	**6** 0.1%	**1028** 25.4%	**0** 0.0%	**0** 0.0%	**0** 0.0%	**99.4%** 0.6%
4	**0** 0.0%	**0** 0.0%	**8** 0.2%	**408** 10.1%	**8** 0.2%	**0** 0.0%	**96.2%** 3.8%
5	**0** 0.0%	**0** 0.0%	**0** 0.0%	**0** 0.0%	**687** 17.0%	**11** 0.3%	**98.4%** 1.6%
6	**0** 0.0%	**0** 0.0%	**0** 0.0%	**0** 0.0%	**6** 0.1%	**249** 6.1%	**97.6%** 2.4%
	98.0% 2.0%	**99.4%** 0.6%	**98.2%** 1.8%	**100.0%** 0.0%	**98.0%** 2.0%	**95.8%** 4.2%	**98.6%** 1.4%

In order to perform the third stage evaluation, both unseen samples were combined and then by using the combined samples, the suitable statistical distribution for each class approximator was fitted and probabilities of obtaining E within the specified ranges were obtained. The summary of the evaluation is given in Table 7-17. In addition, the PDF and CDF plots of the best fitted distribution for each class

approximator are given in Appendix F. To provide further information regarding how the unbounded distributions were ranked using the Kolmogorov-Smirnov test, Table 7-18 provides the statistical parameter D and the rank of each distribution selected. From the table it can be seen that the highest distribution ranking that is chosen as the best fitted distribution listed in Table 7-17 is based on the lowest value of the Kolmogorov-Smirnov statistical parameter D.

From Table 7-17, several observations can be made. As the level of prediction error increases, the probability of getting the prediction error within the range increases as well. This is logical since the wider the error range, the more samples that produce the prediction errors within the range will increase, which increases the probability. In addition, different distributions were found to be the best fitted distribution for E of each class approximator. This was expected as the optimisation of the synaptic weights during the training of the networks to obtain the optimised MSE is different, thus producing different responses and prediction error behaviour

Class Approximators 1, 2 and 5 possess high prediction accuracy since the probability of getting the prediction error between -3 to 3% is more than 0.97. However, by comparison of the three class approximators, Class Approximator 1 is the most superior. This can be clearly seen from Table 7-17 where the probability of having a prediction error between -3 to 3% is almost 1.0. On the other hand, Classes 4 and 6 were seen to possess relatively low probability in maintaining good prediction accuracy compared to the other class approximators. This can also be clearly seen from Table 7-17, as the probability of obtaining predictions between -6 to 6% is around 0.93 for both approximators.

Table 7-17: Summary of the probabilistic analysis of E for each class approximator

		Class Approximator					
		Class 1	**Class 2**	**Class 3**	**Class 4**	**Class 5**	**Class 6**
Best fitted distribution		Logistic	JSU	Cauchy	Cauchy	JSU	Cauchy
		Probability					
Level of error range	T1	0.8299	0.8195	0.7565	0.6440	0.7551	0.5720
	T2	0.9829	0.9678	0.8739	0.8067	0.9308	0.7713
	T3	0.9984	0.9923	0.9153	0.8689	0.9744	0.8462
	T4	0.9999	0.9977	0.9364	0.9011	0.9887	0.8843
	T5	1.0000	0.9992	0.9490	0.9207	0.9944	0.9074
	T6	1.0000	0.9997	0.9575	0.9338	0.9970	0.9228

By comparing the probabilistic values (converted to percentages) given in Table 7-17 and the percentage of samples encompassed within the specified range as given

in Figure 7-8, the magnitudes of deviation between them (taken as absolute values) were calculated and are given in Table 7-19. From the table, it can be seen that the deviation between the two analyses for Classes 1, 2 and 5 are small, especially Classes 1 and 2, with average values of 0.66, 0.59, and 1.64 respectively. This indicates that good agreement between the two analyses was obtained for the three classes. Classes 4 and 3 are found to have slightly higher deviation values indicating that acceptable agreement between the two analyses was obtained. In contrast, the deviation values for Class 6 are found to be considerably higher than the rest of the classes, indicating poor agreement is obtained between the two analyses.

Table 7-18: Rank of the selected distributions generated by EasyFit 5.5

	Class Approximator											
	Class 1		Class 2		Class 3		Class 4		Class 5		Class 6	
Distribution	D	Rank	D	Rank	D	Rank	D	Rank	D	Rank	D	Rank
Cauchy	0.069	8	0.050	5	**0.032**	**1**	**0.032**	**1**	0.048	4	**0.084**	**1**
Error	0.055	4	0.034	2	0.080	4	0.090	4	0.046	3	0.104	7
Error Function	0.057	7	0.084	8	0.159	9	0.150	8	0.132	10	0.109	9
Gumbel Max	0.098	10	0.105	9	0.175	11	0.198	11	0.125	9	0.161	11
Gumbel Min	0.097	9	0.121	10	0.173	10	0.182	10	0.146	11	0.084	2
Hypersecant	0.034	2	0.042	4	0.103	5	0.118	6	0.070	5	0.092	5
Johnson SU	0.037	3	**0.030**	**1**	0.076	2	0.090	5	**0.043**	**1**	0.091	4
Laplace	0.056	6	0.034	3	0.080	3	0.090	3	0.046	2	0.104	8
Logistic	**0.034**	**1**	0.057	6	0.119	6	0.132	7	0.085	6	0.091	3
Normal	0.056	5	0.079	7	0.141	8	0.151	9	0.107	7	0.097	6
Student's t	No fit		No fit		0.137	7	0.059	2	0.114	8	0.116	10

Table 7-19: Magnitude of deviation between two of the analyses

	Class Approximator					
Error range	**Class 1**	**Class 2**	**Class 3**	**Class 4**	**Class 5**	**Class 6**
T1	2.86	2.02	4.17	2.48	6.60	1.86
T2	0.24	0.93	3.77	1.15	1.96	8.37
T3	0.82	0.48	4.34	2.54	0.70	10.04
T4	0.02	0.09	4.34	3.74	0.27	7.75
T5	0.00	0.01	4.33	3.75	0.16	6.97
T6	0.00	0.03	3.87	3.92	0.13	6.96
Average Deviation	0.66	0.59	4.14	2.93	1.64	6.99

The reason for the poor agreement occurring in Class 6 is because the best fitted distribution was unable to provide good fitting at some of the data points, causing large differences between the theoretical and the empirical (observed unseen samples) probability. This can be clearly seen when the probability difference is plotted against the prediction error, E as shown in Figure 7-9. From the figure it can be seen that the

discrepancy of the theoretical and empirical CDFs causes the plot to have data located at a distance from zero.

The effect of the discrepancy between two CDFs can be better seen when the probability difference plot of Class 6 in Figure 7-9 is compared with the plot of Class 5 as given in Figure 7-10. It can be seen that when good agreement is achieved between the empirical and theoretical CDFs, as shown in Figure 7-10, the majority of the data points in the plot will be located very close to zero.

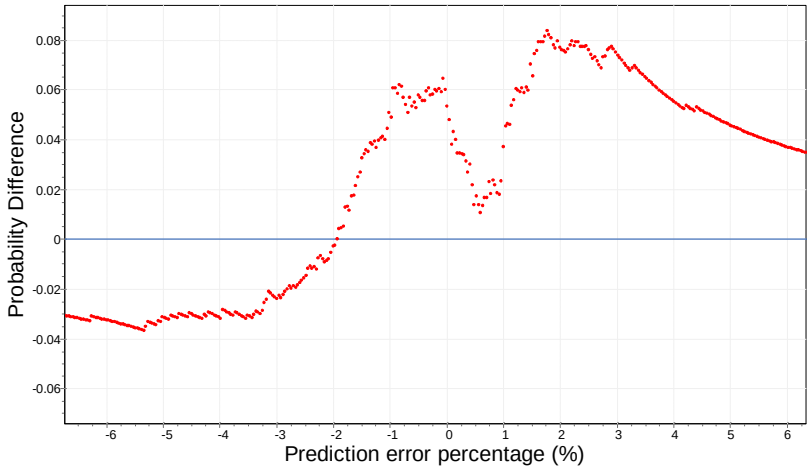

Figure 7-9: Probability difference against E for Class 6 Approximator

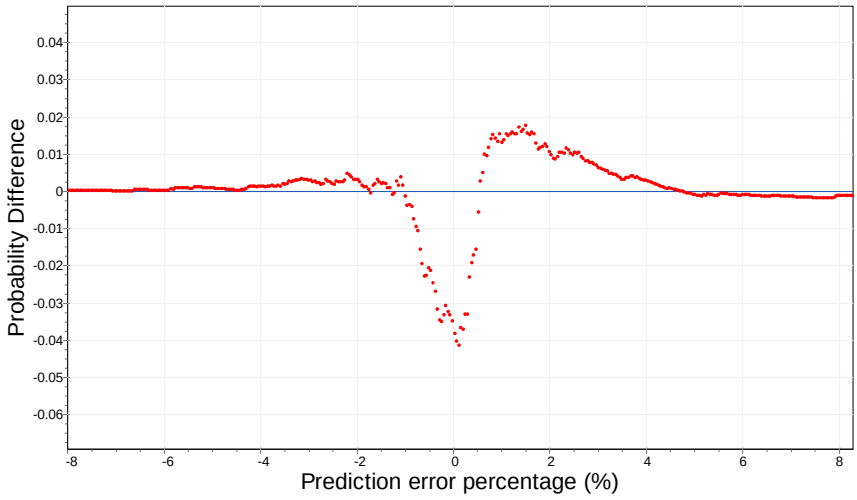

Figure 7-10: Probability difference against E for Class 5 Approximator

It is worth noting that the probability difference graph is a plot of the difference between the empirical CDF calculated using Equation (7-10) and the theoretical CDF calculated using Equation (7-8) at a given $E = x$. In Equation (7-10), $F_n(x)$ denotes the empirical CDF, n_{obs} denotes the observed samples that have $E \leq x$, while n_{total} denotes the total samples.

$$F_n(x) = \frac{1}{n_{total}}[n_{obs} \leq x] \quad \textbf{(7-10)}$$

7.3.1.6 Assessment of the Performance of the Network on a Given Mission Profile

Based on the specified mission profile given in Table 6-9 in Section 6.3 , the mission segments or mission sub-segments (for non-constant operation) operation parameters (altitude, PCN etc.) were inputted into the architecture. Since the architecture uses both classifier and approximators, the mission segments were first applied to the Range Classifier in order to classify the segments into different classes of creep life range. Then each of the classified mission segments (both correct and incorrect) was inputted into its respective Class Approximator to approximate the mission segments' or sub-segments' creep lives. Using the same reference conditions as specified in the previous analysis (refer to Section 6.3), the CF and LF of each mission segment or sub segment together with the CF_M were computed respectively.

The classification outputs of the Range Classifier are summarised in Table 7-20. From the table it can be seen that only one mission sub-segment was not correctly classified which is F2-10. The results again show how good the trained classifier is in providing correct classification.

Table 7-20: Summarised classification output

Sub-segment	Correct class		Sub-segment	Correct class		Sub-segment	Correct class	
	Yes	No		Yes	No		Yes	No
F1	✓		F2-2	✓		F2-3	✓	
F2-4	✓		F2-5	✓		F2-6	✓	
F2-7	✓		F2-8	✓		F2-9	✓	
F2-10		✓	F2-11	✓		F2-12	✓	
F2-13	✓		F2-14	✓		F2-15	✓	
F2-16	✓		F2-17	✓		F2-18	✓	
F3-19	✓		F4-20	✓		F4-21	✓	
F4-22	✓		F4-23	✓		F5-24	✓	
F6-25	✓		F6-26	✓		F6-27	✓	
F6-28	✓		F6-29	✓		F6-30	✓	
F6-31	✓		F6-32	✓		F7-33	✓	
F8-34	✓		F8-35	✓		F8-36	✓	
F8-37	✓		F8-38	✓		F8-39	✓	
F8-40	✓		F8-41	✓		F8-42	✓	
F8-43	✓		F8-44	✓		F8-45	✓	
F8-46	✓		F8-47	✓		F8-48	✓	
F8-49	✓		F8-50	✓		F8-51	✓	
F8-52	✓		F8-53	✓		F9-54	✓	

Figure 7-11 provides a comparison between the CFs calculated from the creep lives predicted using the implemented architecture and the integrated model (extracted from clean engine CFs in Figure 6-32). From the figure it can be clearly seen that the CFs between both model and architecture are similar, causing the plots to overlap each other. The figure also shows that the effects of misclassification in this case study are found to be insignificant as the misclassified approximator is able to provide good creep life prediction.

The comparisons of the calculated LF_M and CF_M produced by the integrated model and the implemented architecture are given in Table 7-21. The table shows that the LF_M and CF_M produced by both model and architecture are similar with errors between them around 2.6 to 2.7%. The low prediction errors were expected since the previous assessments conducted using the training and the unseen samples also demonstrate the ability of the architecture to provide good creep life prediction.

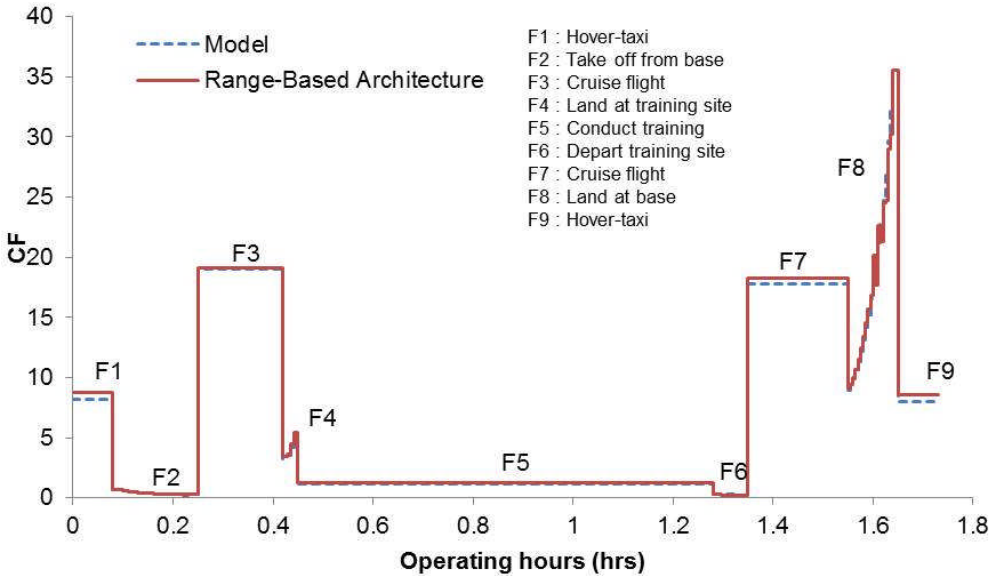

Figure 7-11: CFs for the given mission profile produced by both the integrated model and the neural architecture

Table 7-21: LF_M and CF_M produced by the integrated model and neural architecture

	Model	Architecture	Error (%)
LF_M	5.07E-05	5.20E-05	-2.68
CF_M	1.167	1.136	2.61

7.3.2 Implementation of FB Architecture

In this section, the implementation of the FB neural architecture on the selected engine model is reported.

7.3.2.1 Design Considerations and Realisation

The FB architecture creates mapping between the selected engine operating parameters and individual creep life functional parameters (blade metal temperature and stress) before these functional parameters are mapped to the selected engine model HP turbine blade's creep life. A cascade type of network is applied, as shown in Figure 7-12.

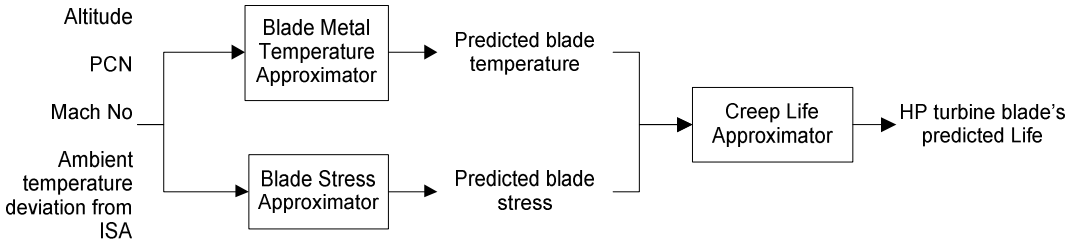

Figure 7-12: Implemented FB Neural Creep Life Estimation Architecture

From the figure, it can be seen that three approximator networks were created which are the Blade Metal Temperature Approximator to predict the blade's metal temperature, the Blade Stress Approximator to predict the blade's maximum stress, and the Creep Life Approximator to predict the blade's creep life. Both the Blade Metal Temperature and Blade Stress Approximator are known as intermediate approximators while the Creep Life Approximator is known as the output approximator.

It is important to emphasise at this stage that the predicted blade's metal temperature and maximum stress are values predicted at the blade's critical location which provides the minimum creep life; therefore the blade's predicted creep life is the blade's minimum creep life along the blade span.

7.3.2.2 Number of Samples to Train the Approximators

Table 7-22 provides the step size used for each parameter and the amount of the initial and final generated samples. Similarly, 60% of the finalised samples were used as training samples, 20% were used for validation samples and the other 20% were used as test samples.

Table 7-22: Step size used for each parameter and the amount of generated samples for the approximators

Parameter	LL	UL	Step size
Altitude	0	4,800	300
PCN	0.94	1	0.006
Mach number	0	0.3	0.06
Ambient temperature deviation from ISA	0	30	3
	Initial samples generated		12,342
	Finalised samples		9,742

Although the same amount of samples was used in each network, the inputs and outputs of individual networks are different. The inputs for the Blade Metal Temperature and Blade Stress Approximators were similar which were the selected parameters listed in Table 7-22, but the targeted outputs were different. For the Blade Metal Temperature Approximator, the targeted output was the blade metal temperature while for the Blade Stress Approximator, the output was the maximum blade stress. Similarly, the inputs for the Creep Life Approximator were both the blade's metal temperature and blade's stress while the targeted output was the blade's minimum creep life.

Extractions of different information from the same generated samples were easy as each sample simulated, by using the Integrated Creep Life Estimation model, contains not only the blade's creep life but also both the blade's metal temperature and blade stress along the blade span.

7.3.2.3 Training of the Approximator Networks

The final sizes of the three approximators are given in Table 7-23. It can be seen from the table that all of the approximators used two hidden layers in order to achieve the best optimised synaptic weights, although the Blade Metal Temperature Approximator used more hidden neurons compared to the other approximators.

Table 7-23: Final sizes of approximator networks

Network	Size of the network
Blade Metal Temperature Approximator	4-30-30-1
Blade Stress Approximator	4-10-10-1
Creep Life Approximator	2-20-20-1

The observed MSE during the training and the corresponding final regression plots before the training was stopped are given in Appendix G while the summary is given in Table 7-24.

Table 7-24: Summary of the final MSE and R for each approximator

	Blade Metal Temperature Approximators	Blade Stress Approximators	Creep Life Approximators
Training samples:			
MSE	1.10E-05	5.79E-07	1.002E-9
R	0.99997	1	1
Validation samples:			
MSE	2.53E-05	6.67E-07	1.038E-09
R	0.99994	1	1
Test samples:			
MSE	2.78E-5	6.58E-07	1.096E-09
R	0.99993	1	1

From the summarised table, it can be clearly seen that the $MSEs$ of the networks are significantly low, suggesting that the error between the normalised predicted and targeted outputs is quite small. In addition, the trends of the $MSEs$ given in Appendix G (Blade Stress Approximator and Creep Life Approximator) are not only similar but the location between them implies a good generalisation. In addition, the table also shows that the R values are unity, suggesting that both predicted and targeted outputs are highly correlated.

7.3.2.4 Assessment of the Performance of the Networks Using the Populated Samples

Table 7-25 provides the E_{Ave} and SD_E produced by individual networks. It can be seen that the predicted outputs produced by the networks possess E_{Ave} very close to zero and small SD_E. These indicate that, individually, all networks are able to produce accurate predictions with small variations of prediction error.

Table 7-25: The predicted outputs E_{Ave} and SD_E of each trained network

	Blade Metal Temperature Approximator	Blade Stress Approximator	Creep Life Approximator
E_{Ave} (%)	-6.52E-04	-1.38E-04	-3.03E-04
SD_E (%)	0.03487	0.00902	0.02074

Having to evaluate the performance of individual networks does not provide the overall picture of how the implemented architecture responds to a given input when those networks are put together to form a cascade system. This is because in the cascade system, the output prediction errors of the intermediate networks will propagate into the Creep Life Approximator, thus increasing the blade's creep life

prediction errors. For this reason, the overall performance of the implemented architecture must be evaluated.

To evaluate the overall performance of the FB architecture, the blade's metal temperatures and stresses, predicted by the Blade Metal Temperature and Blade Stress Approximators respectively, are inputted into the Creep Life Approximator. Then, the predicted blade's creep lives were compared with the targeted creep lives used during the training of the Creep Life Approximator. The blade's creep life E_{Ave} and SD_E were recalculated and are given in Table 7-26.

Table 7-26: The blade's creep life E_{Ave} and SD_E produced by the Creep Life Approximator

	Creep Life Approximator
E_{Ave}(%)	0.04133
SD_E (%)	1.574

It can be seen from the table that when the predicted values were used as inputs to the Creep Life Approximator, both E_{Ave} and SD_E have increased substantially. It was found that the magnitudes of the blade's creep life E_{Ave} and SD_E have increased 136 (0.04133 /-3.03E-04) and 76 (1.574/0.02074) times from their initial values (refer to Table 7-25) respectively. Although the increments appear to be appalling, the increase in E_{Ave} is not crucial since the value is still close to zero. However, the increase in SD_E does indicate that the variation of E has become bigger, although was still at an acceptable level.

Table 7-27: Percentage of samples encompassed within the specified error ranges

Error Range	% Sample encompassed
T1	65.048
T2	86.15
T3	94.625
T4	97.03
T5	98.39
T6	98.97

Using the same error range specified in Table 7-2, the study further investigated how many samples are able to produce a predicted creep life with a prediction error that falls within a given range of E. The results of the investigation are presented in Table 7-27. From the table it can be seen that almost 95% of the samples are able to produce a predicted creep life with E within -3 to 3% while most of the samples (99%) were able to produce E within -6 to 6%.

7.3.2.5 Assessment of Performance of the Network Using Unseen Post Test Samples

The step size for each input parameter and the distribution of samples for both first and second unseen data is given in Appendix H. From the appendix it can be seen that around 13,300 new samples were generated. Using the same prediction error range specified in Table 7-2, the percentage of the unseen samples able to produce a predicted creep life with E within the specified range was independently counted. The plots of the results are given in Figure 7-13.

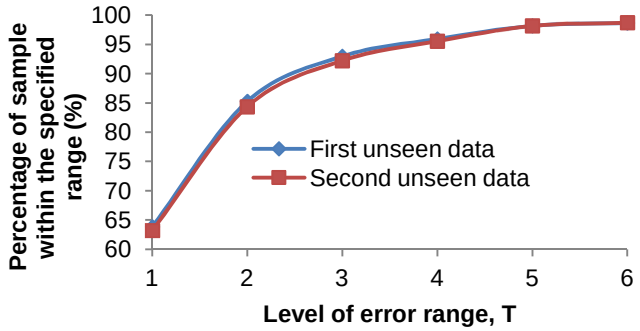

Figure 7-13: Percentage of samples encompassed within the specified error range

The plots of both unseen data given in Figure 7-13 are seen to be overlapping each other, confirming that good generalisation was achieved during the training of the networks. The figure also indicates than almost 96% of the both unseen samples are able to produce a predicted creep life with E within -4 to 4% while almost 99% of both unseen samples are able to produce E within -6 to 6%.

When the results plotted in Figure 7-13 were compared with the results tabulated in Table 7-27, it can be seen that at error range lower than T4, the discrepancies of the values between them is around 2% before they improve considerably at the later ranges.

Table 7-28: Probability of obtaining E within the specified error ranges

Best fitted distribution		Student's t
		Probability
Level of error range	T1	0.609
	T2	0.861
	T3	0.942
	T4	0.972
	T5	0.985
	T6	0.991

Table 7-28 provides the summary of the third stage assessment while Figure 7-14 and Figure 7-15 depict the PDF and CDF of the best fitted distribution. From the results, several observations can be made. The best fitted distribution obtained from the combined unseen data is the Student's t distribution. In addition, both the theoretical and empirical PDF plotted in Figure 7-14 shows that the distribution is symmetrical with the highest occurrence at the average, which is at $E \approx 0\%$. Also, Table 7-28 indicates that as the level of error range increases, the probability of getting the error within the range also increases. It can be seen that the probability of obtaining E within -4 to 4% is 0.97 while a 0.99 probability is achieved when E is within -6 to 6%.

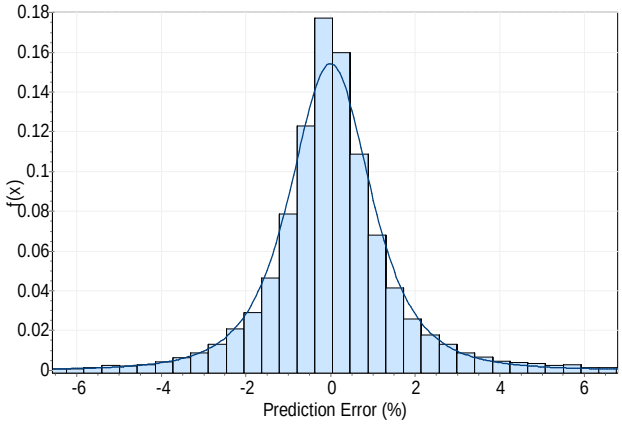

Figure 7-14: PDF of the best fitted distribution

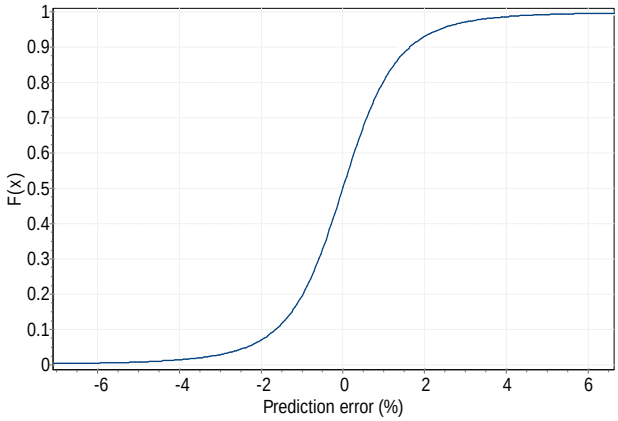

Figure 7-15: CDF of the best fitted distribution

Importantly, it was found that the probabilities calculated at different error range are consistent with the percentage of samples encompassed within the specified range given in Figure 7-13. This can be clearly seen when the magnitudes of the deviation (specified in absolute form) between both of them were calculated; these are given in Table 7-29. The small magnitudes of deviation suggest that the probabilistic analysis is in agreement with the sample distribution analysis

Table 7-29: Magnitude of deviation between the two analyses

Error range	Deviation
T1	2.31
T2	1.75
T3	2.0
T4	1.65
T5	0.291
T6	0.39

7.3.2.6 Assessment of Performance of the Network on a Given Mission Profile

Figure 7-16 provides the comparison between the CFs calculated using the FB architecture and the integrated model (extracted from clean engine CFs in Figure 6-32). The figure clearly shows that the plots of the CFs are overlapping each other, demonstrating the architecture's ability to produce good predictions. As a consequence, the accumulated effect of the prediction errors is minimised, hence producing a good overall mission prediction as given in Table 7-30. The table shows that when both LF_M and CF_M given by the integrated model and architecture are compared, the prediction errors are found to be around 0.9%.

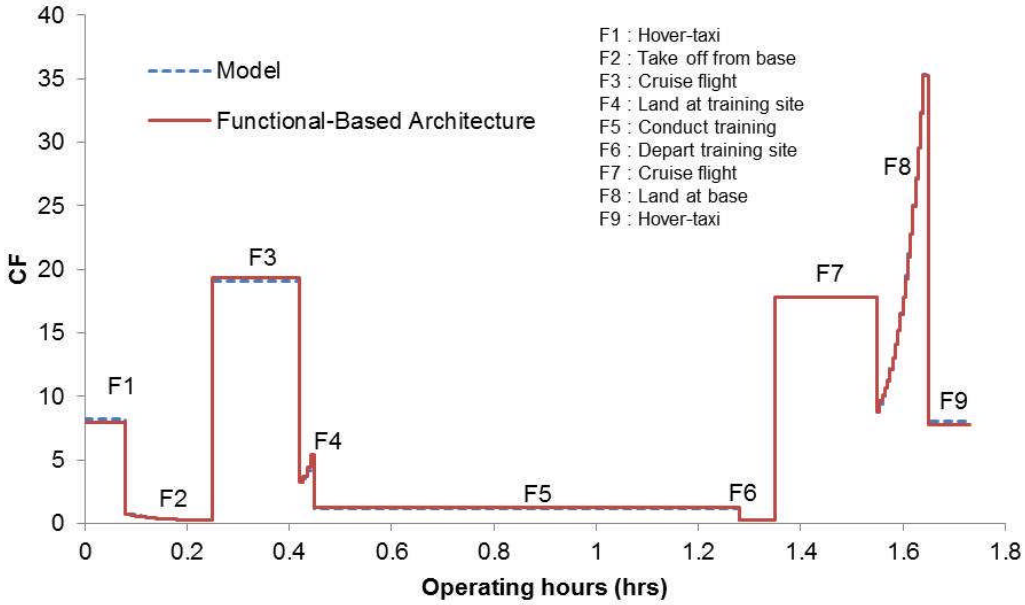

Figure 7-16: CFs for the given mission profile predicted by FB architecture and the integrated model

Table 7-30: LF_M and CF_M produced by the integrated model and FB architecture

	Model	Architecture	Error (%)
LF_M	5.07E-05	5.201E-05	-0.911
CF_M	1.167	1.178	-0.92

7.3.3 Implementation of SB Architecture

This section reports the implementation of the proposed SB architecture on the selected engine model HP turbine blade's creep life estimation.

7.3.3.1 Design Considerations and Realisation

The implemented SB architecture for the selected engine model is illustrated in Figure 7-17. From the figure, it can be seen that eight sensors were selected as the inputs to the cascade network. The selection of the sensors was based on the available engine test rig measurements obtained from the engine manufacturer during the course of the research.

Similar to the FB architecture, three approximator networks were created: the Blade Metal Temperature Approximator, the Blade Stress Approximator, and the Creep Life Approximator. However, during the implementation of the architecture, only the Blade Metal Temperature and Blade Stress Approximators were trained while the Creep Life Approximator was taken out of the FB architecture.

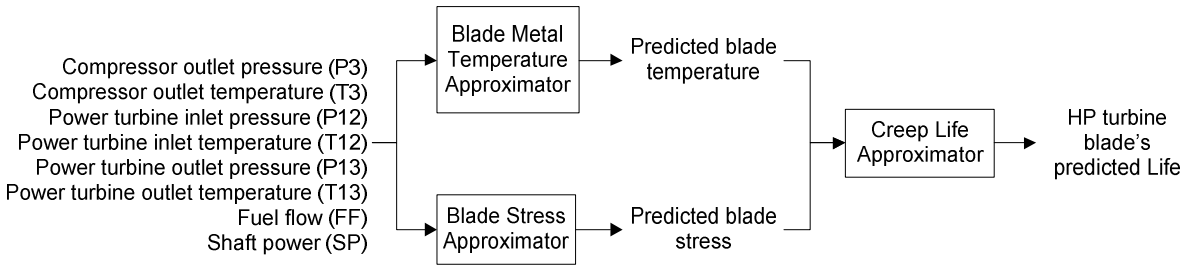

Figure 7-17: Implemented SB Neural Creep Life Estimation Architecture

7.3.3.2 Number of Samples to Train the Approximators

Samples used to train the FB Architecture were taken as the samples to train both approximator networks. Again, extraction of the information was easy as each sample simulated using the Integrated Creep Life Estimation model also contained all of the measurements needed for this architecture.

7.3.3.3 Training of the Approximator Networks

Table 7-31 provides the final sizes of the Blade Metal Temperature and Blade Stress Approximator networks. The table shows that both approximators required two hidden layers in order to achieve the best optimised solution, although the Blade Stress Approximator used more hidden neurons compared to the other approximator.

The plots of the observed MSE and the corresponding final R for the training, validation and test samples are given in Appendix I while the summary is given in Table 7-32. The low $MSEs$ for both samples again indicate that the errors between the normalised predicted and targeted outputs are minimised. Also the location of the

trends of the MSE given in Appendix I between the three samples are extremely close indicating that the good generalisations have been achieved for both approximators. Also from Table 7-32, the Rs are unity, indicating that both predicted and targeted outputs are considerably correlated.

Table 7-31: Final sizes of the two approximator networks

Network	Size of the network
Blade Metal Temperature Approximator	8-10-10-1
Blade Stress Approximator	8-15-15-1

Table 7-32: Summary of the final MSE and R for each approximator

	Blade Metal Temperature Approximators	Blade Stress Approximators
Training samples:		
MSE	1.90E-07	2.41E-07
R	1	1
Validation samples:		
MSE	1.99E-07	3.22E-07
R	1	1
MSE	210E-7	3.72E-07
R	1	1

7.3.3.4 Assessment of the Performance of the Networks Using the Populated Samples

Similar to the previous implemented architectures, the true prediction errors were obtained when the normalised predicted and targeted outputs for each approximator were de-normalised. Table 7-33 depicts the predicted outputs E_{Ave} and SD_E of individual, trained approximators. From the table it can be seen that the performances of the individual network were very good, with the predicted outputs E_{Ave} very close to zero and its corresponding SD_E extremely small.

Table 7-33: E_{Ave} and SD_E of each trained network

	Blade Metal Temperature Approximator	Blade Stress Approximator
E_{Ave} (%)	3.30E-05	9.37E-05
SD_E (%)	0.00375	0.00607

By comparing the performances of the individual networks between the SB (refer to Table 7-33) and the FB architectures (refer to Table 7-25), it was found that the performances of the SB architecture are much better, especially that of the Blade Metal

Temperature Approximator. The magnitudes of both predicted output E_{Ave} and SD_E of the SB Blade Metal Temperature Approximator were found to be 20 and 10 times lower, respectively, than the FB architecture.

The reductions in the predicted output E_{Ave} and SD_E in both approximators, especially the Blade Metal Temperature Approximator, have reduced the effects of the propagating errors coming from the intermediate approximators to the output approximator, hence improving the overall performance of the implemented architecture. This can be clearly seen when the predicted outputs E_{Ave} and SD_E produced by the Creep Life Approximator between the FB (refer to Table 7-26) and the SB architectures are compared in Table 7-34. From Table 7-34, it can be seen that the predicted output E_{Ave} and SD_E of the SB architecture are significantly lower than the FB architecture with both giving values of -0.0022% and 0.17691% respectively.

Table 7-34: Comparison of the Creep Life Approximator predicted output E_{Ave} and SD_E between two implemented architectures

	FB architecture	SB architecture
E_{Ave}	0.04133	-0.0022
SD_E	1.574	0.17691

It is worth remembering that the predicted outputs E_{Ave} and SD_E at this stage were calculated when the predicted blade's metal temperatures and stresses were inputted into the Creep Life Approximator and the predicted and targeted outputs compared.

The percentages of the samples able to produce a predicted creep life with E within the specified ranges were counted and these are given in Table 7-35. From the table it can be seen that all of the samples were able to produce a predicted creep life with E even at the lowest range (-1 to 1%). This shows how superior the SB architecture is in producing accurate creep life prediction. For this reason, lower blade's creep life prediction error ranges were specified in Table 7-36 so that the distribution of samples producing different ranges of E could be further investigated.

Table 7-35: Percentage of samples encompassed within the specified levels of error range

Level of Error Range	%Sample encompassed	Level of Error Range	%Sample encompassed
T1	100	T2	100
T3	100	T4	100
T5	100	T6	100

Table 7-36: Lower levels of error range used to assess the performance of the trained network

Level of Error Range	Description
T0.2	$-0.2\% \leq E \leq 0.2\%$
T0.4	$-0.4\% \leq E \leq 0.4\%$
T0.6	$-0.6\% \leq E \leq 0.6\%$
T0.8	$-0.8\% \leq E \leq 0.8\%$

The results of the investigations using the new specified ranges are given in Table 7-37. From the table, it can be seen that 98% of the samples were able to produce a predicted blade's creep life with E within -0.4 to 0.4%. In addition, almost all of the samples were able to produce E within -0.8 to 0.8%.

Table 7-37: Percentage of samples encompassed within the new specified levels of error range

Level of Error Range	% Sample encompassed
T0.2	73.78
T0.4	98.17
T0.6	99.83
T0.8	99.99

7.3.3.5 Assessment of the Performance of the Network Using Unseen Post Test Samples

Two unseen samples used to perform the post test for the FB architecture were used in the post test of the SB architecture. Using the new specified levels of error range given in Table 7-36, the percentage of the two unseen samples able to produce a predicted creep life with E within the specified range were independently counted. The plots of the results are given in Figure 7-18.

From Figure 7-18, it can be clearly seen that good generalisation is achieved during the training of the networks since both plots of the two unseen samples are overlapping each other. It can also be seen that almost 98% of the two unseen samples are able to produce an estimated creep life with E within -0.4 to 0.4%. Also at the highest level of range specified, almost no samples are seen to have a prediction error that exceeds the value.

By combining the two unseen samples, the statistical distribution fitting was performed and Table 7-38 summarises the results of the distribution fitting and the probabilities of achieving the specified levels of error range given in Table 7-36. Using

the best fitted distribution, both PDF and CDF were plotted and are given in Figure 7-19 and Figure 7-20 respectively.

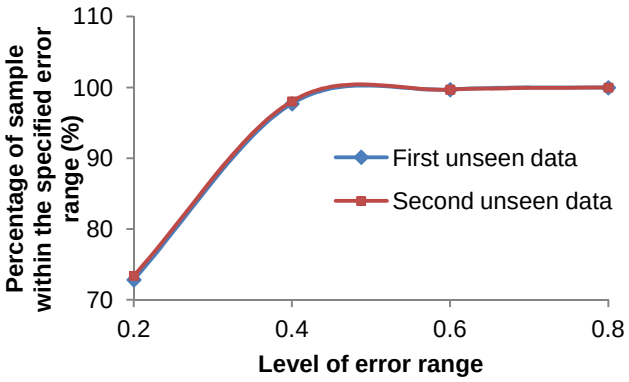

Figure 7-18: Percentage of samples encompassed within the newly specified error ranges

Table 7-38: Probability of obtaining E within the specified range

Best fitted distribution		Normal
		Probability
Level of error range	T0.2	0.7345
	T0.4	0.9741
	T0.6	0.9992
	T0.8	0.9999

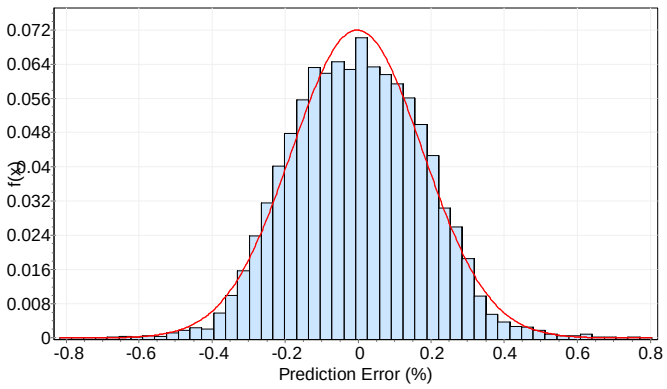

Figure 7-19: PDF of the best fitted distribution

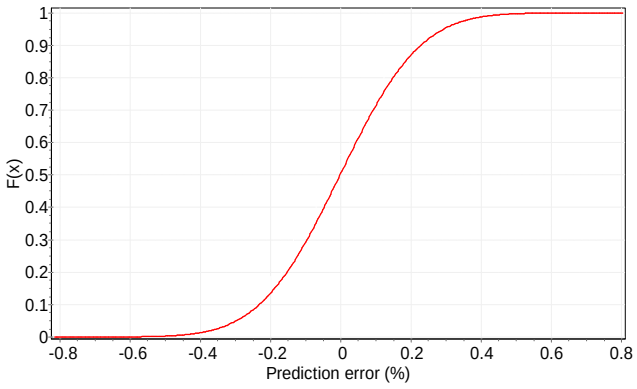

Figure 7-20: CDF of the best fitted distribution

From the table it can be seen that the best distribution that can fit the unseen samples is the normal distribution. Looking at the empirical PDF plotted in Figure 7-19, it can also be seen that the blade's creep life prediction errors were distributed evenly with the highest occurrence located at the mean of the distribution which is at $E \approx 0\%$. Also, the probability of obtaining E within the lowest specified range is around 0.73

before it increases substantially to 0.97 at the next level. Additionally, the probability reaches unity when the range is between -0.8 to 0.8%.

The calculated probabilities were found to be consistent with the percentages of samples encompassed within the specified range given in Figure 7-18. This can be clearly seen when the magnitudes of deviation between the calculated probabilities and the percentages of samples were calculated, as shown in Table 7-39. From the table it can be seen that the small magnitudes of deviation suggest that the probabilistic analysis is in agreement with the sample distribution analysis.

From the results it can be concluded that the SB architecture possesses high probability for obtaining a substantially good blade's creep life prediction accuracy.

Table 7-39: Magnitude of deviation between the two analyses

Error Range	Deviation
T0.2	0
T0.4	0.64
T0.6	0.22
T0.8	0.005

7.3.3.6 Assessment of the Performance of the Network on a Given Mission Profile

Figure 7-21 plots the CFs of each mission segment against their respective operating hour predicted by both the integrated model and the implemented architecture. Similarly to the previous architectures, the overlapping of both plots indicates that the architecture is able to produce good creep life prediction.

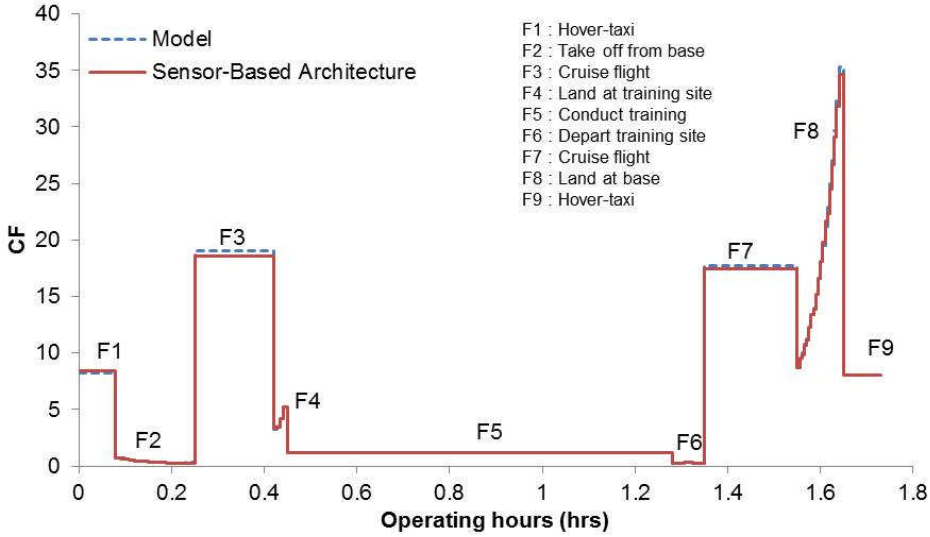

Figure 7-21: CFs for the given mission profile produced by the integrated model and SB architecture

The accumulated effect of the prediction errors when the mission profile was formed can be seen in Table 7-40 where the errors of both LF_M and CF_M between the architecture and the integrated model are around 0.45%. The low errors result from the accurate prediction of the blade's creep life at an individual operating point which has been proved in the previous assessments to be accurate.

Table 7-40: LF_M and CF_M produced by the integrated model and SB architecture

	Model	Architecture	Error (%)
LF_M	5.07E-05	5.04E-05	-0.449
CF_M	1.167	1.172	-0.45

7.3.4 Comparison between the Three Implemented Architectures at Clean Engine Condition

Although the engine operational ranges covered during the implementation of the network (refer to Table 7-4) are similar, the way individual networks are arranged is different, and the number of samples used to train the network is not the same. Figure 7-22 depicts the ratio between the samples used to train the networks for the three implemented architectures, with the samples used for the SB architecture. Figure 7-22 also shows that the RB architecture used twice as many samples as in the other two architectures (samples used in the other two architectures are similar) in order to achieve a similar performance. This was expected since the RB architecture used more networks (six approximators + one classifier) compared to the architectures that used only three approximators.

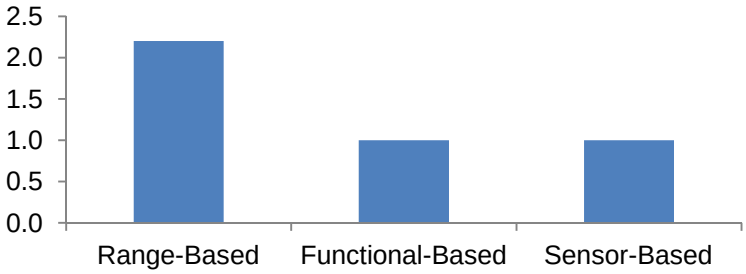

Figure 7-22: Ratio of samples used during network training.

During the post test, when two new unseen samples were generated and tested independently, it can be seen that all three architectures were able to have good generalisations. This can be clearly seen when the plots of the percentage of samples, that are able to provide creep life estimates with E fall within the given ranges for both

unseen samples, are overlapping each other (refer to Figure 7-8, Figure 7-13 and Figure 7-18).

Although all of the architectures were able to provide good generalisations, the SB architecture was found to be more superior compared to the other two in terms of providing accurate creep life predictions. This can be clearly seen in Figure 7-23 when the probabilities of achieving the specified blade's creep life prediction error range for the three architectures were compared.

As shown in Figure 7-23, the SB architecture has reached the probability of unity when E is within -0.6 to 0.6% compared to others where the best probability is given by one of the RB Class Approximators which is a probability of 0.62.

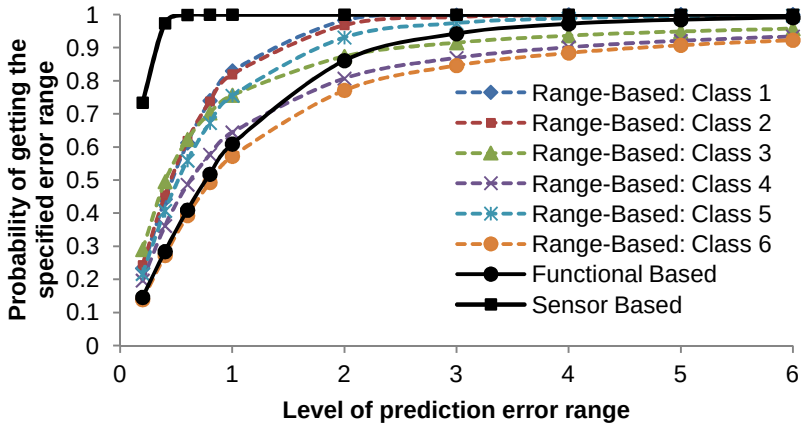

Figure 7-23: Probability of obtaining specified range of E

Comparing the probability trends of both RB and FB architectures, it can be seen that RB Classes 1, 2 and 5 approximators are able to provide higher creep life prediction accuracies than the FB architecture. However, for the RB architecture, Classes 3 and 4, the two approximators are found to be more accurate at the lower range prediction error (-2 to 2%) before the FB architecture takes over at the higher ranges.

When the same mission profile at clean engine condition was inputted into the three architectures, it can be seen that all of the architectures were able to provide good prediction creep life. This can be seen when the plotted CFs predicted by the architectures, as previously shown in Figure 7-11, Figure 7-16 and Figure 7-21, were individually compared with the plotted CFs predicted by the Integrated Creep Life Estimation Model. The plots of the CFs were seen to be overlapping each other, suggesting that the creep lives predicted by the architectures were close to the values predicted by the integrated model. In addition, the good creep life prediction of the

individual mission segment or sub-segment has ensured that the overall prediction errors of the CF_M and LF_M were significantly minimised.

By comparing the mission profile analysis between the three architectures, the SB architecture is found to be more superior than the other architectures in providing accurate mission creep life assessment. This can be clearly seen when the prediction errors (%) of both LF_M and CF_M between the architectures and the integrated model are summarised in Table 7-41. As shown in the table, the prediction errors produced by the SB architecture are six times and two times lower than the RB and the FB architectures respectively.

Table 7-41: Prediction errors of LF_M and CF_M between the architectures and the integrated model

	Prediction error (%)		
	RB	FB	SB
LF_M	-2.68	-0.911	-0.449
CF_M	2.61	-0.92	-0.45

By comparing both RB and FB architectures, the superiority of both architectures will depend on the location of the operation points in the operation envelope. At the lower creep life operational range, RB architecture is found to be more superior than the FB architecture and vice versa. The mission analysis conducted using both architectures shows that FB architecture is better than the RB architecture, suggesting that the operational points in the mission profile have a strong influence in determining which architecture is better than the other.

7.4 Implementation of the Proposed Neural Architectures on the Developed Engine Model at Degraded Engine Condition

The implementation of the proposed neural architectures was extended to the degraded engine conditions using two of the proposed architectures, which are the FB and SB architectures. The decision to implement only two architectures instead of three was because of time constraints in finishing the research.

The operational ranges covered by the developed architectures were first defined and are given in Table 7-42. It can be seen that the upper limits of the operational range in ambient temperature and altitude were lower than those used at the clean engine condition (refer to Table 7-4). In addition, the lower limits of the ambient

temperature was also increased. The decision to lower the upper limits was to simplify the complexity of the current problem thus reducing the number of networks created.

Table 7-42: Range covered by the developed neural-based model

Parameters	Lower limit (LL)	Upper limit (UP)
Altitude (m)	0	4500
PCN	0.94	1
Mach number	0	0.3
Ambient temperature deviation from ISA (K)	10	25

Additionally, the implementations of the proposed architectures were limited to single component degradation with the presence of compressor fouling, and HP and LP turbine erosions. The ranges of the health parameters are presented in Table 7-43. Again, the decisions to consider only single component degradation and limit the degradation magnitudes were to simplify the complexity of the problem. Further, if multiple component degradations are needed to be included later with larger degradation magnitudes, additional approximator networks can be added with some retraining to the classifiers (if used in the architecture).

Table 7-43: Degradation magnitudes covered in this study

Health parameters	Compressor	Turbine
Isentropic efficiency (ETA)	0 to 6% reduction	0 to 6% reduction
Flow capacity (FC)	0 to 6% reduction	0 to 6% increment

7.4.1 Implementation of FB Architecture

In this section the implementation of the FB architecture on the selected engine model at degraded engine condition is explained.

7.4.1.1 Design Considerations and Realisation

The implementation of the architecture was carried out for the case where prior to the estimation of the blade's creep life, the engine component degradation has been isolated and the magnitudes of both health parameters have been quantified. By having that information, three individual FB architectures were built to cater for the three component degradations.

The inputs to the intermediate approximators have two known additional health parameters, as listed in Table 7-43. Since the presence of the two health parameters have added complexity into the network, the degradation magnitude and the

operational space were divided into smaller divisions. For this study, the degradation magnitudes were divided into three successive levels:

a. Low level (LL): <2% degradation
b. Medium level (ML): 2% to 4% degradation,
c. High level (HL): >4% to 6% degradation.

For each degradation level, the altitude was divided into several levels which are given in Table 7-44. Note that for compressor degradation, four altitude levels were specified compared to the rest which used only three altitude levels. The reason to change from four to three levels was because it was found that during the implementation of the architecture, splitting the operational space into three levels was sufficient to produce good prediction accuracy.

Table 7-44: Altitude level for each degradation level of each component degradation

Component degradation	Degradation level	Altitude level	Tag	Range of altitude (m)
Compressor	LL	Level 1	LL1	0 to 1000
		Level 2	LL2	1000 < Altitude ≤ 2000
		Level 3	LL3	2000 < Altitude ≤ 3000
		Level 4	LL4	3000 < Altitude ≤ 4500
	ML	Level 1	ML1	0 to 1500
		Level 2	ML2	1500 < Altitude ≤ 3000
		Level 3	ML3	3000 < Altitude ≤ 4500
	HL	Level 1	HL1	0 to 1500
		Level 2	HL2	1500 < Altitude ≤ 3000
		Level 3	HL3	3000 < Altitude ≤ 4500
HP and LP turbines	LL	Level 1	LL1	0 to 1000
		Level 2	LL2	1000 < Altitude ≤ 2000
		Level 3	LL3	2000 < Altitude ≤ 3000
	ML	Level 1	ML1	0 to 1500
		Level 2	ML2	1500 < Altitude ≤ 3000
		Level 3	ML3	3000 < Altitude ≤ 4500
	HL	Level 1	HL1	0 to 1500
		Level 2	HL2	1500 < Altitude ≤ 3000
		Level 3	HL3	3000 < Altitude ≤ 4500

Figure 7-24 depicts an example of the FB architecture constructed for the compressor degradation. Note that for both HP and LP turbines, similar architectures, as given in Figure 7-24, were applied. From Figure 7-24, it can be seen that only approximator networks were used to construct the architecture for compressor degradation. Based on the operational inputs, degradation level and altitude level, the

blade's metal temperature and maximum stress were predicted by the respective intermediate approximators before the predicted blade's creep life was obtained from the output approximators.

7.4.1.2 Number of Samples to Train the Approximators

Appendix J provides the step sizes used for each input and the final amount of generated samples used to train the approximators for the three component degradation architectures. Note that the step sizes for ETA and FC given in Appendix J were not fixed. The reason for this was that during the samples generation, it was found that at some fixed ETA and FC operational points, PYTHIA was unable to provide the performance simulation outputs either by producing significant unconverged samples or because PYTHIA crashed during simulation. For these reasons these values were changed accordingly (added at different values or totally deleted without being replaced by new values).

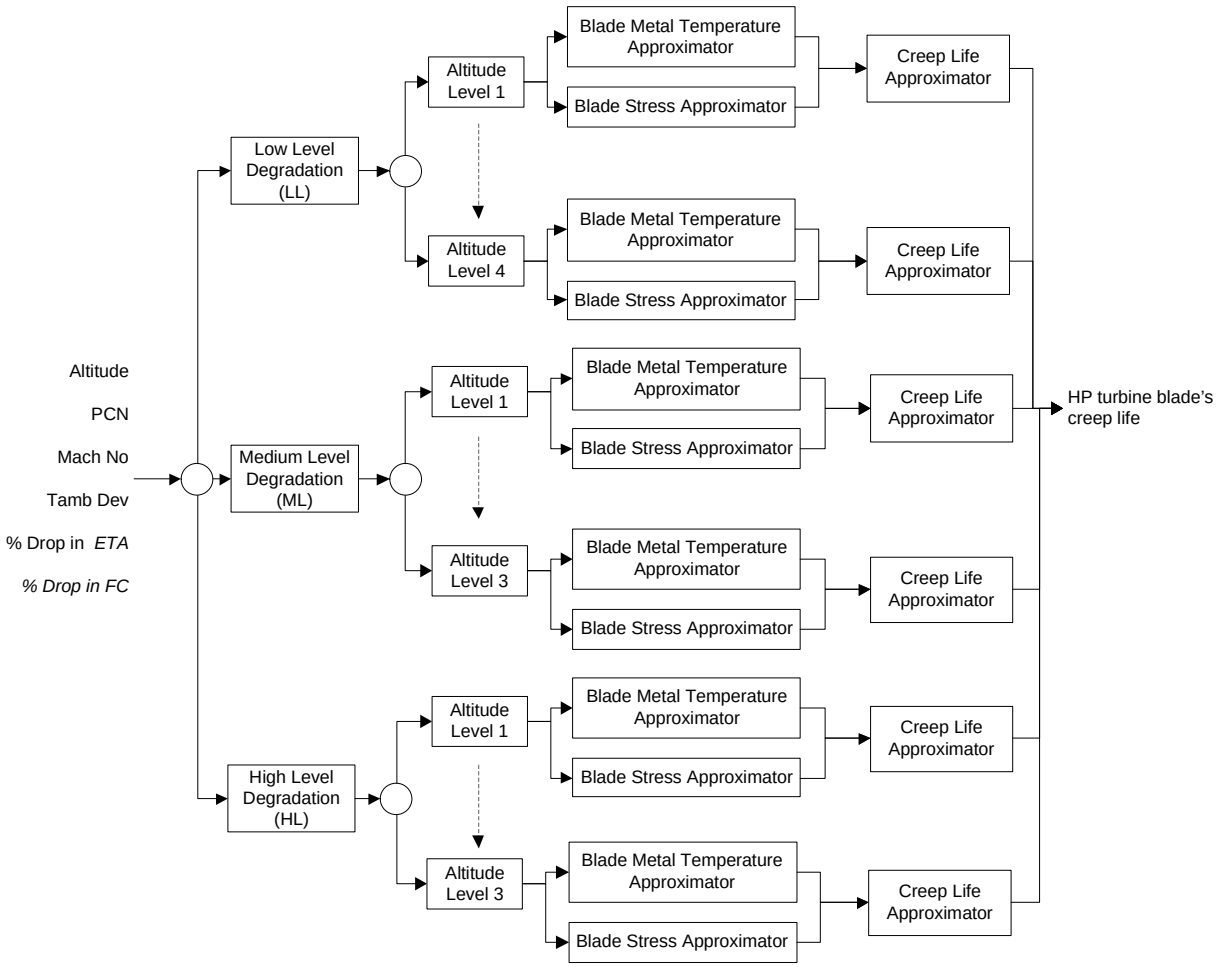

Figure 7-24: FB architecture for compressor degradation

Similarly, 60% of the finalised samples were used as training samples, 20% were used for validation samples and the other 20% were used as test samples. From the appendices it can be seen that samples used for each magnitude and altitude level are around 21,000 to 23,000 for compressor degradation and 28,000 to 30,000 for both turbines' degradation respectively.

7.4.1.3 Training of the Approximator Networks

The final sizes of the approximators for the compressor, HP and LP turbines degradations are given in Appendix K. From the appendix it can be seen that all of the trained approximators for Compressor Degradation were constructed using two hidden layers. The Blade Metal Temperature Approximators were found to use more hidden neurons compared to the other two approximators in order to obtain the final optimal solution.

Similar observations were seen for both the HP and LP turbines' degradation. All of the trained approximators used two hidden layers while the Blade Metal Temperature Approximators were found to have used more neurons than the other approximators.

The final $MSEs$ and Rs for each approximator of the compressor, and HP and LP turbines degradations are given in Appendices L.1, L.2, and L.3 respectively. From the appendices, it can be seen that all of the approximators were able to produce low $MSEs$ indicating that the errors between the normalised predicted and targeted outputs are quite small.

Besides having low values of $MSEs$, the appendices also show that the $MSEs$ between the training, validation and test samples were similar although the majority of training samples have lower $MSEs$ than validation and test samples. This provides an early indication that good generalisation may have been achieved during the training. The slightly higher value in the training samples' $MSEs$ also suggests that for any unseen inputs given into the architectures, the prediction error will be slightly higher than the one used during the training. The appendices also show that R values are unity, suggesting that both predicted and targeted outputs are highly correlated for all the approximators.

7.4.1.4 Assessment of the Performance of the Networks Using the Populated Samples

Both the E_{Ave} and SD_E produced by individual networks of each compressor, HP and LP turbine degradations under different levels of degradation and altitude were calculated and tabulated in Appendix M. The values of E_{Ave} very close to zero with small $SD_{E,}$ as depicted in the appendices, show that individually, all networks were able to predict outputs with small variations of error. By comparing both E_{Ave} and SD_E between the three approximators (intermediates and output approximators) of each compressor, HP and LP turbine degradation, it was found that although the values of E_{Ave} between them are similar, the lowest overall variation of E being produced by the Blade Stress Approximator.

The effects of error propagation were also assessed when the predicted blade's metal temperatures and stresses produced by the intermediate approximators were inputted into the Creep Life Approximator, hence the E_{Ave} and SD_E were recalculated and are shown in Table 7-45. By comparing the initially calculated E_{Ave} and SD_E of the Creep Life Approximators given in Appendix M with the E_{Ave} and SD_E given in Table 7-45, it can be seen that both the E_{Ave} and SD_E have increased significantly. Note that similar effects were seen when the FB architecture was implemented for the clean engine case, as discussed in Section 7.3.2.4.

Table 7-45: The blade's creep life E_{Ave} and SD_E produced by the Creep Life Approximator

	Compressor degradation		HP turbine degradation		LP turbine degradation	
Level	E_{Ave}(%)	SD_E(%)	E_{Ave}(%)	SD_E(%)	E_{Ave}(%)	SD_E(%)
LL1	4.21E-02	0.6120	9.33E-03	0.7201	-4.83E-05	0.5695
LL2	4.90E-02	0.8000	-1.20E-03	0.7002	6.63E-03	0.6819
LL3	2.47E-02	0.6958	2.77E-03	0.6336	4.45E-03	0.4938
LL4	-4.00E-03	0.7620	-	-	-	-
ML1	-8.90E-03	0.6177	1.30E-02	0.4479	-5.16E-04	0.3412
ML2	-1.80E-02	0.4000	7.34E-04	0.3857	5.79E-04	0.5271
ML3	1.80E-03	0.4460	-3.46E-03	0.3776	-2.42E-03	0.3437
HL1	-1.10E-01	0.8790	-3.32E-03	0.2905	-5.76E-06	0.2201
HL2	-9.60E-02	0.8610	8.03E-04	0.4446	-1.21E-04	0.2377
HL3	1.23E-02	0.5980	2.40E-03	0.2857	-6.04E-03	0.3075

Despite having a considerable increase in both E_{Ave} and SD_E, the increase in E_{Ave} is not essential since the values, as shown in Table 7-45, are still close to zero. On the other hand, the increase in SD_E in all of the Creep Life Approximators is considered significant because it indicates that the variation of Es has become higher. Table 7-46 compares the initially calculated SD_E (extracted from Appendix M) and the recalculated SD_E (from Table 7-46) together with the ratio between the recalculated and the initially calculated SD_E. From the table, the effects of the propagating error can be clearly seen as the increase in SD_E is between two and 150 times the initial values. Although the increase of the SD_E is large, the values are still within an acceptable level with the highest recorded SD_E at 0.879%.

Using the same error range specified in Table 7-2, the percentage of samples able to produce E within the specified range in the case of the compressor, HP and LP turbine degradation are given in Appendix N. From the appendix, several observations can be made. In general, all of the output networks were able to produce accurate predictions with a high percentage of samples possessing low prediction error. As the error range is increased, the percentage of samples encompassed within the range also increased.

Table 7-46: Comparisons between the initial and the recalculated SD_E

	Compressor degradation			HP turbine degradation			LP turbine degradation		
Level	Initial SD_E	SD_E	Ratio	Initial SD_E	SD_E	Ratio	Initial SD_E	SD_E	Ratio
LL1	0.022	0.612	27.407	0.043	0.720	16.939	0.016	0.570	35.090
LL2	0.021	0.800	38.223	0.025	0.700	27.862	0.020	0.682	34.197
LL3	0.005	0.696	150.602	0.006	0.634	101.051	0.005	0.494	108.756
LL4	0.012	0.762	65.917	-	-	-	-	-	-
ML1	0.052	0.618	11.946	0.048	0.448	9.397	0.019	0.341	18.148
ML2	0.024	0.400	16.618	0.014	0.386	26.746	0.022	0.527	23.456
ML3	0.011	0.446	38.918	0.015	0.378	24.374	0.012	0.344	28.479
HL1	0.036	0.879	24.122	0.020	0.291	14.198	0.032	0.220	6.856
HL2	0.020	0.861	43.158	0.249	0.445	1.786	0.017	0.238	13.740
HL3	0.006	0.598	101.356	0.055	0.286	5.188	0.013	0.308	22.796

For compressor degradation architecture, on average, 95% of the samples are able to have E within -1 to 1%. A significant increment was witnessed afterwards with 99% of the samples on average able to have E within -3 to 3%. By comparing the distribution of samples between different levels of degradation magnitude, it can be seen that both medium and high levels of degradation magnitude have similar prediction capabilities while the low levels of degradation magnitude are found to be slightly lower.

Similar observations were obtained for both the HP and LP turbines' degradation architectures. At the lowest specified range, both architectures were able to encompass around 96 to 97% of their respective total samples producing E within the range. A significant increment was also witnessed afterwards with both architectures achieving 99% of their respective total samples producing E within -3 to 3%. It was also found that both architectures have better prediction capabilities at medium and high degradation magnitudes.

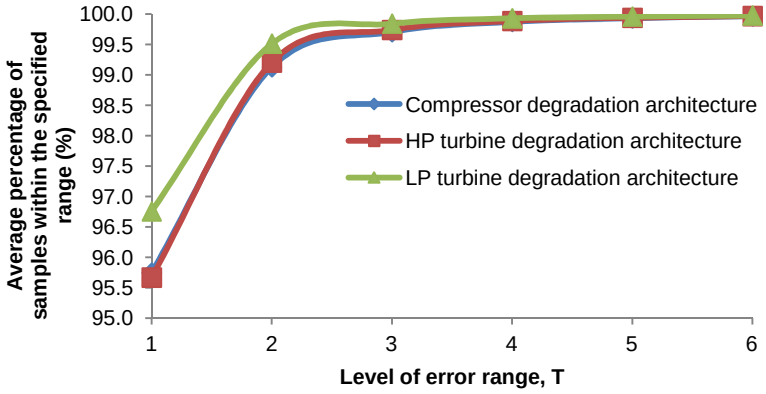

Figure 7-25: Average sample distributions at different error range

Figure 7-25 provides the comparison of average sample distributions at different error range predicted by the three component degradation architectures. From the figure, it can be seen that LP turbine degradation architecture has the best trained approximators able to produce accurate predictions followed by HP turbine degradation architecture and compressor degradation architecture.

7.4.1.5 Assessment of Performance of the Network Using Unseen Post Test Samples

In order to simplify the sample generation process, using the step sizes given in Appendices O.1,and O.2, a large set of samples was first generated for every magnitude and altitude level before the samples were divided randomly into two sets. Note that the information in the appendices contains the step size for each input and the amount of final generated samples used to perform the post test. From the appendices it can be seen that samples used for each magnitude and altitude level are around 14,000 to 27,000 for compressor degradation and 24,000 to 28,000 for both turbines' degradation respectively.

Using the same prediction error range specified in Table 7-2, the percentage of the unseen samples able to produce a predicted creep life with E within the specified

range was independently counted. The plots of the results are given in Appendix P. From the appendix, it can be seen that the plots of both unseen data at all three component degradation architectures were seen to be overlapping each other, validating that good generalisation was achieved during the training of the networks.

Figure 7-26 depicts the average sample distributions at different error range of one of the set of unseen samples. When unseen samples were inputted, it can be seen that the output approximators can still retain the ability to produce good prediction although when compared with the average distribution of samples obtained during the training of the approximators (refer to Figure 7-25), the accuracy of the prediction dropped slightly at the first two error ranges.

Figure 7-26 also shows that the performance of the trained approximators for the HP and LP turbine degradation architectures are similar and slightly higher than the compressor degradation architectures, especially at the first two ranges of error. At error level T1, both turbines' approximators were able to encompass around 93 to 94% of their respective total samples compared to the compressor with only 91%. Significant increments were seen afterwards for all the three component approximators achieving 99% samples able to produce prediction with E within -3 to 3%.

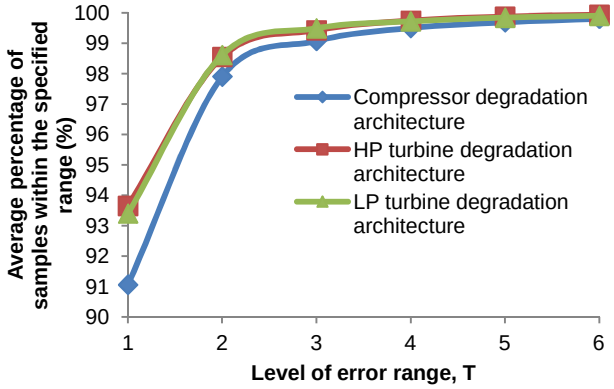

Figure 7-26: Average sample distributions at different error range of one set of unseen data

Appendix Q summarises the results of the stage three assessment for the compressor, HP and LP turbines while the plots of PDFs and CDFs are given in Appendix R. From Appendix Q, several observations can be made. It can be seen that the best fitted distribution for most of the compressor degradation approximators is Johnson SU (six approximators) followed by Cauchy distribution (four approximators). For HP turbine degradation, all of the approximators were seen to fit well with the Johnson SU distribution. For the LP turbine degradation, seven out of nine

approximators were found to fit well with the Johnson SU distribution while the other two approximators were found to fit well with the Cauchy and Hypersecant distribution.

Appendix Q also shows that for compressor degradation, eight out of ten approximators are able to provide a 0.89 to 0.97 probability of obtaining a prediction error within -1 to 1%. The probability increases significantly then where six out of ten approximators are able to produce a probability of 0.97 to 0.99 in producing the prediction error between -2 to 2%. It was also found that all approximators were able to produce a 0.98 probability of producing the prediction error between -5 to 5%.

The probabilistic analysis of the compressor degradation in general is found to be in agreement with the sample distribution analysis given in Appendix P, especially at the higher error range. This can be clearly seen when the magnitude of the deviations between the percentage of samples and the probability of achieving prediction error within the range are calculated, as shown in Table 7-47. From the table it can be seen that the deviations in the majority of the magnitude and altitude levels across the error range are small.

Table 7-47: Deviation magnitude between the sample distribution and probabilistic analyses for compressor degradation

	LL1	LL2	LL3	LL4	ML1	ML2	ML3	HL1	HL2	HL3
Error Level	**Deviation in percentage between the sample distribution and the probability (%)**									
T1	2.24	0.32	0.20	5.38	6.19	5.94	0.51	6.21	2.67	0.40
T2	0.74	1.21	3.76	0.44	4.57	4.27	0.01	0.31	3.17	0.25
T3	0.29	0.94	3.23	0.15	3.02	3.31	0.08	0.72	1.56	0.18
T4	0.11	0.69	2.70	0.19	2.37	2.57	0.03	0.14	1.82	0.07
T5	0.03	0.30	1.02	0.10	1.93	2.07	0.01	0.02	1.77	0.03
T6	0.09	0.15	1.99	0.15	1.76	1.82	0.00	0.16	1.62	0.03

The higher deviations at some magnitude and altitude levels, as shown in Table 7-47, occur when the difference between the empirical (using sample data) and the theoretical (fitted model) probability is significant. Taking LL4 for example, when the difference between the empirical and the fitted model probability is plotted against the error range, as given in Figure 7-27, the 5.38% deviation occurring at error range T1 coincides with the peaking occurring at the plotting of the same error range.

For HP turbine degradation, Appendix Q indicates that six out of nine approximators were able to produce a probability of 0.9 to 0.99 at error range -1 to 1%. Similar to compressor degradation, the probability increases significantly where seven out of nine approximators were able to produce prediction errors with a probability of

0.98 to 0.999 at error range -2 to 2%. Moreover, it can be seen that all of the approximators were able to produce a 0.99 probability of getting a prediction error between -3 to 3%.

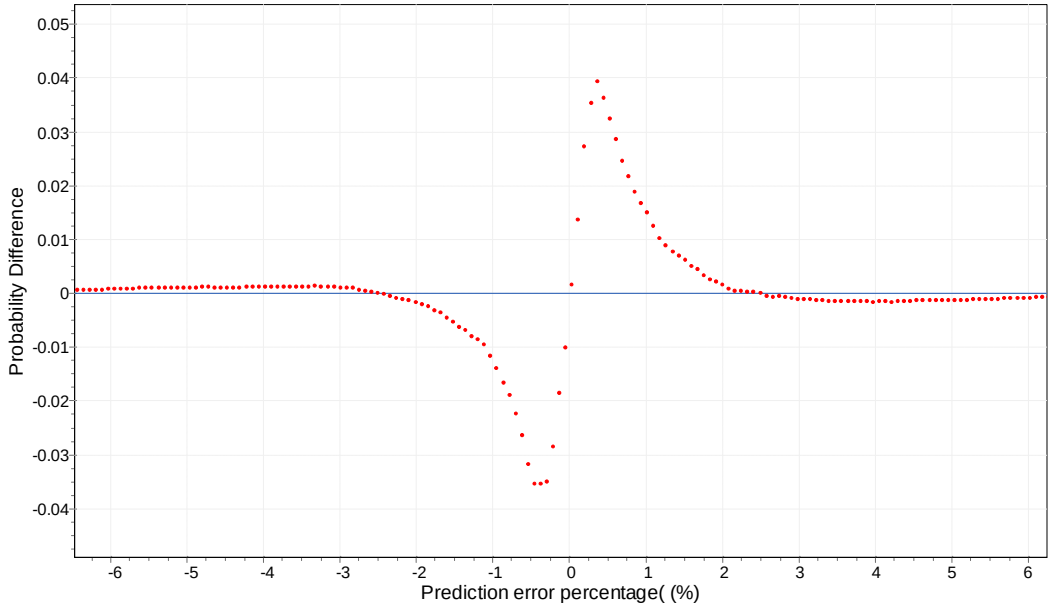

Figure 7-27: Probability difference between empirical data and the fitted model at LL4

From the calculated magnitude of the deviations between the sample distribution analysis and the probabilistic analysis given in Table 7-48, it can be seen that the probabilistic results are in agreement with the sample distribution analysis since the deviations between them are small.

Based on Appendix Q, it can be seen that for LP turbine degradation, six out of nine approximators are able to produce a probability of 0.88 to 0.99 at error range -1 to -1%. In addition, eight out of nine approximators are able to produce a 0.99 or higher probability of getting a prediction error between -3 to 3%.

Table 7-48: Deviation magnitude between the sample distribution and probabilistic analyses for HP turbine degradation

	LL1	LL2	LL3	ML1	ML2	ML3	HL1	HL2	HL3
Error Level	**Deviation in percentage between the sample distribution and the probability (%)**								
T1	1.61	2.69	3.69	0.66	0.16	0.43	0.64	0.83	0.69
T2	0.59	0.20	1.48	0.29	0.03	0.14	0.29	0.49	0.12
T3	0.21	0.24	0.26	0.22	0.02	0.03	0.26	0.22	0.01
T4	0.08	0.32	0.22	0.09	0.03	0.03	0.11	0.16	0.00
T5	0.08	0.23	0.13	0.00	0.02	0.01	0.04	0.05	0.00
T6	0.01	0.11	0.13	0.02	0.00	0.01	0.03	0.03	0.00

From the deviations between the sample distribution analysis and the probabilistic analysis given in Table 7-49, it can be seen that the values of deviation are small across the error ranges, suggesting that good agreement is achieved between the two analyses.

Table 7-49: Deviation magnitude between the sample distribution and probabilistic analyses for LP turbine degradation

	LL1	LL2	LL3	ML1	ML2	ML3	HL1	HL2	HL3
Error Level	**Deviation in percentage between the sample distribution and the probability (%)**								
T1	0.18	2.51	6.12	0.54	2.09	0.47	0.10	0.80	0.38
T2	0.02	0.01	4.25	0.16	0.25	0.33	0.04	0.10	0.21
T3	0.07	0.12	3.13	0.07	0.11	0.10	0.00	0.00	0.02
T4	0.04	0.32	2.56	0.04	0.18	0.06	0.00	0.07	0.01
T5	0.01	0.24	2.18	0.02	0.20	0.05	0.00	0.00	0.01
T6	0.01	0.15	1.67	0.01	0.15	0.04	0.00	0.00	0.00

7.4.1.6 Assessment of the Performance of the Network on a Given Mission Profile

Mission profiles of the three cases of component degradation specified in Section 6.5 were used as inputs to the implemented component degradation architectures. For all the cases of degradation, the mission operating conditions, together with the known health parameters, were inputted into the architectures before the predicted creep lives were estimated. Similar to the clean engine case, using the same reference conditions as specified in the previous chapter (refer to Section 6.3) CF, LF, LF_M and CF_M were then calculated.

Appendix DD.1 compares the plots of the CFs produced by the implemented component degradation architectures with the integrated model. From the figures it can be seen that for all of the degradation cases, the plots of the CFs of both model and architecture are overlapping each other, demonstrating the capability of FB architecture to produce accurate predictions of creep lives, thus minimising the accumulated effects of error prediction for the given mission profiles. This can be clearly seen in Table 7-50 where the prediction errors of both LF_M and CF_M are between -0.3 to 0.3%.

By comparing the errors produced by different degradation cases, it can be seen from Table 7-50 that the compressor degradation case was better predicted, compared to the other two cases, with errors that are three and four times lower than the HP and LP turbine degradation cases respectively.

Table 7-50: LF_M and CF_M produced by the integrated model and component degradation neural architectures

Degradation Case		LF_M	CF_M
Compressor	Model	8.35E-05	0.708
	Architecture	8.36E-05	0.707
	Error (%)	-0.064	0.064
HP turbine	Model	7.82E-05	0.756
	Architecture	7.84E-05	0.754
	Error (%)	-0.213	0.213
LP turbine	Model	6.18E-05	0.957
	Architecture	6.20E-05	0.954
	Error (%)	-0.284	0.283

7.4.2 Implementation of SB Architecture

In this section the implementation of the proposed SB neural Creep Life architectures on the selected engine model at degraded engine condition is presented.

7.4.2.1 Design Considerations and Realisation

The implementation of the architectures follows the same operational ranges specified in Table 7-42. Similarly, only single component degradation, with the ranges given in Table 7-43, is considered in the implementation.

The SB architecture serves the condition where the information regarding the health status of the engine model is unknown prior to the estimation of the blade's creep life. For this reason, the architecture was designed so that prior to the estimation of the blade's creep life, the health status of the engine was determined by means of the Component Health Classifiers which will classify the input pattern into the clean engine case (Class 1), compressor degradation case (Class 2), HP turbine erosion case (Class 3) and LP turbine erosion case (Class 4).

For this implemented architecture, three altitude levels were specified:

a. Level 1: 0 to 1500m,
b. Level 2: 1500m < Altitude ≤ 3000m
c. Level 3: 3000m < Altitude ≤ 4500m.

In addition, for each altitude level, the degradation was divided into three levels:

a. Low level (LL): < 2% degradation,
b. Medium level (ML): 2% to 4% degradation
c. High level (HL): <4% to 6% degradation.

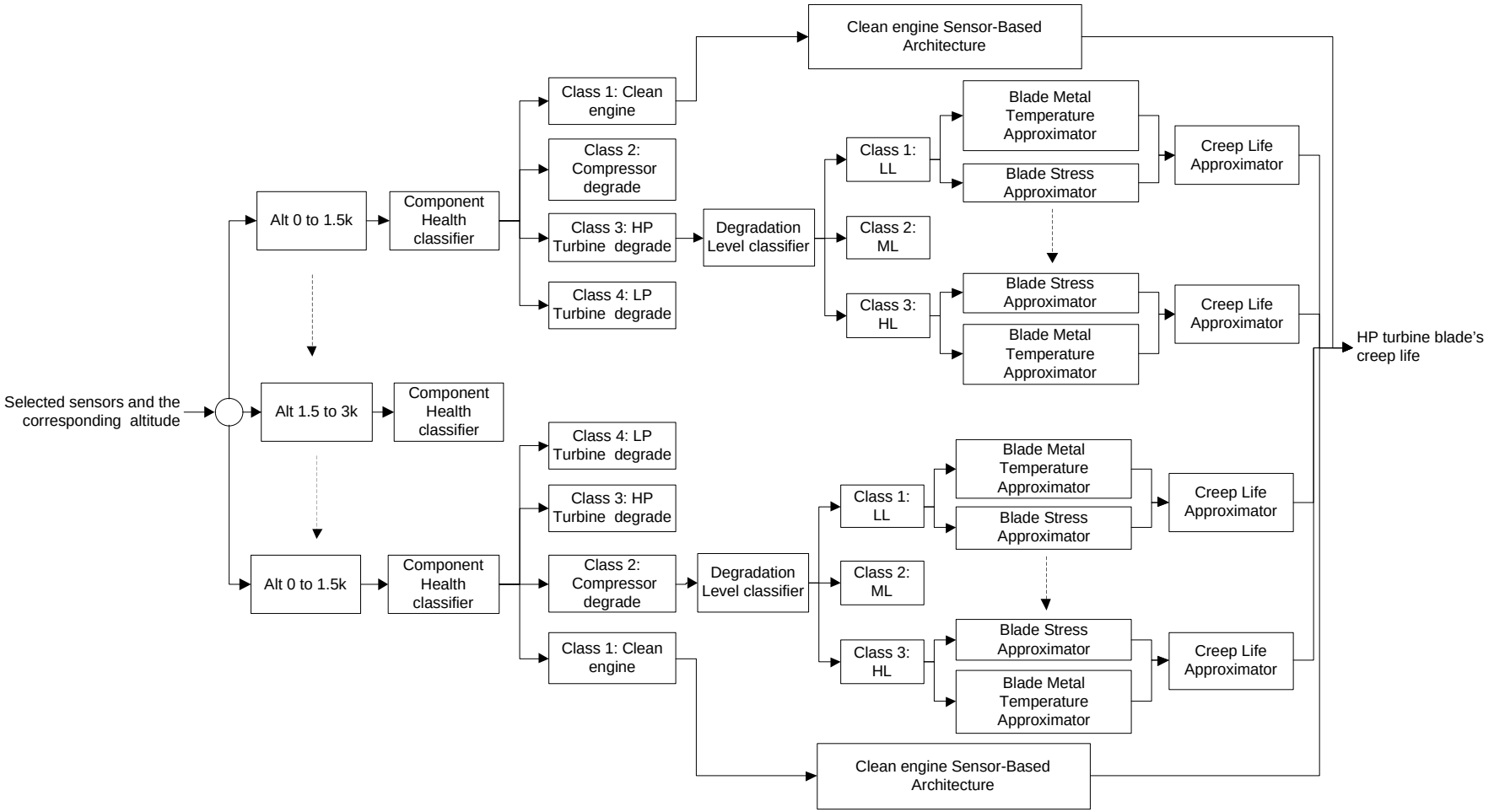

Figure 7-28: Implemented FB Architecture

The tags used for the combined altitude and degradation levels are given in Table 7-51.

Since the degradation is divided into several levels, Degradation Level Classifiers were used in the implemented architecture to classify the input pattern into LL (Class 1), ML (Class 2), and HL (Class 3). Once the input had been classified, the respective outputs were predicted using the approximators.

Table 7-51: Tags used for the combined altitude and degradation levels

Tag	Altitude level	Magnitude level
LL1	Level 1	LL
ML1	Level 1	ML
HL1	Level 1	HL
LL2	Level 2	LL
ML2	Level 2	ML
HL2	Level 2	HL
LL3	Level 3	LL
ML3	Level 3	ML
HL3	Level 3	HL

Figure 7-28 depicts the implemented SB. From the figure it can be seen that measurements from the selected sensor and corresponding altitude were used as inputs to the architecture. Based on the corresponding altitude, the measurements were inputted into the Component Health classifiers where the engine health status will then be identified.

If clean engine status is identified, than the measurements will be inputted into the previously developed clean engine SB architecture (reported in Section 7.3.3). On the other hand, if degraded engine status is identified, the measurements will be inputted into the Degradation Level classifier before the measurements are inputted into the respective intermediate and output approximators.

Two sets of sensors were used as inputs to the classifiers and approximators as shown in Table 7-52. During the initial stage of implementation, Altitude Level 1 with low level degradation (LL1) classifiers and approximators for both HP and LP turbines' degradation were first developed using the first set of sensors. However, during the development of the compressor degradation LL1 classifier, the efficiency of the classifier was found to be significantly low with 85% correct classification (HP and LP turbine classifiers have around 98% efficiency). As a result, two additional sensors (P2 and T2) were included to form the second set of measurements. From that instant, the second set of measurements was applied to the rest of the approximators and classifiers. It is worth noting that both P2 and T2 are the available engine test rig

measurements obtained from the engine manufacturer during the course of the research.

Table 7-52: Sets of measurements for the approximators and classifiers.

Set	Sensors	Approximators Involved	Classifiers Involved
1	Compressor outlet pressure (P3) Compressor outlet temperature (T3) Power turbine inlet pressure (P12) Power turbine inlet temperature (T12) Power turbine outlet pressure (P13) Power turbine outlet temperature (T13) Fuel flow (FF) Shaft power (SP)	HP and LP turbines LL1 approximators which includes: • the Blade Metal Temperature approximator • the Blade Stress approximators	HP and LP turbines LL1 Degradation Level Classifiers
2	Compressor inlet pressure (P2) Compressor inlet temperature (T2) Compressor outlet pressure (P3) Compressor outlet temperature (T3) Power turbine inlet pressure (P12) Power turbine inlet temperature (T12) Power turbine outlet pressure (P13) Power turbine outlet temperature (T13) Fuel flow (FF) Shaft power (SP)	All of the other approximators except for Creep Life approximators	All of the other Classifiers which includes: • Degradation Level Classifier • Component Health Classifier

7.4.2.2 Number of Samples to Train the Approximators and Classifiers

Samples used to train the previously implemented FB Architecture were taken as the samples to train the SB Architecture approximators. Again, the extraction of the information is easy as each sample simulated using the Integrated Creep Life Estimation model also contains all of the measurements needed for this architecture.

Not all the samples generated for the FB architecture were used. Since for compressor degradation, four levels LL1 to LL4 were specified in the previous architecture, the samples used to train the approximators for compressor degradation LL1, LL2 and LL3 of the SB architecture were generated. In addition, since no classifiers were used in the previous architecture, all the samples used to train the classifiers were also generated.

Appendix S provides the step sizes used for each input and the final amount of generated samples. Similar to the FB architecture, the step sizes for ETA and FC given in Appendix S were not fixed. Also 60% of the finalised samples were used as training samples, 20% were used for validation samples and the other 20% as test samples.

As shown in Appendix S.1, around 27,000 to 29,000 samples were used to train the compressor degradation approximators. The amount of samples increased as the Degradation Level classifiers were trained which used around 34,000 samples as shown in Appendix S.2. This was necessary as the classifiers require measurement patterns from all of the three degradation levels (LL, ML and HL). Similarly, the amount of samples needed to train the Component Health classifiers is larger than the Degradation Level classifiers averaging around 43,000 samples. This was again expected as the classifiers require measurement patterns not only from different levels of degradation magnitude but also from different component degradation.

7.4.2.3 Training of the Approximators and Classifiers

For all of the component degradations, the final sizes of the trained approximators and classifiers at different altitude levels are given in Appendices T.1 and T.2 respectively. From both appendices, it can be seen that all of the trained approximators and classifiers were constructed using two hidden layers. For the approximators, it was found that the Blade Metal Temperature approximators required more hidden neurons in order to obtain the final optimal solution. Note also that most of the Creep Life approximators given in Appendix T.1 were taken from the previous FB architecture, except for compressor degradation at LL1, LL2 and LL3. This is again because of the different levels of altitude that were being specified in the previous architectures which were LL1 to LL4.

Appendix U provides the final $MSEs$ and Rs for each approximator of the compressor, HP and LP turbines' degradations at different Altitude Levels. From the appendix it was found that all of the approximators were able to produce low $MSEs$ indicating small errors between the normalised predicted and targeted outputs. In addition, the magnitude of the $MSEs$ between the training, validation and test samples were similar, suggesting that good generalisation had been achieved during the training for all of the approximators. Also the R values given in the appendices suggest that high correlation between the predicted and targeted outputs was obtained.

7.4.2.4 Assessment of the Performance of the Networks Using the Populated Samples

Appendix V summarises the E_{Ave} and SD_E at different altitude levels. Note that the E_{Ave} and SD_E of the prediction errors for most of the Creep Life Approximators were not included in the tables except for the compressor degradation LL1, LL2 and LL3. This is

because most of the Creep Life Approximators were taken from the previous FB architecture.

From the appendix it can be seen that for all of the trained approximators, the E_{Ave} values are very close to zero and the SD_E calculated are very small. However, if the two intermediate approximators (Blade Metal Temperature and Blade Stress Approximators) are compared, it is found that despite having similar E_{Ave}, for compressor degradation, the lowest overall variation of E is being produced by the Blade Metal Temperature Approximator, while for both the HP and LP turbine degradations it is the Blade Stress Approximators.

In order to assess the performance of the cascaded system, the predicted blade's metal temperatures and stresses produced by the corresponding approximators were inputted into the Creep Life Approximator hence the E_{Ave} and SD_E were recalculated. Table 7-53 provides the recalculated values of both E_{Ave} and SD_E for the component degradations at different degradation and altitude levels.

By comparing the initially calculated E_{Ave} and SD_E of the Creep Life Approximators (for compressor degradation LL1 to LL3, refer to Appendix V and for the rest of the approximators, refer to Appendix M), it can be seen that both the E_{Ave} and SD_E have increased significantly. This again is due to the effect of error propagating from the intermediate networks to the Creep Life Approximators.

Table 7-53: The blade's creep life E_{Ave} and SD_E produced by the Creep Life Approximator

	Compressor degradation		HP turbine degradation		LP turbine degradation	
Level	E_{Ave}(%)	SD_E(%)	E_{Ave}(%)	SD_E(%)	E_{Ave}(%)	SD_E(%)
LL1	-0.00252	0.17506	-0.00192	0.2116	-0.00055	0.15091
LL2	0.00402	0.25564	0.00113	0.1444	0.000744	0.14338
LL3	0.00203	0.17997	-0.00161	0.14946	0.00944	0.14852
ML1	-0.01139	0.21801	0.000273	0.16789	-0.00011	0.02067
ML2	0.000123	0.22776	-0.00065	0.14214	-0.00125	0.14238
ML3	0.00525	0.16963	0.00435	0.14712	-0.0002	0.14875
HL1	0.00184	0.14121	-0.00057	0.15287	-0.00034	0.14394
HL2	-0.00167	0.20491	-0.00283	0.28602	-0.00017	0.14043
HL3	0.000165	0.25611	-0.00388	0.15725	-0.00075	0.14614

Although significant increases were seen in both the E_{Ave} and SD_E, the increases in E_{Ave} are not crucial since they are still near to zero. However, the increases in SD_E due to the error propagation become important as they can dictate the final predicted outputs since the variation of the error has becoming higher. Table 7-54 compares the initially calculated SD_E (extracted from Appendix V for compressor

degradation LL1, LL2 and LL3; and from Appendix M for the rest of the approximators) and the recalculated SD_E (from Table 7-53) together with the ratio between the recalculated and the initially calculated SD_E. It can be clearly seen that the increase in SD_E varies considerably between each approximator ranging between 1.0088 to 42.69 times the initial values. Although the increase of the SD_E is large, the values are still within an acceptable level with the highest recorded SD_E being 0.286%.

Table 7-54: Comparisons between the initial and the recalculated SD_E

	Compressor degradation			HP turbine degradation			LP turbine degradation		
Level	Initial SD_E	SD_E	Ratio	Initial SD_E	SD_E	Ratio	Initial SD_E	SD_E	Ratio
LL1	0.015	0.175	11.812	0.043	0.212	4.921	0.016	0.151	9.432
LL2	0.090	0.256	2.837	0.025	0.144	5.776	0.020	0.143	7.169
LL3	0.012	0.180	15.568	0.006	0.149	24.910	0.005	0.149	29.704
ML1	0.052	0.218	4.193	0.048	0.168	3.498	0.019	0.021	1.088
ML2	0.024	0.228	9.490	0.014	0.142	10.153	0.022	0.142	6.472
ML3	0.011	0.170	15.421	0.015	0.147	9.808	0.012	0.149	12.396
HL1	0.036	0.141	3.923	0.020	0.153	7.644	0.032	0.144	4.498
HL2	0.020	0.205	10.246	0.249	0.286	1.149	0.017	0.140	8.261
HL3	0.006	0.256	42.685	0.055	0.157	2.859	0.013	0.146	11.242

Using the error range specified in Table 7-55, the percentage of samples able to produce E within the specified range for the case of compressor, and HP and LP turbine degradation are given in Appendix W. From the appendix, several observations can be made. All the output approximators were found to be able to produce high prediction accuracy at lower error range. This can be clearly seen as high percentages of samples possessed low prediction error. For compressor degradation approximators, on average, 97% of the samples were able to have E within -0.4 to 0.4%. Improvements in the approximators' performance were witnessed afterwards with 99% of the samples on average able to have E within -0.8 to 0.8%.

Table 7-55: Error ranges used to assess the performance of the trained networks

Error Range	Description
T0.2	$-0.2\% \leq E \leq 0.2\%$
T0.4	$-0.4\% \leq E \leq 0.4\%$
T0.6	$-0.6\% \leq E \leq 0.6\%$
T0.8	$-0.8\% \leq E \leq 0.8\%$
T1	$-1\% \leq E \leq 1\%$
T2	$-2\% \leq E \leq 2\%$
T3	$-3\% \leq E \leq 3\%$
T4	$-4\% \leq E \leq 4\%$
T5	$-5\% \leq E \leq 5\%$
T6	$-6\% \leq E \leq 6\%$

Better average performances are seen in HP turbine degradation approximators where on average, 98.76% of the samples are able to produce E within -0.4 to 0.4% while 99.71% of the samples on average were able to have E within the next error range.

LP turbine degradation approximators have the best average performance compared with the two other component degradation approximators where at error range T0.4, 99.86% of the samples were able to produce E within the given range while almost all of the samples were able to produce E within -0.6 to 0.6%.

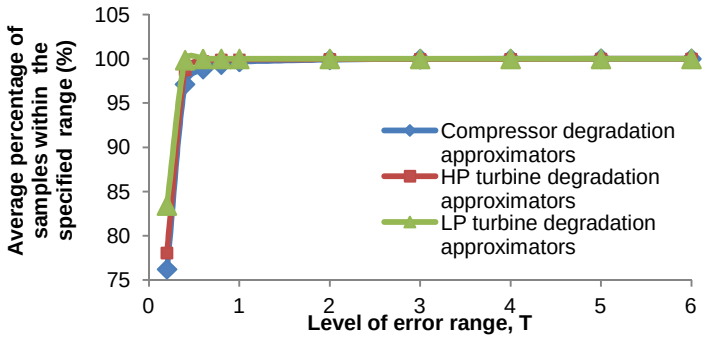

Figure 7-29: Average sample distributions at different error range

Figure 7-29 provides the comparison of average sample distributions at different error range. It can be clearly seen that the LP turbine degradation architecture has the best trained approximators, followed by HP turbine degradation approximators and compressor degradation approximators.

The performances of the trained classifiers were also evaluated by observing the classification accuracy via the confusion matrices of the training, validation and test samples of each component degradation classifier. The confusion matrices of the Degradation Level Classifiers of the three component degradations at different altitude levels are given in Appendices X.1 to X.9. Also the confusion matrices of the Component Health Classifiers at different altitude levels are given in Appendices X.10 to X.12. The overall classification accuracies for the training, validation and test samples (given in Appendices X.1 to X.12) are summarised in Table 7-56.

From the table it can be seen that the overall classification accuracies of all the trained classifiers are high with the lowest accuracy of 99.5% given by the HP turbine Degradation Level Classifier at altitude level 1. In addition, it can be seen that all of the compressor degradation classifiers were able to produce 100% correct classification overall. This shows that the additional two measurements P2 and T2 are able to significantly improve the classifying ability. This can be clearly seen as the training

samples' confusion matrix of the compressor degradation level classifier at altitude level 1 using the first set of measurements (as listed in Table 7-52) is given in Figure 7-30. By comparing the overall classification accuracies between the three samples, it can be clearly seen from the table that all of the samples have similar accuracies indicating good generalisations have been achieved during the training of the classifiers.

Table 7-56: Overall classification accuracy of the trained classifiers

Component Degradation	Classifier	Altitude Level	Classification Accuracy (%)		
			Training Samples	Validation Samples	Test Samples
Compressor	Degradation level	Level 1	100	100	100
		Level 2	100	100	100
		Level 3	100	100	100
HP turbine	Degradation level	Level 1	99.6	99.5	99.5
		Level 2	100	99.9	99.9
		Level 3	99.9	99.7	99.8
LP turbine	Degradation level	Level 1	100	100	100
		Level 2	100	99.9	99.9
		Level 3	100	100	100
	Component Health	Level 1	99.9	99.9	99.9
		Level 2	99.9	99.8	99.9
		Level 3	99.9	99.8	99.8

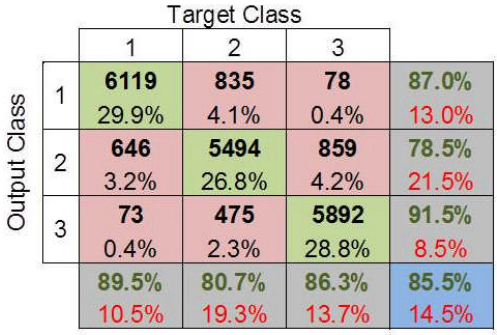

Figure 7-30: Confusion matrix of the compressor degradation level classifier using 1st set of measurements

7.4.2.5 Assessment of Performance of the Network Using Unseen Post Test Samples

To validate the generalisation of the output approximators, two sets of unseen samples generated during the post test of the FB architectures were utilised. However, for compressor degradation, two new sets of unseen samples were generated for levels LL1, LL2, and LL3. The new sets were randomly divided from a pool of samples,

generated using the step sizes given in Appendix Y.1. In addition, new unseen samples were also generated to validate the Degradation Level Classifiers and the Component Health Classifiers. The step size of each parameter and the finalised samples used to test the corresponding classifiers are given in Appendices Y.2 and Y.3 respectively.

From the appendices it can be seen that around 26,000 new samples were generated to validate the compressor degradation approximators. Also around 29,000 samples were generated for each Degradation Level Classifier and around 177,000 to 210,000 samples were used to test the Component Health Classifiers.

Using the same prediction error range specified in Table 7-55, the percentages of unseen samples able to produce a predicted creep life with E within the specified range were independently counted. The plots of the results are given in Appendix Z. From the appendix, it can be seen that the plots of both unseen data for the three component degradation approximators were seen to be overlapping each other hence validating that good generalisations have been achieved during the training.

Figure 7-31 depicts the average sample distributions at different error range of one of the set of unseen samples predicted by the three component degradation approximators. Several observations were made. When unseen samples were inputted into the approximators, both the HP and LP turbine degradation approximators were able to retain the ability to produce good prediction. However, when the sample distributions of both the HP and LP turbines were compared with the distributions obtained during the training of the approximators (Figure 7-29), the HP turbine approximators produced similar sample distributions as opposed to the LP turbine approximators that experienced slight drops at error range T0.8 and below. Further investigation (refer to Appendix Z.3 (a), (d), and (g)) revealed that the slight drops were contributed by the approximators at LL1, ML1, and HL1. As a result, HP turbine degradation is seen to have better approximators compared to LP turbine degradation.

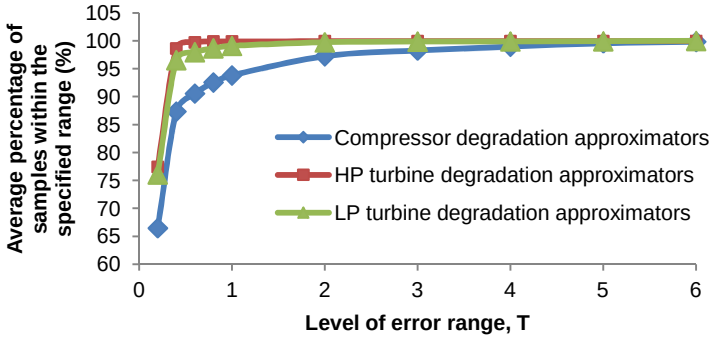

Figure 7-31: Average sample distributions at different error range of one set of unseen data

Although good prediction accuracies were achieved during the training of the compressor degradation approximators, it can be seen from Figure 7-31 that the prediction accuracies of the approximators reduced substantially at lower parts of the error range. This can be clearly seen when both average sample distributions during the training and post test are compared in Figure 7-32. The figure shows that at error range of T2 and below, the deviations between the training and the post test sample distributions are relatively large. However, after error range T2, the deviation reduced significantly with the highest deviation found to be around 2% at T2.

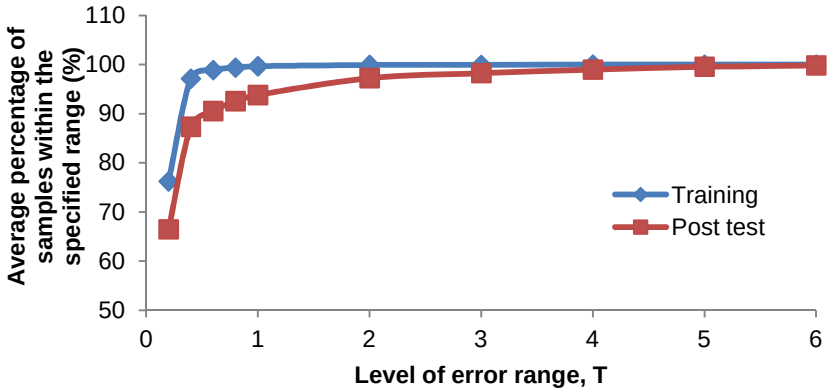

Figure 7-32: Average sample distributions of compressor degradation approximators during training and post test

Figure 7-31 also shows that for compressor degradation, on average, 90% of the samples were able to have E within -0.6 to 0.6%. Significant improvements were seen afterwards as 97% of the samples were able to have E within -2 to 2% before achieving 99% at E within -4 to 4%.

As for HP turbine degradation approximators, since the performance of the approximators were retained, it can be seen that averagely, 98.76% of the samples were able to produce E within -0.4 to 0.4% while 99.71% of the samples were able to have E within the next error range.

Since the performance of the LP turbine degradation approximators dropped slightly, it was found that at error range T0.4, 97% of the samples were able to produce E within the given range while 99% of all the samples were able to produce E within -1 to 1%.

The summary of the results of the third stage assessment is given in Appendix AA and the plots of individual PDF and CDF are given in Appendix BB. From the summarised results, several observations can be made. The best fitted distribution for most of the compressor degradation approximators is Cauchy distribution (seven

approximators) while the other two approximators are Johnson SU (one approximator) and Hypersecant (one approximator). Looking at HP turbine degradation, the majority of the approximators (eight approximators) are best fitted with Normal distribution while only one is best fitted with Cauchy distribution. For the LP turbine, six out of nine approximators are found to be best fitted with Normal distribution, followed by Cauchy distribution (two approximators) and Johnson SU distribution (one approximator).

For compressor degradation it can be seen that seven out of nine approximators are able to provide 0.85 to 0.97 probability of obtaining prediction error within -0.6 to 0.6%. The probability increases as the error range is widened, where eight out of nine approximators are able to produce 0.95 to 0.99 probabilities in obtaining the error between -2 to 2%. Further at T4, eight out of nine approximators have around 0.98 to 1 probability of obtaining E within -4 to 4%.

Table 7-57 provides the percentage deviation between the sample distribution (Appendix Z.1) and the probabilistic analyses (Appendix AA) for compressor degradation approximators. From the table it can be seen that the probabilistic analysis conducted on the compressor degradation is in good agreement at error range T1 and higher as the deviations at that range are found to be small. However, at the lower error range, the deviations between the two analyses are relatively high indicating that at the lower range, the chosen distribution models are unable to fit well with the empirical unseen samples. This can be clearly seen when the difference between the empirical and the fitted model probability for HL1 is plotted against the error range as given in Figure 7-33. The peaking of the plot occurring between -1 to 1% shows that at that interval, poor fitting happens, thus increasing the deviations between the sample distribution and the probabilistic analyses.

Table 7-57: Deviation magnitude between the sample distribution and probabilistic analyses for compressor degradation

	LL1	LL2	LL3	ML1	ML2	ML3	HL1	HL2	HL3
Error Level	**Deviation in percentage between the sample distribution and the probability (%)**								
T0.2	5.0	3.1	2.6	2.2	7.2	3.2	11.0	10.0	2.4
T0.4	5.4	8.9	0.3	4.6	13.5	8.2	12.6	6.1	5.7
T0.6	1.5	6.2	4.5	0.9	9.5	5.4	8.0	0.9	2.9
T0.8	1.0	4.7	5.4	0.3	7.5	4.9	5.2	0.3	1.3
T1	0.4	3.7	5.4	1.0	6.1	3.6	4.3	0.5	0.9
T2	0.1	4.1	3.5	1.2	3.2	2.7	0.8	0.2	0.3
T3	0.0	1.7	3.3	2.5	2.2	2.5	1.9	0.0	0.6
T4	0.0	1.6	1.6	2.4	1.7	1.9	1.1	0.0	0.5
T5	0.0	1.6	1.2	1.9	1.4	1.7	1.0	0.0	0.5
T6	0.0	1.4	1.9	1.6	1.2	1.0	0.8	0.0	0.1

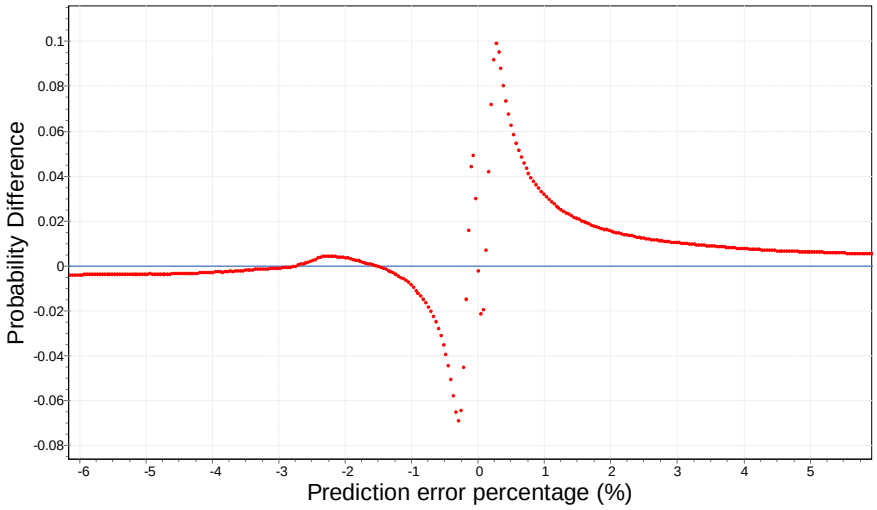

Figure 7-33: Probability difference between empirical data and the fitted model at HL1

For HP turbine degradation, Appendix AA indicates that seven out of nine approximators were able to produce a probability of 0.98 to 0.99 at error range -0.4 to 0.4%. As the error ranges are widened, the probability increases as well, where eight out of nine approximators are able to produce a 0.99 to 1.0 probability of obtaining the error between -0.6 to 0.6%. Further, at T0.8, eight out of nine approximators have a 1.0 probability of obtaining E within -0.8 to 0.8%.

Table 7-58: Deviation magnitude between the sample distribution and probabilistic analyses for HP turbine degradation

	LL1	LL2	LL4	ML1	ML2	ML3	HL1	HL2	HL3
Error Level	**Deviation in percentage between the sample distribution and the probability (%)**								
T0.2	0.5	1.6	1.8	1.3	1.2	1.5	0.6	13.6	1.7
T0.4	0.0	0.6	0.7	0.3	0.5	0.8	0.0	12.0	0.7
T0.6	0.2	0.0	0.0	0.3	0.0	0.0	0.2	7.7	0.0
T0.8	0.0	0.0	0.0	0.0	0.0	0.0	0.1	2.1	0.0
T1	0.0	0.0	0.0	0.0	0.0	0.0	0.0	0.7	0.0
T2	0.0	0.0	0.0	0.0	0.0	0.0	0.0	0.4	0.0
T3	0.0	0.0	0.0	0.0	0.0	0.0	0.0	0.3	0.0
T4	0.0	0.0	0.0	0.0	0.0	0.0	0.0	0.2	0.0
T5	0.0	0.0	0.0	0.0	0.0	0.0	0.0	0.1	0.0
T6	0.0	0.0	0.0	0.0	0.0	0.0	0.0	0.0	0.0

From the calculated magnitude of the deviations between the sample distribution analysis and the probabilistic analysis given in Table 7-58, it can be seen that good agreements are achieved between the two analyses in the majority of the

approximators. However, for approximator HL2, good agreement is achieved at error range T0.8 and above. Similarly the high deviations at the lower error range are caused by poor fitting between the empirical data and the chosen distribution model at that particular range.

Appendix AA also shows that for the LP turbine degradation, seven out of nine approximators were able to produce a 0.98 to 1.0 probability at error range -0.8 to 0.8%. The probability increase afterwards where seven out of nine approximators are able to produce 1.0 probability at error range T2.0.

When the percentage deviation between the sample distribution and the probabilistic analyses were measured, as provided in Table 7-59, it was found that good agreement was achieved between the two analyses. Despite that, approximators at LL1 and HL1 depict relatively higher deviations compared to the other approximators at the lower end of the error range before reducing to less than 4% at error range T2.

Validation of the generalisations of the classifier was done by observing the classification accuracy via the confusion matrices of the two unseen samples. Both of the matrices are given in Appendix CC. However, the summary of the overall classification accuracies is given in Table 7-60.

Table 7-59: Deviation magnitude between the sample distribution and probabilistic analyses for LP turbine degradation

	LL1	LL2	LL4	ML1	ML2	ML3	HL1	HL2	HL3
Error Level	**Deviation in percentage between the sample distribution and the probability (%)**								
T0.2	1.7	1.8	1.6	3.7	1.1	1.1	8.4	0.8	1.2
T0.4	6.7	0.7	0.8	2.5	0.6	0.9	13.7	0.5	0.6
T0.6	5.9	0.0	0.0	0.4	0.0	0.0	8.7	0.0	0.0
T0.8	6.9	0.0	0.0	1.0	0.0	0.0	7.6	0.0	0.0
T1	4.8	0.0	0.0	0.4	0.0	0.0	4.9	0.0	0.0
T2	3.4	0.0	0.0	0.0	0.0	0.0	2.6	0.0	0.0
T3	2.0	0.0	0.0	0.0	0.0	0.0	2.3	0.0	0.0
T4	1.4	0.0	0.0	0.0	0.0	0.0	1.8	0.0	0.0
T5	1.3	0.0	0.0	0.0	0.0	0.0	1.4	0.0	0.0
T6	1.5	0.0	0.0	0.0	0.0	0.0	1.2	0.0	0.0

From Table 7-60, it can be seen that the classification accuracy between the two sets of unseen samples were similar with small deviations, hence validating the generalisation of the trained classifiers. If the classification accuracies of the first set of unseen samples (Table 7-60) are compared with the accuracies measured using the training samples (Table 7-56), as shown in Table 7-61, the absolute percentage deviations are small, averaging at 1% deviation. This suggests that the classification

accuracy can still retain its ability to produce good classification, despite having a large size of unseen samples being inputted into the classifiers.

Table 7-60: Overall classification accuracy of the trained classifiers using sets of unseen samples

Component Degradation	Classifier	Altitude Level	Classification Accuracy (%)	
			First set unseen samples	Second set unseen samples
Compressor	Degradation level	Level 1	99.5	99.6
		Level 2	98.5	98.3
		Level 3	97.5	97.3
HP turbine	Degradation level	Level 1	98.7	98.4
		Level 2	98.9	98.8
		Level 3	99	99.3
LP turbine	Degradation level	Level 1	98.8	98.9
		Level 2	98.2	98.3
		Level 3	98.5	98.7
	Component Health	Level 1	99.8	99.8
		Level 2	99.7	99.7
		Level 3	99.7	99.7

Table 7-61: Comparison of classification accuracy between the training samples and the first set of unseen samples

Component Degradation	Classifier	Altitude Level	Classification Accuracy (%)		Absolute Deviation (%)
			Training samples	First set unseen samples	
Compressor	Degradation level	Level 1	100	99.5	0.5
		Level 2	100	98.5	1.5
		Level 3	100	97.5	2.5
HP turbine	Degradation level	Level 1	99.6	98.7	0.9
		Level 2	100	98.9	1.1
		Level 3	99.9	99	0.9
LP turbine	Degradation level	Level 1	100	98.8	1.2
		Level 2	100	98.2	1.8
		Level 3	100	98.5	1.5
	Component Health	Level 1	99.9	99.8	0.1
		Level 2	99.9	99.7	0.2
		Level 3	99.9	99.7	0.2
				Average	1.03

The effects of the misclassification on the prediction accuracy given by incorrect Degradation Level approximators are shown in Table 7-62. From the table it can be seen that although incorrect approximators were used to estimate the blade's creep life, the prediction errors were still at the acceptable level with small E_{Ave} and SD_E.

From the table, it was found that if misclassified inputs were inputted into any of the HP and LP turbine approximators, the prediction error would still be acceptable with maximum and minimum errors seen to be around 2.3% and -2%. However, if the misclassified inputs were inputted into any of the compressor degradation approximators, prediction errors depicted in the table will be relatively higher with the maximum and minimum errors reaching 7% and -9% respectively.

Table 7-62: Summary of the prediction using misclassified Degradation Level approximators

Component Degradation	Altitude Level	E_{Ave}(%)	SD_E (%)	Max error (%)	Min error (%)
Compressor	Level 1	-0.68	1.73	0.33	-8.96
	Level 2	-1.7	2.5	1.3	-8.5
	Level 3	-0.2	2.0	7.1	-9.4
HP turbine	Level 1	0.03	0.25	2.31	-0.95
	Level 2	-0.01	0.14	0.37	-0.33
	Level 3	0.01	0.15	0.39	-0.32
LP turbine	Level 1	0.03	0.33	1.05	-1.99
	Level 2	0.0	0.1	0.4	-0.4
	Level 3	-0.01	0.15	0.37	-0.42

7.4.2.6 Assessment of the Performance of the Network on a Given Mission Profile

Similar to the FB architectures, the three cases of component degradations' mission segment or sub-segment inputs were then inputted into the implemented SB architecture. Since two types of classifier were used, the Component Health classifiers were first utilised to isolate the component degradation. Table 7-63 provides the summary of the classification outputs for all the respective altitude levels of the component degradation cases. As shown in the table, 100% correct classification was obtained for each of the degradation cases, which exhibits the capability of the classifiers to isolate the correct component degradations.

Table 7-63: Summary of Component Health classifier outputs

Component degradation	% of correct classification	% of misclassification
Compressor	100	0
HP turbine	100	0
LP turbine	100	0

Based on the classification outputs, each mission segment was inputted into the corresponding Degradation Level classifiers and the summary of the classification

outputs is presented in Table 7-64. Similar to the previous classifiers, the Degradation Level classifiers for all the degradation cases are able to provided 100% correct classification thus proving the capability of the classifiers to provide accurate classification.

Table 7-64: Summary of Degradation Level classifier outputs

Component degradation	% of correct classification	% of misclassification
Compressor	100	0
HP turbine	100	0
LP turbine	100	0

From the classification output, the mission inputs were inputted into the respective approximators in order to obtain the blade's metal temperatures, maximum stresses and hence the blade's creep lives. Finally the CF, LF, CF_M and CF_M were calculated. Appendix DD.2 provides the plots of the CFs produced by the implemented component degradation architectures with the integrated model for the compressor, HP turbine and LP turbine degradations. Similar to the FB architecture, it can be seen from the figures that the plots of the CFs of both model and architecture for all of the degradation cases are overlapping each other suggesting that the values of creep life predicted by both model and architecture are very similar, hence demonstrating the ability to produce accurate creep lives' prediction.

The effect of error accumulation in the given mission profile creep life prediction can be observed in Table 7-65. From the table it can be seen that the errors between the architecture and the model for both LF_M and CF_M are between -0.3 to 0.3%. This suggests that if the prediction accuracy of an individual mission segment or sub-segment is high, then the effect of accumulated errors in a given mission profile would be insignificant.

Table 7-65: LF_M and CF_M produced by the integrated model and SB architecture

Degradation Case		LF_M	CF_M
Compressor	Model	8.35E-05	0.708
	Architecture	8.36E-05	0.7077
	Error (%)	-0.036	0.036
HP turbine	Model	7.82E-05	0.756
	Architecture	7.84E-05	0.754
	Error (%)	-0.267	0.2665
LP turbine	Model	6.18E-05	0.957
	Architecture	6.19E-05	0.956
	Error (%)	-0.108	0.108

Comparison of both errors (LF_M and CF_M) between the three degradation cases will reveal that the compressor degradation case was better predicted compared to the other two cases. It can be seen from Table 7-65 that the errors for predicting the compressor degradation are seven and three times lower than the HP and LP turbine degradation cases respectively.

7.4.3 Comparison Analysis between the Two Implemented Neural-Based Creep Life Estimation Architectures at Degraded Engine Condition

In this section, comparison between the FB and SB architectures will be discussed. The most obvious difference between the two architectures lies with why these architectures are supposed to be used. FB architectures were implemented for the case where prior to the creep life estimation, the engine component degradation has been isolated and the magnitudes of both health parameters have been quantified. On the other hand, the SB architecture was implemented for the case where the health status of the engine is unknown thus embedding the process of isolating the degradation within the architecture itself.

Because of different functionality, different inputs were required. FB architectures required six inputs (operating and health parameter) while for SB architecture eight to ten inputs (selected sensors) were utilised in order to train the networks. Despite using the same cascaded system, FB architectures require only approximator networks to approximate the desired outputs. However, since the engine health status is unknown, for SB architecture, classifier networks are also utilised to isolate the component degradation and also to classify different magnitudes of degradation.

To ensure accurate creep life prediction, FB architectures used 84 approximators while for SB architecture, 81 approximators and 12 classifiers were created. In addition, around 21,000 to 23,000 samples for compressor degradation and 28,000 to 30,000 samples for both turbines' degradation were populated to train each FB architecture approximator. The sizes used to train the SB architecture were found to be similar – around 27,000 to 30,000 samples for each approximator. However, additional samples were required for the SB architecture in order to train the classifiers.

Both architectures used two hidden layers in each of their approximators in order to obtain the optimised solution. Additionally, for the majority of the training, the blade's metal temperature approximators were found to require more neurons than the other approximators. Using the two-hidden-layer network, both architectures were able to possess low $MSEs$ either for their training, validation or test samples. Apart from that

both architectures possess a strong correlation between their predicted and the targeted output with R to be so close to unity.

When tested with two sets of unseen sample, both architectures were found to possess good generalisations in their approximators with both sets having the same percentage of samples able to provide E within the specified error range. Although good generalisations were obtained for both architectures, the HP turbine degradation approximators were found to be better than the other two component degradation approximators.

By using statistical distribution fitting software, it was found that the distributions of creep life prediction errors of both architectures are different. For FB architecture, the Johnson SU distribution is seen to be the most suitable for the three component degradations' approximators. On the other hand, for SB architecture, the Cauchy and Normal distributions are the two most suitable for compressor degradation and both turbines respectively.

Appendices EE.1, EE.2, and EE.3 provide the comparison of the probabilities of achieving the specified blade's creep life prediction error range between both architectures' approximators for compressor, HP and LP turbines' degradations respectively. Several observations can be made:

a. Compressor degradation approximators: From Appendix EE.1, it can be seen that at low degradation magnitude, FB approximators are more superior in producing accurate creep life prediction except for the approximator at LL1. On the other hand, at medium level degradation, SB approximators are found to be better than FB approximators except for the approximator at ML3. At high level degradation magnitude, the FB approximator is more accurate at H3 while the SB approximator is more accurate at HL2. For HL1, it can be seen that the SB approximator is better at error range lower than T2.
b. HP turbine degradation approximators: As shown in Appendix EE.2, it was found that the SB approximators are better than the FB approximators at all degradation and altitude levels.
c. LP turbine degradation approximators: It can be seen from Appendix EE.3 that at low degradation magnitude, SB approximators are better at all LL2 and LL3. However for LL1, the FB approximators become more accurate at error range higher than T1. Superiority of the SB approximators continues at medium level degradation with all approximators being more accurate than

the FB approximators. At high level degradation, again SB approximators are seen to be better than the FB approximators at HL2 and HL3.

When the results from the probabilistic analyses were compared with the sample distribution analyses, it was found that the majority of the approximators for both architectures achieved good agreement with each other. However, there was also evidence that some approximators were found to have better distribution fitting when they surpassed certain a specified error range.

The mission profile analyses of both architectures provide the same observations. Both architectures depict good prediction accuracy for each mission segment or sub-segment, thus creating overlapping plots of CFs between those predicted by both architectures and the one predicted by the Integrated Creep Life Estimation Model. Also the prediction errors of LF_M and CF_M between both architectures and the integrated model were found to be very small, hence minimising the effects of error accumulation on a given mission profile, especially the compressor degradation case.

The above comparison analysis is summarised in Table 7-66.

7.5 Chapter Conclusion

In this chapter, the implementations of the proposed neural-based creep life architectures on the developed engine model for both clean and degraded engine conditions are summarised.

The study looks at the implementation of the neural architectures for clean engine condition first before extending the work to degraded engine condition. For the clean engine condition, all of the three proposed architectures, RB, FB and SB were implemented. However for degraded engine condition, only FB and SB architectures were implemented.

Using the Integrated Life Estimation Model, samples were generated and were used to train each created approximator or classifier network. The amount of samples were determined by considering the sensitivity of each of the selected operating and health parameters obtained in Section 6.4 which were then translated into step sizes that dictate how the samples were being spaced.

For all of the networks created, MFBP neural network was used together with Levenberg-Marquardt and Conjugate-Scaled-Gradient training algorithms. As tools to initially determine the accuracy and the generalisation of the train approximators, both

MSE and R were observed during the training. Similarly, confusion matrices were used to observe both accuracy and generalisation of the trained classifiers.

Table 7-66: Summary of the comparison analyses

No	Comparison parameters	FB Architecture	SB Architecture
1	Utilisation of architecture	When status of engine health parameters are known	When status of engine health parameters are unknown
2	Type of network utilised	Approximator network only	Approximator and classifier networks
3	Number of inputs	6	8-10
4	Number of network created	84	93
5	Samples used to train each approximator:		
	Compressor degradation	21,000 to 23,000	27,000 to 28,000
	HP and LP turbines degradation	28,000 to 30,000	28,000 to 30,000
6	Size of hidden layers	2 layers	2 layers
7	MSE of each approximator:		
	Blade Metal Temperature	$\approx \times 10^{-6}$	$\approx \times 10^{-7}$
	Blade Stress	$\approx \times 10^{-7}$ to 10^{-8}	$\approx \times 10^{-6}$ (compressor) $\approx \times 10^{-8}$ (turbines)
	Creep Life	$\approx \times 10^{-12}$	$\approx \times 10^{-12}$
8	R of each approximator	$\approx\ 1$	$\approx\ 1$
9	Generalisation of the approximators	Achieved	Achieved
10	Best output approximators	HP turbine degradation	HP turbine degradation
11	Distribution of prediction errors:		
	Compressor degradation	Johnson SU distribution	Cauchy distribution
	HP turbine degradation	Johnson SU distribution	Normal distribution
	LP turbine degradation	Johnson SU distribution	Normal distribution
12	Probabilistic analysis comparison:		
	Compressor degradation	Better in LL2,LL3, LL4 Better in ML3 Better in H3 and HL1(above error range T2)	Better in LL1 Better in ML1, ML2 Better in H2 and HL1(below error range T2)
	HP turbine degradation		Better in all LLs, MLs and HLs
	LP turbine degradation	Better in LL1 for error range above T1 Better in HL1	Better in all LLs except LL1 (range below T1) Better in all MLs Better in HL2 and HL3
13	Agreement between probabilistic and sample distribution analyses:		
	Compressor degradation	Good agreement especially above error range T3	Good agreement especially above error range T2
	HP turbine degradation	Good agreement at all error range	Good agreement at all error range
	LP turbine degradation	Good agreement at all error range except LL3 above T3	Good agreement at all error range except LL1 and HL1 above T2
14	Mission profile prediction accuracy	Good prediction with low prediction errors especially compressor degradation case	Good prediction with low prediction errors especially compressor degradation case

Several criteria were introduced for both approximators and classifiers to assist with the search for the best trained networks. During the training, the size of the network was changed repeatedly until those criteria were met.

Evaluations regarding the performance of the trained networks were done in four stages. In the first stage, assessment was done using the previously used populated samples, aiming to observe the samples distribution in obtaining several specified error ranges together with assessing the average and standard deviation of the prediction errors given by the trained approximators. For classifiers, further investigation regarding the classification accuracy was done for each class via confusion matrices.

The second stage of the evaluation involved the generation of two sets of new unseen samples used to validate the generalisation of the trained approximators and classifiers independently. Sample distribution analysis was conducted using the approximators in order to evaluate the consistency of the predicted outputs hence validating the networks if consistency were observed during the analysis. For classifiers, consistency of the classification efficiencies was observed via the confusion matrices for both sets of unseen samples. If consistency were attained, then the trained classifiers are said to achieve generalisation.

Statistical analysis was performed in the third stage, aiming to obtain the overall picture of how the trained networks responded to given unseen inputs. Using EasyFit 5.5, the best fitted distributions were searched in order to provide realistic probability of obtaining specific ranges of prediction error. Based on the fitted distribution, the theoretical PDF and CDF were constructed hence the probability of obtaining the specified prediction error ranges were calculated. In this stage, the results obtained from the statistical analysis were compared with the previous sample distribution analysis with the intention of assessing the suitability of the fitted distribution with the empirical data.

The final stage of the evaluation was conducted to see the effects of accumulated predicted errors on a given mission profile. Using the previously created mission profiles, the mission segments or sub-segments were inputted into the trained network before the CF, LF, CF_M and LF_M were computed.

All of the implemented architectures whether for clean or degraded engine conditions have almost the same observations. Good generalisations with good prediction accuracy were observed in the entire trained network across all architectures. In the first evaluation stage, all of the trained networks have low MSE with R closed to unity. Not only that, the E_{Ave} of the creep life prediction errors for each

trained approximator was very close to zero with some degree of variation. Moreover, the classification networks were able to produce good classification.

In the second stage of the evaluation, the implemented architectures were seen to be able to retain their creep life prediction accuracy or classification accuracy when two sets of unseen data were inputted into them independently. From the sample distribution analysis or confusion matrix, there was evidence that some approximators or classifiers were experiencing a slight drop in accuracy, although the majority of the networks across the architectures did not. Nevertheless, it was observed that the consistencies of the predicted outputs or classifications, when both sets of unseen samples were inputted, have validated that the trained networks are producing good generalisations.

The statistical analysis conducted in the third stage of the evaluation revealed that the distributions of the prediction errors produced by the approximators are different between architectures. However, the three most common distributions observed were Johnson SU, Cauchy and Normal distributions. When the results of the statistical analysis were compared with the sample distribution analysis (conducted in the second stage of the evaluation), small discrepancies between the two analyses were observed. The small discrepancies show that both analyses are in agreement with each other. However, there was also evidence that some approximators were found to achieve good agreement only when they surpassed a certain specified error range.

Using the mission profiles created in the previous study for both clean and degraded engine conditions, the effects of accumulated errors on the mission profile were investigated. Based on the calculated mission segments or sub-segments' CF and the comparison with the CFs predicted using the Integrated Creep Life Estimation Model, it was observed that both CFs were very similar, producing overlapping trends when they were plotted together. As a result of this, it was found that the effects of the accumulated errors on the mission profile were minimal thus producing low errors in both LF_M and CF_M.

For clean engine condition, SB architecture is seen to be most superior in producing accurate creep life prediction with a probability of unity at error range between -0.6 to 0.6%. In addition, the prediction errors of both LF_M and CF_M during the mission profile analysis are six times and two times lower than the RB and the FB architectures respectively.

When both RB and FB architectures were compared, it was found that the superiority of both architectures will depend on the location of the operation points in the operation envelope. At lower creep range operation points, the RB architecture was found to be superior to the FB architecture and vice versa. Both Classes 1 and 2 of the RB architecture were able to have probabilities of near unity at error between -3 to 3% compared to the FB approximator with only 0.942.

Despite having the chance of being misclassified to the wrong class, it has been observed that the misclassifications in the Range Classifiers of the RB architecture occur at the operation points that produce creep lives located very close to the class upper and lower limits. Because of the closeness of the values to the limits, the creep life prediction errors were still at the acceptable level with small E_{Ave} and SD_E.

For the degraded engine condition, it was found that the SB approximators, in the majority, are able to offer better creep life prediction than the FB architectures, especially in predicting the blade's creep life of degraded HP and LP turbines. By comparing the three component degradation approximators, it was found that for both architectures, HP turbine degradation approximators were better than the other two component degradation approximators. For the FB architecture, seven out of nine HP turbine degradation approximators were able to produce prediction errors with a probability of 0.98 to 0.999 at error range -2 to 2%. For the SB architecture, seven out of nine HP turbine degradation approximators were able to produce prediction errors with a probability of 0.98 to 0.99 at error range -0.4 to 0.4%

Similarly, with the clean engine conditions, the effects of accumulated errors in the respective degraded mission profiles can also be neglected. Good prediction accuracy of CF in each mission segment or sub-segment was observed, hence reducing the prediction errors of both LF_M and CF_M, especially for the compressor degradation case.

Overall, it can be concluded that the implementations of the proposed architectures have been done successfully for both clean and degraded engine conditions.

8 INFLUENCE OF INPUT UNCERTAINTIES ON CREEP LIFE PREDICTION

In Chapter 7, the capabilities of the implemented neural architectures in producing good creep life prediction, either for single or multiple point operations, have been shown. Since during the implementation of the architectures, only 'true' values of the input (input with no uncertainty/noise) were used to train and hence test the architectures, the effects of input uncertainties on the accuracy of the creep life prediction need to be carried out.

In this chapter, the influence of input uncertainties on creep life prediction accuracy using the implemented neural-based architectures is reported. This will include discussions on the objectives and methodology, assumptions and considerations, results and discussions. At the end, the conclusion is given.

8.1 Objectives and Methodology of the Input Uncertainty Analysis

The objectives of the input uncertainty analysis are as follows:

a) To obtain the behaviour of the architectures' prediction and classification accuracies at different levels of input uncertainty.
b) To determine which of the two intermediate approximators (Blade Metal Temperature Approximator or Blade Stress Approximator) is more sensitive to input uncertainty for both FB and SB architectures.
c) To measure the impact of obtaining creep life prediction error within the assigned error range at different input uncertainty levels.
d) To determine which of the implemented architectures is more sensitive to input uncertainty.

In order to achieve the objectives in a 'timely' manner, the study was limited to the three implemented architectures for the clean engine condition. The reason for this is because the architectures for the degraded engine condition possess the same network arrangement as the clean engine condition, hence the influence of the input uncertainty on the creep life prediction accuracy will be similar.

The methodology of performing the study is summarised in Figure 8-1.

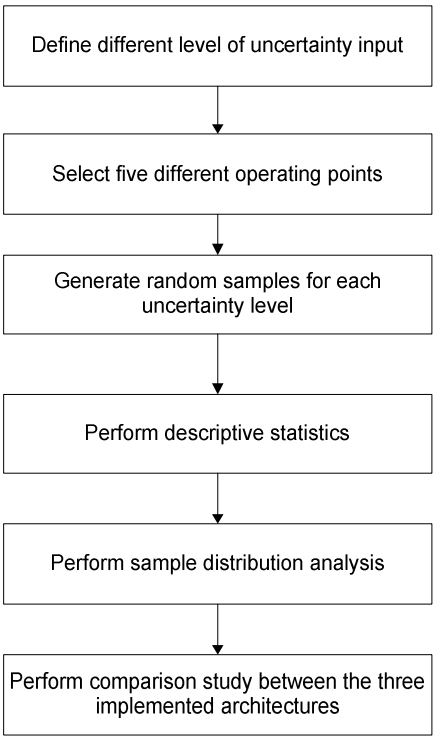

Figure 8-1: Methodology to perform the input uncertainty study

8.1.1 Defining Different Levels of Uncertainty Input

The levels of uncertainty were defined based on typical errors of the respective inputs as shown in Table 8-1. From Table 8-1 it can be seen that most of the typical errors listed were obtained from typical measurement error or allowable tolerance published in the open literatures or from PYTHIA. However, for the Mach number, the typical error has been reasonably assumed.

The typical errors provide the upper and lower bounds of the respective input. In this study it is assumed that the uncertainty of the inputs follows a Normal distribution with the upper and lower bounds, as given in Table 8-1, taken as the limits of the '2σ' of the Normal distribution. This enables the study to randomly generate normally distributed samples when the mean value, μ and the standard deviation, σ are specified.

Eight levels of input uncertainty were defined, as listed in Table 8-2. From the table it can be seen that the uncertainty levels represent the degree of uncertainty when the typical error or 2σ is multiplied by a certain percentage of level multiplier. The higher percentage of level multiplier means the higher the degree of input uncertainty.

Table 8-1: Typical errors of the respective neural architecture input

Input	Typical Error	Source
PCN	$\pm$ 0.1%	Obtained from [213]
T2, T3, T12, and T13	<290°C : $\pm$3.3°C, 290-1000°C: $\pm\sqrt{2.5^2+(0.0075T)^2}$ 1000-1300°C: : $\pm\sqrt{3.5^2+(0.0075T)^2}$	Obtained from [213]
P2, P3, P12, and P13	$\pm$ 0.5%	Obtained from [213]
Fuel Flow	Up to 0.0694 kg/s: $\pm$0.01153 kg/s Up to 0.125 kg/s: $\pm$0.00952 kg/s Up to 0.25 kg/s: $\pm$0.00817 kg/s Up to 0.378 kg/s: $\pm$0.00658 kg/s Up to 0.504 kg/s: $\pm$0.00578 kg/s Up to 0.63 kg/s: $\pm$0.00639 kg/s Up to 0.757 kg/s: $\pm$0.00719 kg/s Up to 1.008 kg/s: $\pm$0.01006 kg/s Up to 1.5139 kg/s: $\pm$0.0176 kg/s Up to 3.406 kg/s: $\pm$0.03964 kg/s	Obtained from [213]
Altitude	Up to 304.8 m : $\pm$6.096 m Up to 457.2 m: $\pm$7.62 m Up to 914.4 m: $\pm$9.144 m Up to 1219.2 m: $\pm$10.668 m Up to 1828.8 m: $\pm$12.192 m Up to 2438.4 m: $\pm$18.288 m Up to 3048 m: $\pm$24.384 m Up to 3657.6 m: $\pm$27.432 m Up to 4267 m: $\pm$30.48 m Up to 4876.8 m: $\pm$33.528 m Up to 5486.4 m: $\pm$36.576 m	Obtained from [214]
Shaft Power	$\pm$0.5%	PYTHIA
Ambient Temp	0.1%	PYTHIA
Mach No	$\pm$0.5%	Assumed value

Table 8-2: Level of uncertainty used in this study

Uncertainty Level	Magnitude of Uncertainty	Uncertainty Level	Magnitude of Uncertainty
Level 1	5% of 2σ	Level 5	50% of 2σ
Level 2	10% of 2σ	Level 6	100% of 2σ
Level 3	15% of 2σ	Level 7	150% of 2σ
Level 4	20% of 2σ	Level 8	200% of 2σ

8.1.2 Selecting Five Different Operating Points

Five different operating points, with each of them being randomly selected from different creep life range classes (Classes 1 to 5) of the RB architecture, were specified as case studies. This is to allow different approximators being assessed during the study. The lists of the specified operating points are given in Table 8-3.

Table 8-3: Operating points selected in the study

Point	Altitude	PCN	Mach Number	Ambient Temperature Deviation from ISA
1	1000	0.99	0.1	18
2	2100	0.982	0.2	13
3	3200	0.958	0.15	22
4	4500	0.97	0.27	13
5	4800	0.964	0.24	10

For each of the operating points, a performance simulation of the selected engine model was carried out using PYTHIA to obtain the gas path measurements. Then the measurements which have been selected as inputs to the SB architecture (T3, P3, T12, P12, T13, P13, FF and SP) were recorded.

These measurements, together with the altitude, PCN, Mach number and ambient temperature deviations, were treated as 'true' inputs. The term 'true' used in this context represents inputs predicted when no uncertainty is present. These 'true' inputs were then inputted into the implemented architectures to predict the blade's metal temperatures, stresses and creep lives. These predicted outputs were taken as the reference outputs, z_{ref} which were later used to quantify the effect of input uncertainty on the prediction accuracy.

8.1.3 Generating Random Samples for Each Uncertainty Level

15,000 samples which consist of a set of inputs suited to different implemented architecture were then generated for each uncertainty level (Table 8-2) at each specified operating point (Table 8-3). This was done using a normal distribution random number generator available in Microsoft Excel which requires the input of:

a) the input mean value which is taken from the true input value, and
b) the magnitude of uncertainty (Table 8-2) which is the by-product of the multiplication of the percentage of level multiplier with the input 2σ .

Figure 8-2 and Figure 8-3 show examples of the randomly recorded simulated altitude (1000m mean value) of the first 100 points at four different uncertainty levels and the PDF generated at 150% uncertainty multiplier plotted using EasyFit. As shown in Figure 8-2, as the uncertainty level increases, the fluctuation of altitude also increases. Additionally, Figure 8-3 indicates that the random generator used by the author was able to provide a normally distributed input.

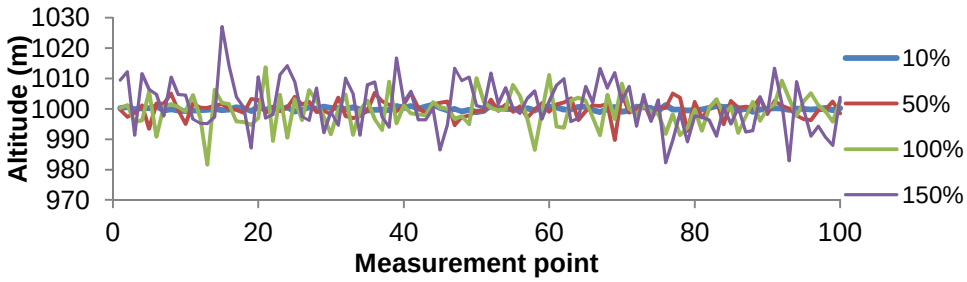

Figure 8-2: First 100 points generated by the normal distribution random for mean altitude of 1000m

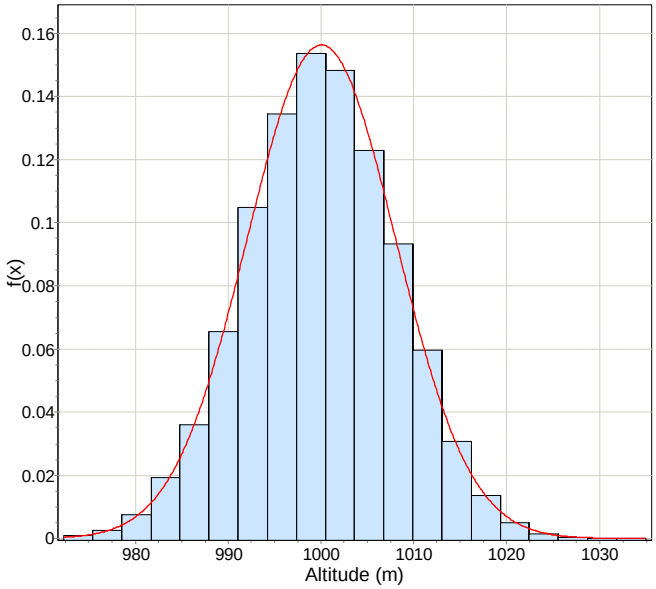

Figure 8-3: PDF of the generated altitudes at 150% uncertainty level

8.1.4 Performing Descriptive Statistics and Sample Distribution Analysis

Once the entire samples have been generated, the samples were inputted into the three implemented architectures in order to predict the corresponding creep lives. For the FB and SB architectures, the blade's metal temperatures and the maximum blade stresses were also predicted. Then the error E between each predicted output,

$\hat{z}_{Uncertain}$ (creep life, blade's metal temperature or stress) with its reference output, z_{ref} was calculated using Equation (8-1).

$$E = \frac{\hat{z}_{Uncertain} - z_{true}}{z_{true}} \times 100\% \quad \textbf{(8-1)}$$

Using the calculated Es, descriptive statistics, which basically describe the main features of the generated samples [215], were performed. In this study, three descriptive statistics parameters or test parameters were used to describe the features of the calculated Es which are the standard deviation SD_E, minimum and maximum values. The SD_E describes how diverse the Es will be from its mean value. If the SD_E is large, the variations of the Es are significant thus reducing the prediction accuracy. The maximum and the minimum values, E_{min} and E_{max}, will indicate to what extent the uncertain inputs can affect the prediction accuracy at both the positive and negative sides of the error.

Having to perform the descriptive analysis enables the study to measure the effect of the input uncertainty on the prediction accuracy. In addition, it helps to determine which of the two intermediate approximators (Blade Metal Temperature Approximator or Blade Stress Approximator) is more sensitive to input uncertainty for both FB and SB architectures.

Apart from the descriptive analysis, sample distribution analysis was also carried out. This analysis was divided into two parts. In the first part, the percentage of samples able to produce E within the error range of -5 to 5% is calculated for each given uncertainty level. The error range specified acts as a yardstick to assess the effect of the input uncertainty on the creep life prediction accuracy. If the sample percentage calculated is high throughout the entire uncertainty levels, then it shows that the architecture is insensitive to input uncertainty or vice versa.

In the second part of the sample distribution analysis, the percentage of the sample able to produce correct classification via the use of the Range Classifier was calculated. This part of the analysis was only applied to the RB architecture since only this architecture uses a classifier to classify the predicted creep life into the several creep life ranges. Similarly, if high classification efficiency is obtained throughout the entire uncertainty levels, the classifier is said to be insensitive to input uncertainty and vice versa.

8.1.5 Performing the Comparison Study between the Three Implemented Architectures

The comparison study between the three implemented architectures was done by comparing the sample distribution analysis of the individual architecture. The architecture which possesses the lowest sample percentages able to produce E within the specified error range will be the most sensitive to input uncertainty or vice versa.

8.2 Results and Discussions

In this section, the results obtained from the study will be presented and discussed.

8.2.1 RB Architecture

Figure 8-4 provides the plots of creep life SD_E against the uncertainty multiplier at different operating points. From the figure it can be seen that as the uncertainty multiplier was increased, the $SD_E s$ increased linearly. The increase shows that the presence of the input uncertainty has caused the creep life prediction errors to spread even more, hence reducing the creep life prediction accuracy. Furthermore, although the behaviours of the SD_E are similar, the magnitudes of the SD_E at most of the operating conditions are different. At 200% uncertainty multiplier, the $SD_E s$ for operating points 1 to 5 are 8.0%, 3%, 17.8% , 8.3% and 10% respectively. This was expected since during the optimisation of the synaptic weights, the minimisation of error for points at different operating spaces is different which affects the way the points will behave when uncertainty is present.

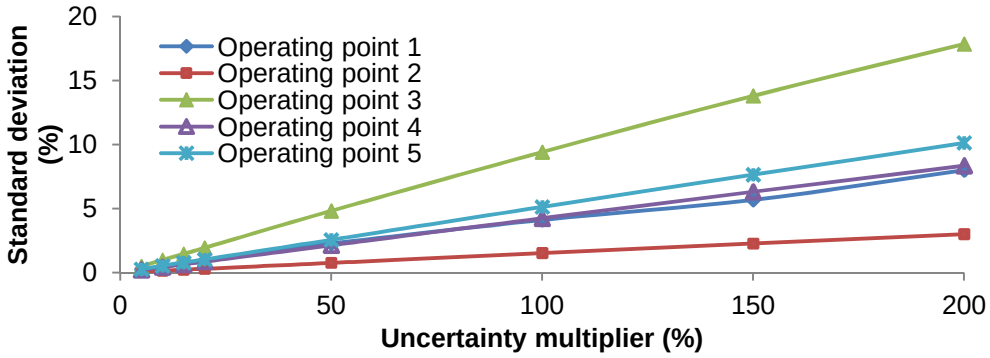

Figure 8-4: Plots of SD_E against uncertainty multiplier produced by the RB architecture

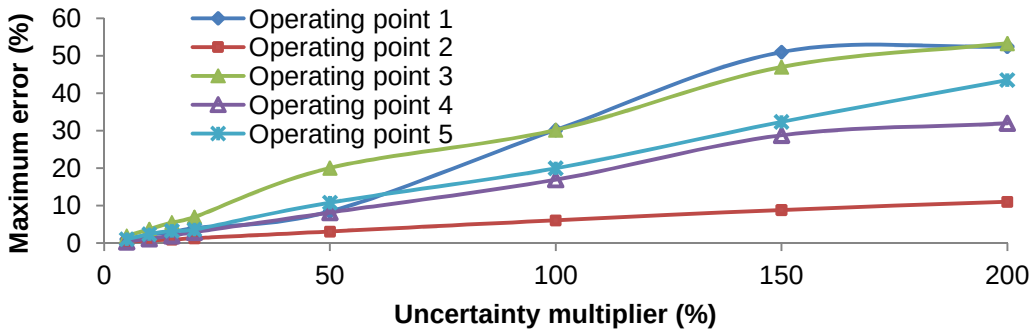

Figure 8-5: Plots of E_{max} against uncertainty multiplier produced by the RB architecture

The increase in the uncertainty has also caused both the E_{max} and E_{min} to increase fairly linearly. This can be clearly seen when both parameters are plotted against the uncertainty multiplier, as shown in Figure 8-5 and Figure 8-6 respectively. From both figures, it can be seen that at 200% uncertainty multiplier, the E_{max} at points 1 to 5 have increased significantly to around 52%, 11%, 53%, 31% and 43% while the E_{min} at the same points have increased negatively to -8%, -11%, -53%, -28%, and -33% respectively. Also, the magnitude of increase between the E_{max} and $E_{min}$was different, especially at point 1, indicating that the distribution of the E has a longer tail on the positive side than the negative side.

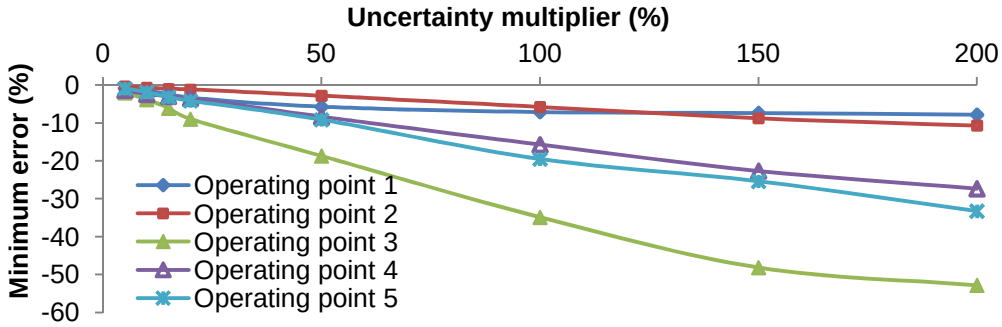

Figure 8-6: Plots of E_{min} against uncertainty multiplier produced by the RB architecture

As the SD_E, E_{max} and E_{min} increase, the amount of samples able to produce low prediction error will consequently reduce. This can be clearly seen when the percentage of the samples able to produce E within -5 to 5% is plotted in Figure 8-7. From the figure it can be seen that except for operation point 2, the amount of sample encompassed reduced exponentially after reaching 50% (points 1, 4 and 5) and 20% (point 3) of uncertainty multipliers. At 200% uncertainty multiplier, the percentages of samples encompassed within -5 to 5% of error for points 1 to 5 are 46.7%, 90.4%, 20.7%, 44.0% and 37.4% respectively.

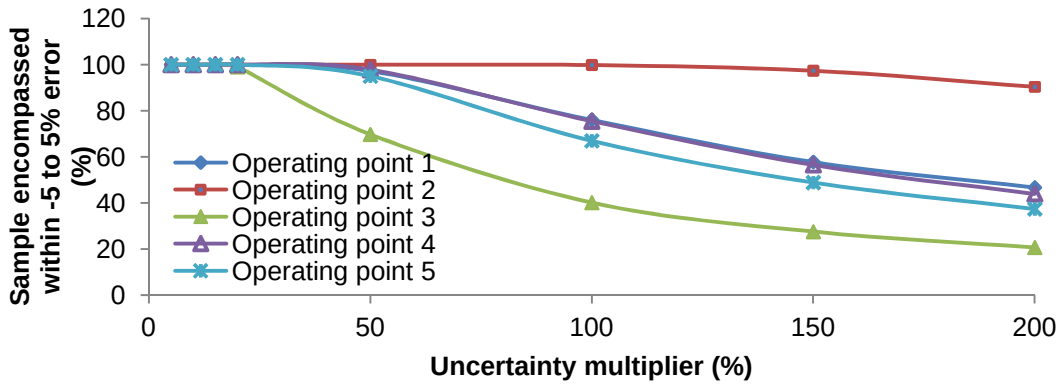

Figure 8-7: Percentage of samples encompassed within the specified error range

By comparing all of the operating points, point 2 was found to be more resilient to input uncertainty with the sample percentage being maintained above 90% throughout the test. This was again expected since the SD_E, E_{max} and $E_{min}$of point 2 were the least of all the selected operating points. On the other hand, point 3 was seen to be most vulnerable to input uncertainty due to the fact that the SD_E, E_{max} and E_{min} of point 3 were the highest among all of the selected operating points.

The overall effect of input uncertainty on the sample distribution can be seen when the prediction error PDF of the generated samples were plotted. Figure 8-8 provides an example of the prediction error PDF at operating point 1 for several uncertainty multipliers. From the figure, it can be seen that the width of the PDF increases as the input uncertainty increases, suggesting a rise in the prediction error variation, hence reducing the probability of obtaining good prediction accuracy. Similar trends were observed in other operating points as shown in Appendix FF.1.

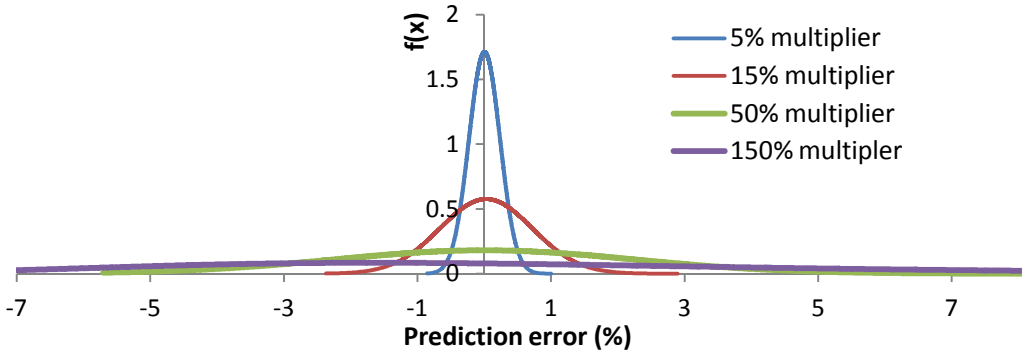

Figure 8-8: Prediction error PDF of the generated samples at point 1 for several uncertainty multipliers

Figure 8-9 plots the classification accuracy of the Range Classifier against the uncertainty multiplier. The figure shows that points 2, 3 and 4 are able to maintain good classification accuracy throughout the uncertainty multiplier. However, for points 1 and

5, classification accuracies were seen to reduce after surpassing the 20% uncertain multiplier. At 200% multiplier, classification accuracies of both points are 59% and 62% respectively.

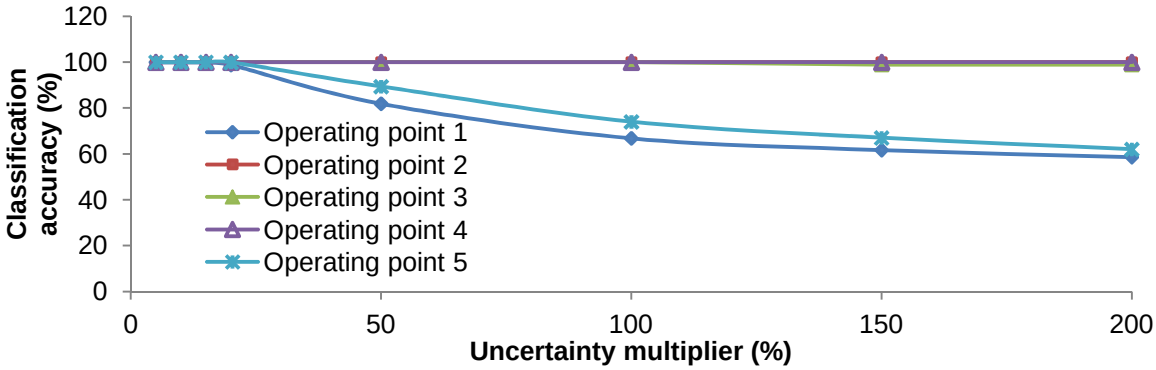

Figure 8-9: Classification accuracy against uncertainty multiplier

Further investigation reveals that the classification accuracy depends very much on the operating point. If the operating point produces a predicted creep life very close to the respective upper or lower limits of the creep life class range, reduction in the classification accuracy is seen. In contrast, if the predicted creep life is far from the limits, then the variation of the inputs from its true value will not change the classification output thus maintaining its classification ability.

This can be clearly seen when the percentage deviation between the operating point's reference creep life and its corresponding class range upper limit is calculated and graphed in Figure 8-10. From the figure it can be seen that both points 1 and 5 have low percentage deviation. This indicates that the reference creep lives at both points are close to the upper limits, thus causing the classification accuracy to deteriorate.

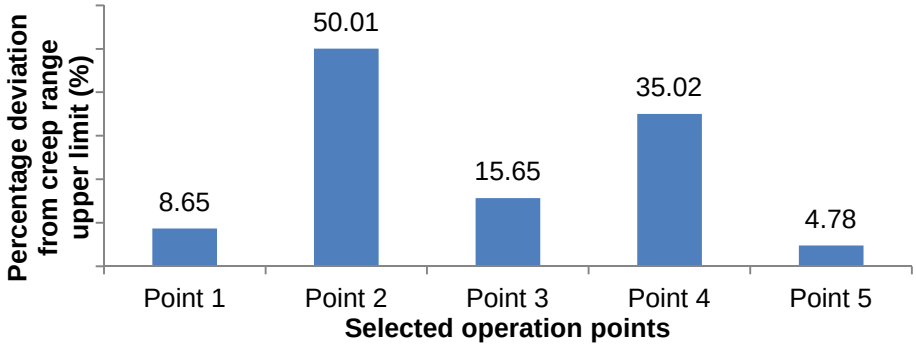

Figure 8-10: Percentage deviation of operating point's reference life with its respective class range upper limit.

Overall, the RB approximators are found to be sensitive to input uncertainty. As input uncertainty increases, the SD_E, E_{max} and E_{min} increase as well. Consequently, the

ability to provide good creep life prediction is degraded. This can be seen as the percentage of samples able to produce a prediction error within -5 to 5% reduces exponentially after a certain percentage of uncertainty multiplier. The magnitude of the accuracy reduction is also found to be a function of the engine operational envelope. This can be seen as different selected points having different resistance towards input uncertainty.

8.2.2 FB Architecture

Before the effect of input uncertainty on the creep life prediction accuracy was investigated, the effects of input uncertainty on the blade's metal temperature and stress prediction accuracies were studied. Figure 8-11 and Figure 8-12 depict the SD_E of the blade's metal temperature and stress respectively. From the figure it can be seen that both $SD_E s$ increase linearly when the input uncertainty increases. At 200% multiplier, the $SD_E s$ for the blade metal temperature at points 1 to 5 are 0.05%, 0.037%, 0.246%, 0.12% and 0.19% respectively. Similarly, $SD_E s$ for the blade stress at the same points are seen to be 0.22%, 0.2%, 0.3%, 0.2% and 0.21% respectively.

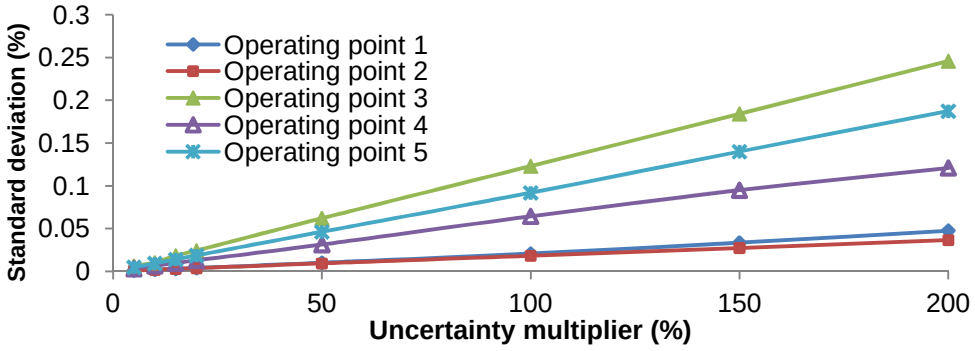

Figure 8-11: Plots of the blade's metal temperature SD_E produced by the FB architecture

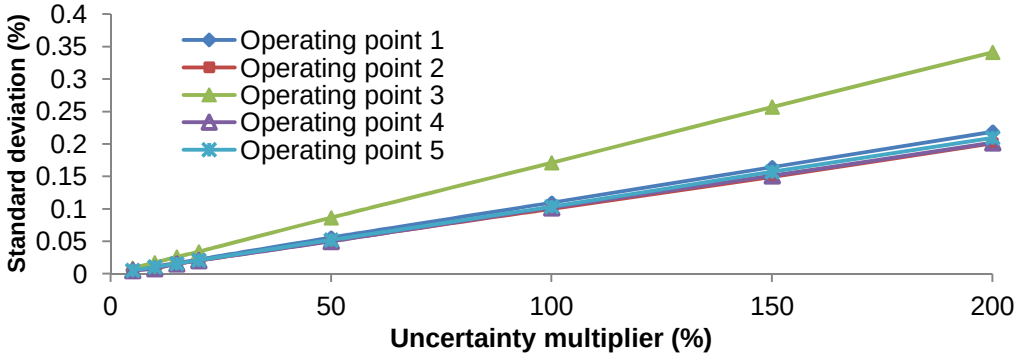

Figure 8-12: Plots of the blade's stress SD_E produced by the FB architecture

By comparing the behaviour of $SD_E s$ between the blade's metal temperature and stress, it can be seen that the magnitude of the $SD_E s$ for the blade's metal temperature is strongly influenced by the operation point compared to the blade stress which in contrast shows similarity to the $SD_{Es} s$ for the majority of the operating points.

Despite having a consistent increase in the $SD_{Es} s$, the magnitudes of the SD_{Es} for the blade stress are seen to be higher than the blade's metal temperature. This can be clearly seen when both $SD_{Es} s$ are compared, as shown in Appendix GG.1 for each selected operating point. From the appendix it can be seen that all of the plots of the $SD_{Es} s$ for the blade's stress are higher than the blade's metal temperature.

The effect of input uncertainty on the blade's creep life was then investigated. Using the predicted blade's metal temperatures and stresses, the blade's creep lives were then predicted. The creep life $SD_E s$ were then calculated and plotted as shown in Figure 8-13. From the figure it can be seen that as the uncertainty multiplier was increased, the $SD_E s$ increased linearly. Although the behaviour of the SD_E is similar for each operating point, the magnitudes are found to be different from one operating point to another. For example, at 200% uncertainty multiplier, the $SD_E s$ for points 1 to 5 are 3.2%, 2.7%, 17.1%, 7.1% and 10.13% respectively. This significant difference in the magnitude suggests that for this architecture, the effect of input uncertainty has a strong influence on the operating points selected in this study.

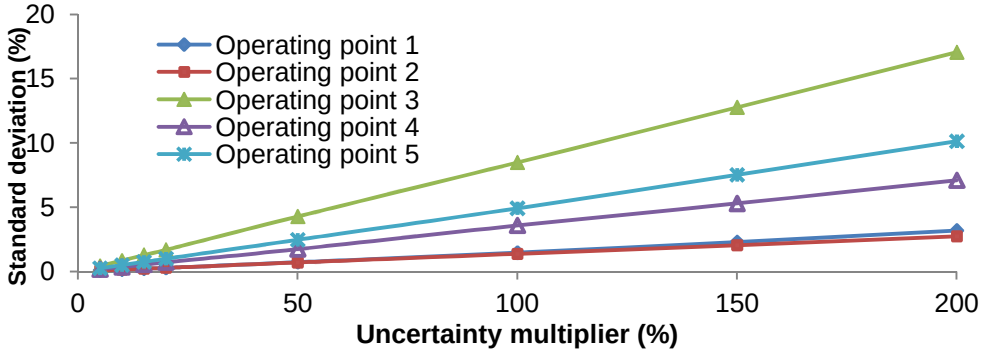

Figure 8-13: Plots of SD_E of the blade's creep life produced by the FB architecture

Similar effects were seen on E_{max} and E_{min}. As the SD_E increases linearly, the spreading of the errors has caused the E_{max} and E_{min} to increase linearly as well. This can be clearly seen in Figure 8-14 and Figure 8-15 as E_{max} and E_{min} were plotted against the uncertainty multiplier. At 200% uncertainty multiplier, the $E_{max} s$ at points 1 to 5 have increased to around 21%, 11%, 81%, 32%, 53% respectively while the $E_{min} s$ at the same points have dropped to -5%, -11%, -50%, -22% and -32% respectively.

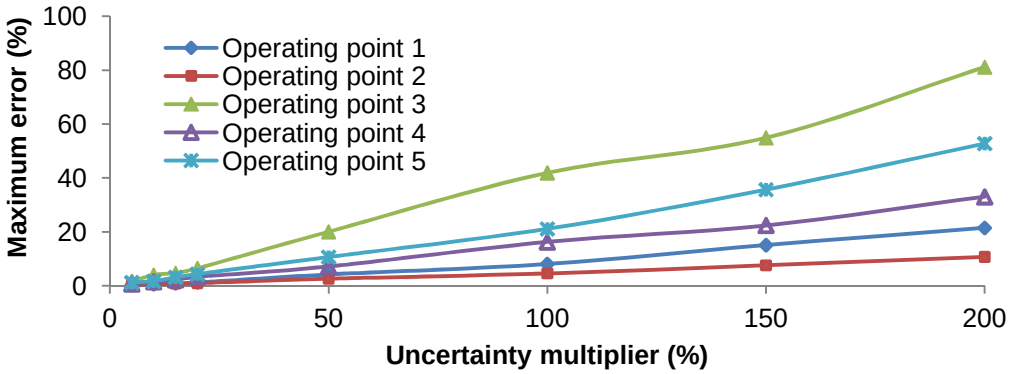

Figure 8-14: Plots of E_{max} against uncertainty multiplier produced by the FB architecture

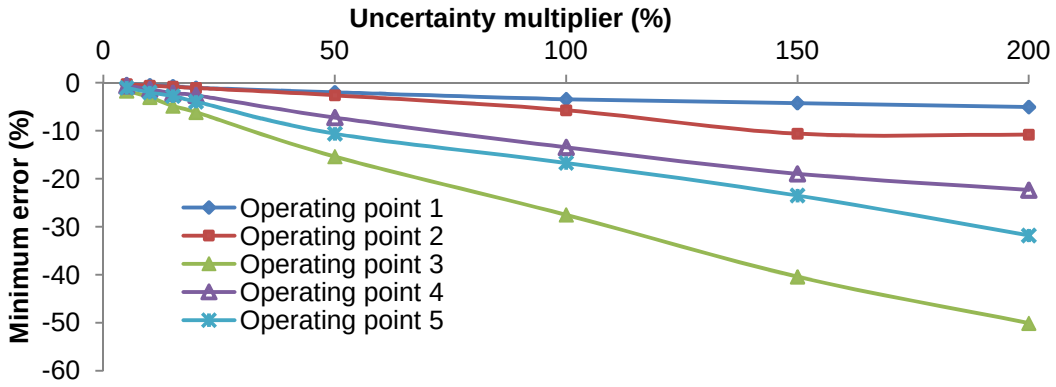

Figure 8-15: Plots of E_{min} against uncertainty multiplier produced by the FB architecture

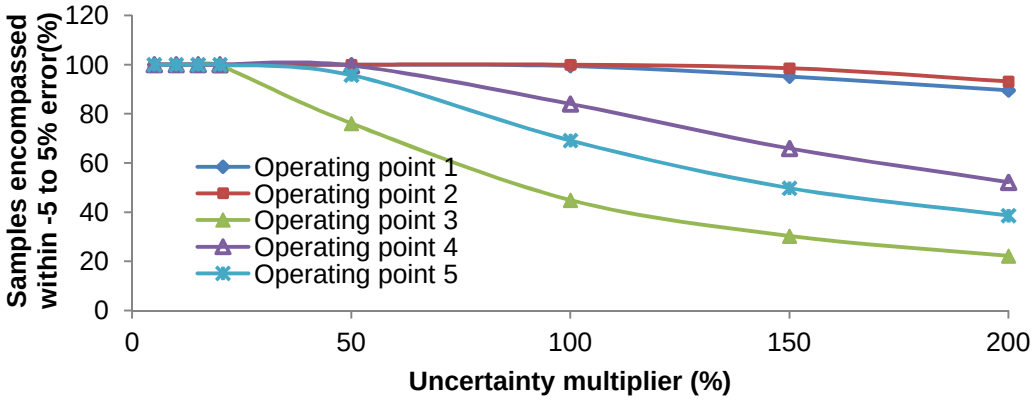

Figure 8-16: Percentage of samples encompassed within the specified error range

Figure 8-16 depicts the outcomes of the sample distribution analysis. As the input uncertainty increases, the percentage of samples able to produce E within -5 to 5% drops exponentially, especially at operating point 3. The drops were seen to happen

only when the uncertainty multiplier was increased beyond 100% for points 1 and 2, 50% for points 4 and 5 or 20% for point 3. This was expected since the SD_E, E_{max} and E_{min} were found to be increasing as the input uncertainty increased. At 200% uncertainty multiplier, the percentages of samples encompassed within -5 to 5% of error for points 1 to 5 are 90%, 93%, 22%, 52% and 39% respectively.

Both points 1 and 2 were found to be the most resilient to input uncertainty when their samples' percentages were compared to the other operating points. Both points were able to retain 90% of their samples producing E within -5 to 5%. This was, again, expected since the $SD_E s$, $E_{max} s$ and $E_{min} s$ of both points were the smallest. In contrast, point 3 was the most sensitive to input uncertainty. Not only was the point only able to retain its prediction accuracy up to 20% uncertainty multiplier, the samples' percentages producing E within -5 to 5% were the lowest among all other points throughout the entire test. This is because the SD_E, E_{max} and E_{min} of point 3 were the highest among all of the selected operating points.

Figure 8-17 depicts the prediction error PDFs created using the generated samples of several uncertainty multipliers at operating point 1. The plot provides a good visual representation of how the overall generated samples were distributed when different levels of input uncertainty were applied. The trends of the PDF are found to be similar to the trends plotted for the RB architecture with the width of the PDF increases, thus reducing the probability of obtaining good prediction accuracy as the input uncertainty increases. Similar behaviours have been observed at other PDFs plotted at different operating points, as shown in Appendix FF.2.

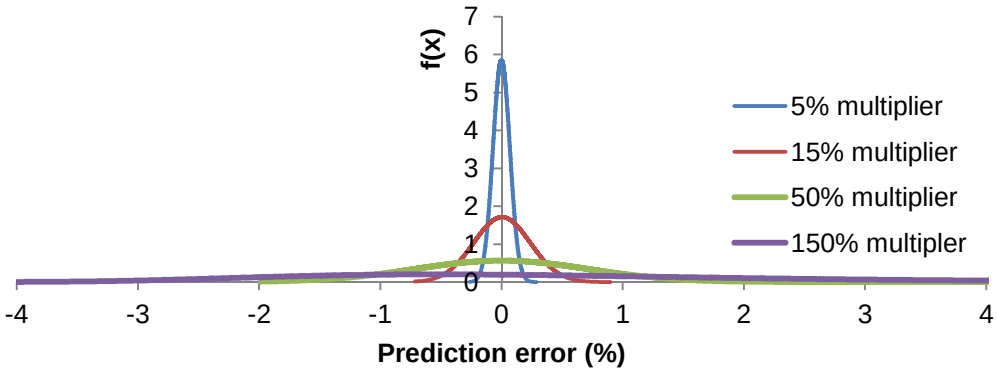

Figure 8-17: Prediction error PDF of the generated samples at point 1 for several uncertainty multipliers

In general, the study conducted on the implemented FB architectures shows that the effect of input uncertainty on the blade's metal temperature, stress and creep life prediction accuracies is significant. By comparing the $SD_E s$ of blade's metal

temperatures and stresses, the blade stresses were found to be more sensitive than the blade metal temperatures to input uncertainty. Also the magnitude of the $SD_E s$ for the blade's metal temperatures is strongly influenced by the operation point compared to the blade stresses which show consistency in the $SD_E s$ for the majority of the operating points.

As the input uncertainty increases, the creep life SD_E, E_{max} and E_{min} increase as well. The effects of the reductions in these test parameters are translated into the loss of the architecture's ability to retain good prediction accuracy beyond a certain level of uncertainty multiplier. The magnitude of the accuracy reduction is also dictated by the location of the engine operation point. Based on the sample distribution analysis, it can be seen that different selected points have different resistance towards input uncertainty.

8.2.3 SB Architecture

Since the SB architecture has the same network arrangement as the FB architecture, a similar procedure was used to perform the test. Figure 8-18 plots the creep life SD_E against the uncertainty multiplier at all of the selected operating points. From the figure it can be seen that only up to 20% uncertainty multipliers were applied. The restriction imposed on the test was because the architecture can no longer function beyond this uncertainty multiplier. It was found that beyond 20%, the prediction errors not only exceed 600%, but that some of the predicted creep lives have negative values.

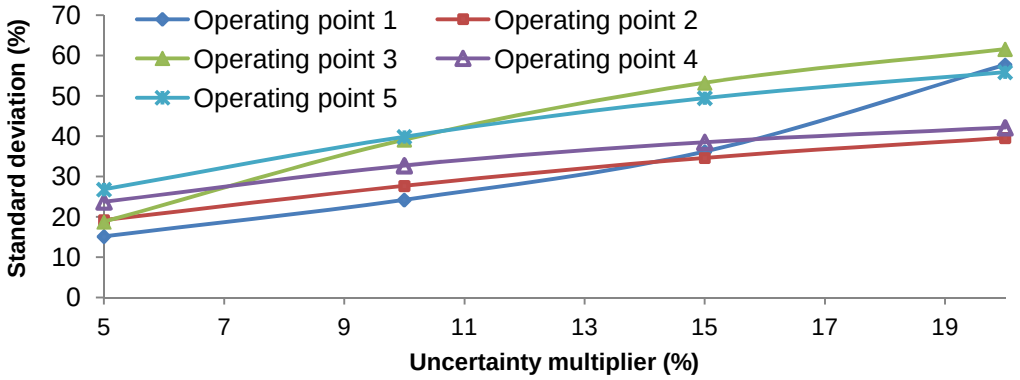

Figure 8-18: Plots of the creep life $SD_E s$ produced by the SB architecture

In addition, if the values of the $SD_E s$ given in Figure 8-18 are compared with both the RB (Figure 8-4) and FB (Figure 8-13) architectures, the $SD_E s$ produced by the SB architecture are considerably higher than the other two architectures. At 20% uncertainty multiplier, the $SD_E s$ recorded are 57.7%, 39.6%, 61.6%, 42.1% and 55.9% for operating points 1 to 5 respectively. Taking point 3 as an example, at 20%

multiplier, creep life SD_E for the SB, FB, and RB architectures are 61.6%, 1.68%, and 1.44% respectively. From these values it can be seen that the creep life SD_E for the SB is approximately 40 times higher than the values produced by both the FB and RB architectures at the same operating point.

The high creep life SD_Es mean that the distribution of the prediction errors are highly scattered hence increase the variations of the errors from their mean values. It also increases the E_{max} and E_{max} as shown in Figure 8-19 and Figure 8-20 respectively. Since the creep life SD_E increases as uncertainty increases, both figures show the same trends with an increasing of both values and with increasing uncertainty. At 20% uncertainty multiplier, the $E_{max}s$ at points 1 to 5 have increased to around 169.1%, 75.8%, 133.3%, 77.7%, and 104.7% respectively while the E_{min} at the same points have reduced to -121.4%, -98.8%, -99.94%, and -99.98% respectively.

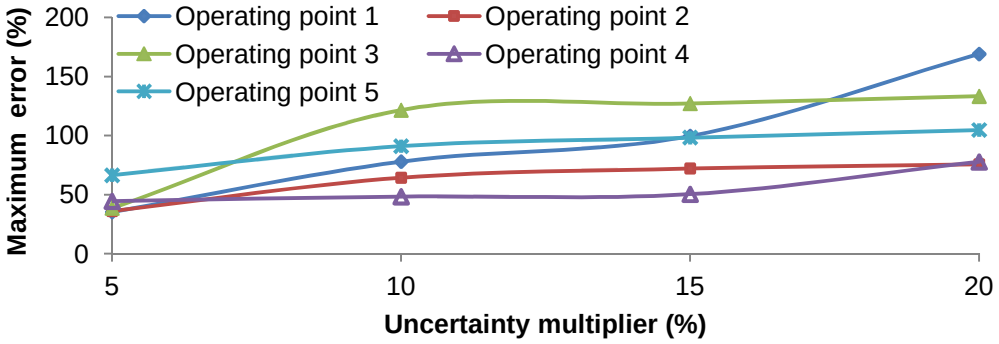

Figure 8-19: Plots of E_{max} against uncertainty multiplier produced by the SB architecture

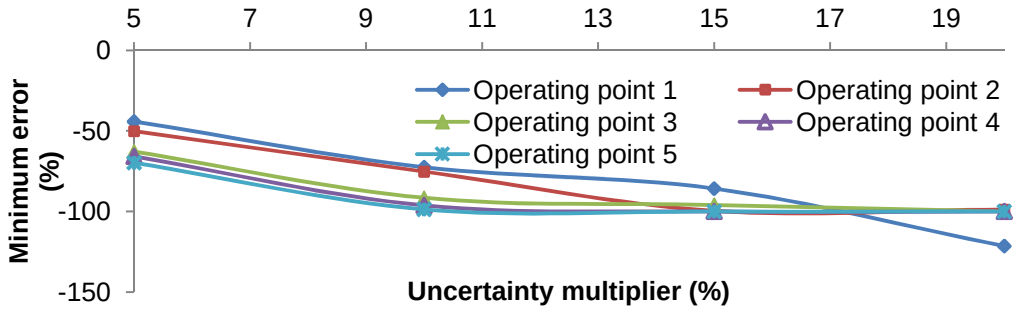

Figure 8-20: Plots of E_{min} against uncertainty multiplier produced by the SB architecture

Figure 8-21 depicts the results of the sample distribution analysis. From the figure it can be seen that when the input uncertainty increases, the amount of samples able to produce E within -5 to 5% are reduced exponentially. At 20% uncertainty multiplier, the percentages of samples encompassed within the error range for points 1 to 5 are 5.5%, 5.3%, 4.35%, 4.66% and 3.47% respectively. The significantly low sample percentages

suggest that the effects of input uncertainty on the architecture were so detrimental that even with the smallest input uncertainty, the architecture was unable to retain good creep life prediction.

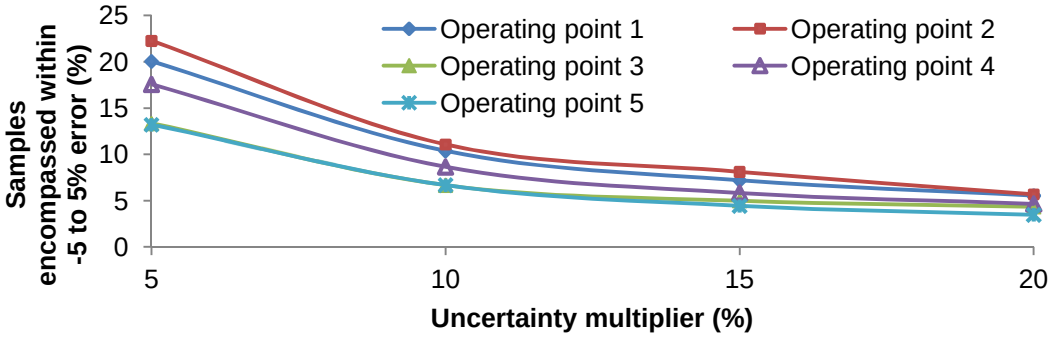

Figure 8-21: Percentage of samples encompassed within the specified error range

The detrimental effect of the input uncertainty is visually represented in Figure 8-22 when the prediction error PDFs created using the generated samples at point 1 were plotted. From the figure it can be seen that although the mean of the distribution (the peak of the PDF) is located very close to zero, the increase in the variation of the prediction error has caused the PDF to be 'stretched' to a bigger range of error, hence creates fatter and shortened distributions. Similar behaviours are observed at other PDFs plotted at different operating points, as shown in Appendix FF.3. However, for both point 3 and point 4, some distributions were seen to have negative bias as the means value moved slightly to the negative side of the error.

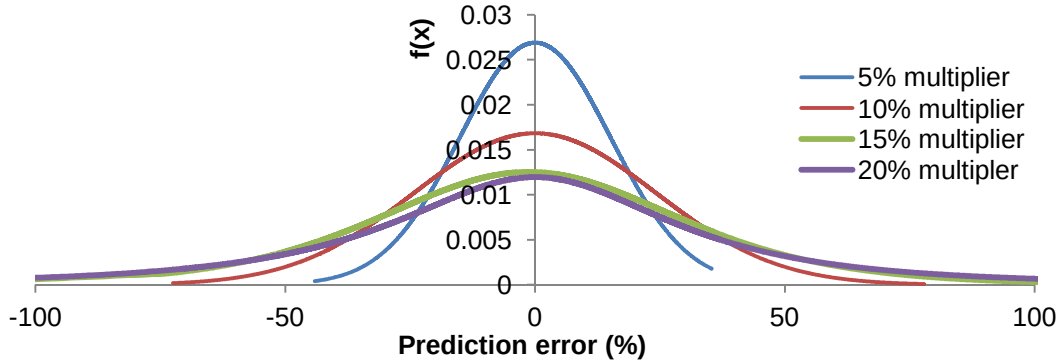

Figure 8-22: Prediction error PDF of the generated samples at point 1 for different uncertainty multipliers

The effects of input uncertainty on the blade's metal temperatures and stresses can be seen in Figure 8-23 and Figure 8-24 in which the $SD_E s$ of both outputs were calculated and plotted. Several observations were made. The trends of the $SD_E s$ of

both outputs are different with linear increments seen in the metal temperature and exponential increments in the blade stress.

When both values are compared with those obtained using the FB architecture (Figure 8-12), it can be seen that the SB architecture possesses considerably higher SD_Es for both the temperature and stress. For example, at point 1 the SD_Es of the SB blade's metal temperature and stress are 1.1% and 4.5% respectively. Meanwhile for the FB blade's metal temperature and stress, the SD_Es are 0.00388% and 0.02167% respectively. Based on these values, the SD_Es of the SB blade's metal temperature and stress at point 1 are found to be 283 and 208 times larger than the FB values.

By comparing Figure 8-23 and Figure 8-24, it can be seen that the magnitudes of the SD_Es of the blade stress are higher than the blade's metal temperature. The difference between the two $SD_{Es}s$ can be much clearer when both $SD_{Es}s$ are compared, as shown in Appendix GG.2.

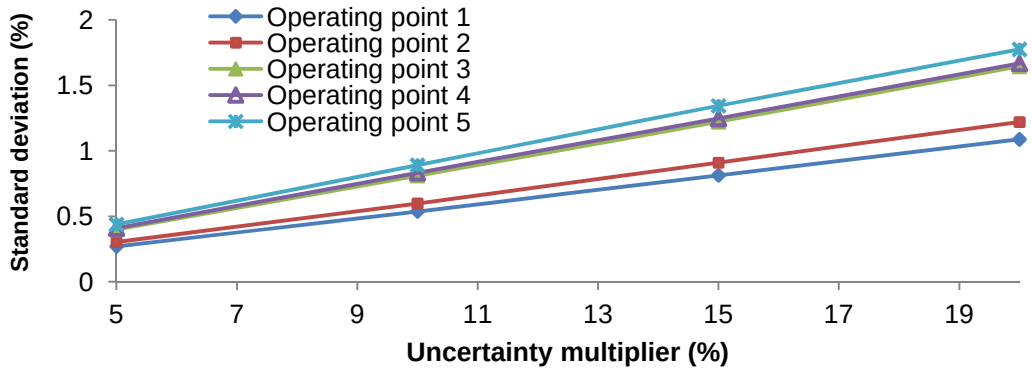

Figure 8-23: Plots of the blade's metal temperature SD_E produced by the SB architecture

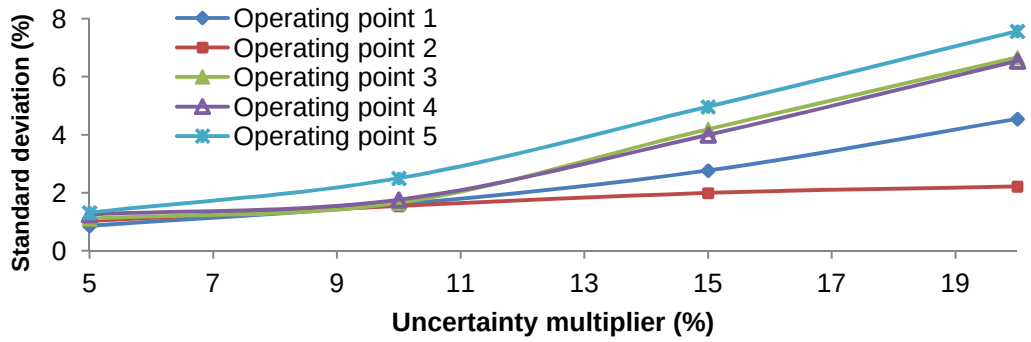

Figure 8-24: Plots of the blade's stress SD_E produced by the SB architecture

The substantial increase in $SD_{Es}s$ for both metal temperatures and stresses are seen as the main cause why the architecture is so sensitive to the input uncertainty. It has already been established in a previous chapter that by utilising a cascaded type of

network arrangement, error propagation from the intermediate networks to the output network can never be avoided. Since both metal temperatures and stresses have high prediction error variations shown as high $SD_{Es}s$, the effects of error propagation becomes more significant.

The root cause of this problem lies at how the architecture was being developed. Because the SB architecture uses twice the inputs as the other architectures, the amount of synaptic weights available in the SB architecture increases. These additional synaptic weights help the training process to reduce the $MSEs$ even more since more weights can be adjusted in the search for the best optimised solution.

On the other hand, because more inputs were used in the SB architecture, the collective input uncertainties were larger than the other architectures. The increase in the collective uncertainties will create a bigger disturbance to the larger sized synaptic weights hence creating bigger output variations in both of the intermediate approximators. Consequently this will create situations where the outputs produced by the intermediate approximators will be much larger than the input limits used to train the output approximators. Table 8-4 and Table 8-5 provide the percentages of samples that produced the predicted blade's metal temperatures and stresses exceeding the temperature and stress limits of the trained Creep Life Approximator. From both tables it can be seen that for the blade's metal temperature, only point 5 has samples that exceed the temperature limits. However, the effect of uncertainty is more significant in the blade's stress. Almost all of the points possess samples that produced stresses exceeding the limit beyond the 5% multiplier.

Table 8-4: Percentages of samples exceeding the blade's metal temperature limits of the trained Creep Life Approximator

Uncertainty Multiplier	% of samples exceeding blade's metal temperature limit				
	Point 1	Point 2	Point 3	Point 4	Point 5
5%	0.00	0.00	0.00	0.00	0.00
10%	0.00	0.00	0.00	0.00	0.52
15%	0.01	0.00	0.00	0.00	4.53
20%	0.13	0.00	0.00	0.00	9.73

The effect of error propagation from the intermediate approximators to the output approximator has also worsened the situation. The error propagation has amplified the existing output variation to bigger values causing the architecture to fail even at a small fraction of uncertainty.

Table 8-5: Percentages of samples exceeding the blade's stress limit of the trained Creep Life Approximator

Uncertainty Multiplier	% of samples exceeding blade's stress limit				
	Point 1	Point 2	Point 3	Point 4	Point 5
5%	0.00	0.00	0.00	0.00	0.00
10%	0.02	0.01	0.04	0.13	0.06
15%	1.19	1.14	1.81	1.56	1.83
20%	5.83	4.52	7.96	6.96	6.99

Overall, the study has shown that the effects of the input uncertainty on the SB architecture prediction accuracies were unacceptable. The high $SD_E s$ in both blade's metal temperatures and stresses have created a massive impact on the functionality of the Creep Life Approximator. Based on the test conducted, it can be seen that as the creep life prediction accuracy significantly degraded, the Creep Life Approximator failed to function properly beyond 20% of the uncertainty multiplier.

Moreover, it was found that the magnitude of the SD_E, E_{min}, E_{max} and the percentages of samples encompassed within the specified range have strong relations with the selected operating points. It can be clearly seen that, although the behaviours of those mentioned parameters are similar, the magnitudes of those parameters are different at different operating points.

8.2.4 Comparison Analysis between the Three Implemented Architectures

The results and discussions given in this Chapter have so far focused on the effects of input uncertainty on individual implemented architecture prediction accuracy. However, in this section a comparison between the three implemented architectures is given.

When the inputs were inputted into the architectures at different uncertainty levels, several similar outcomes were observed. Firstly, all of the architectures were found to be significantly affected by uncertainties. For both the RB and FB architectures, the ability to retain their prediction accuracies were limited to certain levels of input multipliers. The results show that most of the operating points selected were able to provide good creep life prediction up to 50% uncertainty multiplier. On the other hand, the SB architecture was seen to be the most vulnerable to input uncertainty with the architecture failing to function after the uncertainty multiplier goes beyond 20%.

Secondly, most of the test parameters and percentage of samples able to produce E within the specified error range were strongly influenced by the operating points selected. This can be clearly seen as different operating points were seen to have different magnitudes of test parameters and samples' percentage.

Thirdly, for both the RB and SB architectures, the variations of the blade's stress prediction error were seen to be higher than the blade's metal temperature. This can be clearly seen when the SD_E of both temperature and stress were plotted together for each selected operating point.

Figure 8-25 provides the comparison of the results of the sample distribution analysis between the three architectures at operating point 1. It can be seen that at operating point 1, the FB architecture has the highest percentage of samples able to produce E within -5 to 5% followed by the RB architecture and the SB architecture. When the results of the sample distribution analysis of the other points are plotted in Appendix HH, similar outcomes were observed. Collectively it can be said that the FB architecture is the least sensitive to input uncertainty, followed by the RB architecture and the SB architecture.

The study conducted on the three implemented architectures for the clean engine condition shows the need to treat the incoming inputs before the inputs can be used to predict the blade's creep life. By treating the inputs, the existing uncertainty could be eliminated or minimised, hence retaining the ability to produce good prediction accuracy.

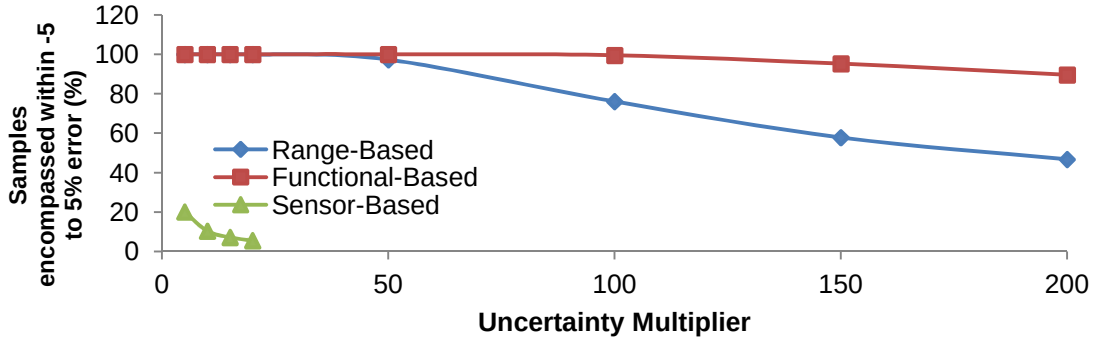

Figure 8-25: Comparison of the sample distribution analysis results between the three architectures at operating point 1

8.3 Chapter Conclusion

This chapter reports on the study conducted by the author in order to investigate the effects of input uncertainty on the accuracy of the creep life prediction using the three

implemented neural architectures for clean engine condition. Four objectives have been laid out which are:

a) To obtain the behaviour of the architectures' prediction and classification accuracies at different levels of input uncertainty.
b) To determine which of the two intermediate approximators (Blade Metal Temperature Approximator or Blade Stress Approximator) is more sensitive to input uncertainty for both FB and SB architectures.
c) To measure the impact of obtaining creep life prediction error within the assigned error range at different input uncertainty levels.
d) To determine which of the implemented architectures is more sensitive to input uncertainty.

The uncertainties of the inputs are based on typical errors which provide the upper and lower limits of the respective input. By taking the Normal distribution as the basis to generate the uncertain inputs, 15,000 samples were randomly generated for each of uncertainty levels. Five different operating points were selected as case studies, with each one of them being randomly selected from each creep life range class of the RB architecture.

Once the samples for each uncertainty level at each operating point were generated, the samples were inputted into the three implemented architectures in order to predict the corresponding blade's metal temperatures, stresses and creep lives. Descriptive statistical and sample distribution analyses were then performed in order to assess the effects of the input uncertainty on the prediction accuracy of each implemented architecture before a comparison study was conducted to compare the three implemented architecture.

Based on the analyses conducted, several observations were made:

a) All of the architectures were found to be significantly affected by uncertainties. As the uncertainty level increases, the test parameters such as the SD_E, E_{max} and E_{min} increases, indicating an increase in the effects of the input uncertainty.
b) For both the RB and FB architectures, the $SD_E s,\ E_{max} s$ and $E_{min} s$ change fairly linearly to the change of the input uncertainty.
c) The behaviour of the test parameters of the SB architecture is found to be slightly different from the previous two architectures. The trend of the SD_E is found to be increasing fairly linearly as the levels of input uncertainty are

increased. However for both the E_{max} and E_{min}, the trends of both parameters are found to be changing non-linearly.

d) The classification accuracy of the Range Classifier depends very much on the locations of the operating point. If the location of the operating point that produces a predicted creep life is very close to the respective upper or lower limits of the creep life class range, than the classification accuracy will degrade. Nevertheless, if the location is far from the limits, the variation of the inputs will not change the classification outcome hence maintaining its classification ability.

e) For both FB and SB architectures, the blade's stress was found to be more affected by input uncertainty at all the selected operating points.

Table 8-6: Summary of the conclusions

No	Observable item	Implemented Neural Architecture		
		RB	FB	SB
1	Prediction accuracy in the presence of input uncertainty	Reduce	Reduce	Reduce
2	Behaviour of the test parameters:			
	Creep life SD_E	Linear	Linear	Linear
	Prediction error maximum and minimum values	Linear	Linear	Non-linear
	Classification accuracy	Operating point dependent	-	-
3	Blade temperature vs. stress	-	Stress is more sensitive	Stress is more sensitive
4	Trend of the sample's percentage drop	Exponential after exceeding certain uncertainty level	Exponential after exceeding a certain uncertainty level	Exponential
5	Impact of obtaining creep life within the assigned error range	Operating point dependent	Operating point dependent	Operating point dependent
6	Sensitivity to input uncertainty	Rank 2	Rank 3	Rank 1

f) For all of the architectures, the percentage of the samples able to produce E within the error range of -5 to 5% dropped exponentially as the levels of input uncertainty were increased. However, for both the RB and FB architectures, the drop in the percentages only occurs when a certain level of uncertainty is surpassed. Although the behaviours of the percentage drop are observed to be similar across all operating points, the magnitude of the drop differs from one point to another suggesting that the engine operating envelope has a strong influence in dictating the ability to retain a good creep life prediction.

g) It was observed that the FB architecture is the least sensitive to input uncertainty, followed by the RB architecture and the SB architecture.

Table 8-6 provides the summary of the conclusions that have been discussed in the previous chapters.

9 CONCLUSIONS AND FUTURE WORK

9.1 Conclusions

The aim of this research is to develop an alternative creep life estimation model that is able to reduce the complexity of the current estimation framework, perform rapid calculation while maintaining a certain level of accuracy. In order to achieve this aim, four objectives have been laid out:

a. To create an integrated creep life estimation model that enables the prediction of component creep life at different operating and health conditions.
b. To study the effects of different operating and health conditions on component creep life consumption using a simple relative analysis technique.
c. To construct an alternative neural-based creep life estimation model that enables a direct link between the gas turbine operating and health conditions with the components' corresponding life
d. To study the impact of input uncertainties on the creep life prediction accuracy obtained using the alternative creep life estimation method.

In order to achieve the research objectives, a research methodology has been proposed. Tasks required to complete the research objectives have been detailed and the links between one specific task and the others have been established. Based on the research objectives and the proposed methodology, the conclusions are given in the next sections.

9.1.1 Creating an Integrated Creep Life Estimation Model

An integrated creep life estimation model has been developed and incorporated in the existing Cranfield University performance simulation and diagnostics software called PYTHIA in order to produce a new version of the program with a creep life prediction capability. This enables users to perform single or multiple stage, cooled or uncooled HP turbine blade's creep life prediction under any given operating and health conditions either for a single operation point or for any given mission profile automatically. In addition, a new impact analysis parameter called Creep Factor has been introduced. Using the new parameter, performance parameter impact analysis can be done using the proposed Creep Factor approach.

This integrated model serves several purposes of the research work which includes:

a. generation of training samples for the construction of the proposed neural-based creep life prediction architectures
b. generation of post test samples to validate each proposed neural network architecture,
c. studying the effects of different operating and health conditions on a selected engine model HP turbine blade's creep life.

The integrated model consists of five sub models:

a. Operation/Mission Profile Model that simulates the performance of a model engine for a given operation/mission profile, a single operating point or a user-defined reference operating condition
b. Blade Stress Model that calculates the blades stresses
c. Blade Thermal Model that performs the blade thermal analysis
d. Life Estimation Model that calculates the blade's creep life
e. Life Usage Model that provides the percentage of blade creep life usage for a given operation history.

Using the PYTHIA platform, four program interfaces have been created in order to incorporate the developed integrated model with PYTHIA:

a. Initial Blade Setting Interface to input the engine's blade data and choose the mode of thermal analysis
b. Flight Segment Setting Interface which allows users to define a single or multiple mission/operation segment of clean and degraded engine model
c. Life Estimation Analysis Interface to carry out the blade's creep life assessment for each mission/operation segment or for the entire mission/operation
d. Overall Life Calculation Interface to calculate the blade's life usage.

The benefits of the developed integrated model include:

a. flexibility to change and update turbine design features
b. ability to calculate the tangential and axial loading
c. ability to calculate the drop in gas temperature at the inlet of the blade due to the presence of cooling in the NGV
d. ability to predict the metal temperature variation across the blade span
e. ability to simulate individual a mission/operation segment or the entire mission/operation profile for both a clean and degraded engine
f. ability to perform impact analysis for an individual flight/operation segment or the entire mission/operation profile

g. the model is relatively simple and requires only one person to perform the predictions

Having successfully developed the integrated model, it can be said that the first research objective has been successfully accomplished.

9.1.2 Investigation into the Effects of Different Operating and Health Conditions on Component Creep Life Consumption Using a Simple Relative Analysis Technique

Using a helicopter turbo-shaft engine model, impact analyses of several selected operating and health parameters on the blade's creep life consumption have been investigated. The impact study was divided into two parts where in the first part, the influence of engine rotational speed, altitude, ambient temperature, Mach number, compressor fouling, HP and LP turbine erosions were quantified using the introduced Creep Factor which forms a simple relative analysis technique. In the second part of the study, the effects of clean and degraded mission profiles (with the inclusion of compressor fouling and turbine erosion) on the nominal blade's creep life were investigated using the same Creep Factor approach.

Prior to the impact analyses, the engine model was constructed in PYTHIA. In order to improve the engine performance prediction accuracy at both DP and OD conditions, DP and OD performance adaptations were carried out. After the adaptations, at DP the average error of the targeted parameters reduced from 0.998% initially to 5.08E-5% while at OD conditions, the overall performance prediction error reduced from a total average error of 4% to around 0.75%.

When the calculated impact weight of the operating parameters were compared, it was found that for the clean engine condition, the engine rotation speed is the most influential in changing the blade's creep life. Not only that the magnitude of the impact weight is the highest (-0.591$\log CF$); the logarithmic term indicates that the reduction in the blade's creep life is accelerating. On the other hand, altitude is the least sensitive as the impact weight compared to the other operating parameters is the lowest (-0.0292CF). By comparing the impact weight of different health parameters, it can be seen that compressor fouling has the highest threat in reducing the blade's creep life with an impact weight of -0.1121$\log CF$. On the other hand, the LP turbine erosion is seen to have the lowest threat as the value of the impact weight is the lowest at -0.0477 LogCF. In addition, the logarithmic terms used in the impact weight indicate that

component degradation will have an accelerated impact on the consumption of the blade's creep life.

Investigations into the effects of clean and degraded mission profiles on the nominal blade's creep life were done by calculating each mission segment CF and CF_M. By comparing each mission segment CF, it was found that the clean engine possesses higher CFs, compared to the degraded engine, over the entire mission. With the degraded engine, compressor fouling is seen to give the lowest CFs at all mission segments followed by HP turbine erosion and LP turbine erosion. Moreover, for both the clean and degraded engine, the calculated mission CFs were able to identify which mission segments have a relatively lower creep life. The calculated CF_Ms of the clean and degraded mission profiles provide the overall weight of the impact. The CF_M for the clean, compressor fouled, HP turbine eroded and LP turbine eroded mission profiles are 1.17, 0.71, 0.76, and 0.96 respectively which indicate that the nominal creep lives are 17% more, 29% less, 24% less and 4% less than the life calculated at reference condition respectively.

The impact analysis has been very useful in recognising the sensitivity of each operating and health parameter in changing the blade's creep life. The results obtained have been used to determine the samples required to train the proposed neural network model.

Having successfully performed the impact analyses using the Creep Factor approach, the second research objective has been achieved.

9.1.3 Construction of the Alternative Neural-Based Creep Life Estimation Models

The construction of the alternative neural-based creep life estimation models started by analysing the process of the author's integrated creep life estimation prediction model via the use of an output-input process tree. Using the process tree, the overall process of predicting the minimum creep life can be visualised. It was found that the entire creep life prediction requires two main parameters and two main inputs which are the calculated parameters, simulated parameters, primary input and secondary input.

Based on the process tree, clustering of the parameters and inputs was done. Using the clustered parameters, four mappings that linked the clustered parameters were created. Once the mappings were established, the parameter(s) for each cluster were finalised hence three neural-based architectures were formed which are the RB, FB and SB architectures.

The application of the proposed architecture for a clean and degraded engine was done using the same helicopter turbo-shaft engine model. For the clean engine case, all the three proposed architectures were applied while for the degraded engine case, only the FB and SB architectures were implemented.

Using the author's integrated creep life estimation model, both training and post test samples were generated. The amount of samples populated to train the proposed architectures were determined by considering the sensitivity of each of the selected operating and health parameters obtained from the impact analyses.

In this study, an MFBP neural network was used as the basis to construct the neural-based model. When an approximator type of network was used to approximate any form of value, such as the blade's creep life or the blade's metal temperature, the Levenberg-Marquardt training algorithm was used. However, when a classifier type of network was used to classify any output from a given input, the Scaled-Conjugate-Gradient algorithm was applied. In addition, the study uses the Hyperbolic-Tangent Function as the activation function for its hidden neurons and the Linear Function for its output neurons.

As tools to initially determine the accuracy and generalisation of the trained approximators, both MSE and R were observed during the training. Similarly, confusion matrices were used to observe both accuracy and generalisation of the trained classifiers. Several criteria were then specified and observed. If the criteria were met, the network would be selected. Otherwise training would be repeated using either the same, or with the new hidden layer size.

Evaluations of the performance of the proposed architectures were done in four stages. In the first stage, assessments were done via the sample distribution analyses and the confusion matrices, to see how accurate the prediction and classification of the trained networks are when the training samples are presented. In the second stage, validations of the networks were done using two sets of new, unseen samples. These were again done via the sample distribution analyses and the confusion matrices. In the third stage, statistical analysis was performed, in order to obtain the overall picture of how the trained networks responded to given unseen inputs. In the final stage, evaluations were conducted to see the effects of accumulated predicted errors on given mission profiles.

All of the implemented architectures, whether for clean or degraded engine conditions have almost the same observations. Good generalisations with good prediction accuracy were observed in the entire trained network across all

architectures. In the first stage of evaluation, the trained networks produced low MSE with R closed to unity. Not only that, E_{Ave} for each trained approximator was very close to zero with some degree of variations. Additionally the classification networks were able to produce good classification.

In the second stage of the evaluation, the implemented architectures were seen to be able to retain their creep life prediction accuracy or classification accuracy when two sets of unseen data were inputted into them independently. However, there was also evidence that some approximators or classifiers were experiencing a slight drop in accuracy although the majority of the networks across the architectures did not.

The statistical analysis conducted in the third stage of the evaluation reveals that the distributions of the prediction errors produced by the approximators are different between architectures with Johnson SU, Cauchy and Normal distributions being among most common. When the statistical analysis was compared with the sample distribution analysis, small discrepancies between the two analyses were observed indicating good agreement was achieved between the two analyses. However, there was also evidence that some approximators were found to achieve good agreement only when they surpassed a certain specified error range.

In the fourth stage assessment, when the same mission profiles (both clean and degraded missions) were presented to the proposed architectures, the mission segment CFs were very similar to the CFs predicted using the Integrated Creep Life Estimation Model.

By comparing the proposed architecture, it was found that the SB architecture for both clean and degraded engines were able to offer a better creep life prediction. Similarly, with the clean engine conditions, there was good prediction accuracy for each mission segment CF, especially for the compressor degradation case.

Overall, it can be concluded that the implementations of the proposed architectures have been done successfully for both clean and degraded engine conditions, hence achieving the third research objective.

9.1.4 Investigation of the Effects of Input Uncertainties on Creep Life Prediction Accuracy Obtained Using the Alternative Creep Life Estimation Method

In this investigation, only the clean engine case was considered. The uncertainties of the inputs are based on typical errors of the respective inputs. By assuming that the input uncertainties are normally distributed, 15,000 samples were randomly generated

for each of the uncertainty levels. Five different operating points were randomly selected as case studies. The generated samples were inputted into the three implemented architectures in order to predict the corresponding outputs (T_M, σ, or L_{CMin}). Descriptive statistical and sample distribution analyses were performed to assess the input uncertainty effects on the prediction accuracy before a comparison study was conducted to compare the three proposed architectures.

Based on the analyses conducted, several observations were made. All of the architectures were found to be significantly affected by input uncertainties. As the level of uncertainty increases, the test parameters (i.e. SD_E, E_{max} and E_{min}) increases. The $SD_E s$, $E_{max} s$ and $E_{min} s$ were found to change linearly for both the RB and FB architectures while for the SB architecture, only SD_E was found to change linearly.

The classification accuracy of the RB architecture was found to be a function of the location of the operating point. If the location of the operating point that produces a predicted creep life is very close to the respective upper or lower limits of the creep life class range, then the classification accuracy will degrade or vice versa.

For both the FB and SB architectures, the blade's stress was found to be more affected by input uncertainty than the blade's metal temperature at all the selected operating points.

For all of the architectures, the percentage of the samples able to produce E within the error range of -5 to 5% dropped exponentially as the levels of input uncertainty were increased. However, for both the RB and FB architectures, the drop occurred only when a certain level of uncertainty was surpassed. Although the behaviours of the percentages drop were observed to be similar across all operating points, the magnitude of the drop differed from one point to another suggesting that the engine operating envelope has a strong influence in dictating the ability to retain good creep life prediction.

Based on all the results, it was found that the FB architecture is the least sensitive to input uncertainty, followed by the RB architecture and the SB architecture.

Having successfully completed the uncertainty analysis, the fourth research objective has been achieved.

9.1.5 Significant Contributions of the Research

As all of the objectives outlined in this research have been successfully achieved, the research has produced several significant contributions. In the development of the model-based creep life estimation approach as discussed in Chapter 4, a new relative

creep life analysis approach called the Creep Factor approach has been introduced. Using the Creep Factor approach, the impact of the operating and health conditions on changing the blade's creep life can be individually quantified. The impact weight calculated via the Creep Factor value will enable the users to assess how much has the blade's creep life changes when the engine operating and health conditions deviates from a user defined reference condition. Thus will produce a realistic impact analysis and eliminate the dependency on the given OEM baseline operation estimated creep life which sometimes is not reachable when the engine operating conditions are far from the suggested baseline operation.

In addition, using the Creep Factor approach, the impact of a given mission profile in changing the blades creep life can also be measured. The calculated individual mission segment Creep Factor will provide insight on how each mission segment could influence the blade's creep life while the introduced Mission Creep Factor will provide the overall impact weight of the given mission relative to a user defined reference condition.

The research has also developed a generic Integrated Creep Life Estimation model which is capable of performing 0D and 1D creep life analyses, for both cooled and uncooled turbine blades. Using the model, the blades creep life of single and multiple operating conditions for both clean and degraded engine can be estimated. As the model is able to predict variations of creep life along the blade span, users will be able to know where the minimum creep life is occurring along the blade span hence producing a realistic creep life assessment.

Another significant contribution produced by this research is the introduction of an alternative creep life estimation method that is capable of reducing the complexity of the present model-based creep life estimation method using an ANN approach. Such alternative will be very useful for creep life consumption estimation of production engines in operation where relatively simple and quick solutions are desired.

Although ANN has been used by some researchers to perform material creep life analysis, the research is the first to implement ANN in a large-scale component creep life prediction by replacing all of the complicated analyses required to perform the prediction for aero-engine applications. With different forms of proposed architecture, the research provides options to those who decided to implement the new alternative method in component creep life prediction. In addition to that, the systematic approach of designing the architecture as reported in this thesis will guide readers in creating

new and improved architectures not only suitable for the creep life prediction but also other forms of damage mechanism prediction as well.

9.2 Future Work

Although the works conducted have successfully achieved their objective, there is plenty of room for improvements to be considered in future work. In this section, the recommendations for future work are divided into two categories:

a. future work for improving the integrated life estimation model
b. future work for improving the alternative neural-based life estimation model.

9.2.1 Future Work for Improving the Integrated Life Estimation Model

a. Improvement to the blade stress model by including the thermal stress effects: In the current blade stress model, centrifugal stress, bending moment stress due to pressure and velocity different have been considered. In order to improve the prediction accuracy, thermal stress should also be considered since variation in the metal temperature can be predicted using the present model.
b. Improvement to the thermal model by considering 2D thermal analysis: In the present model, 1D thermal analysis has been utilised. For further improvement, a 2D thermal analysis model should be considered.
c. Inclusion of other component life assessment: The current model has been developed for HP turbine blade creep life estimation. For future work, consideration of including other components for life estimation should be done, such as the LP turbine blades, turbine disc and burner.
d. Inclusion of other damage mechanisms: The work at present only focuses on creep life estimation. It is recommended that other damage mechanisms such as LCF, HCF, TMF etc. should be considered in future work.
e. Expanding the uses of the Creep Factor approach: In the present work, the Creep Factor has been successfully used to perform impact analysis of a single performance parameter. For future work it is recommended that the Creep Factor approach is used to perform multiple parameter impact analysis. In addition, the application of the approach for optimisation purposes should be looked into, such as including the Creep Factor in optimising the operation condition or flight trajectory. The application of the Creep Factor as a decision

parameter can also be examined, such as using the Creep Factor for gas turbine selection.

9.2.2 Future Work for the Alternative Neural-Based Life Estimation Model

a. Implementation of mapping 4: In Section 5.2.2: Conceptual Design of the Neural Architecture, four mappings that linked the clustered parameters created from the process analysis have been proposed. However, due to the limited amount of time available to test all of the proposed architectures, mapping 4 has been left out. For future work, implementation of mapping 4 should be done in order to assess its prediction capability and then compare it with the other three (RB, SB, and FB) implemented architectures.
b. Implementation of RB architecture on the developed engine model at degraded engine condition: In this present work, the implementation of the proposed neural architectures has been extended to the degraded engine conditions using two of the proposed architectures, i.e. FB and SB. For future work, the implementation of the RB architecture to the degraded engine condition should be considered.
c. Solving the problems with input uncertainties: Chapter 8 in this thesis acts as a bridge for continuation of the existing work. At present, although the proposed neural architectures can provide good creep life prediction, Chapter 8 has proved that the proposed architectures are vulnerable to input uncertainties. For future work, the vulnerability of the input uncertainty needs to be addressed either by incorporating the model with measurement noise reduction algorithm or retraining the output approximators and classifiers by including tolerance in the network.
d. Reduction in the training samples to train the network: In order to make the approach more effective, an improved method is needed to ensure that minimal training samples can be used to train the network while maintaining or improving the prediction accuracy.
e. Implementation of the neural-based approach to other gas turbine applications: Implementation of the proposed neural architectures was carried out using a helicopter turbo-shaft model. For future work, implementation of the proposed architecture can be done using an aircraft gas turbine model or industrial gas turbine model.

f. Implementation of the neural-based approach as an alternative to other creep life estimation approach: The scope of the present work is limited to developing an alternative model for the present complex integrated creep life estimation model. For future work, the same approach can be applied to build an alternative neural-based model for other forms of life estimation approach.
g. Utilisation of other neural network type: The present work uses MFBP to create both a classifier and approximator network. In order to improve the current model, different types of network can be considered.
h. Creating a dynamic neural-based creep life estimation approach: At present, the proposed architectures already have the capability to predict the blade's creep life for a single or multiple operation point without consideration of time spent for each operation point since linear damage accumulation theory has been used to account for the progressive damage or to calculate the mission's nominal creep life. For future work, the progressive damage can be incorporated to form a dynamic neural-based creep life estimation.
i. Application of the neural-based approach to other damage mechanism: At present the development of the neural-based approach focuses on the creep deformation mechanism. For future work, a neural-based approach can be developed for other damage mechanisms such as LCF, HCF, TMF, etc.

REFERENCES

[1] Forecast International Power System Group, “The market for gas turbine electrical power generation,” Forecast International, Newtown, CT, F646, Sep. 2010.

[2] R. K. Bhargava, “Global energy resources-recent trends,” *Global Gas Turbine News, ASME*, vol. 42, no. 3, pp. 14-18, 2002.

[3] L. Wood, “Research and markets: global large gas turbine market,” *Reuters*, 14-May-2009.

[4] L. S. Langston, “Gas turbine industry overview,” *Global Gas Turbine News, ASME*, vol. 40, no. 1, pp. 5-8, 2000.

[5] D. R. Ballal and J. Zelina, “Progress in aero engine technology (1939-2003),” in *39th AIAA/ASME/SAE/ASEE Joint Propulsion Conference and Exhibit*, Huntsville, Alabama, 2003.

[6] B. Koff, “Gas Turbine Technology Evolution: A Designer’s Perspective,” *Journal of Propulsion and Power*, vol. 20, no. 4, pp. 577-595, 2004.

[7] J.A. Latcovich Jr., “Condition monitoring and its effect on the insurance of new advance gas turbine,” presented at the Turbine Power System and Condition Monitoring Workshop, Texas, 2002.

[8] R. W. Evans and B. Wilshire, *Introduction to Creep*. London: IOM Communication Ltd, 1999.

[9] M. P. Boyce and J. A. Latcovich, “Condition monitoring and its effect on the life of new advanced gas turbine,” *Global Gas Turbine News, ASME*, vol. 42, no. 3, pp. 4-9, 2002.

[10] G. F. Harrison and T. Homewood, “The Application of the Graham and Walles Creep Equation to Aeroengines Superalloys,” *Journal of Strain Analysis*, vol. 129, no. 3, pp. 177-184, 1994.

[11] P. Rubini, “Turbine Blade Cooling. MSc Course Notes.” Cranfield, 2006.

[12] C. Kilroy, “Accident Database,” 2008.

[13] Bureau of Transport and Regional Economics, “Report 113: Cost of Aviation Accidents and Incidents,” Department of Transport and Regional Services, Canberra, Australia, BTRE Report 113, 2006.

[14] L. Marinai, D. Probert, and R. Singh, “Prospects for aero gas-turbine diagnostics: a review,” *Applied Energy*, vol. 79, no. 1, pp. 109-126, 2004.

[15] G. Parthasarathy et al., “Neural Network Models for Usage Based Remaining Life Computation,” *Journal of Engineering for Gas Turbines and Power*, vol. 130, 2008.

[16] B. Weber, J. Huitang, R. Pistor, and P. Lowden, “Application of an integrated engineering approach for LM1600 blade life on-line assessment (05-IAGT-2.2),” in *16th Symposium on Industrial Application of Gas Turbine*, Alberta, Canada, 2005.

[17] S. Ackert, “Elements of Engine Shop Maintenance Costs: Engine Maintenance Concepts for Financiers Version 1.” Macquarie AirFinance, 15-Mar-2010.

[18] Rolls Royce, “Analyst presentation for Citigroup Aerospace and Defence Conference 2007,” 2008.

[19] J. Huitang, R. Pistor, P. Lowden, B. Weber, and R. Grant, “Prediction of Gas Turbine Blade Life-An Interdisplinary Engineering Approach for Condition-Based Maintenance,” in *ASME Turbo Expo 2006: Power for Land, Sea and Air*, 2006, vol. Barcelona, Spain, p. 1.

[20] B. Meherwan P., “9 - Axial-Flow Turbines,” in *Gas Turbine Engineering Handbook (Third Edition)*, Burlington: Gulf Professional Publishing, 2006, pp. 354-386.

[21] D. M. Knowles, “Gas turbine assest management research,” *Gas Today*, May-2008.

[22] F. J. Cunha, M. T. Dahmer, and M. K. Chyu, “Thermal-mechanical life prediction system for anisotropic turbine components,” *Journal of Turbomachinery*, vol. 128, pp. 240-250, 2006.
[23] E. Marcus, “A Parametric Physics Based Creep Life Prediction Approach to a Gas Turbine Blade Conceptual Design,” Georgia Institute of Technology, Atlanta, Georgia, 2008.
[24] R. P. Y. Wei and R. P. Gangloff, *Fracture Mechanics: Perspectives and Directions (Twentieth Symposium)*, vol. 1. Philadelphia: ASTM International, 1989.
[25] N. Boutarek, D. Saïdi, M. A. Acheheb, M. Iggui, and S. Bouterfaïa, “Competition between three damaging mechanisms in the fractured surface of an Inconel 713 superalloy,” *Materials Characterization,*, vol. 59, no. 7, pp. 951-956, 2008.
[26] A. S. Haslam and R. A. Cookson, *Mechanical Design of Turbomachinery. MSc Lecture Notes*, vol. 1. Cranfield, UK: Cranfield University, 2007.
[27] M. H. Sabour, “Creep-fatigue interaction in aircraft gas turbine components by simulation and testing at scaled temperatures,” PhD Thesis, Concordia University, Canada, 2005.
[28] R. Viswanathan, *Damage mechanisms and life assessment of high-temperature components*. ASM International, 1989.
[29] P. Mestanek, “Low cycle fatigue analysis of a last stage steam turbine blade,” *Applied and Computational Mechanics*, vol. 2, pp. 71-82, Oct. 2008.
[30] L. Jacobsson, C. Persson, and S. Melin, “Experimental method for thermomechanical fatigue in gas turbine materials,” in *15th European Conference of Fracture*, Stockholm, Sweden, 2004.
[31] T. J. Carter, “Common failures in gas turbine blades,” *Engineering Failure Analysis,*, vol. 12, no. 2, pp. 237-247, 2005.
[32] M. T. Naeem, S. A. Jazayeri, and N. Razamahdi, “Failure Analysis of Gas Turbine Blades,” in *IJAC-IJME International Conference 2008*, 2008, vol. Nashville, Tenesse.
[33] M. E. Kassner and M.-T. Peres-Prado, *Fundamentals of creep in metals and alloys*. Oxford: Elsevier Science Ltd, 2004.
[34] M. Naeem, “Implications of day temperature variation for an aero-engine’s HP turbine-blade’s creep life-consumption,” *Aerospace Science and Technology,*, vol. 13, no. 1, pp. 27-35, 2009.
[35] G. A. Webster and R. A. Ainsworth, *High Temperature Component Life Assessment*, vol. 1. London: Chapman & Hall, 1994.
[36] K. Brun and R. Kurz, “GAS TURBINE CORROSION - 2,” 2010. [Online]. Available: http://findarticles.com/p/articles/mi_qa5385/is_201003/ai_n53928165/. [Accessed: 13-Sep-2011].
[37] G. Y. Lai, *High-temperature corrosion and materials applications*. ASM International, 2007.
[38] A. Dibbert, “Extending Gas Turbine Life,” *Turbomachinery International*, vol. 47, no. 2, pp. 36-37, 2006.
[39] T. Sourmail, “Coatings for Turbine Blades,” Jan-2009. [Online]. Available: http://www.msm.cam.ac.uk/phase-trans/2003/Superalloys/coatings/index.html.
[40] M. Naeem, R. Singh, and D. Probert, “Consequences of aero-engine deteriorations for military aircraft,” *Applied Energy,*, vol. 70, no. 2, pp. 103-133, 2001.
[41] G. E. Dieter, *Mechanical Metallurgy*, SI Metric ed 3 Revised ed. McGraw-Hill Higher Education, 1989.
[42] Z. Mazur, A. Luna-Ramírez, J. A. Juárez-Islas, and A. Campos-Amezcua, “Failure analysis of a gas turbine blade made of Inconel 738LC alloy,” *Engineering Failure Analysis*, vol. 12, no. 3, pp. 474-486, 2005.

[43] S.-gab Kim, Y.-ha Hwang, T.-gu Kim, and C.-min Shu, “Failure analysis of J85 Engine turbine blades,” *Engineering Failure Analysis,*, vol. 15, no. 4, pp. 394-400, 2008.
[44] J. Zhao, S.-qi Han, H.-bo Gao, and L. Wang, “Remaining life assessment of a CrMoV steel using the Z-parameter method,” *International Journal of Pressure Vessels and Piping,*, vol. 81, no. 9, pp. 757-760, 2004.
[45] G. Marahleh, A. R. I. Kheder, and H. F. Hamad, “Creep-life prediction of service-exposed turbine blades,” *Materials Science*, vol. 42, no. 4, pp. 476-481, Jul. 2006.
[46] J. A. Daleo and J. R. Wilson, “GTD111 Alloy Material Study,” *Journal of Engineering for Gas Turbines and Power*, vol. 120, pp. 375-382, 1998.
[47] A. K. Koul and R. Castillo, “Assessment of service induced microstructural damage and its rejuvenation in turbine blades,” *Metallurgical Transactions A*, vol. 19, pp. 2049-2066, Aug. 1988.
[48] J. A. Daleo, K. A. Ellison, and D. H. Boone, “Metallurgical Considerations for Life Assessment and the Safe Refurbishment and Requalification of Gas Turbine Blades,” *Journal of Engineering for Gas Turbines and Power*, vol. 124, no. 3, pp. 571-579, Jul. 2002.
[49] P. Henderson and J. Komenda, “A Metallographic Technique for High Temperature Creep Damage Assessment in Single Crystal Alloys,” *Journal of Engineering for Gas Turbines and Power*, vol. 121, no. 4, pp. 683-686, Oct. 1999.
[50] J. A. Daleo, K. A. Ellison, and D. A. Woodford, “Application of Stress Relaxation Testing in Metallurgical Life Assessment Evaluations of GTD111 Alloy Turbine Buckets,” *Journal of Engineering for Gas Turbines and Power*, vol. 121, no. 1, pp. 129-137, 1999.
[51] S. Watson, “Creep Prediction and Extrapolation,” 2004.
[52] J. F. R. Sobrinho and L. O. Bueno, “Correlation between Creep and Hot Tensile Behaviour for 2.25Cr-1Mo Steel from 500 to 700 deg C. Part 2: An Assessment According to Different Parameterization Methodologies,” *Revista Materia*, vol. 10, no. 3, pp. 463-471, 2005.
[53] M. Naeem, “Implication of aero-engine deterioration for a military aircraft’s performance.,” Cranfield University, United Kingdom, 1999.
[54] G. F. Harrison and M. R. Winstone, “Modelling and lifing of structural materials for future aeroengine components,” *Advanced Performance Materials*, vol. 3, no. 3-4, pp. 263-278, 1996.
[55] B. J. Cane and P. F. Aplin, “Creep Life Assessment Method,” *Journal of Strain Analysis*, vol. 29, no. 3, pp. 225-232, 1994.
[56] J. Harris, “Fuzzy logic methods in fatigue and creep,” *Journal of Strain Analysis*, vol. 36, no. 4, pp. 411-420, 2001.
[57] J. Li and A. Dasgupta, “Failure-mechanism models for creep and creep rupture,” *IEEE Transactions on Reliability*, vol. 42, no. 3, pp. 339-353, Sep. 1993.
[58] F. C. Monkman and N. J. Grant, “An empirical relationship between rupture life and minimum creep rate,” in *Deformation and Fracture at Elevated Temperatures*, Boston: MIT Press, 1965.
[59] F. Dobes and K. Milicka, “Relation between minimum creep rate and time to fracture,” *Met Sci*, vol. 10, no. 11, pp. 382-384, Nov. 1976.
[60] A. K. Koul, R. Castillo, and K. Willett, “Creep life predictions in nickel-based superalloys,” *Materials Science and Engineering*, vol. 66, no. 2, pp. 213-226, Sep. 1984.
[61] B. Wilshire and D. R. J. Owen, *Recent Advances in Creep and Fracture of Engineering Materials and Structures*. Pineridge Press Ltd, 1982.
[62] M. Evans, “Predicting times to low strain for 1CrMoV rotor steel using a 6 theta projection technique,” *Journal of Materials Science*, vol. 35, no. 12, pp. 2937-2948, 2000.

[63] K. Monden, “Creep Life Assessment of Tin-Based Lead-Free Solders Based on Imaginary Initial Strain Rate,” *Journal of Electronic Materials*, vol. 36, pp. 1691-1696, Sep. 2007.
[64] E. Pink, “Physical Significance and Reliability of Larson Miller and Manson Haferd Parameters,” *Material Sceince and Technology*, vol. 10, no. 4, pp. 340-344, 1994.
[65] H. Nickel, P. J. Ennis, and W. J. Quadakkers, “The Creep Rupture Properties of 9% Chromium Steels and the Influence of Oxidation on Strength,” *Mineral Processing and Extractive Metallurgy Review*, vol. 22, pp. 181-195, Jan. 2001.
[66] L. O. Bueno and V. L. Sordi, “Creep behaviour of Fe–Mn–Al steel from 500 °C to 800 °C: Part 2: Aspects of rupture strength and parametric analysis,” *Materials Science and Engineering: A*, vol. 483-484, pp. 560-563, 15 2008.
[67] D. R. Eno and G. A. Young, “A Unified View of Engineering Creep Parameters,” in *Proceeding of Pressure Vessel and Piping Division Conference*, 2008, vol. Chicago, Illinois.
[68] M. G. Leinster, “A method of creep rupture data extrapolation based on physical processes,” *International Journal of Pressure Vessels and Piping*, vol. 85, no. 10, pp. 701-710, Oct. 2008.
[69] J. Betten, S. Sklepus, and A. Zolochevsky, “A Microcrack Description of Creep Damage in Crystalline Solids with Different Behaviour in Tension and Compression,” *International Journal of Damage Mechanics*, vol. 8, no. 3, pp. 197 - 232, Jul. 1999.
[70] J. L. Chaboche, “Continuum damage mechanics: Present state and future trends,” *Nuclear Engineering and Design*, vol. 105, no. 1, pp. 19-33, Dec. 1987.
[71] B. J. Cane, “Remaining creep life estimation by strain assessment on plant,” *International Journal of Pressure Vessels and Piping*, vol. 10, no. 1, pp. 11-30, Jan. 1982.
[72] M. . Wood, “Gas turbine hot section life assessment and extension: status and issues,” *OMMI*, vol. 3, no. 2, 2004.
[73] M. O. Dedekind, “Implementation of creep-fatigue model into finite element code to assess cooled turbine blade,” *International Journal of Pressure Vessels and Piping*, vol. 59, no. 1-3, pp. 13-19, 1994.
[74] R. Hagmeijer et al., “Towards integrated analysis of gas turbine components for life prediction,” National Aerospace Laboratory, Unclassified NLR-TP-2000-196, May 2000.
[75] T. Tinga, W. P. J. Visser, and W. B. Wolf, “Integrated Lifing Analysis for Gas Turbine Components,” National Aerospace Laboratory, Amsterdam, NLR-TP-2000-049, 2000.
[76] D. A. Rosario and R. M. Tilley, “LIFE ASSESSMENT OF CRITICAL BOILER AND TURBINE COMPONENTS USING EPRI’s Creep-FatiguePro SOFTWARE.”
[77] S. Sampath, L. Marinai, R. Singh, and A. Gulati, “``SMART ENGINE'': A Gas Turbine Fault Diagnostics and Life Management Tool,” *ASME Conference Proceedings*, vol. 2006, no. 42401, pp. 639-648, Jan. 2006.
[78] G. Cerri, G. Marco, and S. Borghetti, “Hot Section Life Assessment by a Creep Model to Plan Gas Turbine Based Power Plant Electricity Production,” in *The Futue of Gas Turbine Technology, 3rd International Conference*, 2006, vol. Brussel, Belgium.
[79] Y. Assoul, S. Benbelaid, V. S. Zeravcic, G. Bakic, and M. Dukic, “Life Estimation of First Stage High Pressure Gas Turbine Blades,” *Scientific Technical Review*, vol. LVIII, no. 2, p. 8, 2008.
[80] D. S. Pascovici, “Thermo economic and risk analysis for advance long range aero engines,” PhD Thesis, Cranfield University, Cranfield, UK, 2008.
[81] S. Eshati, M. F. Abdul Ghafir, P. Laskaridis, and Y. G. Li, “Impact of operating condition and design parameters on gas turbine hot section (GT2010-22334),”

presented at the Proceedings of ASME Turbo Expo 2010: Power for Land, Sea and Air, Glasgow, UK, 2010.
[82] W. Mohamed, S. Eshati, P. Pilidis, S. O. T. Ogaji, P. Laskaridis, and A. Nasir, “A method to evaluate the impact of power demand on HPT blade creep life (GT2011-45092),” presented at the Proceedings of ASME Turbo Expo 2011: Power for Land, Sea and Air, Vancouver, Canada, 2011.
[83] M. F. Abdul Ghafir, Y. G. Li, R. Singh, K. Huang, and X. Feng, “Impact of operating and health conditions on aero gas turbine hot section creep life using a creep factor approach (GT2010-22332),” presented at the Proceedings of ASME Turbo Expo 2010: Power for Land, Sea and Air, Glasgow, UK, 2010.
[84] P. E. DiCristoforo and M. Elledge, “Stress Redistribution for Increased Creep Life in the GE MS6001 B Second-Stage Blade,” *Journal of Engineering for Gas Turbines and Power*, vol. 126, no. 1, p. 127, 2004.
[85] M. Aghaie-Khafri and M. Hajjavady, “The effect of thermal exposure on the properties of a Ni-base superalloy,” *Materials Science and Engineering: A,*, vol. 487, no. 1-2, pp. 388-393, 25 2008.
[86] M. Aghaie-Khafri and M. Noori, “Life prediction of a Ni-base superalloy,” *Bulletin of Materials Science*, vol. 34, no. 2, pp. 305-309, Aug. 2011.
[87] H. Kaftelen and A. Baldan, “Comparative creep damage assessments using the various models,” *Journal of Materials Science*, vol. 39, pp. 4199-4210, Jul. 2004.
[88] M. Evans, “A comparative assessment of creep property predictions for a 1CrMoV rotor steel using the CRISPEN, CDM, Omega and Theta projection techniques,” *Journal of Materials Science*, vol. 39, pp. 2053-2071, 2004.
[89] A. R. Ibanez, A. Saxena, and J. Kang, “Creep deformation and rupture behaviour of direct solidified GTD 111 superalloy,” *Strength, Fracture and Complexity*, vol. 4, pp. 75-81, 2006.
[90] K. E. Bagnoli, Z. . Cater-Cyker, and B. S. Budiman, “Evaluation of the theta projection technique for estimating the remaining creep life of GTD-111DS turbine blades,” presented at the ASME Turbo Expo 2007: Power for Land, Sea and Air, Motreal, Canada, 2007, vol. GT2007-28345.
[91] A. Baldan and E. Tascioglu, “Assessment of θ-projection concept and fracture cavitation,” *Journal of Materials Science*, vol. 43, pp. 4592-4606, May 2008.
[92] J.-T. Yeom, J.-Y. Kim, Y.-S. Na, and N.-K. Park, “Creep strain and creep-life prediction for alloy 718 using the omega method,” *Metals and Materials International*, vol. 9, no. 6, pp. 555-560, Dec. 2003.
[93] A. . Miodownik, X. Li, N. Saunders, and J.-P. Schille, “Modelling of Creep in Nickel Based Superalloys,” in *Sixth International Charles Parsons Turbine Conference*, Dublin, Ireland, 2003.
[94] G. . Harrison, P. . Tranter, D. . Shepherd, and T. Ward, “Application of multi-scale modelling in aeroengine component life assessment,” *Materials Science and Engineering: A*, vol. 365, no. 1-2, pp. 247-256, Jan. 2004.
[95] D. . Sheperd, T. J. Ward, A. Wisbey, B. Vermeulen, and A. . Boyd Lee, “Life extension methods in aero-engines,” *OMMI*, vol. 3, no. 1, Apr. 2004.
[96] R. Daniel, T. Tinga, M. . Handerson, and T. J. Ward, “Deformation modelling of the single crystal superalloy CM186 LC,” National Aerospace Laboratory, Netherland, NLR-TP-2002-597, 2002.
[97] J. Cormier and G. Cailletaud, “Constitutive modelling of the creep behaviour of single crystal superalloys under non-isothermal conditions inducing phase transformation,” *Technische Mechanik*, vol. 30, no. 1-3, pp. 56-73, 2010.
[98] E. L. Robinson, “Effect of temperature variation on the creep strength of steels,” *Trans. Am. Soc. Mech. Engrs*, vol. 60, pp. 253-259.

[99] C. Rinaldi, V. Bicego, and P. P. Colombo, “Validation of CESI Blade Life Management System by Case Histories and in situ NDT,” *Journal of Engineering for Gas Turbines and Power*, vol. 128, pp. 73-80, 2006.
[100] M. F. Abdul Ghafir, Y. G. Li, L. Wang, and W. Zhang, “Impact analysis on aero-engine performance parameter variation on hot section’s creep life using creep factor approach (ISABE-2011-1609),” in *International Symposium on Air Breathing Engines*, Gothenburg, Sweden, 2011.
[101] J. Lemaitre, “How to use damage mechanics,” *Nuclear Engineering and Design*, vol. 80, no. 2, pp. 233-245, Jul. 1984.
[102] W. Qi and A. Bertram, “Anisotropic continuum damage modeling for single crystals at high temperatures,” *International Journal of Plasticity*, vol. 15, no. 11, pp. 1197-1215, 1999.
[103] W. Qi, W. Brocks, and A. Bertram, “An FE-analysis of anisotropic creep damage and deformation in the single crystal SRR99 under multiaxial loads,” *Computational Materials Science*, vol. 19, no. 1-4, pp. 292-297, Dec. 2000.
[104] W. Brocks and W. Qi, “Numerical investigation of creep damage developement in the Ni-Based superalloy IN738LC at 850C,” *Computer Modeling in Engineering & Sciences*, vol. 3, no. 3, pp. 313-320, 2002.
[105] D. W. MacLachlan and D. M. Knowles, “Creep-behavior modeling of the single-crystal superalloy CMSX-4,” *Metallurgical and Materials Transactions A*, vol. 31, no. 5, pp. 1401-1411, May 2000.
[106] D. W. MacLachlan and D. M. Knowles, “Modelling and prediction of the stress rupture behaviour of single crystal superalloys,” *Materials Science and Engineering A*, vol. 302, no. 2, pp. 275-285, Apr. 2001.
[107] V. G. Karaivanov, D. W. Mazzotta, M. K. Chyu, W. S. Slaughter, and M. A. Alvin, “Three-Dimensional Modeling of Creep Damage in Airfoils for Advanced Turbine Systems,” in *Volume 5: Structures and Dynamics, Parts A and B*, Berlin, Germany, 2008, pp. 225-234.
[108] D. W. Maclachlan and D. M. Knowles, “The effect of material behaviour on the analysis of single crystal turbine blades: Part I – Material model,” *Fatigue & Fracture of Engineering Materials & Structures*, vol. 25, no. 4, pp. 385-398, Apr. 2002.
[109] D. W. Maclachlan and D. M. Knowles, “The effect of material behaviour on the analyisis of single crystal turbine blade: Part II-component analysis,” *Fatigue and Fracture of Engineering Materials and Structures*, vol. 25, no. 4, pp. 399-409, 2002.
[110] D. . Knowles and D. . MacLachlan, “The effect of material behaviour on the analysis of single crystal turbine blades: material model development,” *Current Applied Physics*, vol. 4, no. 2-4, pp. 300-303, Apr. 2004.
[111] I. N. Vladimirov, S. Reese, and G. Eggeler, “Constitutive modelling of the anisotropic creep behaviour of nickel-base single crystal superalloys,” *International Journal of Mechanical Sciences*, vol. 51, no. 4, pp. 305-313, Apr. 2009.
[112] L. Meric, P. Poubanne, and G. Cailletaud, “Single crystal modeling for structural calculations: part I-model presentation,” *Trans. Am. Soc. Mech. Engrs*, vol. 70, pp. 133-162, 1991.
[113] Q. M. Yu, Z. F. Yue, and Z. X. Wen, “Creep damage evolution in a modeling specimen of nickel-based single crystal superalloys air-cooled blades,” *Materials Science and Engineering: A*, vol. 477, no. 1-2, pp. 319-327, Mar. 2008.
[114] L. Esposito and N. Bonora, “Time-independent formulation for creep damage modeling in metals based on void and crack evolution,” *Materials Science and Engineering: A*, vol. 510-511, no. 0, pp. 207-213, Jun. 2009.
[115] F. Ashby and B. F. Dyson, “Creep damage mechanics and micromechanisms,” in *Advances in Fracture Research*, vol. 1, Oxford: Pergamon Press, 1984, pp. 3-30.

[116] B. Dyson, “Use of CDM in Materials Modeling and Component Creep Life Prediction,” *Journal of Pressure Vessel Technology*, vol. 122, no. 3, pp. 281-296, 2000.
[117] A. Djakovic, H. C. Basoalto, B. F. Dyson, and M. McLean, “Physics based modelling of creep behaviour of aluminium alloy 2650-T8,” *Metalurgija*, vol. 11, no. 4, pp. 257-265, 2005.
[118] International Atomic Energy Agency, “Non-destructive testing for plant life assessment.,” IAEA, Training course report IAEA-TCS-26, 2005.
[119] J. Saniie, B. Panda, T. Wang, and D. T. Nagle, “Life assessment of creep degraded super alloy materials using ultrasound,” in *Ultrasonics Symposium, 1990. Proceedings., IEEE 1990*, 1990, pp. 987-990 vol.2.
[120] J. Pitkänen et al., “NDT methods for revealing anamolies and defects in gas turbine blades,” in *15th World Conference on Non-Destructive Testing*, Rome, 2000.
[121] P. Auerkari, J. Pitkänen, M. Pihkakoski, L. Muurinen, M. Kemppainen, and P. Kangas, “Maintenance of gas turbine-impact and implication for NDT,” in *European Conference on Nondestructive Testing*, Barcelona, Spain, 2002.
[122] P. Kumar Raja, V. Ganesan, T. Saravanan, S. Bagavathiappan, and K. Balasubramaniam, “Detection of micro-crack in the HP turbine blades using phase array and radiography techniques and enhancement of radiographic images by image processing,” in *National Seminar and Exhibition on Non-Destructive Evaluation*, Tiruchy, India, 2009.
[123] W. Abbasi and S. Rahman, “NDE Inspections and Lifetime Assessmentof Turbine Equipment,” in *Power-Gen International*, Orlando, Florida, 2008.
[124] J. Vagn Hansen, “Non-destructive metallography used on-site, possibilities and experience,” in *7th European Conference on Non-Destructive Testing*, Copenhagen, 1998.
[125] D. Zuljan and J. Grum, “Non-destructive metallographic analysis of surface and microstructures by means of replicas,” in *The 8th International Comference of the Slovenian Society for Non-Destructive Testing*, Slovenia, 2005, pp. 359-368.
[126] B. Neubauer and U. Wedel, “Restlife estimation of creeping component by means of replicas,” in *Advances in Life Prediction Methods*, New York: American Society of Mechancial Engineering, 1983, pp. 307-314.
[127] R. Viswanathan, “Residual life techniques for plant life extension,” *Materials Science and Engineering: A*, vol. 103, no. 1, pp. 131-139, Aug. 1988.
[128] D. J. Gooch, “Plant-life extension-remanent-life assessment of high-temperaturecomponents,” *Power Engineering Journal*, vol. 2, no. 6, pp. 323-331, Nov. 1988.
[129] S. Bret et al., “Residual life assessment and microstructure,” ECCC, Italy, ECCC Recommendation AC/MC/93, 2005.
[130] M. Vaezi and M. Soleymani, “Creep life prediction of Inconel 738 gas turbine blade,” *Journal of Applied Sciences*, vol. 9, no. 10, pp. 1950-1955, 2009.
[131] S. R. Holdsworth and R. B. Davies, “A recent advance in the assessment of creep rupture data,” *Nuclear Engineering and Design*, vol. 190, no. 3, pp. 287-296, Jun. 1999.
[132] British Standard Institute, “Guidance on the methodology for assessment-Part 1: Procedure for derivation of strength values,” British Standard Institute, UK, British Standard 6605-1:1998, Dec. 1998.
[133] British Standard Institute, “Guidance on the methodology for assessment-Part 2: Computing methods,” British Standard Institute, UK, British Standard 6605-1:1998, Nov. 1998.

[134] S. Chandra, R. Cotgrove, S. R. Holdsworth, and M. Schwienheer, “Creep rupture data assessment of Alloy 617,” in *Creep & Fracture in High Temperature Components: Design & Life Assessment Issues*, DEStech Publications, Inc, 2005.
[135] J. Bolton, “The extrapolation of creep rupture data by PD6605 - An independent case study,” *International Journal of Pressure Vessels and Piping*, vol. 88, no. 4, pp. 158-165, Apr. 2011.
[136] A. K. Koul, S. Bhanot, A. Tiku, and B. Junkin, “Improving component life prediction accuracy and reliability through physics based prognosis: A probabilistic turbine blade case study,” in *TURBOEXPO 2008*, Berlin, Germany, 2008, vol. GT 2008-51526.
[137] A. K. Koul, S. Bhanot, A. Tiku, and B. Junkin, “Importance of physics-based prognosis for improving turbine reliability - RRA KB gas turbine blade case study,” in *Proceedings of POWER 2007*, Texas, USA, 2007, pp. 1-6.
[138] A. K. Koul, A. Tiku, S. Shankar, and J. Zhao, “Probabilistic creep life prediction of turbine disc (GT2010-22169),” in *Proceeding of ASME Turbo Expo 2010*, Glasgow, UK, 2010, pp. 1-6.
[139] Z. Liu, D. Mavris, and V. Volovoi, “Creep life prediction of gas turbine components under varying operating conditions,” in *ASME International Joint Power Generation Conference2001*, 2001, vol. Louisiana, USA.
[140] Z. Liu, V. Volovoi, and D. Mavris, “Probabilistic Remaining Creep Life Assessment for Gas Turbine Components under Varying Operating Conditions,” in *43rd AIAA/ASME/ASCE/AHS/ASC Structures, Structural Dynamics, and Materials Conference*, 2002, vol. Denver, Colorado, p. 1.
[141] Zhimin Liu and Dimitri Mavris, “A Methodology for Probabilistic Creep-Fatigue Life Assessment of Hot Gas Path Components,” presented at the 45th AIAA/ASME/ASCE/AHS/ASC Structures, Structural Dynamics and Materials Conference, Palm Springs, California, 2004, vol. AIAA-2004-1990.
[142] J. Wallace, R. Wang, and D. Mavris, “Creep Life Uncertainty Assessment of a Gas Turbine Airfoil,” in *44th AIAA/ASME/ASCE/AHS/ASC Structures, Structural Dynamics, and Materials Conference*, 2003, vol. Norfolk, Virginia, p. 1.
[143] M. Voigt, R. Mu cke, K. Vogeler, and M. Oevermann, “Probabilistic Lifetime Analysis for Turbine Blades Based on a Combined Direct Monte Carlo and Response Surface Approach,” 2004, pp. 327-335.
[144] T. Sourmail, H. K. D. H. Bhadeshia, and D. J. C. MacKay, “Neural network model of creep strength of austenitic stainless steels,” *Materials Science and Technology*, vol. 18, no. 6, pp. 655-663, Jun. 2002.
[145] M. C. Maritza, V. . Alberto, P. Demetrios, V. Apostolos, and C. C. Antonio, “Design of a creep resistant iron-base superalloy for Herreshoff furnaces. Part I-Mechanical properties modelling and phase diagram simulation,” *Minería y Geología*, vol. 24, no. 3, pp. 1-17, 2008.
[146] Y. S. Yoo, C. Y. Jo, and C. N. Jones, “Compositional prediction of creep rupture life of single crystal Ni base superalloy by Bayesian neural network,” *Materials Science and Engineering A*, vol. 336, no. 1-2, pp. 22-29, Oct. 2002.
[147] a. R. Ibanez, V. S. Srinivasan, and A. Saxena, “Creep deformation and rupture behaviour of directionally solidified GTD 111 superalloy,” *Fatigue & Fracture of Engineering Materials & Structures*, vol. 29, no. 12, pp. 1010-1020, Dec. 2006.
[148] O. Frovola, E. Roos, K. Maile, and W. Muller, “Representation of the heat specific creep rupture Behaviour of 9%Cr steels using neural networks,” *Transactions on Machine Learning and Data Mining*, vol. 4, no. 1, pp. 1-16, 2011.
[149] V. K. Gupta, N. Kwatra, and S. Ray, “Artificial neural network modeling of creep behavior in a rotating composite disc,” *Engineering Computations*, vol. 24, pp. 151-164, 2007.

[150] H. Jeong and D.-H. Kim, “Estimation of Creep Voids Using a Progressive Damage Model and Neural Networks,” *Research in Nondestructive Evaluation*, vol. 14, pp. 33-45, Jan. 2002.
[151] K. Zarrabi, K. W. Hendrata, and H. P. Halim, “An Artificial Neural Network Approach to Elastic-creep Life Assessment,” in *Australasian Structural Engineering Conference 2008*, Melbourne, Australia, 2008, pp. 184-191.
[152] L. . Dobrzanski, W. Sitek, M. Krupinski, and J. Dobrzanski, “Computer aided method for evaluation of failure class of materials working in creep conditions,” *Journal of Materials Processing Technology*, vol. 157-158, no. 0, pp. 102-106, Dec. 2004.
[153] L. . Dobrzanski, M. Sroka, and J. Dobrzanski, “Application of neural networks to classification of internal damage in steels working in creep service,” *Journal of Achievements in Materials and Manufacturing Engineering*, vol. 20, no. 1-2, pp. 303-306, Feb. 2007.
[154] Y. G. Li and R. Singh, “An advance gas turbine gas path diagnostic system - PYTHIA,” in *XVII International Symposium on Air Breathing Engines (ISABE)*, 2005, vol. Munich, Germany.
[155] J. G. Kaufman, *Parametric analyses of high-temperature data for aluminum alloys*. ASM International, 2008.
[156] W. Gracey, *Measurement of static pressure on aircraft*. Langley Research Center: NACA, 1958.
[157] W. Blake, *Jet Transport Performance Methods*. [[Seattle]]: Boeing Commercial Airplanes, 2009.
[158] EUROCONTROL Experimental Centre, “User manual for the base of aircraft data (BADA) revision 3.7,” European Organisation for Safety of Air Navigation, France, Technical/Scientific 11/03/08-08, March 2019.
[159] K. W. Ramsden, *Gas turbine fundamentals and turbomachinery MSc course notes*. UK: Cranfield University, 2009.
[160] D. R. Kirk, “MAE 4261 Air-Breathing Engine Lecture: Velocity triangles example,” Florida Institut of Technology, 03-Nov-2009.
[161] F. E. Wu, “Aero-engine’s life evaluated for combined creep and fatigue, and extended by trading-off excess thrust,” PhD Thesis, Cranfield University, Cranfield, UK, 1994.
[162] J. H. Horlock and L. Torbidoni, “Turbine Blade Cooling: The Blade Temperature Distribution,” *Proceedings of the Institution of Mechanical Engineers, Part A: Journal of Power and Energy*, vol. 220, no. 4, pp. 343-353, 2006.
[163] M. . Holland and T. . Thake, “Rotor blade cooling in high pressure turbines,” *J. Aircraft*, vol. 17, pp. 418-418, 1980.
[164] Je-Chin Han, Sandip Dutta, and V. E. Srinath, *Gas Turbine Heat Transfer and Cooling Technology*, vol. 1. London: Taylor & Francis, 2000.
[165] H. I. H. Saravanamuttoo, P. G. F. C. Rogers, H. Cohen, and P. P. Straznicky, *Gas Turbine Theory*, 6th ed. Prentice Hall, 2008.
[166] B.-M. Genick, *Basics of fluid mechanics*, Version 0.3.0.4 ed. Chicago, IL: Free Software Foundation, Inc., 2011.
[167] F. P. Incropera and D. P. DeWitt, *Fundamentals of Heat and Mass Transfer, 5th Edition*, 5th ed. Wiley, 2001.
[168] F. R. Larson and J. Miller, “A time-temperature relationship for rupture and creep stresses,” *Trans. Am. Soc. Mech. Engrs*, vol. 74, pp. 765-775, 1952.
[169] C. M. Bishop, *Neural Networks for Pattern Recognition*, 1st ed. Oxford University Press, USA, 1996.
[170] R. J. Schalkoff, *Artificial Neural Networks*. McGraw-Hill Companies, 1997.
[171] H.K.D.H Bhadeshia, “Neural Network in Materials Science,” *ISIJ International*, vol. 39, no. 10, pp. 966-979, 1999.

[172] H. K. D. . Bhadeshia, “Neural Networks and Information in Materials Science,” *Statistical Analysis and Data Mining*, vol. 1, pp. 296-305, 2009.
[173] H. K. D. . Bhadeshia, R. . Dimitriu, S. Forsik, J. H. Pak, and J. H. Ryu, “Performance of neural networks in materials science,” *Material Secinece and Technology*, vol. 25, no. 4, pp. 504-510, 2009.
[174] W. Sha and K. L. Edwards, “The use of artificial neural networks in materials science based research,” *Materials & Design*, vol. 28, no. 6, pp. 1747-1752, 2007.
[175] A. J. Skinner and J. Q. Broughton, “Neural networks in computational materials science: training algorithms,” *Modelling and Simulation in Materials Science and Engineering*, vol. 3, no. 3, pp. 371-390, May 1995.
[176] J. Schumann, *Applications of Neural Networks in High Assurance Systems*. Springer, 2010.
[177] K. Gurney, *Introduction to Neural Networks*. CRC Press, 1997.
[178] E. Kandel, J. Schwartz, and T. Jessell, *Principles of Neural Science*, 4th ed. McGraw-Hill Medical, 2000.
[179] S. Haykin, *Neural Networks: A Comprehensive Foundation*, 2nd ed. Pearson Education, 1997.
[180] P. S. Churchland and T. J. Sejnowski, *The Computational Brain*. A Bradford Book, 1994.
[181] P. Dayan, “Unsupervised learning,” 23-Aug-2011. [Online]. Available: http://www.gatsby.ucl.ac.uk/~dayan/papers/dun99b.pdf.
[182] S. Becker, “Unsupervised learning procedures for neural network,” *International Journal of Neural System*, vol. 2, pp. 17-33, 1991.
[183] J. T. Tou, “Feature extraction in pattern recognition,” *Pattern Recognition*, vol. 1, no. 1, pp. 3-11, Jul. 1968.
[184] Z. Zainuddin and P. Ong, “Function approximation using artificial neural networks,” *WSEAS Transaction on Mathematics*, vol. 7, no. 6, pp. 333-338, Jun. 2008.
[185] G. Cybenko, “Approximation by superposition of sigmoidal function,” *Mathematics Control Signal Systems*, vol. 2, pp. 303-314, 1989.
[186] K. Hornik, “Multilayer feedforward networks are universal approximators,” *Neural Networks*, vol. 2, no. 5, pp. 359-366, 1989.
[187] D. E. Rumelhart, G. E. Hinton, and R. J. Williams, “Learning representations by back-propagating errors,” *Nature*, vol. 323, no. 6088, pp. 533-536, Oct. 1986.
[188] S. Samarasinghe, *Neural Networks for Pattern Recognition in Scientific Data*, 1st ed. Auerbach Publications, 2006.
[189] M. T. Hagan, H. B. Demuth, and M. H. Beale, *Neural Network Design*, Har/Dis. PWS Pub. Co., 1995.
[190] M. Moller, “A scaled conjugate gradient algorithm for fast supervised learning,” *Neural Networks*, vol. 6, no. 4, pp. 525-533, 1993.
[191] Y. G. Li, P. Pilidis, and M. A. Newby, “An adaptation approach for gas turbine design-point performance simulation,” *Journal of Engineering for Gas Turbines and Power*, vol. 128, no. 4, pp. 789-795, Oct. 2006.
[192] S. O. T. Ogaji, S. Sampath, R. Singh, and S. D. Probert, “Parameter selection for diagnosing a gas-turbine’s performance-deterioration,” *Applied Energy*, vol. 73, no. 1, pp. 25-46, 2002.
[193] Y. Le Cun, “Efficient learning and second-order method,” Denver, Colorado, United States, 1993.
[194] H. Demuth, M. Beal, and M. Hagan, *Neural Network Toolbox 6 User’s Guide*. Massachussetts: Mathwork Inc., 2009.
[195] W. S. Sarle, “Stopped Training and Other Remedies for Overfitting,” *PROCEEDINGS OF THE 27TH SYMPOSIUM ON THE INTERFACE OF COMPUTING SCIENCE AND STATISTICS*, p. 352--360, 1995.

[196] A. Stamatis, K. Mathioudakis, and K. D. Papailiou, “Adaptive Simulation of Gas Turbine Performance,” *Journal of Engineering for Gas Turbines and Power*, vol. 112, no. 2, pp. 168-175, Apr. 1990.
[197] B. Lambiris, K. Mathioudakis, A. Stamatis, and K. Papailious, “Adaptive Modeling of Jet Engine Performance with Aplication to Condition Monitoring,” *Journal of Propulsion and Power*, vol. 10, no. 6, pp. 890-896, 1994.
[198] C. Kong, J. Ki, and M. Kang, “A New Scaling Method for Component Maps of Gas Turbine Using System Identification,” *Journal of Engineering for Gas Turbines and Power*, vol. 125, no. 4, pp. 979-985, Oct. 2003.
[199] B. Roth, D. L. Doel, D. Mavris, and D. Beeson, “High-Accuracy Matching of Engine Performance Models to Test Data,” *ASME Conference Proceedings*, vol. 2003, no. 36843, pp. 129-137, Jan. 2003.
[200] E. L. Gatto, Y. G. Li, and P. Pilidis, “Gas Turbine Off-Design Performance Adaptation Using a Genetic Algorithm,” *ASME Conference Proceedings*, vol. 2006, no. 42371, pp. 551-560, Jan. 2006.
[201] L. Wang, Y. G. Li, and R. Singh, “Gas Turbine Off-Design Performance Model Improvement for Diagnostics (CM-2009-970),” presented at the Sixth International Conference on Condition Monitoring and Machinery Failure Prevention Technologies, 2009.
[202] C. Kong, S. Kho, and J. Ki, “Component Map Generation of a Gas Turbine Using Genetic Algorithms,” *ASME Conference Proceedings*, vol. 2004, no. 41723, pp. 469-474, Jan. 2004.
[203] M. Gholamrezaei and K. Ghorbanian, “Compressor map generation using a feed-forward neural network and rig data,” *Proceedings of the Institution of Mechanical Engineers, Part A: Journal of Power and Energy*, vol. 224, no. 1, pp. 97-108, Jan. 2010.
[204] Y. G. Li, M. F. Abdul Ghafir, L. Wang, R. Singh, K. Huang, and X. Feng, “Non–linear multiple points gas turbine off-design performance adaptation using a genetic algorithm (GT2010-22285),” presented at the Proceedings of ASME Turbo Expo 2010, Glasgow, UK, 2010.
[205] P. P. Walsh and P. Fletcher, *Gas Turbine Performance*, vol. 2. USA: Blackwell Publishing, 2004.
[206] G. R. Guenette, G. Pappas, and A. H. Epstein, “The Influence of Non-Uniform Spanwise Inlet Temperature on Turbine Rotor Heat Transfer,” in *AGARD Heat Transfer and Cooling in Gas Turbine*, 1992, vol. 527, pp. 5-1-5-10.
[207] S. Colantuoni, A. Colella, L. Di Nola, D. Carbone, and D. Marotta, “Aero-Thermal Design of a Cooled Transonic NGV and Comparison with Experimetal Result,” in *AGARD Heat Transfer and Cooling in Gas Turbine*, 1992, vol. Turkey, pp. 33-1-33-25.
[208] N. P. Padture, M. Gell, and E. H. Jordan, “Thermal Barrier Coatings for Gas-Turbine Engine Applications,” *Science*, vol. 296, no. 5566, pp. 280 -284, Apr. 2002.
[209] Y. G. Li, “Gas Turbine Performance and Health Status Estimation Using Adaptive Gas Path Analysis,” *Journal of Engineering for Gas Turbines and Power*, vol. 132, no. 4, pp. 041701-9, Apr. 2010.
[210] S. . Suhr, “Preliminary turboshaft engine design methodology for rotorcraft application,” M.Sc, Georgia Institute of Technology, USA, 2006.
[211] P. Pilidis, *Gas turbine theory and performance MSc. course note*. Cranfield, UK: Cranfield University, 2007.
[212] MathWave Technologies, “EasyFit 5.5 User’s Manual.” MathWave Technologies, 2004.
[213] R. J. . Dyson and D. L. Doel, “CF6-80 condition monitoring-the engine manufacturer’s involvement in data acquisition and analysis. AIAA-84-1412,” *American Institute of Aeronautics and Astronautics*, 1984.

[214] Federal Aviation Administration, “Code of Federal Regulation, Tittle 14 Part 43, Appendix E: Altimeter System Test and Installation,” FAA, Washington, USA, Code of Federal Regulation 14CFR, Part 43, Jan. 2006.
[215] P. S. Mann, *Introductory Statistics, 5Th Ed*. Wiley India Pvt. Ltd., 2007.

Appendix A : Algorithm for the Integrated Creep Life Prediction Model

LIST OF SYMBOLS

$\%T_{drop}$	Temperature drop percentage of each turbine stage
ΔT_{ISA}	Ambient temperature deviation from ISA condition
ΔV_{Axial}	Blade axial velocity difference
ΔV_{TanMid}	Tangential velocity difference at blade mid
$\Delta V_{TanRoot}$	Tangential velocity difference at blade root
Δp_{Mid}	Blade mid static pressure difference
Δp_{Tip}	Blade tip static pressure difference
A_{AnAve}	Blade average annulus area
$A_{AnSec1/2RDS}$	Root-mid blade section annulus area
$A_{AnSecTDS1/2}$	Mid-tip blade section annulus area
$A_{CrosSec1/2RDS}$	Average cross section area for root-mid blade section
$A_{CrosSecTDS1/2}$	Average cross section area for mid-tip blade section
A_{In}	Annulus area at inlet of blade
A_{Out}	Annulus area at outlet of blade
AR	Blade angle ratio
BMP_{Root}	Pressure bending moment about blade root
BMP_{mid}	Pressure bending moment about blade mid
$BM_{ResAxMid}$	Blade mid resulting bending moment at axial direction
$BM_{ResAxRoot}$	Blade root resulting bending moment at axial direction
$BM_{ResTanMid}$	Blade mid resulting bending moment at tangential direction
$BM_{ResTanRoot}$	Blade root resulting bending moment at tangential direction
BMV_{AxMid}	Axial momentum bending moment about blade mid
BMV_{AxRoot}	Axial momentum bending moment about blade root
BMV_{TanMid}	Tangential momentum bending moment about blade mid
$BMV_{TanRoot}$	Tangential momentum bending moment about blade root
C	Larson Miller constant
$CF_{1/2Height}$	Accumulated centrifugal force at blade mid
$CF_{1/2RDS}$	Centrifugal force for root-mid blade section
CF_{M}	Mission Creep Factor
$CF_{M\ Overall}$	Overall mission Creep Factor
CF_{RDS}	Accumulated centrifugal force at blade root
CF_{Shroud}	Centrifugal force of the shroud
CF_{TDS}	Accumulated centrifugal force at blade tip
$CF_{TDS1/2}$	Centrifugal force for mid-tip blade section
CP_{hot}	Specific heat at constant pressure for hot gas
CP_{cold}	Specific heat at constant pressure for cold gas
CP_{cold}	Specific heat of cold gas
H	Blade convective heat transfer coefficient
H_{Sec}	Blade section convective heat transfer coefficient
I_{maxMid}	Blade maximum mid-section second moment of area
$I_{maxRoot}$	Blade maximum root-section second moment of area
I_{minMid}	Blade minimum mid-section second moment of area
$I_{minRoot}$	Blade minimum root-section second moment of area
L_C	Predicted creep life

$L_{C\ 25\%}$	Predicted creep life at the 25% distance of the blade root
$L_{C\ 75\%}$	Predicted creep life at the 25% distance of the blade root
$L_{C\ M}$	Mission/operation nominal creep life
L_{CMid}	Predicted creep life at the blade mid
$L_{C\ Min}$	Minimum predicted creep life
L_{CRoot}	Predicted creep life at the blade root
$L_{C\ Overall}$	Overall nominal creep life
L_{Ref}	User defined reference point minimum predicted creep life
L_{Rem}	Blade remnant life
LF	Life fraction
LF_M	Mission/operation life fraction
$LF_{Overall}$	Overall life fraction
LMP	Larson-Miller parameter
LR	Lapse rate
$LU\%$	Life usage percentage
M	Mach number
M_{XXMid}	Blade mid bending moment about blade direction X
M_{XXRoot}	Blade mid bending moment about blade direction Y
N	Rotational speed
N_b	Number of blade
N_{design}	Absolute rotational speed
NGV	Nozzle guide vane
NGV_{PR}	NGV pressure recovery
$NGV_{mass\ frac}$	NGV coolant stage mass fraction
Nu	Blade Nusselt number
Nu_{Sec}	Blade section Nusselt number
Nu_g^*	Nominal mean Nusselt number
$Nu_g^*{}_{Sec}$	Average nominal mean Nusselt number of each blade section
$Nu_g^*{}_{bottom}$	Blade section bottom nominal mean Nusselt number
$Nu_g^*{}_{top}$	Blade section top nominal mean Nusselt number
OH	Operating hour
$OH_{Overall}$	Overall operating hour
OH_{Tot}	Total operating hour
P_{hz}	Pressure at the given altitude
$P_{oINStage}$	Blade inlet stagnation pressure
P_{oNGV}	NGV inlet stagnation pressure
P_{oOUT}	Blade outlet stagnation pressure
$P_{oOUTStage}$	Blade outlet stagnation pressure
P_{trop}	Pressure at the corresponding Tropopause temperature
PCN	Relative compressor rotational speed
$PF_{1/2RDS}$	Root-mid blade section pressure force
$PF_{TDS1/2}$	Mid-tip blade section pressure force
Pr	Prandtl number
Q_{Guess}	Guess value of $m\sqrt{T_o}/(AP_o)$
$Q_{RotorIn}$	Blade inlet $m\sqrt{T_o}/(AP_o)$
$Q_{RotorOut}$	Blade outlet $m\sqrt{T_o}/(AP_o)$
Q_{Target}	$m\sqrt{T_o}/(AP_o)$ obtained from Pressure Bending Moment Model

R	Idea gas constant
$RTDF$	Radial temperature distribution factor
Re_{Sec}	Average Reynolds number of each blade section
Re	Reynolds number
Re_{bottom}	Blade section bottom Reynolds number
Re_{top}	Blade section top Reynolds number
R_k	Ratio between the blade section wall temperature and the gas temperature
$Rotor_{massfrac}$	Blade mass fraction
SF_{ac}	Safety factor
$Suth$	Sutherland constant
Th_{TBC}	Thickness of thermal barrier coating
T_{hz}	Temperature at a given altitude
T_{BurIn}	Burner inlet temperature
T_{CiSec}	Blade section inlet coolant temperature
T_{CoSec}	Blade section coolant exit temperature
$T_{CoolantExit}$	Coolant exit temperature
$T_{CoolantIn}$	Coolant inlet temperature
T_G	Blade gas temperature profile
$T_{G25\%}$	Blade gas temperature profile at 25% distance from root
$T_{G75\%}$	Blade gas temperature profile at 75% distance from root
T_{GRoot}	Blade gas temperature profile at blade root
T_{GSec}	Average gas temperature of each blade section
T_{GTip}	Blade gas temperature profile at blade tip
$T_{Gbottom}$	Blade section bottom gas temperature
T_{Gmid}	Blade gas temperature profile at blade mid
T_{Gtop}	Blade section top gas temperature
T_{ISA}	Temperature at ISA condition
T_M	Metal temperature
T_{MSec}	Blade section metal temperature
$T_{MSec\ Top}$	Upper blade section metal temperature
$T_{MSec\ Bottom}$	Lower blade section metal temperature
$T_{MixingStage}$	Blade inlet stagnation temperature before mixing
T_{NGV}	NGV metal temperature
$T_{OINstage}$	Blade inlet temperature after mixing
T_{Ref}	Combustor temperature rise
T_{SL}	Sea level temperature
T_{drop}	Temperature drop across the turbine
T_{io}	Reference temperature used in the Sutherland equation
T_{max}	Maximum gas temperature
T_{min}	Minimum gas temperature
T_{oNGV}	NGV inlet stagnation temperature
$T_{oNGVStage}$	Stage NGV inlet stagnation temperature
T_{oOUT}	Turbine outlet stagnation temperature
$T_{oOUTStage}$	Blade outlet stagnation temperature
T_{trop}	Tropopause temperature
$U_{25\%In}$	Blade speed at 25% root of the blade inlet
$U_{25\%Out}$	Blade speed at outlet of 25% distance from root
$U_{75\%In}$	Blade speed at 75% root of the blade inlet

$U_{75\%Out}$	Blade speed at outlet of 75% distance from root
U_{MidIn}	Blade speed at the mid of the blade inlet
U_{MidOut}	Blade speed at the tip of the blade outlet
U_{RootIn}	Blade speed at the root of the blade inlet
$U_{RootOut}$	Blade speed at the tip of the blade outlet
U_{TipIn}	Blade speed at the tip of the blade inlet
U_{TipOut}	Blade speed at the tip of the blade outlet
$V_{Abs25\%In}$	Blade absolute inlet velocity at 25% distance from root
$V_{Abs25\%Out}$	Blade absolute outlet velocity at 25% distance from root
$V_{Abs75\%In}$	Blade absolute inlet velocity at 75% distance from root
$V_{Abs75\%Out}$	Blade absolute outlet velocity at 75% distance from root
V_{AbsIn}	Blade absolute inlet velocity
$V_{AbsMidIn}$	Blade mid absolute inlet velocity
$V_{AbsMidOut}$	Blade mid absolute outlet velocity
V_{AbsOut}	Blade absolute outlet velocity
$V_{AbsRootIn}$	Blade root absolute inlet velocity
$V_{AbsRootOut}$	Blade root absolute outlet velocity
$V_{AbsTipIn}$	Blade tip absolute inlet velocity
$V_{AbsTipOut}$	Blade tip absolute outlet velocity
V_{AxIn}	Blade inlet axial velocity
V_{AxOut}	Blade outlet axial velocity
V_{CAS}	Calibrated air speed
$VF_{Ax1/2RDS}$	Momentum force due to axial velocity difference of root-mid blade section
$VF_{AxTDS1/2}$	Momentum force due to axial velocity difference of mid-tip blade section
$VF_{Tan1/2RDS}$	Momentum force due to tangential velocity difference for root-mid blade section
$VF_{TanTDS1/2}$	Momentum force due to tangential velocity difference for mid-tip blade section
V_{TAS}	True air speed
$V_{Tan25\%In}$	Blade tangential inlet velocity at 25% distance from root
$V_{Tan75\%In}$	Blade tangential inlet velocity at 75% distance from root
V_{TanIn}	Blade tangential inlet velocity
$V_{TanMidIn}$	Blade mid tangential inlet velocity
$V_{TanMidOut}$	Blade mid tangential outlet velocity
$V_{TanRootIn}$	Blade root tangential inlet velocity
$V_{TanRootOut}$	Blade root tangential outlet velocity
$V_{TanTipIn}$	Blade tip tangential inlet velocity
$V_{TanTipOut}$	Blade tip tangential outlet velocity
$W_{TanTipOut}$	Blade tip relative tangential outlet velocity
W_{TipIn}	Gas relative velocity at blade inlet
W_{TipOut}	Gas relative velocity at blade outlet
X	Constant used in the Heat Transfer Data for Conventional Blade Profile plot
X_{BckMid}	X distance between back of the blade to the blade mid CG
$X_{BckRoot}$	X distance between back of the blade to the blade root CG
X_{LEMid}	X distance between LE to the blade mid CG
X_{LERoot}	X distance between LE to the blade root CG
X_{Sec}	Average constant X of each blade section
X_{TEMid}	X distance between TE to the blade mid CG

X_{TERoot}	X distance between TE to the blade root CG
X_{bottom}	Blade section bottom constant X
X_{top}	Blade section top constant X
Y	Exponent used for calculating the empirical Nusselt number
Y_{BckMid}	Y distance between back of the blade to the blade mid CG
$Y_{BckRoot}$	Y distance between back of the blade to the blade root CG
Y_{LEMid}	Y distance between LE to the blade mid CG
Y_{LERoot}	Y distance between LE to the blade root CG
Y_{Sec}	Average constant Y of each blade section
Y_{TEMid}	Y distance between TE to the blade mid CG
Y_{TERoot}	Y distance between TE to the blade root CG
Y_{bottom}	Blade section bottom constant Y
Y_{top}	Blade section top constant Y
a_s	Speed of sound
c	Blade chord
$c_{25\%}$	Blade chord at 25% distance from root
$c_{75\%}$	Blade chord at 75% distance from root
c_{Mid}	Blade chord at mean
c_{Root}	Blade chord at root
c_{Sec}	Average chord of each blade section
c_{Tip}	Blade chord at tip
c_{bottom}	Blade section bottom chord
c_{top}	Blade section top chord
g	Acceleration of gravity
$h_{1/2RDS}$	Blade height for root-mid blade section
h_{Sec}	Height of the blade section
$h_{TDS1/2}$	Blade height for mid-tip blade section
h_{blade}	Blade height
$h_{trop(ISA)}$	Tropopause altitude at ISA condition
h_{trop}	Tropopause altitude
h_z	Altitude
k_{GSec} / k_G	Thermal conductivity for average gas temperature profile
k_T	ISA temperature gradient with altitude below the Tropopause
k_{TBC}	Thermal conductivity of thermal barrier coating
$m_{coolant}$	Coolant mass flow
$m_{NGV}{}^*$	NGV non-dimension coolant mass flow
mg_{Area}	Blade mass flow per unit area
m_{gas}	Gas mass flow
m_{intake}	Intake mass flow
m_{shroud}	Shroud mass
$p_{25\%}$	Blade outlet static pressure at 25% distance from root
$p_{75\%}$	Blade outlet static pressure at 75% distance from root
$p_{Av1/2RDS}$	Root-mid blade section average pressure difference
$p_{AvTDS1/2}$	Mid-tip blade section average pressure difference
p_{In}	Blade inlet static pressure
p_{MidIn}	Blade mid inlet static pressure
p_{Midout}	Blade mid outlet static pressure
p_{Out}	Blade outlet static pressure

$p_{RootOut}$	Blade mid outlet static pressure
p_{TipIn}	Blade tip inlet static pressure
p_{TipOut}	Blade tip outlet static pressure
$r_{Mean1/2}$	Blade mid average radius
r_{MeanIn}	Leading edge mean radius
r_{MeanIn}	Blade leading edge mean radius
$r_{MeanOut}$	Training edge mean radius
$r_{MeanOut}$	Blade trailing edge mean radius
$r_{MeanRDS}$	Blade root average radius
$r_{MeanTDS}$	Blade tip average radius
r_{RootIn}	Leading edge blade root radius
$r_{RootOut}$	Trailing edge blade root radius
r_{TipIn}	Leading edge blade tip radius
r_{TipOut}	Trailing edge blade tip radius
$s_{25\%}$	Blade perimeter at 25% distance from root
$s_{75\%}$	Blade perimeter at 75% distance from root
s_{Mid}	Blade perimeter at mean
s_{Root}	Blade perimeter at root
s_{Sec}	Average perimeter of each blade section
s_{Tip}	Blade perimeter at tip
s_{bottom}	Blade section bottom perimeter
s_{top}	Blade section top perimeter
$t_{25\%}$	Blade outlet static temperature at 25% distance from root
$t_{75\%}$	Blade outlet static temperature at 75% distance from root
t_{Ave}	Blade average static temperature
t_{In}	Blade inlet static temperature
t_{MidOut}	Blade mid outlet static temperature
t_{Out}	Blade outlet static temperature
$t_{RootOut}$	Blade root outlet static temperature
t_{TipIn}	Blade tip inlet static temperature
t_{TipOut}	Blade tip outlet static temperature
$\alpha_{o25\%}$	NGV outlet angle at 25% distance from the blade root
$\alpha_{o75\%}$	NGV outlet angle at 75% distance from the blade root
α_{oMid}	NGV mid outlet angle
α_{oRoot}	NGV root outlet angle
α_{oTip}	NGV tip outlet angle
γ_{hot}	Specific heat ratio for hot gas
ε_{NGV}	NGV cooling effectiveness
ε_{R}	Blade cooling effectiveness
η_{P}	Polytrophic efficiency
η_{conv}	NGV convection effectiveness
η_{t}	Turbine isentropic efficiency
θ_{Mid}	Blade mid stager angle
θ_{Root}	Blade root stager angle
μ_{Ave}	Blade average gas viscosity
μ_{o}	Reference viscosity used in Sutherland equation
ρ_{hz}	Density at a given altitude
ρ_{Ave}	Blade average gas density

ρ_{ISA}	Density at ISA condition
ρ_{SL}	Sea level density
ρ_{blade}	Blade density
ρ_g	Blade outlet gas density
ρ_{gIn}	Blade inlet gas density
ρ_{trop}	Density at the corresponding Tropopause temperature
$\sigma_{1/2Height}$	Centrifugal stress at blade mid
σ_{BckMid}	Back of the blade stress at blade mid
$\sigma_{BckRoot}$	Back of the blade stress at blade root
σ_{LEMid}	LE stress at blade mid
σ_{LERoot}	LE stress at blade root
σ_{MaxMid}	Maximum stress at blade mid
$\sigma_{MaxRoot}$	Maximum stress at blade root
σ_{RDS}	Centrifugal stress at blade root
σ_{TDS}	Centrifugal stress at blade tip
σ_{TEMid}	TE stress at blade mid
σ_{TERoot}	TE stress at blade root
$\sigma_{TotBckMid}$	Back of the blade total stress at blade mid
$\sigma_{TotBckRoot}$	Back of the blade total stress at blade root
$\sigma_{TotLEMid}$	LE total stress at blade mid
$\sigma_{TotLERoot}$	LE total stress at blade root
$\sigma_{TotTEMid}$	TE total stress at blade mid
$\sigma_{TotTERoot}$	TE total stress at blade root
$\sigma_{max25\%Root}$	Maximum stress at 25% distance of the blade root
$\sigma_{max75\%Root}$	Maximum stress at 75% distance of the blade root
φ_{NGV}	Coolant mass flow percentage that enters NGV
μ	Blade outlet as viscosity
ω	Angular velocity
α_1	Blade inlet gas relative angle
α_2	Blade outlet angle
$\alpha_{2\ 25\%}$	Blade outlet angle at 25% distance from the blade root
$\alpha_{2\ 75\%}$	Blade outlet angle at 75% distance from the blade root
α_{2Mid}	Blade mid outlet angle
α_{2Root}	Blade root outlet angle
α_{2Tip}	Blade tip outlet angle

A.1 Algorithm for the Atmospheric and Air Speed Model

The algorithm is divided into two conditions which are for altitude below Tropopause and for altitude in Tropopause.

A.1.1 For altitude below Tropopause

1. Obtain the altitude h_z, and the ambient temperature deviation from ISA condition ΔT_{ISA}
2. Calculate the Tropopause altitude, h_{trop} with LR = 6.5°/1000m.

$$h_{trop} = h_{trop(ISA)} + \frac{\Delta T_{ISA}}{LR} \quad \textbf{(A-1)}$$

3. Calculate the sea level temperature T_{SL} and density ρ_{SL}.

$$T_{SL} = T_{ISA} + \Delta T_{ISA} \quad \textbf{(A-2)}$$

$$\rho_{SL} = \frac{\rho_{ISA} \times T_{ISA}}{T_{SL}} \quad \textbf{(A-3)}$$

4. Calculate the viscosity, μ with $\gamma = 1.4$

$$\mu = \frac{\gamma - 1}{\gamma} \quad \textbf{(A-4)}$$

5. Calculate the temperature at the given altitude, T_{hz}.

$$T_{hz} = T_{SL} - (LR \times h_z) \quad \textbf{(A-5)}$$

6. Calculate the density at the given altitude, ρ_{hz} with $k_T = -0.0065\,°/m$

$$\rho_{hz} = \rho_{SL}\left(\frac{T_{hz}}{T_{SL}}\right)^{-\frac{g}{k_t R}-1} \quad \textbf{(A-6)}$$

7. Calculate the pressure at the given altitude, P_{hz}.

$$P_{hz} = P_{ISA}\left(\frac{T_{hz}}{T_{SL}}\right)^{-\frac{g}{k_t R}} \quad \textbf{(A-7)}$$

8. Calculate TAS, V_{TAS} from given CAS, V_{CAS}

$$V_{TAS} = \left[\frac{2}{\mu}\frac{P}{\rho}\left\{\left(1 + \frac{P_{ISA}}{P}\left[\left(1 + \frac{\mu}{2}\frac{\rho_{ISA}}{P_{ISA}}{V_{CAS}}^2\right)^{1/\mu} - 1\right]\right)^{\mu} - 1\right\}\right]^{1/2} \quad \textbf{(A-8)}$$

9. Calculate the speed of sound,a_s

$$a = \sqrt{\gamma R T_{hz}} \quad \textbf{(A-9)}$$

10. Calculate the Mach number, M

$$M = \frac{V_{TAS}}{a_s} \quad \textbf{(A-10)}$$

A.1.2 For altitude in Tropopause

1. Obtain the altitude h_z, and the ambient temperature deviation from ISA condition ΔT_{ISA}
2. Calculate the Tropopause altitude, h_{trop} using Equation (A-1)
3. Calculate sea level temperature T_{SL} and density ρ_{SL} using Equation (A-2) and (A-3) respectively
4. Calculate the viscosity, μ using Equation (A-4)
11. Take the temperature at the given altitude, T_{hz} to be equal to Tropopause temperature T_{trop} which is 216.65 °K
12. Calculate the density at the corresponding Tropopause temperature, ρ_{trop}

$$\rho_{trop} = \rho_{SL}\left(\frac{T_{trop}}{T_{SL}}\right)^{-\frac{g}{k_t R}-1} \quad \textbf{(A-11)}$$

13. Calculate the density at the given altitude, ρ_{hz}.

$$\rho_{hz} = \rho_{trop} \times e^{-\left(\frac{g}{RT_{trop}}\right)(h_z - h_{trop})} \quad \textbf{(A-12)}$$

14. Calculate the pressure at the corresponding Tropopause temperature, P_{trop}

$$P_{trop} = P_{ISA}\left(\frac{T_{trop}}{T_{SL}}\right)^{-\frac{g}{k_t R}} \quad \textbf{(A-13)}$$

15. Calculate the pressure at the given altitude, P_{hz}.

$$P = P_{trop} \times e^{-\left(\frac{g}{RT_{trop}}\right)(h_z - h_{trop})} \quad \textbf{(A-14)}$$

16. Calculate TAS, V_{TAS} from given CAS, V_{CAS} using Equation (A-8)
17. Calculate the speed of sound,a_s using Equation (A-9)
18. Calculate the Mach number, M using Equation (A-10)

A.2 Algorithm for Blade Stress Model

A.2.1 Algorithm for Centrifugal Stress Model

1. Calculate the rotational speed, N

$$N = PCN \times N_{design} \quad \textbf{(A-15)}$$

2. Calculate the angular velocity, ω

$$\omega = \frac{2\pi N}{60} \quad \textbf{(A-16)}$$

3. For each stage, calculate the blade tip, mid and root average radius, $r_{MeanTDS}$, $r_{MeanRDS}$ and $r_{Mean1/2}$ (refer to Figure A.2-1)

$$r_{MeanTDS} = 0.5\left(r_{TipIn} + r_{TipOut}\right) \quad \textbf{(A-17)}$$

$$r_{MeanRDS} = 0.5(r_{RootIn} + r_{RootOut}) \quad \textbf{(A-18)}$$

$$r_{Mean1/2} = 0.5(r_{MeanTDS} + r_{MeanRDS}) \quad \textbf{(A-19)}$$

4. Calculate the LE and TE mean radius for each blade stage, r_{MeanIn} and $r_{MeanOut}$as shown in Figure A.2-1

$$r_{MeanIn} = 0.5\left(r_{TipIn} + r_{RootIn}\right) \quad \textbf{(A-20)}$$

$$r_{MeanOut} = 0.5(r_{RootIn} + r_{RootOut}) \quad \textbf{(A-21)}$$

5. Calculate for each stage the average cross section area for mid-tip and root-mid blade section, $A_{CrosSecTDS1/2}$, and $A_{CrosSec1/2RDS}$ respectively.

$$A_{CrosSecTDS1/2} = 0.5\left(A_{CrosSecTDS} + A_{CrosSec1/2}\right) \quad \textbf{(A-22)}$$

$$A_{CrosSec1/2RDS} = 0.5\left(A_{CrosSec1/2} + A_{CrosSecRDS}\right) \quad \textbf{(A-23)}$$

6. Calculate for each stage, the blade height for mid-tip and root-mid blade section $h_{TDS1/2}$ and $h_{1/2RDS}$ respectively.

$$h_{TDS1/2} = r_{meanTDS} - r_{mean1/2} \quad \textbf{(A-24)}$$

$$h_{1/2RDS} = r_{mean1/2} - r_{meanRDS} \quad \textbf{(A-25)}$$

7. Calculate for each stage, distance from section CG to rotation axis for mid-tip and root-mid blade section, $d_{CGTDS1/2}$ and $d_{CG1/2RDS}$ respectively as shown in Figure A.2-2.

$$d_{CGTDS1/2} = r_{mean1/2} + 0.5h_{TDS1/2} \quad \textbf{(A-26)}$$

$$d_{CG1/2RDS} = r_{meanRDS} + 0.5h_{1/2RDS} \quad \textbf{(A-27)}$$

8. Calculate for each stage, the centrifugal force of the shroud, CF_{Shroud}

$$CF_{Shroud} = m_{shroud} \times \omega^2 \times r_{MeanTDS} \quad \textbf{(A-28)}$$

9. Calculate for each stage, centrifugal force for mid-tip and root-mid blade section, $CF_{TDS1/2}$ and $CF_{1/2RDS}$ respectively

$$CF_{TDS1/2} = \rho_{blade} \times A_{CrosSecTDS1/2} \times \omega^2 \times d_{CGTDS1/2} \times h_{TDS1/2} \quad \textbf{(A-29)}$$

$$CF_{1/2RDS} = \rho_{blade} \times A_{CrosSec1/2RDS} \times \omega^2 \times d_{CG1/2RDS} \times h_{1/2RDS} \quad \textbf{(A-30)}$$

10. Calculate for each stage, the accumulated centrifugal force at blade tip, mid and root, $CF_{TDS}, CF_{1/2Height}$ and CF_{RDS} respectively as shown in Figure A.2-3

$$CF_{TDS} = CF_{Shroud} \quad \textbf{(A-31)}$$

$$CF_{1/2Height} = CF_{TDS} + CF_{TDS1/2} \quad \textbf{(A-32)}$$

$$CF_{RDS} = CF_{1/2Height} + CF_{1/2RDS} \quad \textbf{(A-33)}$$

11. Calculate for each stage, the centrifugal stress at blade tip, mid and root, σ_{TDS}, $\sigma_{1/2Height}$, and σ_{RDS} respectively

$$\sigma_{TDS} = CF_{TDS}/A_{CrosSecTDS} \quad \textbf{(A-34)}$$

$$\sigma_{1/2Height} = CF_{1/2Height}/A_{CrosSec1/2} \quad \textbf{(A-35)}$$

$$\sigma_{RDS} = CF_{RDS}/A_{CrosSecRDS} \quad \textbf{(A-36)}$$

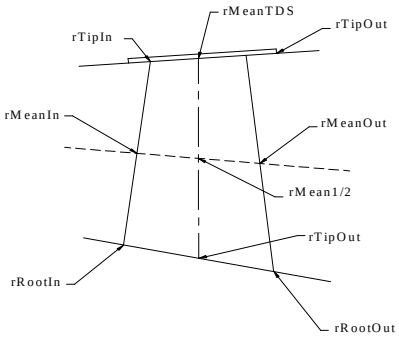

Figure A.2-1

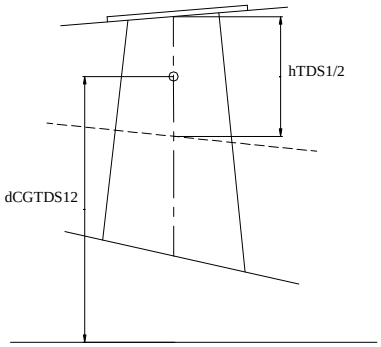

Figure A.2-2

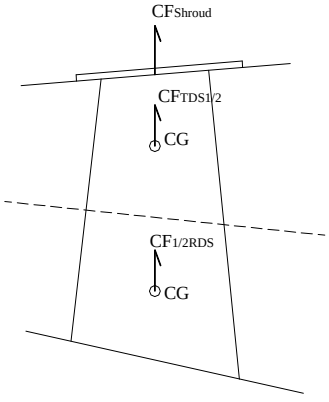

Figure A.2-3

A.2.2 Algorithm for Pressure Bending Moment Model

1. Calculate the polytrophic efficiency, η_P

$$\eta_P = \frac{ln\left(1 - \eta_t\left(1 - \left(\frac{P_{oOUT}}{P_{oNGV}}\right)^{\frac{\gamma_{hot}-1}{\gamma_{hot}}}\right)\right)}{\frac{\gamma_{hot}-1}{\gamma_{hot}} ln\left(\frac{P_{oOUT}}{P_{oNGV}}\right)} \quad \textbf{(A-37)}$$

2. Calculate the temperature drop across the turbine, T_{drop} (Figure A.2-4)

$$T_{drop} = T_{oNGV} - T_{oOUT} \quad \textbf{(A-38)}$$

3. Calculate for each stage, the NGV inlet stagnation temperature, $T_{oNGVStage}$ (refer to Figure A.2-4)

$$T_{oNGVStage} = T_{oNGV} \text{ (if only single stage turbine)} \quad \textbf{(A-39)}$$

OR

$$T_{oNGVStage} = T_{oOUTStage} \text{ (of previous stage for multi-stage design)} \quad \textbf{(A-40)}$$

4. Calculate for each stage, the NGV inlet stagnation pressure, $P_{oNGVStage}$ (refer to Figure A.2-4)

$$P_{oNGVStage} = P_{oNGV} \text{ (If only single stage turbine)} \quad \textbf{(A-41)}$$

OR

$$P_{oNGVStage} = P_{oOUTStage} \text{ (of previous stage for multi-stage design)} \quad \textbf{(A-42)}$$

5. Calculate for each stage, the blade outlet stagnation temperature, $T_{oOUTStage}$ (refer to Figure A.2-4)

$$T_{oOUTStage} = T_{oOUT} \text{ (If only single stage turbine)} \quad \textbf{(A-43)}$$

OR

$$T_{oOUTStage} = T_{oNGVStage} - \left(\%T_{drop} \times T_{drop}\right) \text{ (for multi-stage design)} \quad \textbf{(A-44)}$$

6. Calculate for each stage, the blade outlet stagnation pressure, $P_{oOUTStage}$ (refer to Figure A.2-4)

$$P_{oOUTStage} = P_{oOUT} \text{ (If only single stage turbine)} \quad \textbf{(A-45)}$$

OR

$$P_{oOUTStage} = P_{oNGVStage}\left(\frac{T_{oOUTStage}}{T_{oNGV}}\right)^{\frac{\gamma_{hot}}{\eta_P(\gamma_{hot}-1)}} \text{ (for multi-stage design)} \quad \textbf{(A-46)}$$

7. Calculate for each stage, annulus area at inlet and outlet of blade, A_{In} and A_{Out} respectively as shown in Figure A.2-5.

$$A_{In} = \pi\left(r_{TipIn}^2 - r_{RootIn}^2\right) \quad \textbf{(A-47)}$$

$$A_{Out} = \pi\left(r_{TipOut}^2 - r_{RootOut}^2\right) \quad \textbf{(A-48)}$$

8. Calculate for each stage, blade inlet stagnation temperature before mixing, $T_{MixingStage}$ (refer to Figure A.2.6). Note that $T_{CoolantExit}$ are obtained from the Blade Thermal Model.

$$T_{MixingStage} = T_{oNGVStage} - \frac{NGV_{mass\ frac} \times m_{coolant} CP_{cold}}{m_{gas} CP_{hot}}\left(T_{CoolantExit} - T_{CoolantIn}\right) \quad \textbf{(A-49)}$$

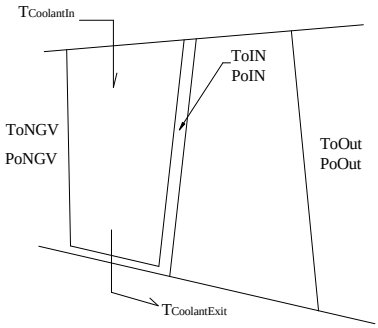

Figure A.2-4

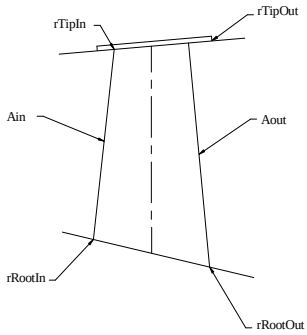

Figure A.2.5

9. Calculate for each stage, blade inlet temperature after mixing, $T_{OINstage}$(refer to Figure A.2-6)

$$T_{OINstage} = \frac{m_{gas}CP_{hot}T_{MixingStage} + (NGV_{mass\ frac} \times m_{coolant})CP_{cold}T_{Coolant\ Exit}}{\left(m_{gas} + (NGV_{mass\ frac} \times m_{coolant})\right)CP_{hot}} \quad \textbf{(A-50)}$$

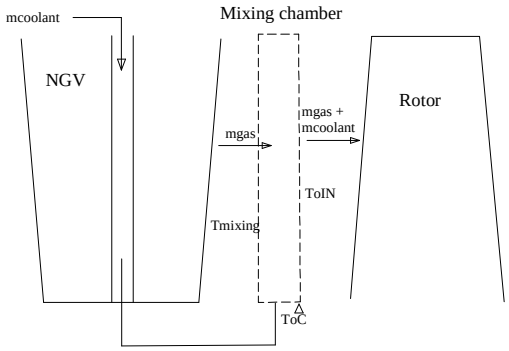

Figure A.2-6

10. Calculate for each stage, blade inlet stagnation pressure, $P_{oINStage}$

$$P_{oINStage} = NGV_{PR} \times P_{oNGVStage} \quad \textbf{(A-51)}$$

11. Calculate for each stage, blade inlet and outlet $m\sqrt{T_o}/(AP_o)$ denotes as $Q_{RotorIn}$ and $Q_{RotorOut}$ respectively

$$Q_{RotorIn} = \frac{m_{gas}\sqrt{T_{oINStage}}}{A_{In}P_{oINStage}} \quad \textbf{(A-52)}$$

$$Q_{RotorOut} = \frac{m_{gas}\sqrt{T_{oOUTStage}}}{A_{Out}P_{oOUTStage}} \quad \textbf{(A-53)}$$

12. Obtain for each stage, blade inlet and outlet axial velocity, $V_{AxialIn}$ and $V_{AxialOut}$ from the Axial Velocity Model for given $Q_{RotorIn}$ and $Q_{RotorOut}$ respectively.

FOR BLADE TIP

13. Calculate for each stage, the blade speed at the tip of the blade inlet and outlet U_{TipIn}(Figure A.2-7) and U_{TipOut}(Figure A.2-8) respectively.

$$U_{TipIn} = \omega \times r_{TipIn} \quad \textbf{(A-54)}$$

$$U_{TipOut} = \omega \times r_{TipOut} \quad \textbf{(A-55)}$$

14. Calculate for each stage, the relative tangential velocity at the tip of the blade outlet, $W_{TanTipOut}$ (refer to Figure A.2-8).

$$W_{TanTipOut} = V_{AxOut} \times tan\alpha_{2Tip} \quad \textbf{(A-56)}$$

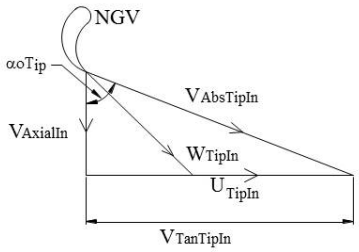

Figure A.2-7

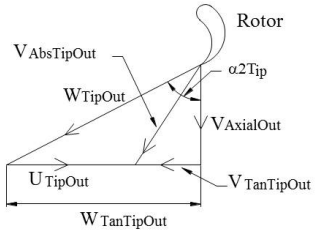

Figure A.2.8

15. Calculate for each stage, the tangential velocity at the tip of the blade inlet and outlet, $V_{TanTipIn}$ (Figure A.2-7) and $V_{TanTipOut}$ (Figure A.2-8) respectively.

$$V_{TanTipIn} = V_{AxIn} \times tan\alpha_{oTip} \quad \textbf{(A-57)}$$

$$V_{TanTipOut} = U_{TipOut} - W_{TanTipOut} \quad \textbf{(A-58)}$$

16. Calculate for each stage, the absolute velocity at the tip of blade inlet and outlet, $V_{AbsTipIn}$ (Figure A.2-7) and $V_{AbsTipOut}$ (Figure A.2-8) respectively.

$$V_{AbsTipIn} = \sqrt{V_{AxIn}^2 + V_{TanTipIn}^2} \quad \textbf{(A-59)}$$

$$V_{AbsTipOut} = \sqrt{V_{AxOut}^2 + V_{TanTipOut}^2} \quad \textbf{(A-60)}$$

17. Calculate for each stage, the static temperature at the tip of blade inlet and outlet, t_{TipIN} and t_{TipOut} respectively.

$$t_{TipIn} = T_{oINStage} - \frac{V_{AbsTipIn}^2}{2CP_{hot}} \quad \textbf{(A-61)}$$

$$t_{TipOut} = T_{oOUTStage} - \frac{V_{AbsTipOut}^2}{2CP_{hot}} \quad \textbf{(A-62)}$$

18. Calculate for each stage, the static pressure at the tip of blade inlet and outlet p_{TipIn}, and p_{TipOut} respectively.

$$p_{TipIn} = P_{oINStage}\left(\frac{t_{TipIn}}{T_{oIN}}\right)^{\frac{\gamma_{hot}}{\gamma_{hot}-1}} \quad \textbf{(A-63)}$$

$$p_{TipOut} = P_{oOutStage}\left(\frac{t_{TipOut}}{T_{oOut}}\right)^{\frac{\gamma_{hot}}{\gamma_{hot}-1}} \quad \textbf{(A-64)}$$

19. Calculate for each stage, the pressure difference, Δp_{Tip} at the tip of the blade

$$\Delta p_{Tip} = p_{TipIn} - p_{TipOut} \quad \textbf{(A-65)}$$

FOR BLADE MID

20. Repeat step 13 to 19 to calculate the corresponding properties at the mid of the blade. Hence the term 'Tip' using in the equations corresponding to those steps should be

replaced to the term 'Mid'. The final calculation should be the pressure difference, Δp_{Mid} at the mid of the blade.

$$\Delta p_{Mid} = p_{MidIn} - p_{Midout} \quad \textbf{(A-66)}$$

FOR BLADE ROOT

21. Repeat step 13 to 19 to calculate the corresponding properties at the root of the blade. Hence the term 'Tip' using in the equations corresponding to those steps should be replaced to the term '$Root$. The final calculation should be the pressure difference, Δp_{Root} at the root of the blade.

$$\Delta p_{Root} = p_{RootIn} - p_{Rootout} \quad \textbf{(A-67)}$$

22. Calculate for each stage, the annulus area for each blade section, $A_{AnSecTDS1/2}$ (mid-tip blade section) and $A_{AnSec1/2RDS}$ (root-mid blade section) respectively

$$A_{AnSecTDS1/2} = \pi\left(r^2_{MeanTDS} - r^2_{Mean1/2}\right) \quad \textbf{(A-68)}$$

$$A_{AnSec1/2RDS} = \pi\left(r^2_{Mean1/2} - r^2_{MeanRDS}\right) \quad \textbf{(A-69)}$$

23. Calculate for each stage, the distance between section GC to blade root for each blade section, $d_{CGRootTDS1/2}$ (mid-tip blade section) and $A_{AnSec1/2RDS}$ (root-mid blade section) respectively as shown in Figure A.2-9

$$d_{CGRootTDS1/2} = d_{CGTDS1/2} - r_{MeanRDS} \quad \textbf{(A-70)}$$

$$d_{CGRoot1/2RDS} = d_{CG1/2RDS} - r_{MeanRDS} \quad \textbf{(A-71)}$$

24. Calculate for each stage, the average pressure difference for each section $p_{AvTDS1/2}$ (mid-tip blade section) and $p_{Av1/2RDS}$ (root-mid blade section) respectively

$$p_{AvTDS1/2} = 0.5\left(\Delta p_{Tip} - \Delta p_{Mid}\right) \quad \textbf{(A-72)}$$

$$p_{Av1/2RDS} = 0.5(\Delta p_{Mid} - \Delta p_{Root}) \quad \textbf{(A-73)}$$

25. Calculate for each stage, force due to pressure difference for each section,

$$PF_{TDS1/2} = \frac{A_{AnSecTDS1/2} \times p_{AvTDS1/2}}{N_b} \quad \textbf{(A-74)}$$

$$PF_{1/2RDS} = \frac{A_{AnSec1/2RDS} \times p_{Av1/2RDS}}{N_b} \quad \textbf{(A-75)}$$

26. Calculate for each stage, the bending moment due to pressure difference about the root (BMP_{Root}) and the mid (BMP_{mid}) of the blade as shown in Figure A.2-10 respectively

$$BMP_{Root} = \left(PF_{TDS1/2} \times d_{CGRootTDS1/2}\right) + \left(PF_{1/2RDS} \times d_{CGRoot1/2RDS}\right) \quad \textbf{(A-76)}$$

$$BMP_{mid} = PF_{TDS1/2} \times \left(d_{CGRootTDS1/2} - h_{1/2RDS}\right) \quad \textbf{(A-77)}$$

A.2.3 Algorithm for Axial Velocity Model

1. Obtain for each stage the blade inlet and outlet $m\sqrt{T_o}/(AP_o)$, $Q_{RotorIn}$ and $Q_{RotorOut}$ from the Pressure Bending Moment Model
2. Guess the axial Mach Number
3. Calculate for each stage, the blade inlet and outlet stagnation and static temperature ratio, T/t

$$\frac{T}{t} = 1 + \frac{\gamma_{hot} - 1}{2} M^2 \quad \textbf{(A-78)}$$

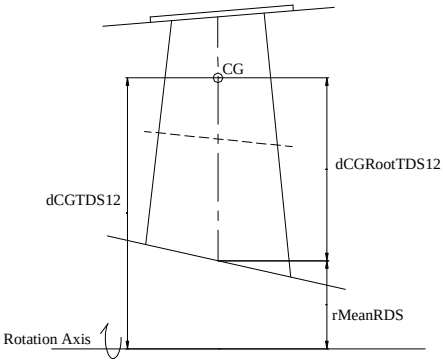

Figure A.2-9

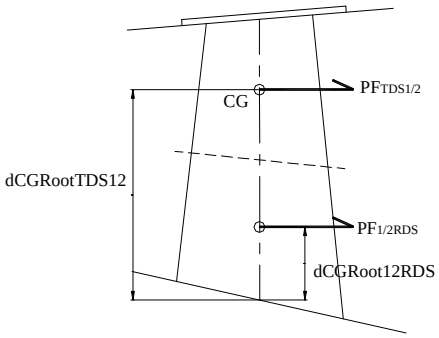

Figure A.2-10

4. Calculate for each stage, the blade inlet and outlet $m\sqrt{T_o}/(AP_o)$, Q_{Guess}

$$Q_{Guess} = M\sqrt{\frac{\gamma_{hot}}{R}}\left(\frac{T}{t}\right)^{\frac{-(\gamma_{hot}+1)}{2(\gamma_{hot}-1)}} \quad \textbf{(A-79)}$$

5. Calculate error value,

$$E = \frac{Q_{Target} - Q_{Guess}}{Q_{Guess}} \times 100 \quad \textbf{(A-80)}$$

6. If the calculated E is bigger that the threshold error margin, then repeat step 2 to 5 with a new guess Mach number value. If the calculated E is within the threshold error margin, then continue to step 7. The threshold error margin used in this research is given in Equation (A-81).

$$-0.005\% < E < 0.005\% \quad \textbf{(A-81)}$$

7. Calculate for each stage, the value of $V/\sqrt{T}$ for blade inlet and outlet

$$\frac{V}{\sqrt{T}} = M\sqrt{\gamma R}\left(\frac{T}{t}\right)^{-1/2} \quad \textbf{(A-82)}$$

8. Calculate for each stage, the axial velocity for blade inlet and outlet, V_{AxIn} and V_{AxOut} respectively

$$V_{AxIn} = \frac{V}{\sqrt{T}} \times T_{oINStage} \quad \textbf{(A-83)}$$

$$V_{AxOut} = \frac{V}{\sqrt{T}} \times T_{oOutStage} \quad \textbf{(A-84)}$$

9. Forward both V_{AxIn} and V_{AxOut}values to the Pressure Bending Moment Model

A.2.4 Algorithm for Momentum Bending Moment Model

The algorithm is divided into two parts. In the first part the algorithm to calculate the bending moment due to axial velocity difference while for the second part, steps to calculate the bending moment due to tangential velocity difference is presented.

A.2.4.1 Bending Moment due to Axial Velocity Difference

1. Calculate for each stage, the blade average annulus area, A_{AnAve} as shown in Figure A-2-11.

$$A_{AnAve} = 0.5(A_{In} + A_{Out})$$ **(A-85)**

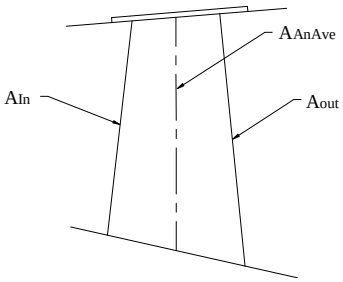

Figure A.2-11

2. Calculate for each stage, the mass flow per unit area, mg_{Area}

$$mg_{Area} = \frac{mg}{A_{AnAve}}$$ **(A-86)**

3. Calculate for each stage, the axial velocity difference, ΔV_{Axial}

$$\Delta V_{Axial} = V_{AxIn} - V_{AxOut}$$ **(A-87)**

4. Calculate for each stage, the force due to axial velocity difference for each section $VF_{AxTDS1/2}$ (for mid-tip blade section) and $VF_{Ax1/2RDS}$ (for root-mid blade section)

$$VF_{AxTDS1/2} = \frac{mg_{Area} \times A_{AnSecTDS1/2} \times \Delta V_{Axial}}{N_b}$$ **(A-88)**

$$VF_{Ax1/2RDS} = \frac{mg_{Area} \times A_{AnSec1/2RDS} \times \Delta V_{Axial}}{N_b}$$ **(A-89)**

5. Calculate for each stage, the axial bending moment about blade root and about the blade mid, BMV_{AxRoot} and BMV_{AxMid}

$$BMV_{AxRoot} = \left(VF_{AxTDS1/2} \times d_{CGRootTDS1/2}\right) + \left(VF_{Ax1/2RDS} \times d_{CGRoot1/2RDS}\right)$$ **(A-90)**

$$BMV_{AxMid} = VF_{AxTDS1/2} \times \left(d_{CGRootTDS1/2} - h_{1/2RDS}\right)$$ **(A-91)**

A.2.4.2 Bending Moment due to Tangential Velocity Difference

1. Calculate for each stage, the tangential velocity difference at blade tip, mid and root, ΔV_{TanTip}, ΔV_{TanMid}, and $\Delta V_{TanRoot}$ respectively as shown in Figure A.2-12

$$\Delta V_{TanTip} = V_{TanTipIn} - V_{TanTipOut}$$ **(A-92)**

$$\Delta V_{TanMid} = V_{TanMidIn} - V_{TanMidOut}$$ **(A-93)**

$$\Delta V_{TanRoot} = V_{TanRootIn} - V_{TanRootOut}$$ **(A-94)**

2. Calculate for each stage, the average tangential velocity difference for each section, $\Delta V_{TanAvTDS1/2}$(mid-tip blade section) and $\Delta V_{TanAv1/2RDS}$ (root-mid blade section) respectively as shown in Figure A. 2-12.

$$\Delta V_{TanAvTDS1/2} = 0.5\left(\Delta V_{TanTip} + \Delta V_{TanMean}\right)$$ **(A-95)**

$$\Delta V_{TanAv1/2RDS} = 0.5(\Delta V_{TanMean} + \Delta V_{TanRoot})$$ **(A-96)**

3. Calculate for each stage, the force due to tangential velocity of each section, $VF_{TanTDS1/2}$ (mid-tip blade section) and $VF_{Tan1/2RDS}$ (root-mid blade section) respectively.

$$VF_{TanTDS1/2} = \frac{mg_{Area} \times A_{AnSecTDS1/2} \times \Delta V_{TanAvTDS1/2}}{N_b} \quad \textbf{(A-97)}$$

$$VF_{Tan1/2RDS} = \frac{mg_{Area} \times A_{AnSec1/2RDS} \times \Delta V_{TanAv1/2RDS}}{N_b} \quad \textbf{(A-98)}$$

4. Calculate for each stage, the tangential bending moment about blade root and about the blade mid.

$$BMV_{TanRoot} = \left(VF_{TanTDS1/2} \times d_{CGRootTDS1/2}\right) + \left(VF_{Tan1/2RDS} \times d_{CGRoot1/2RDS}\right) \quad \textbf{(A-99)}$$

$$BMV_{TanMid} = VF_{TanTDS1/2} \times \left(d_{CGRootTDS1/2} - h_{1/2RDS}\right) \quad \textbf{(A-100)}$$

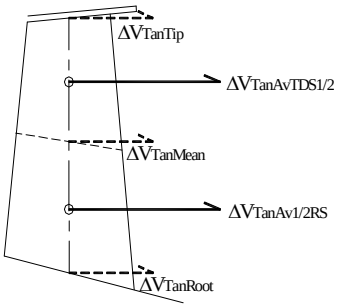

Figure A.2-12

A.2.5 Algorithm for Maximum Stress Model

1. Calculate for each stage, the resulting bending moment at axial and for blade mid and root, $BM_{ResAxMid}$, and $BM_{ResAxRoot}$ respectively.

$$BM_{ResAxMid} = BMP_{Mid} + BMV_{AxMid} \quad \textbf{(A-101)}$$

$$BM_{ResAxRoot} = BMP_{Root} + BMV_{AxRoot} \quad \textbf{(A-102)}$$

2. Calculate for each stage, the resulting bending moment at tangential and for blade mid and root, $BM_{ResTanMid}$, and $BM_{ResTanRoot}$ respectively.

$$BM_{ResTanMid} = BMV_{TanMid} \quad \textbf{(A-103)}$$

$$BM_{ResTanRoot} = BMV_{TanRoot} \quad \textbf{(A-104)}$$

3. Convert for each stage, blade mid and root bending moment about blade direction X (refer to Figure A.6-1), M_{XXMid} and M_{XXRoot} respectively

$$M_{XXMid} = BM_{ResAxMid} sin\theta_{Mid} + BM_{ResTanMid} cos\theta_{Mid} \quad \textbf{(A-105)}$$

$$M_{XXRoot} = BM_{ResAxRoot} sin\theta_{Root} + BM_{ResTanRoot} cos\theta_{Root} \quad \textbf{(A-106)}$$

4. Convert for each stage, blade mid and root bending moment about blade direction X (refer to Figure A.2-13), M_{YYMid} and M_{YYRoot} respectively

$$M_{YYMid} = BM_{ResAxMid} cos\theta_{Mid} - BM_{ResTanMid} sin\theta_{Mid} \quad \textbf{(A-107)}$$

$$M_{YYRoot} = BM_{ResAxRoot} cos\theta_{Root} - BM_{ResTanRoot} sin\theta_{Root} \quad \textbf{(A-108)}$$

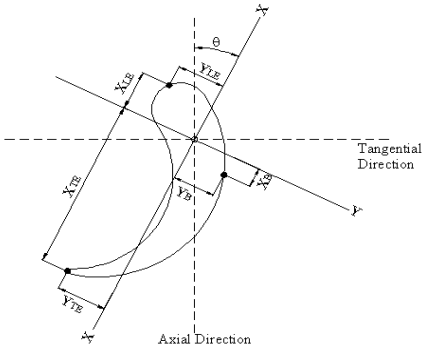

Figure A.2-13

5. Calculate for each stage, LE stress at the blade root and mid, σ_{LEMid} and σ_{LERoot} respectively.

$$\sigma_{LEMid} = \frac{M_{XXMid} Y_{LEMid}}{I_{minMid}} + \frac{M_{YYMid} X_{LEMid}}{I_{maxMid}} \quad \textbf{(A-109)}$$

$$\sigma_{LERoot} = \frac{M_{XXRoot} Y_{LERoot}}{I_{minRoot}} + \frac{M_{YYRoot} X_{LERoot}}{I_{maxRoot}} \quad \textbf{(A-110)}$$

6. Calculate for each stage, TE stress at the blade root and mid, σ_{TEMid} and σ_{TERoot} respectively.

$$\sigma_{TEMid} = \frac{M_{XXMid} Y_{TEMid}}{I_{minMid}} + \frac{M_{YYMid} X_{TEMid}}{I_{maxMid}} \quad \textbf{(A-111)}$$

$$\sigma_{TERoot} = \frac{M_{XXRoot} Y_{TERoot}}{I_{minRoot}} + \frac{M_{YYRoot} X_{TERoot}}{I_{maxRoot}} \quad \textbf{(A-112)}$$

7. Calculate for each stage, back of the blade stress at the blade root and mid, σ_{BckMid} and $\sigma_{BckRoot}$ respectively.

$$\sigma_{BckMid} = \frac{M_{XXMid} Y_{BckMid}}{I_{minMid}} + \frac{M_{YYMid} X_{BckMid}}{I_{maxMid}} \quad \textbf{(A-113)}$$

$$\sigma_{BckRoot} = \frac{M_{XXRoot} Y_{BckRoot}}{I_{minRoot}} + \frac{M_{YYRoot} X_{BckRoot}}{I_{maxRoot}} \quad \textbf{(A-114)}$$

8. Calculate for each stage, the total stress at LE, TE, and back of blade at the blade mid, $\sigma_{TotLEMid}$, $\sigma_{TotTEMid}$, and $\sigma_{TotBckMid}$ respectively

$$\sigma_{TotLEMid} = \sigma_{1/2Height} + \sigma_{LEMid} \quad \textbf{(A-115)}$$

$$\sigma_{TotTEMid} = \sigma_{1/2Height} + \sigma_{TEMid} \quad \textbf{(A-116)}$$

$$\sigma_{TotBckMid} = \sigma_{1/2Height} + \sigma_{BckMid} \quad \textbf{(A-117)}$$

9. Calculate for each stage, the total stress at LE, TE, and back of blade at the blade root, $\sigma_{TotLERoot}$, $\sigma_{TotTERoot}$, and $\sigma_{TotBckRoot}$ respectively

$$\sigma_{TotLERoot} = \sigma_{RDS} + \sigma_{LERoot} \quad \textbf{(A-118)}$$

$$\sigma_{TotTERoot} = \sigma_{RDS} + \sigma_{TERoot} \quad \textbf{(A-119)}$$

$$\sigma_{TotBckRoot} = \sigma_{RDS} + \sigma_{BckRoot} \quad \textbf{(A-120)}$$

10. Select for each stage, maximum stress at blade mid and root, σ_{MaxMid}, and $\sigma_{MaxRoot}$.

$$\sigma_{MaxMid} = \max\{\sigma_{TotLEMid}, \sigma_{TotTEMid}, \sigma_{TotBckMid}\} \quad \textbf{(A-121)}$$

$$\sigma_{MaxRoot} = \max\{\sigma_{TotLERoot}, \sigma_{TotTERoot}, \sigma_{TotBckRoot}\} \quad \textbf{(A-122)}$$

11. Approximate the maximum stress at 25% and 75% distance from blade root, $\sigma_{max25\%Root}$, and $\sigma_{max75\%Root}$

$$\sigma_{max25\%Root} = 0.5(\sigma_{MaxRoot} + \sigma_{MaxMid}) \quad \textbf{(A-123)}$$

$$\sigma_{max75\%Root} = 0.5(\sigma_{MaxMid} + \sigma_{TDS}) \quad \textbf{(A-124)}$$

A.3 Algorithm for Blade Thermal Model

The algorithm is divided into three sub-models which are the Cooled Blade 0D Thermal Model, Cooled Blade 1D Thermal Model, Uncooled Blade 1D Thermal Model.

A.3.1 Cooled Blade 0D Thermal Model

1. Calculate for each stage coolant mass flow percentage that enters NGV, φ_{NGV}

$$\varphi_{NGV} = \frac{NGV_{massfrac} \times m_{coolant}}{m_{intake}} \quad \textbf{(A-125)}$$

2. Calculate for each stage NGV non-dimension coolant mass flow, ${m_{NGV}}^*$

$${m_{NGV}}^* = \frac{\varphi_{NGV}}{2.5} \quad \textbf{(A-126)}$$

3. Calculate for each stage convection efficiency, η_{conv}

$$\eta_{conv} = \frac{\varepsilon_{NGV}}{{m_{NGV}}^* - ({m_{NGV}}^* \times \varepsilon_{NGV})} \quad \textbf{(A-127)}$$

4. Calculate for each stage NGV metal temperature, T_{NGV} (Figure A.3-1)

$$T_{NGV} = T_{oNGVStage} - \varepsilon_{NGV}\left(T_{oNGVStage} \times T_{CoolantIn}\right) \quad \textbf{(A-128)}$$

5. Calculate for each stage NGV coolant exit temperature, $T_{CoolantExit}$ (Figure A.3-2)

$$T_{CoolantExit} = T_{CoolantIn} - \eta_{conv}(T_{NGV} \times T_{CoolantIn}) \quad \textbf{(A-129)}$$

6. Calculate for each stage blade metal temperature (Figure A.3-2)

$$T_{Rotor} = T_{OINstage} - \varepsilon_R\left(T_{OINstage} \times T_{CoolantIn}\right) \quad \textbf{(A-130)}$$

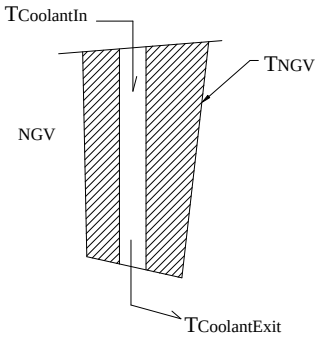

Figure A.3-1

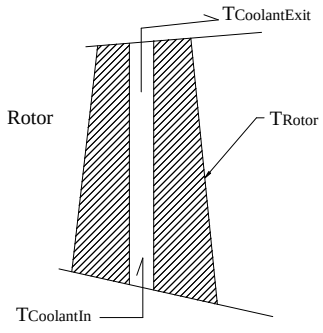

Figure A.3-2

A.3.2 Cooled Blade 1D Thermal Model

1. For each stage, calculate the blade reference temperature, T_{Ref}

$$T_{Ref} = T_{oNGVstage} - T_{BurIn} \quad \textbf{(A-131)}$$

2. Calculate for each stage the maximum and minimum gas temperature, T_{max} and T_{min} respectively.

$$T_{max} = T_{oINstage} + \left(T_{Ref} \times RTDF\right) \quad \textbf{(A-132)}$$

$$T_{min} = \frac{\left(5T_{oINstage} - 2T_{max}\right)}{3} \quad \textbf{(A-133)}$$

3. Create for each stage the temperature profile at the blade span locations, T_{GRoot}, $T_{G25\%}$, T_{mid}, $T_{G75\%}$, and T_{GTip}.

$$T_{GRoot} \text{ or } T_{GTip} = T_{min} \quad \textbf{(A-134)}$$

$$T_{G25\%} = T_{min} + \frac{2(T_{max} - T_{min})}{3} \quad \textbf{(A-135)}$$

$$T_{GMid} = T_{min} + \frac{(T_{max} - T_{min})}{3} \quad \textbf{(A-136)}$$

$$T_{G75\%} = T_{max} \quad \textbf{(A-137)}$$

4. Calculate for each stage % coolant mass flow that enters NGV, φ_{NGV} using Equation (A-125)
5. Calculate for each stage NGV non-dimension coolant mass flow $m_{NGV}{}^{*}$, using Equation (A-126)
6. Calculate for each stage NGV convection efficiency, η_{conv} using Equation (A-127)
7. Calculate for each stage NGV metal temperature, T_{NGV} using Equation (A-128)
8. Calculate for each stage NGV coolant exit temperature, $T_{CoolantExit}$ using Equation (A-129)

9. Calculate for each stage the blade height, h_{blade}

$$h_{blade} = r_{MeanTDS} - r_{MeanRDS} \quad \textbf{(A-138)}$$

10. Calculate for each stage the blade chord at 25% and 75% distance from blade root, $c_{25\%}$, $c_{75\%}$.

$$c_{25\%} = 0.5(c_{root} + c_{Mid}) \quad \textbf{(A-139)}$$

$$c_{75\%} = 0.5\left(c_{Mid} + c_{Tip}\right) \quad \textbf{(A-140)}$$

11. Calculate for each stage the blade perimeter at 25% and 75% distance from blade root, $s_{25\%}$, $s_{75\%}$.

$$s_{25\%} = 0.5(s_{root} + s_{Mid}) \quad \textbf{(A-141)}$$

$$s_{75\%} = 0.5\left(s_{Mid} + s_{Tip}\right) \quad \textbf{(A-142)}$$

12. Calculate for each stage outlet static pressure at 25% and 75% distance from blade root, $p_{25\%}$, $p_{75\%}$

$$p_{25\%} = 0.5(p_{RootOut} + p_{MidOut}) \quad \textbf{(A-143)}$$

$$p_{75\%} = 0.5\left(p_{TipOut} + p_{MidOut}\right) \quad \textbf{(A-144)}$$

13. Calculate for each stage outlet static temperature at 25% and 75% distance from blade root, $t_{25\%}$, $t_{75\%}$

$$t_{25\%} = 0.5(t_{RootOut} + t_{MidOut}) \quad \textbf{(A-145)}$$

$$t_{75\%} = 0.5\left(t_{MidOut} + t_{TipOut}\right) \quad \textbf{(A-146)}$$

14. Calculate for each stage outlet absolute velocity at 25% and 75% distance from blade root, $V_{Abs25\%Out}$, $V_{Abs75\%Out}$

$$V_{Abs25\%Out} = 0.5(V_{AbsRootOut} + V_{AbsMidOut}) \quad \textbf{(A-147)}$$

$$V_{Abs75\%Out} = 0.5(V_{AbsMidOut} + V_{AbsTipOut}) \quad \textbf{(A-148)}$$

15. Calculate for each stage NGV exit blade angle at 25% and 75% distance from blade root, $\alpha_{o25\%}$, $\alpha_{o75\%}$

$$\alpha_{o25\%} = 0.5(\alpha_{oRoot} + \alpha_{oMid}) \quad \textbf{(A-149)}$$

$$\alpha_{o75\%} = 0.5(\alpha_{oMid} + \alpha_{oTip}) \quad \textbf{(A-150)}$$

16. Calculate for each stage blade exit blade angle at 25% and 75% distance from blade root, $\alpha_{2\,25\%}$, $\alpha_{2\,75\%}$

$$\alpha_{2\,25\%} = 0.5(\alpha_{2Root} + \alpha_{2Mid}) \quad \textbf{(A-151)}$$

$$\alpha_{2\,75\%} = 0.5(\alpha_{2Mid} + \alpha_{2Tip}) \quad \textbf{(A-152)}$$

17. Calculate for each stage outlet blade speed at 25% and 75% distance from blade root, $U_{25\%Out}$, $U_{75\%Out}$

$$U_{25\%Out} = 0.5(U_{RootOut} + U_{MidOut}) \quad \textbf{(A-153)}$$

$$U_{75\%Out} = 0.5(U_{MidOut} + U_{TipOut}) \quad \textbf{(A-154)}$$

18. Calculate for each stage the tangential inlet velocity for 25%, and 75% distance from blade root, $V_{Tan25\%In}$ and $V_{Tan75\%In}$.

$$V_{Tan25\%In} = V_{AxIn} \tan \alpha_{o25\%} \quad \textbf{(A-155)}$$

$$V_{Tan75\%In} = V_{AxIn} \tan \alpha_{o75\%} \quad \textbf{(A-156)}$$

19. Calculate for each stage the blade inlet gas relative angle α_1 for root, mid, tip, 25%, and 75% distance from blade root as shown in Figure A.3-3

$$\alpha_1 = \tan^{-1}\left(\frac{V_{TanIn} - U_{RootIn}}{V_{AxIn}}\right) \quad \textbf{(A-157)}$$

20. Calculate for each stage the blade angle ratio, AR for root, 25%, 75%, and tip

$$AR = \alpha_1/\alpha_2 \quad \textbf{(A-158)}$$

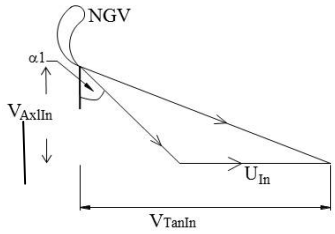

Figure A.3-3

21. Obtain for each stage the constant X from the Heat Transfer Data for Conventional Blade Profile plot (see Figure A.3-4) for root, 25%, 75%, and tip.
22. Obtain for each stage the nominal mean Nusselt number Nu_g^* from the Heat Transfer Data for Conventional Blade Profile plot (see Figure A.3-4) for root, 25% root, mid, 75% root, and tip.

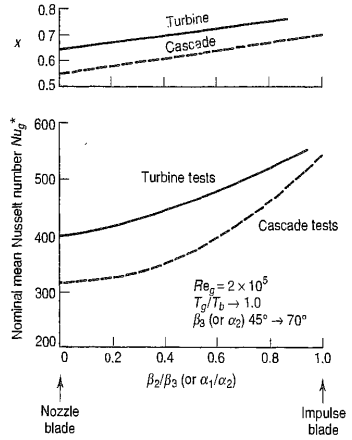

Figure A.3-4: Heat transfer data for conventional blade profile

23. Calculate for each stage the blade outlet gas density, ρ_g for root, 25% root, mid 75% root, and tip.

$$\rho_g = p_{out} / \left(R \times t_{out} \right) \quad \textbf{(A-159)}$$

24. Using Sutherland Equation, calculate for each stage the blade outlet gas viscosity, μ for root, 25% root, mid, 75% root, and tip.

$$\mu = \mu_o \frac{0.555 T_{io} + Suth}{0.555 t_{out} + Suth} \left(\frac{t_{out}}{T_{io}} \right)^{3/2} \quad \textbf{(A-160)}$$

where μ_o=0.00001257 N_{sec}/m^2 , T_{io}=524.07K, and $Suth$=120

25. Calculate for each stage the Reynolds number, Re for root, 25% root, mid, 75% root, and tip of the exit of the blade.

$$\mathrm{Re} = \frac{\rho_g \times V_{AbsOut} \times c}{\mu} \quad \textbf{(A-161)}$$

26. Calculate for each stage the exponential Y for root, 25% root, mid, 75% root, and tip

$$Y = 0.14 \left(\frac{\mathrm{Re}}{2 \times 10^5} \right)^{-0.4} \quad \textbf{(A-162)}$$

27. Divide the blade into four sections as shown in Figure A.3-5

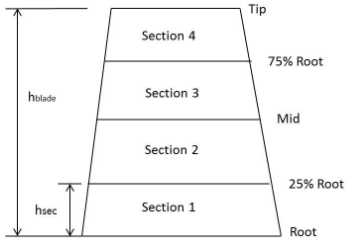

Figure A.3-5

28. Calculate the mean height of the blade, h_{Blade}

$$h_{Blade} = r_{MeanTDS} - r_{MeanRDS} \quad \textbf{(A-163)}$$

29. Calculate height of the blade section, h_{Sec}

$$h_{Sec} = h_{Blade} / 4 \quad \textbf{(A-164)}$$

30. Calculate for each stage, average chord, c_{Sec} of each blade section

$$c_{Sec} = \frac{c_{top} - c_{bottom}}{2} \quad \textbf{(A-165)}$$

Note: For blade section 1: c_{top} is the chord at 25% root while for c_{bottom}, it is chord of the blade root.

31. Calculate for each stage, average perimeter, s_{Sec} of each blade section

$$s_{Sec} = \frac{s_{top} - s_{bottom}}{2} \quad \textbf{(A-166)}$$

32. Calculate for each stage average Reynolds number of each blade section, Re_{Sec}

$$Re_{Sec} = \frac{Re_{top} - Re_{bottom}}{2} \quad \textbf{(A-167)}$$

33. Calculate for each stage average constant X of each blade section, X_{Sec}

$$X_{Sec} = \frac{X_{top} - X_{bottom}}{2} \quad \textbf{(A-168)}$$

34. Calculate for each stage average exponential Y of each blade section, Y_{Sec}

$$Y_{Sec} = \frac{Y_{top} - Y_{bottom}}{2} \quad \textbf{(A-169)}$$

35. Calculate for each stage average nominal mean Nusselt number $Nu_g{}^*$ of each blade section, $Nu_g{}^*{}_{Sec}$

$$Nu_g{}^*{}_{Sec} = \frac{Nu_g{}^*{}_{top} - Nu_g{}^*{}_{bottom}}{2} \quad \textbf{(A-170)}$$

36. Calculate for each stage the average gas temperature profile for each blade section, T_{GSec}

$$T_{GSec} = \frac{T_{Gtop} - T_{Gbottom}}{2} \quad \textbf{(A-171)}$$

37. For each average gas temperature, T_{GSec}, obtain the thermal conduction of air, k_{GSec}.
38. Calculate for each stage the blade section metal temperature, T_{MSec} starting from the root to the top section

$$T_{MSec} = T_{GSec} - \varepsilon_R(T_{GSec} - T_{CiSec}) \quad \textbf{(A-172)}$$

Note: The coolant inlet temperature, T_{CiSec} for each subsequent section is taken as the coolant exit temperature, T_{CoSec} of the lower section as shown in Figure A.3-6. For blade section 1, $T_{CiSec} = T_{CoolantIn}$.

39. Calculate for each stage, the blade section Nusselt number, Nu_{Sec}

$$Nu_{Sec} = Nu^*{}_{Sec}\left(\frac{Re_{Sec}}{2 \times 10^5}\right)^{X_{Sec}}\left(\frac{T_{Gsec}}{T_{Msec}}\right)^{Y_{sec}} \quad \textbf{(A-173)}$$

40. Calculate for each stage, the blade section convective heat transfer coefficient, H_{Sec}

$$H_{Sec} = \frac{Nu_{Sec} \times k_{GSec}}{c_{sec}} \quad \textbf{(A-174)}$$

41. Calculate for each stage, the blade section coolant exit temperature, T_{CoSec}

$$T_{CoSec} = T_{CiSec} + \left[\frac{H_{Sec}S_{Sec}h_{Sec}\varepsilon_R(T_{Gsec} - T_{CiSec})}{\left(\frac{m_{coolant}Rotor_{massfrac}}{N_b}\right)CP_{cold}}\right] \quad \textbf{(A-175)}$$

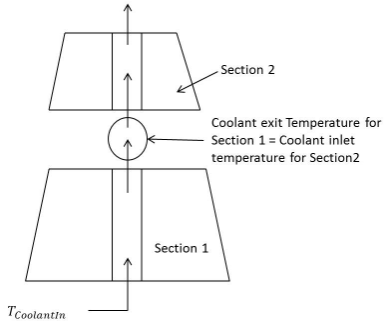

Figure A.3-6

42. Take coolant exit temperature, T_{CoSec} to be the next section coolant inlet temperature, T_{CiSec} and repeat Step 37 to 40 until calculation of blade section 4 is completed.

43. Calculate for each stage the metal temperature, T_M at blade root, 25% root, mid, 75% root, and tip

$$T_M = 0.5(T_{MSec\,Top} + T_{MSec\,Bottom}) \quad \textbf{(A-176)}$$

Note: Metal temperature at the mid is the average of metal temperature at blade section 2 and 3 as shown in A.3-5

A.3.3 Uncooled Blade 1D Thermal Model

1. For each stage, calculate the blade reference temperature, T_{Ref} using Equation (A-131).

2. Calculate for each stage the maximum and minimum gas temperature, T_{max} and T_{min} respectively using Equation (A-132) and (A-133) respectively.

3. Create for each stage the temperature profile at the blade span locations, T_{GRoot}, $T_{G25\%}$, T_{mid}, $T_{G75\%}$, and T_{GTip} using Equation (A-134), (A-135), (A-136), and (A-137) respectively.

4. Calculate for each stage % coolant mass flow that enters NGV, φ_{NGV} using Equation (A-125)

5. Calculate for each stage NGV non-dimension coolant mass flow $m_{NGV}{}^{*}$, using Equation (A-126)

6. Calculate for each stage NGV convection efficiency, η_{conv} using Equation (A-127)

7. Calculate for each stage NGV metal temperature, T_{NGV} using Equation (A-128)

8. Calculate for each stage NGV coolant exit temperature, $T_{CoolantExit}$ using Equation (A-129)

9. Calculate for each stage the blade height, h_{blade} using Equation (A-138)

10. Calculate for each stage the blade chord at 25% and 75% distance from blade root, $c_{25\%}$,and $c_{75\%}$ using Equation (A-139) and (A-140) respectively.

11. Calculate for each stage the blade perimeter at 25% and 75% distance from blade root, $s_{25\%}$, and $s_{75\%}$ using Equation (A-141) and (A-142) respectively.

12. Calculate for each stage outlet static pressure at 25% and 75% distance from blade root, $p_{25\%}$, and $p_{75\%}$ using Equation (A-143) and (A-144).

13. Calculate for each stage outlet static temperature at 25% and 75% distance from blade root, $t_{25\%}$, and $t_{75\%}$ using Equation (A-145) and (A146) respectively.

14. Calculate for each stage outlet absolute velocity at 25% and 75% distance from blade root, $V_{Abs25\%Out}$, and $V_{Abs75\%Out}$ using Equation (A-147) and (A-148).

15. Calculate for each stage inlet absolute velocity at 25% and 75% distance from blade root, $V_{Abs25\%Out}$, and $V_{Abs75\%Out}$

$$V_{Abs25\%In} = 0.5(V_{AbsRootIn} + V_{AbsMidIn}) \quad \textbf{(A-177)}$$

$$V_{Abs75\%In} = 0.5\left(V_{AbsMidIn} + V_{AbsTipIn}\right) \quad \textbf{(A-178)}$$

16. Calculate for each stage the blade outlet gas density, ρ_g for root, 25% root, mid 75% root, and tip using Equation (A-159).

17. Calculate for each stage the blade inlet gas density, ρ_{gIn} for root, 25% root, mid 75% root, and tip.

$$\rho_{gIn} = \frac{p_{In}}{R \times t_{In}} \quad \textbf{(A-179)}$$

18. Calculate for each stage the blade outlet gas viscosity, μ for root, 25% root, mid, 75% root, and tip using Equation (A-160).

19. Calculate for each stage the blade inlet gas viscosity, μ_{In} for root, 25% root, mid, 75% root, and tip

$$\mu_{In} = \mu_o \frac{0.555T_{io} + Suth}{0.555t_{In} + Suth}\left(\frac{t_{In}}{T_{io}}\right)^{3/2} \quad \textbf{(A-180)}$$

where $\mu_o = 0.00001827 \frac{Nsec}{m^2}$, $T_{io} = 524.07K$, and $Suth = 120$

20. Calculate for each stage the blade average gas density, ρ_{Ave} at root, 25% root, mid,75% root and tip

$$\rho_{Ave} = 0.5\left(\rho_{gIn} + \rho_g\right) \quad \textbf{(A-181)}$$

21. Calculate for each stage the blade average gas viscosity, μ_{Ave} at root, 25% root, mid,75% root and tip

$$\mu_{Ave} = 0.5(\mu_{In} + \mu) \quad \textbf{(A-182)}$$

22. Calculate for each stage the blade average absolute velocity, V_{AveAbs} at root, 25% root, mid,75% root and tip

$$V_{AveAbs} = 0.5(V_{AbsIn} + V_{AbsOut}) \quad \textbf{(A-183)}$$

23. Calculate for each stage the blade average static temperature, t_{Ave} at root, 25% root, mid,75% root and tip

$$t_{Ave} = 0.5(t_{In} + t_{Out}) \quad \textbf{(A-184)}$$

24. Calculate for each stage the blade Reynolds number at root, 25% root, mid,75% root and tip

$$Re = \frac{\rho_{Ave} \times V_{AveAbs} \times c}{\mu_{Ave}} \quad \textbf{(A-185)}$$

25. Calculate for each stage the blade Nusselt number at root, 25% root, mid,75% root and tip using flat plate empirical relation

$$Nu = 0.037Re^{4/5}Pr^{1/3} \quad \textbf{(A-186)}$$

26. For each blade average static temperature,t_{Ave}, obtain the gas thermal conductivity, k_G.

27. Calculate for each stage the blade external convective heat transfer coefficient, H at root, 25% root, mid,75% root and tip

$$H = \frac{Nu \times k_G}{c} \quad \textbf{(A-187)}$$

28. Divide the blade into four sections as shown in Figure A.3-7

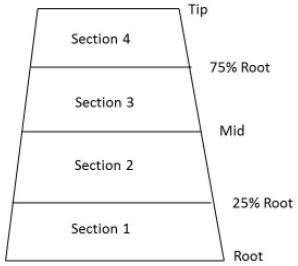

Figure A.3-7

29. Calculate for each stage the blade section average convective heat transfer coefficient

$$H_{Sec} = \frac{H_{top} - H_{bottom}}{2} \quad \textbf{(A-188)}$$

Note: For blade section 1: H_{top} is the convective heat transfer coefficient at 25% root while for H_{bottom}, it is convective heat transfer coefficient at the blade root.

30. Calculate for each stage the blade section temperature ratio $\left(\frac{T_M}{T_G}\right)_{Sec}$

$$\left(\frac{T_M}{T_G}\right)_{Sec} = R_k - \left[\frac{H_{Sec} \times Th_{TBC}}{k_{TBC}}(1 - R_k)\right] \quad \textbf{(A-189)}$$

31. Calculate for each stage the average gas temperature profile for each blade section, T_{GSec} using Equation (A-171)

32. Calculate for each stage the blade section metal temperature, T_{MSec}

$$T_{MSec} = T_{GSec}\left(\frac{T_M}{T_G}\right)_{Sec} \quad \textbf{(A-190)}$$

33. Calculate for each stage the blade metal temperature, T_M at root, 25% root, mid,75% root and tip using Equation (A-176)

A.4 Algorithm for Life Estimation Model

The model algorithm is divided into two sub-models. The first model is used to predict the blade minimum creep life of a single operating point; while the later model is used to predict the minimum nominal and mission/operation profile creep life for a given mission/operation profile.

A.4.1 Single Operating Creep Life Prediction

1. For each stage, determine the blade LMP value (for a given the maximum stress obtained from the Maximum Stress Model) using the corresponding material LMP master curve of each specified locations along the blade span (blade root, 25% root, mid, and 75% root,

2. Calculate for each stage, the blade time to failure, t_f of each specified locations along the blade span

$$t_f = 10^{\left(\frac{1000LMP}{T_M} - C\right)} \quad \textbf{(A-191)}$$

3. Calculate for each stage, the blade predicted creep life, L_C of each specified location along the blade span

4.

$$L_C = \frac{t_f}{SF_{ac}} \quad \textbf{(A-192)}$$

5. Obtain for each stage, the blade minimum predicted creep life, $L_{C\,Min}$ of each specified location along the blade span and display the corresponding location.

$$L_{C\,Min} = \min\{L_{CRoot}, L_{C\,25\%}, L_{Mid}, L_{C725\%},\} \quad \textbf{(A-193)}$$

6. Calculate for each stage, the operating point blade Creep Factor, CF

$$CF = \frac{L_{CMin}}{L_{Ref}} \quad \textbf{(A-194)}$$

A.4.2 Mission / Operation Profile Creep Life Prediction

1. Determine for each stage, the profile point blade LMP of each specified locations along the blade span.

2. Calculate for each stage, the profile point blade time to failure, t_f of each specified locations along the blade span using Equation (A-191)

3. Calculate for each stage, the profile point blade predicted creep life, L_C of each specified location along the blade span using Equation (A-192)

4. Obtain for each stage, the minimum profile point blade predicted creep life, $L_{C\,Min}$ of each specified location along the blade span using Equation (A-193). Also display the corresponding location.

5. Calculate for each stage, the profile point blade life fraction, LF

$$LF = \frac{OH}{L_{C\,Min}} \quad \textbf{(A-195)}$$

6. Calculate for each stage, the mission/operation blade life fraction, LF_M

$$LF_M = \sum LF \quad \textbf{(A-196)}$$

7. Calculate the total operating hour, OH_{Tot}

$$OH_{Tot} = \sum OH \quad \textbf{(A-197)}$$

8. Calculate for each stage, the mission/operation blade nominal creep life, $L_{C\,M}$

$$L_{C\,M} = \frac{OH_{Tot}}{LF_M} \quad \textbf{(A-198)}$$

9. Calculate for each stage, the profile point Creep Factor, CF using Equation A-194

10. Calculate for each stage, the mission Creep Factor, CF_M

$$CF_M = \frac{L_{C\,M}}{L_{Ref}} \quad \textbf{(A-199)}$$

11. Save the mission/operation blade life fraction, LF_M and the total operating hour, OH_{Tot}

A.5 Algorithm for Life Usage Model

1. Upload the present and the previous mission/operation profile blade life fractions, LF_M and total operating hour, OH_{Tot}

2. For each stage, calculate each mission/operation profile blade nominal creep life using Equation (A-198)

3. Calculate for each stage, the blade overall life fraction, $LF_{Overall}$ and operating hours

$$LF_{Overall} = \sum LF_M \quad \textbf{(A-200)}$$

$$OH_{Overall} = \sum OH_{Tot} \quad \textbf{(A-201)}$$

4. Calculate the blade overall nominal creep life, $L_{C\ Overall}$

$$L_{C\ Overall} = \frac{OH_{Overall}}{LF_{Overall}} \quad \textbf{(A-202)}$$

5. Obtain reference operation life, L_{ref}

6. Calculate the blade overall mission Creep Factor, $CF_{M\ Overall}$

$$CF_{M\ Overall} = \frac{L_{C\ Overall}}{L_{Ref}} \quad \textbf{(A-203)}$$

7. Calculate the blade overall life usage percentage, $LU\%$

$$LU\% = LF_{Overall} \times 100 \quad \textbf{(A-204)}$$

8. Calculate the blade remnant life, L_{Rem}

$$L_{Rem} = \left(CF_{M\ Overall} \times L_{Ref}\right) - OH_{Overall} \quad \textbf{(A-205)}$$

Appendix B : Process Tree of the Developed Integrated Creep Life Prediction model

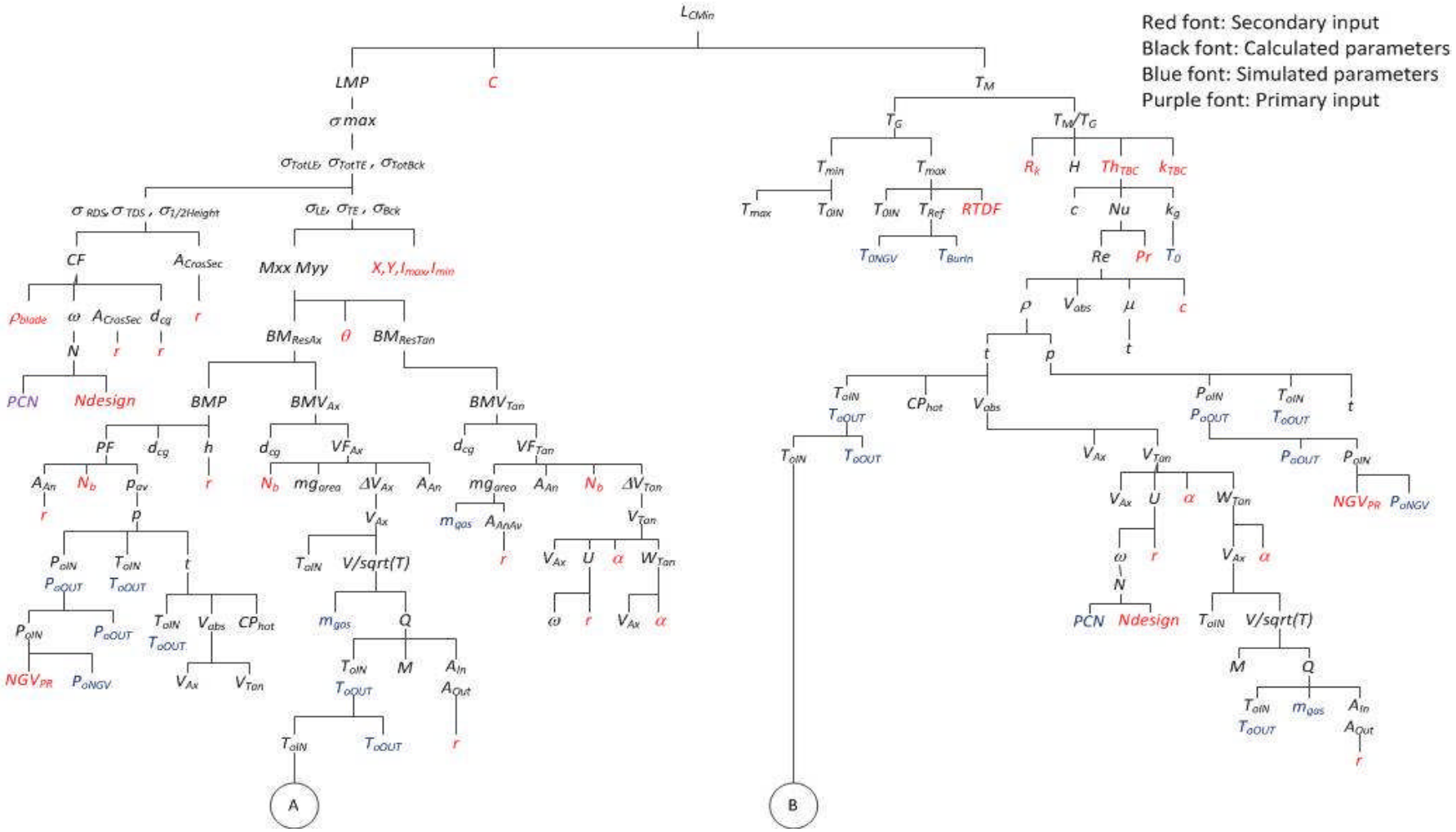

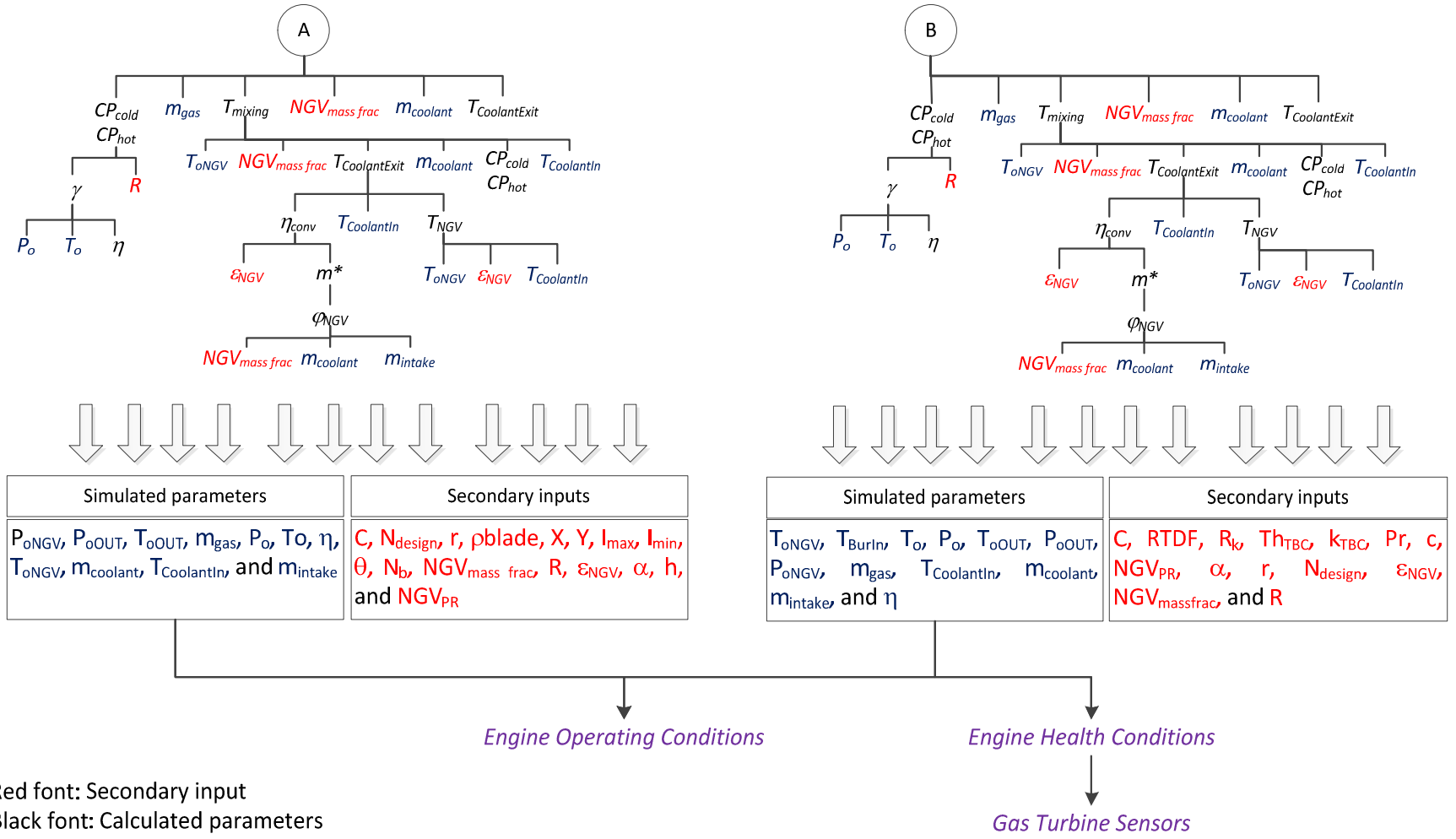

Red font: Secondary input
Black font: Calculated parameters
Blue font: Simulated parameters
Purple font: Primary input

Appendix C : Plots of MSE, Final Regression and Confusion Matrix for Each Trained Network of RB Architecture at Clean Engine Condition

C.1 : Plots of MSE for Each Trained Network of RB Architecture

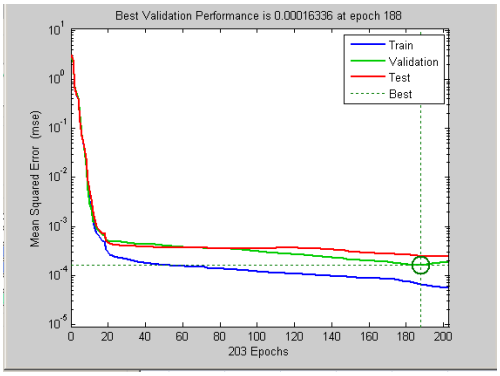

Figure C.1-1: MSE plot for Class 1 Approximator

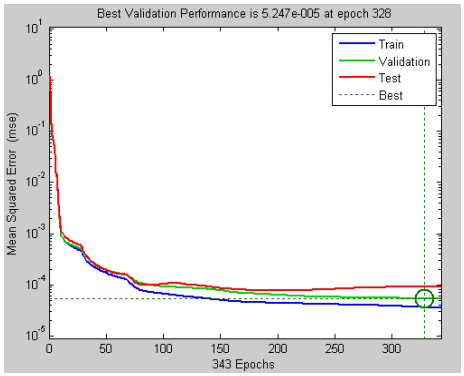

Figure C.1-2: MSE plot for Class 2 Approximator

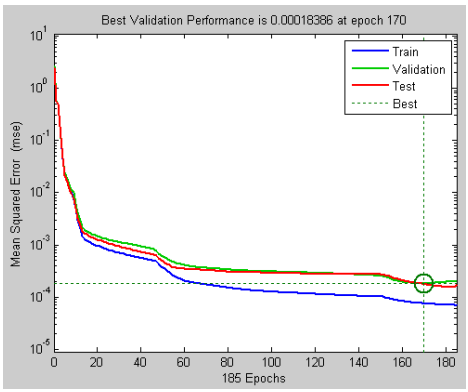

Figure C.1-3: MSE plot for Class 3 Approximator

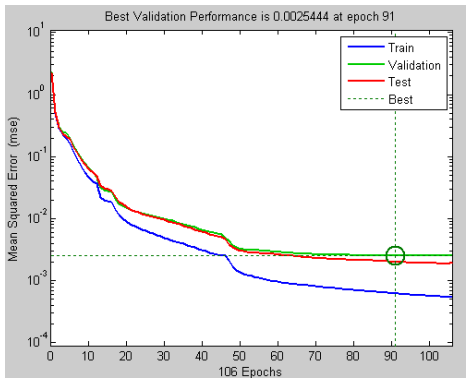

Figure C.1-4: MSE plot for Class 4 Approximator

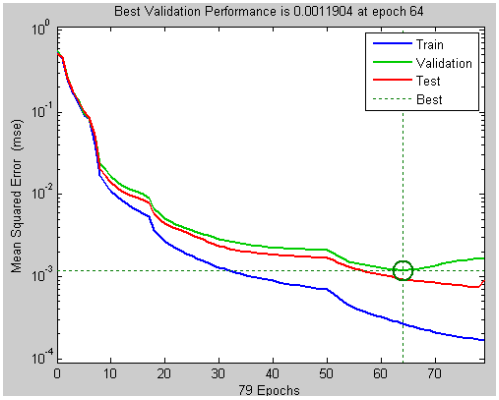

Figure C.1-5: MSE plot for Class 5 Approximator

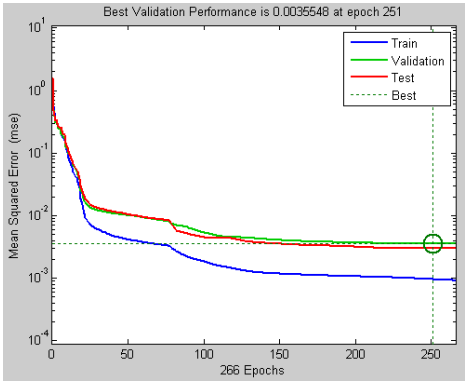

Figure C.1-6: MSE plot for Class 6 Approximator

C.2 : Plots of Final Regressions for Each Trained Network of RB Architecture

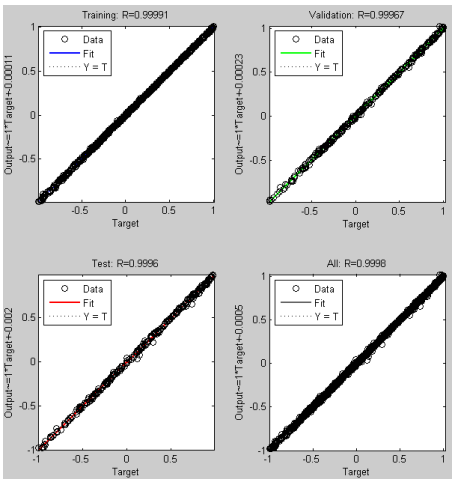

Figure C.2-1: Final regression plot for Class 1 Approximator

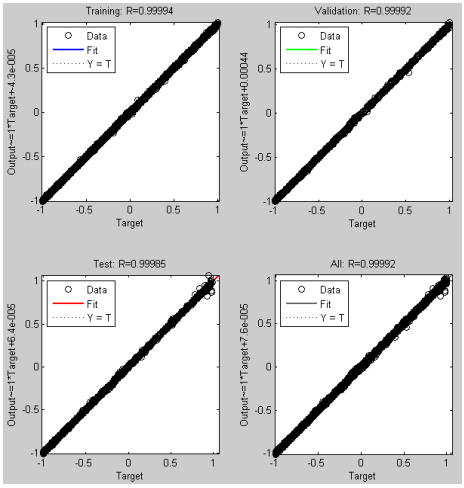

Figure C.2-2: Final regression plot for Class 2 Approximator

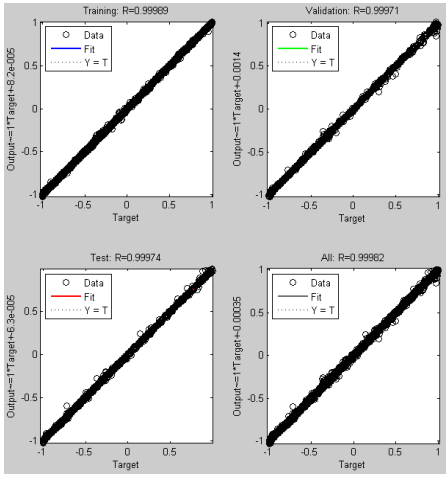

Figure C.2-3: Final regression plot for Class 3 Approximator

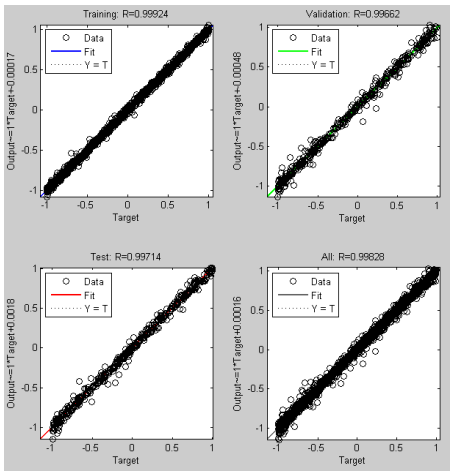

Figure C.2-4: Final regression plot for Class 4 Approximator

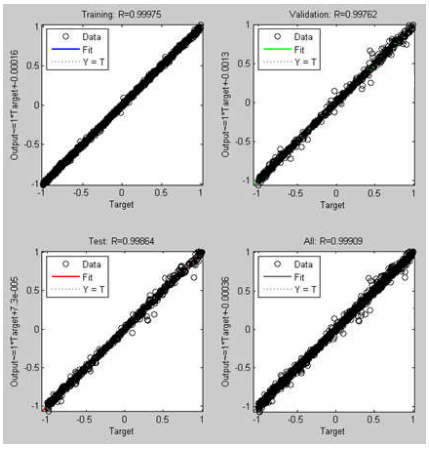

Figure C.2-5: Final regression plot for Class 5 Approximator

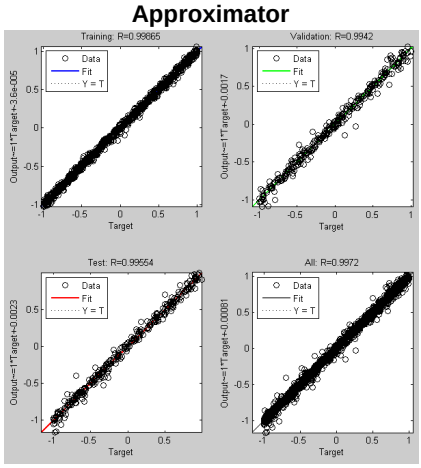

Figure C.2-6: Final regression plot for Class 6 Approximator

C.3 Plots of Confusion Matrices Produce by Range Classifier

Table C.3-1: Confusion matrix produced using the training samples

Output Class \ Target Class	1	2	3	4	5	6	
1	**861** 6.7%	**3** 0.0%	**0** 0.0%	**0** 0.0%	**0** 0.0%	**0** 0.0%	**99.7%** 0.3%
2	**1** 0.0%	**4457** 34.7%	**0** 0.0%	**0** 0.0%	**0** 0.0%	**0** 0.0%	**100.0%** 0.0%
3	**0** 0.0%	**0** 0.0%	**3197** 24.9%	**8** 0.1%	**0** 0.0%	**0** 0.0%	**99.8%** 0.2%
4	**0** 0.0%	**0** 0.0%	**4** 0.0%	**1270** 9.9%	**9** 0.1%	**0** 0.0%	**99.0%** 1.0%
5	**0** 0.0%	**0** 0.0%	**0** 0.0%	**4** 0.0%	**2086** 16.2%	**7** 0.1%	**99.5%** 0.5%
6	**0** 0.0%	**0** 0.0%	**0** 0.0%	**0** 0.0%	**3** 0.0%	**947** 7.4%	**99.7%** 0.3%
	99.9% 0.1%	**99.9%** 0.1%	**99.9%** 0.1%	**99.1%** 0.9%	**99.4%** 0.6%	**99.3%** 0.7%	**99.7%** **0.3%**

Table C.3-2: Confusion matrix produced using the validation samples

Output Class \ Target Class	1	2	3	4	5	6	
1	**277** 6.5%	**7** 0.2%	**0** 0.0%	**0** 0.0%	**0** 0.0%	**0** 0.0%	**97.5%** 2.5%
2	**5** 0.1%	**1494** 34.9%	**8** 0.2%	**0** 0.0%	**0** 0.0%	**0** 0.0%	**99.1%** 0.9%
3	**0** 0.0%	**7** 0.2%	**1077** 25.1%	**8** 0.2%	**0** 0.0%	**0** 0.0%	**98.6%** 1.4%
4	**0** 0.0%	**0** 0.0%	**12** 0.3%	**383** 8.9%	**14** 0.3%	**0** 0.0%	**93.6%** 6.4%
5	**0** 0.0%	**0** 0.0%	**0** 0.0%	**11** 0.3%	**674** 15.7%	**8** 0.2%	**97.3%** 2.7%
6	**0** 0.0%	**0** 0.0%	**0** 0.0%	**0** 0.0%	**7** 0.2%	**293** 6.8%	**97.7%** 2.3%
	98.2% 1.8%	**99.1%** 0.9%	**98.2%** 1.8%	**95.3%** 4.7%	**97.0%** 3.0%	**97.3%** 2.7%	**98.0%** **2.0%**

Table C.3-3: Confusion matrix produced using the test samples

Output Class \ Target Class	1	2	3	4	5	6	
1	**262** 6.1%	**4** 0.1%	**0** 0.0%	**0** 0.0%	**0** 0.0%	**0** 0.0%	**98.5%** 1.5%
2	**4** 0.1%	**1529** 35.7%	**16** 0.4%	**0** 0.0%	**0** 0.0%	**0** 0.0%	**98.7%** 1.3%
3	**0** 0.0%	**6** 0.1%	**1041** 24.3%	**9** 0.2%	**0** 0.0%	**0** 0.0%	**98.6%** 1.4%
4	**0** 0.0%	**0** 0.0%	**9** 0.2%	**412** 9.6%	**13** 0.3%	**0** 0.0%	**94.9%** 5.1%
5	**0** 0.0%	**0** 0.0%	**0** 0.0%	**13** 0.3%	**657** 15.3%	**11** 0.3%	**96.5%** 3.5%
6	**0** 0.0%	**0** 0.0%	**0** 0.0%	**0** 0.0%	**9** 0.2%	**290** 6.8%	**97.0%** 3.0%
	98.5% 1.5%	**99.4%** 0.6%	**97.7%** 2.3%	**94.9%** 5.1%	**96.8%** 3.2%	**96.3%** 3.7%	**97.8%** **2.2%**

Appendix D : Step Size Used for Each Parameter and the Distribution of Samples for the Post Tests of RB Architecture

First Unseen Data							
Parameter	LL	UL	Step size	Parameter	LL	UL	Step size
Altitude	100	4900	200	Mach number	0.03	0.27	0.06
PCN	0.946	0.994	0.012	Ambient temperature deviation from ISA	1	29	4
Initial samples generated			4375	Final samples generated			4060
Distribution of finalised sampled							
Class 1 approximator			205	Class 2 approximator			1447
Class 3 approximator			1041	Class 4 approximator			407
Class 5 approximator			698	Class 6 approximator			262
Second Unseen Data							
Parameter	LL	UL	Step size	Parameter	LL	UL	Step size
Altitude	125	4925	200	Mach number	0.03	0.27	0.06
PCN	0.946	0.994	0.012	Ambient temperature deviation from ISA	1	29	4
Initial samples generated			4375	Final samples generated			4051
Distribution of finalised sampled							
Class 1 approximator			203	Class 2 approximator			1432
Class 3 approximator			1047	Class 4 approximator			408
Class 5 approximator			701	Class 6 approximator			260

Appendix E : Percentage of Samples within the Specified Levels of Error Range for Post Test

First Unseen Data							
Level of Error Range	% of Samples Within the Specified Level of Range						
	Class 1	Class 2	Class 3	Class 4	Class 5	Class 6	Average
T1	85.85	83.97	79.82	61.92	68.91	55.34	72.64
T2	98.05	95.85	91.16	81.82	91.12	85.50	90.58
T3	99.02	98.75	95.87	89.43	98.14	94.66	95.98
T4	100.00	99.86	97.98	93.85	99.14	96.18	97.84
T5	100.00	99.93	99.23	95.82	99.28	97.71	98.66
T6	100.00	100.00	99.62	97.30	99.57	99.24	99.29
Second Unseen Data							
Level of Error Range	% of Samples Within the Specified Level of Range						
	Class 1	Class 2	Class 3	Class 4	Class 5	Class 6	Average
T1	87.19	84.63	80.23	62.00	68.62	56.53	73.20
T2	98.03	96.24	91.69	80.15	91.73	84.62	90.41
T3	99.50	98.75	95.70	88.24	96.43	94.23	95.48
T4	100.00	99.65	97.52	91.18	98.29	99.23	97.65
T5	100.00	99.79	98.37	93.87	98.25	99.23	98.25
T6	100.00	99.89	99.33	96.32	97.28	99.23	98.68

Appendix F : PDF and CDF Plots of the Best Fitted Distribution for Each Class Approximator Using the Combined Unseen Samples

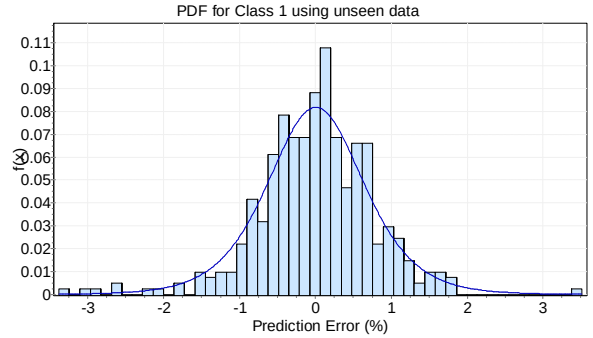

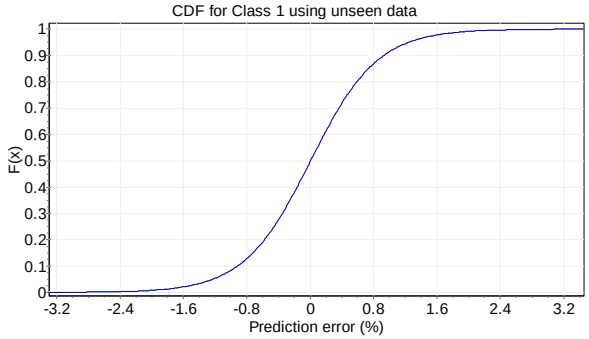

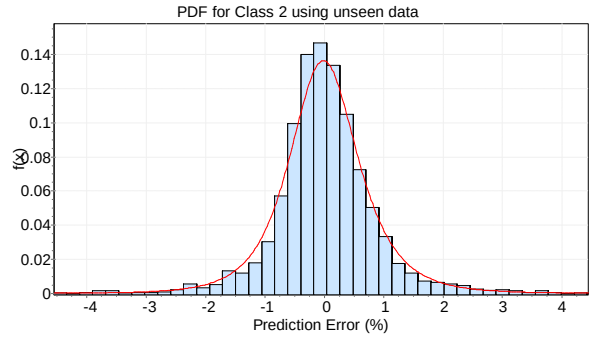

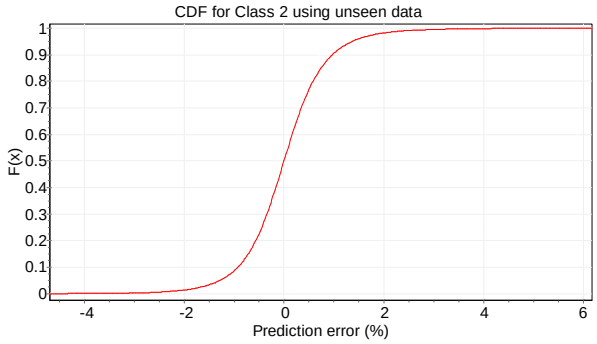

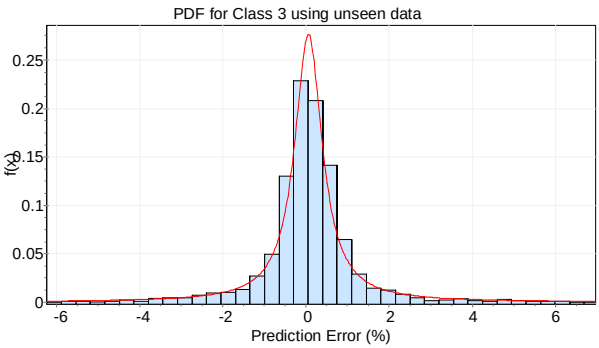

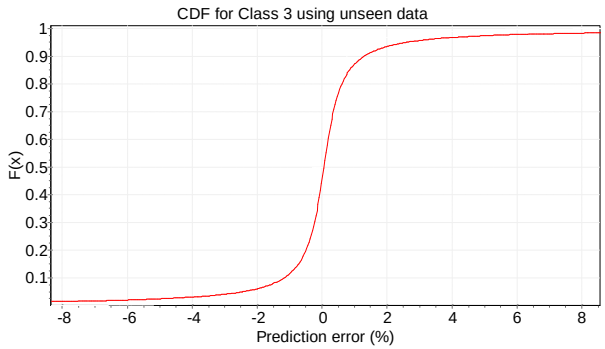

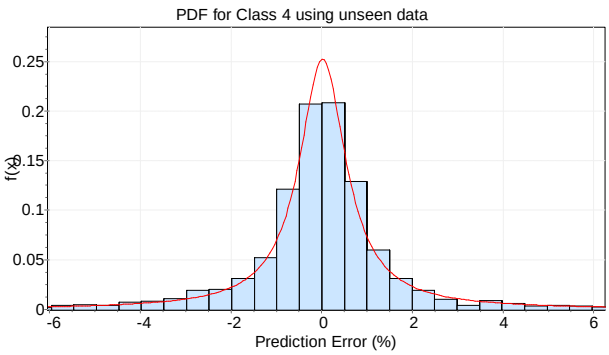

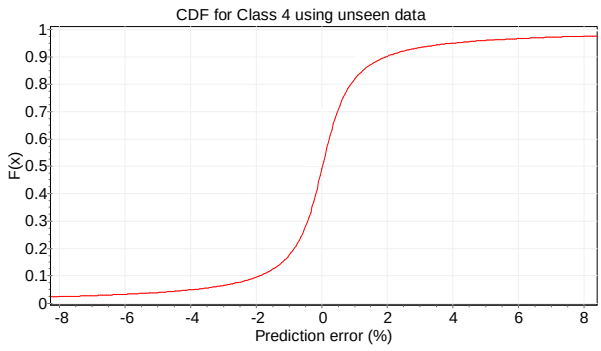

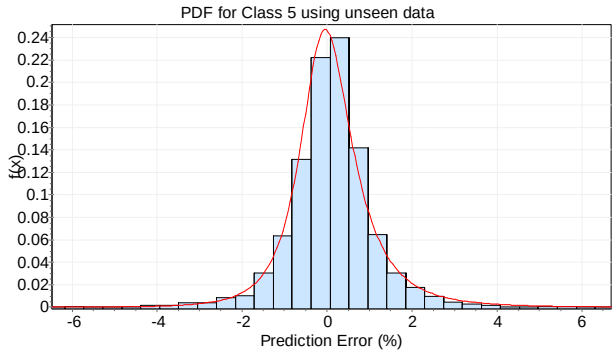
PDF for Class 5 using unseen data
f(x)
Prediction Error (%)

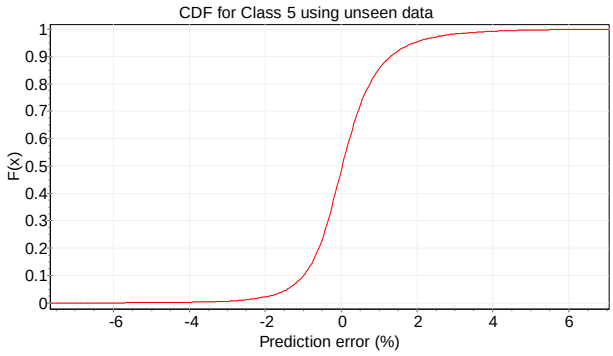
CDF for Class 5 using unseen data
F(x)
Prediction error (%)

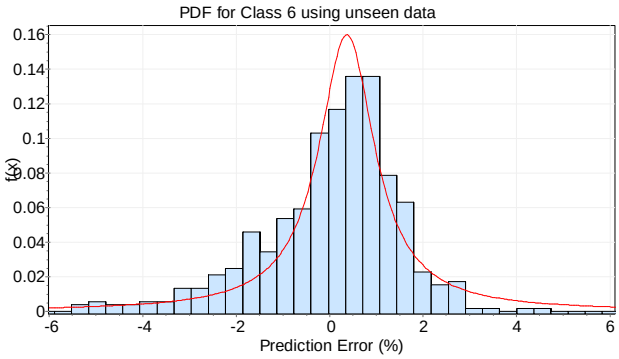
PDF for Class 6 using unseen data
f(x)
Prediction Error (%)

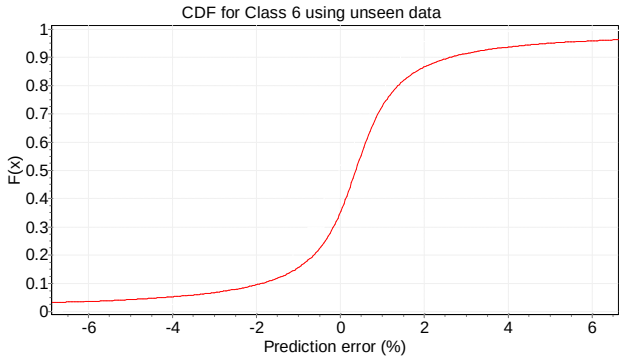
CDF for Class 6 using unseen data
F(x)
Prediction error (%)

Appendix G : Plots of MSE and Final Regressions for Each Trained Network of FB Architecture at Clean Engine Condition

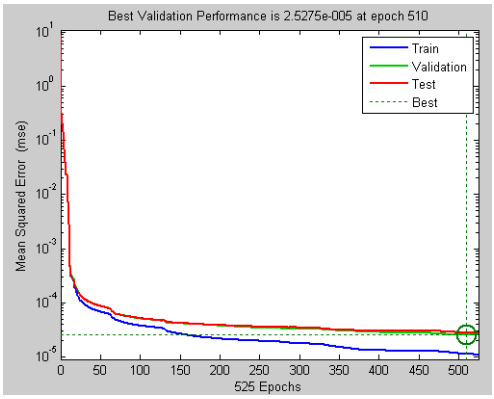

Figure G-1: MSE plot for Blade Temp Approximator

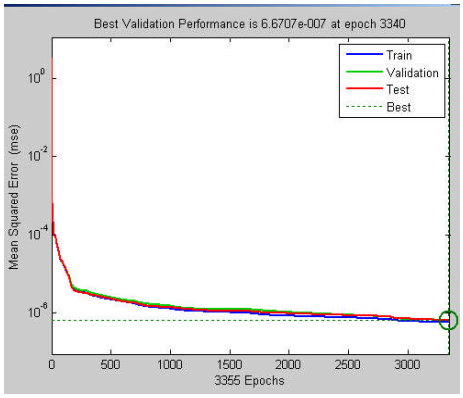

Figure G-2: MSE plot for Blade Stress Approximator

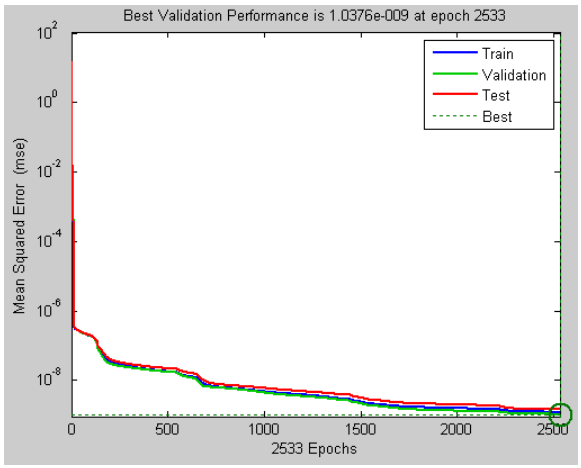

Figure G-3: MSE plot for Creep Life Approximator

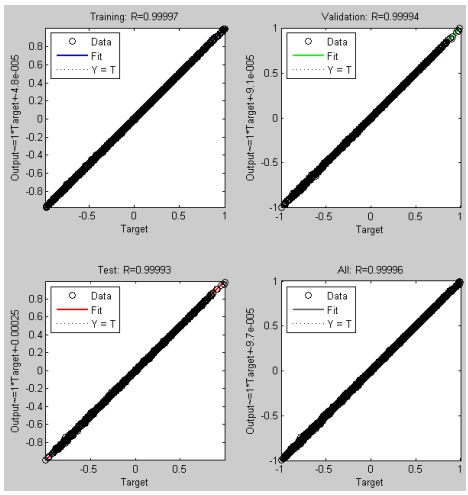

Figure G-4: Final regression plot for Blade Temp Approximator

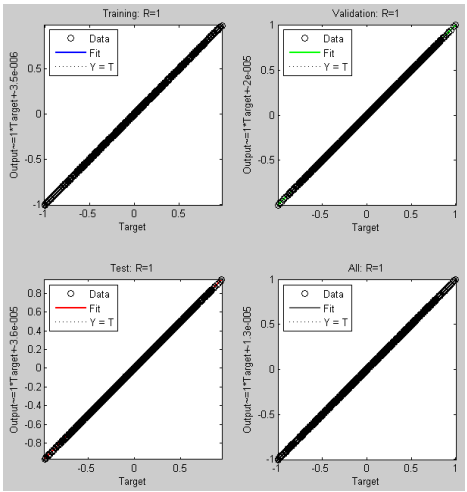

Figure G-5: Final regression plot for Blade Stress Approximator

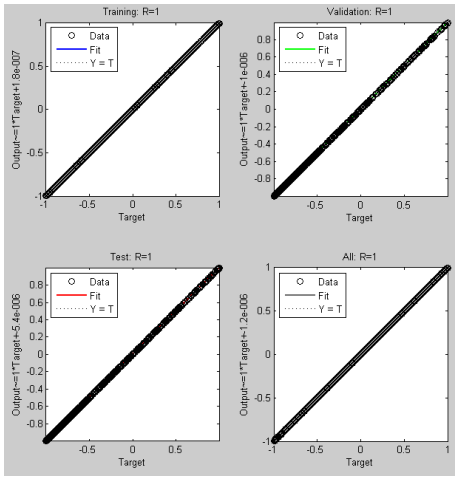

Figure G-6: Final regression plot for Creep Life Approximator

Appendix H : Step Size Used for Each Parameter and the Amount of Initial and Finalised Samples for the Post Tests of FB Architecture

First Unseen Data							
Parameter	LL	UL	Step size	Parameter	LL	UL	Step size
Altitude	150	4,650	300	Mach number	0.03	0.27	0.06
PCN	0.943	0.997	0.006	Ambient temperature deviation from ISA	2	29	3
Initial samples			8,000	Finalised samples			6,635
Second Unseen Data							
Parameter	**LL**	**UL**	**Step size**	**Parameter**	**LL**	**UL**	**Step size**
Altitude	70	4,575	300	Mach number	0.03	0.27	0.06
PCN	0.943	0.997	0.006	Ambient temperature deviation from ISA	2	29	3
Initial samples			8,000	Finalised samples			6,740

Appendix I : Plots of MSE and Final Regressions for Each Trained Network of Sensor-Based Architecture at Clean Engine Condition

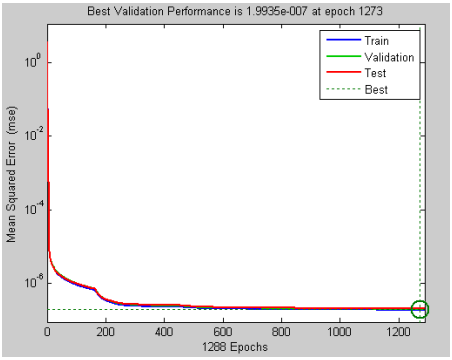

Figure I-1: MSE plot for Blade Temp Approximator

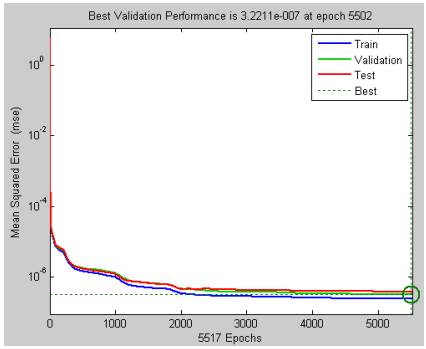

Figure I-2: MSE plot for Blade Stress Approximator

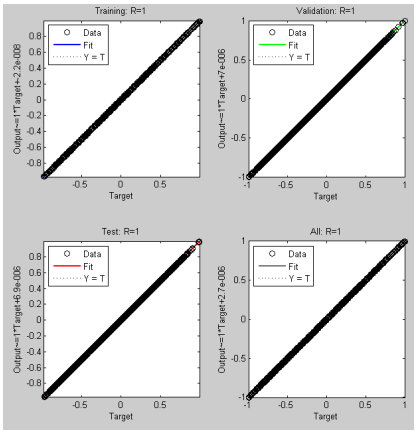

Figure I-3: Final regression plot for Blade Temp Approximator

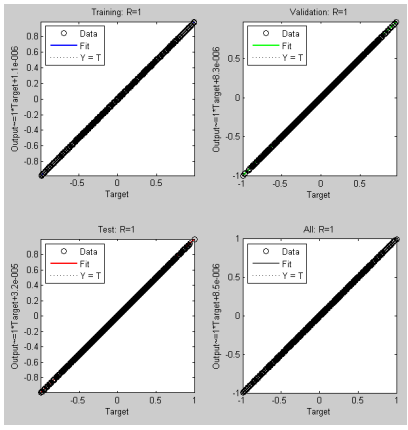

Figure I-4: Final regression plot for Blade Stress Approximator

Appendix J : Step Size for Each Parameter and Samples Size for FB Architecture Approximators of Degraded Engine Condition.

J.1 : Step Size for Each Parameter and Samples Used to Train Compressor Degradation for FB Architecture

LL1							
Parameter	LL	UL	Step size	Parameter	LL	UL	Step size
Altitude	0	900	300	PCN	0.94	1	0.006
Mach number	0	0.3	0.06	Tamb dev.	10	25	3
% in ETA and FC	-0.5	-2	0.5 (approx.)		Finalised samples		21,791
LL2							
Parameter	LL	UL	Step size	Parameter	LL	UL	Step size
Altitude	1000	1900	300	PCN	0.94	1	0.006
Mach number	0	0.3	0.06	Tamb dev.	10	25	3
% in ETA and FC	-0.5	-2	0.5 (approx.)		Finalised samples		22,769
LL3							
Parameter	LL	UL	Step size	Parameter	LL	UL	Step size
Altitude	2000	2900	300	PCN	0.94	1	0.006
Mach number	0	0.3	0.06	Tamb dev.	10	25	3
% in ETA and FC	-0.5	-2	0.5 (approx.)		Finalised samples		23,581
LL4							
Parameter	LL	UL	Step size	Parameter	LL	UL	Step size
Altitude	3000	4500	300	PCN	0.94	1	0.0075
Mach number	0	0.3	0.06	Tamb dev.	10	25	3
% in ETA and FC	-0.5	-2	0.5 (approx.)		Finalised samples		23,421
ML1							
Parameter	LL	UL	Step size	Parameter	LL	UL	Step size
Altitude	0	1500	300	PCN	0.94	1	0.0075
Mach number	0	0.3	0.06	Tamb dev.	10	25	3
% in ETA and FC	-2.5	-4	0.5 (approx.)		Finalised samples		29,490
ML2							
Parameter	LL	UL	Step size	Parameter	LL	UL	Step size
Altitude	1500	3000	300	PCN	0.94	1	0.0075
Mach number	0	0.3	0.06	Tamb dev.	10	25	3
% in ETA and FC	-2.5	-4	0.5 (approx.)		Finalised samples		30,745
ML3							
Parameter	LL	UL	Step size	Parameter	LL	UL	Step size
Altitude	3000	4500	300	PCN	0.94	1	0.0075
Mach number	0	0.3	0.06	Tamb dev.	10	25	3
% in ETA and FC	-2.5	-4	0.5 (approx.)		Finalised samples		30,086
HL1							
Parameter	LL	UL	Step size	Parameter	LL	UL	Step size
Altitude	0	1500	300	PCN	0.94	1	0.0075
Mach number	0	0.3	0.06	Tamb dev.	10	25	3
% in ETA and FC	-4.5	-6	0.5 (approx.)		Finalised samples		30,089
HL2							
Parameter	LL	UL	Step size	Parameter	LL	UL	Step size
Altitude	1500	3000	300	PCN	0.94	1	0.0075
Mach number	0	0.3	0.06	Tamb dev.	10	25	3
% in ETA and FC	-4.5	-6	0.5 (approx.)		Finalised samples		30,008
HL3							
Parameter	LL	UL	Step size	Parameter	LL	UL	Step size
Altitude	3000	4500	300	PCN	0.94	1	0.0075
Mach number	0	0.3	0.06	Tamb dev.	10	25	3
% in ETA and FC	-4.5	-6	0.5 (approx.)		Finalised samples		30,064

J.2 : Step Size for Each Parameter and Samples Used to Train HP and LP Turbine Degradation for FB Architecture

LL1							
Parameter	LL	UL	Step size	Parameter	LL	UL	Step size
Altitude	0	1500	300	PCN	0.94	1	0.0075
Mach number	0	0.3	0.06	Tamb dev.	10	25	3
% in ETA	-0.5	-2	0.5 (approx.)	Finalised samples (HP Turbine)			28,455
% in FC	0.5	2	0.5 (approx.)	Finalised samples (LP Turbine)			26,695

LL2							
Parameter	LL	UL	Step size	Parameter	LL	UL	Step size
Altitude	1500	3000	300	PCN	0.94	1	0.0075
Mach number	0	0.3	0.06	Tamb dev.	10	25	3
% in ETA	-0.5	-2	0.5 (approx.)	Finalised samples (HP Turbine)			28,225
% in FC	0.5	2	0.5 (approx.)	Finalised samples (LP Turbine)			27,526

LL3							
Parameter	LL	UL	Step size	Parameter	LL	UL	Step size
Altitude	3000	4500	300	PCN	0.94	1	0.0075
Mach number	0	0.3	0.06	Tamb dev.	10	25	3
% in ETA	-0.5	-2	0.5 (approx.)	Finalised samples (HP Turbine)			29,307
% in FC	0.5	2	0.5 (approx.)	Finalised samples (LP Turbine)			29,545

ML1							
Parameter	LL	UL	Step size	Parameter	LL	UL	Step size
Altitude	0	1500	300	PCN	0.94	1	0.0075
Mach number	0	0.3	0.06	Tamb dev.	10	25	3
% in ETA	-2.5	-4	0.5 (approx.)	Finalised samples (HP Turbine)			28,537
% in FC	2.5	4	0.5 (approx.)	Finalised samples (LP Turbine)			31,086

ML2							
Parameter	LL	UL	Step size	Parameter	LL	UL	Step size
Altitude	1500	3000	300	PCN	0.94	1	0.0075
Mach number	0	0.3	0.06	Tamb dev.	10	25	3
% in ETA	-2.5	-4	0.5 (approx.)	Finalised samples (HP Turbine)			30,292
% in FC	2.5	4	0.5 (approx.)	Finalised samples (LP Turbine)			29,910

ML3							
Parameter	LL	UL	Step size	Parameter	LL	UL	Step size
Altitude	3000	4500	300	PCN	0.94	1	0.0075
Mach number	0	0.3	0.06	Tamb dev.	10	25	3
% in ETA	-2.5	-4	0.5 (approx.)	Finalised samples (HP Turbine)			30,228
% in FC	2.5	4	0.5 (approx.)	Finalised samples (LP Turbine)			30,132

HL1							
Parameter	LL	UL	Step size	Parameter	LL	UL	Step size
Altitude	0	1500	300	PCN	0.94	1	0.0075
Mach number	0	0.3	0.06	Tamb dev.	10	25	3
% in ETA	-4.5	-6	0.5 (approx.)	Finalised samples (HP Turbine)			30,337
% in FC	4.5	6	0.5 (approx.)	Finalised samples (LP Turbine)			29,243

HL2							
Parameter	LL	UL	Step size	Parameter	LL	UL	Step size
Altitude	1500	3000	300	PCN	0.94	1	0.0075
Mach number	0	0.3	0.06	Tamb dev.	10	25	3
% in ETA	-4.5	-6	0.5 (approx.)	Finalised samples (HP Turbine)			30,328
% in FC	4.5	6	0.5 (approx.)	Finalised samples (LP Turbine)			25,246

HL3							
Parameter	LL	UL	Step size	Parameter	LL	UL	Step size
Altitude	3000	4500	300	PCN	0.94	1	0.0075
Mach number	0	0.3	0.06	Tamb dev.	10	25	3
% in ETA	-4.5	-6	0.5 (approx.)	Finalised samples (HP Turbine)			30,573
% in FC	4.5	6	0.5 (approx.)	Finalised samples (LP Turbine)			26.978

Appendix K : Final sizes of the trained approximators for all component degradation

Magnitude And Altitude Level	Blade Metal Temperature Approximator	Blade Stress Approximator	Creep Life Approximator
Compressor degradation			
LL1	6-30-40-1	6-10-10-1	2-15-15-1
LL2	6-30-30-1	6-15-15-1	2-20-20-1
LL3	6-30-30-1	6-17-17-1	2-20-20-1
LL4	6-30-30-1	6-18-18-1	2-22-22-1
ML1	6-30-30-1	6-19-19-1	2-22-22-1
ML2	6-30-30-1	6-19-19-1	2-22-22-1
ML3	6-30-30-1	6-19-19-1	2-22-22-1
HL1	6-30-30-1	6-20-20-1	2-22-22-1
HL2	6-30-35-1	6-20-22-1	2-22-24-1
HL3	6-30-35-1	6-20-22-1	2-22-24-1
HP turbine degradation			
LL1	6-30-32-1	6-20-22-1	2-21-22-1
LL2	6-30-30-1	6-20-23-1	2-21-22-1
LL3	6-30-40-1	6-20-23-1	2-22-23-1
ML1	6-35-35-1	6-25-25-1	2-23-23-1
ML2	6-33-33-1	6-25-25-1	2-23-23-1
ML3	6-33-33-1	6-25-25-1	2-25-25-1
HL1	6-35-35-1	6-25-25-1	2-23-23-1
HL2	6-35-35-1	6-25-25-1	6-23-23-1
HL3	6-35-35-1	6-25-25-1	2-25-25-1
LP turbine degradation			
LL1	6-35-35-1	6-25-25-1	2-25-25-1
LL2	6-35-35-1	6-25-25-1	2-25-25-1
LL3	6-35-35-1	6-25-25-1	2-25-25-1
ML1	6-35-40-1	6-25-25-1	2-25-25-1
ML2	6-35-40-1	6-25-25-1	2-25-25-1
ML3	6-35-40-1	6-25-25-1	2-25-25-1
HL1	6-35-40-1	6-25-25-1	2-25-25-1
HL2	6-35-40-1	6-25-25-1	2-25-25-1
HL3	6-35-40-1	6-25-25-1	2-25-25-1

Appendix L : The training, validation and test samples' MSE and R of the Approximators during the Training and After the Training Was Stopped.

L.1 : The final MSE and R of the Approximators for Compressor Degradation

Low Level Degradation												
	LL1			LL2			LL3			LL4		
	Temp	Stress	Creep	Temp	Stress	Creep	Temp	Stress	Creep	Temp	Stress	Creep
Training sample												
MSE	1.98E-06	1.69E-06	1.37E-12	3.77E-06	5.75E-07	8.92E-12	2.4E-06	2.95E-07	3.35E-13	2.04E-06	1.58e-07	1.66E-13
R	1	1	1	1	1	1	0.99999	1	1	0.99999	1	1
Validation sample												
MSE	3.77E-06	1.67E-06	1.19E-11	5.17E-06	6.81E-07	9.38E-12	4.57E-06	3.547E-07	3.69E-13	4.28E-06	1.94E-07	3.92E-13
R	0.99999	1	1	0.99999	1	1	0.99999	1	1	0.99999	1	1
Test sample												
MSE	3.87E-06	1.74E-06	1.11E-10	6.66E-06	6.23E-7	1.07E-11	5.99E-06	3.9E-07	4.2E-13	7.13E-06	2.08e-7	1.67E-12
R	0.99999	1	1	0.99999	1	1	0.99999	1	1	0.99998	1	1
Medium Level Degradation												
	ML1			ML2			ML3					
	Temp	Stress	Creep	Temp	Stress	Creep	Temp	Stress	Creep			
Training sample												
MSE	5.85E-07	1.12E-07	1.08E-12	6.98E-07	5.81E-08	1.14E-11	1.04E-06	8.92E-08	2.10E-12			
R	1	1	1	1	1	1	1	1	1			
Validation sample												
MSE	1.27E-06	1.55E-07	1.27E-11	1.12E-06	7.55E-08	1.86E-11	1.54E-06	1.03E-07	2.35E-12			
R	1	1	1	1	1	1	1	1	1			
Test sample												
MSE	1.35E-06	1.42E-07	1.56E-11	1.06E-6	7.38E-08	2.05E-11	1.66E-06	1.05E-07	2.28E-12			
R	1	1	1	1	1	1	1	1	1			
High Level Degradation												
	HL1			HL2			HL3					
	Temp	Stress	Creep	Temp	Stress	Creep	Temp	Stress	Creep			
Training sample												
MSE	6.43E-07	1.55E-07	1.26E-11	6.13E-07	8.13E-08	1.47E-12	1.28E-06	5.86E-08	7.53E-13			

R	1	1	1	1	1	1	1	1	1			
Validation sample												
MSE	1.02E-06	1.65E-07	8.03E-12	1.39E-06	9.57E-08	2.44E-12	1.95E-06	7.15E-08	8.18E-13			
R	1	1	1	1	1	1	1	1	1			
Test sample												
MSE	1.37E-06	1.77E-07	1.21E-11	1.33E-06	1.1E-07	2.47E-12	2.02E-06	7.18E-08	8.88E-13			
R	1	1	1	1	1	1	1	1	1			

L.2 : The final MSE and R of the Approximators for HP Turbine Degradation

Low Level Degradation									
	LL1			LL2			LL3		
	Temp	Stress	Creep	Temp	Stress	Creep	Temp	Stress	Creep
Training sample									
MSE	2.97E-06	3.24E-07	1.17E-11	2.61E-06	3.56E-07	2.00E-11	2.04E-06	1.66E-07	1.04E-12
R	0.99999	1	1	0.99999	1	1	0.99999	1	1
Validation sample									
MSE	4.71E-06	4.09E-07	8.36E-11	4.75E-06	4.29E-07	2.09E-11	4.80E-06	2.16E-07	2.21E-12
R	0.99999	1	1	0.99999	1	1	0.99998	1	1
Test sample									
MSE	4.85E-06	3.70E-07	1.83E-11	5.99E-06	4.41E-07	2.34E-11	3.51E-06	2.49E-07	2.57E-12
R	0.99999	1	1	0.99999	1	1	0.99999	1	1
Medium Level Degradation									
	LL1			LL2			LL3		
	Temp	Stress	Creep	Temp	Stress	Creep	Temp	Stress	Creep
Training sample									
MSE	8.47E-07	1.67E-07	2.62E-11	7.92E-07	1.23E-07	2.23E-12	7.58E-07	1.30E-07	4.62E-12
R	1	1	1	1	1	1	1	1	1
Validation sample									
MSE	2.30E-06	2.46E-07	3.04E-11	1.48E-06	1.99E-07	3.81E-12	1.24E-06	1.68E-07	4.87E-12
R	1	1	1	1	1	1	1	1	1
Test sample									
MSE	2.42E-06	2.25E-07	4.73E-11	1.37E-06	1.73E-07	2.86E-12	1.46E-06	1.71E-07	6.23E-12
R	1	1	1	1	1	1	1	1	1

High Level Degradation									
	LL1			LL2			LL3		
	Temp	Stress	Creep	Temp	Stress	Creep	Temp	Stress	Creep
Training sample									
MSE	3.85E-07	1.25E-07	3.41E-12	6.87E-07	2.13E-07	3.27E-10	4.71E-07	3.48E-08	2.27E-10
R	1	1	1	1	1	1	1	1	1
Validation sample									
MSE	7.05E-07	2.21E-07	5.11E-12	1.45E-06	2.34E-07	3.93E-10	7.69E-07	4.49E-08	3.15E-10
R	1	1	1	1	1	1	1	1	1
Test sample									
MSE	6.98E-07	2.24E-07	7.17E-12	1.20E-06	2.94E-07	3.67E-10	7.85E-07	4.14E-08	3.46E-10
R	1	1	1	1	1	1	1	1	1

L.3 : The final MSE and R of the Approximators for LP Turbine Degradation

Low Level Degradation									
	LL1			LL2			LL3		
	Temp	Stress	Creep	Temp	Stress	Creep	Temp	Stress	Creep
Training sample									
MSE	1.90E-06	1.37E-07	1.36E-12	2.92E-06	9.76E-08	6.70E-12	1.49E-06	6.17E-08	3.27E-13
R	1	1	1	0.99999	1	1	1	1	1
Validation sample									
MSE	3.23E-06	1.74E-07	1.87E-12	5.63E-06	1.31E-07	8.11E-12	2.94E-06	8.82E-08	6.55E-13
R	0.99999	1	1	0.99999	1	1	0.99999	1	1
Test sample									
MSE	3.47E-06	1.59E-07	2.00E12	4.38E-06	1.28E-07	9.09E-12	3.95E-06	8.61E-08	8.73E-13
R	0.99999	1	1	0.99999	1	1	0.99999	1	1
Medium Level Degradation									
	LL1			LL2			LL3		
	Temp	Stress	Creep	Temp	Stress	Creep	Temp	Stress	Creep
Training sample									
MSE	5.90E-07	4.02E-08	4.85E-12	1.69E-06	2.06E-08	8.73E-12	7.94E-07	3.27E-08	5.73E-12
R	1	1	1	1	1	1	1	1	1

Validation sample									
MSE	1.23E-06	5.92E-08	9.75E-12	2.23E-06	3.02E-08	1.49E-11	1.36E-06	3.88E-08	1.05E-11
R	1	1	1	1	1	1	1	1	1
Test sample									
MSE	1.12E-06	5.90E-08	6.69E-12	2.85E-06	2.92E-08	1.17E-11	1.29E-06	3.97E-08	1.02E-11
R	1	1	1	1	1	1	1	1	1
High Level Degradation									
	LL1			LL2			LL3		
	Temp	Stress	Creep	Temp	Stress	Creep	Temp	Stress	Creep
Training sample									
MSE	2.34E-07	2.88E-08	7.91E-12	3.06E-07	1.40E-08	2.64E-12	5.54E-07	2.29E-08	4.94E-12
R	1	1	1	1	1	1	1	1	1
Validation sample									
MSE	3.97E-07	3.78E-08	5.81E-12	5.98E-07	1.92E-08	1.67E-12	1.04E-06	3.26E-08	5.57E-12
R	1	1	1	1	1	1	1	1	1
Test sample									
MSE	4.08E-07	3.11E-08	1.38E-11	5.72E-07	2.36E-08	2.43E-12	1.07E-06	3.55E-08	8.77E-12
R	1	1	1	1	1	1	1	1	1

Appendix M : The Predicted Outputs E_{Ave} and SD_E for the entire Component Degradation Trained Networks.

		Compressor Deg.		HP Turbine Deg.		LP Turbine Deg.	
Level	Approx. Network	E_{Ave}	SD_E	E_{Ave}	SD_E	E_{Ave}	SD_E
LL1	Blade Temp	-3.90E-05	0.01365	-1.34E-04	0.01635	3.91E-05	0.01294
	Blade Stress	-3.18E-05	0.01177	-1.90E-04	0.00558	6.53E-06	0.00324
	Creep Life	-4.88E-05	0.02233	-6.7E-05	0.04251	0.000113	0.01623
LL2	Blade Temp	-3.63E-05	0.01702	7.49E-05	0.01626	-3.89E-05	0.01558
	Blade Stress	-2.99E-05	0.00698	1.49E-05	0.00573	-2.94E-04	0.00292
	Creep Life	-7.77E-05	0.02093	-3.9E-05	0.02513	4.77E-05	0.01994
LL3	Blade Temp	2.58E-05	0.01558	-3.13E-05	0.01456	-6.12E-05	0.01114
	Blade Stress	4.43E-05	0.00493	3.15E-05	0.00374	5.22E-06	0.00223
	Creep Life	-2.02E-06	0.00462	3.69E-05	0.00627	2.99E-05	0.00454
LL4	Blade Temp	2.65E-04	0.01555				
	Blade Stress	-2.32E-05	0.00356				
	Creep Life	1.60E-04	0.01156				
ML1	Blade Temp	6.90E-05	0.00821	-1.90E-04	0.01067	7.76E-06	0.00779
	Blade Stress	1.21E-05	0.00337	-1.17E-04	0.00428	2.98E-05	0.00206
	Creep Life	5.25E-04	0.05171	0.00141	0.04767	-0.00015	0.0188
ML2	Blade Temp	-7.32E-05	0.00768	8.19E-06	0.00872	1.12E-05	0.01208
	Blade Stress	1.16E-07	0.00232	8.19E-06	0.00872	6.51E-06	0.0014
	Creep Life	-4.11E-05	0.02407	6.95E-05	0.01442	-0.00019	0.02247
ML3	Blade Temp	-2.07E-05	0.00904	9.90E-05	0.00853	6.76E-05	0.00785
	Blade Stress	3.28E-05	0.00263	-3.63E-05	0.00329	4.95E-06	0.00156
	Creep Life	1.07E-04	0.01146	4.34E-05	0.01549	-5.9E-05	0.01207
HL1	Blade Temp	-3.43E-05	0.00844	9.60E-05	0.00654	1.25E-06	0.00495
	Blade Stress	-1.44E-05	0.00385	-1.86E-05	0.00401	-1.46E-07	0.00168
	Creep Life	-2.06E-04	0.03644	0.000342	0.02046	-0.00017	0.0321
HL2	Blade Temp	-2.24E-05	0.00826	-9.34E-06	0.00839	1.15E-05	0.00546
	Blade Stress	8.32E-06	0.00273	-2.39E-05	0.00446	-5.21E-06	0.00118
	Creep Life	-1.87E-04	0.01995	-0.0003	0.24893	8.59E-05	0.0173
HL3	Blade Temp	-8.27E-06	0.01009	-3.35E-05	0.0064	1.47E-04	0.00706
	Blade Stress	-1.03E-05	0.00215	1.25E-05	0.00167	1.79E-05	0.00142
	Creep Life	1.30E-05	0.0059	0.000667	0.05508	3.34E-05	0.01349

Appendix N : Percentage of Component Degradation Samples Encompassed within the Specified Range

Compressor Degradation											
Error Range	Degradation Magnitude and Altitude Level										
	LL1	LL2	LL3	LL4	ML1	ML2	ML3	HL1	HL2	HL3	Average
T1	93.44	89.19	92.78	93.89	98.42	98.65	97.31	98.89	98.28	96.62	**95.75**
T2	98.7	97.55	98.37	98.75	99.6	99.77	99.68	99.76	99.68	99.39	**99.13**
T3	99.6	99.24	99.36	99.49	99.88	99.93	99.92	99.87	99.9	99.86	**99.71**
T4	99.8	99.7	99.67	99.77	99.94	99.98	99.98	99.97	99.95	99.96	**99.87**
T5	99.9	99.87	99.8	99.86	99.97	99.99	99.99	99.97	99.97	99.99	**99.93**
T6	99.95	99.94	99.86	99.92	99.99	100	100	99.98	99.98	100	**99.96**

HP Turbine Degradation											
Error Range	Degradation Magnitude and Altitude Level										
	LL1	LL2	LL3	LL4	ML1	ML2	ML3	HL1	HL2	HL3	Average
T1	88.78	90.92	93.05	-	96.93	97.94	97.91	99.24	97.13	99.12	**95.67**
T2	98.01	98.1	98.7	-	99.34	99.71	99.78	99.85	99.42	99.94	**99.21**
T3	99.39	99.34	99.49	-	99.83	99.91	99.94	99.96	99.8	99.99	**99.74**
T4	99.75	99.71	99.77	-	99.92	99.95	99.98	99.98	99.92	100	**99.89**
T5	99.91	99.82	99.86	-	99.95	99.98	99.98	99.99	99.96	100	**99.94**
T6	99.97	99.91	99.91	-	99.98	99.99	99.99	99.997	99.97	100	**99.97**

LP Turbine Degradation											
Error Range	Degradation Magnitude and Altitude Level										
	LL1	LL2	LL3	LL4	ML1	ML2	ML3	HL1	HL2	HL3	Average
T1	93.92	91.08	96.44	-	98.25	95.18	98.29	99.65	99.32	98.69	**96.76**
T2	99.05	98.33	99.44	-	99.78	99.32	99.89	99.96	99.95	99.91	**99.51**
T3	99.77	99.43	99.76	-	99.94	99.82	99.96	99.98	99.98	99.96	**99.84**
T4	99.93	99.74	99.86	-	99.98	99.91	99.99	99.99	100	99.99	**99.93**
T5	99.97	99.86	99.92	-	99.99	99.93	99.993	99.997	100	99.99	**99.96**
T6	99.97	99.93	99.95	-	99.99	99.96	99.996	99.997	100	100	**99.98**

Appendix O : Step Size and Unseen Samples Size for Each Parameter Used During Post Test of the FB Architecture Approximators of Degraded Engine Condition

O.1 : Step Size for Each Parameter and Unseen Samples Used during Post Test of Compressor Degradation Functional Based Architecture

LL1							
Parameter	LL	UL	Step size	Parameter	LL	UL	Step size
Altitude	200	800	200	PCN	0.943	0.997	0.006
Mach number	0.03	0.27	0.06	Tamb dev.	11	23	3
% in ETA	-0.25	-1.75	0.5 (approx.)	% in FC	-0.4	-1.6	0.4 (approx.)
					Finalised samples		14,195
LL2							
Parameter	LL	UL	Step size	Parameter	LL	UL	Step size
Altitude	1200	1800	200	PCN	0.943	0.997	0.006
Mach number	0.03	0.27	0.06	Tamb dev.	11	23	3
% in ETA	-0.25	-1.75	0.5 (approx.)	% in FC	-0.4	-1.6	0.4 (approx.)
					Finalised samples		14,776
LL3							
Parameter	LL	UL	Step size	Parameter	LL	UL	Step size
Altitude	2200	2800	200	PCN	0.943	0.997	0.006
Mach number	0.03	0.27	0.06	Tamb dev.	11	23	3
% in ETA	-0.25	-1.75	0.5 (approx.)	% in FC	-0.4	-1.6	0.4 (approx.)
					Finalised samples		14,291
LL4							
Parameter	LL	UL	Step size	Parameter	LL	UL	Step size
Altitude	3200	4400	200	PCN	0.943	0.997	0.006
Mach number	0.03	0.27	0.06	Tamb dev.	11	23	3
% in ETA	-0.25	-1.75	0.5 (approx.)	% in FC	-0.4	-1.6	0.4 (approx.)
					Finalised samples		25,262
ML1							
Parameter	LL	UL	Step size	Parameter	LL	UL	Step size
Altitude	200	1400	200	PCN	0.943	0.997	0.006
Mach number	0.03	0.27	0.06	Tamb dev.	11	23	3
% in ETA	-2.25	-3.75	0.5 (approx.)	% in FC	-2.4	-3.6	0.4 (approx.)
					Finalised samples		27,183
ML2							
Parameter	LL	UL	Step size	Parameter	LL	UL	Step size
Altitude	1700	2900	200	PCN	0.943	0.997	0.006
Mach number	0.03	0.27	0.06	Tamb dev.	11	23	3
% in ETA	-2.25	-3.75	0.5 (approx.)	% in FC	-2.4	-3.6	0.4 (approx.)
					Finalised samples		27,482
ML3							
Parameter	LL	UL	Step size	Parameter	LL	UL	Step size
Altitude	3200	4400	200	PCN	0.943	0.997	0.006
Mach number	0.03	0.27	0.06	Tamb dev.	11	23	3
% in ETA	-2.25	-3.75	0.5 (approx.)	% in FC	-2.4	-3.6	0.4 (approx.)
					Finalised samples		27,855
HL1							
Parameter	LL	UL	Step size	Parameter	LL	UL	Step size
Altitude	200	1400	200	PCN	0.943	0.997	0.006
Mach number	0.03	0.27	0.06	Tamb dev.	11	23	3
% in ETA	-4.25	-5.75	0.5 (approx.)	% in FC	-4.4	-5.6	0.4 (approx.)
					Finalised samples		27,743
HL2							

Parameter	LL	UL	Step size	Parameter	LL	UL	Step size
Altitude	1700	2900	200	PCN	0.943	0.997	0.006
Mach number	0.03	0.27	0.06	Tamb dev.	11	23	3
% in ETA	-4.25	-5.75	0.5 (approx.)	% in FC	-4.4	-5.6	0.4 (approx.)
					Finalised samples		27,733

HL3

Parameter	LL	UL	Step size	Parameter	LL	UL	Step size
Altitude	3200	4400	200	PCN	0.943	0.997	0.006
Mach number	0.03	0.27	0.06	Tamb dev.	11	23	3
% in ETA	-4.25	-5.75	0.5 (approx.)	% in FC	-4.4	-5.6	0.4 (approx.)
					Finalised samples		27,868

O.2 : Step Sizes and Unseen Samples Sizes for Each Parameter Used during Post Test of HP and LP Turbine Degradation FB Architecture

LL1

Parameter	LL	UL	Step size	Parameter	LL	UL	Step size
Altitude	200	1400	200	PCN	0.943	0.997	0.006
Mach number	0.03	0.27	0.06	Tamb dev.	11	23	3
% in ETA	-0.25	-1.75	0.5 (approx.)	Finalised samples (HP Turbine)			24,651
% in FC	0.4	1.6	0.4 (approx.)	Finalised samples (LP Turbine)			24,639

LL2

Parameter	LL	UL	Step size	Parameter	LL	UL	Step size
Altitude	1700	2900	200	PCN	0.943	0.997	0.006
Mach number	0.03	0.27	0.06	Tamb dev.	11	23	3
% in ETA	-0.25	-1.75	0.5 (approx.)	Finalised samples (HP Turbine)			26,276
% in FC	0.4	1.6	0.4 (approx.)	Finalised samples (LP Turbine)			26,012

LL3

Parameter	LL	UL	Step size	Parameter	LL	UL	Step size
Altitude	3200	4400	200	PCN	0.943	0.997	0.006
Mach number	0.03	0.27	0.06	Tamb dev.	11	23	3
% in ETA	-0.25	-1.75	0.5 (approx.)	Finalised samples (HP Turbine)			27,131
% in FC	0.4	1.6	0.4 (approx.)	Finalised samples (LP Turbine)			27,142

ML1

Parameter	LL	UL	Step size	Parameter	LL	UL	Step size
Altitude	200	1400	200	PCN	0.943	0.997	0.006
Mach number	0.03	0.27	0.06	Tamb dev.	11	23	3
% in ETA	-2.25	-3.75	0.5 (approx.)	Finalised samples (HP Turbine)			26,678
% in FC	2.4	3.6	0.4 (approx.)	Finalised samples (LP Turbine)			26,562

ML2

Parameter	LL	UL	Step size	Parameter	LL	UL	Step size
Altitude	1700	2900	200	PCN	0.943	0.997	0.006
Mach number	0.03	0.27	0.06	Tamb dev.	11	23	3
% in ETA	-2.25	-3.75	0.5 (approx.)	Finalised samples (HP Turbine)			27,630
% in FC	2.4	3.6	0.4 (approx.)	Finalised samples (LP Turbine)			27,559

ML3

Parameter	LL	UL	Step size	Parameter	LL	UL	Step size
Altitude	3200	4400	200	PCN	0.943	0.997	0.006
Mach number	0.03	0.27	0.06	Tamb dev.	11	23	3
% in ETA	-2.25	-3.75	0.5 (approx.)	Finalised samples (HP Turbine)			27,843
% in FC	2.4	3.6	0.4 (approx.)	Finalised samples (LP Turbine)			26,758

HL1

Parameter	LL	UL	Step size	Parameter	LL	UL	Step size
Altitude	200	1400	200	PCN	0.943	0.997	0.006
Mach number	0.03	0.27	0.06	Tamb dev.	11	23	3
% in ETA	-4.25	-5.75	0.5 (approx.)	Finalised samples (HP Turbine)			27,611
% in FC	4.4	5.6	0.4 (approx.)	Finalised samples (LP Turbine)			27,488

HL2

Parameter	LL	UL	Step size	Parameter	LL	UL	Step size
Altitude	1700	2900	200	PCN	0.943	0.997	0.006
Mach number	0.03	0.27	0.06	Tamb dev.	11	23	3
% in ETA	-4.25	-5.75	0.5 (approx.)	Finalised samples (HP Turbine)			27,691
% in FC	4.4	5.6	0.4 (approx.)	Finalised samples (LP Turbine)			27,905

HL3

Parameter	LL	UL	Step size	Parameter	LL	UL	Step size
Altitude	3200	4400	200	PCN	0.943	0.997	0.006
Mach number	0.03	0.27	0.06	Tamb dev.	11	23	3
% in ETA	-4.25	-5.75	0.5 (approx.)	Finalised samples (HP Turbine)			27,873
% in FC	4.4	5.6	0.4 (approx.)	Finalised samples (LP Turbine)			27,204

Appendix P : Percentage of Samples with E Within the Specified Range Predicted by the FB Architectures of Degraded Engine Case

P.1 : Samples Distribution Predicted by Compressor Degradation Architecture

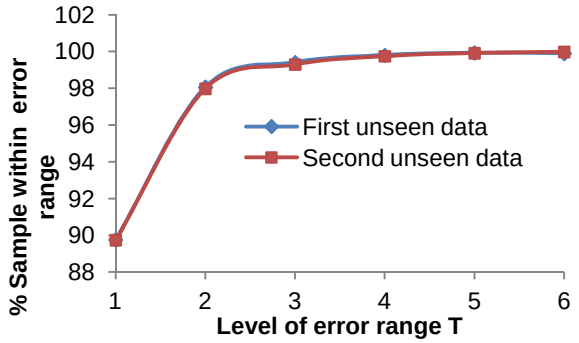

(a) LL1

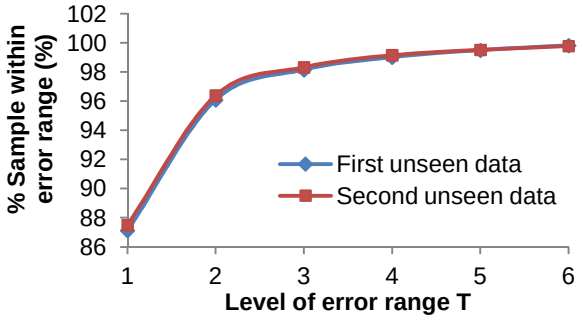

(b) LL2

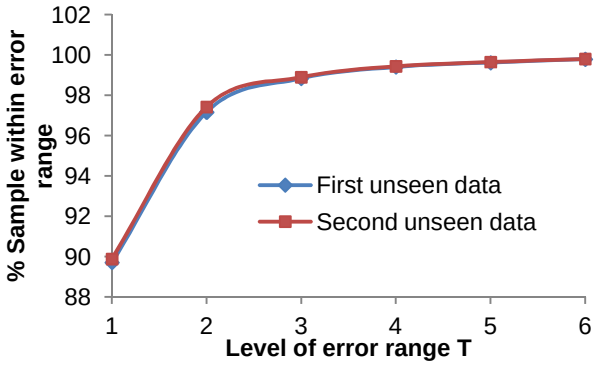

(c) LL3

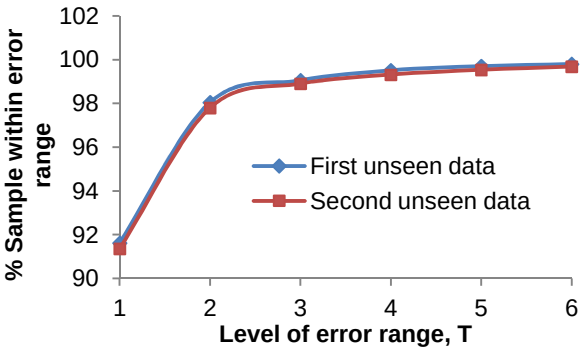

(d) LL4

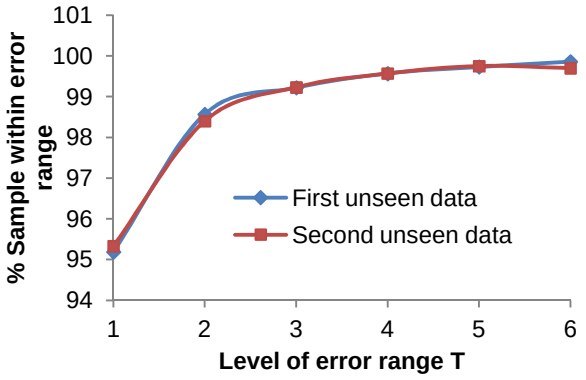

(e) ML1

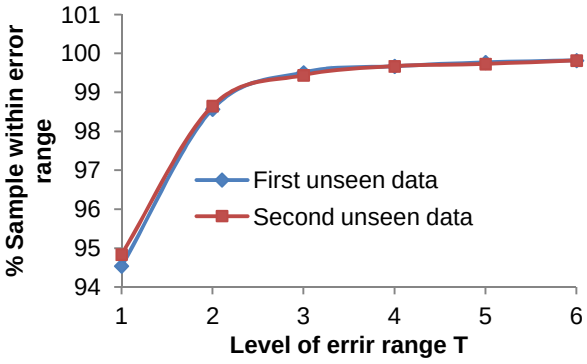

(f) ML2

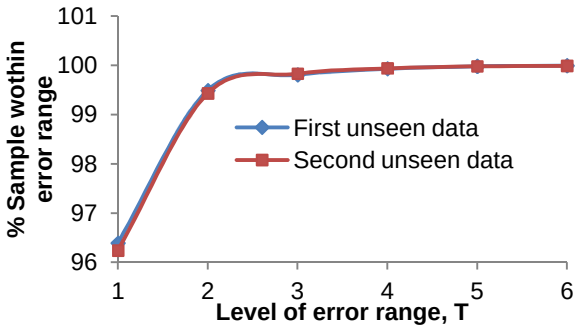

(g) ML3

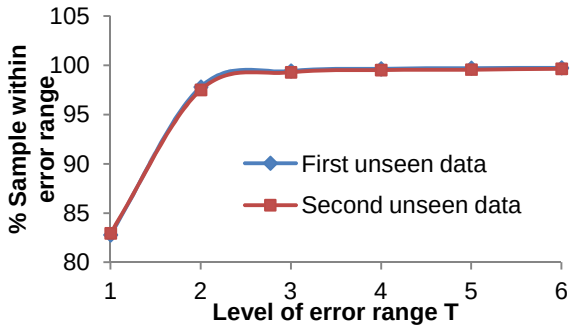

(h) HL1

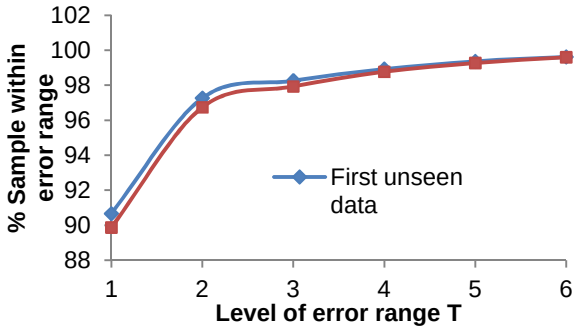

(i) HL2

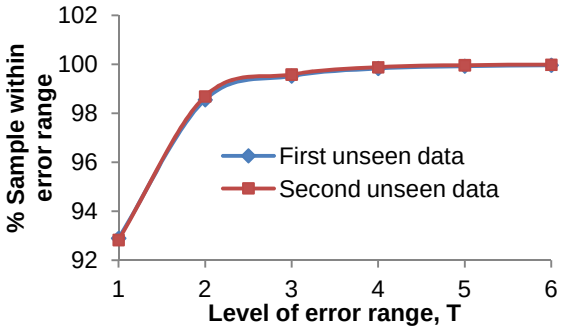

(j) HL3

P.2 : Samples Distribution Predicted By HP Turbine Degradation Architecture

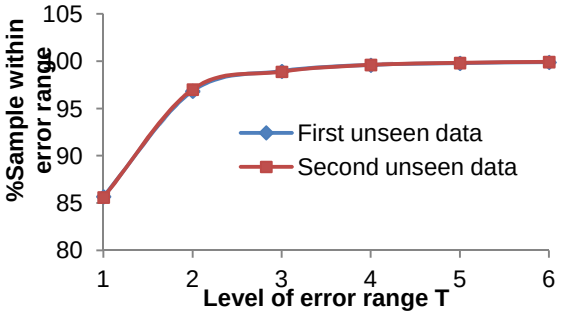

(a) LL1

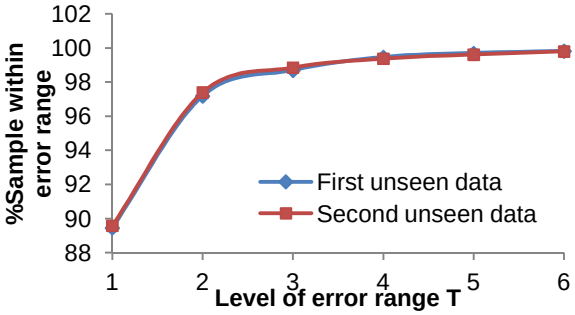

(b) LL2

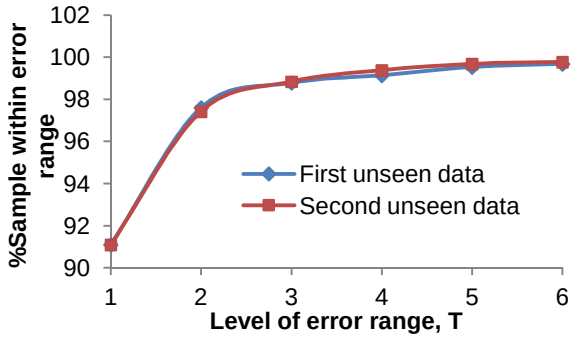

(c) LL3

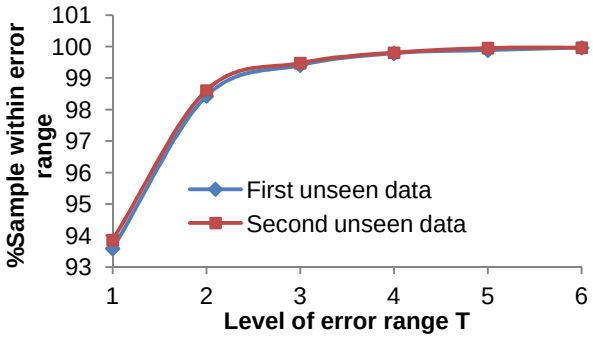

(d) ML1

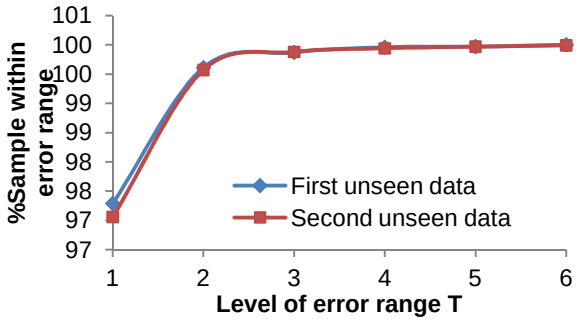

(e) ML2

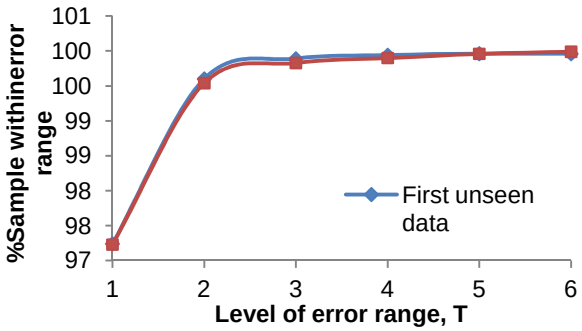

(f) ML3

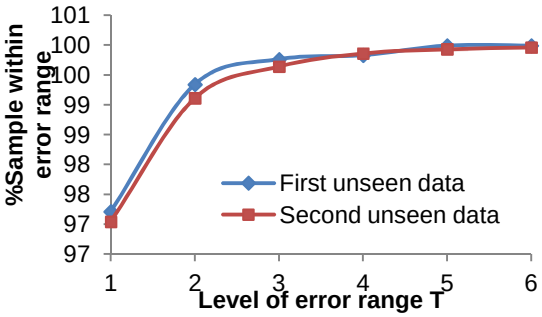

(g) HL1

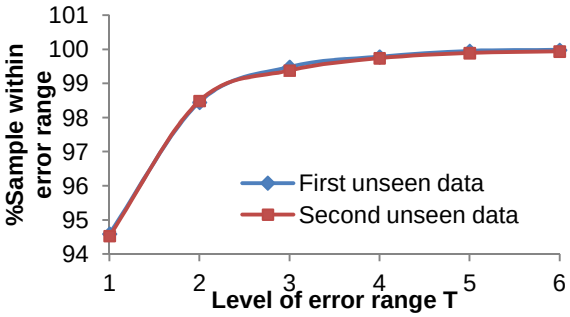

(h) HL2

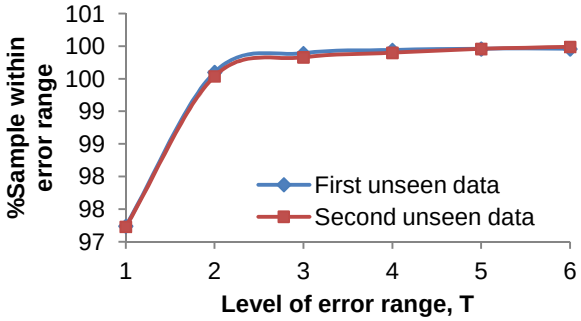

(i) HL3

P.3 : Samples Distribution Predicted By LP Turbine Degradation Architecture

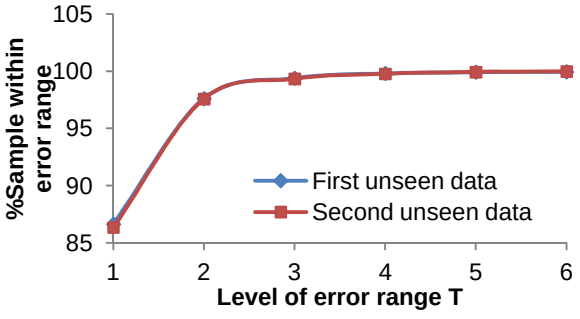

(a) LL1

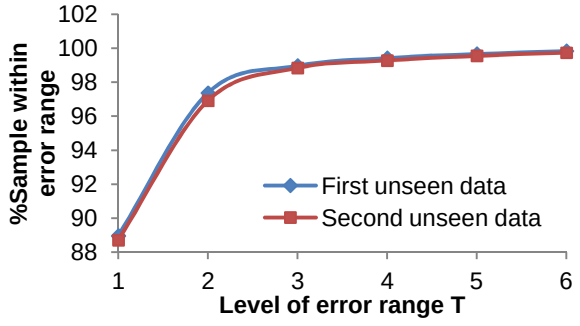

(b) LL2

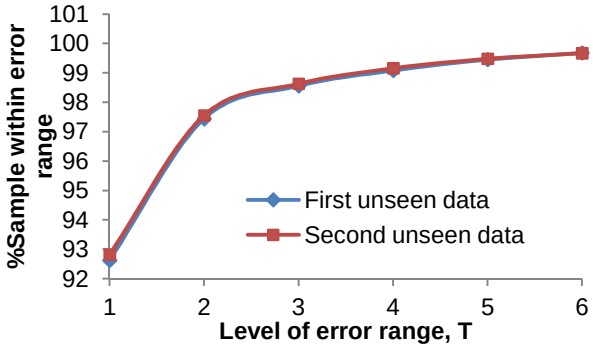

(c) LL3

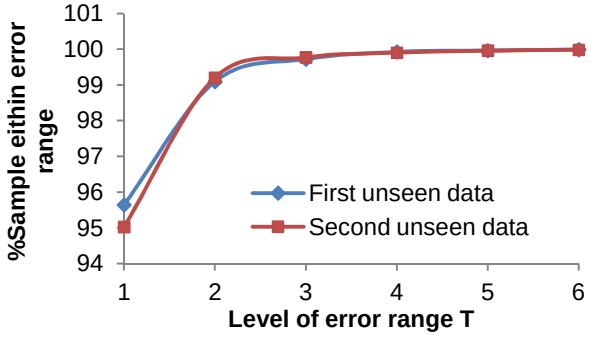

(d) ML1

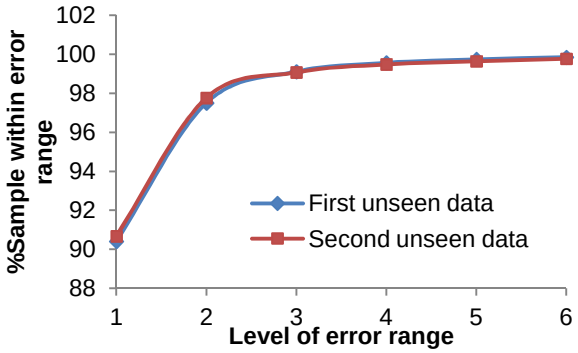

(e) ML2

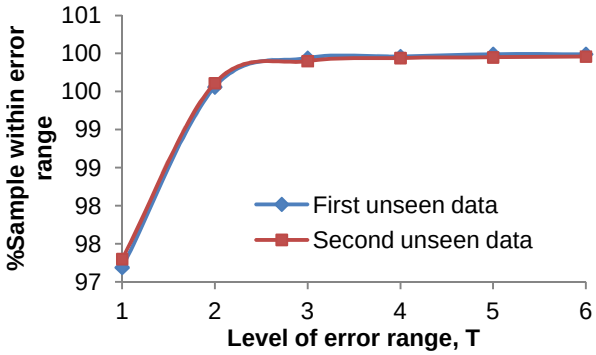

(f) ML3

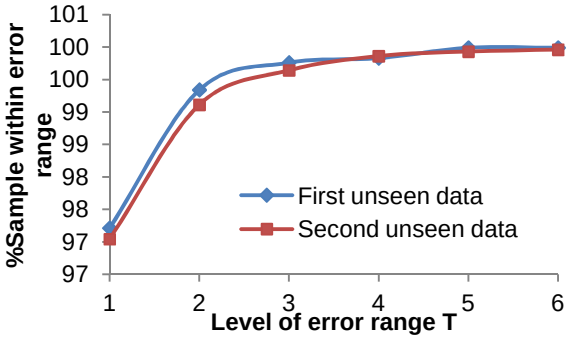

(g) HL1

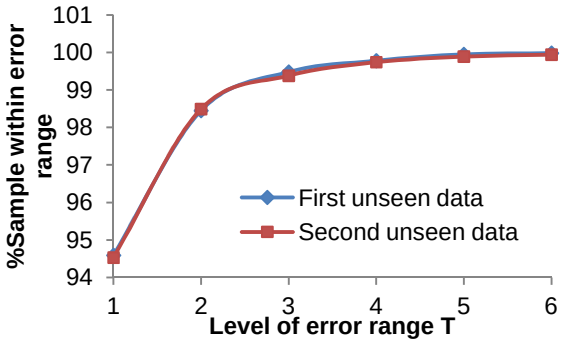

(h) HL2

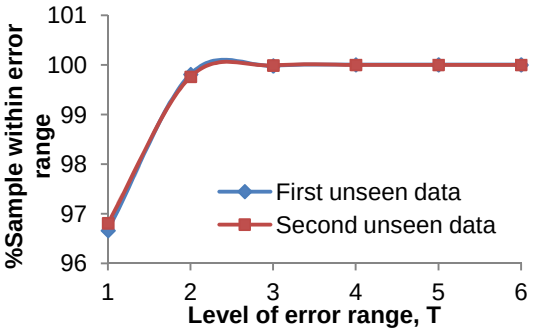

(i) HL3

Appendix Q : Summarised Results of the Probabilistic Analyses Conducted On the Component Degradation FB Architectures

	LL1	LL2	LL3	LL4	ML1	ML2	ML3	HL1	HL2	HL3
Compressor degradation:										
Best fitted distribution	Johnson SU	Johnson SU	Cauchy	Johnson SU	Cauchy	Cauchy	Johnson SU	Johnson SU	Cauchy	Johnson SU
Error Range	Probability									
T1	0.9200	0.8680	0.8990	0.9700	0.8900	0.8860	0.9690	0.8900	0.8800	0.9250
T2	0.9880	0.9730	0.9340	0.9760	0.9400	0.9430	0.9950	0.9750	0.9410	0.9880
T3	0.9970	0.9910	0.9560	0.9920	0.9620	0.9620	0.9989	0.9870	0.9670	0.9970
T4	0.9991	0.9970	0.9670	0.9970	0.9720	0.9710	0.9996	0.9950	0.9710	0.9990
T5	0.9996	0.9980	0.9860	0.9980	0.9780	0.9770	0.9999	0.9970	0.9760	0.9995
T6	0.9999	0.9997	0.9780	0.9995	0.9810	0.9800	0.9999	0.9990	0.9800	0.9999
HP turbine degradation:										
Best fitted distribution	Johnson SU	Johnson SU	Johnson SU		Johnson SU	Johnson SU	Johnson SU	Johnson SU	Johnson SU	Johnson SU
Error Range	Probability									
T1	0.8400	0.8690	0.8740		0.9320	0.9690	0.9680	0.9640	0.9370	0.9750
T2	0.9760	0.9720	0.9890		0.9890	0.9960	0.9940	0.9940	0.9898	0.9988
T3	0.9910	0.9910	0.9910		0.9970	0.9990	0.9980	0.999	0.9960	0.9998
T4	0.9970	0.9970	0.9960		0.9990	0.9997	0.9993	0.9997	0.9990	1.0000
T5	0.9990	0.9985	0.9981		0.9995	0.9999	0.9997	0.9997	0.9994	1.0000
T6	0.9994	0.9992	0.9990		0.9998	0.9999	0.9998	0.9999	0.9997	1.0000
LP turbine degradation:										
Best fitted distribution	Johnson SU	Johnson SU	Cauchy		Johnson SU	Johnson SU	HyperSec	Johnson SU	Johnson SU	Johnson SU
Error Range	Probability									
T1	0.8617	0.8620	0.8670		0.9556	0.8858	0.9683	0.9899	0.9530	0.9670
T2	0.9760	0.9690	0.9330		0.9936	0.9751	0.9994	0.9993	0.9958	0.9970
T3	0.9940	0.9896	0.9550		0.9984	0.9918	1.0000	0.9999	0.9993	0.9994
T4	0.9981	0.9960	0.9660		0.9994	0.9966	1.0000	1.0000	0.9999	0.9998
T5	0.9993	0.9980	0.9730		0.9998	0.9984	1.0000	1.0000	1.0000	0.9999
T6	0.9997	0.9989	0.9800		0.9999	0.9992	1.0000	1.0000	1.0000	1.0000

Appendix R : PDF and CDF Plots for the Component Degradation FB Approximator.

R.1 : PDF and CDF Plots for the Compressor Degradation

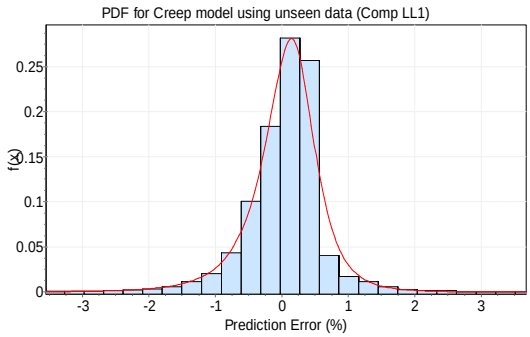

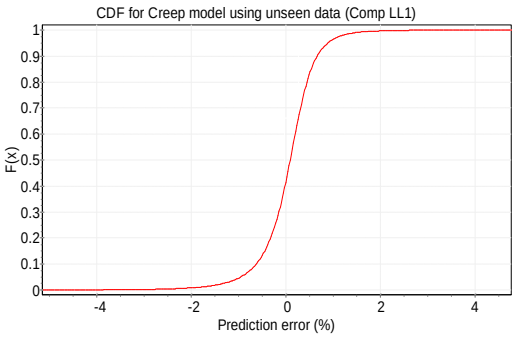

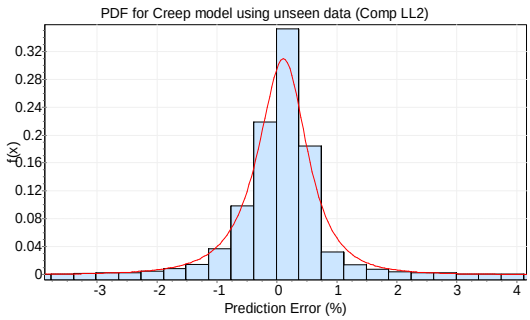

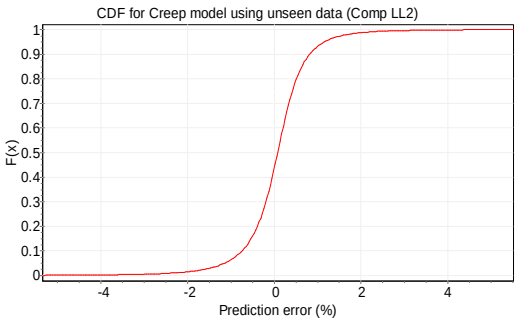

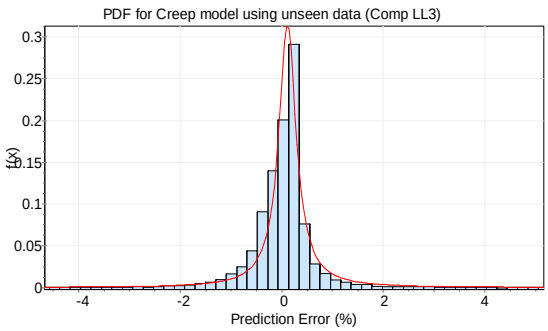

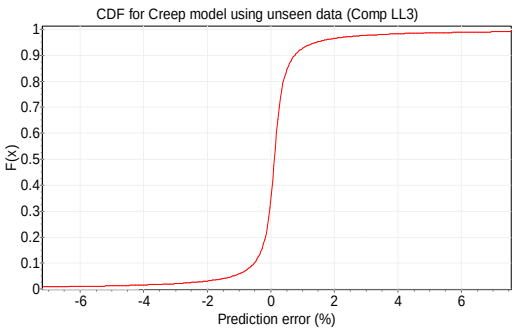

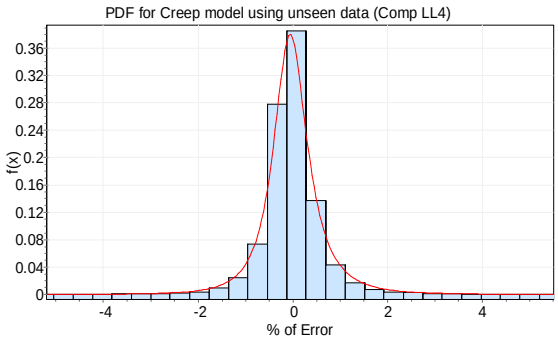

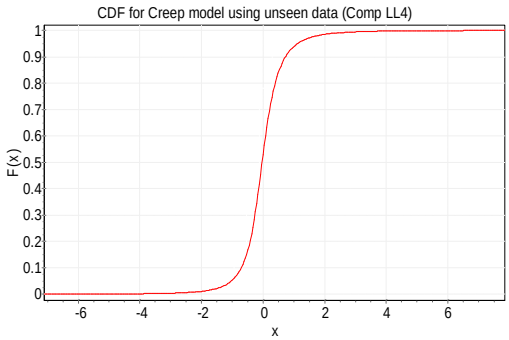

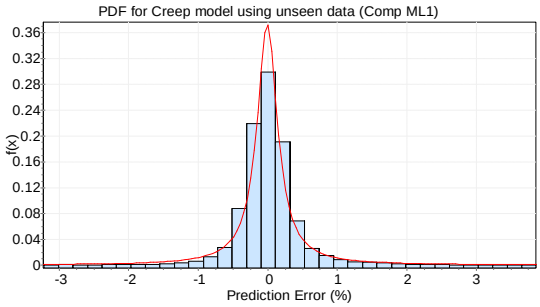
PDF for Creep model using unseen data (Comp ML1)
f(x)
Prediction Error (%)

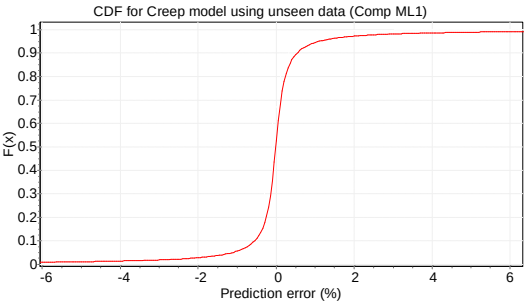
CDF for Creep model using unseen data (Comp ML1)
F(x)
Prediction error (%)

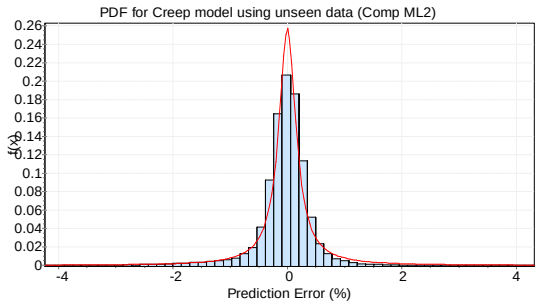
PDF for Creep model using unseen data (Comp ML2)
f(x)
Prediction Error (%)

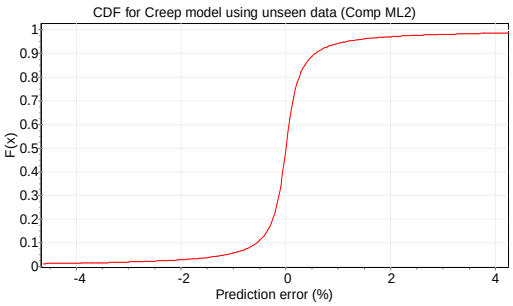
CDF for Creep model using unseen data (Comp ML2)
F(x)
Prediction error (%)

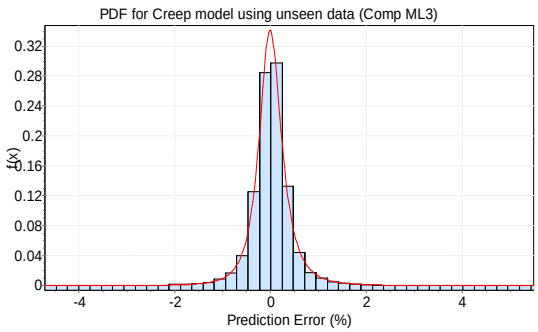
PDF for Creep model using unseen data (Comp ML3)
f(x)
Prediction Error (%)

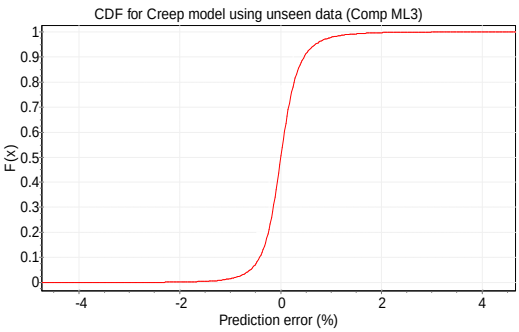
CDF for Creep model using unseen data (Comp ML3)
F(x)
Prediction error (%)

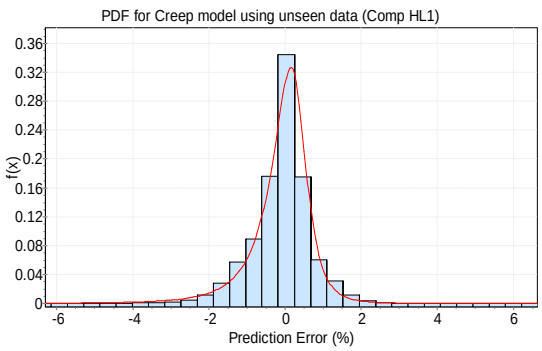
PDF for Creep model using unseen data (Comp HL1)
f(x)
Prediction Error (%)

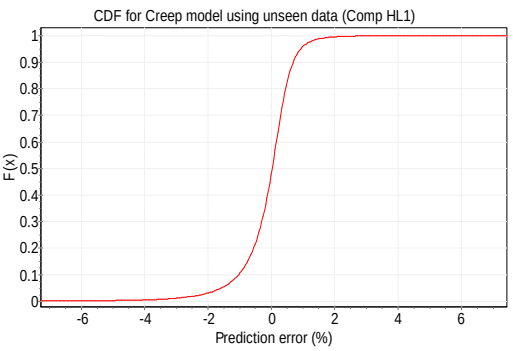
CDF for Creep model using unseen data (Comp HL1)
F(x)
Prediction error (%)

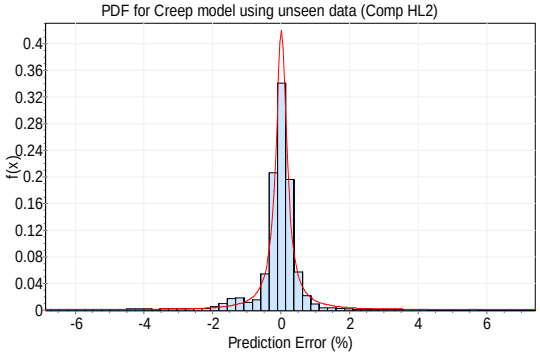
PDF for Creep model using unseen data (Comp HL2)
f(x)
Prediction Error (%)

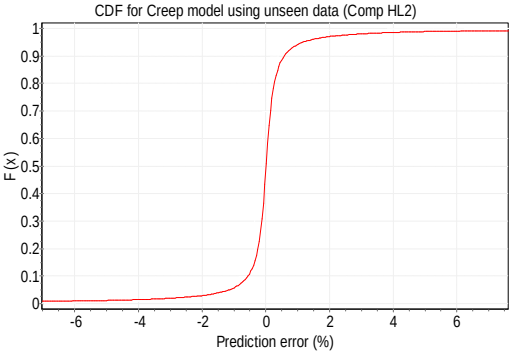
CDF for Creep model using unseen data (Comp HL2)
F(x)
Prediction error (%)

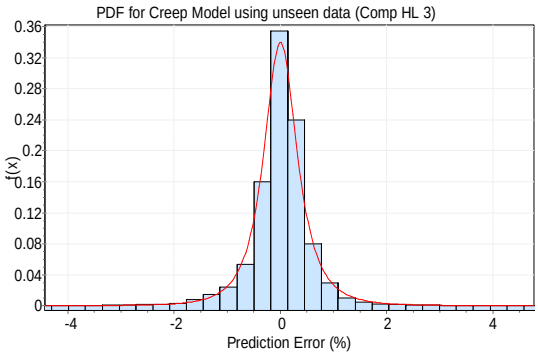

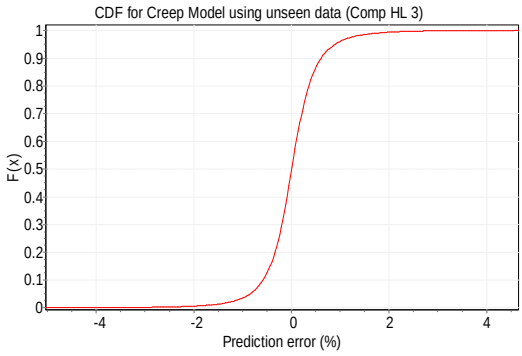

R.2 PDF and CDF Plots for the HP Turbine Degradation

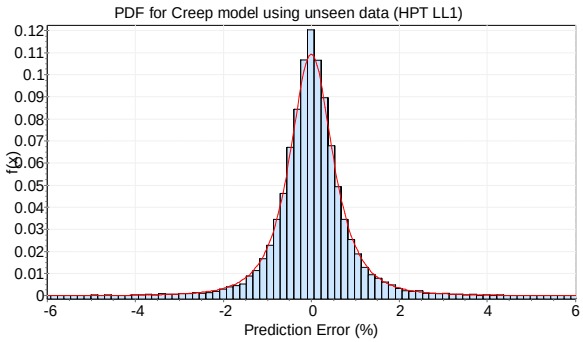

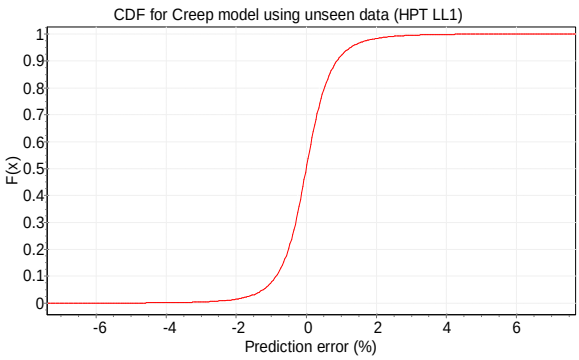

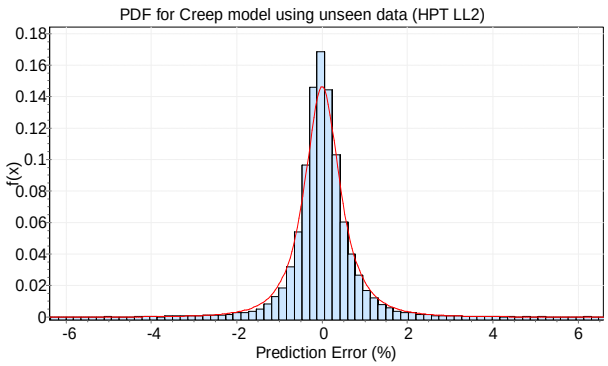

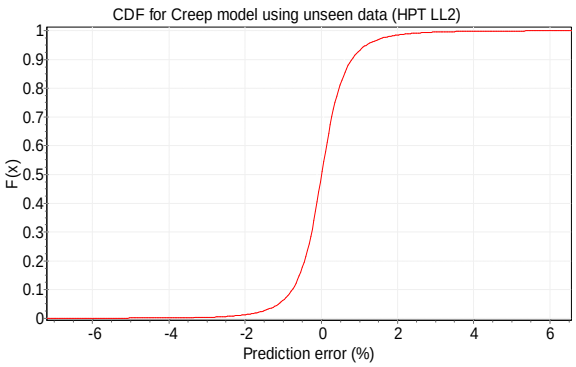

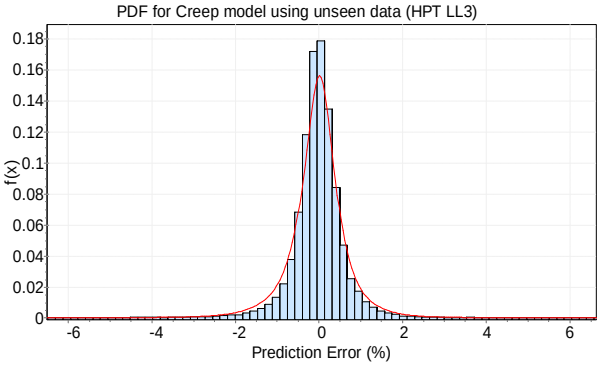

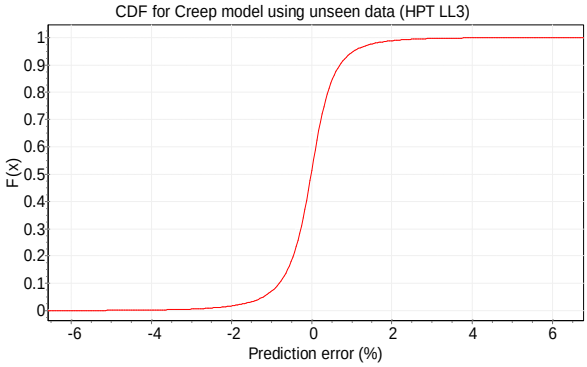

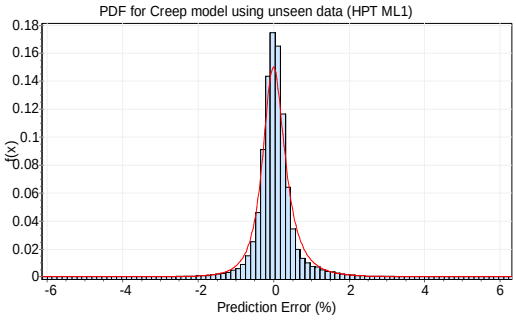
PDF for Creep model using unseen data (HPT ML1)
f(x)
Prediction Error (%)

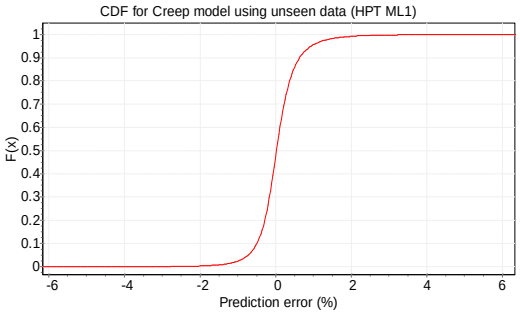
CDF for Creep model using unseen data (HPT ML1)
F(x)
Prediction error (%)

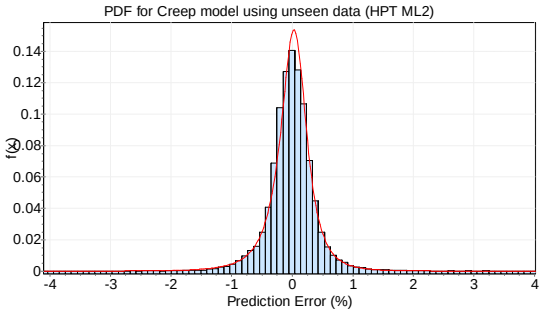
PDF for Creep model using unseen data (HPT ML2)
f(x)
Prediction Error (%)

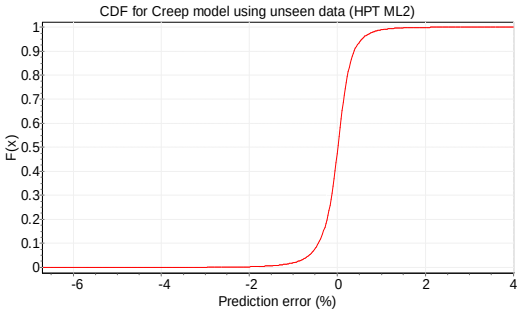
CDF for Creep model using unseen data (HPT ML2)
F(x)
Prediction error (%)

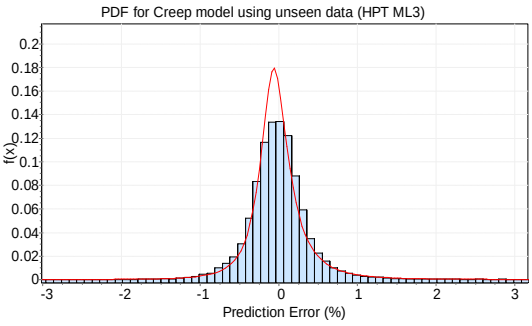
PDF for Creep model using unseen data (HPT ML3)
f(x)
Prediction Error (%)

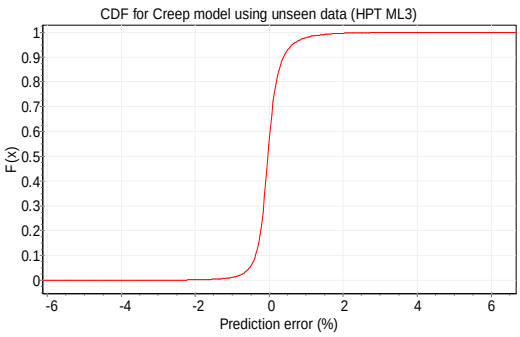
CDF for Creep model using unseen data (HPT ML3)
F(x)
Prediction error (%)

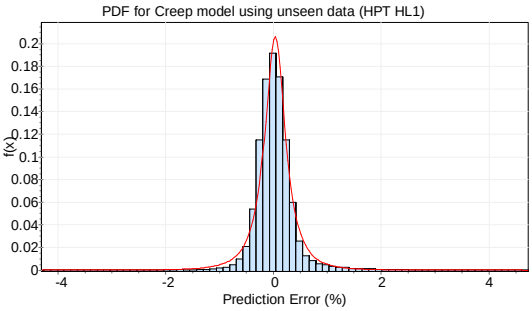
PDF for Creep model using unseen data (HPT HL1)
f(x)
Prediction Error (%)

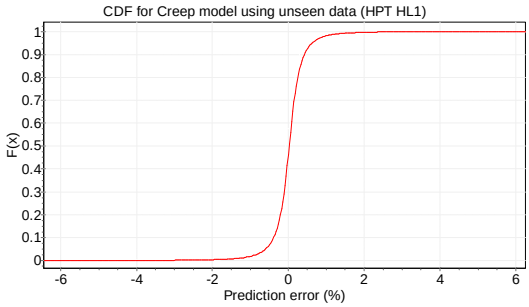
CDF for Creep model using unseen data (HPT HL1)
F(x)
Prediction error (%)

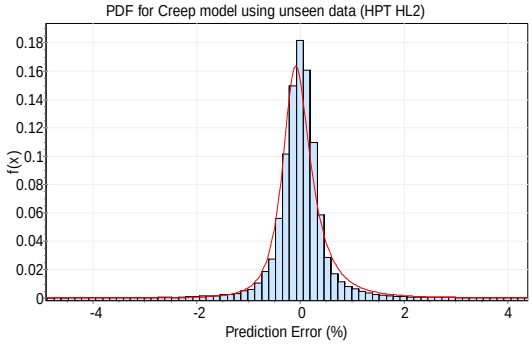
PDF for Creep model using unseen data (HPT HL2)
f(x)
Prediction Error (%)

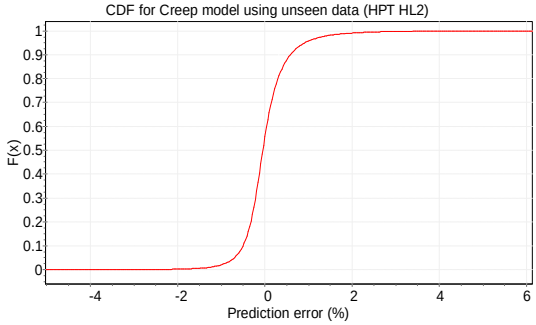
CDF for Creep model using unseen data (HPT HL2)
F(x)
Prediction error (%)

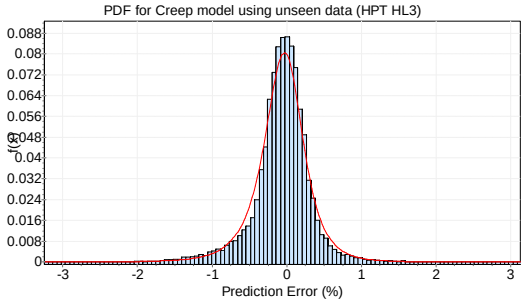

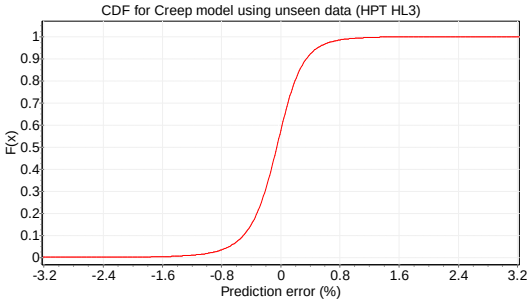

R.3 PDF and CDF Plots for the LP Turbine Degradation

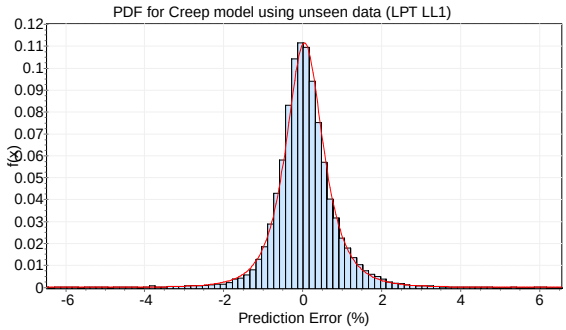

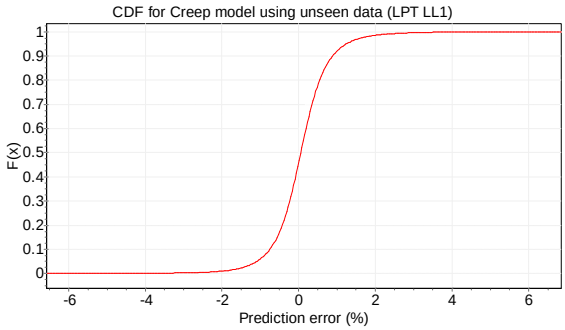

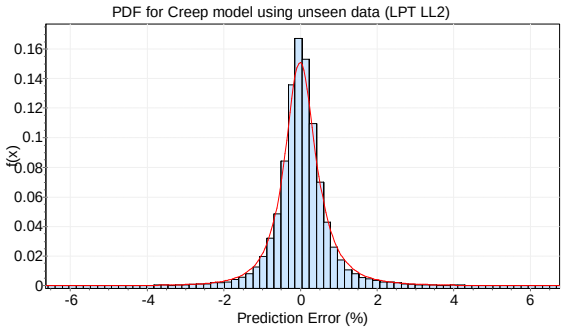

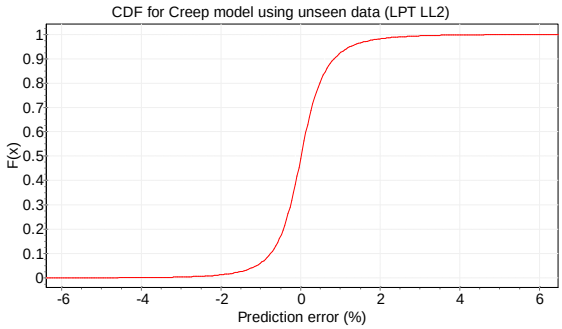

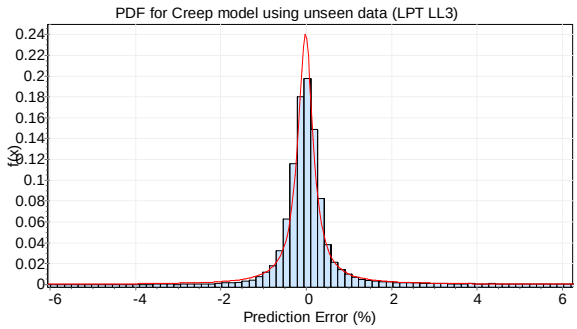

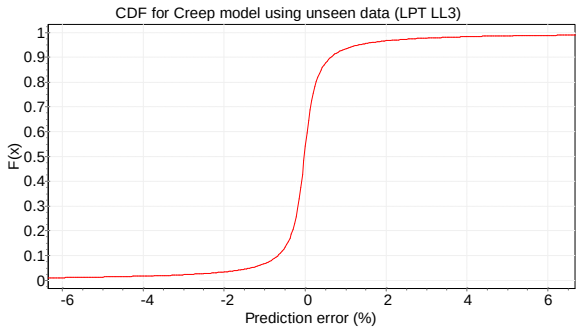

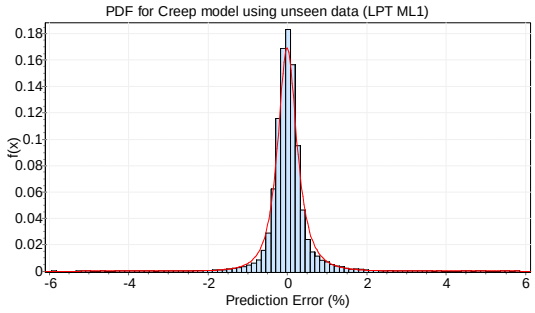
PDF for Creep model using unseen data (LPT ML1)
f(x)
Prediction Error (%)

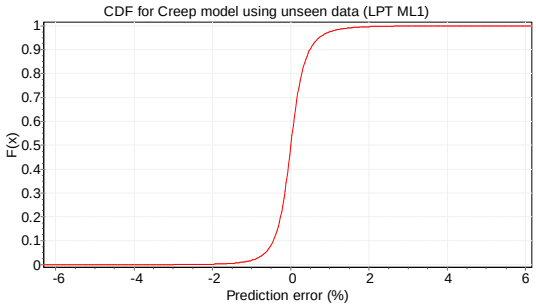
CDF for Creep model using unseen data (LPT ML1)
F(x)
Prediction error (%)

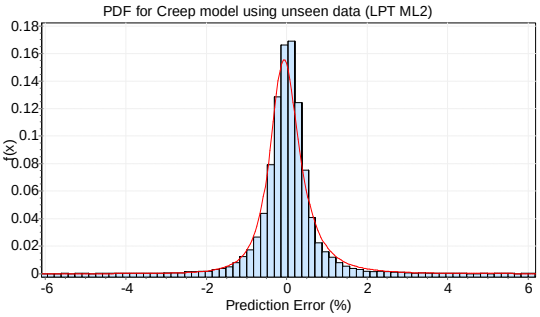
PDF for Creep model using unseen data (LPT ML2)
f(x)
Prediction Error (%)

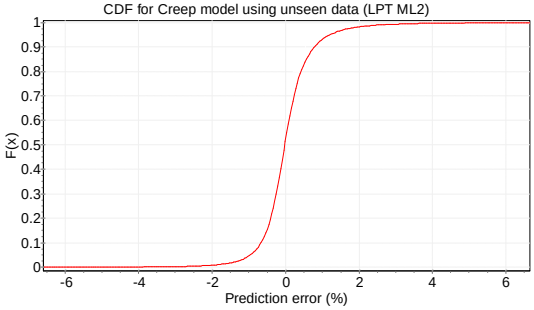
CDF for Creep model using unseen data (LPT ML2)
F(x)
Prediction error (%)

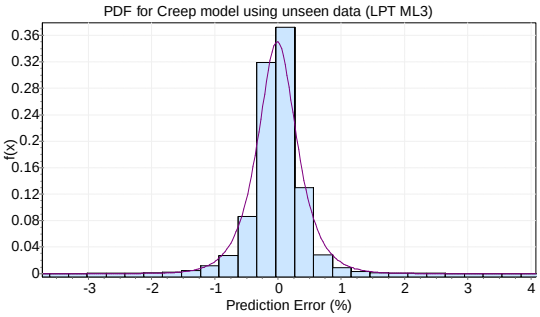
PDF for Creep model using unseen data (LPT ML3)
f(x)
Prediction Error (%)

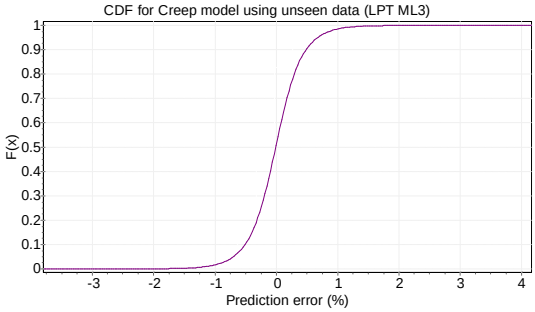
CDF for Creep model using unseen data (LPT ML3)
F(x)
Prediction error (%)

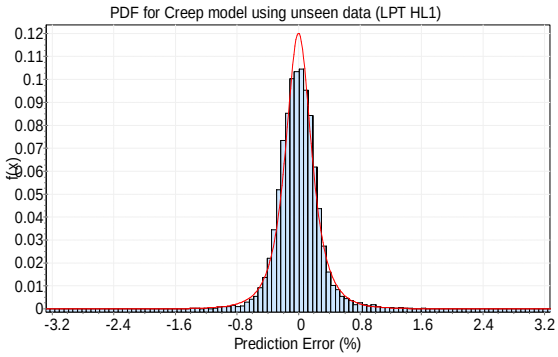
PDF for Creep model using unseen data (LPT HL1)
f(x)
Prediction Error (%)

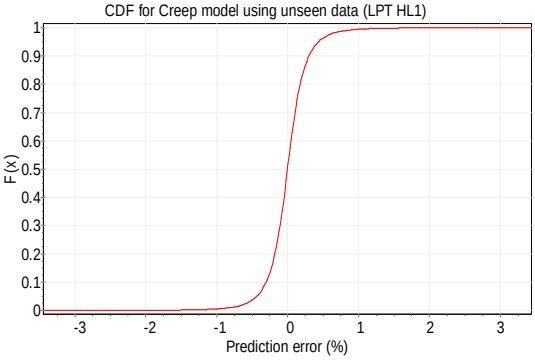
CDF for Creep model using unseen data (LPT HL1)
F(x)
Prediction error (%)

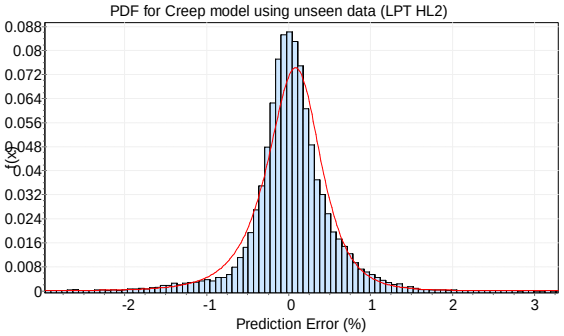
PDF for Creep model using unseen data (LPT HL2)
f(x)
Prediction Error (%)

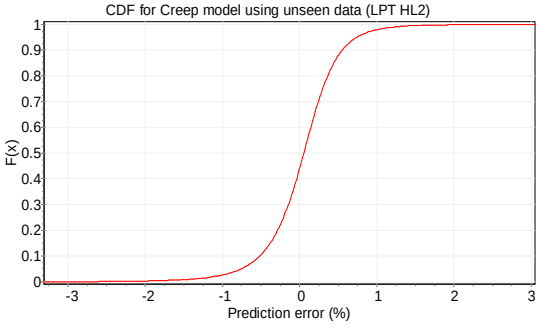
CDF for Creep model using unseen data (LPT HL2)
F(x)
Prediction error (%)

Appendix S : Step Size for Each Parameter and Samples Used for SB Architecture of Degraded Engine Condition.

S.1 : Step Size and Samples Size Used to Train Compressor Degradation Approximators

LL1							
Parameter	LL	UL	Step size	Parameter	LL	UL	Step size
Altitude	0	1500	300	PCN	0.94	1	0.0075
Mach number	0	0.3	0.06	Tamb dev.	10	25	3
% in ETA	-0.5	-2	0.5 (approx.)		Initial samples		31,104
% in FC	-0.5	-2	0.5 (approx.)		Finalised samples		27,005
LL2							
Parameter	LL	UL	Step size	Parameter	LL	UL	Step size
Altitude	1500	3000	300	PCN	0.94	1	0.0075
Mach number	0	0.3	0.06	Tamb dev.	10	25	3
% in ETA	-0.5	-2	0.5 (approx.)		Initial samples		31,104
% in FC	-0.5	-2	0.5 (approx.)		Finalised samples		28,613
LL3							
Parameter	LL	UL	Step size	Parameter	LL	UL	Step size
Altitude	3000	4500	300	PCN	0.94	1	0.0075
Mach number	0	0.3	0.06	Tamb dev.	10	25	3
% in ETA	-0.5	-2	0.5 (approx.)		Initial samples		31,104
% in FC	-0.5	-2	0.5 (approx.)		Finalised samples		29,421

S.2 : Step Size and Samples Size Used to Train Degradation Level Classifier at All Altitude Levels

Operating parameter							
Parameter	LL	UL	Step size	Parameter	LL	UL	Step size
Altitude Level 1	0	1500	375	PCN	0.94	1	0.012
Altitude Level 2	1500	3000	375	Tamb dev.	10	25	3
Altitude Level 3	3000	4500	375	Mach number	0	0.3	0.1
Compressor degradation							
% in ETA	-0.5	-2	0.5 (approx.)	% in FC	-0.5	-2	0.5 (approx.)
	-2.5	-4	0.5 (approx.)		-2.5	-4	0.5 (approx.)
	-4.5	-6	0.5 (approx.)		-4.5	-6	0.5 (approx.)
HP and LP Turbine degradation							
% in ETA	-0.5	-2	0.5 (approx.)	% in FC	0.5	2	0.5 (approx.)
	-2.5	-4	0.5 (approx.)		2.5	4	0.5 (approx.)
	-4.5	-6	0.5 (approx.)		4.5	6	0.5 (approx.)

Finalised samples					
Altitude Level 1		Altitude Level 2		Altitude Level 3	
Compressor	34,119	Compressor	34,087	Compressor	34,289
HP Turbine	34,157	HP Turbine	34,256	HP Turbine	34,447
LP Turbine	34,303	LP Turbine	34,064	LP Turbine	33,644

S.3 : Step Size for Each Parameter and Samples Used to Train Component Health Classifier

Operating parameter for Clean Engine							
Parameter	LL	UL	Step size	Parameter	LL	UL	Step size
Altitude Level 1	0	1500	250	PCN	0.94	1	0.006
Altitude Level 2	1500	3000	250	Tamb dev.	10	25	2.5
Altitude Level 3	3000	4500	250	Mach number	0	0.3	0.06
Operating parameter for Degraded Engine							
Parameter	LL	UL	Step size	Parameter	LL	UL	Step size

Altitude Level 1	0	1500	500	PCN	0.94	1	0.015
Altitude Level 2	1500	3000	500	Tamb dev.	10	25	3.75
Altitude Level 3	3000	4500	500	Mach number	0	0.3	0.1
Compressor degradation (approx.)							
% in ETA (LL)	-0.3	-1.98	0.3 to 0.66	% in FC (LL)	-0.3	-1.98	0.3 to 0.66
% in ETA (ML)	-2.66	-3.98	0.66	% in FC (ML)	-2.66	-3.98	0.66
% in ETA (HL)	-4.66	-5.98	0.66	% in FC (HL)	-4.66	-5.98	0.66
HP/LP Turbine degradation (approx.)							
% in ETA (LL)	-0.3	-1.98	0.3 to 0.66	% in FC (LL)	0.3	1.98	0.3 to 0.66
% in ETA (ML)	-2.66	-3.98	0.66	% in FC (ML)	2.66	3.98	0.66
% in ETA (HL)	-4.66	-5.98	0.66	% in FC (HL)	4.66	5.98	0.66
Finalised samples							
Altitude Level 1	43,677		Altitude Level 2	43,467		Altitude Level 3	43,542

Appendix T : Final sizes of the trained approximators and classifiers for all component degradation

T.1 : Final sizes of the trained approximators for all component degradation at All Altitude Levels

Magnitude And Altitude Level	Blade Metal Temperature Approximator	Blade Stress Approximator	Creep Life Approximator
Altitude Level 1			
Compressor degradation:			
LL1	10-30-35-1	10-35-40-1	2-35-35-1
ML1	10-35-40-1	10-20-20-1	Taken from previous architecture
HL1	10-35-40-1	10-40-40-1	
HP turbine degradation			
LL1	8-30-35-1	8-20-22-1	Taken from previous architecture
ML1	8-35-35-1	8-20-22-1	
HL1	8-35-35-1	8-25-25-1	
LP turbine degradation			
LL1	8-35-35-1	8-25-25-1	Taken from previous architecture
ML1	8-35-40-1	8-25-25-1	
HL1	8-35-40-1	8-25-25-1	
Altitude Level 2			
Compressor degradation:			
LL2	10-30-35-1	10-35-35-1	2-35-35-1
ML2	10-35-35-1	10-25-25-1	Taken from previous architecture
HL2	10-35-35-1	10-25-25-1	
HP turbine degradation			
LL2	10-30-30-1	10-20-23-1	Taken from previous architecture
ML2	10-33-33-1	10-25-25-1	
HL2	10-35-35-1	10-25-25-1	
LP turbine degradation			
LL2	10-35-35-1	10-25-25-1	Taken from previous architecture
ML2	10-35-40-1	10-25-25-1	
HL2	10-35-40-1	10-25-25-1	
Altitude Level 3			
Compressor degradation:			
LL3	10-25-25-1	10-35-35-1	
ML3	10-25-25-1	10-35-40-1	Taken from previous

HL3	10-25-25-1	10-35-35-1	architecture
HP turbine degradation			
LL3	10-30-40-1	10-20-23-1	Taken from previous architecture
ML3	10-33-33-1	10-25-25-1	
HL3	10-35-35-1	10-25-25-1	
LP turbine degradation			
LL3	10-25-25-1	10-25-25-1	Taken from previous architecture
ML3	10-25-25-1	10-25-25-1	
HL3	10-25-25-1	10-25-25-1	

T.2 : Final sizes of the Trained Classifier Classifiers at All Altitude Levels

	Altitude Level 1	Altitude Level 2	Altitude Level 3
Degradation level classifiers:			
Compressor	10-35-35-4	10-25-25-3	10-35-35-3
HP turbine	8-40-40-3	10-35-35-3	10-35-35-3
LP turbine	8-35-40-3	10-35-35-3	10-35-35-3
Component health classifiers:	10-35-35-4	10-35-35-4	10-35-35-4

Appendix U : The Training, Validation and Test Samples' Final MSE and R of the Approximators during the Training.

	LL			ML		HL	
	Temp	**Stress**	**Creep**	**Temp**	**Stress**	**Temp**	**Stress**
Altitude Level 1							
Compressor Approximator:							
Training sample							
MSE	1.33E-07	2.10E-06	8.03E-13	1.23E-07	6.57E-06	1.14E-07	2.69E-08
R	1	0.99999	1	1	1	1	1
Validation sample							
MSE	1.50E-07	4.86E-06	2.43E-12	1.38E-07	1.05E-05	1.25E-07	1.97E-07
R	1	0.99999	1	1	0.99999	1	1
Test sample							
MSE	1.50E-07	5.85E-06	1.09E-11	1.37E-07	1.16E-05	1.24E-07	6.11E-07
R	1	0.99999	1	1	0.99999	1	1
HP Turbine Approximator:							
Training sample							
MSE	1.76E-07	4.99E-06	-	1.56E-07	1.27E-07	1.42E-07	1.35E-07
R	1	0.99999	-	1	1	1	1
Validation sample							
MSE	1.85E-07	5.26E-06	-	1.73E-07	1.81E-07	1.57E-07	2.06E-07
R	1	0.99999	-	1	1	1	1
Test sample							
MSE	1.88E-07	5.28E-06	-	1.75E-07	1.7E-07	1.56E-07	1.71E-07
R	1	0.99999	-	1	1	1	1
LP Turbine Approximator:							
Training sample							
MSE	1.52E-07	6.22E-08	-	1.35E-07	1.72E-08	1.21E-07	4.44E-09
R	1	1	-	1	1	1	1
Validation sample							
MSE	1.90E-07	9.02E-08	-	1.63E-07	3.30E-08	1.35E-07	5.66E-09
R	1	1	-	1	1	1	1
Test sample							
MSE	1.93E-07	8.69E-08	-	1.64E-07	2.78E-08	1.36E-07	5.61E-09
R	1	1	-	1	1	1	1
Altitude Level 2							
Compressor Approximator:							

Training sample							
MSE	1.47E-07	6.4E-06	3.54E-10	1.37E-07	6.77E-06	1.26E-07	4.99E-06
R	1	0.99999	1	1	0.99999	1	0.99999
Validation sample							
MSE	1.64E-07	1.70E-05	4.31E-10	1.51E-07	1.45E-05	1.36E-07	7.58E-06
R	1	0.99996	1	1	0.99997	1	0.99999
Test sample							
MSE	1.58E-07	1.57E-05	1.43E-09	1.50E-07	1.27E-05	1.38E-07	1.09E-05
R	1	0.99997	1	1	0.99998	1	0.99998
HP Turbine Approximator:							
Training sample							
MSE	1.49E-07	1.07E-08	-	1.33E-07	7.00E-09	1.28E-07	8.89E-09
R	1	1	-	1	1	1	1
Validation sample							
MSE	1.53E-07	1.35E-08	-	1.52E-07	1.00E-08	1.54E-07	1.56E-08
R	1	1	-	1	1	1	1
Test sample							
MSE	1.57E-07	1.35E-08	-	1.57E-07	1.02E-08	1.67E-07	1.11E-08
R	1	1	-	1	1	1	1
LP Turbine Approximator:							
Training sample							
MSE	1.59E-07	6.19E-09	-	1.36E-07	5.42E-09	1.28E-07	6.43E-09
R	1	1	-	1	1	1	1
Validation sample							
MSE	1.75E-07	7.59E-09	-	1.63E-07	6.79E-09	1.56E-07	8.80E-09
R	1	1	-	1	1	1	1
Test sample							
MSE	1.74E-07	4.84E-09	-	1.63E-07	6.44E-09	1.74E-07	8.33E-09
R	1	1	-	1	1	1	1
Altitude Level 3							
Compressor Approximator:							
Training sample							
MSE	1.71E-07	1.49E-06	1.71E-13	1.62E-07	1.17E-06	1.59E-07	8.58E-6
R	1	1	1	1	1	1	0.99998
Validation sample							
MSE	1.78E-07	4.81E-06	3.92E-13	1.72E-07	4.70E-06	1.63E-07	1.80E-05
R	1	0.99999	1	1	0.99999	1	0.99995
Test sample							
MSE	1.74E-07	6.84E-06	1.71E-12	1.69E-07	3.56E-06	1.64E-07	2.86E-05
R	1	0.99999	1	1	0.99999	1	0.99996
HP Turbine Approximator:							
Training sample							
MSE	1.57E-07	2.05E-08	-	1.44E-07	1.86E-08	1.52E-07	9.87E-08
R	1	1	-	1	1	1	1
Validation sample							
MSE	1.62E-07	2.53E-08	-	1.51E-07	2.60E-08	1.61E-07	1.10E-07
R	1	1	-	1	1	1	1
Test sample							
MSE	1.64E-07	2.69E-08	-	1.52E-07	2.94E-08	1.57E-07	1.1E-07
R	1	1	-	1	1	1	1
LP Turbine Approximator:							
Training sample							
MSE	2.09E-07	1.12E-08	-	1.72E-07	3.32E-08	1.55E-07	1.99E-08
R	1	1	-	1	1	1	1
Validation sample							
MSE	2.19E-07	1.30E-08	-	1.84E-07	5.00E-08	1.62E-07	2.78E-08
R	1	1	-	1	1	1	1
Test sample							
MSE	2.23E-07	1.24E-08	-	1.83E-07	4.16E-08	1.66E-07	3.29E-08
R	1	1	-	1	1	1	1

Appendix V : The Predicted Outputs E_{Ave} and SD_E for the entire Component Degradation Trained Networks.

		Compressor Deg.		HP Turbine Deg.		LP Turbine Deg.	
Level	**Approx. Network**	E_{Ave}	SD_E	E_{Ave}	SD_E	E_{Ave}	SD_E
Altitude Level 1:							
LL1	Blade Temp	4.64E-05	0.00317	1.37E-05	0.00361	1.71E-05	0.00338
	Blade Stress	1.08E-04	0.01758	-6.73E-05	0.04251	5.63E-06	0.00223
	Creep Life	7.83E-05	0.01482	-	-	-	-
ML1	Blade Temp	-5.19E-05	0.00316	2.76E-05	0.00355	-6.44E-07	0.00327
	Blade Stress	2.18E-03	0.02783	4.95E-06	0.0036	-6.04E-06	0.00139
HL1	Blade Temp	-3.85E-05	0.00315	2.38E-05	0.00347	5.29E-06	0.0032
	Blade Stress	-1.60E-05	0.00395	-1.56E-06	0.00381	2.01E-06	0.000661
Altitude Level 2:							
LL2	Blade Temp	-3.26E-05	0.00323	-2.55E-05	0.00323	-1.55E-05	0.00322
	Blade Stress	-2.53E-04	0.02903	1.06E-05	0.000966	1.02E-05	0.000717
	Creep Life	0.000456	0.09011	-	-	-	-
ML2	Blade Temp	2.08E-05	0.0032	1.74E-05	0.00322	2.59E-05	0.0032
	Blade Stress	-9.96E-05	0.02753	2.42E-07	0.000831	-2.66E-06	0.000684
HL2	Blade Temp	-1.47E-06	0.0032	6.16E-05	0.00327	7.82E-06	0.00317
	Blade Stress	2.51E-04	0.023	-2.55E-06	0.000964	-3.86E-06	0.000769
Altitude Level 3:							
LL3	Blade Temp	-2.66E-05	0.00335	3.76E-05	0.00335	-2.09E-04	0.00334
	Blade Stress	-7.89E-05	0.01519	1.11E-05	0.00125	-4.98E-06	0.00088
	Creep Life	0.00016	0.01156	-	-	-	-
ML3	Blade Temp	-1.05E-04	0.00332	-9.65E-05	0.0033	2.14E-06	0.00335
	Blade Stress	-4.20E-05	0.01285	3.52E-06	0.00125	8.99E-06	0.00163
HL3	Blade Temp	3.08E-06	0.00331	1.08E-04	0.00332	2.01E-05	0.0033
	Blade Stress	1.89E-04	0.03205	-1.55E-05	0.00273	-2.46E-05	0.00129

Appendix W : Percentage of Component Degradation Samples Encompassed within the Specified Range

Table W-1: Percentage of Samples Encompassed for Compressor Degradation

Error Range	Degradation Magnitude and Altitude Level									
	LL1	**LL2**	**LL3**	**ML1**	**ML2**	**ML3**	**HL1**	**HL2**	**HL3**	**Average**
T0.2	78.1	68.95	76.23	72.7	73.94	77.93	84.74	75.73	77.69	**76.22**
T0.4	98.46	93.84	98.75	95.92	95.74	99	99.92	95.94	96.61	**97.13**
T0.6	99.62	97.72	99.68	98.49	97.62	99.76	99.95	98.12	98.75	**98.86**
T0.8	99.8	98.83	99.83	99.28	98.47	99.9	99.97	98.9	99.3	**99.36**
T1	99.88	99.30	99.90	99.6	98.9	99.93	99.98	99.94	99.5	**99.66**
T2	99.98	99.86	99.96	99.96	99.62	99.98	99.99	99.94	99.85	**99.90**
T3	99.99	99.96	99.98	99.98	99.85	99.997	100	99.95	99.93	**99.96**
T4	100	100.00	100.00	100	99.94	100	100	99.99	99.97	**99.99**
T5	100	100.00	100.00	100	99.97	100	100	99.996	99.98	**99.99**
T6	100	100.00	100.00	100	99.99	100	100	100	99.99	**100.00**

Table W-2: Percentage of Samples Encompassed for HP Turbine Degradation

Error Range	Degradation Magnitude and Altitude Level									
	LL1	LL2	LL3	ML1	ML2	ML3	HL1	HL2	HL3	Average
T0.2	66.13	81.8	80.23	76.89	80.9	81.4	80.25	75.57	79.47	**78.07**
T0.4	94.52	99.95	99.97	98.55	99.8	99.96	99.57	97	99.5	**98.76**
T0.6	99.15	100	100	99.78	99.97	99.997	99.97	98.7	99.84	**99.71**
T0.8	99.85	100	100	99.95	100	100	99.99	99.1	99.94	**99.87**
T1	99.95	100	100	99.97	100	100	100	99.21	99.98	**99.90**
T2	100	100	100	100	100	100	100	99.53	99.997	**99.95**
T3	100	100	100	100	100	100	100	99.68	100	**99.96**
T4	100	100	100	100	100	100	100	99.76	100	**99.97**
T5	100	100	100	100	100	100	100	99.92	100	**99.99**
T6	100	100	100	100	100	100	100	99.96	100	**100.00**

Table W-3: Percentage of Samples Encompassed for LP Turbine Degradation

Error Range	Degradation Magnitude and Altitude Level									
	LL1	LL2	LL3	ML1	ML2	ML3	HL1	HL2	HL3	Average
T0.2	81.26	81.22	80.76	99.95	80.83	80.688	83.4	80.92	81.88	**83.43**
T0.4	99.52	99.95	99.95	99.99	99.88	99.94	99.8	99.74	99.97	**99.86**
T0.6	99.94	100	100	100	100	99.997	99.97	100	100	**99.99**
T0.8	99.98	100	100	100	100	100	99.99	100	100	**100.00**
T1	100	100	100	100	100	100	99.993	100	100	**100.00**
T2	100	100	100	100	100	100	100	100	100	**100.00**
T3	100	100	100	100	100	100	100	100	100	**100.00**
T4	100	100	100	100	100	100	100	100	100	**100.00**
T5	100	100	100	100	100	100	100	100	100	**100.00**
T6	100	100	100	100	100	100	100	100	100	**100.00**

Appendix X : Confusion Matrices of the Training, Validation and Test Samples of the Component Degradation Classifiers.

X.1 : Compressor Degradation Level Classifier at Altitude Level 1

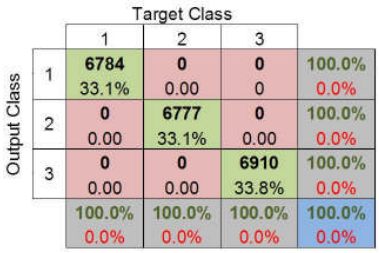

(a) Training samples

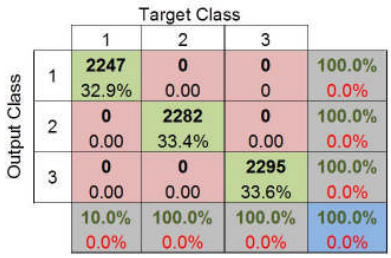

(b) Validation samples

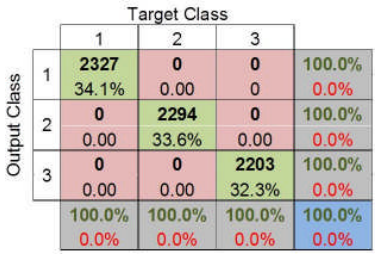

(b) Test samples

X.2 : HP Turbine Degradation Level Classifier at Altitude Level 1

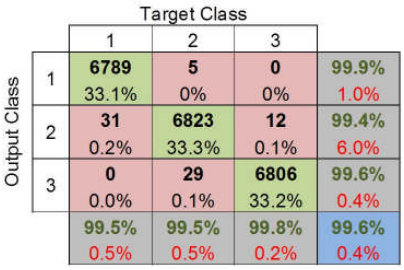

(a) Training samples

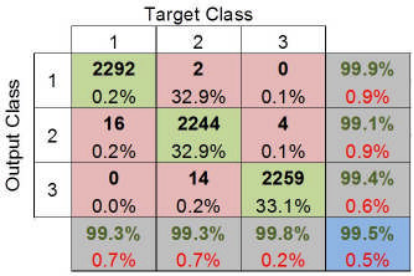

(b) Validation samples

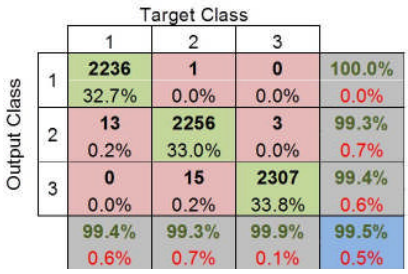

(b) Test samples

X.3 : LP Turbine Degradation Level Classifier at Altitude Level 1

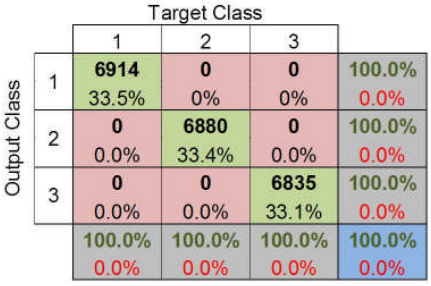

(a) Training samples

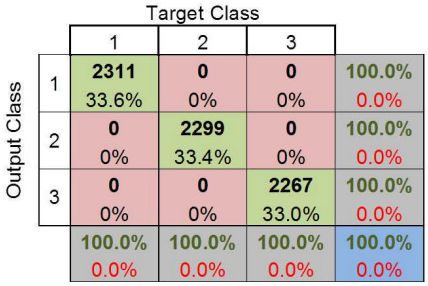

(b) Validation samples

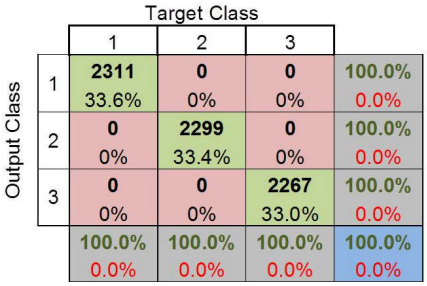

(b) Test samples

X.4 : Compressor Degradation Level Classifier at Altitude Level 2

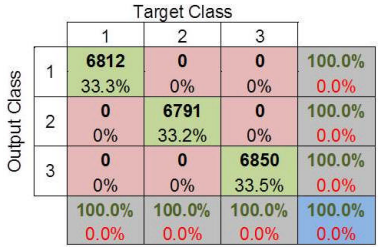

(a) Training samples

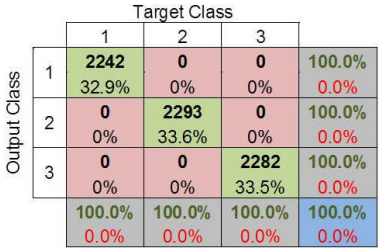

(b) Validation samples

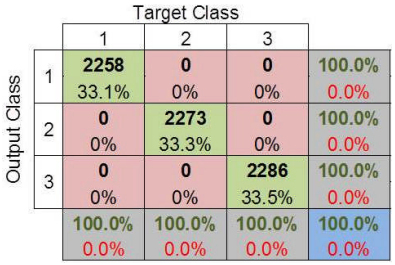

(b) Test samples

X.5 : HP Turbine Degradation Level Classifier at Altitude Level 2

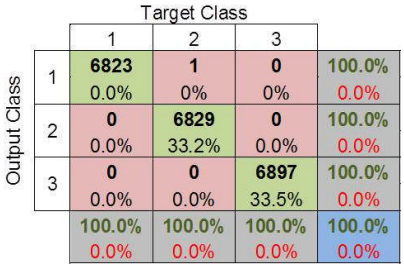

(a) Training samples

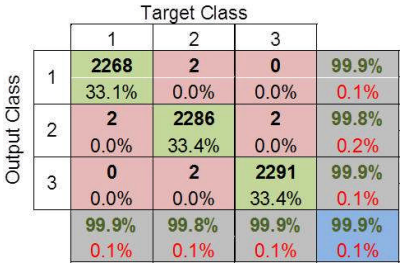

(b) Validation samples

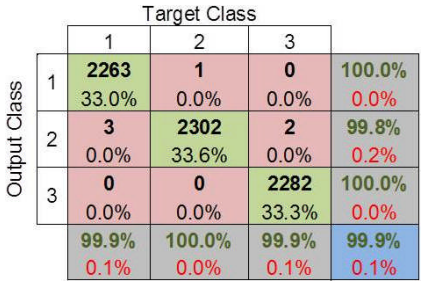

(b) Test samples

X.6 : LP Turbine Degradation Level Classifier at Altitude Level 2

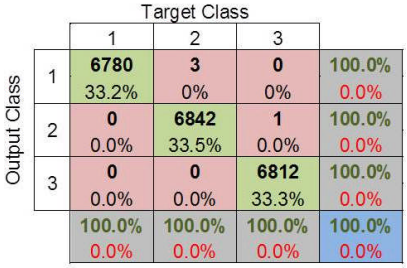

(a) Training samples

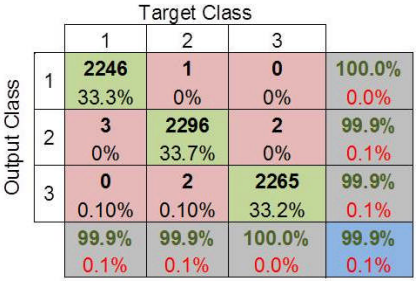

(b) Validation samples

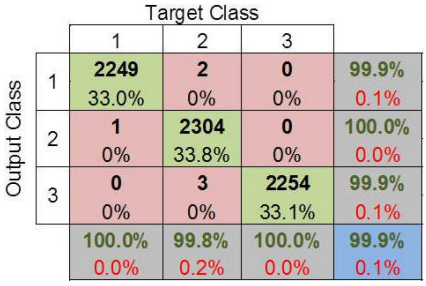

(b) Test samples

X.7 : Compressor Degradation Level Classifier at Altitude Level 3

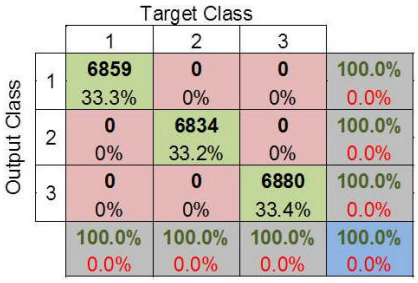

(a) Training samples

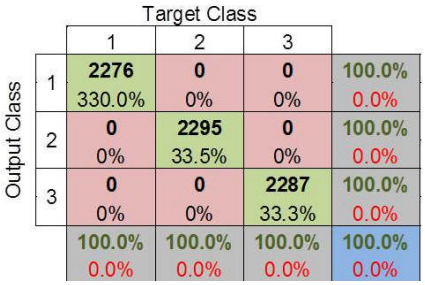

(b) Validation samples

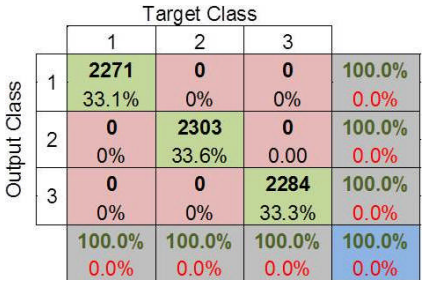

(b) Test samples

X.8 : HP Turbine Degradation Level Classifier at Altitude Level 3

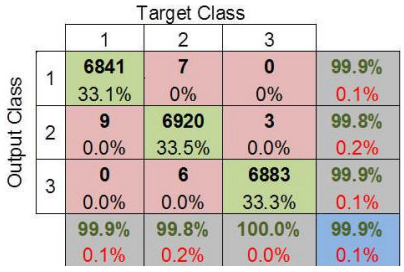

(a) Training samples

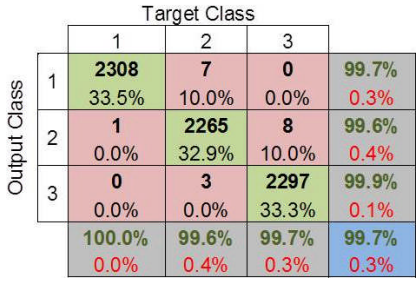

(b) Validation samples

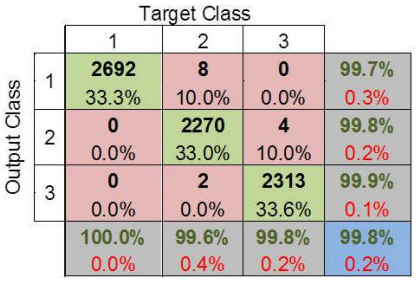

(b) Test samples

X.9 : LP Turbine Degradation Level Classifier at Altitude Level 3

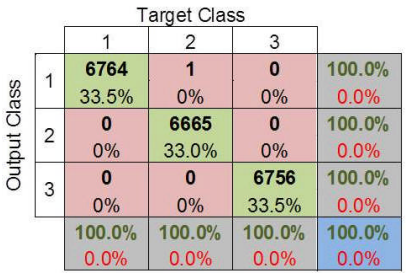

(a) Training samples

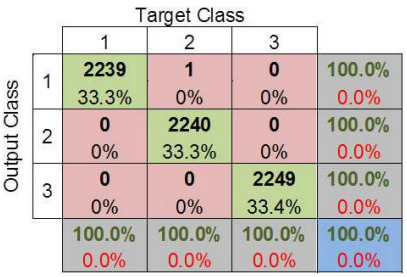

(b) Validation samples

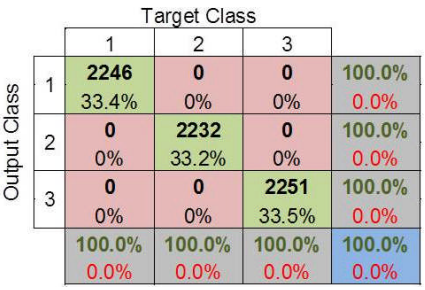

(b) Test samples

X.10 : Confusion Matrices of Component Health Classifier at Altitude Level 1

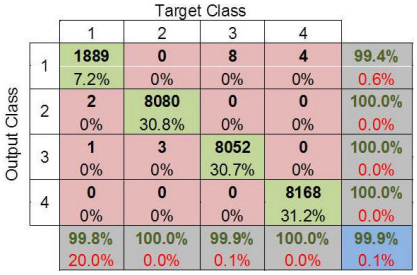

Output Class \ Target Class	1	2	3	4	
1	1889 7.2%	0 0%	8 0%	4 0%	99.4% 0.6%
2	2 0%	8080 30.8%	0 0%	0 0%	100.0% 0.0%
3	1 0%	3 0%	8052 30.7%	0 0%	100.0% 0.0%
4	0 0%	0 0%	0 0%	8168 31.2%	100.0% 0.0%
	99.8% 20.0%	100.0% 0.0%	99.9% 0.1%	100.0% 0.0%	99.9% 0.1%

(a) Training samples

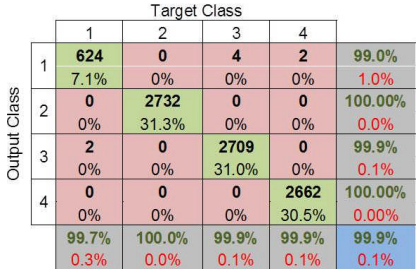

Output Class \ Target Class	1	2	3	4	
1	624 7.1%	0 0%	4 0%	2 0%	99.0% 1.0%
2	0 0%	2732 31.3%	0 0%	0 0%	100.00% 0.0%
3	2 0%	0 0%	2709 31.0%	0 0%	99.9% 0.1%
4	0 0%	0 0%	0 0%	2662 30.5%	100.00% 0.00%
	99.7% 0.3%	100.0% 0.0%	99.9% 0.1%	99.9% 0.1%	99.9% 0.1%

(b) Validation samples

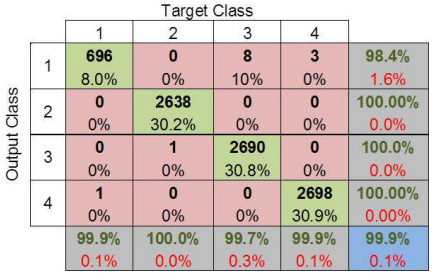

Output Class \ Target Class	1	2	3	4	
1	696 8.0%	0 0%	8 10%	3 0%	98.4% 1.6%
2	0 0%	2638 30.2%	0 0%	0 0%	100.00% 0.0%
3	0 0%	1 0%	2690 30.8%	0 0%	100.0% 0.0%
4	1 0%	0 0%	0 0%	2698 30.9%	100.00% 0.00%
	99.9% 0.1%	100.0% 0.0%	99.7% 0.3%	99.9% 0.1%	99.9% 0.1%

(b) Test samples

X.11 : Confusion Matrices of Component Health Classifier at Altitude Level 2

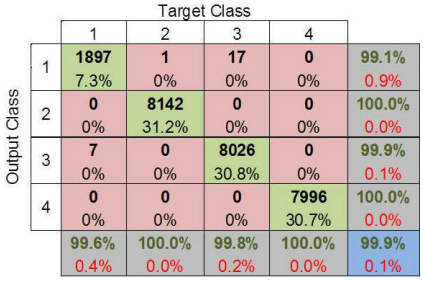

Output Class \ Target Class	1	2	3	4	
1	1897 7.3%	1 0%	17 0%	0 0%	99.1% 0.9%
2	0 0%	8142 31.2%	0 0%	0 0%	100.0% 0.0%
3	7 0%	0 0%	8026 30.8%	0 0%	99.9% 0.1%
4	0 0%	0 0%	0 0%	7996 30.7%	100.0% 0.0%
	99.6% 0.4%	100.0% 0.0%	99.8% 0.2%	100.0% 0.0%	99.9% 0.1%

(a) Training samples

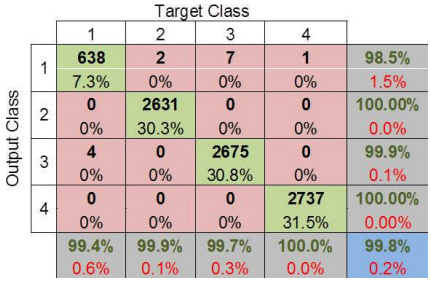

Output Class \ Target Class	1	2	3	4	
1	638 7.3%	2 0%	7 0%	1 0%	98.5% 1.5%
2	0 0%	2631 30.3%	0 0%	0 0%	100.00% 0.0%
3	4 0%	0 0%	2675 30.8%	0 0%	99.9% 0.1%
4	0 0%	0 0%	0 0%	2737 31.5%	100.00% 0.00%
	99.4% 0.6%	99.9% 0.1%	99.7% 0.3%	100.0% 0.0%	99.8% 0.2%

(b) Validation samples

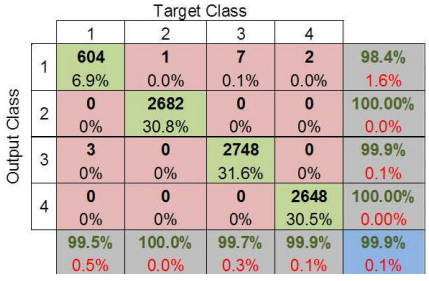

Output Class \ Target Class	1	2	3	4	
1	604 6.9%	1 0.0%	7 0.1%	2 0.0%	98.4% 1.6%
2	0 0%	2682 30.8%	0 0%	0 0%	100.00% 0.0%
3	3 0%	0 0%	2748 31.6%	0 0%	99.9% 0.1%
4	0 0%	0 0%	0 0%	2648 30.5%	100.00% 0.00%
	99.5% 0.5%	100.0% 0.0%	99.7% 0.3%	99.9% 0.1%	99.9% 0.1%

(b) Test samples

X.12 : Confusion Matrices of Component Health Classifier at Altitude Level 3

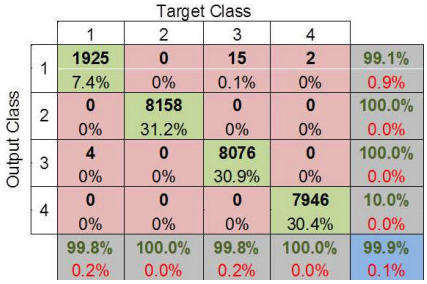

Output Class \ Target Class	1	2	3	4	
1	1925 7.4%	0 0%	15 0.1%	2 0%	99.1% 0.9%
2	0 0%	8158 31.2%	0 0%	0 0%	100.0% 0.0%
3	4 0%	0 0%	8076 30.9%	0 0%	100.0% 0.0%
4	0 0%	0 0%	0 0%	7946 30.4%	10.0% 0.0%
	99.8% 0.2%	100.0% 0.0%	99.8% 0.2%	100.0% 0.0%	99.9% 0.1%

(a) Training samples

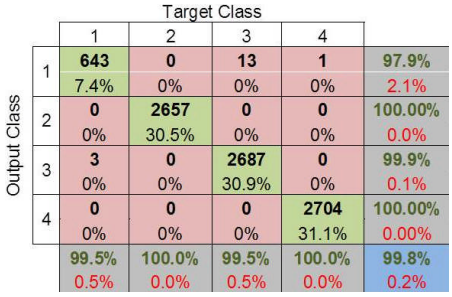

Output Class \ Target Class	1	2	3	4	
1	643 7.4%	0 0%	13 0%	1 0%	97.9% 2.1%
2	0 0%	2657 30.5%	0 0%	0 0%	100.00% 0.0%
3	3 0%	0 0%	2687 30.9%	0 0%	99.9% 0.1%
4	0 0%	0 0%	0 0%	2704 31.1%	100.00% 0.00%
	99.5% 0.5%	100.0% 0.0%	99.5% 0.5%	100.0% 0.0%	99.8% 0.2%

(b) Validation samples

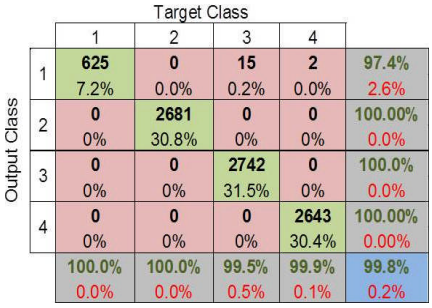

Output Class \ Target Class	1	2	3	4	
1	625 7.2%	0 0.0%	15 0.2%	2 0.0%	97.4% 2.6%
2	0 0%	2681 30.8%	0 0%	0 0%	100.00% 0.0%
3	0 0%	0 0%	2742 31.5%	0 0%	100.0% 0.0%
4	0 0%	0 0%	0 0%	2643 30.4%	100.00% 0.00%
	100.0% 0.0%	100.0% 0.0%	99.5% 0.5%	99.9% 0.1%	99.8% 0.2%

(b) Test samples

Appendix Y : Step Size and Unseen Samples Size Used during Post Test for SB Architecture Approximators at Degraded Engine Condition

Y.1 : Step Size for Each Parameter and Unseen Samples Used during Post Test of Compressor Degradation

LL1							
Parameter	LL	UL	Step size	Parameter	LL	UL	Step size
Altitude	200	1400	200	PCN	0.943	0.997	0.006
Mach number	0.03	0.27	0.06	Tamb dev.	11	23	3
% in ETA	-0.25	-1.75	0.5 (approx.)				
% in FC	-0.4	-1.6	0.4 (approx.)		Finalised samples		25,156
LL2							
Parameter	LL	UL	Step size	Parameter	LL	UL	Step size
Altitude	1700	2900	200	PCN	0.943	0.997	0.006
Mach number	0.03	0.27	0.06	Tamb dev.	11	23	3
% in ETA	-0.25	-1.75	0.5 (approx.)				
% in FC	-0.4	-1.6	0.4 (approx.)		Finalised samples		26,489
LL3							
Parameter	LL	UL	Step size	Parameter	LL	UL	Step size
Altitude	3200	4400	200	PCN	0.943	0.997	0.006
Mach number	0.03	0.27	0.06	Tamb dev.	11	23	3
% in ETA	-0.25	-1.75	0.5 (approx.)				
% in FC	-0.4	-1.6	0.4 (approx.)		Finalised samples		25,287

Y.2 Step Size for Each Parameter and Unseen Samples Used during Post Test of Degradation Level Classifier at All Altitude Levels

Operating parameter							
Parameter	LL	UL	Step size	Parameter	LL	UL	Step size
Altitude Level 1	200	1400	300	PCN	0.946	0.994	0.012
Altitude Level 2	1700	2900	300	Tamb dev.	14	23	3
Altitude Level 3	3200	4400	300	Mach number	0.05	0.275	0.075
Compressor degradation							
% in ETA	-0.25	-1.95	0.5 (approx.)	% in FC	-0.4	-1.8	0.4 (approx.)
	-2.25	-3.95	0.5 (approx.)		-2.4	-3.8	0.4 (approx.)
	-4.25	-5.95	0.5 (approx.)		-4.4	-5.8	0.4 (approx.)
HP and LP Turbine degradation							
% in ETA	-0.25	-1.95	0.5 (approx.)	% in FC	0.4	1.8	0.4 (approx.)
	-2.25	-3.95	0.5 (approx.)		2.4	3.8	0.4 (approx.)
	-4.25	-5.95	0.5 (approx.)		4.4	5.8	0.4 (approx.)

Finalised samples					
Altitude Level 1		Altitude Level 2		Altitude Level 3	
Compressor	28,705	Compressor	29,567	Compressor	29,734
HP Turbine	29,648	HP Turbine	29,319	HP Turbine	29,792
LP Turbine	29,936	LP Turbine	29,685	LP Turbine	29,099

Y.3 : Step Size and Unseen Samples Used during Post Test of Component Health Classifier

Operating parameter for Clean Engine							
Parameter	LL	UL	Step size	Parameter	LL	UL	Step size
Altitude Level 1	75	1275	150	PCN	0.943	0.997	0.006
	150	1350	150	Tamb dev.	11	29	3
Altitude Level 2	1545	2745	300	Mach number for Alt Level 1	0.03	0.27	0.06

	1575	2775	300	Mach number for Alt Level 2 and 3	0.01	0.28	0.03
	1650	2850	300				
Altitude Level 3	3045	4295	250				
	3075	4325	250				
	3150	4400	250				
Operating parameter for Degraded Engine							
Parameter	LL	UL	Step size	Parameter	LL	UL	Step size
Altitude Level 1	200	1400	200	PCN (all except comp deg. @ Alt level 3)	0.943	0.997	0.006
Altitude Level 2	1700	2900	200	PCN (comp deg. @ Alt level 3)	0.94	0.997	0.003
Altitude Level 3	3200	4400	200	Tamb dev.	11	23	3
				Mach number	0.03	0.27	0.06
Compressor degradation							
% in ETA (LL)	-0.25	-1.75	0.5 (approx.)	% in FC (LL)	-0.4	-1.6	0.4 (approx.)
% in ETA (ML)	-2.25	-3.75	0.5 (approx.)	% in FC (ML)	-2.4	-3.6	0.4 (approx.)
% in ETA (HL)	-4.25	-5.75	0.5 (approx.)	% in FC (HL)	-4.4	-5.6	0.4 (approx.)
HP/LP Turbine degradation							
% in ETA (LL)	-0.25	-1.75	0.5 (approx.)	% in FC (LL)	0.4	1.6	0.4 (approx.)
% in ETA (ML)	-2.25	-3.75	0.5 (approx.)	% in FC (ML)	2.4	3.6	0.4 (approx.)
% in ETA (HL)	-4.25	-5.75	0.5 (approx.)	% in FC (HL)	4.4	5.6	0.4 (approx.)
Finalised samples							
Altitude Level 1	216,289		Altitude Level 2	177,425	Altitude Level 3		179,051

Appendix Z : Percentage of Samples with E Within the Specified Range Predicted by the SB Architectures of Degraded Engine Case

Z.1 : Samples Distribution Predicted by Compressor Degradation Architecture

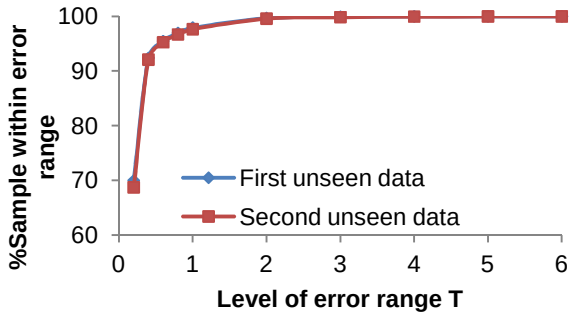

(a) LL1

(b) LL2

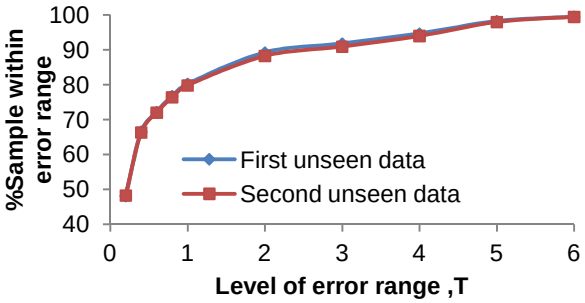

(c) LL3

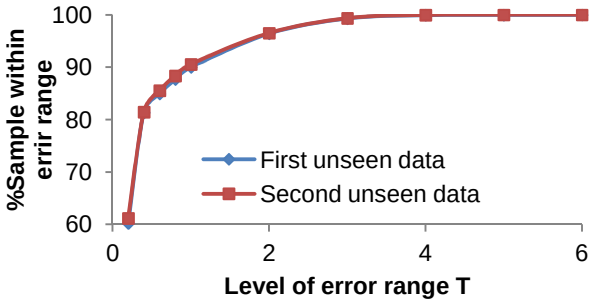

(d) ML1

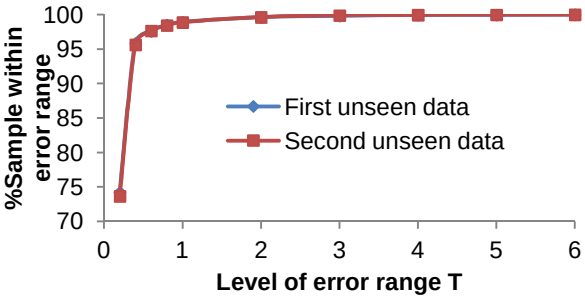

(e) ML2

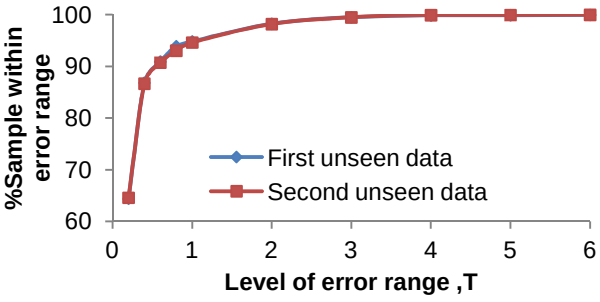

(f) ML3

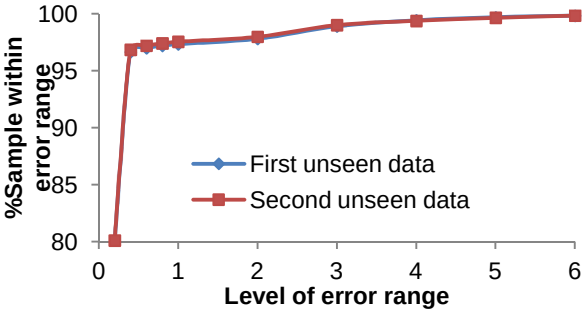

(g) HL1

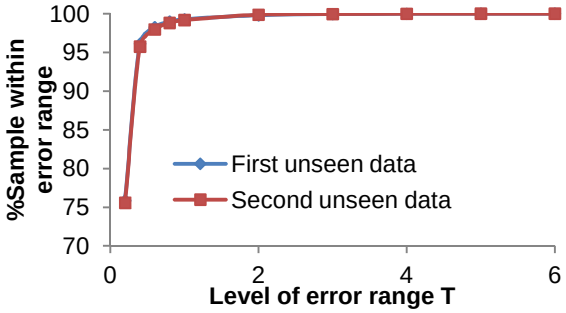

(h) HL2

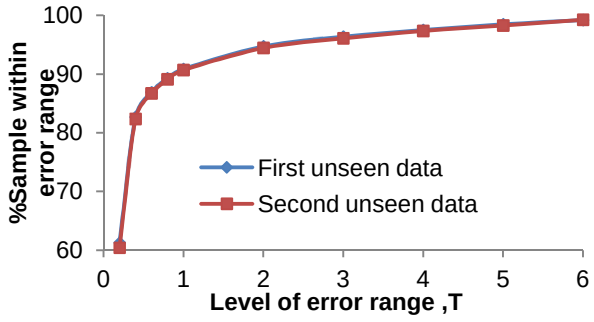

(i) HL1

Z.2 : Samples Distribution Predicted by HP Turbine Degradation Architecture

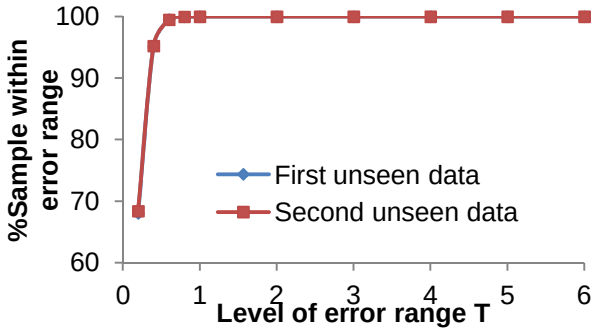

(a) LL1

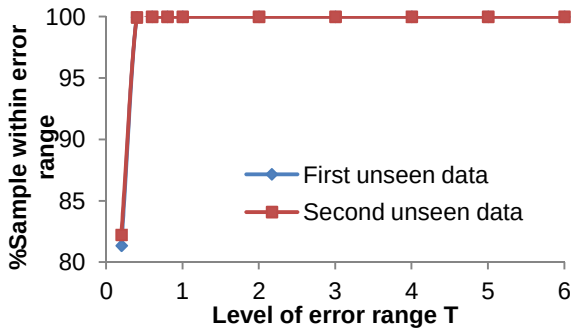

(b) LL2

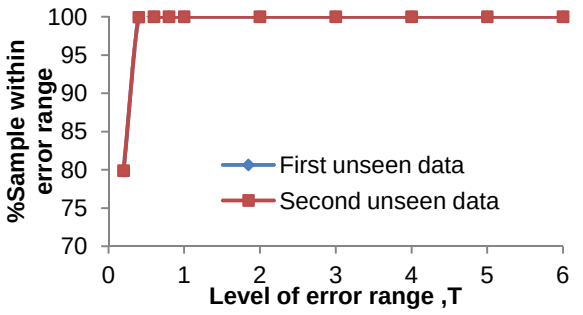

(c) LL3

(d) ML1

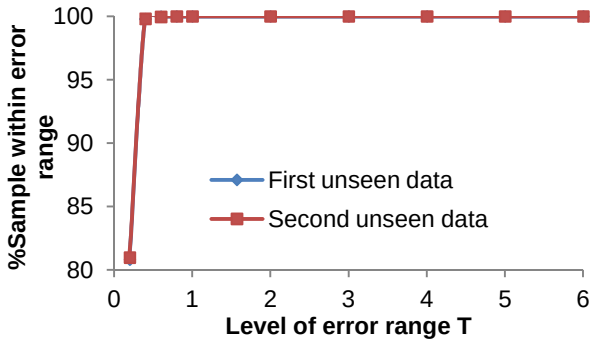

(e) ML2

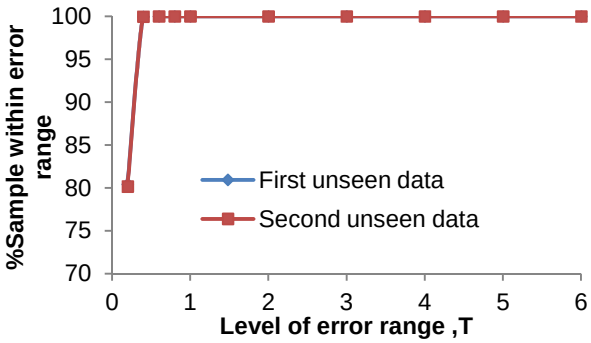

(f) ML3

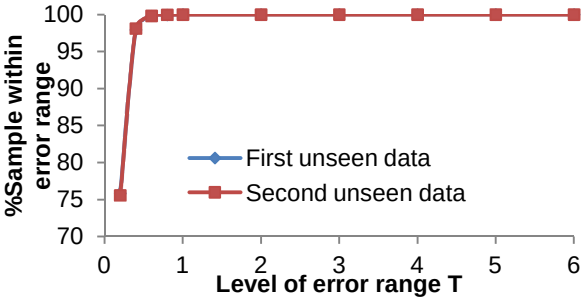

(g) HL1

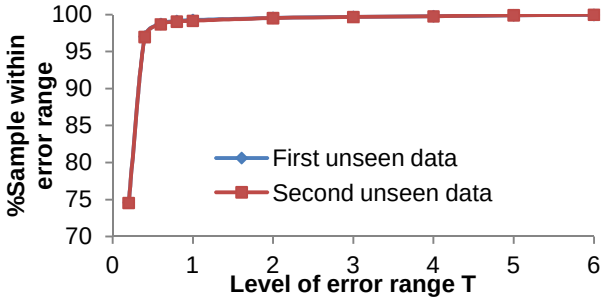

(h) HL2

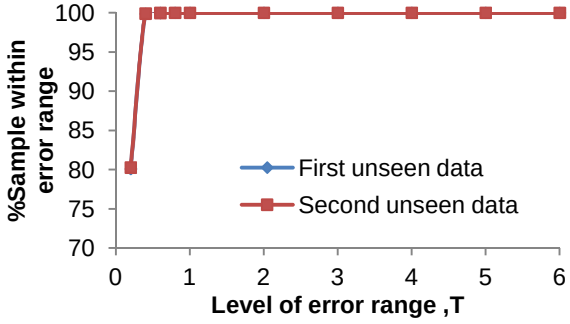

(i) HL3

Z.3 Samples Distribution Predicted by LP Turbine Degradation Architecture

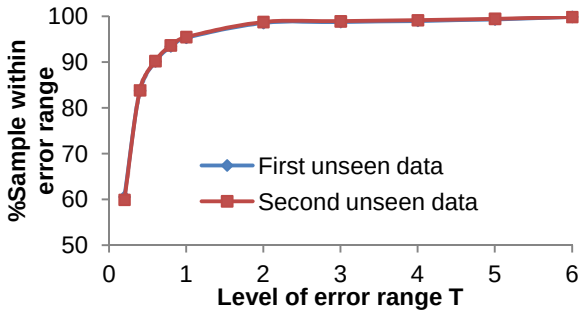

(a) LL1

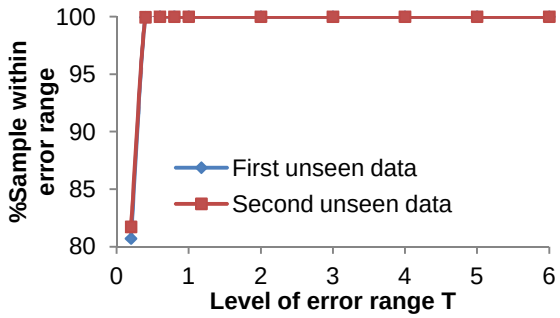

(b) LL2

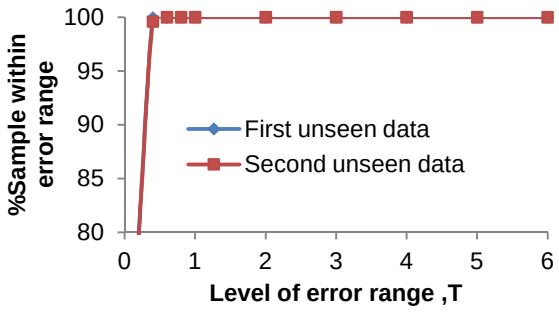

(c) LL3

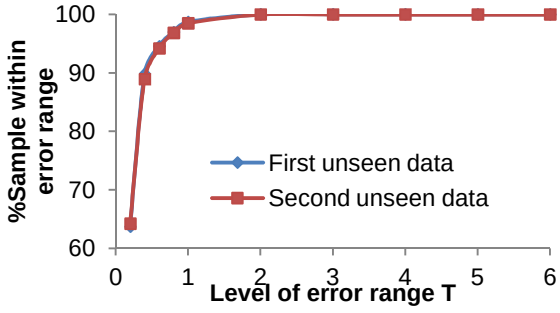

(d) ML1

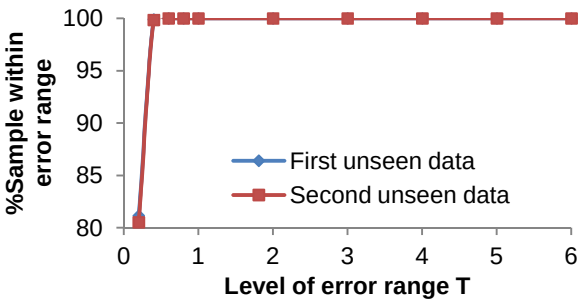

(e) ML2

(f) ML3

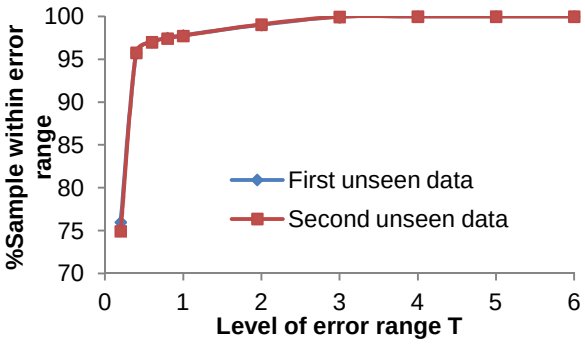

(g) HL1

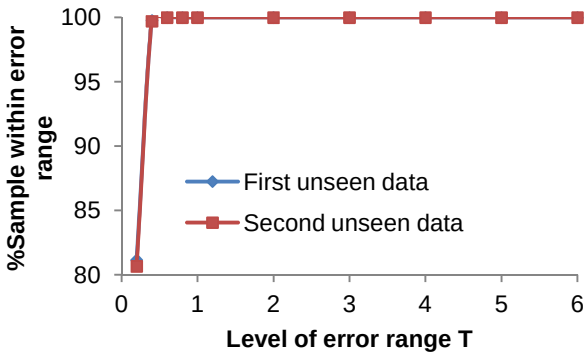

(h) HL2

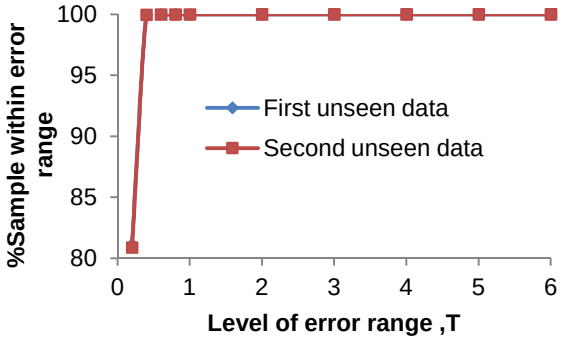

(i) HL3

Appendix AA : Summarised Results of the Probabilistic Analyses Conducted On the Component Degradation Sensor-Based Architectures

	LL1	LL2	LL3	ML1	ML2	ML3	HL1	HL2	HL3
Compressor degradation:									
Best fitted distribution	Johnson SU	Cauchy	Cauchy	Cauchy	Cauchy	Cauchy	Cauchy	HyperSec	Cauchy
Error Range	Probability								
T0.2	0.650	0.610	0.456	0.580	0.670	0.612	0.690	0.659	0.589
T0.4	0.870	0.787	0.668	0.768	0.824	0.786	0.840	0.900	0.770
T0.6	0.940	0.855	0.767	0.840	0.881	0.855	0.890	0.974	0.846
T0.8	0.980	0.890	0.822	0.880	0.910	0.890	0.920	0.993	0.880
T1	0.983	0.912	0.856	0.910	0.928	0.912	0.930	0.998	0.900
T2	0.998	0.956	0.927	0.952	0.964	0.956	0.970	1.000	0.950
T3	0.999	0.970	0.951	0.968	0.976	0.970	0.970	1.000	0.970
T4	1.000	0.978	0.963	0.976	0.982	0.980	0.983	1.000	0.980
T5	1.000	0.982	0.970	0.981	0.986	0.982	0.987	1.000	0.990
T6	1.000	0.985	0.976	0.984	0.988	0.990	0.990	1.000	0.993
HP turbine degradation:									
Best fitted distribution	Normal	Normal	Normal	Normal	Normal	Normal	Normal	Cauchy	Normal
Error Range	Probability								
T0.2	0.6752	0.829	0.816	0.7473	0.820	0.819	0.752	0.61	0.818
T0.4	0.9511	0.994	0.992	0.9778	0.993	0.992	0.979	0.79	0.992
T0.6	0.9969	1.000	1.000	0.9994	1.000	1.000	0.9995	0.91	1.000
T0.8	0.9992	1.000	1.000	1.000	1.000	1.000	1.000	0.970	1.000
T1	1.000	1.000	1.000	1.000	1.000	1.000	1.000	0.986	1.000
T2	1.000	1.000	1.000	1.000	1.000	1.000	1.000	1.000	1.000
T3	1.000	1.000	1.000	1.000	1.000	1.000	1.000	1.000	1.000
T4	1.000	1.000	1.000	1.000	1.000	1.000	1.000	1.000	1.000
T5	1.000	1.000	1.000	1.000	1.000	1.000	1.000	1.000	1.000
T6	1.000	1.000	1.000	1.000	1.000	1.000	1.000	1.000	1.000
LP turbine degradation:									
Best fitted distribution	Cauchy	Normal	Normal	Johnson SU	Normal	Normal	Cauchy	Normal	Normal
Error Range	Probability								
T0.2	0.589	0.825	0.814	0.6	0.822	0.818	0.676	0.820	0.823
T0.4	0.771	0.993	0.992	0.873	0.993	0.990	0.821	0.993	0.993
T0.6	0.843	1.000	1.000	0.95	1.000	1.000	0.883	1.000	1.000
T0.8	0.865	1.000	1.000	0.98	1.000	1.000	0.899	1.000	1.000
T1	0.9050	1.000	1.000	0.9910	1.000	1.000	0.9290	1.000	1.000
T2	0.9520	1.000	1.000	0.9998	1.000	1.000	0.9640	1.000	1.000
T3	0.9680	1.000	1.000	1.0000	1.000	1.000	0.9760	1.000	1.000
T4	0.9760	1.000	1.000	1.0000	1.000	1.000	0.9820	1.000	1.000
T5	0.9810	1.000	1.000	1.0000	1.000	1.000	0.9860	1.000	1.000
T6	0.9840	1.000	1.000	1.0000	1.000	1.000	0.9880	1.000	1.000

Appendix BB : PDF and CDF Plots for the Component Degradation SB Approximator

BB.1 : PDF and CDF Plots for the Compressor Degradation Approximators

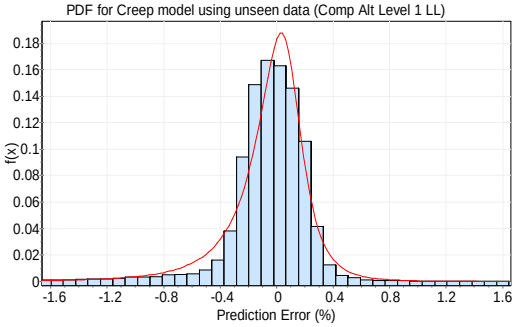

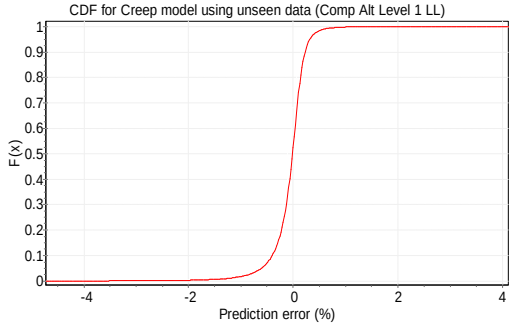

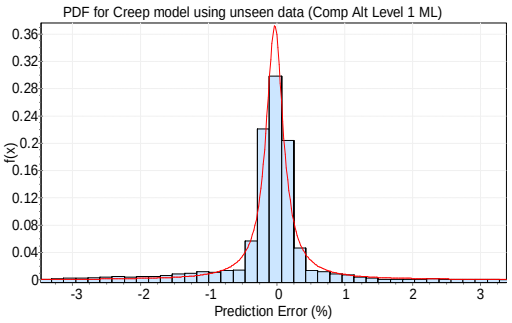

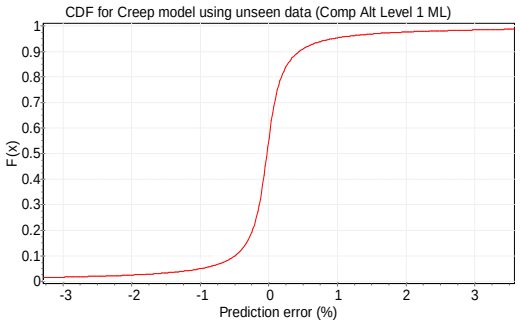

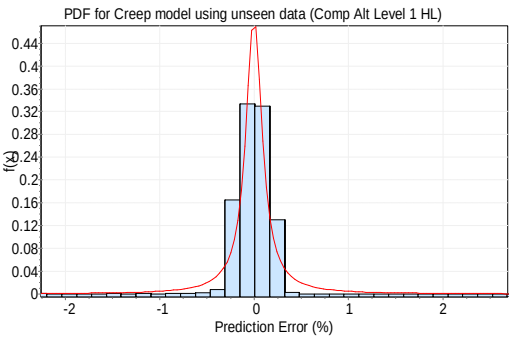

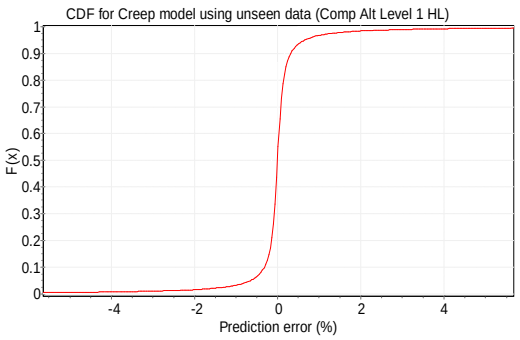

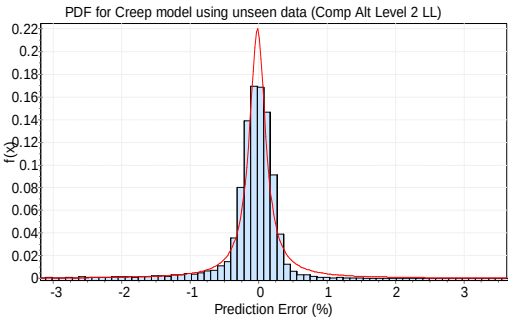

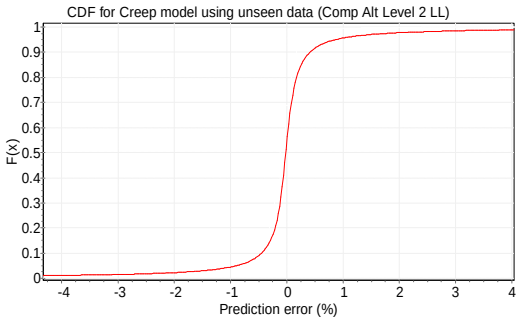

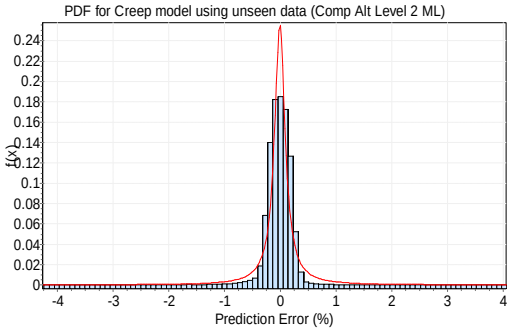
PDF for Creep model using unseen data (Comp Alt Level 2 ML)
f(x)
Prediction Error (%)

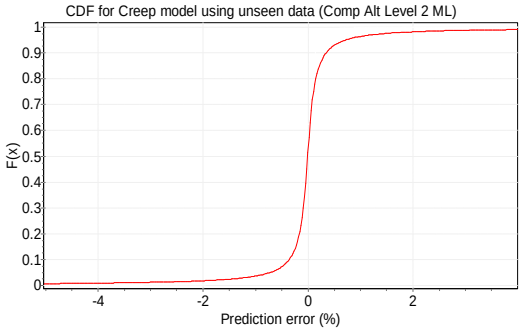
CDF for Creep model using unseen data (Comp Alt Level 2 ML)
F(x)
Prediction error (%)

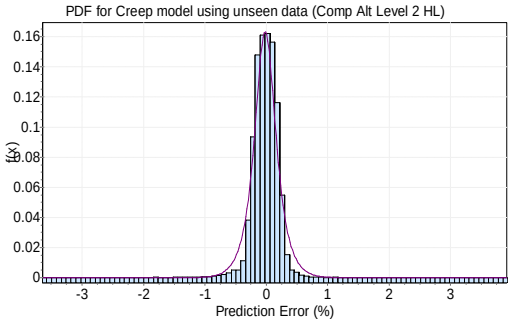
PDF for Creep model using unseen data (Comp Alt Level 2 HL)
f(x)
Prediction Error (%)

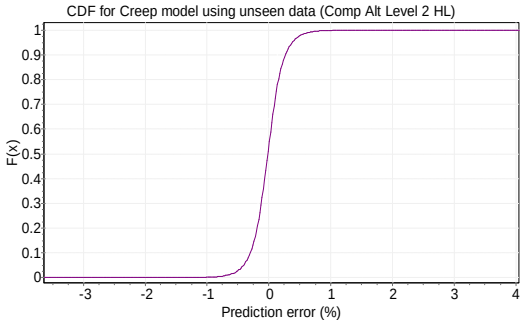
CDF for Creep model using unseen data (Comp Alt Level 2 HL)
F(x)
Prediction error (%)

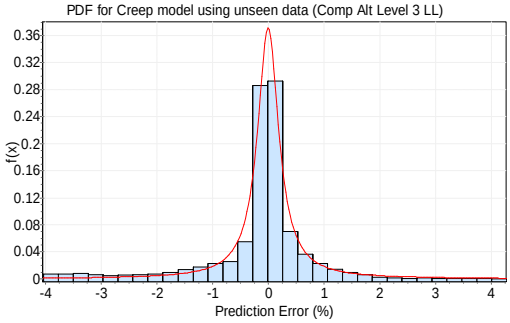
PDF for Creep model using unseen data (Comp Alt Level 3 LL)
f(x)
Prediction Error (%)

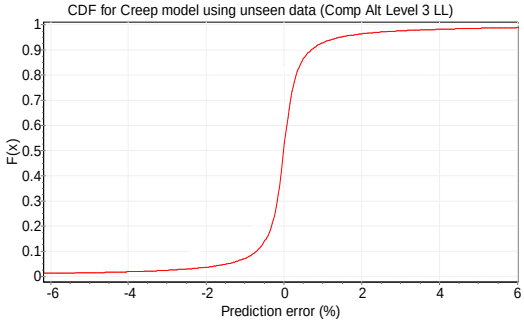
CDF for Creep model using unseen data (Comp Alt Level 3 LL)
F(x)
Prediction error (%)

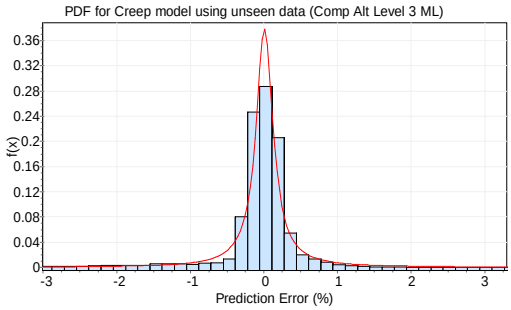
PDF for Creep model using unseen data (Comp Alt Level 3 ML)
f(x)
Prediction Error (%)

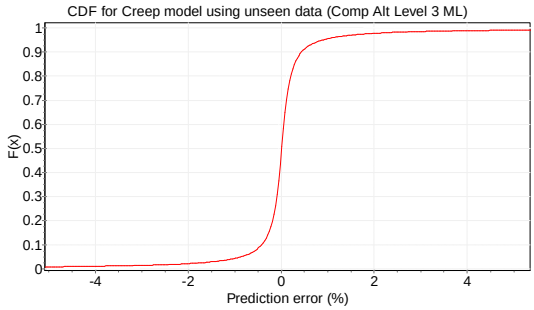
CDF for Creep model using unseen data (Comp Alt Level 3 ML)
F(x)
Prediction error (%)

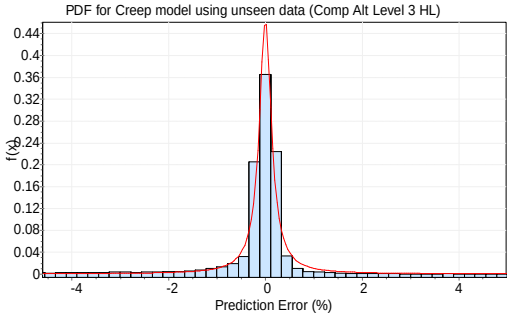
PDF for Creep model using unseen data (Comp Alt Level 3 HL)
f(x)
Prediction Error (%)

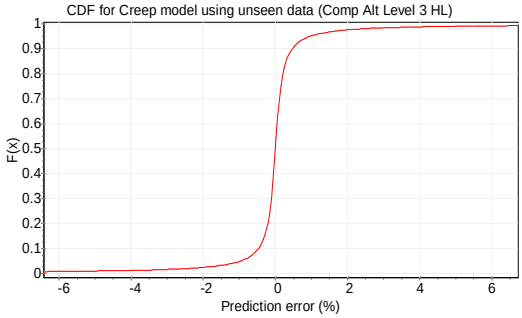
CDF for Creep model using unseen data (Comp Alt Level 3 HL)
F(x)
Prediction error (%)

BB.2 : PDF and CDF Plots for the HP Turbine Degradation Approximators

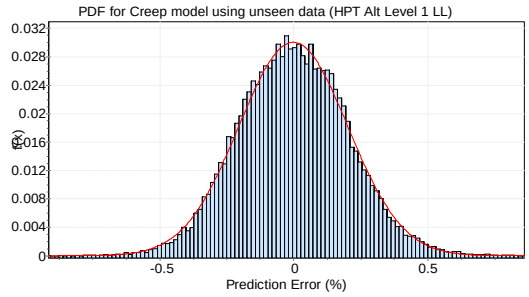

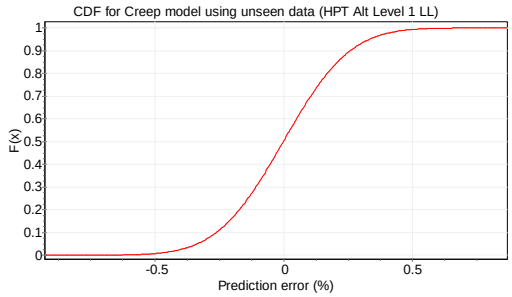

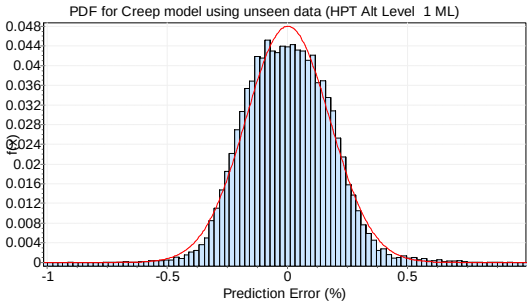

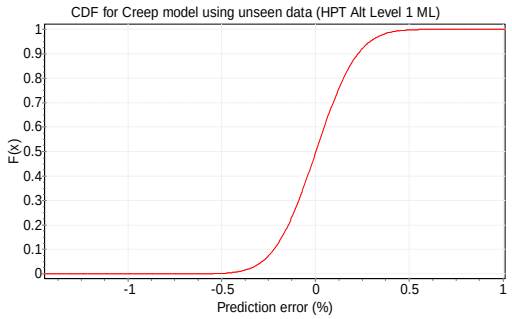

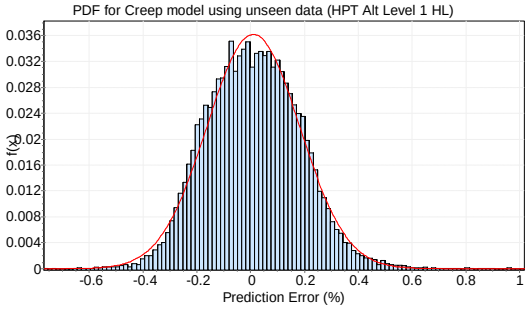

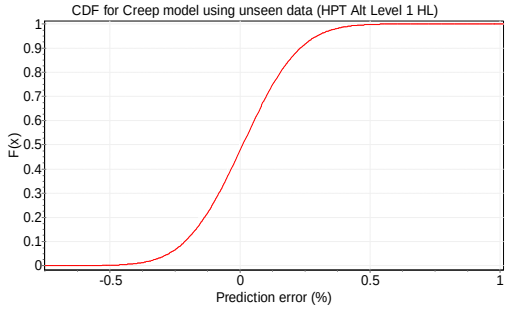

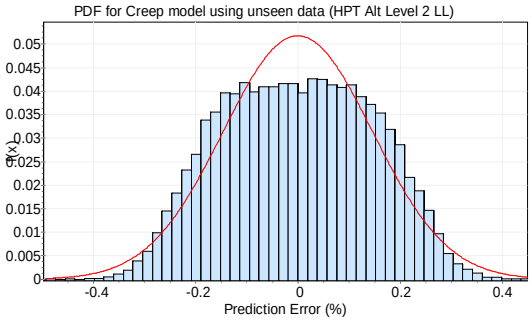

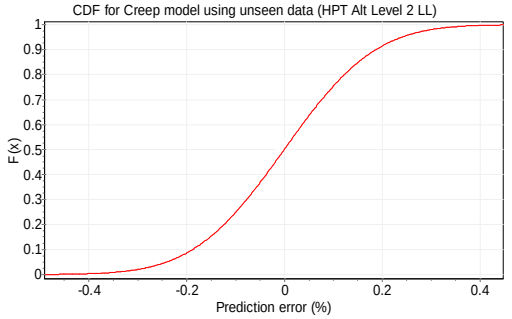

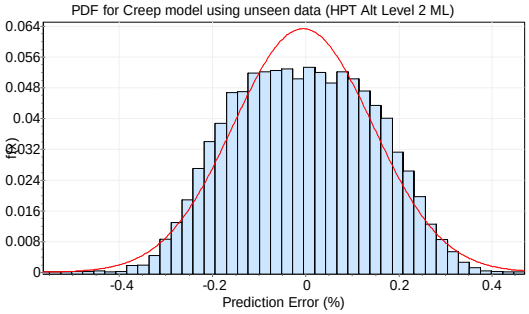

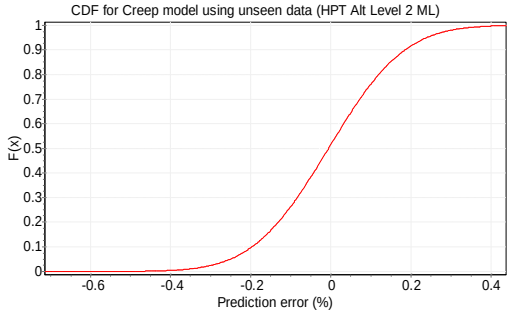

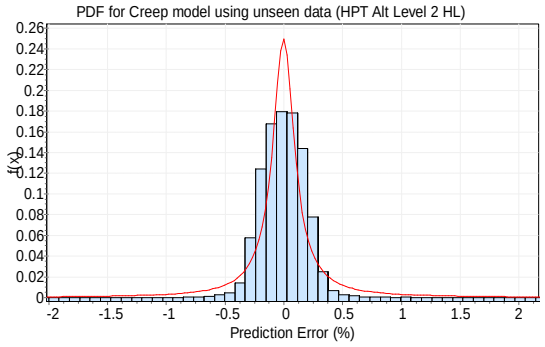
PDF for Creep model using unseen data (HPT Alt Level 2 HL)
f(x)
Prediction Error (%)

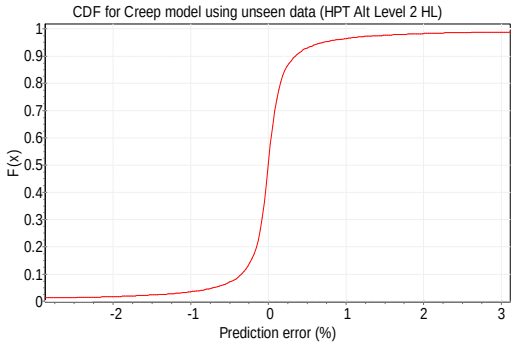
CDF for Creep model using unseen data (HPT Alt Level 2 HL)
F(x)
Prediction error (%)

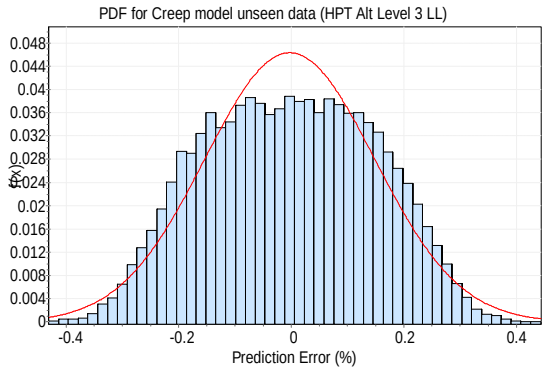
PDF for Creep model unseen data (HPT Alt Level 3 LL)
f(x)
Prediction Error (%)

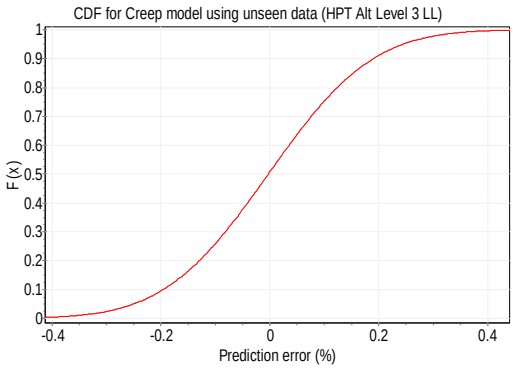
CDF for Creep model using unseen data (HPT Alt Level 3 LL)
F (x)
Prediction error (%)

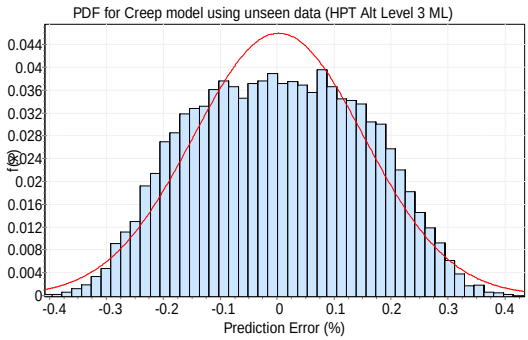
PDF for Creep model using unseen data (HPT Alt Level 3 ML)
f(x)
Prediction Error (%)

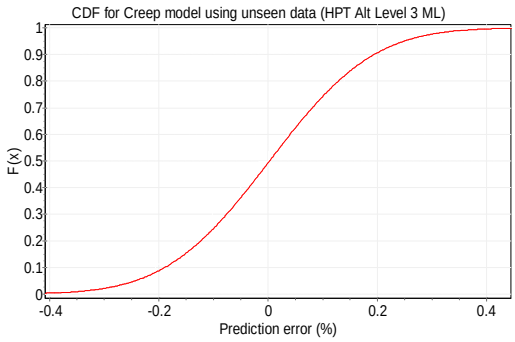
CDF for Creep model using unseen data (HPT Alt Level 3 ML)
F(x)
Prediction error (%)

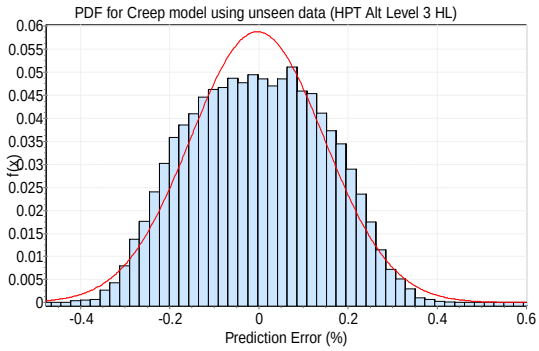
PDF for Creep model using unseen data (HPT Alt Level 3 HL)
f(x)
Prediction Error (%)

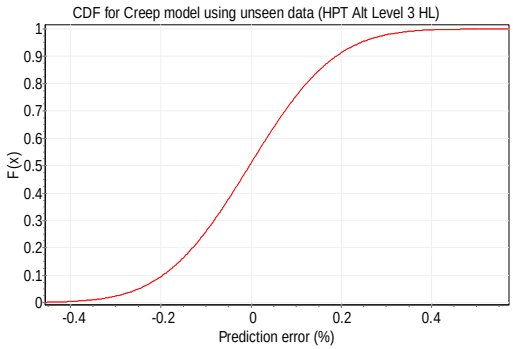
CDF for Creep model using unseen data (HPT Alt Level 3 HL)
F(x)
Prediction error (%)

BB.3 : PDF and CDF Plots for the LP Turbine Degradation Approximators

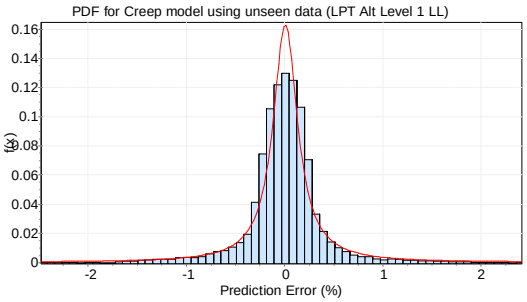

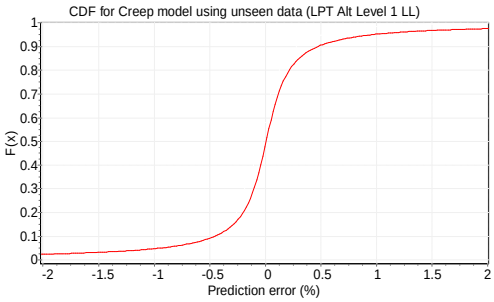

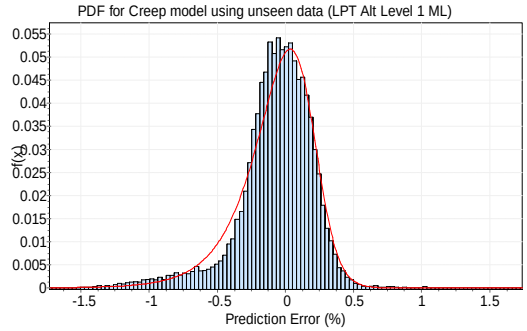

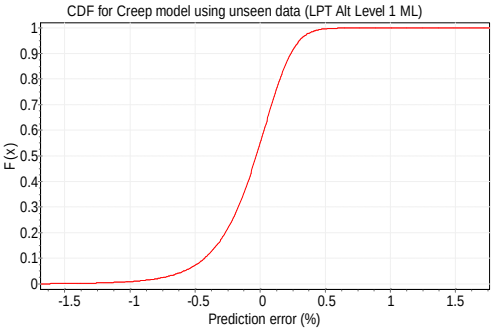

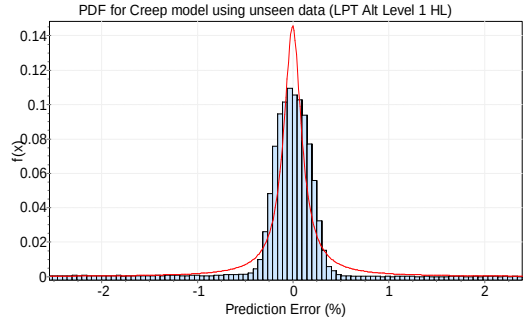

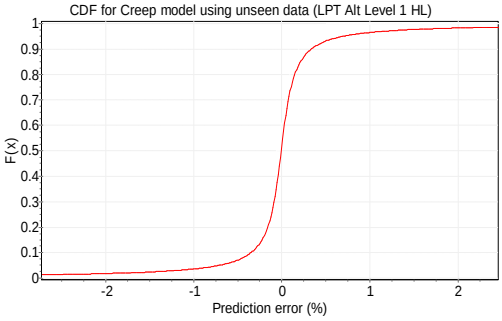

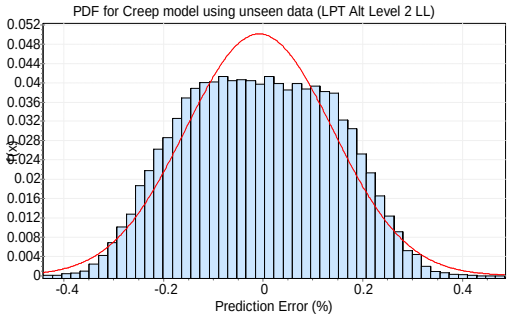

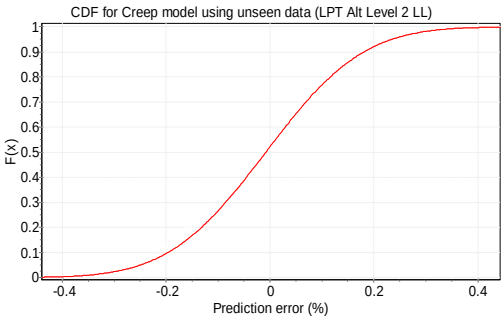

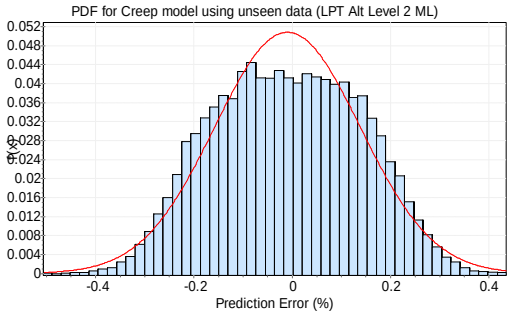

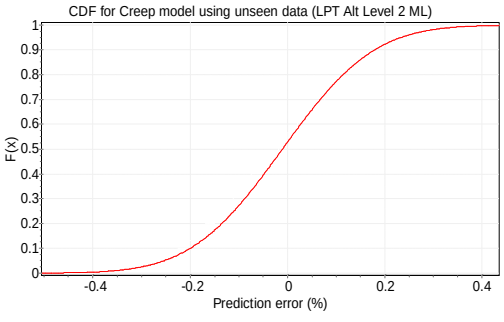

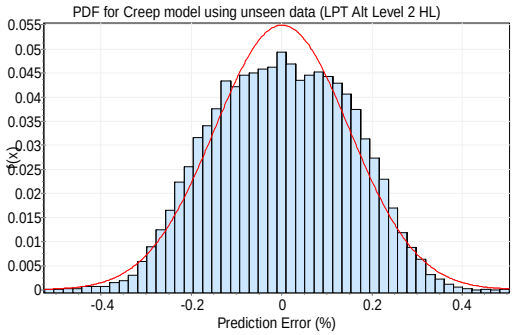
PDF for Creep model using unseen data (LPT Alt Level 2 HL)
f(x)
Prediction Error (%)

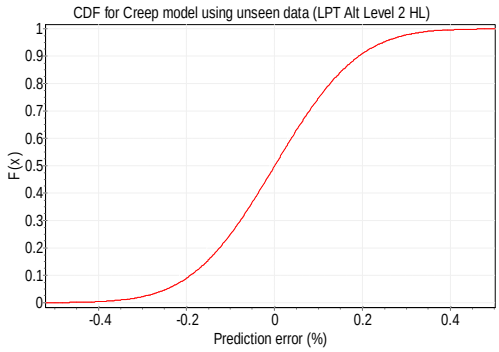
CDF for Creep model using unseen data (LPT Alt Level 2 HL)
F(x)
Prediction error (%)

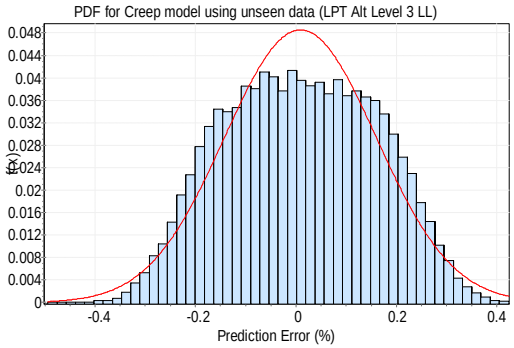
PDF for Creep model using unseen data (LPT Alt Level 3 LL)
f(x)
Prediction Error (%)

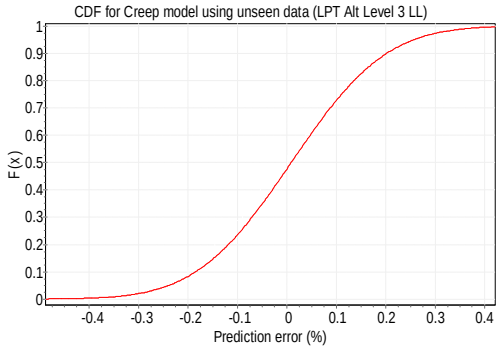
CDF for Creep model using unseen data (LPT Alt Level 3 LL)
F(x)
Prediction error (%)

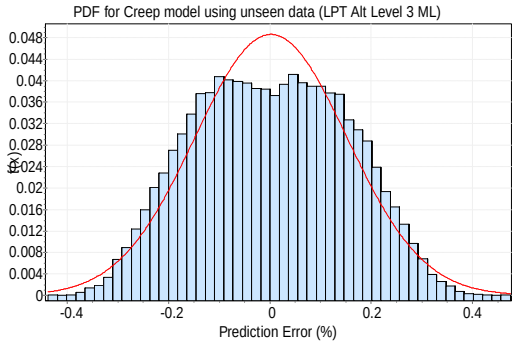
PDF for Creep model using unseen data (LPT Alt Level 3 ML)
f(x)
Prediction Error (%)

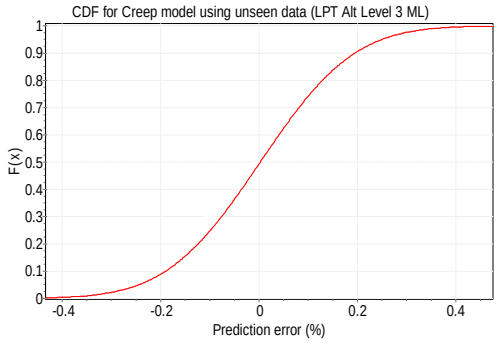
CDF for Creep model using unseen data (LPT Alt Level 3 ML)
F(x)
Prediction error (%)

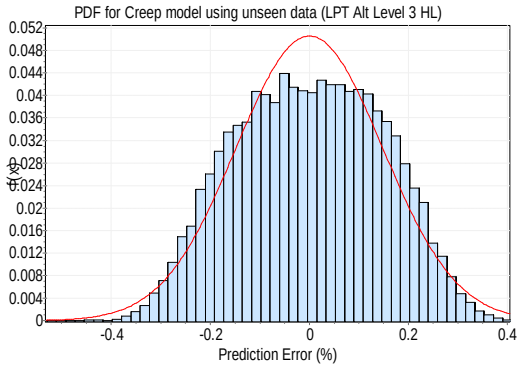
PDF for Creep model using unseen data (LPT Alt Level 3 HL)
f(x)
Prediction Error (%)

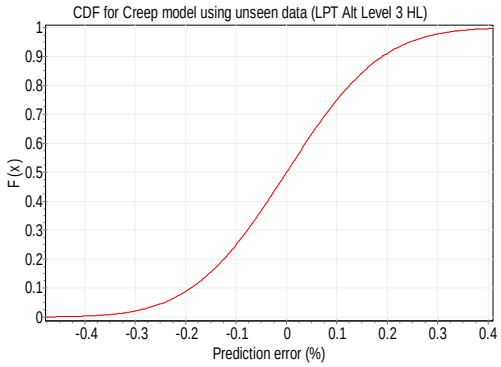
CDF for Creep model using unseen data (LPT Alt Level 3 HL)
F(x)
Prediction error (%)

Appendix CC : Confusion Matrices of Unseen Samples of the Component Degradation Classifiers.

CC.1 : Compressor Degradation Level Classifier at Altitude Level 1

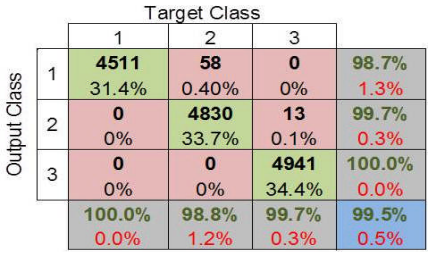

Output Class \ Target Class	1	2	3	
1	**4511** 31.4%	**58** 0.40%	**0** 0%	**98.7%** 1.3%
2	**0** 0%	**4830** 33.7%	**13** 0.1%	**99.7%** 0.3%
3	**0** 0%	**0** 0%	**4941** 34.4%	**100.0%** 0.0%
	100.0% 0.0%	**98.8%** 1.2%	**99.7%** 0.3%	**99.5%** 0.5%

(a) 1st unseen data

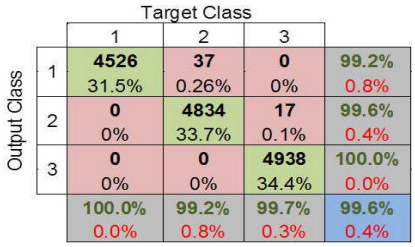

Output Class \ Target Class	1	2	3	
1	**4526** 31.5%	**37** 0.26%	**0** 0%	**99.2%** 0.8%
2	**0** 0%	**4834** 33.7%	**17** 0.1%	**99.6%** 0.4%
3	**0** 0%	**0** 0%	**4938** 34.4%	**100.0%** 0.0%
	100.0% 0.0%	**99.2%** 0.8%	**99.7%** 0.3%	**99.6%** 0.4%

(b) 2nd unseen data

CC.2 : HP Turbine Degradation Level Classifier at Altitude Level 1

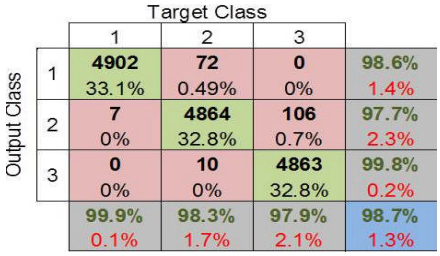

Output Class \ Target Class	1	2	3	
1	**4902** 33.1%	**72** 0.49%	**0** 0%	**98.6%** 1.4%
2	**7** 0%	**4864** 32.8%	**106** 0.7%	**97.7%** 2.3%
3	**0** 0%	**10** 0%	**4863** 32.8%	**99.8%** 0.2%
	99.9% 0.1%	**98.3%** 1.7%	**97.9%** 2.1%	**98.7%** 1.3%

(a) 1st unseen data

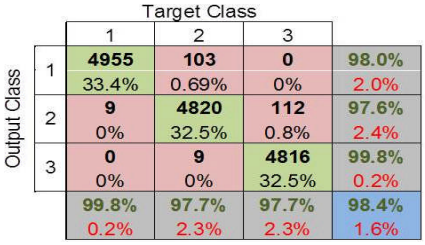

Output Class \ Target Class	1	2	3	
1	**4955** 33.4%	**103** 0.69%	**0** 0%	**98.0%** 2.0%
2	**9** 0%	**4820** 32.5%	**112** 0.8%	**97.6%** 2.4%
3	**0** 0%	**9** 0%	**4816** 32.5%	**99.8%** 0.2%
	99.8% 0.2%	**97.7%** 2.3%	**97.7%** 2.3%	**98.4%** 1.6%

(b) 2nd unseen data

CC.3 LP Turbine Degradation Level Classifier at Altitude Level 1

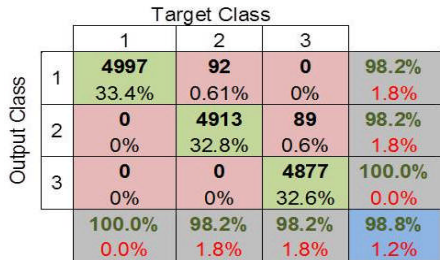

Output Class \ Target Class	1	2	3	
1	**4997** 33.4%	**92** 0.61%	**0** 0%	**98.2%** 1.8%
2	**0** 0%	**4913** 32.8%	**89** 0.6%	**98.2%** 1.8%
3	**0** 0%	**0** 0%	**4877** 32.6%	**100.0%** 0.0%
	100.0% 0.0%	**98.2%** 1.8%	**98.2%** 1.8%	**98.8%** 1.2%

(a) 1st unseen data

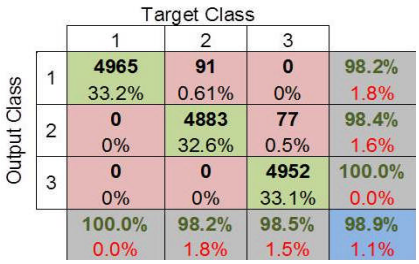

Output Class \ Target Class	1	2	3	
1	**4965** 33.2%	**91** 0.61%	**0** 0%	**98.2%** 1.8%
2	**0** 0%	**4883** 32.6%	**77** 0.5%	**98.4%** 1.6%
3	**0** 0%	**0** 0%	**4952** 33.1%	**100.0%** 0.0%
	100.0% 0.0%	**98.2%** 1.8%	**98.5%** 1.5%	**98.9%** 1.1%

(b) 2nd unseen data

CC.4 : Compressor Degradation Level Classifier at Altitude Level 2

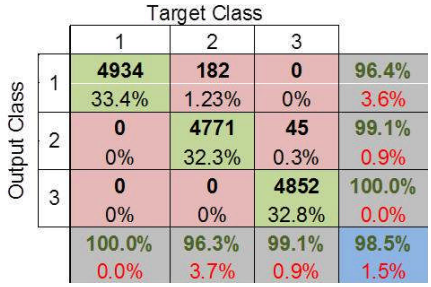

Output Class \ Target Class	1	2	3	
1	**4934** 33.4%	**182** 1.23%	**0** 0%	**96.4%** 3.6%
2	**0** 0%	**4771** 32.3%	**45** 0.3%	**99.1%** 0.9%
3	**0** 0%	**0** 0%	**4852** 32.8%	**100.0%** 0.0%
	100.0% 0.0%	**96.3%** 3.7%	**99.1%** 0.9%	**98.5%** 1.5%

(a) 1st unseen data

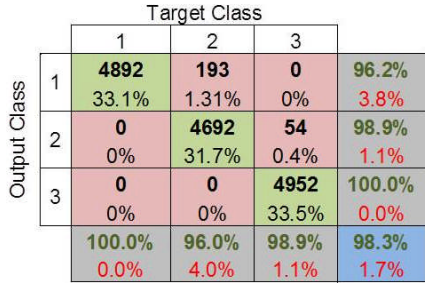

Output Class \ Target Class	1	2	3	
1	**4892** 33.1%	**193** 1.31%	**0** 0%	**96.2%** 3.8%
2	**0** 0%	**4692** 31.7%	**54** 0.4%	**98.9%** 1.1%
3	**0** 0%	**0** 0%	**4952** 33.5%	**100.0%** 0.0%
	100.0% 0.0%	**96.0%** 4.0%	**98.9%** 1.1%	**98.3%** 1.7%

(b) 2nd unseen data

CC.5 : HP Turbine Degradation Level Classifier at Altitude Level 2

Output Class \ Target Class	1	2	3	
1	**4740** 32.3%	**71** 0.48%	**0** 0%	**98.5%** 1.5%
2	**0** 0%	**4839** 33.0%	**93** 0.6%	**98.1%** 1.9%
3	**0** 0%	**3** 0%	**4914** 33.5%	**99.9%** 0.1%
	100.0% 0.0%	**98.5%** 1.5%	**98.1%** 1.9%	**98.9%** 1.1%

(a) 1st unseen data

Output Class \ Target Class	1	2	3	
1	**4716** 32.2%	**81** 0.55%	**0** 0%	**98.3%** 1.7%
2	**0** 0%	**4879** 33.3%	**94** 0.6%	**98.1%** 1.9%
3	**0** 0%	**1** 0%	**4888** 33.3%	**100.0%** 0.0%
	100.0% 0.0%	**98.3%** 1.7%	**98.1%** 1.9%	**98.8%** 1.2%

(b) 2nd unseen data

CC.6 : LP Turbine Degradation Level Classifier at Altitude Level 2

Output Class \ Target Class	1	2	3	
1	**4788** 32.3%	**81** 0.55%	**0** 0%	**98.3%** 1.7%
2	**44** 0%	**4928** 33.2%	**146** 1.0%	**96.3%** 3.7%
3	**0** 0%	**1** 0%	**4855** 32.7%	**100.0%** 0.0%
	99.1% 0.9%	**98.4%** 1.6%	**97.1%** 2.9%	**98.2%** 1.8%

(a) 1st unseen data

Output Class \ Target Class	1	2	3	
1	**4888** 32.9%	**102** 0.69%	**0** 0%	**98.0%** 2.0%
2	**36** 0%	**4864** 32.8%	**117** 0.8%	**97.0%** 3.0%
3	**0** 0%	**0** 0%	**4835** 32.6%	**100.0%** 0.0%
	99.3% 0.7%	**97.9%** 2.1%	**97.6%** 2.4%	**98.3%** 1.7%

(b) 2nd unseen data

CC.7 : Compressor Degradation Level Classifier at Altitude Level 3

Output Class \ Target Class	1	2	3	
1	**4958** 33.3%	**250** 1.68%	**0** 0%	**95.2%** 4.8%
2	**0** 0%	**4709** 31.7%	**128** 0.9%	**97.4%** 2.6%
3	**0** 0%	**0** 0%	**4822** 32.4%	**100.0%** 0.0%
	100.0% 0.0%	**95.0%** 5.0%	**97.4%** 2.6%	**97.5%** 2.5%

(a) 1st unseen data

Output Class \ Target Class	1	2	3	
1	**4895** 32.9%	**253** 1.70%	**0** 0%	**95.1%** 4.9%
2	**0** 0%	**4720** 31.7%	**146** 1.0%	**97.0%** 3.0%
3	**0** 0%	**0** 0%	**4853** 32.6%	**100.0%** 0.0%
	100.0% 0.0%	**94.9%** 5.1%	**97.1%** 2.9%	**97.3%** 2.7%

(b) 2nd unseen data

CC.8 : HP Turbine Degradation Level Classifier at Altitude Level 3

Output Class \ Target Class	1	2	3	
1	**4851** 32.6%	**63** 0.42%	**0** 0%	**98.7%** 1.3%
2	**0** 0%	**4962** 33.3%	**80** 0.5%	**98.4%** 1.6%
3	**0** 0%	**1** 0%	**4939** 33.2%	**100.0%** 0.0%
	100.0% 0.0%	**98.7%** 1.3%	**98.4%** 1.6%	**99.0%** 1.0%

(a) 1st unseen data

Output Class \ Target Class	1	2	3	
1	**4961** 33.3%	**51** 0.34%	**0** 0%	**99.0%** 1.0%
2	**0** 0%	**4911** 33.0%	**57** 0.4%	**98.9%** 1.1%
3	**0** 0%	**1** 0%	**4915** 33.0%	**100.0%** 0.0%
	100.0% 0.0%	**99.0%** 1.0%	**98.9%** 1.1%	**99.3%** 0.7%

(b) 2nd unseen data

CC.9 : LP Turbine Degradation Level Classifier at Altitude Level 3

Output Class \ Target Class	1	2	3	
1	4923 33.8%	106 0.73%	0 0%	97.9% 2.1%
2	0 0%	4708 32.4%	112 0.8%	97.7% 2.3%
3	0 0%	0 0%	4701 32.3%	100.0% 0.0%
	100.0% 0.0%	97.8% 2.2%	97.7% 2.3%	98.5% 1.5%

(a) 1st unseen data

Output Class \ Target Class	1	2	3	
1	4806 33.0%	104 0.71%	0 0%	97.9% 2.1%
2	0 0%	4681 32.2%	92 0.6%	98.1% 1.9%
3	0 0%	0 0%	4866 33.4%	100.0% 0.0%
	100.0% 0.0%	97.8% 2.2%	98.1% 1.9%	98.7% 1.3%

(b) 2nd unseen data

CC.10 : Confusion Matrices of Component Health Classifier at Altitude Level 1

Output Class \ Target Class	1	2	3	4	
1	2260 2.1%	82 0%	26 0%	96 0%	91.7% 8.3%
2	5 0%	39916 36.9%	0 0%	0 0%	99.99% 0.0%
3	8 0%	26 0%	26613 24.6%	1 0%	99.9% 0.1%
4	8 0%	0 0%	0 0%	39104 36.2%	99.98% 0.02%
	99.1% 0.9%	99.7% 0.3%	99.9% 0.1%	99.8% 0.2%	99.8% 0.2%

(a) 1st unseen data

Output Class \ Target Class	1	2	3	4	
1	2184 2.0%	86 0%	25 0%	98 0%	91.3% 8.7%
2	7 0%	39573 36.6%	0 0%	0 0%	99.98% 0.0%
3	7 0%	16 0%	26753 24.7%	1 0%	99.9% 0.1%
4	5 0%	0 0%	0 0%	39389 36.4%	99.99% 0.01%
	99.1% 0.9%	99.7% 0.3%	99.9% 0.1%	99.7% 0.3%	99.8% 0.2%

(b) 2nd unseen data

CC.11 : Confusion Matrices of Component Health Classifier at Altitude Level 2

Output Class \ Target Class	1	2	3	4	
1	4987 5.6%	0 0%	112 0%	36 0%	97.1% 2.9%
2	29 0%	27859 31.4%	0 0%	0 0%	99.9% 0.1%
3	87 0%	12 0%	27796 31.3%	1 0%	99.6% 0.4%
4	0 0%	0 0%	0 0%	27794 31.3%	100.0% 0.0%
	97.7% 2.3%	100.0% 0.0%	99.6% 0.4%	99.9% 0.1%	99.7% 0.3%

(a) 1st unseen data

Output Class \ Target Class	1	2	3	4	
1	4975 5.6%	1 0%	91 0%	30 0%	97.6% 2.4%
2	23 0%	27983 31.5%	0 0%	0 0%	99.9% 0.1%
3	92 0%	4 0%	27852 31.4%	0 0%	99.7% 0.3%
4	0 0%	0 0%	0 0%	27661 31.2%	100.0% 0.0%
	97.7% 2.3%	100.0% 0.0%	99.7% 0.3%	99.9% 0.1%	99.7% 0.3%

(b) 2nd unseen data

CC.12 : Confusion Matrices of Component Health Classifier at Altitude Level 3

Output Class \ Target Class	1	2	3	4	
1	5403 6.0%	0 0%	94 0%	30 0%	97.8% 2.2%
2	6 0%	27895 31.2%	0 0%	0 0%	100.0% 0.0%
3	154 0%	0 0%	28313 31.6%	2 0%	99.5% 0.5%
4	10 0%	0 0%	0 0%	27619 30.9%	100.0% 0.0%
	96.9% 3.1%	100.0% 0.0%	99.7% 0.3%	99.9% 0.1%	99.7% 0.3%

(a) 1st unseen data

Output Class \ Target Class	1	2	3	4	
1	5291 5.9%	0 0%	82 0%	26 0%	98.0% 2.0%
2	1 0%	27811 31.1%	0 0%	0 0%	100.0% 0.0%
3	152 0%	0 0%	28317 31.6%	0 0%	99.5% 0.5%
4	6 0%	0 0%	0 0%	27839 31.1%	100.0% 0.0%
	97.1% 2.9%	100.0% 0.0%	99.7% 0.3%	99.9% 0.1%	99.7% 0.3%

(b) 2nd unseen data

Appendix DD : Plots of CF from Different Implemented Neural Architectures for the Given Mission Profile

DD.1 : Predicted CF from Component Degradation FB Architectures and the Integrated Model

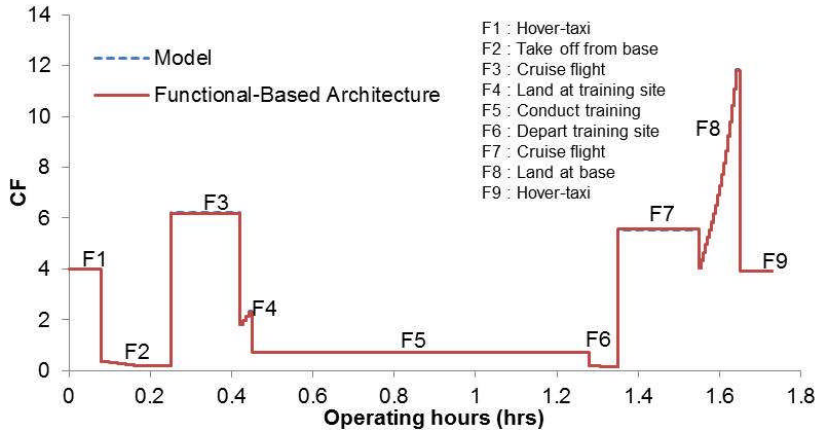

Figure DD.1-1: Compressor degradation mission profile plot

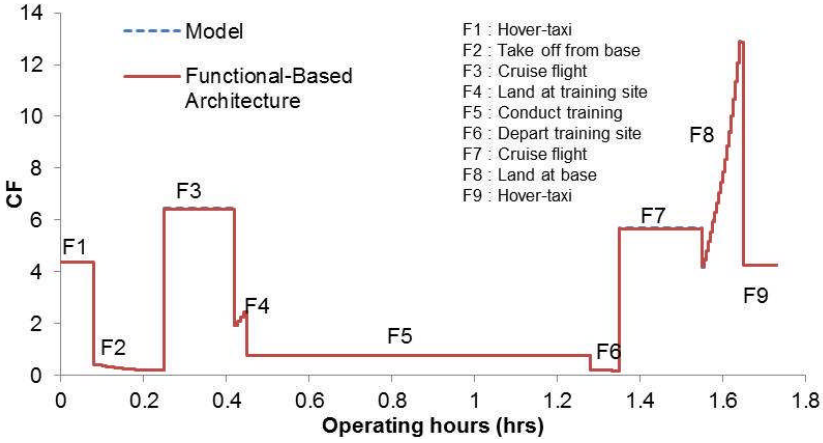

Figure DD.1-2: HP turbine degradation mission profile plot

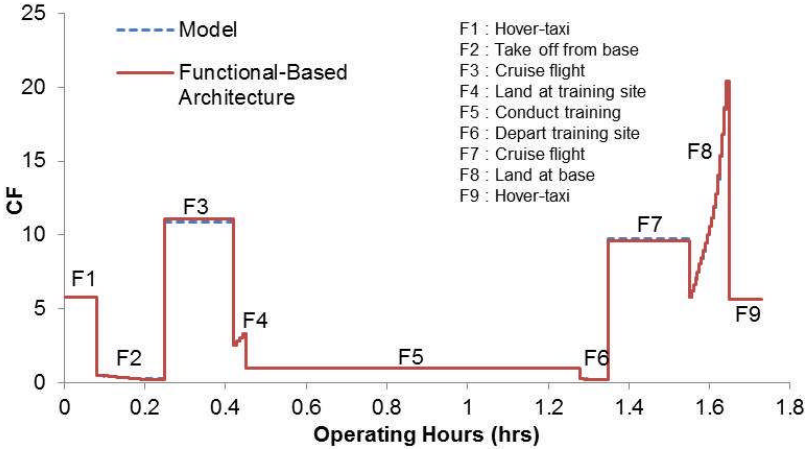

Figure DD.1-3: LP turbine degradation mission profile plot

DD.2 : Predicted CF from Component Degradation SB Architectures and the Integrated Model

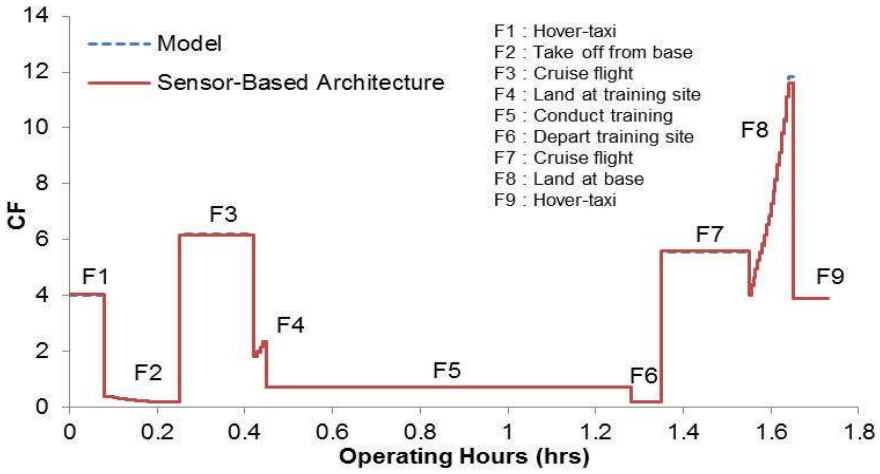

Figure DD.2-1: Compressor degradation mission profile plot

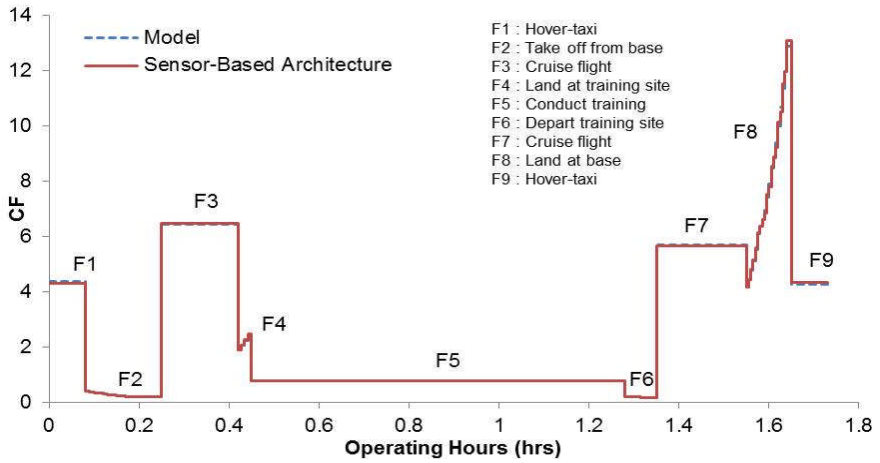

Figure DD.2-2: HP turbine degradation mission profile plot

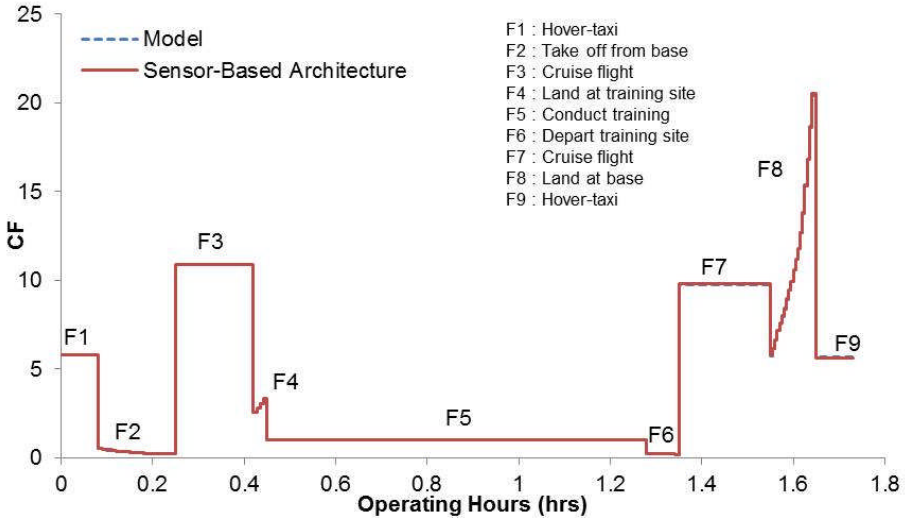

Figure DD.2-3: LP turbine degradation mission profile plot

Appendix EE : Comparison of the Calculated Probabilities between the FB and SB Architecture for Degraded Engine Condition.

EE.1 : Probability Comparison for Compressor Degradation

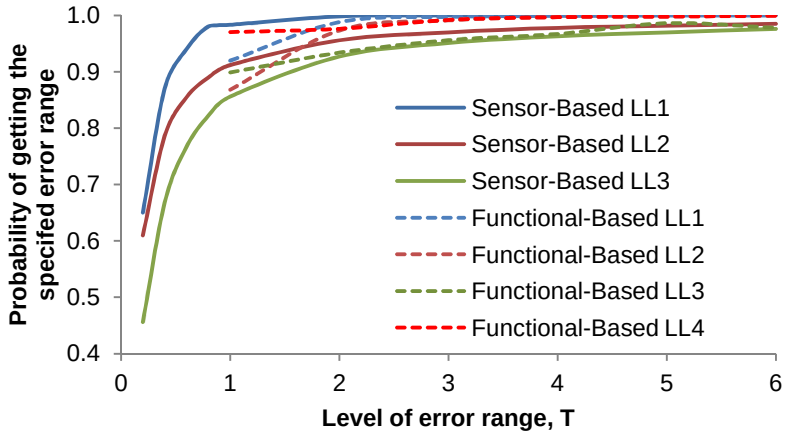

Figure EE.1-1: Probability of obtaining specified E range at low level degradation

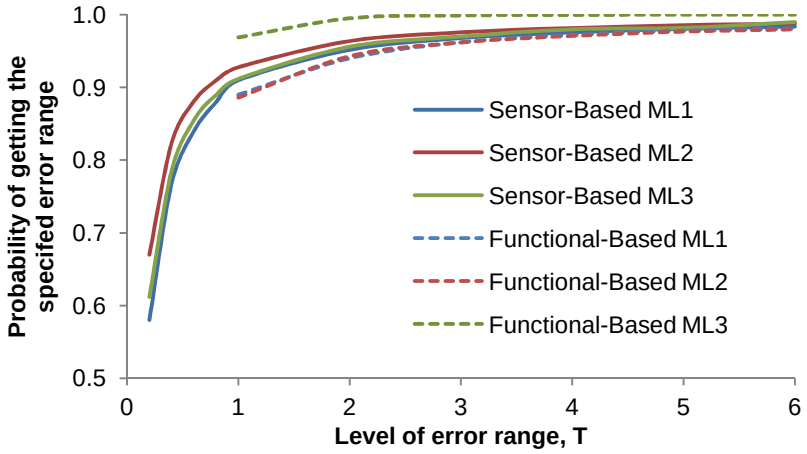

Figure EE.1-2: Probability of obtaining specified E range at medium level degradation

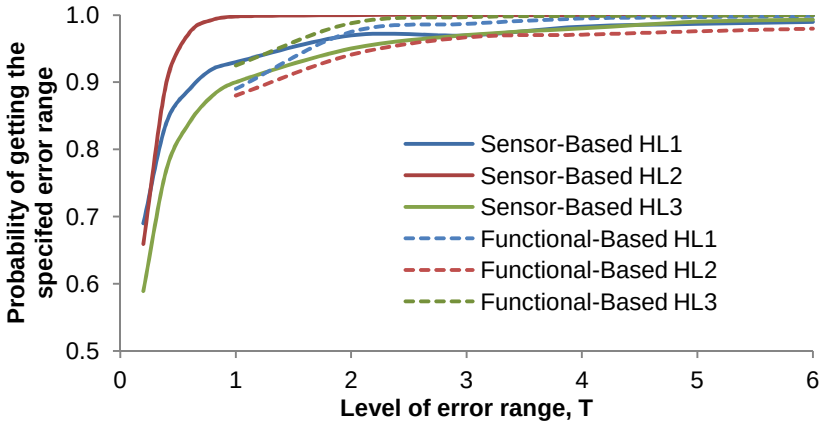

Figure EE.1-3: Probability of obtaining specified E range at high level degradation

EE.2 : Probability Comparison for HP Turbine Degradation

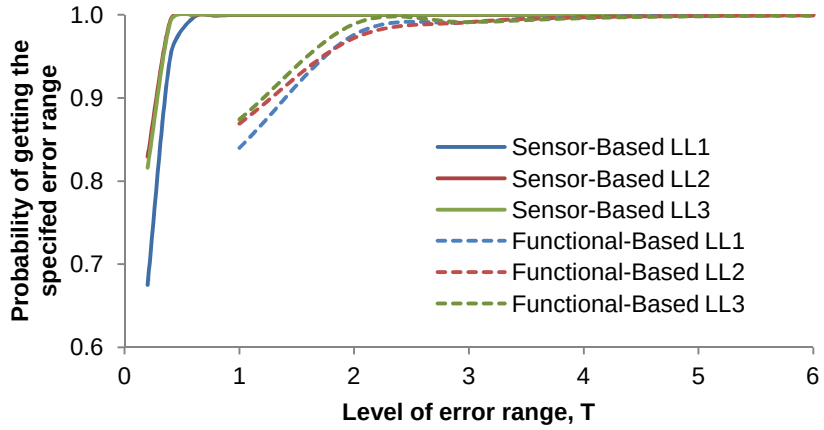

Figure EE.2-1: Probability of obtaining specified E range at low level degradation

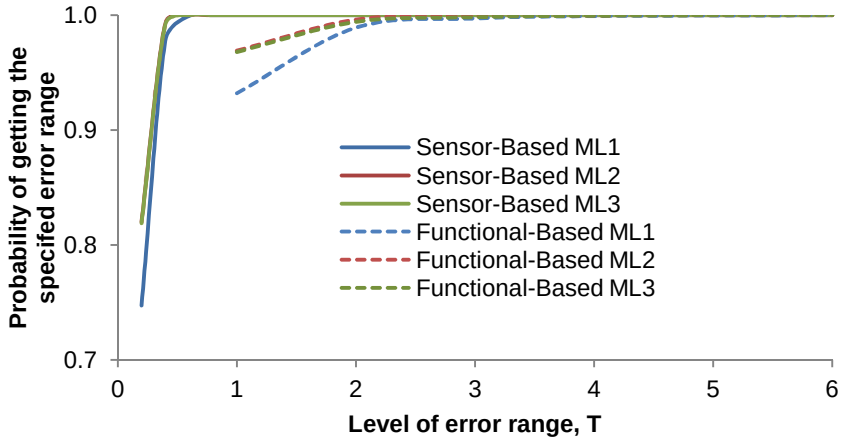

Figure EE.2-2: Probability of obtaining specified E range at medium level degradation

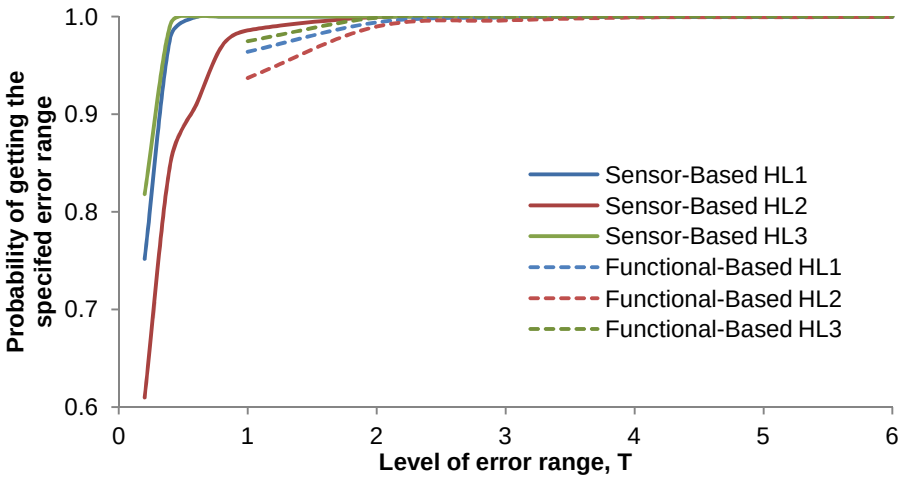

Figure EE.2-3: Probability of obtaining specified E range at high level degradation

EE.3 : Probability Comparison for LP Turbine Degradation

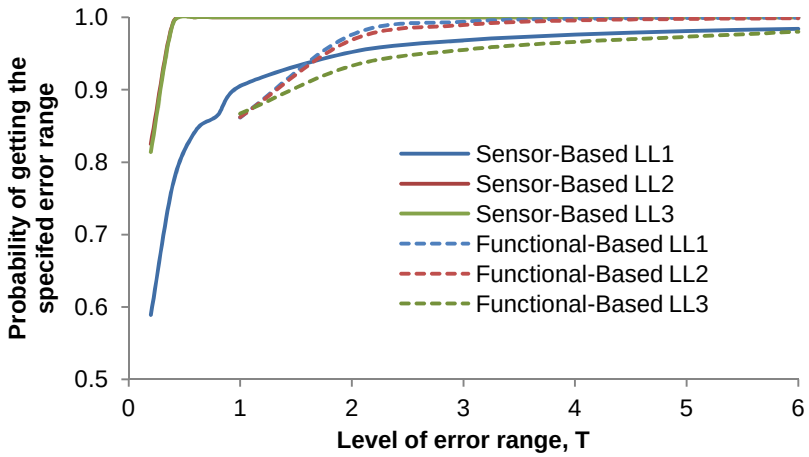

Figure EE.3-1: Probability of obtaining specified E range at low level degradation

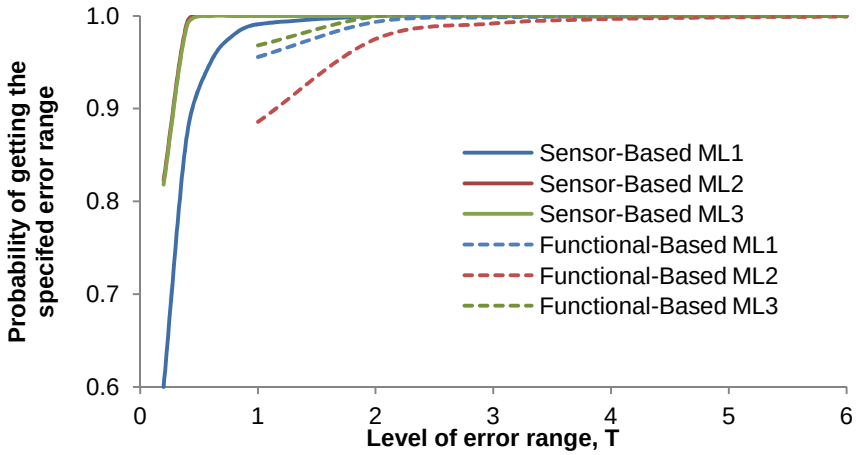

Figure EE.3-2: Probability of obtaining specified E range at medium level degradation

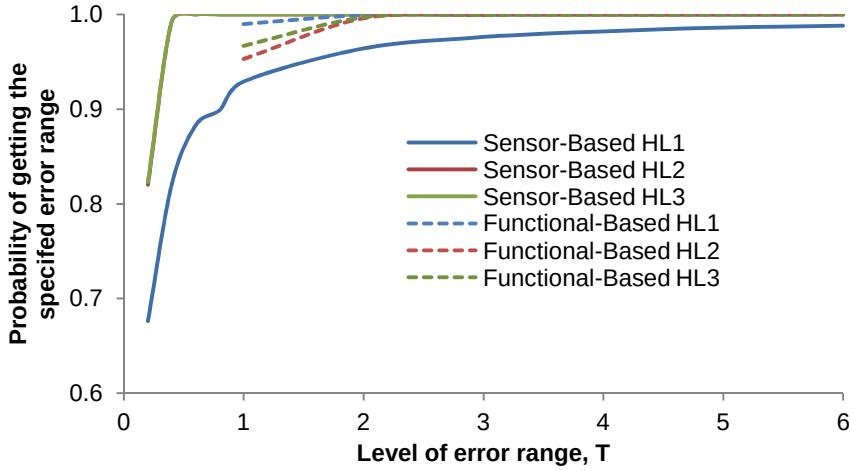

Figure EE.3-3: Probability of obtaining specified E range at high level degradation

Appendix FF : Prediction error PDF of the Generated Samples Obtained Using the Implement Neural Architectures.

FF.1 : Prediction Error PDF Obtained Using the RB Architecture

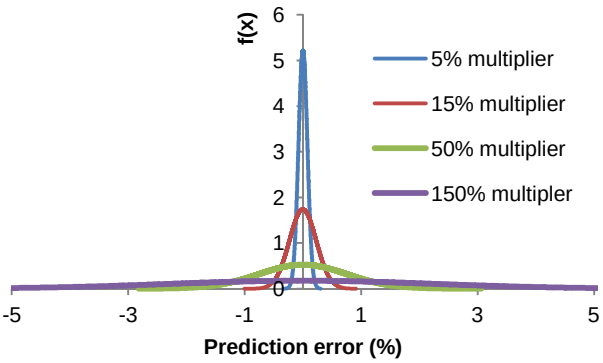

(a) Point 2 for several uncertainty multiplier

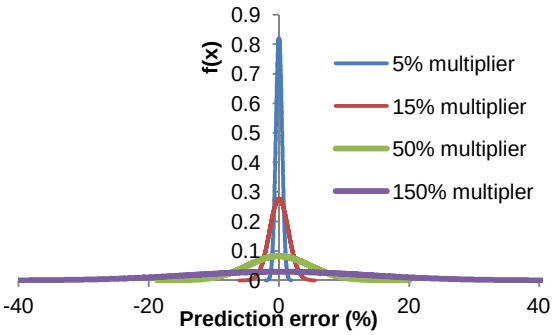

(b) Point 3 for several uncertainty multiplier

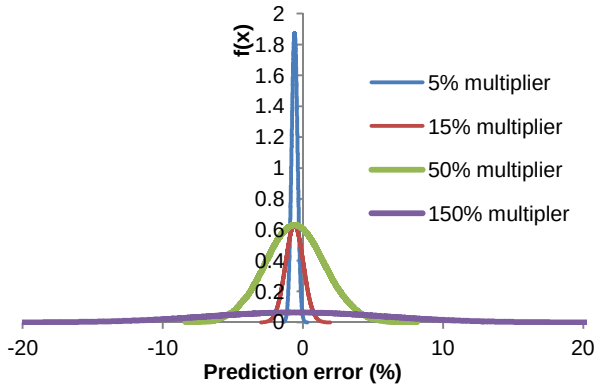

(c) Point 4 for several uncertainty multiplier

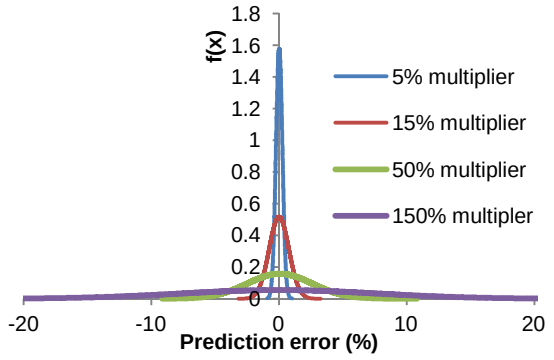

(d) Point 5 for several uncertainty multiplier

FF.2 : Prediction Error PDF Obtained Using the FB Architecture

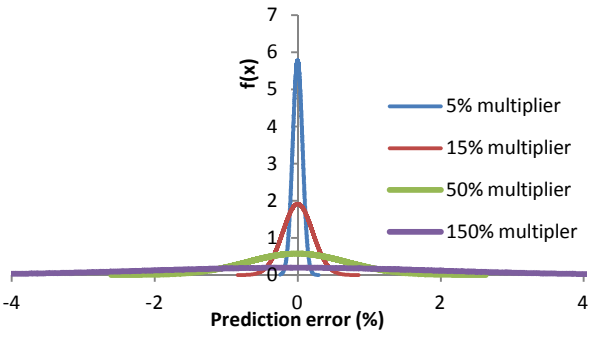

(a) Point 2 for several uncertainty multiplier

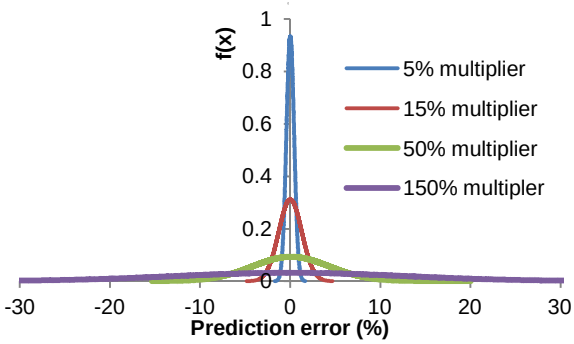

(b) Point 3 for several uncertainty multiplier

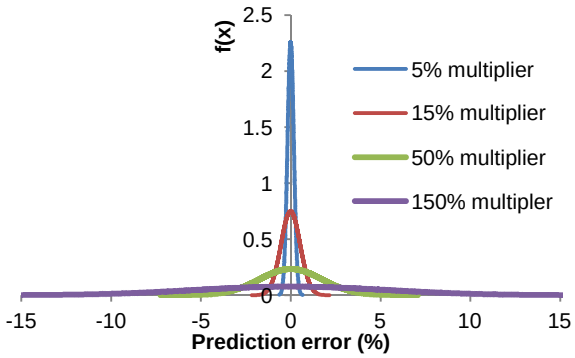

(c) Point 4 for several uncertainty multiplier

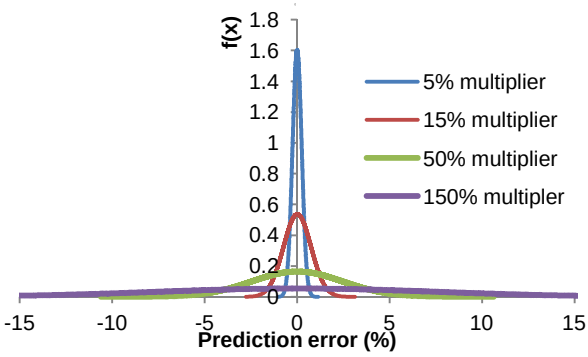

(d) Point 5 for several uncertainty multiplier

FF.3 : Prediction Error PDF Using the SB Architecture

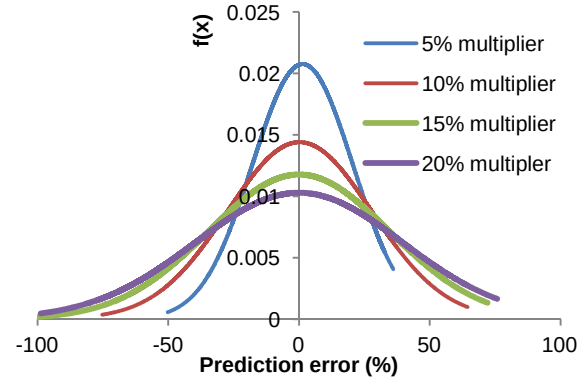

(a) Point 2 for several uncertainty multiplier

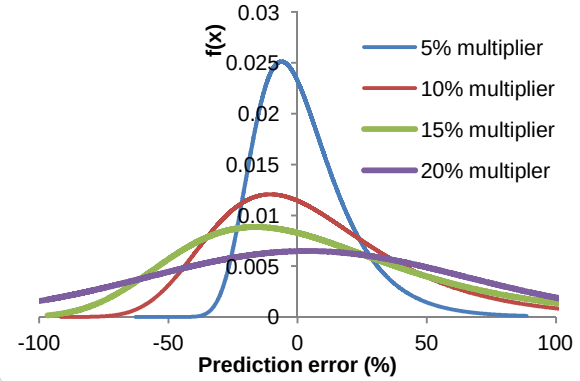

(b) Point 3 for several uncertainty multiplier

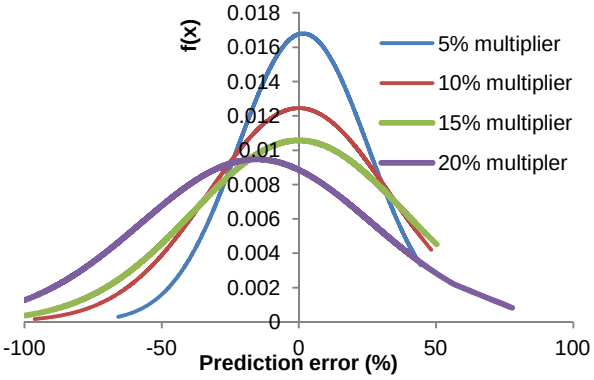

(c) Point 4 for several uncertainty multiplier

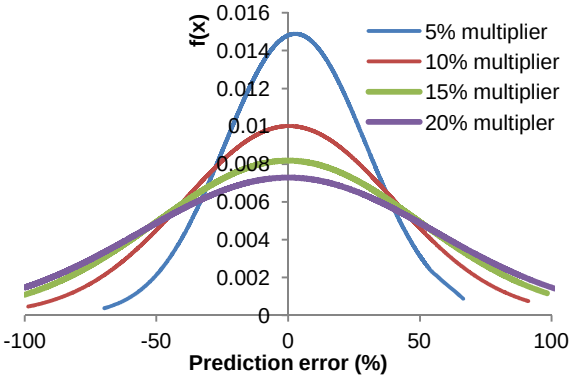

(d) Point 5 for several uncertainty multiplier

Appendix GG : Comparison of SD_E between the Blade's Metal Temperature and Stress of the FB and SB Approximators.

GG.1 : SD_E of the Blade's Metal Temperature and Stress of the FB Approximators

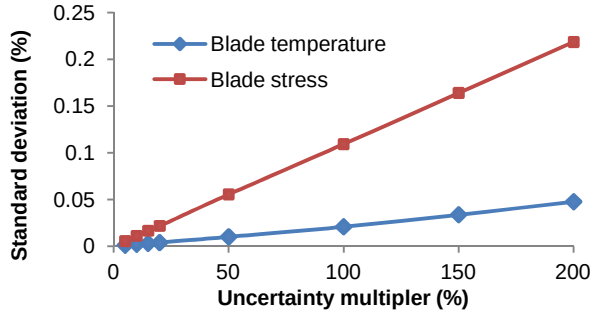

(a) $SD_E s$ at point 1

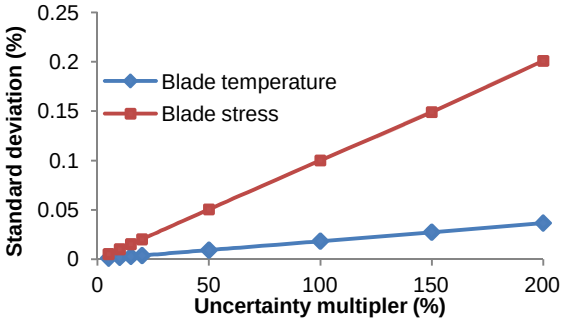

(b) $SD_E s$ at point 2

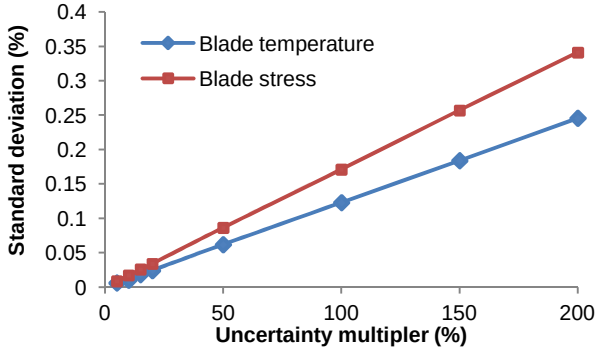

(c) $SD_E s$ at point 3

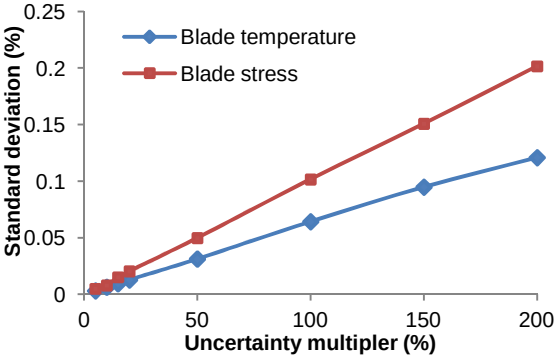

(d) $SD_E s$ at point 4

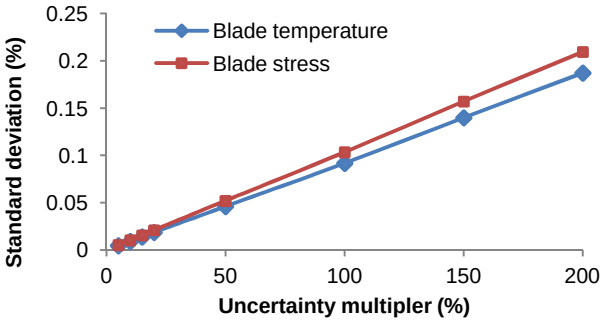

(e) $SD_E s$ at point 5

GG.2 : SD_E of the Blade's Metal Temperature and Stress of the SB Approximators

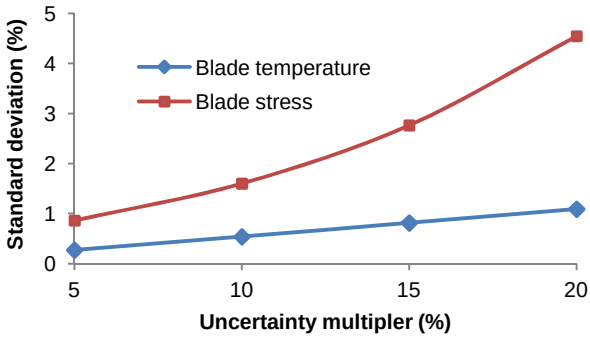

(a) $SD_E s$ at point 1

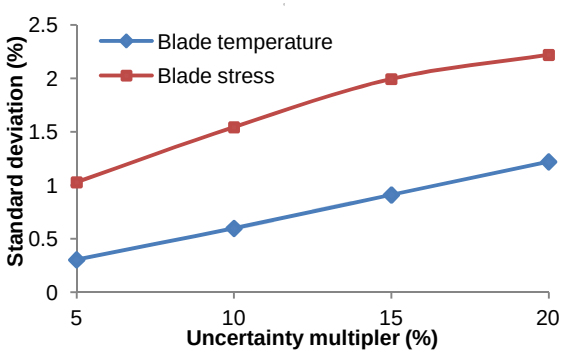

(b) $SD_E s$ at point 2

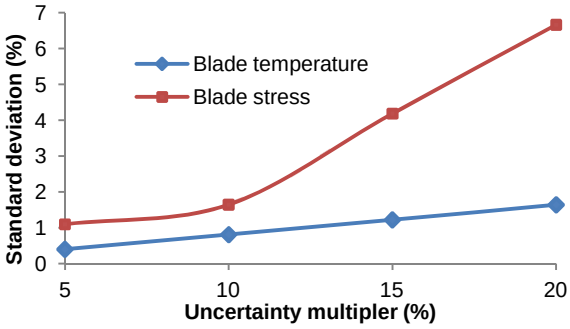

(c) $SD_E s$ at point 3

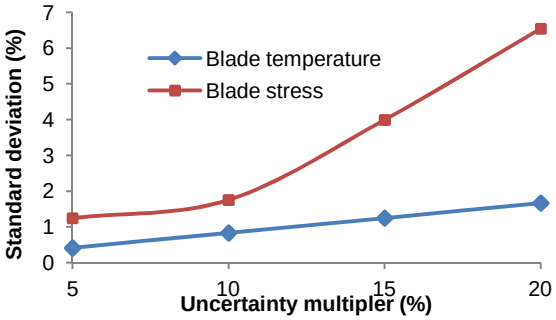

(d) $SD_E s$ at point 4

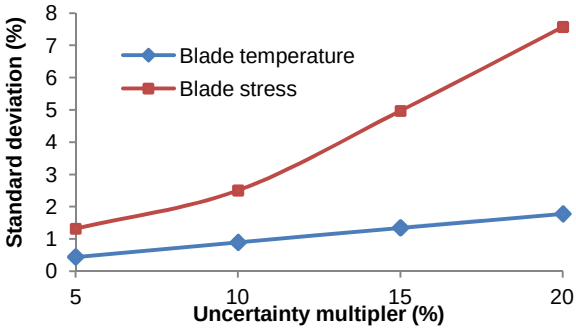

(e) $SD_E s$ at point 5

Appendix HH : Comparison of the Sample Distribution Analysis Results between the Three Implemented Architectures.

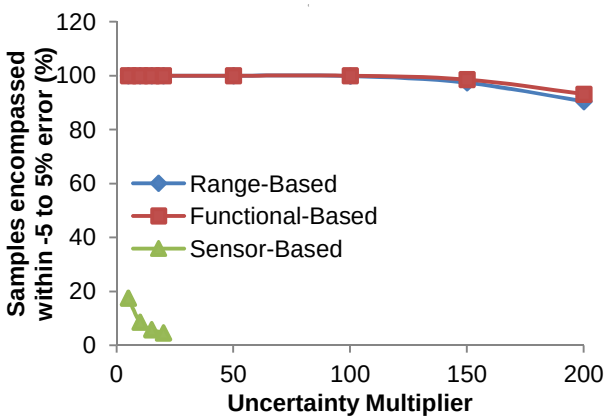

(a) Sample distribution analysis at point 2

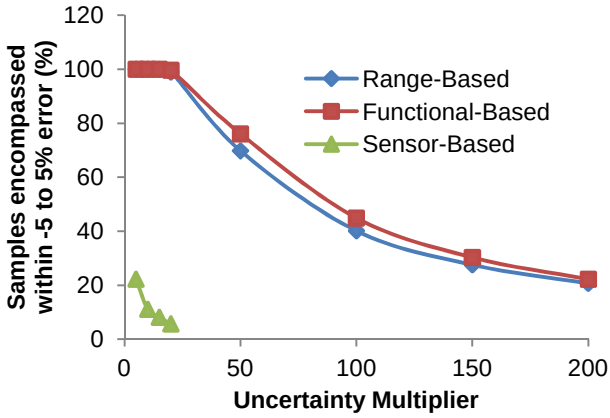

(b) Sample distribution analysis at point 3

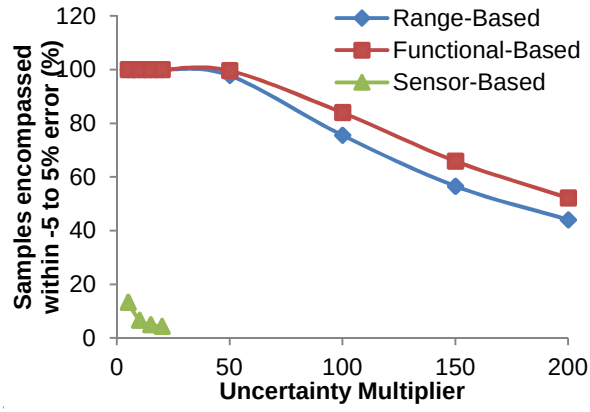

(c) Sample distribution analysis at point 4

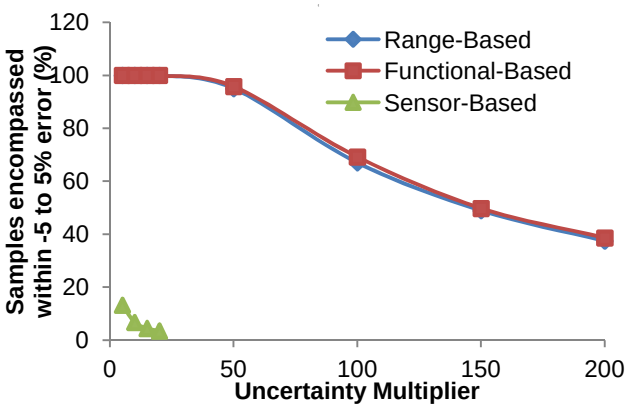

(d) Sample distribution analysis at point 5